

INAUGURAL-DISSERTATION

zur

Erlangung der Doktorwürde

der

Naturwissenschaftlich-Mathematischen Gesamtfakultät

der

RUPRECHT-KARLS-UNIVERSITÄT

HEIDELBERG

vorgelegt von

Dipl.-Ing. Kai Henning Koch

aus Berlin Tempelhof

Tag der mündlichen Prüfung

....., 2015

Using Model-based Optimal Control for Conceptual
Motion Generation for the Humannoid Robot HRP-2 14
and Design Investigations for Exo-Skeletons

Gutachter

PROFESSOR DR. KATJA MOMBAUR

Zusammenfassung

Das zweibeinige Laufen ist ein Forschungsfeld, welches bereits seit einigen Jahrzehnten sehr aktiv ist. Zum einen besitzt die Fortbewegung auf Beinen das Potential robuste und flexible Fortbewegung für technische Anwendungen zu verwirklichen. Zum anderen kann ein umfassendes Verständnis der Fortbewegung auf Beinen Ärzten und Ingenieuren dabei helfen, effektiv Patienten zu unterstützen, welche ihre Fortbewegungsfähigkeiten z.B. durch einen Unfall teilweise oder ganz verloren haben.

Mit dem Fortschritt der Technologie sind unzählige Roboter, darunter auch viele Humanoide, entstanden. Hierbei wird die Fortbewegung auf Beinen durch das Prinzip von Abstraktion und Abbilden auf ein technisches Erzeugnis erforscht. Des Weiteren wurden Geräte mit direkter Interaktion mit dem Menschen entwickelt, unter anderem passive und aktive Orthesen und Exo-Skelette. In der Entwicklung der Exo-Skelette für medizinische Zwecke wurden in der letzten Zeit erfolgreiche Versuche mit gesunden und bewegungseingeschränkten Patienten aus verschiedenen Laboren aus der gesamten Welt gemeldet. Während hierbei eine Entlastung des medizinischen Personals (z.B. während der Gangtherapie) deutlich erkennbar war, war die Benutzung für den Patienten häufig mit großen Anstrengungen und schneller Ermüdung verbunden. Grundsätzlich wird davon ausgegangen, dass der immer noch große Unterschied zwischen der maschinellen und der menschlichen Leistungsfähigkeit in Bezug auf Robustheit, Fortbewegungsgeschwindigkeit und allgemeine Bewegungsform nicht nur von den dynamisch begrenzten Eigenschaften der eingesetzten Technologie abhängt, sondern auch durch die eingesetzten Methoden zur Bewegungsgenerierung beschränkt wird.

In der humanoiden Robotik teilt sich die Bewegungsgenerierung in heuristische und optimierungsbasierte Methoden auf. Diese Methoden unterscheiden sich vor allem durch die Komplexität des zu lösenden Problems (Rechenaufwand) und dem resultierenden dynamischen Fehler. Die Ausführung der Bewegung wird dann durch ein in Echtzeit stabilisierendes Regelungssystem begleitet, welches den dynamischen Fehler identifiziert und herausregelt. Diese Arbeit beinhaltet einen **wissenschaftlichen Beitrag** zur generellen Berechnung des Modells basierend auf inverser Dynamik, sowie zur Formulierung von Optimalsteuerungsproblemen, für die dynamisch stabile Bewegungsgenerierung. Es wurde ein neuer Inversdynamikalgorithmus für nicht genügend beschränkte, unter-aktuierte Systeme zum Einsatz in der direkten Multiple-Shooting-Methode (Bock et. al.) entwickelt, ausgiebig getestet und mit dem vorwärtsdynamischen Ansatz basierend auf verschiedenen Modellen verglichen.

Ausgehend von diesem **wissenschaftlichen Beitrag** wurden zunächst verschiedene Optimalsteuerungsprobleme formuliert, um den Einfluss verschiedener biologischer Optimalitätskriterien auf die finale Laufbewegung abbilden und einordnen zu können. Des Weiteren wurde das vollständige Modell des Humanoiden Roboters HRP-2 N° 14 um den Kollisionsabsorber im Fersengelenkkomplex erweitert. Mit diesem Modell war die Berechnung zum dynamischen Übersteigen eines Hindernisses mit nur zwei Schritten zwischen zwei statischen Posen des Roboters möglich. In der Simulation und in realen Experimenten konnte ein geringer Korrekturaufwand des stabilisierenden Regelungssystems gemessen werden. Somit war es möglich mit der dynamisch stabilen Übersteigung eines Hindernisses von 20cm x 11cm (Höhe x Breite) einen neuen Rekord für diese Plattform mit einem optimierungsbasierten Ansatz aufzustellen.

Des Weiteren wird in dieser Arbeit eine auf Optimalsteuerung basierte, iterative und umfassende Designmethode für die Konzeption eines Exo-Skeletts für die unteren Gliedmaßen vorgestellt, welche die mechatronische Form des Systems beachtet. In diesem **wissenschaftlichen Beitrag** wird das Gesamtsystem, bestehend aus Mensch und Exo-Skelett modelliert und optimiert. Von einer Anfangsschätzung folgt eine iterative Konkretisierung der Systemparameter, jedoch immer auf Basis des Gesamtsystems, unter Erfassung aller Wechselwirkungen zwischen den einzelnen Systemkomponenten. Der Ansatz beruht auf Optimierungsstudien, mit welchen, ausgehend von der Laufbewegung eines gesunden Menschen (ebenerdig, sowie auf verschiedenen Steigungen), die notwendigen Eigenschaften des Mensch-Exo-Skelett Systems ermittelt werden. Auf Basis dieser Ergebnisse werden erste Ansätze zur Realisierung einzelner Systemkomponenten formuliert und diskutiert.

Abstract

The research field of bipedal locomotion has been active since a few decades now. At one hand, the legged locomotion principle comprises highly flexible and robust mobility for technical applications. At the other hand, a thorough technical understanding of bipedalism supports efforts of clinicians and engineers to help people, suffering from reduced locomotion capabilities caused by fatal incidents.

Since the technology enabled the construction of numerous robotic devices, among them: various humanoids, researchers started to investigate bipedalism by abstraction and adoption for technical applications. Findings from humanoid robotics are further exploited for the construction of devices for human performance augmentation and mobility support or gait rehabilitation, among them: orthosis and exo-skeletons.

Although this research continuously progresses, the motion capacities of humanoid robots still lack far behind those of humans in terms of forward velocity, robustness and appearance of the overall motion. Generally, it is claimed that the difference of performance between humans and robotics is not only due to the limiting characteristics of the employed technology, e.g. constructive lack of specific determinants of gait for bipedalism or dynamic limits of the actuation system, but as well to the adopted methods for motion generation and control.

For humanoid robotics, methods for motion generation are classified into optimization-based methods and those that employ heuristics, that are mostly distinguished based on the problem complexity (computation time) and the resulting dynamic error between the generated motion and the dynamics of the real robot. The implementation of the dynamic motion on the robotic platform is usually comprised with an on-line stabilizing control system. This control system must then identify and resolve instantaneously the dynamic error to maintain a continuously stable operation of the device. A large dynamic error and breach of the dynamic limits of the actuation system can quickly lead to a fatal destabilization of the device.

This work proposes a **contribution** to the model computation and the strategy of the problem formulation of direct multiple-shooting based optimal control (Bock et. al.) for dynamically stable optimization-based motion generation. The computation of the whole-body dynamic model inside the optimization relies either on forward or inverse dynamics approach. As the inverse dynamics approach has frequently been perceived as less resource intensive than the forward dynamics approach, a new generic algorithm for insufficiently constrained, under-actuated dynamic systems has been developed and thoroughly tested to comply with all numerical restrictions of the enveloping optimization algorithm.

Based on this **contribution**, various optimal control problems for the humanoid platform HRP-2 N° 14 have been formulated to assess the influence of different biologically inspired optimization criteria on the final motion characteristics of walking motions. From thorough bibliographic researches a dynamically more accurate model was comprised, by taking into account the impact absorbing element in the ankle joint complex. Based on the experiences of the previous study, a problem formulation for the limiting case of, dynamically overstepping an obstacle of 20cm x 11cm (height x width) with only two steps, while maintaining its stable operation was accomplished. This is a new record for this platform.

In a further part, this work proposes an iterative comprehensive model-based optimal control approach for the conception of a lower limb exo-skeleton that respects the integrated nature of such a mechatronic device. In this **contribution**, a human effectively wearing such a lower limb exo-skeleton is modeled. The approach then substantiates all system components in an iterative procedure, based on the complete system model, effectively resolving all complex inter-dependencies between the different components of the system. The study in this work is conducted on an important benchmark motion, walking, of a healthy human being. From this study the limiting characteristics of the system are determined and substantial propositions to the realization of various system components are formulated.

Acknowledgments

The following work, about optimal control based motion generation for the Humanoid HRP-2 N° 14, has been conducted in cooperation between the group *ORB¹-IWR, Heidelberg University, Germany* and group *Gepetto, LAAS-CNRS, Toulouse, France*. The author would like to express his grateful acknowledgments to its supervisors Prof. Katja Mombaur (Head of the Group ORB-IWR, Heidelberg University, Germany) and Dr. Philippe Souères (Head of the Group Gepetto, LAAS-CNRS, Toulouse, France) as well as to his second supervisors Dr. Jean-Paul Laumond from *LAAS-CNRS, Toulouse, Collège de France, Paris, France* and Dr. Johannes Schlöder from *IWR, Heidelberg University* for their guidance, support and fruitful discussions during this research project.

The conception and implementation of the new inverse dynamics algorithm was conducted together with Dr. Christian Kirches & Manuel Kudruss from *OUS²-IWR, Heidelberg University, Germany*. The author would like express his grateful acknowledgment for the help and various fruitful discussions that made this algorithm a success and a highly valuable contribution to the various optimization studies conducted in the following work.

The author would like to thank the permanent members of the team *Gepetto, LAAS-CNRS, Toulouse, France*: Dr. Olivier Stasse, Dr. Nicolas Mansard and Dr. Florent Lamiroux for their continuous guidance and support towards and during the experiments on HRP-2 N° 14. Furthermore, the preparation and execution of simulations and real experiments would not have been possible without the help of: Dr. Thomas Moulard from *Google Robotics, Japan*, Dr. Antonio El Khoury from *Dassault Systèmes, France*, Maxime Reis, Maxime Naveau, Justin Carpentier and Dr. Mehdi Benallegue from *Gepetto, LAAS-CNRS, Toulouse, France*.

The initial idea of the improvement of the dynamic accuracy of the model of HRP-2 N° 14 and essential directions to the deeper understanding of the online stabilizing control system to successfully accomplish the subsequent optimization studies on HRP-2 N° 14 spun off from fruitful discussion with 秀司梶田先生 (Dr. Shuuji Kajita) from *AIST³ Tokyo, Japan* and 光一西脇先生 (Dr. Koichi Nishiwaki) from *Google Robotics, Japan*, during ICRA 2013 in Karlsruhe, Germany, IROS 2013 in Tokyo, Japan and HLR-2014 in Heidelberg, Germany, as well as subsequent communications. The author would like to express his grateful acknowledgment to both researches for their time to discuss these scientific aspects in detail.

Furthermore, a subsequent part of this work, on conceptional design studies, has been conducted in the bridge: Medical Technology for Health (MTH), of the research partnership HEiKA between the Heidelberg University and the Karlsruhe Institute of Technology (KIT). This cooperation was established between the Group *ORB-IWR, Heidelberg University, Germany* and the *Humanoids and Intelligence Systems Lab - Institute for Anthropomatics - KIT, Germany*. Support of Prof. Tamim Asfour during this research period is acknowledged.

Investigations on the conceptional design studies for exo-skeletons would not have been possible without the comprehensive data records of walking motion, recorded under clinical conditions at the Heidelberg MotionLab. The author would like to thank Dr. Sebastian Wolf

¹Optimization in Robotics & Biomechanics - IWR, Heidelberg University

²Junior Research Group - Optimization of Uncertain Systems - IWR, Heidelberg University

³The National Institute of Advanced Industrial Science and Technology, Japan

as well as Daniel Heitzmann, Julia Block, Khai-Long Ho Hoang and the rest of the team of *Heidelberg Motionlab*⁴, *Germany* for the opportunity to conduct these measurements and the support during the study.

All optimization-based studies have been built on top of the optimal control framework MUSCOD-II. The author would like to thank the SimOpt team of Prof. Hans Georg Bock from *IWR - University of Heidelberg, Germany* for providing the optimal control code MUSCOD-II.

The author would like to his gratefully acknowledge the received financial support for this work from the following resources:

- DFG Graduate School 220 (Heidelberg Graduate School of Mathematical and Computational Methods for the Science) – German Excellence Initiative of the University of Heidelberg
- HEiKA - Heidelberg Karlsruhe Research Partnership, Heidelberg University, Karlsruhe Institut of Technology (KIT)
- European FP7 project ECHORD (GOP)
- European Project KORoIBOT (GA No. 600911)

The work on this manuscript involved several iterations and reviews. The author would like to thank his colleagues: Dr. Manish Sreenivasa, Dr. Debora Clever, Alexander Schubert, Martin Felis, Khai-Long Ho Hoang and Sascha Debasteh from *ORB-IWR, University of Heidelberg, Germany* as well as Dr. Christian Kirches & Manuel Kudruss from *OUS-IWR, Heidelberg University, Germany* for the time they spent to read the manuscript and numerous fruitful discussions that lead to the final form of this document.

Finally, the author would like to thank Dr. Hubert Koch, Karin Patermann-Koch and 美奈子高木様 (Minako Takagi) as well as Klaus Rombach, Manuel Engler, Gloria Steger, Livia Steger, Natasha Shilla Sharma, Sara Lee, Juiletta Yuan Mertens and Sun Hwa Lee for their patience and psychological support during the time of this work and especially for the period of writing the manuscript.

The publication of image material for public use by [Capraro, 2014, Dang, 2013, Häggström, 2008] that has been adopted for the presentation of this work, his gratefully acknowledged.

⁴Heidelberg University Clinics, Department Orthopedic Surgery

Contents

1	Introduction & Related Work	1
1	Anthropomorphic Walking Characteristics	1
2	Humanoid Robots	3
3	Motion Generation Methods	6
4	Exo-Skeletons	11
5	Contribution & Organization	13
 Modeling & Optimal Control of Anthropomorphic Walking Systems		17
2	Mechanical Modeling	19
1	Classical Representation	19
2	Kinematics	20
3	Multiple Rigid Bodies and Hybrid Dynamics	26
4	Concluding Remarks	33
3	<i>DYNAMOD</i> - Efficient Mechanical Modeling	34
1	Development	34
2	Structure and Configuration	35
3	Concluding Remarks	41
4	Direct Approach for Optimal Control	42
1	Transcription of the Continuous Problem	43
2	Theory of Constrained Nonlinear Optimization	46
3	Sequential Quadratic Programming	50
5	Computation of Model Dynamics	54
1	Expression in the Optimization Context	55
2	Algorithms for Rank Deficient Inverse Dynamics Optimization	59
3	Numerical Results for an Inverted Pendulum on a Cart	66
 Optimal Control for HRP-2 Motions		77
6	Modeling of the Humanoid Robot HRP-2	80
1	The Humanoid Robot HRP-2 N° 14	80
2	Modeling of the HRP-2 N° 14 Robot	86
7	Inelastic Model Approach	93
1	A Walking Study	93
2	Optimization Results	99
3	Conclusion	106

- 8 Towards Real Motion Implementation 112**
 - 1 Motion Generation for Obstacle Overstepping 113
 - 2 Problem Formulation for Obstacle Overstepping 113
 - 3 Optimization Results of the Overstepping Motion 117
- 9 A More Realistic Modeling Approach 124**
 - 1 Difference Between Reality and Modeling 124
 - 2 Comparison: FdOP & IdOP for HRP-2 N° 14 129
 - 3 Results 136
- 10 Implementation on the Real HRP-2 N° 14 142**
 - 1 General Idea & Realization 142
 - 2 Results 145

Optimal Control for Exo-Skeletons

153

- 11 Integrated Modeling Approach for Exo-Skeletons 156**
 - 1 Examples of Different Exo-Skeleton Conception Approaches 157
 - 2 Optimization Based - Comprehensive Approach 163
- 12 Exoskeleton Modeling for Optimization 165**
 - 1 Modeling of a Human Inside an Exo-Skeleton 165
 - 2 Estimation of Structural Load 177
 - 3 Concluding Remarks 179
 - 4 Equations of Motion 182
- 13 Problem Formulation - Walking Studies 185**
 - 1 Scope of this Simulation 185
 - 2 Tool-Chain 190
 - 3 Verification & Tuning of Problem Formulation 191
- 14 Walking Studies 193**
 - 1 The Level-Ground Case 193
 - 2 Concluding Remarks 207
- 15 Conclusions 212**
 - 1 OCP Formulations and Dynamic Modeling 212
 - 2 Modeling and Optimal Control for HRP-2 N° 14 212
 - 3 Conceptual Work for Exos 213

Appendices 217

- A Computation of Dynamic Characteristics 218**
 - 1 Preliminaries 218
 - 2 Constructive Solid Geometry 222
 - 3 Polygonal Representation 225
 - 4 Concluding Remarks 228
- B Modeling of Technical Components 230**
 - 1 Actuation Systems 230
 - 2 Modeling Friction 236

3	Modeling of Surface Contacts	236
C	Human Body Data	239
1	Kinematic Data	239
2	Dynamic Data	241
3	Data-Set from McConville et. al. and Young et. al.	241
4	Data-Set from Zatsiorsky et. al.	242
5	Concluding Remarks	243
D	Conception of Bearings	244
1	Bearing Classes	244
2	Conception of Ball Bearings	245
E	Meta Motion Capture Data	247
F	Model Description of DYNAMOD	250
1	Kinematics	250
2	Dynamics	251
3	Tags & Contacts	252
G	FdOP and IdOP based OCP-Formulations	253
1	Formulations of the Dynamic System	253
	Bibliography	257

1 Introduction & Related Work

Mobility in unstructured terrain is a crucial aspect of all kinds of transport problems. Let us consider the following scenarios:

- We are standing in front of a disaster site where human help and some equipment are urgently requested. As a healthy human-being, one could just walk inside carrying the necessary equipment, but only up to a certain maximum weight and after taking precautions with regard to hazardous environmental conditions.
- In another scenario, some experimental equipment is sitting on a remote planet with a highly cluttered surface and is to be moved to some place else.
- Finally, in a rather domestic scenario, a partially paralyzed person suffering from the long time effects of a stroke is sitting in a wheel chair. This person would urgently need to move up a staircase.

Is there a flexible and energy efficient solution to these transport problems? - Engineers are usually employing purely technical solution to deal with these kind of problems (e.g. big wheels, 4WD and 6WD or catapillar for unstructured terrain) in a comprehensive work [Nachtigall, 2002] formulated the suggestion to consider the natural evolution as a portfolio of optimized solutions for a large variety of problems - such as mobility in unstructured terrain. The exploitation of these solutions should not be based on a pure copy, but an intelligent abstraction of the principle and subsequent transfer into a technical application [Nachtigall, 2002].

For the above mentioned scenario, the legged locomotion principle¹ is a suitable abstraction from natural locomotion principles, that would clearly out-perform a purely technical solution – wheels. This directly follows from the underlying technical principle [Albers et al., 2009] of functional surfaces that are in contact. The wheel needs a continuous, planar surface it can roll on, the leg only needs small, disjoint contact surface patches, frequently present in a cluttered environment.

Furthermore, flexibility and adaption are two important aspects that would clearly give priority to bipedal locomotion techniques. First, the fewer contact surface patches necessary and therefore smaller body size to support the selected locomotion principle, the more flexible it is. Second, most of the environment in which a robot should cooperate with a human are specifically designed for humans. Thus, the decision to technically employ the bipedal locomotion principle is reasonable.

1 Anthropomorphic Walking Characteristics

As previously outlined, a pure copy of the nature for technical application is pointless [Nachtigall, 2002]. For a successful implementation of a technical solution, abstraction starts with a

¹This is a choice that has been explicitly done by the author before-hand, being well aware that other promising biological inspired approaches for terrestrial locomotion exist, e.g. snake locomotion - refer to [Gray, 1946, Transeth et al., 2009] for the first publication into this direction, known to the author, and a comprehensive overview of the recent state of art, respectively.

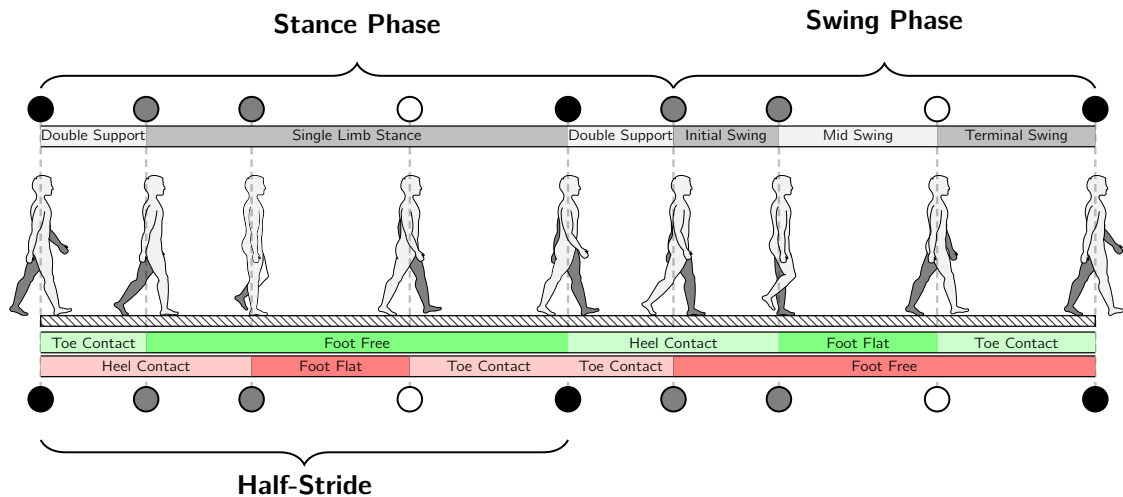


Figure 1.1: Typical phase sequence during an anthropomorphic walking motion as it is shown in [Perry and Burnfield, 2010]. The contact states of the left and right foot are marked with green and red stripes, respectively. Contact-state transition between the phases of the gait sequence are marked with circles. Black circles mark transitions with discontinuities in the motion trajectories, grey and white transitions are continues.

study of the natural example at hand to understand and extract its functional principles. A typical bipedal human motion cycle of walking is given in Figure 1.1 [Perry and Burnfield, 2010]. The motion cycle consists of alternating stance and swing phase for both legs with a contralateral phase shift of a half-stride. A foot enters into ground-contact upon heel strike soon followed by the toe-strike. During the double support phase the support of the body is accepted from the contralateral leg. The body travels over the support leg during the single limb stance. The heel lifts off before the contralateral heel-strike. During the next double support phase the body support is shifted over to the contralateral leg and the toes lift off ground. The knee goes flexes keeping the foot off ground while it travels in front of the body. The knee is then again extended and it comes to a heel-strike. This type of locomotion called walking is clearly distinguished, by forward velocity and motion sequence, from running gaits in the sense that it is slower and does not contain flight-phases (non-contact phases). In the following, only walking locomotion will be of interest.

1.1 Gait Characteristics

In early works of gait analysis on humans [Saunders et al., 1953], bipedal locomotion is described as the translation of the Center of Mass/Gravity (CoM) based on a complex sequence of motion trajectories in three anatomic planes² following least energetic effort. Similar results are found in [Beckett and Chang, 1968, Chou et al., 1995]. Based on the individual geometry the motion is described similar to a pendulum with a specific timing. Furthermore, results reveal that the hip torque seems to have a high contribution to the locomotion, while the knee torque seems to accomplish only motion control purposes. As unifying principle to assess this complex motion, [McMahon, 1984, Saunders et al., 1953] formulated six aspects, called Determinante of Gait (DoG), being:

²coronal (frontal) plane, sagittal plane, transverse plane

- | | |
|--|--|
| 1. compass gait (vertical arc motion of hip) | 4. lateral translation of the pelvis, |
| 2. pelvis transverse rotation, | 5. knee flexion (stance leg) |
| 3. pelvic tilt, | 6. plantar flexion of ankle (stance leg) |

While the loss of one determinant may be compensated by exaggeration of complementary determinants the loss of more than one is generally problematic.

[McMahon, 1984] thoroughly investigates human locomotion (walking and running), e.g. observing effects of gravity, load carrying as well as dynamic energy storage and the influence of terrains with different stiffness. Furthermore, [McMahon, 1984] discusses extension to ballistic walking (compass walker with knees) using the previously discussed DoG towards a more accurate assessment of the vertical ground contact reactions. Among these improvements are, a lateral motion of the pelvis combined with a vertical and tilt rotation of the pelvis. An important statement found in this publication is the fact that from measurements, delay time of electro-myographic activities towards muscles to trigger reflexes does not allow for active control of the lower limb muscles during the first quarter of the foot-ground contact while running [McMahon, 1984].

In a subsequent study [Pandy and Berme, 1989a,b], formulate the idea that the implementation of stable bipedal locomotion might be possible in open-loop. Findings of their 3D model based analysis suggest that importance of pelvic tilt is inferior compared to the other DoM [Pandy and Berme, 1989a]. In [Pandy and Berme, 1989b] the authors suggest that plantar flexion of the stance-ankle alone can be compensated, however, a combined lack of knee and ankle poses a severe problem.

1.2 Abstraction of Characteristics for Technical Application

More recent studies [Dollar and Herr, 2008] assume a clear distinction between the hip, knee and ankle joint complex, following their mechanical contribution to level-ground walking. Besides stabilizing, it is suggested that the hip joint complex contributes the mechanical power output for the locomotion process. Following the different modes of either swing (ballistic motion) or stance the knee joint may be characterized as free-moving or equipped with a spring with a specific stiffness [Shamaei and Dollar, 2011]. In the same way, the plantar-flexion joint of the ankle joint complex is characterized as a spring-damper system during the stance phase. During the toe transition it is replaced by a spring system with suitable stiffness combined with a power output element to accomplish the propulsion.

The complex kinematic characteristics based on the human anatomy of the hip [Menschik, 1997], the knee [Grood and Suntay, 1983] and the ankle joint complex [Isman and Inman, 1969, Sheehan, 2010] have been investigated by different anthropomorphic studies. Furthermore, various studies have been devoted to the determination of the dynamic characteristics, of the human soft-tissue [de Leva, 1996a,b, Dumas et al., 2007a,b] for dynamic motion analysis. A comprehensive discussion of all characteristics the following parts of this work are based on, has been devoted to the Appendix C on page 239.

2 Humanoid Robots

From the previous discussion, the direct questions are then - how are these technical characteristics efficiently represented with recent technology and how will the DoG be considered based on the motion control system, such that a given mechanism can actively perform bipedal locomotion?

In the following, it is important to make a clear distinction between two different methods to accomplish walking. At one hand there are active walking devices such as Humanoid Robots [Hirai et al., 1998, Hirukawa et al., 2004]. These are usually focused towards high flexibility away from the anthropomorphic characteristics relying on sophisticated control systems and actuation technology [Hirai, 1998]. However, their motion performance is only conforme to a subset of DoGs, usually resulting in high energy consumption. At the other hand, passive dynamic walkers [Collins et al., 2001] exploit their intrinsic structural dynamics, combined with only simple control technology being conform to most of the DoGs resulting in lower energy consumption [Collins and Ruina, 2005] during stable and autonomous walking. In this work, modeling and optimization is done for the former type of systems - Humanoid Robots.

2.1 Technological Aspects

The mathematical modeling of technical features, as it will be thoroughly discussed in subsequent chapters, must always obey the principle - *as realistic as necessary - as simple as possible*. Modeling is based on assumptions and consistent modeling always starts with a thorough study of the system at hand, including its technological line of development to identify necessary assumptions to make. Furthermore, a cross-comparison of similar platforms frequently provides complementary information to improve the technical comprehension of the system design and its physical implications, particularly when specific documentation is not available. In the following, two exemplary common characteristics of different platforms are outlined to form the common line through the discussion of the subsequent chapters.

Interaction Problem

Despite being substantially different with respect to their system architecture, all mentioned platforms need to accomplish - omni-directional, bipedal locomotion. This translates for example to a dynamic interaction with their environment, at least with their feet, to maintain their dynamic equilibrium. Thus, from the viewpoint of control-engineering, the system can not rely entirely on pure position control [Heimann et al., 2007]. It has to provide some sort of compliance, either active in form of a compliance control [Vanderborgh et al., 2013] or passive e.g. as an impact absorber unit [Nakaoka et al., 2007]. In chapter 6 - 10 the technical characteristics to accomplish this interaction and its implications on the modeling of the system are given.

Motion Appearance

Furthermore, the aspect of natural motion appearance is not only linked to the employed algorithms for motion generation [Xiang et al., 2010] that might in some case yield high energy consumption [De Michieli et al., 2008, Sun and Roos, 2014], but as well to the design of the system architecture [Hirai, 1998, Hirukawa et al., 2004, Yamaguchi et al., 1999] that implies that some DoGs may be difficult to satisfy, due e.g. to singularities [Baerlocher, 2001] or absence of degrees of freedom for example in the upper torso³. As various works discuss the fact that energy efficiency is a governing principle of bipedal locomotion, e.g. [Beckett and Chang, 1968, Chou et al., 1995, Saunders et al., 1953], a basic motivation of this work

³Compared to the HRP-4C [Kaneko et al., 2009], the HRP-x [Kaneko et al., 2011] series is only equipped with a Yaw-Pitch joint in the link between the pelvis and the upper torso which does not allow a tilt motion of the pelvis without important rotation of the upper torso.

is to employ optimization, not to make a robot move perfectly as a human, but to improve its locomotion capacities with respect to its given design.

2.2 Related Architectures

Research on Humanoid Robots all over the world has been active for a few decades now, leading to a huge variety of different devices. What follows, is a short discussion of the important development lines to explain where the complementary information for the modeling of HRP-2 14 was obtained from.

From the knowledge of the author the first legged walking devices built to investigate biped locomotion were constructed in the '70s [Chew et al., 2003] at Waseda University Tokyo, Japan. With these walking devices researchers experimented with different actuation systems, e.g. hydraulic WL-3,5 or pneumatic WAP-1,2,3, artificial toes WL-3 [Machado and Silva, 2006]. Quasi-static [Kato et al., 1983] and dynamic [Takanishi et al., 1985] locomotion following fixed motion trajectories from dynamic simulation, was realized and ground interaction was based on compliance control. Pioneering work led as well to Wabian series [Yamaguchi et al., 1999], powered by 35 Degree of Freedom (dof)s equipped with a complete upper trunk, head and arms. A particularity of this robot series is its trunk-roll dof, which allows for a tilt motion of the pelvis (compare DoG) in walking direction and walking with stretched knees as performed by its successor wabian-2 [Ogura et al., 2006].

Around the year 1986 Honda secretly started its own project to investigate the bipedal locomotion principle and build the E0-6 series as lower limb devices with 12 dof and later the P1 through P3 full-body humanoid robots [Hirai, 1998]. Development was not made public before the official announcement of P2 a full featured humanoid robot with rigid upper torso, 30 dof position control, and a shock absorbing mechanism in the ankle joint complex, explicitly mentioned as low pass filter [Hirai et al., 1998]. Construction of further robots progressed rapidly and the Humanoid Robotics Project (HRP) [Hirukawa et al., 2004] was initialized based on the hardware of P3, previously developed by Honda. The project soon released their own robot HRP-1 [Yokoi et al., 2001].

Around the same time, a research team at Tokyo University built a series of humanoid robots called H5 [Nagasaka et al., 1999], H6 [Nishiwaki et al., 2000] and H7 [Nishiwaki et al., 2007]. These robots were built from aluminum sheet bending techniques for light-weight and stiff body characteristics and were similarly equipped with foot force sensors and shock absorber units.

The development was continuously ongoing and while Honda presented its next generation of Humanoid Robots under the name of Asimo [Sakagami et al., 2002], to perform as well dynamically stable running [Takenaka et al., 2009d], the HRP developed different successful platforms. Most important for this work are the 12 dof lower limb modul HRP-2LR [Kajita et al., 2005] used for hopping and running studies [Kajita et al., 2004, 2007b], the 30 dof prototype HRP-2 [Kaneko et al., 2002] and the improved HRP-2 Prometh platform [Kagami et al., 2007, Kaneko et al., 2004] a 30 dofs robot equipped a stiffer structure, with various extensions, designed for collaborative tasks. These robots are equipped with pure position control and a shock absorber unit in the ankle joint complex. The characteristics of the platform has been as well found among its successors, HRP-3 [Kaneko et al., 2008], HRP-4 [Kaneko et al., 2011] and the cybernetic robot HRP-4C [Kaneko et al., 2009].

High-speed walking is as well investigated at the University of Munich and led to construction of two architectures Johnnie [Löffler et al., 2003] with 17 dofs and Lola [Buschmann et al., 2009] with 25 dof and a hybrid position/force control system. Another recent development in this area is the torque controlled robot ToRo from DLR [Engelsberger et al., 2014, Ott et al., 2010] based on the KUKA light-weight arm [Bischoff et al., 2010].

Besides, various other architectures exist all over the world, e.g. KHR-3 [Park et al., 2005] from KAIST, Atlas from Boston Dynamics, SDR-4X [Ishida et al., 2003] from Sony, the Partner robot Series [Ota, 2010] from Toyota, Nao [Gouaillier et al., 2009] from Aldebaran or Reem B [Tellez et al., 2008] and his recently developed successor Reem C from PAL Robotics. Their discussion however is out of the scope of this work.

3 Motion Generation Methods

Similarly numerous as the previously presented humanoid robot architectures are the different motion generation methods. Usually these have been built around each of the robots during their construction, to provide the platform at hand with the necessary motion performance capabilities for stable operation. From literature, motion generation methods are divided into various classes. At one hand [Buschmann et al., 2005] distinguishes between lumped-mass model and optimization based methods. At the other hand [Xiang et al., 2010] classifies different approaches into Zero Moment Point (ZMP)-, optimization- and control-based methods. The following discussion will concentrate on two classes: *methods based on heuristics*, which regroup most of the specialized, *ZMP-based* (e.g. [Hirai, 1998]) and generic, *inverted pendulum* (e.g. [Kajita et al., 2001a]) approaches as well as *optimization based method*. The

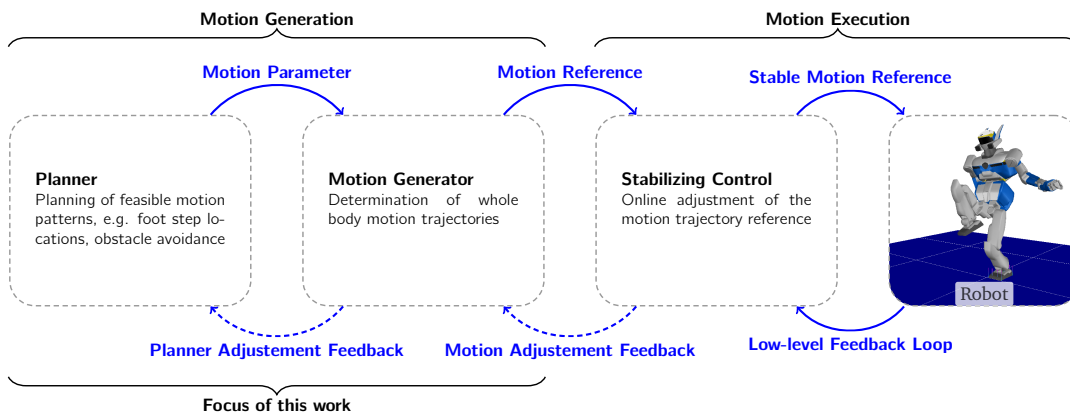


Figure 1.2: Schematics of a typical online motion generation process, from high-level information such as walking direction, goal-location and obstacle locations, towards the final dynamically stable motion that is executed on the real robot.

general procedure of motion generation methods is shown in Figure 1.2. Usually high-level motion parameters, such as possible foot step placements, goal-position, goal-orientation or obstacle locations to be avoided, are processed to generate specifically tailored parameters for the subsequent motion generation process. These frequently apply only for shorter time horizon. The motion generator is then based on these parameters and possible feedback from the online execution process to compute the reference trajectories. Before execution of the reference trajectories with the real robot, they usually undergo adjustment with respect to external perturbations and dynamic errors of the generation process with respect to the real robot. The resulting trajectories are performed on the real robot, closely monitoring its dynamic equilibrium.

Optimization-based methods employ more accurate models when compared to methods based on heuristics and therefore produce reference trajectory with a lower dynamic error [Takanaka et al., 2009a]. However, they still encounter problems related to environmental disturbances and physical phenomena that have not been modeled to keep the computational efforts at a reasonable level. Hence, in both situations execution of a given motion trajectory

is usually only successful by the intermediate of an online stabilizing control system. Thus, the distinction between optimization-based and heuristic methods only concerns the part *Motion Generation* from Figure 1.2 on the preceding page. The part *Motion Execution* remains untouched in both cases.

3.1 Methods Based on Heuristics

Methods that employ heuristics usually break-down the high complexity of the nonlinear system dynamics to simple, single or multiple lumped mass models [Buschmann et al., 2005, Xiang et al., 2010]. These methods are easy parameterized and finalize with smaller computation times than the high-level control cycle. Thus, the complete chain from Figure 1.2 on the facing page is allowed to perform in real-time, acting on command input e.g. from an operator [Kajita et al., 2002, Kanehiro et al., 2010] and re-act at the same time on environmental disturbances [Kajita et al., 2007b, Takenaka et al., 2009c] and modeling of errors [Kajita et al., 2010, Takenaka et al., 2009b].

In an earlier work [Kajita et al., 2001a], divided efforts to build such algorithms into two classes, a generic approach, based on a simple physical model and a more specialized one, related to a specific model. The first one is generally valid for a wide range of different robots. As little knowledge of the dynamics is available, the approach needs a feedback controller to accomplish a stable real walking situation [Kajita et al., 2003a]. The second one must be adjusted to each robot model, it is supposed to work on. However, it reaches higher accuracy with respect to the real world [Hirai et al., 1998] and therefore requires less feedback control effort.

Generic Approach - Example: 3D Linear Inverted Pendulum Mode (3D-LIPM)

From a study of walking on rugged terrain [Kajita and Tani, 1991] expressed a control principle for the motion of an arbitrary device linking a CoM to an unstructured ground profile. The CoM is restricted to move inside a plane, effectively linearizing the resulting control law. Controls are split into those that maintain the CoM inside the previously defined layer and into torques that control the motion inside the layer. Without the latter control the dynamic system acts as a 3D-LIPM [Kajita et al., 2001a] conserving a quantity called orbital energy⁴. The idea is now to let the pendulum swing and to patch dynamically consistent configurations together, effectively preserving the orbital energy. From the desired CoM-velocity and direction, suitable step-locations and stepping times are determined to build a dynamically consistent single-support, double-support walking scheme that is re-actively controllable [Kajita et al., 2002]. The transfer to a complete multi-body structure is then achieved by construction of a controller based on preview control [Kajita et al., 2003a]. This marks the introduction of the popular table-cart model by Kajita et. al. that is tracked with a preview controller computing the necessary CoM trajectory that would result into a given ZMP-trajectory⁵. The dynamic error of the multi-body model is then compensated for, with the same approach [Kajita et al., 2003a]. The works of [Kajita et al., 2003a] are the basis of a wide range of different pattern generators, e.g. for running with speed around $\sim 0.58 \frac{km}{h}$ [Kajita et al., 2005, 2007b], with extension of the CoM moving on a surface defined with spline-interpolation [Morisawa et al., 2005] to improve knee joint trajectories, using auxiliary feedback from the real robot [Kajita et al., 2006] for stable rough terrain walking and adaption to the low-pass filter dynamics [Ka-

⁴This quantity coming from celestial mechanics and has been further analyzed e.g. for motion without the restriction to a layer and dynamic stability - refer to [Pratt et al., 2006, Pratt and Drakunov, 2007]

⁵A criteria for dynamic stability based on works of [Vukobratović and Stepanenko, 1972] that will be outlined more in detail in a subsequent section of this work

jita et al., 2001b] of the ankle elasticity [Kajita et al., 2010].

With respect to the scheme depicted in Figure 1.2 on page 6, one plans the overall trajectory towards the goal position and orientation specifying the locations of the foot steps. Based on a method related to the table-cart model [Kajita et al., 2003a] a CoM trajectory is computed. Motion of the limbs (arms, legs) are usually parameterized. A popular method is to compute the whole body motion with respect to a fixed linear and angular momentum reference [Kajita et al., 2003b]. The motion reference is then corrected by the online stabilizing control [Kajita et al., 2005, 2007b] based on the feedback from the real robot to yield a dynamically stable motion performance.

Specialized Approach - Example: Divergent Component of Motion

From the previous outline, it sounds reasonable to build a generic approach to walking and use sophisticated feedback-control to resolve the resulting, larger dynamic error between the simplified model and the nonlinear whole-body dynamics. However, it is possible to minimize the dynamic error before-hand and hence, improve the walking performance as the resolution of the dynamic error is probably less difficult. This leads to the approaches, e.g. employed by [Hirai et al., 1998, Yamaguchi et al., 1999]. In the following, the approach used by [Hirai et al., 1998] for the robot series Px [Hirai, 1998] and the later Asimo series [Sakagami et al., 2002] will be shortly outlined. The complete motion generation system comprises walking [Takenaka et al., 2009a] and running [Takenaka et al., 2009d]. The dynamic error between the generated motion and a detailed dynamic whole-body model of the robot is reduced [Takenaka et al., 2009b], before the trajectories are passed to the online stabilizing control system that tracks the dynamic equilibrium of the robot, whilst performing the desired motion [Takenaka et al., 2009c].

In contrast to the generic approach in [Kajita et al., 2003a], the walking motion is generated based on a three mass model. The dynamics of the simplified system are formulated similar to the form of the 3D-LIPM [Kajita et al., 2001a]. Their analysis of the dynamic equation reveals that the motion consists of a *convergent* and a *divergent component* (with time) and that only the *divergent component* needs to be controlled [Takenaka et al., 2009a]. This leads to the formulation of a Boundary Value Problem (BVP) which is solved analytically based on specific assumptions.

The constructed three mass-based motion pattern is then altered such that it respects continuity of the divergent component of motion during the complete horizon of the generated motion. For the walking motion the vertical trajectory of the CoM is kept on a horizontal plane [Takenaka et al., 2009a], this assumption is dropped with additional corrections to the three mass model, when it comes to running [Takenaka et al., 2009d].

The dynamic error of the simplified trajectories with respect to the detailed whole-body model of the robot is determined and corrected with feed forward control methods that additionally respect the maximum limits of the external contact reactions that the robot is able to transmit between the feet and the ground [Takenaka et al., 2009b]. The stabilizing control algorithms works similar to the one outlined above. In addition, a strong feedback towards the motion generation system and even the planner exists [Takenaka et al., 2009b,c].

The complete system outline in [Takenaka et al., 2009a,b,c,d] has proved to work remarkably well. It could reach stable walking around $4.05 \frac{km}{h}$ [Takenaka et al., 2009a] and running around $10 \frac{km}{h}$ [Takenaka et al., 2009d] on a robot with similar characteristics to [Sakagami et al., 2002].

Another motion generation method that uses the divergent component of motion for rough terrain walking has recently been proposed by [Englsberger et al., 2013].

3.2 Methods Based on Optimization

As it was observable in the previous discussion, an increase of the precision of the dynamic model inside the motion generation algorithms results in a lower dynamic error with respect to the real robot. Hence, the online control effort to resolve this error for a stable motion execution of the motion trajectory on the real robot is smaller and the overall performance of the system usually improves. In [Takenaka et al., 2009a,b,c,d] the motion generation process starts from a three mass model with telescopic legs and corrects the resulting motion with respect to the detailed whole-body model of the robot, before it is passed to the online stabilizing control system.

From the above outlines it is clearly visible that these *pattern generators* adopt various assumptions, such as, single [Kajita and Tani, 1991] or three mass model [Takenaka et al., 2009a], ZMP-trajectory fixed before-hand [Kajita et al., 2003a] or whole-body motion with a given linear and angular momentum reference [Kajita et al., 2003b]. However, the influence on the characteristics of the final motion is not always clear.

Despite the fact that with an increasing model precision the computational complexity to solve the formulated problem gets problematic, at least for real-time applications, a dynamic error close to zero is usually unrealistic. However, these methods give a more abstract access to the motion characteristics, such that its application is more and more interesting with the recent achievements in computational performance.

Optimization-based Motion Generation

Optimization-based motion generation techniques had its first application in bipedal gait analysis in the early seventies [Chow and Jacobson, 1971]. In this pioneering work an approach based on dynamic programming with penalty functions and minimization of a quadratic performance criterion is proposed for bipedal motion generation. Subsequent publications show that this approach has soon been replaced by indirect and direct optimal control approaches. An OCP formulation represents an optimization problem that is solved subject to a multi-point BVP [Betts, 2009] and box constraints on all optimization variables. An examples for an indirect approach is the Pontryagin's Maximum Principle, applied for walking motion generation in [Bessonnet et al., 2002]. Direct approaches are distinguished in collocation [Ackermann and van den Bogert, 2010, Channon et al., 1992, Hardt et al., 1999, Martin and Bobrow, 1997, Saidouni and Bessonnet, 2003] and shooting techniques [Mombaur et al., 2001, Rousset et al., 1997, 1998]. Both approaches differ in the employed strategy of transcription as follows:

In the collocation method the system trajectories and controls are discretized in parallel [Hargraves and Paris, 1987]. The system states are usually expressed as a set of polynomials [Hargraves and Paris, 1987, Hu et al., 1999] or truncated Fourier series [Rousset et al., 1997] as well as B-splines [Martin and Bobrow, 1997] or cubic splines [Saidouni and Bessonnet, 2003] on a time grid. The controls are approximated e.g. as piece-wise linear functions [Hargraves and Paris, 1987, von Stryk and Bulirsch, 1992]. This leads then to a high dimensional sparse optimization problem.

The shooting method discretizes the controls with similar approaches as in collocation, e.g. piece-wise constant or linear [Leineweber, 1995]. The system state trajectories, however, are determined based on forward integration. A technique to improve robustness of the numerical solution of the multi-point BVP is the parametrization of the time horizon by a series of Initial Value Problems (IVPs) with additional continuity constraints to suppress defects in the resulting system trajectory [Betts, 2009]. This again results in a nonlinear program with a particular structure. Improved algorithms in terms of convergence and computation time

have been proposed by [Bock and Plitt, 1984].

Both methods have been successfully applied to solve complex problem formulations arising from the domain of bipedal motion analysis. A small choice of important examples is outlined below:

Asymptotically stable bipedal walking [Mombaur et al., 2001] and in later works, stable human-like running [Mombaur, 2009] in 2D and running motions [Schultz and Mombaur, 2010] in 3D motion trajectories have been computed by Mombaur et al. based on a multiple shooting method. The problem formulation consisted of minimization of a Lagrange-type or Bolza-type objective, subject to multiple phases with discontinuous phase transitions, each described by a multi-point boundary value problem. Maximization of open-loop stability was performed as minimization of the eigenvalues of the Monodromy-matrix, also known as Floquet multipliers [Mombaur, 2009, Mombaur et al., 2001]. The human-like full body model used in 2D [Mombaur, 2009] and in 3D [Schultz and Mombaur, 2010] was modeled with torque controlled joints and additional parameterized spring-damper systems. In the case of the stability, optimization results showed that it is possible to build torque controlled robots and find actuation profiles such that walking motions can be performed based on periodic feed-forward control under small perturbations without destabilization [Mombaur et al., 2001]. Similar results are found for the 2D running motion [Mombaur, 2009]. These findings encourage further efforts to investigate mechanically self-stabilizing characteristics of robotic walking devices to minimize the effort of a potential online stabilizing control system. For the 3D running case of [Schultz and Mombaur, 2010] the minimum energy criterion led to running motions which compared reasonably well to human running motions.

A collocation and Inverse Dynamics (ID) based approach can be found in [Mordatch et al., 2013], wherein the authors generate whole-body motions using contact-invariant optimization. Contact events are added to the optimization procedure as degrees of freedom. An example of algorithms based on optimal control applied to full-scale models of humanoids can be found in [Tassa et al., 2014]. The authors use a dynamic programming technique, based on the dedicated simulation environment *MuJoCo* [Todorov et al., 2012] for simulation, and apply contact smoothing algorithms [Todorov, 2010], complementarity relaxation and least-squares treatment of virtual actuation [Erez and Todorov, 2012]. The method is also used for whole-body model predictive control (MPC) in simulation [Erez et al., 2013], that rolls out the current system state by forward integration and calculates an optimal correction backwards, using a quadratic approximation of the *cost-to-go* function at each time instant. The simulation and derivative generation of multi-body dynamics, is based on their contact smoothing algorithms [Todorov, 2010]. In [Erez and Todorov, 2012] they also investigated ID optimal control with contacts based on complementarity relaxation and least-square treatment of virtual actuation. These methods are also used for whole-body model predictive control in simulation (compare [Erez et al., 2013]).

The problem of task prioritization and incorporation of equality as well as inequality constraints is addressed with an approach called the *stack of tasks* [Mansard, 2012, Ramos et al., 2011, Saab et al., 2011] and based on ID. A series of subsequent quadratic programs, minimizing a system of slack variables, is solved, each operating in the null-space of the constraints of the previous stage. From this constraints prioritization scheme [Nakamura, 1990], the authors solve for a redundant setting of joint accelerations, actuation torques and contact constraint forces, for one time step. Dependent system states are then determined through integration to build the configuration the next iteration is based on. The highest priority is always given, to the ID and contact constraint formulation, followed by various motion tasks. The layers are stacked until all redundancy is consumed to yield a stable motion result. In this approach redundant contact modeling is generally not problematic and the computational scheme can

be tuned for cost-reduction and good numerical stability [Mansard, 2012].

At one hand, the above discussed approaches work on the full whole-body model and therefore should result in a small dynamic error. At the other hand their computational complexity limits the application to offline use and hence, the online stabilizing control system is still necessary (see Figure 1.2 on page 6) to successfully perform the motion on the real robot.

Combination of Optimization and Control

Despite the computational complexity in mixed heuristic and optimization-based approaches, optimization can make a valuable contribution to the motion quality as seen in the following examples:

An important control scheme is the orthogonal decomposition⁶ based control of floating base systems, which has been successfully applied to legged devices [Buchli et al., 2009, Righetti et al., 2011b]. The proposed control scheme [Righetti et al., 2011b] is a dynamic model-based feed-forward control under external contact constraints. However, resolution of the internal coupling between actuation and external contact reactions as projection into the sub-manifold of the external contacts is achieved on purely kinematic quantities and hence, computationally robust to inaccuracy in the inertia matrix of the model. The separate identification of actuation joint-torque and the contact constraint forces provides further opportunities of exploitation. In [Righetti et al., 2011a] these quantities are employed to establish compliant feed-forward control [Mistry et al., 2010] and to optimize the contact reaction forces for robust interaction, e.g. during locomotion [Righetti et al., 2011a]. However, this formalism has an important short coming - it suffers from potential physical inconsistency in the case of under-actuated configurations. As it is explained in [Hutter, 2013], one may easily choose configurations that are physically not tractable.

An identification of non-controllable and controllable acceleration space of under-actuated systems is given in [Sentis and Khatib, 2005]. The analysis is conducted with respect to the motion space of the desired tasks, extending the prioritized task control for floating base systems. Further extensions explore multi-contact and internal linkage representations, e.g. [Sentis et al., 2010].

4 Exo-Skeletons

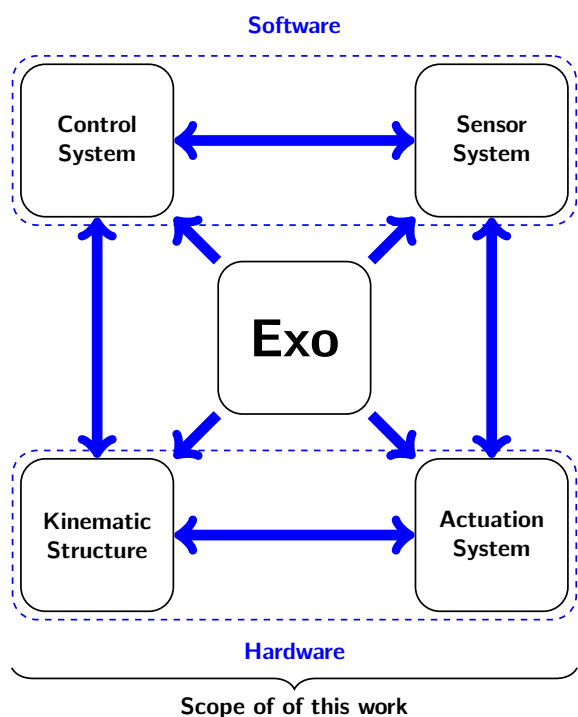
Revisiting once again the third scenario from above. Despite the research conducted in humanoid robots and related algorithms for stable motion generation. Isn't there an opportunity to put the human inside the loop? One could directly exploit this added intelligence for robust and stable motion generation. Also this situation could compensate some disabilities in mobility of the given human, such that he can walk up the staircase, even though, he/she cannot actively move its legs due to a previous spinal cord injury.

The vision to build a *robotic suite* for humans, that inspired researchers and engineers [Mizen, 1969], developed into an active research field with mostly complementary directions, namely military logistics and support in mobility and rehabilitation for medical engineering [del Ama et al., 2012, Dollar and Herr, 2008, Herr, 2009, Herr and Kornbluh, 2004, Pons, 2010]. Besides various technical studies that never left the drawing stage. One of the first prototypes built was Hardiman I [Fick, 1969, Fick and Makinson, 1971] in the '70s (see Figure 1.3b on the next page). A massive hydraulic driven construction, weighing around 680kg, that aimed

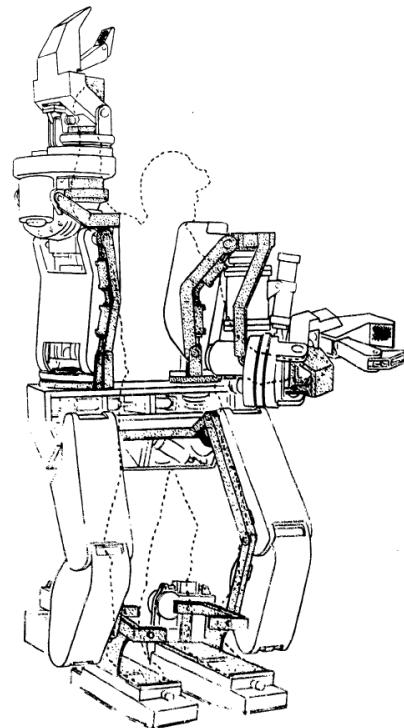
⁶Orthogonal decomposition was originally originally applied for modal analysis [Flashner, 1986]

to mimic the kinematics of a human and provide a potential operator with high force amplification ($\sim 25:1$) for logistic purposes. Although it was never powered on with a human inside, the gain of knowledge, on how to apply modern technology to accomplish a device that would work to together with a human in concert, was considerable [Dollar and Herr, 2008]. Among these technical challenges are, safety of the operator [Zeilig et al., 2012], compliant actuation systems [Kwa et al., 2009, Vanderborght et al., 2013], energetic autonomy [Raade et al., 2003], human machine interface [Raj et al., 2011] and stability in control, e.g. handling of human induced instabilities [Kazerooni and Snyder, 1995].

A new impulsion was set with the *EHPA* program towards development of exoskeletons



(a) Different components of and Exo-Skeleton construction and its crossed interdependencies that need to be carefully considered during the design process.



(b) Hardiman I - Prototyp with silhouette of human operator inside [Fick and Makinson, 1971]

Figure 1.3: On the left side the abstract main components of an exo skeleton construction are shown. During conception these components should not be considered separately - as it is frequently done but packed into a comprehensive approach. On the right side Hardiman I Prototype is shown.

for human performance augmentation [Chu et al., 2005, Kazerooni et al., 2005, Valiente, 2005]. Around the '70s, university laboratories and later industrial concerns started to invest considerable efforts of time and financial resources into the development of exoskeletons for support in mobility or rehabilitation of people with gait disabilities [Kagawa and Uno, 2009, Kawamoto and Sankai, 2002, Quintero et al., 2011, Raj et al., 2011, Vukobratovic et al., 1974, Wang et al., 2011, Zeilig et al., 2012].

In the following, the focus is set on the conception of an untethered lower-limb exo-skeleton for rehabilitation purposes. Conception of such an exo-skeleton must accomplish the implementation of various system components (see Figure 1.3a), such that they work in concert

with the human operator [Chu et al., 2005, Kazerooni et al., 2005, Kwa et al., 2009, Raj et al., 2011].

As depicted on Figure 1.3a on the preceding page these systems are classified into software and hardware. The software consists of various sensor and control systems to detect perturbations on the mechanism by the actual operator of the exo-skeleton [Chu et al., 2005], or human machine interaction to follow the intention of the operator as closely as possible, e.g. by using EMG or muscle tension measurements [Kasaoka and Sankai, 2001, Kawamoto et al., 2003] and effectively generating the corresponding motions [Hayashi et al., 2005, Kazerooni et al., 2005]. As a disabled operator frequently lacks sensory feedback from its legs, support to the estimation of its present dynamic situation is effectively provided with a particular human machine interface [Raj et al., 2011].

The hardware consists of the kinematic structure and the actuation system [Chu et al., 2005]. The kinematic structure acts as partial functional substitute to the human soft-tissue structure [Dollar and Herr, 2008]. The actuation system can either be passive or active [del Ama et al., 2012]. In the passive case it acts mainly as a spring-damper system for scheduled energy storage and dissipation, supporting the human muscle system in the case of healthy operators [Valiente, 2005], or to build the control complement to synthesized muscle activation for patients with partial gait-disabilities wearing the device [del Ama et al., 2012].

A huge problem of these highly complex devices is their operational efficiency [Dollar and Herr, 2008]. At least in the case of military logistics there is only little data available that shows an effective improvement of the metabolic efficiency of an operator wearing such a robotic suite [Dollar and Herr, 2008]. A technical issue that is frequently stated [Dollar and Herr, 2008, Herr, 2009, Pons, 2010] is the problem of mis-alignment between the human soft-tissue and the rigid kinematic structure of the exoskeleton, surrounding the human. The rigid kinematic chain of the exoskeleton only establishes a discrete number of dof and hence, creates additional kinematic constraints on the complex kinematic of human lower limb joint complexes (compare to Appendix C). The individual geometry and the compliance of the human soft-tissue structure creates mis-alignment between the human and the technical joint structure and combined with the kinematic constraints could lead to hyperstaticity [Cempini et al., 2013] and parasitic loads on the human joint structure causing discomfort and injury [Esmaeili et al., 2011, Malosio et al., 2011].

The above aspect is directly related to the safety of the user during operation, especially for patients with gait-disabilities [Zeilig et al., 2012]. Besides single devices, such as *Rex*⁷ that provides the operator with stable locomotion, most of these devices only provide a subset of the full human lower limb kinematic such that all DoG are not equally represented. Therefore most of the devices can only be used with additional support of clutches [Vukobratovic et al., 1974], need further assistance of technical staff [Raj et al., 2011] and usually lead to quick fatigue of the wearing person [del Ama et al., 2012].

5 Contribution & Organization

This thesis has three major contributions in the domain of optimization-based offline motion generation. First, a new algorithm has been developed and studied to allow ID based computations based on a direct multiple shooting algorithm to solve OCPs. Second, OCPs were formulated to investigate motion characteristics of different optimization criteria and modeling decisions. Third, motion generation was applied to investigate design decisions in the comprehensive mechatronic conception of a lower-limb exo-skeleton.

⁷*Rex* is manufactured from Rex Bionics • Auckland Neusseeland, publication are however not available

5.1 Contribution to Optimization-based Motion Generation

In the field of optimization-based motion generation methods, computation of the model dynamics is performed following either forward or ID. It is generally believed that ID seems to be mathematically much simpler and hence should be computationally less involving than the Forward Dynamics (FD). Furthermore, the employed direct multiple-shooting method implies additional numerical constraints on the algorithm, used to solve the model dynamics. Therefore a new ID algorithm for the computation of under-actuated systems for the employed multiple shooting algorithm is developed and tested based on an academic model and a full-featured dynamic model of the humanoid robotics platform HRP-2 14. The developed algorithm has then been used to effectively support the investigations for motion generation.

5.2 Contribution to Modeling and Conceptional Motion Generation

The huge variety of previously published approaches dealing with problems of online and offline motion generation, raises the importance to clearly specify the scope of the contribution of this work in the domain of motion generation for humanoid robots.

As depicted in Figure 1.2 on page 6 motion generation is done for the offline-case. Motion generation is done for the robot platform HRP-2 14. However, the employed approach is generic and can be applied for any robot that comes with a sufficiently accurate dynamic model. Motions are generated from dedicated problem formulations, based on complex whole-body model dynamics to minimize the error between the motion trajectories and the real robot, solved with direct multiple-shooting techniques.

In a first study, motions are computed using different optimization criteria and dropping for example, the conservative ZMP constraint to assess the motion characteristics one could expect with these optimization criteria. Optimal motions with respect of their appearance were not expected to be human-like, as the robot platform HRP-2 14 lacks a suitable dof configuration to perform e.g. pelvis tilt motions (compare [McMahon, 1984, Saunders et al., 1953]).

In a second study, the optimization setup was tuned to work in concert with the online stabilizing control system, such that the offline motion result could then be performed on the real robot. This approach is effectively used to drop all additional assumptions that are made upon the physical situation before-hand in most of the motion generation methods and to investigate the gain in performance of the motion.

As an example, the effect of an inelastic and elastic mathematical modeling of the robot platform HRP-2 14 is investigated with respect to the dynamic error of the resulting motion trajectories, effectively solving the ground interaction problem. The minimization of the dynamic error is exploited to effectively push the robot towards its dynamic limits, while overstepping an obstacle with dynamic stability was successfully executed on the real robot. The overstepped obstacle had a dimension of 20cm × 11cm (height × width). The experiment broke the record of Stasse et. al. with 18cm × 11cm.

5.3 Contribution to Conceptional Design of Exo-Skeletons

From the conceptional investigation of the motion generation problem this section goes one step further. The focus is no longer on a fixed kinematic structure, but deals with a variable one. The proposed approach replaces the classic over-the-wall engineering or divide and conquer techniques, by the formulation of subsequent optimization problem. In this optimization problem, the human operator is effectively inserted in the exo-skeleton in simulation. This set-up is then iterated, but always on the comprehensive human – exo-skeleton system model. Most of the system properties, more than one can determine with sufficient confidence during the first iteration, are not known before-hand. However, they may be approximated with a

reasonable initial effort and formulated in a large set of system parameters. The optimization set-up gives then the possibility to substantiate these parameters in an iterative manner, but always on top of the comprehensive system model, such that complex inter-dependencies and interactions between the various system components and the human in the loop are effectively resolved and considered during the conception.

The study is conducted on an important benchmark motion - walking. Walking motion have been obtained from a healthy human for level ground walking and up-slope (2.5 DEG, 5.0 DEG, 7.5 DEG) and down-slope (2.5 DEG, 5.0 DEG, 7.5 DEG) walking. The complete human-exo-skeleton model is fitted against these motions. The simulation setup then gives important information about the whole body dynamics, the kinematics and the actuation system. Based on this information the next iteration is prepared to continuously substantiate an optimal design.

This method aims to contribute an iterative optimization-based approach which considers at each level the comprehensive model to improve the complex conception of such a mechatronic device and to resolve the complex inter-dependencies between the system components with reasonable effort, e.g human machine interaction during walking.

5.4 Organization

The work is split into three distinct parts. Part one covers the state of art in modeling, optimal control and explains the modeling tools constructed during this work. The part closes with a thorough discussion of the developed ID algorithm that is integrated with the direct multiple shooting method to solve the formulated OCPs. The algorithm is first analyzed on an academic model⁸ and later on the full featured model of HRP-2 14 with included ankle elasticity. The second part discusses the offline optimization-based motion generation for the robotic platform HRP-2 14. The part starts with a thorough investigation of the hardware and the control software of the robot from literature. Then optimal control problems are discussed to assess the influence of different biologically inspired optimization criteria on the resulting motion characteristics. These experiences are exploited to minimize the dynamic error between the real robot and the simulation such that the robot can be pushed to its limits, while the online stabilizing control system maintains a stable operation.

The last part deals with motion generation to support a comprehensive conceptual study of a lower limb exo-skeleton. The part outlines the various technical problems that emerge during the conception of such a device with a thorough discussion of two well documented exo-skeletons: *Mina* & *BLEEX* from literature. Based on this presentation the choices of the following study is outlined. The part closes with a thorough discussion of a subset of the conducted computational study and the resulting design decisions for the conception of a real lower-limb exo-skeleton.

The document then closes with a comprehensive conclusion on all three parts. Various sections that have been decided not to be essential to the central discussion of this work have been devoted to the appendix. However, these deliver complementary, but non-redundant information to this document and hence, are important to the understanding of all details of this thesis.

⁸Cart-Pendulum Model

Part

**Modeling & Optimal Control of
Anthropomorphic Walking Systems**

High quality modelization is essential to all kinds of optimization. As a projection from the reality onto a virtual system that captures on a varying level of complexity the governing characteristics of a system one would like to investigate, the modeling process itself takes great importance and must be conducted very carefully. This work will be limited to mechatronical systems [Buur and Andreasen, 1990] in the scope of bipedal locomotion. The top question of this chapter is then: how to get a sufficiently generic access to mechatronical-system modelization to ease parametrization for an efficient exploitation during optimal control.

First the engineering mechanics [Gross et al., 2006, 2011, 2004] of rigid bodies (in contrast to continuum mechanics [Gross et al., 2011]), this work is based on, are intensively reviewed. Mathematical preliminaries [Merzinger and Wirth, 2002] as well as methods for their dynamic representation are discussed to find a generic access to all governing mechanical characteristics for an efficient subsequent exploitation during the final optimization process.

Then, state of the art methods are discussed to express the hybrid-dynamics of multiple rigid body systems under contact constraints and instantaneous collisions. Focus is parallel given to a deeper analysis of mechanical properties e.g. structural load. Again, the discussion is focused on methods to establish a generic access to hybrid-dynamic characteristics, building on top of the previously explained approach.

As soon as the pure mechanical basics are sufficiently discussed, the review is expanded to further aspects and components of mechatronical [Buur and Andreasen, 1990] systems, such as: transmissions, motors, control systems, bearings and friction. The discussion is brought back to the same common aspect of how to get the formulation sufficiently generic to be exploited during optimization.

At this point the open-sourcetool *DYNAMOD* is introduced to comprise efficient state of the art algorithms [Featherstone and Orin, 2000] for rigid multiple body system with the generic modeling idea of [Wieber et al., 2006] and the efficient formulation of 6D spatial algebra [Featherstone, 2006] to offer the required generic access to the finally modeled system that was previously discussed.

In a next step, literature on state of the art optimal control is reviewed to describe the highly efficient multiple shooting approach that will be used during the remainder of this work. As for the solution of a classical rigid multiple body system problem there exists a forward and an inverse solution, these are reviewed in literature, showing that the proposed inverse formulation does not work correctly in the employed optimal control approach. Consequently, an improved inverse dynamics formulation had to be established. Finally, the application of forward and inverse problem formulations are intensively evaluated on an academic model and later on the full dynamic model of HRP-2 14.

Related Publications: The scientific work conducted in the following chapter has been issued for publication in:

- Kai Henning Koch, Manuel Kudruss, Christian Kirches, Katja Mombaur. Inverse Dynamics Optimal Control of Under-actuated Multi-Body Systems with Changing Constraint Sets. *Journal Autonomous Robots - Special Issue on whole-body control of contacts and dynamics for humanoid robots*, 2014 [submitted on 15th of November 2014]

2 Mechanical Modeling

In the following sections principles in engineering mechanics are reviewed to support the subsequent discussions in rigid multi-body dynamics. The literature on engineering mechanics is vast - for a comprehensive introduction you may refer to [Featherstone, 2007, Gross et al., 2004, Khalil and Dombre, 2002]. Although, engineers and researchers discuss the same mechanical problems, the notations originate from different conventions. With respect to the usual complexity of engineering mechanics, a clear view on the critical aspects of the modeling conducted in this thesis, is efficiently supported by the spatial notation from [Featherstone, 2007]. This notation, a transformation to a more convenient coordinate basis, provides a compact and straight-forward form to express the usually highly complex and error-prone equations from classical 3D engineering mechanics. However, from the general case some important assumptions are adopted, which are more obvious in the classical representation and thus should be explained briefly before all subsequent discussions are exclusively shifted into spatial notation.

1 Classical Representation

In classical engineering mechanics one distinguishes between kinematics and kinetics. Kinematics expresses the motion and possible constraints of a rigid body and kinetics the relationship between the motion of the rigid-body and the given external forces and torques acting on the system. An important decision that is common to all kinetic and kinematic representations is the proper selection of the reference system, which will be outlined below.

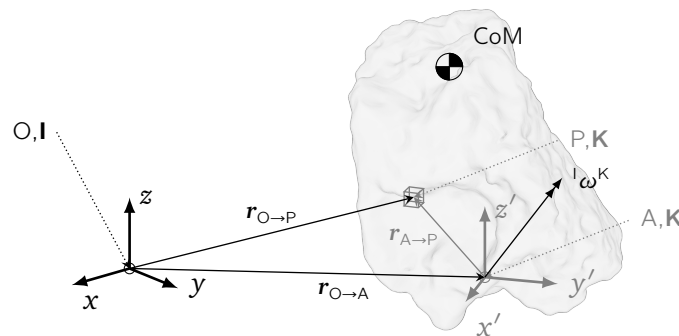


Figure 2.1: Kinematics of a freely moving rigid body. The representation is done based on the fixed global reference frame **I** and on the body fixed moving local reference frame **K**. All quantities that are fixed with respect to the reference frame **I** or **K** are drawn in black or gray, respectively. The origin of **K** is different from the body's CoM. The body **K** is moving with a rotational velocity ω with respect to the reference **I**

2 Kinematics

For this work the focus is set on motion description of a rigid body with respect to different reference systems. This description results as special case from the general kinematic description of point masses [Gross et al., 2004]. For the subsequent discussion on the dynamics of free geometry rigid bodies with respect to different reference systems a rigorous derivation of expressions for the location, velocity and acceleration is essential and will be the final result of this section.

2.1 Preliminaries

Given a moving point P in space. The observation of its trajectory $\mathbf{r}_{O \rightarrow P}(t)$ looks different regarded from fixed and a moving view point, even though, it is physically the same trajectory. This is a convenient fact that helps to efficiently express the complex kinematics of relative moving coordinate frames in a simple and straight-forward manner. In the case of rigid bodies this technique allows to separate the integration of geometry from the temporal derivation.

Let $\mathbf{r}_{O \rightarrow P}$ be a vector between the point O and P be a point in Figure 2.3 that is perceived from the *fixed* reference system I , $\underline{\mathbf{r}}_{O \rightarrow P I}^1$ and from the *moving* reference system K , $\underline{\mathbf{r}}_{O \rightarrow P K}$. The reference I is represented with the orthonormal basis of,

$$C_I = \{\mathbf{e}_x, \mathbf{e}_y, \mathbf{e}_z\} \subset \mathbb{R}^3, \quad (2.1a)$$

and the reference K is represented on the orthonormal basis,

$$C_K = \{\mathbf{e}_{x'}, \mathbf{e}_{y'}, \mathbf{e}_{z'}\} \subset \mathbb{R}^3, \quad (2.1b)$$

in the euclidean vector space U^3 . A vector $\mathbf{r}_{O \rightarrow P K}$ is then represented as coordinate vector $\underline{\mathbf{r}}_{O \rightarrow P}$ in the basis of K ,

$$\mathbf{r}_{O \rightarrow P} = C_K \underline{\mathbf{r}}_{O \rightarrow P K} = \underline{x}'_{O \rightarrow P K} \mathbf{e}_{x'} + \underline{y}'_{O \rightarrow P K} \mathbf{e}_{y'} + \underline{z}'_{O \rightarrow P K} \mathbf{e}_{z'}. \quad (2.2)$$

A let $\underline{\mathbf{p}}$ be a coordinate vector,

$$\underline{\mathbf{p}} = \sum_{i=0}^N b_i \underline{\mathbf{p}}_{i,B} = B \underline{\mathbf{p}}_{\cdot,B}, \quad B = \{e_1, e_2, \dots, e_{n_{\text{vec}}}\} \subset \mathbb{R}^{n_{\text{vec}}} \quad (2.3a)$$

expressing $\underline{\mathbf{p}}$ with respect to a moving base B . The derivative of this coordinate vector is expressed in terms of the vector $\dot{\underline{\mathbf{p}}}$ following [Featherstone, 2006] as,

$$\dot{\underline{\mathbf{p}}} = \frac{\partial}{\partial t} (B \underline{\mathbf{p}}_{\cdot,B}) = \dot{B} \underline{\mathbf{p}}_{\cdot,B} + B \dot{\underline{\mathbf{p}}}_{\cdot,B}, \quad (2.3b)$$

$$B^{-1} \dot{\underline{\mathbf{p}}} = \underbrace{B^{-1} \dot{B}}_1 \underline{\mathbf{p}}_{\cdot,B} + \underbrace{\dot{\underline{\mathbf{p}}}_{\cdot,B}}_2. \quad (2.3c)$$

The basis C_K of the frame K only change with respect to the frame I by rotation of $\underline{\boldsymbol{\omega}}$. Under this assumption it is possible to show [Featherstone, 2006],

$$C^{-1} \dot{C} = \underline{\boldsymbol{\omega}} \times, \quad \underline{\boldsymbol{\omega}} \in C. \quad (2.4)$$

¹Reference-frames \cdot are type-set in bold. A coordinate vector $\mathbf{r}_{\bullet \rightarrow \bullet}$ expresses a vector from the point \bullet towards the point \bullet expressed in the bases of the reference system I .

The coordinate vector For the derivative of the coordinate vector $\underline{r}_{A \rightarrow PK}$ representing the vector $\underline{r}_{A \rightarrow P}$ in the reference frame \mathbf{K} (2.2) it follows from (2.3c),

$$\begin{aligned} \frac{\partial}{\partial t} \underline{r}_{A \rightarrow PK} &= \underbrace{(C_K^{-1} \dot{C}_K)}_{\boldsymbol{\omega}^\times} \underline{r}_{A \rightarrow PK} + \dot{\underline{r}}_{A \rightarrow PK}, \\ &= {}^I \boldsymbol{\omega}_{,K}^K \times \underline{r}_{A \rightarrow PK} + \dot{\underline{r}}_{A \rightarrow PK}. \end{aligned} \quad (2.5)$$

with the coordinate vector of the angular velocity ${}^I \boldsymbol{\omega}_{,K}^K$.

2.2 Free Motion of Rigid-Bodies

In the case of a rigid body \mathbf{K} , one may assume [Gross et al., 2004],

$$\dot{\underline{r}}_{A \rightarrow P, K} = 0, \quad (2.6a)$$

as the coordinate vector from the body-fixed origin \mathbf{A} towards the body-fixed point \mathbf{P} is constant with respect to the chosen coordinate base \mathbf{K} . Therefore the representation of the coordinate vector $\underline{r}_{O \rightarrow PI}$ can be written as [Gross et al., 2004]:

$$\underline{r}_{O \rightarrow PI} = \underline{r}_{O \rightarrow AI} + {}^I R_K \underline{r}_{A \rightarrow PK}. \quad (2.6b)$$

The derivative with respect to time then follows directly to [Gross et al., 2004]:

$$\frac{\partial}{\partial t} \underline{r}_{O \rightarrow PI} = \underbrace{\dot{\underline{r}}_{O \rightarrow AI}}_{\dot{\underline{r}}_{O \rightarrow AI}} + {}^I \boldsymbol{\omega}_{,I}^K \times {}^I R_K \underline{r}_{A \rightarrow PK}. \quad (2.6c)$$

The second derivative by time follows from analog reasoning. The expression (2.6c) will be exploited rigorously in the next sections. From this results it is obvious that the free motion of all geometric parts of the rigid body is solely defined by the linear velocity of a given point of the rigid body and its rotational velocity [Gross et al., 2004]. For the sake of rotational simplicity the following sections will drop the explicit $\underline{\quad}$ coordinate vector sign whenever this is clear from the context.

...a Word on Coordinate Transformations

The orthonormal matrix ${}^I R_K$ (2.7b), (2.7c) has as its columns the coordinates of the basis $\{\mathbf{e}_x, \mathbf{e}_y, \mathbf{e}_z\}$ with respect to the basis of \mathbf{K} and the rows are the coordinates of the basis $\{\mathbf{e}_{x'}, \mathbf{e}_{y'}, \mathbf{e}_{z'}\}$ with respect to the basis of \mathbf{I} [Diebel, 2006, Khalil and Dombre, 2002]. Hence, coordinate transformation is performed from the reference \mathbf{K} towards the reference \mathbf{I} . Further mathematical characteristics are,

$${}^I R_K = C_I (C_K)^{-1}, \quad (2.7a)$$

$$({}^I R_K)^T {}^I R_K = \mathbf{1}, \quad (2.7b)$$

$$\det |{}^I R_K| = 1. \quad (2.7c)$$

Although, the orthonormal matrix ${}^I R_K$ is an essential part to represent the rotational coordinate transformation in the kinematic and dynamic expressions, the closer explanation of its construction [Diebel, 2006, Featherstone, 2007, Khalil and Dombre, 2002, Siciliano and Khatib, 2007] has been circumvented in the past section. The construction of ${}^I R_K$ is usually

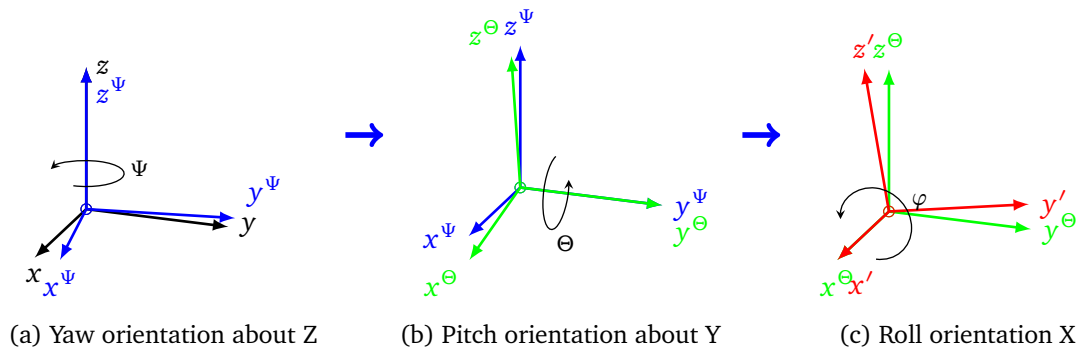


Figure 2.2: Euler-Angle parametrization for example of the angle-sequence Z (Yaw/Heading) \rightarrow Y (Pitch/Attitude) \rightarrow X (Roll/Bank), the so-called Cardan convention frequently used in engineering applications.

parameterized with three (Euler Angles, Angle-Vector representation) or four (Caley-Klein Parameters, Unit Quaternions) parameters. Three parameters are independent, the fourth parameter is always related to the previous three, based on a quadratic norm. The decision to adopt a specific parametrization method usually depends on a large number of different aspects including geometric relation [Featherstone, 2007], desired precision for integration, singularities [Diebel, 2006] and further constraints related to optimization algorithms in applied mathematics. The selection then decides about the formulation of the terms ${}^I R_K$, ${}^I \omega_{\mathcal{I}}^K \times$ and ${}^I \dot{\omega}_{\mathcal{I}}^K \times$.

While the three parameter-based construction of Euler-Angles has a clear geometrical relation to technological joints in engineering mechanics, it suffers from singularities, so-called Gimbal-locks [Diebel, 2006], at different configurations with respect to the selected angle sequence convention. A mathematical more elegant parametrization is achieved by a quaternion-based representation. Compared to the Euler-Angle parametrization this representation is singularity free and yields higher accuracy during the numerical integration from angular velocity [Diebel, 2006]. However, further effort during the integration [Featherstone, 2007] and optimization is necessary to enforce the quadratic norm-based constraint relating the four parameters. This usually done adopting re-normalization or penalty-term techniques [Diebel, 2006, Nocedal and Wright, 2000]. A further alternative is the reprojection of the redundant four quantity parameterization into an unconstrained three parameter sub-manifold consisting of a unit rotation vector and a related rotation angle. This method is adopted by the angle-vector parameterization [Diebel, 2006, Khalil and Dombre, 2002].

The modeling in all subsequent parts of this work is exclusively designed for straight-forward integration with optimal control based on direct multiple-shooting techniques. Furthermore, modeling of the coordinate transformations is closely bound to their technological realization [Kaneko et al., 2004] and the risk of singularities in the resulting motion trajectories is minimized as most of the critical configurations are located outside the technical feasible range [Baerlocher and Boulic, 2001]. Hence, decision was made for the Euler-Angle-based parametrization to keep the mathematical representation as simple as possible and allow direct access to geometric relations.

The parametrization of Euler-Angles is based on the fact that a sequences of three elementary rotational transformations about subsequently different axes $\{X, Y, Z\}$ are sufficient to represent any given re-orientation in space. The latter constraint leads to 12 distinct angle

sequences conventions. Conventions used in this work are the $\{Z, Y, X\}$ Cardan-convention,

$${}^I R_K = {}^{I(xyz)} R_{(xyz)^\psi}(\Psi) {}^{(xyz)^\psi} R_{(xyz)^\theta}(\Theta) {}^{(xyz)^\theta} R_{K(xyz)'}(\varphi), \quad (2.8a)$$

(shown in Figure 2.2). The velocity vector with respect to the reference I then follows to:

$$\begin{aligned} {}^I \boldsymbol{\omega}_{I}^K &= \begin{bmatrix} 0 \\ 0 \\ \dot{\Psi} \end{bmatrix} + {}^{I(xyz)} R_{(xyz)^\psi}(\Psi) \begin{bmatrix} 0 \\ \dot{\Theta} \\ 0 \end{bmatrix} \\ &+ {}^{I(xyz)} R_{(xyz)^\psi}(\Psi) {}^{(xyz)^\psi} R_{(xyz)^\theta}(\Theta) \begin{bmatrix} \dot{\varphi} \\ 0 \\ 0 \end{bmatrix} \\ &= {}^{I(xyz)} E_{(\Psi\Theta\varphi)}(\varphi, \Theta, \Psi) \begin{bmatrix} \dot{\varphi} \\ \dot{\Theta} \\ \dot{\Psi} \end{bmatrix}. \end{aligned} \quad (2.8b)$$

Another convention that is frequently used for the modeling of human kinematics is $\{Y, X, Z\}$. The construction of the comprehensive transformation matrix ${}^I R_K$ follows by matrix multiplication of the elementary transformation matrices (2.8a). The distinction between the angular velocity ${}^I \boldsymbol{\omega}_{I}^K$ and the Euler-angle rates $\dot{\varphi}$, $\dot{\Theta}$ and $\dot{\Psi}$ with respect to the reference I is defined in (2.8b), definition similar for ${}^I \dot{\boldsymbol{\omega}}_{I}^K$.

Unified View

The previous techniques only handle the re-orientation of the Cartesian coordinate frame with respect to an orthonormal transformation. However, for a complete kinematic description of the location of any given point in an arbitrary reference frame a little more computational effort has to be invested. Among the various available methods, the relatively popular one is based on projection geometry or so called homogeneous coordinates [Diebel, 2006, Khalil and Dombre, 2002, Siciliano and Khatib, 2007]. This method is frequently found in computer graphics and engineering applications such as the Denavit-Hartenberg Convention [Heimann et al., 2007]. For this purpose the three-dimensional space \mathbb{R}^3 is augmented by a further projection subspace dimension of the field K leading to the basis B ,

$$B = \{w (\mathbf{e}_x, \mathbf{e}_y, \mathbf{e}_z) : w \in K\}, \quad (2.9a)$$

representing a point p as line through the origin with respect to t ,

$$p = \begin{bmatrix} x & y & z & w \end{bmatrix}^T. \quad (2.9b)$$

With respect to the initial three dimensional space this brings the advantage that scaling, rotation and shear operations are combined with translation operations through four dimensional matrix multiplication ${}^B H_A$,

$${}^B H_A = \left[\begin{array}{c|c} {}^A R_B & r_{\text{ref}(B) \rightarrow \text{ref}(A)B} \\ \hline \mathbf{0} & 1 \end{array} \right]. \quad (2.9c)$$

This matrix embeds the previously discussed coordinate transformation ${}^A R_B$ and the translation $r_{\text{ref}(B) \rightarrow \text{ref}(A)B}$ between both reference frames expressed in the target reference. As the usual rules for matrix multiplications apply, concatenation of multiple transformations for position and orientation transformations is possible in a unified method. Re-orientation of frame B through a chain of transformations towards a frame A is obtained from propagation of an identity matrix and estimation of the Euler parameters from the resulting $\mathbb{R}^{3 \times 3}$ matrix block [Khalil and Dombre, 2002].

2.3 Dynamics

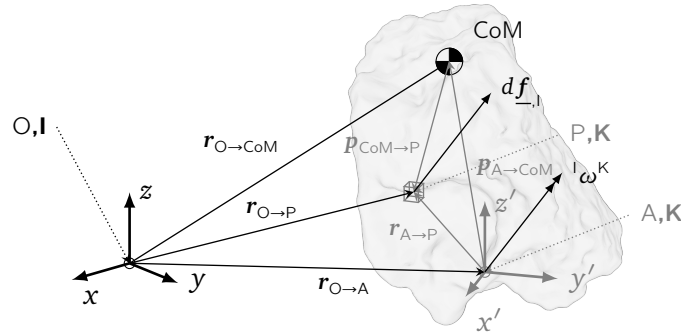


Figure 2.3: Kinematics of a freely moving rigid body. The representation is done based on the fixed global reference frame \mathbf{I} and on the body fixed moving local reference frame \mathbf{K} . All quantities that are fixed with respect to the reference frame \mathbf{I} or \mathbf{K} are drawn in black or gray, respectively. The origin of \mathbf{K} is different from the bodies center of mass (in the following CoM). The body \mathbf{K} is moving with a rotational velocity $\boldsymbol{\omega}$ with respect to the reference \mathbf{I}

Given the free motion of the rigid body, based on its free geometry the focus is now directed towards the determination of the present configuration of external forces. In the following, the rigid body in Figure 2.3 consist of infinitesimal mass elements dm on which an infinitesimal force $d\mathbf{f}$ is acting. From Newton's first two axioms of mechanics the external force configuration on a mass point is bound to the change of its vectorial velocity $\mathbf{f} = m\mathbf{a}$ proportional to its mass being expressed as the temporal derivative of its momentum. Analogously, from [Gross et al., 2004] this aspect can be adopted for a collection of rigidly bound mass points and stated in the form of,

$$\begin{aligned} \mathbf{f}_{,\mathbf{I}} &= \int_{\mathbf{K}} d\mathbf{f}_{,\mathbf{I}} = \frac{\partial}{\partial t} \int_{\mathbf{K}} \dot{\mathbf{r}}_{\mathbf{O} \rightarrow \mathbf{P},\mathbf{I}} dm, \\ &= \frac{\partial}{\partial t} \mathbf{p}_{,\mathbf{I}}, \end{aligned} \quad (2.10a)$$

being the law of linear momentum $\mathbf{p}_{,\mathbf{I}}$ and,

$$\begin{aligned} \mathbf{m}_{,\mathbf{I}}^0 &= \int_{\mathbf{K}} d\mathbf{m}_{,\mathbf{I}}^0 = \int_{\mathbf{K}} \mathbf{r}_{\mathbf{O} \rightarrow \mathbf{P},\mathbf{I}} \times d\mathbf{f}_{,\mathbf{I}} = \frac{\partial}{\partial t} \int_{\mathbf{K}} \mathbf{r}_{\mathbf{O} \rightarrow \mathbf{P},\mathbf{I}} \times \dot{\mathbf{r}}_{\mathbf{O} \rightarrow \mathbf{P},\mathbf{I}} dm, \\ &= \frac{\partial}{\partial t} \mathbf{h}_{,\mathbf{I}}^0, \end{aligned} \quad (2.10b)$$

being the law of angular momentum $\mathbf{h}_{,I}^O$, respectively. In case of the first quantity, the linear momentum, a direct substitution of (2.6c) into (2.10a) and derivation leads to the linear momentum change,

$$\frac{\partial}{\partial t} \mathbf{p}_{,I} = m \left(\mathbf{a}_{O \rightarrow A, I} + {}^I \dot{\boldsymbol{\omega}}_{,I}^K \times {}^I R_K^T \mathbf{r}_{A \rightarrow \text{CoM}, K} + {}^I \boldsymbol{\omega}_{,I}^K \times {}^I \boldsymbol{\omega}_{,I}^K \times {}^I R_K \mathbf{r}_{A \rightarrow \text{CoM}, K} \right). \quad (2.11a)$$

Hence, the linear acceleration of the bodies CoM is directly related to the sum of the forces $\mathbf{f}_{,I}$ acting on the rigid body. For the second quantity, the absolute angular momentum, the substitution of (2.6b) and (2.6c) into (2.10b) breaks the integral into 4 terms,

$$\begin{aligned} \mathbf{h}_{,I}^O &= \int_K \left(\mathbf{r}_{O \rightarrow A, I} + {}^I R_K \mathbf{r}_{A \rightarrow P, K} \right) \times \left(\mathbf{v}_{O \rightarrow A, I} + {}^I \boldsymbol{\omega}_{,I}^K \times {}^I R_K \mathbf{r}_{A \rightarrow P, K} \right) dm, \\ &= \left(\mathbf{r}_{O \rightarrow A, I} \times \mathbf{v}_{O \rightarrow A, I} \right) \int_K dm + \left(\mathbf{r}_{O \rightarrow A, I} \times \right) \int_K \left({}^I R_K \mathbf{r}_{A \rightarrow P, K} \right) dm \\ &+ \underbrace{\int_K \left({}^I R_K \mathbf{r}_{A \rightarrow P, K} \right) dm}_{\int_K \left({}^I R_K \mathbf{r}_{A \rightarrow P, K} \right) dm = m \mathbf{r}_{A \rightarrow \text{CoM}, I}} \times \mathbf{v}_{O \rightarrow A, I} + \underbrace{\int_K \left(\left({}^I R_K \mathbf{r}_{A \rightarrow P, K} \right) \left({}^I R_K \mathbf{r}_{A \rightarrow P, K} \right)^T \right) dm}_{\mathbf{h}_{,I}^A = {}^I R_K {}^I I_{,K}^A {}^I R_K^T \boldsymbol{\omega}_{,I}^K} {}^I \boldsymbol{\omega}_{,I}^K. \end{aligned} \quad (2.11b)$$

Terms $(\cdot \times)$ signify the representation of the skew matrix of the cross product formulated as a skew-matrix vector multiplication. The last two terms contain the local vector to the CoM $\mathbf{r}_{A \rightarrow \text{CoM}, K}$ and the relative momentum $\mathbf{h}_{,I}^A$ with respect to the reference I . The term $I_{,K}^A$ from (2.11b) is the rotational inertia matrix. Its determination based on parameterized flexible geometries will be discussed in subsequent sections. Now the free choice of the reference K is efficiently exploited to simplify the term $I_{,K}^A$ and keep it constant with respect to time. Solution of the integrals, derivation by time and re-arrangement of (2.11b) leads to,

$$\mathbf{m}_{,I}^O = \frac{\partial}{\partial t} \mathbf{h}_{,I}^O = m \mathbf{r}_{O \rightarrow A, I} \times \mathbf{a}_{O \rightarrow \text{CoM}, I} + m \mathbf{r}_{A \rightarrow \text{CoM}, I} \times \mathbf{a}_{O \rightarrow A, I} + \frac{\partial}{\partial t} \mathbf{h}_{,I}^A. \quad (2.12a)$$

From a final substitution of (2.11a) into (2.12a) the expression is reformulated into,

$$\begin{aligned} \mathbf{m}_{,I}^A &= \mathbf{m}_{,I}^O - \mathbf{r}_{O \rightarrow A, I} \times \mathbf{f} = \mathbf{m}_{,I}^O - m \mathbf{r}_{O \rightarrow A, I} \times \mathbf{a}_{O \rightarrow \text{CoM}, I} \\ &= m \mathbf{r}_{A \rightarrow \text{CoM}, I} \times \mathbf{a}_{O \rightarrow A, I} + \frac{\partial}{\partial t} \mathbf{h}_{,I}^A, \end{aligned} \quad (2.12b)$$

with respect of the reference point A . Equation (2.12b) shows some important characteristics. In case the body-fixed reference point A is either a fixed point $\mathbf{a}_{O \rightarrow A, I} = 0$ in space or coincides with the CoM of the rigid body $\mathbf{r}_{O \rightarrow A, I} = 0$, (2.12b) can be simplified further. Equation (2.11a) and (2.12b) are the dynamic equilibrium equations to relate a free motion a given rigid-body to its external torque and force configuration. The motion trajectories of the described rigid body then follows simply from integration of the developed set of differential equations. In most cases these differential equations are complicated and need to be integrated numerically.

Additionally, as soon as a structure of multiple rigid bodies is involved in the motion determination problem, these equations tend to get complex and relatively elaborate, as they provide more information than necessary. However, they are indispensable if one wishes to determine the dynamic equilibrium of a given rigid-body particularly in a structure of multiple bodies

to analyze its internal stress configuration based on externally acting force and torque configuration. For motion determination problems of whole structures specific methods, such as principle of d'Alembert and Lagrange 2nd order [Gross et al., 2004] exist, which will be discussed in sections 3. In this work both methods will be applied to efficiently determine the structural dynamics and to compute the complementary information about the structural stress for a comprehensive mechanical analysis.

3 Multiple Rigid Bodies and Hybrid Dynamics

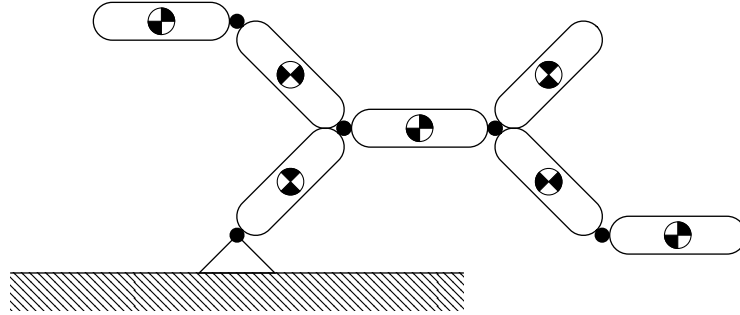


Figure 2.4: Typical tree structure of a multiple rigid body structure. The CoM of each body as well as the joints between the rigid bodies are displayed (black dots).

After all governing quantities of the dynamic equilibrium equations (2.11a) and (2.12b) have been thoroughly discussed in section 1 on page 19 and A on page 218 its exploitation for mechanics of tree structures of multiple rigid bodies is the logical next step towards the algorithmic portfolio that results of the subsequently described optimization studies are based on. A typical tree structure is shown in Figure 2.4. The direct approach to determine the motion of the whole structure would be to formulate (2.11a) and (2.12b) for each body and to solve for all unknowns. However, this would result in $6k$ highly complex equation for k rigid bodies to be solved and hence would not be efficient. Even though each body has a total of 6 global degrees of freedom the complete structure only has a total of n (2.13) degrees freedom with $\dim(Z_i)$ constraint reactions per each joint- (i) and it would be desirable to solve for this usually limited number $n \ll 6k$ of *real* degrees of freedom in a unified scheme, such that development of the differential equations is directly exploitable for computational purposes.

$$n = 6r - \sum_{i=0}^k \dim(Z_i) \quad (2.13)$$

3.1 Spatial Notation Based on Plücker Coordinates

Spatial algebra, a brilliant and highly efficient notation, has been proposed and elaborated for a large number of various mechanical applications by Featherstone [Featherstone, 2006, Featherstone and Orin, 2000, Featherstone, 2007]. Beside the theoretical foundation the reader is referred to [Featherstone, 2010a,b] for a highly understandable, *hands-on* introduction into the topic of *6-D vectors*.

The spatial algebra notation is based on 6D plücker coordinates [Plücker, 1866] and defines a dual basis pair D_A ,

$$D_{O,I} = \{d_{Ox}, d_{Oy}, d_{Oz}, d_x, d_y, d_z\} \subset M^6, \quad (2.14a)$$

on the vector space M^6 for motion and E_A ,

$$E_{O,I} = \{ \mathbf{e}_x, \mathbf{e}_y, \mathbf{e}_z, \mathbf{e}_{Ox}, \mathbf{e}_{Oy}, \mathbf{e}_{Oz} \} \subset F^6, \quad (2.14b)$$

on the vector space F^6 for forces and torques, respectively. The basis D_O defines three elementary rotations \mathbf{d}_{Ox} , \mathbf{d}_{Oy} and \mathbf{d}_{Oz} around the corresponding axes passing through the point O and the translations \mathbf{d}_x , \mathbf{d}_y and \mathbf{d}_z of the reference point O , respectively. The resulting motion vector $\hat{\mathbf{v}}_O$,

$$\hat{\mathbf{v}}_{O,I} = \omega_x \mathbf{d}_{Ox} + \omega_y \mathbf{d}_{Oy} + \omega_z \mathbf{d}_{Oz} + v_{Ox} \mathbf{d}_x + v_{Oy} \mathbf{d}_y + v_{Oz} \mathbf{d}_z, \quad (2.14c)$$

then describes the linear and rotational velocity flow of body particles that happen to coincide with the reference point O at the current instant in time. From this information, $\hat{\mathbf{v}}_A$ based on (2.5), the velocity configuration for any given point of the same rigid body P is then obvious [Featherstone, 2006, Gross et al., 2004]. Analogously, one may construct a dual basis $E_{O,I}$ (2.14b) in F^6 to $D_{O,I}$. Besides the reference point $\mathbf{1}$, $\mathbf{2}$ is outlined separately to mark the orientation of the basis $E_{\mathbf{1},\mathbf{2}}$ with respect to a specific coordinate frame. The basis $E_{O,I}$ describes the three elementary torques \mathbf{e}_x , \mathbf{e}_y and \mathbf{e}_z about the corresponding axis at the reference point O and three elementary forces \mathbf{e}_{Ox} , \mathbf{e}_{Oy} and \mathbf{e}_{Oz} acting on a line through O , respectively. The resulting force vector $\hat{\mathbf{f}}_O$,

$$\hat{\mathbf{f}}_{O,I} = m_{Ox} \mathbf{e}_x + m_{Oy} \mathbf{e}_y + m_{Oz} \mathbf{e}_z + f_x \mathbf{e}_{Ox} + f_y \mathbf{e}_{Oy} + f_z \mathbf{e}_{Oz}, \quad (2.14d)$$

then describes the force configuration about a line passing through O and a torque configuration at the reference point O of the rigid body. Let $\hat{\mathbf{f}}_O$ be the torque and force configuration at O from the first term of (2.12b). Then, the force and torque configuration of the rigid body about any given point A is obvious [Featherstone, 2007, Gross et al., 2004]. Basis transformations from a frame and reference point I,O to another K,P are expressed with ${}^{A,K}X_{O,I}$ and ${}^{A,K}X_{O,I}$ for M^6 and F^6 , respectively. From this observation the vectors $\hat{\mathbf{v}}_O$ and $\hat{\mathbf{f}}_O$ are established from their Cartesian counterparts of torque $\mathbf{m}_{\mathbf{I}}^O$, force $\mathbf{f}_{\mathbf{I}}$, linear velocity $\mathbf{v}_{O,I}$ and the rotational velocity ${}^1\boldsymbol{\omega}_{\mathbf{I}}^K$, respectively, by a simple basis transformation [Featherstone, 2006]. Derivatives of the vectors $\hat{\mathbf{v}}_O$ and $\hat{\mathbf{f}}_O$ are defined analogously to (2.3c) [Featherstone, 2006] employing the basis (2.14a) towards,

$$\left(E_{O,I} \right)^{-1} \dot{\hat{\mathbf{f}}} = \underbrace{\left(E_{O,I} \right)^{-1} \dot{E}_{O,I}}_{=\hat{\mathbf{v}}_O \times^*} \hat{\mathbf{f}}_{\mathbf{I}} + \dot{\hat{\mathbf{f}}}_{\mathbf{I}}, \quad (2.15a)$$

and (2.14b) towards,

$$\left(D_{O,I} \right)^{-1} \dot{\hat{\mathbf{s}}} = \underbrace{\left(D_{O,I} \right)^{-1} \dot{D}_{O,I}}_{=\hat{\mathbf{v}}_O \times} \hat{\mathbf{s}}_{\mathbf{I}} + \dot{\hat{\mathbf{s}}}_{\mathbf{I}}, \quad (2.15b)$$

respectively. Basically, the derivation is done in a moving basis. The point O has a velocity and thus $D_{O,I}$ is dependent on time. However, this *motion*, indirectly related to the geometric motion of the reference frame, is described from the linear velocity $\hat{\mathbf{v}}_{O,I_{\text{lin}}} = \begin{bmatrix} 0 & \mathbf{v}_{O,I} \end{bmatrix}^T$ of

the reference point O . The correct interpretation of,

$$\begin{aligned}
 (D_{O,I})^{-1} \dot{\hat{\mathbf{v}}} &= \dot{\hat{\mathbf{v}}}_{O,I} + \hat{\mathbf{v}}_{O,I|lin} \times \hat{\mathbf{v}}_{O,I} \\
 &= \begin{bmatrix} \dot{\underline{\boldsymbol{\omega}}}_{,I} \\ \dot{\underline{\mathbf{v}}}_{O,I} \end{bmatrix} + \begin{bmatrix} \mathbf{0} \\ \underline{\mathbf{v}}_{O,I} \end{bmatrix} \times \begin{bmatrix} \underline{\boldsymbol{\omega}}_{,I} \\ \underline{\mathbf{v}}_{O,I} \end{bmatrix}, \\
 &= \begin{bmatrix} \dot{\underline{\boldsymbol{\omega}}}_{,I} \\ \ddot{\underline{\mathbf{r}}}_{O,I} \end{bmatrix} + \begin{bmatrix} \mathbf{0} \\ \dot{\underline{\mathbf{r}}}_{O,I} \times \underline{\boldsymbol{\omega}}_{,I} \end{bmatrix}
 \end{aligned} \tag{2.16}$$

is as difficult as it is important for the following discussions. As soon as, the relative position of O as r is re-defined with respect to a fixed datum the coordinate vector entries $\underline{\mathbf{v}}_{O,I}$ and $\dot{\underline{\mathbf{v}}}_{O,I}$ reflect the vector values $\dot{\underline{\mathbf{r}}}_{,I}$ and $\ddot{\underline{\mathbf{r}}}_{,I}$, respectively. With $\dot{\hat{\mathbf{v}}}_{O,(...)}$ being the spatial acceleration and a suitable basis $C_{(...)}$ in the Cartesian space, these values reflect the quantities of the classical acceleration $a_{O,(...)}$ and velocity $v_{O,(...)}$ of the point O [Featherstone, 2006, 2007]. This relation expresses the difference between the spatial and the classical acceleration to be intensively exploited for the definition of contacts and kinematic loops in subsequent discussions.

With this highly compact notational toolbox the dynamic equilibrium equations (2.11a) and (2.12b) are expressed with respect to any given reference point A and orientation equal to the frame \mathbf{K} in one unified 6D equation,

$$\sum \hat{\mathbf{f}}_{A,K} = \hat{I}_{A,K} \hat{\mathbf{a}}_{A,K} + \hat{\mathbf{v}}_{A,K} \times^* \hat{I}_{A,K} \hat{\mathbf{v}}_{A,K}, \tag{2.17a}$$

employing the spatial inertia,

$$\hat{I}_{A,I} = \begin{bmatrix} I_{CoM,K} + m_K r_{A \rightarrow CoM,K} \times (r_{A \rightarrow CoM,K} \times)^T & m_K r_{A \rightarrow CoM,K} \times \\ m_K (r_{A \rightarrow CoM,K} \times)^T & m_K I \end{bmatrix}. \tag{2.17b}$$

The terms $(\cdot) \times$ and $(\cdot) \times^*$ follow from the definition in (2.15b) and (2.15a), respectively (see [Featherstone, 2010a,b] for more information). The spatial inertia contains a construction of the classical inertia matrix $I_{CoM,K}$, from Section A on page 218, with respect to the body's CoM, combined with the Parallel Axis Theorem, from Section 1.4 on page 221.

The initial equations are simply recovered evaluating the expression (2.17a) together with (2.16) to solve for the classic acceleration. Henceforth, the classical representation is dropped for the spatial one. With a simple and unified notation at hand an efficient method to solve for motion of multiple rigid-body tree-structures, such as in Figure 2.4, will be explored.

3.2 Principle of D'Alembert

Let \mathbf{K} be a rigid body that moves along a given path $\mathbf{x}(\mathbf{q}) \in \mathbb{R}^6$ that is solely described on a given number of independent parameters $\mathbf{q} \in \mathbb{R}^n$, then X defines a set of holonomic and skleronomic motion constraints. In the following, this set of independent parameters will be called *minimal set of coordinates*. The constraints set, is called rheonome with a dependencies to time or non-holonomic with dependencies to higher order derivations of the coordinate vector with respect to time, e.g. refer to [Wieber, 2000]. With the focus again back on equation (2.17a), one may as well state the equation as a spatial force balance,

$$\sum_i \mathbf{f}_i = \mathbf{f}^e + \mathbf{f}^c + \mathbf{f}_T, \tag{2.18a}$$

featuring the external forces \mathbf{f}^e , the forces based on the constraint set \mathbf{f}^c and a virtual force based on the inertia effects \mathbf{f}_T ,

$$\mathbf{f}_T = -I\mathbf{a} - \mathbf{v} \times^* I\mathbf{v}. \quad (2.18b)$$

With the virtual displacement $\delta \mathbf{r}$,

$$\delta \mathbf{r} = \begin{bmatrix} \delta s_x(\mathbf{q}) & \delta s_y(\mathbf{q}) & \delta s_z(\mathbf{q}) & \delta s_{Ox}(\mathbf{q}) & \delta s_{Oy}(\mathbf{q}) & \delta s_{Oz}(\mathbf{q}) \end{bmatrix}^T = J(\mathbf{q}) \delta \mathbf{q}, \quad (2.19)$$

definition of virtual work quantities,

$$\delta W^e + \delta W_T + \delta W^c = (\mathbf{f}^e - I\mathbf{a} - \mathbf{v} \times^* I\mathbf{v}) J(\mathbf{q}) \delta \mathbf{q} = 0, \quad (2.20a)$$

for the constraint reactions,

$$\delta W^c = (\mathbf{f}^c)^T J(\mathbf{q}) \delta \mathbf{q} = 0, \quad (2.20b)$$

the external forces,

$$\delta W^e = (\mathbf{f}^e)^T J(\mathbf{q}) \delta \mathbf{q}, \quad (2.20c)$$

as well as the virtual inertia force,

$$\delta W_T = (\mathbf{f}_T)^T J(\mathbf{q}) \delta \mathbf{q}, \quad (2.20d)$$

are possible. The principle of *d'Alembert* [Gross et al., 2004] then states that the motion constraint reactions and the motion direction are always orthogonal (2.20b). From the principle of virtual work the rigid body must always move in concert with the balance (2.20a) between the virtual work of the external forces (2.20c) and the virtual inertia forces (2.20d).

This principle is directly transferable to a tree structure of stiff linked rigid bodies (see Figure 2.4), which is adoptable as good approximation for all modeling examples that will be discussed in subsequent chapters. Furthermore, the expression from (2.20a) is then re-arranged to feature a kinetic energy term E_{kin} and a term E_{pot} , resulting from a flux-free potential field, to describe a set of differential equations for each existent degree of freedom. The resulting scheme is easily exploitable for computational purposes. The resulting equations are called the *Second Order Lagrange's Equations* that are developed through an easy scheme from the *Lagrange Function* L ,

$$L = E_{kin} - E_{pot}. \quad (2.21a)$$

The development of the differential equations for all minimal coordinates is conducted following,

$$\frac{\partial}{\partial t} \left[\frac{\partial}{\partial \dot{\mathbf{q}}} L \right] - \frac{\partial}{\partial \mathbf{q}} L = \sum_{l=0}^{f_{\text{external}}} J_l^T \mathbf{f}_l^e. \quad (2.21b)$$

After substitution of all terms and careful arrangement the final set of differential equations results in,

$$M(\mathbf{q}) \ddot{\mathbf{q}} + N(\dot{\mathbf{q}}, \mathbf{q}) = \boldsymbol{\tau}. \quad (2.21c)$$

This set of equations then features the joint space inertia matrix,

$$M(\mathbf{q}) = \sum_{i=0}^{n_{\text{Bodies}}} (J_i^T I_i J_i), \quad (2.21d)$$

the joint space nonlinear effects including the gravity-term,

$$N(\dot{\mathbf{q}}, \mathbf{q}) = \sum_{i=0}^{n_{\text{Bodies}}} J_i^T \left(I_i \left(\sum_{j=0}^{n_{\text{dofs}}} \frac{\partial}{\partial \mathbf{q}} J_j \frac{\partial \mathbf{q}}{\partial t} \dot{q}_j \right) - \dot{\mathbf{q}}^T J_i^T \times I_i J_i \dot{\mathbf{q}} \right) + \sum_{i=0}^{n_{\text{Bodies}}} J_i^T I_i \mathbf{a}_g, \quad (2.21e)$$

as well as the generalized forces,

$$\boldsymbol{\tau} = \sum_l^{f_{\text{external}}} J_l^T \mathbf{f}_l^e. \quad (2.21f)$$

Correspondant results are found in [Chardonnet, 2009, Featherstone, 2007, Wieber, 2000].

3.3 Hybrid Dynamics: Contacts and Kinematic Loops

The complex whole-body optimization problems that will be discussed in the subsequent chapters are about bipedal locomotion, being a complex, highly dynamic motion in Cartesian space (compare Section 1 on page 1) featuring emerging and vanishing complex contact conditions with the external environment, collisions, friction etc. - hence, the pure dynamic model should be extended to reflect these characteristics.

The OCP formulations presented in this work are closely related to the domain of dynamic simulation. However, it is important to note that the employed optimization method requires a technical representation that substantially differs from a dynamic simulation (e.g. based on forward integration). The system is simulated based on its governing physics. Switches of the dynamic configuration and discontinuous transitions occur at previously unknown instants in time. However, the sequence of these switches is assumed to be known before-hand. A further basic requirement is that all model evaluations, be it continuous with respect to a given dynamic configuration or discontinuous during a transition, need to be continuously differentiable with respect to their dependent model parameters [Mombaur, 2001]. The governing mathematical constraints that actually lead to this reasoning will be presented in the subsequent Chapter 4. However, the following modeling decision should be considered within this context. The equation,

$$M(\mathbf{q}) \ddot{\mathbf{q}} + N(\dot{\mathbf{q}}, \mathbf{q}) + (J_{\text{uni}}(\mathbf{q}))^T \boldsymbol{\lambda}_{\text{uni}} + (J_{\text{bi}}(\mathbf{q}))^T \boldsymbol{\lambda}_{\text{bi}} = \boldsymbol{\tau}, \quad (2.22a)$$

$$\mathbf{c}_{\text{uni}}(\mathbf{q}) \geq 0, \quad \boldsymbol{\lambda}_{\text{uni}} \geq 0, \quad (\mathbf{c}_{\text{uni}}(\mathbf{q}))^T \boldsymbol{\lambda}_{\text{uni}} = 0, \quad (2.22b)$$

$$\mathbf{c}_{\text{bi}}(\mathbf{q}) = 0, \quad r(t, \mathbf{q}) \leq 0, \quad (2.22c)$$

shows the default Lagrangian form of a dynamic equation under unilateral constraints (2.22b) and bilateral constraints (2.22c) with an activation function $r(t, \mathbf{q})$.

Bilateral versus Unilateral Contact Modeling

As discussed in Section 1 on page 1 a natural characteristic of bipedal locomotion is the unilateral contact of the foot with the ground. The foot-ground contact is only active as long as the

foot touches the ground. Hence, the foot does not stick but immediately lifts as soon as the pressure force in the ground-contact vanishes. From the vast and comprehensive literature review about simulations of dynamic systems under contacts in [Brogliato et al., 2002], the principle question are then - how should this contact be technically modeled in the context of the optimal control problem formulation? - how are complex contact configurations, such as pivoting or hinging with respect to a complex parametrized geometry are expressed in a simple and unified way?

Following [Brogliato et al., 2002] the uni-lateral contact condition implies changes on the contact configuration upon appearance or disappearance of a single contact. Imagine for example a simple cube dynamically tumbling over corners and edges. The detection of the events is done with resolution of the detachment conditions (Delassus problem), which leads in the simplest case to a linear, for more complex contact modeling to a nonlinear complementary problem. The vast diversity of the different formalisms to solve these Linear Complementary Problems (LCPs) or Nonlinear Complementary Problems (NCPs) is outside of the scope of this discussion. In direct comparison, the bilateral contact formulation leads to a pure Differential Algebraic Equation (DAE).

The numerical solution of this DAE is efficiently done based on index reduction and forward integration equivalent to an Ordinary Differential Equation (ODE) with respect to consistent initial conditions. Usually, for correct integration of the DAEs with respect to the algebraic consistency equation, some sort of numerical stabilization is necessary. The most popular for engineering applications is the *Baumgarte's Stabilization* [Ascher et al., 1994]. Other techniques that need less tuning, but provide more complexity are, e.g. state-space formulations and projection methods (refer to [Brogliato et al., 2002]). While methods exist to integrate the prevention of consistency violation closely with the forward integration of the DAE for bilateral constraints, numerical treatment of a system based on unilateral constraints is relatively complex. The quality of the solution highly depends on the correct discretization of the LCP contained in the constrained dynamic system formulation [Brogliato et al., 2002].

Besides the necessary numerical efforts arising from the unilateral contact formulation, full control over the temporal structure of the contact configurations is essential for the employed optimization problem formulation. In the following, both, 1 bilateral and unilateral contacts, are modeled as bilateral contacts adding further constraints to enforce the physical correctness of the resulting motion. In that sense, suppression of sliding as well as management of collisions as contact-events (touch-down) and detachments (lift-off) of contacts in a fixed sequence order was then modeled based on an appropriate constraint set (refer to Section 3 on page 236 for complementary information about the expression of surface contacts).

From simple checks of forward integration on the typical time horizons $\sim 1-5s$ used for most of the optimization problem formulations, numerical accuracy was considered sufficient. Even without explicit stabilization, the dynamic contact modeling was implemented as pure indexed reduced DAE to further simplify the model and use the available standard integration techniques.

Compliant versus Rigid Contact Modeling - Collision

A clear distinction of contact models into rigid and compliant modeling is included in [Brogliato et al., 2002, Chardonnet, 2009, Wieber, 2000]. As stated in [Brogliato et al., 2002] decision about the former or the latter is in most cases a tedious trade-off between model simplicity, simulation horizon and desired accuracy of selected resulting quantities of the simulation.

The compliant modeling employs a spring-damper equivalent arrangement to simulate elastic deformation. Different approaches exist to express the modeling related to geometric contact

phenomena, global or local deformation e.g. Hertz [Hertz, 1882]. Control over its physical parameters is achieved by damping and stiffness parameters. However, the identification of generally realistic parameters is problematic and especially for contacts with higher stiffness, further efforts on tuning the numerical integration (e.g. using implicit methods) is essential to maintain the quality of the resulting trajectory. Especially for high number of contacts this might result into high computation times [Brogliato et al., 2002].

From the point of physical modelization the rigid contact modeling is the worst, however, simplest approach, as it does not track the force trajectory during the impact, but just its impulsive value and its related discontinuities of the motion velocities. Furthermore, it suffers from the issue of hyperstaticity, which mathematically results in a rank-deficiency of J_{bi} or J_{uni} in (2.22a) and feature non-unique solutions for the Lagrange multiplier λ_{un} and λ_{uni} . Parametrization of its physical characteristics is achieved with the Parameter of Restitution (PoR)² to control its dissipative and vibrational behavior during collisions. From experience [Brogliato et al., 2002] this modeling scheme is highly tractable to analyze a given system on a global scale, if the focus is not set on high accuracy of the simulation of the collision behavior.

As the purpose of the following work is to assess the whole body dynamics of bipedal walking tasks, decision was made to keep the modeling of the local contacts as simple as possible and to avoid hyperstaticity (compare to [Saab et al., 2011]). Consequently, the rigid contact modeling with restitution of $e = 0$ being perfectly inelastic was adopted during the remainder of this work.

Mathematical Formulation

The final index reduced DAE for one contact point follows to,

$$M(\mathbf{q})\ddot{\mathbf{q}} + N(\dot{\mathbf{q}}, \mathbf{q}) + (\hat{J}(\mathbf{q}))^T \left({}^K\hat{X}_{\text{Contact}}^M \right)^{-T} \hat{S}^T \hat{\boldsymbol{\lambda}} = \boldsymbol{\tau}, \quad (2.23a)$$

$$\hat{S}^K \hat{X}_{\text{Contact}}^M \hat{J}(\mathbf{q})\ddot{\mathbf{q}} + \hat{S}^K \hat{X}_{\text{Contact}}^M \hat{\boldsymbol{\gamma}}(\dot{\mathbf{q}}, \mathbf{q}) + \hat{S} \begin{bmatrix} \mathbf{0} \\ {}^I\boldsymbol{\omega}_{\text{Contact}} \times \mathbf{v}_{\text{Contact}} \end{bmatrix} = \mathbf{0}. \quad (2.23b)$$

The contact collision is written, following [Featherstone, 2007] as,

$$M(\mathbf{q}) (\dot{\mathbf{q}}^+ - \dot{\mathbf{q}}^-) + (\hat{J}(\mathbf{q}))^T \left({}^K\hat{X}_{\text{Contact}}^M \right)^{-T} \hat{S}^T \hat{\boldsymbol{\Lambda}} = \mathbf{0}, \quad (2.24a)$$

$$\hat{S}^K \hat{X}_{\text{Contact}}^M \hat{J}(\mathbf{q}) (\dot{\mathbf{q}}^+ e + \dot{\mathbf{q}}^-) = \mathbf{0}. \quad (2.24b)$$

Spatial quantities are marked with a hat. At this point an important advantage of the spatial notation becomes obvious. The contact equations (2.23b) and (2.24b) are easily transformable to any given local reference frame (rigid body) with the contact point as origin. By application of a further unitary selection matrix \hat{S} revolute and translational degrees of freedom with respect to the local coordinates frame axes can be selected or deselected for the rigid contact model [Featherstone, 2007].

Based on this formalism any complex hinge, pivot and prismatic contact model is conveniently realizable by simple re-configuration of the transformation matrix ${}^K\hat{X}_{\text{Contact}}^M$ and the selection matrix \hat{S} . The contact model is defined with respect to the local reference frame of the moving rigid body. The follows for the physical representation of the Lagrange multipliers $\hat{\boldsymbol{\lambda}}$ and $\hat{\boldsymbol{\Lambda}}$, being the torques, forces and angular and linear collision impulse arising from the mechanical

²In this thesis the PoR is denoted e , refer to equation (2.24b).

interaction in the contact point, respectively. With respect to the global frame the local 6D-contact model bears the numerical convenience of being singularity-free, which is not the case for globally expressed 3D-point contact models. From experience with a vast number of trials for the underlying optimization problem formulation, this is a highly valuable improvement for the globalization quality of the model. Thus, even when started from initial conditions that are physically infeasible or far away from the anticipated result the model computes physically reasonable values, which helps to initialize the optimization computation far from the final solution. Furthermore, this contact model formulation is not exclusively limited to holonomic constraints. Thus, re-formulation of the rigid contact model enables as well the expression of momentum pole-based rolling motions on surfaces.

Kinematic loops are handled over strictly the same contact notation. The general scheme is outlined in [Featherstone, 2007, Khalil and Dombre, 2002]. The model-structure is first implemented with all loops cut open. Then, loops are successively closed over rigid-contact models. In the remainder of this work the non-redundant re-parametrization from [Featherstone, 2007] to a new set of minimal coordinates is dropped, to keep the model description technically consistent through the complete optimization problem setup.

4 Concluding Remarks

In this chapter, the necessary aspect for the mechanical modeling of rigid multiple body tree structures have been discussed. For the sake of clarity the context of this chapter was reduced to the scope necessary to support the following technical discussion about optimal control and dynamic algorithms. However, the conducted modeling in the subsequent parts of this work refer to more realistic and hence elaborate formulations, being out of the scope of this part and thus have found there place in the Appendix.

The reader is referred to Appendix A on page 218 for methods to compute the dynamic characteristics of single rigid bodies with free forms. Appendix B on page 230 gives a review of the modeling of technical components, such as electric motors, dynamics of gearbox and common physical phenomena, such as friction and hyper-static surface contacts.

3 *DYNAMOD* - Efficient Mechanical Modeling

After the essential aspects of the mechanical modeling have been thoroughly discussed, the final question is how to implement the complete formalism in a highly flexible, accessible and testable construction, that further allows direct exploitation of third party tools for pre- and post-processing, e.g. establishment of initial values, visualization [Felis, 2014a], simulation and dynamic verification [Hirukawa et al., 2003]. As the formulation of the dynamic equations for such complex systems is simply out of question, it is important to state clearly why building a new tool from scratch was worth the effort, despite the various mature solutions in spatial notation [Felis, 2014b, Naveau et al., 2014] and classic 3D mechanics [Saab et al., 2011, Wieber et al., 2006, Yoshida et al., 2008] that are already successfully in use in different laboratories.

The resulting tool has been inspired from the dynamic software package *HuMAnS* [Wieber et al., 2006] and performs symbolic computations based on the commercial third party package Maple™ [Char et al., 1983] and the spatial notation from R. Featherstone [Featherstone, 2006, 2007] to establish a highly optimized and comprehensively parametrized dynamic model representation for efficient computation in optimal control. The contributions incorporated into this software are:

- Controlled build process, tracking of dependencies for re-active and safe code manufacturing [Martin and Hoffman, 2007] (see Section 2.1 on page 36)
- Clear separation of common and model related code (see Section 2 on the facing page)
- Compatibility with popular model description formats (see Section 2.1 on page 36 and Section 2.2 on page 37)
- Code quality supported by various automatic self-checks, test builds, cross-checks to external tools, e.g. *RBDL* [Felis, 2014b], and benchmark procedures (see Section 2.1 on page 36 and 2.3 on page 39)
- Highly efficient symbolic model representation based on 6D spatial notation [Featherstone, 2006] (see Section 2.2 on page 37)
- Extended contact modeling [Brogliato et al., 2002, Featherstone, 2006] (see Section 2.2 on page 37 based on Section 3.3 on page 30)
- Extended access to model characteristics (see Section 2.2 on page 37)
- Easy access to full parametrization of all model characteristics (see Section 2.2 on page 37)

1 Development

Initial development was based on the *HuMAnS*-Toolbox [Wieber et al., 2006]. However, during various optimization studies, different issues came into existence. These issues notably

were found as well among other tools and finally lead to the decision to re-base the development on a new, but compatible framework, with respect to the existing packages. A small summary is given below:

1.1 Accessibility & Testability

Confidence in a code portion of a given package is a highly valuable aspect that, by experience, seems to be frequently underestimated by its architects. In most cases code portions are written with a clear purpose in mind. In case this initial purpose was not explicitly stated in the documentation, re-use by any third person not directly involved in the initial development, bears the risk that a given portion is applied for different purpose it was originally targeted for. In most cases this is unproblematic as the formalism in the given code portion is not brought to its limits. However, as soon as any given code portion is part of an optimal control problem formulation the context is different. By experience this case requires high precision and a well defined behavior in the limits of the code governing formalism to efficiently support convergence of the embracing optimization algorithm. This essential level of code quality requires thorough and frequent testing during the integration, which is difficult to achieve with a reasonable amount of coding effort in case the code has not been written with explicitly this purpose in mind.

1.2 Monolithic versus Modular, Code Base & Configuration:

is an important decision, that has to be considered in the early stage of the development. From the large variety of functionality that needs to be implemented the KISS-principle [Rich, 1995] clearly suggests that a modular structure of small autonomous units, should be always preferred over huge and complex monolithic structures. Though, using different tools, each for a small and well defined purpose, subsequently combined together is the strategy that was adopted during the creation of this package. However, as the previous section suggested the combination of tools from different sources always led to the case of an inhomogeneous code base and a non centralized source of information, such as the model kinematics, dynamics, joint characteristics or self-collision data.

1.3 Conclusion

Although, the code development started with a clear strategy about a modular structure in mind and mostly relying on external software packages, the code base continuously underwent massive structural manipulation, keeping its modularity but introducing rigorous automatic testing. Consequently, functionality of non-conform external packages, with respect to numerical requirements for the embracing optimization algorithm, was replaced against specifically tailored self written code portions. Some modules of this code base grouped together to form the symbolic dynamic processor *DYNAMOD* which will be briefly outlined in the following.

2 Structure and Configuration

As it was previously explained *DYNAMOD* is a group of modules (similar to [Wieber et al., 2006]) that were regrouped from a larger code base and as such, it is not able to work autonomously as to other dynamic packages for example [Felis, 2014b, Naveau et al., 2014]. Thus, the common use-case, model-description goes in at one side and the finally processed dynamics comes out at the other side, does not work. The tool was conceived with different

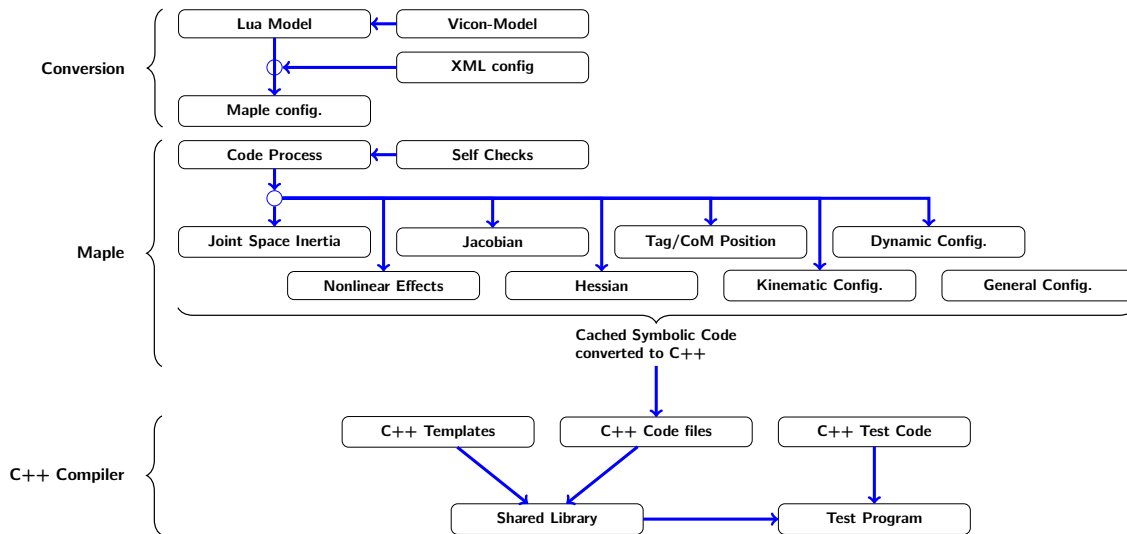


Figure 3.1: Structure of DYNAMOD - during the model build process

purposes in mind. Among those was for example the investigation of forward versus inverse dynamics application in optimal control for motion generation. Consequently, the tool processes a dynamic model description from a monolithic source and produces a generic code set. This code set then gives direct access to the dynamic information in a format to support efficient dynamic computations. The algorithms to conduct these dynamic computations are explicitly not part of this package, e.g. solution of the DAE-System and Contact-Model manipulations. They are part of the comprehensive code base, however, kept in a different module as for the previously discussed reasons (compare Chapter 5). Thus, integration of a model still requires a higher amount of interface code to be written explicitly for one model. From the experience that each model is highly specific with respect to the targeted problem formulation, this decision reveals as a reasonable trade-off. This trade-off arises between the flexibility of the model formulation, compared to the technical constraints that would result from a common interface formalism, and code-recycling as well as separation between common code that is used among all models during the model-building and model-specific code that explicitly remains inside the model block (where it belongs).

2.1 The Model Build

The package *DYNAMOD* is based on MapleTM [Char et al., 1983] (for symbolic representation of the model dynamics), Extensible Markup Language (XML) (for static configuration files), *xdkwrl* [D ecoret, 2003], Lua [Ierusalimschy et al., 2006] (for a unified model configuration syntax - compare [Felis, 2014a]), *SymbolicC++* [Hardy et al., 2008] (for internal symbolic computations), *Boost* and *Eigen* [Guennebaud et al., 2010] (for computations of linear algebra). The main language is *C++* and the build process is controlled using the tools *bash*, *cmake* [Martin and Hoffman, 2007] and the underlying *make* program for auto-tracking of changes and dependencies in the common and model related code base, such that only relevant portions are rebuild on re-factoring.

Figure 3.1 shows the structure of the model process. A model description in Lua or another semantic (basic support exists for Vicon models, Virtual Reality Modeling Language (VRML) and Unified Robotic Description (URDF) are in preparation but not yet finished) will be first converted to a Lua model and then into a configuration file format compatible to *HuMANs* [Wieber

et al., 2006]. The XML file contains configuration parameters that are common to the symbolic representation but may not be used in the Lua-based model description. After a quick self-check of all relevant code snippets and the formalism of the model, the processor begins to explore the model and writes a symbolic model representation of the kinematics, the contact model description and dynamics. The symbolic expressions are cached for equivalent expression to minimize arithmetic effort, converted to C++ code and written into separate source files, with an additional header. This header file is then combined with the model specific interface code in form of templates, configured and build into a shared library. In parallel, model specific template based test code is configured in a separate build instance and combined with the shared library into a test executable which is run on per request-base to confirm correct operation of the model library.

The package itself provides an automatic bootstrap script for the common code base to be prepared, tested and installed into a desired prefix, including environment configuration to assist subsequent builds of related model code projects. On demand the script runs further generic test builds, cross-checks and benchmark procedures to check integrity of the common code base.

2.2 Symbolic Representation

An important contribution of [Wieber et al., 2006] that has considerably been improved, is the parametrization of the model description and access to all characteristics of the symbolic model description. As it was common in [Wieber et al., 2006], one could distribute parameters in the symbolic model description. These parameters then survived the build-process and where then found in the resulting C-Code of the model. However, the resulting files then had to be prepared manually to render access to these parameter during its integration into the problem formulation. A tedious and error-prone process.

Contributions to the Existing Formalism

As in *HuMANs* [Wieber et al., 2006], the model description is separated into three different categories: Kinematics, Dynamics and Additional. Although, the description syntax was kept compatible to the semantics of *HuMANs* [Wieber et al., 2006] important changes in the interpretation occurred that should be outlined in the following. Example of a full configuration set is given in the Appendix F.

Kinematics: The tree structure of the dynamic model without loops (compare Figure 2.4) is described on a per frame base giving translations and rotations in Euler cardan convention based on the homogeneous coordinate (2.9a) representation (compare Section 2.2 on page 23). The type of the joint is configured with special parameters for degrees of freedom that are included into the symbolic representation where necessary. Contributed features for the model kinematics are:

- Parent to child linker for recursive model exploration
- Frame identification by name and index
- Parametric velocity masks [Featherstone and Orin, 2000] description of joints
- Full parametric description of location, spatial 6D velocity and acceleration

Dynamics: The dynamic description on per frame basis has been kept essentially the same as in *HuMANs* [Wieber et al., 2006]. Besides the CoM with respect to the local reference frame, the inertia with respect to the CoM in the local reference frame and the mass of each body, the transmission ratio and the rotor-inertia (of each motor) as been

added (compare Section 1 on page 230) to allow for dynamic couplings of the simplified gearbox-effects. The dynamic effects of the gearboxes are not directly added to the inertia matrix but provided in vector-form for further manipulations. This particularly supports debugging purposes of the complex nonlinear implications on the comprehensive model dynamics. Contributed features of the dynamic representation are:

- Fully parametrized, simplified gearbox effects
- Parametric angular and linear momentum and its first derivation for each frame, respectively
- Parametric CoM position with respect to the global and local reference frame, respectively
- Computation of parametric 6D spatial inertia matrix with respect to each local reference frame

Additional: A distinct feature of the *HuMANs*-Package [Wieber et al., 2006] is the computation of global point positions as well as its first and second derivation with respect to the global reference frame. This information was mainly subject to use for 3D point contact modeling and motion re-targeting purposes. In *DYNAMOD* the notion of tag positions has been maintained for compatibility purposes. The contact modeling, however, was re-based on 6D spatial notion and referenced to the local frame. As from Section 3.3 on page 30 it is obvious that any contact interface can be re-formulated from the 6D spatial Jacobian-Matrix \hat{J} and the Hessian-Vector $\hat{\gamma}$ of the local reference frame with a spatial transformation. The computation of explicit point Jacobian-Matrices are not necessary any more and can be skipped for computational performance. Consequently, the contact selector has been re-formulated to compute explicit Jacobian-Matrices and Hessian-Vectors for each local reference frame in which a contact definition is desired.

- Identification of tags on per name and index basis.
- Selective computation of parametric contact Jacobian-Matrix and Hessian-Vector per desired reference frame for 6D spatial contact modeling
- Computation of parametric tag positions with respect to local and global reference frame, respectively

Algorithmic Representation

On one hand from an algorithmic point of view it would have been most desirable to represent the quantities $M(\mathbf{q})$, $N(\dot{\mathbf{q}}, \mathbf{q})$ in the form (2.21d) and (2.21e) (compare Section 2.20a). On the other hand, the recursive caching that is applied to all subsequent symbolic operations to optimize for a minimum arithmetic expressions to be performed in the resulting C-Code would prefer a recursive representation during the establishment of the generic code base, as the caching process then would translate simply as a further operation to be applied in each step.

Consequently, symbolic representation of the joint space inertia matrix $M(\mathbf{q})$ was based on the *Composite Rigid Body Algorithm* (in the following Composite Rigid Body Algorithm (CRBA)) and the *Recursive Newton Euler Algorithm* (in the following Recursive Newton Euler Algorithm (RNEA)) as described in [Featherstone, 2010a,b, Featherstone and Orin, 2000]. The representation of the Jacobian-Matrix $J(\mathbf{q})$ of the local reference frame was implemented as accumulation and transformation of velocity masks and the Hessian-Vector $\gamma(\dot{\mathbf{q}}, \mathbf{q})$ as accumulation of its resulting cross terms [Featherstone, 2010a,b, Featherstone and Orin, 2000].

Testing

The complete package is subject to thorough pre- and post checks during the model build process to confirm consistency of the model description and resulting symbolic model representation. A huge convenience of the symbolic representation is that consistency checks are possible symbolically and numerically. The common strategy is to compute the quantity to verify based on a symbolic representation following two different methods and compare the resulting expressions. The same is then applied by substituting randomized numerically values.

Framework Tests: These checks are applied, before each run of the model processor, for all elements of the spatial notation, the 3D classic and 4D homogeneous transformations as well as the C-Code conversion functionality, to confirm integrity of the framework prior to model processing.

Model Tests: Verification of the integrity of the model representation is divided into two categories. Common model checks and model specific consistency checks, e.g. of the interface code that belongs to a certain model. The common model checks exist as an annexe module that is invoked during bootstrap for fully parametric models and models arising from a common Lua-Model representation. The tests are implemented as numerical random sampling tests. The following quantities are subject to verification.

- All provided components of the spatial notation, such as skew operators and transformation matrices.
- Contact model quantities: Jacobian-Matrices against spatial velocities as well as Jacobian-Matrices and Hessian-Vectors against spatial accelerations including check for classic acceleration extension (compare Section 3.3 on page 30 (2.23b))
- All quantities of the dynamic equation (2.21c), such as $M(\mathbf{q})$ and $N(\dot{\mathbf{q}}, \mathbf{q})$ built from (2.21d) and (2.21e), checked against the internal symbolic implementation of CRBA and RNEA, respectively.

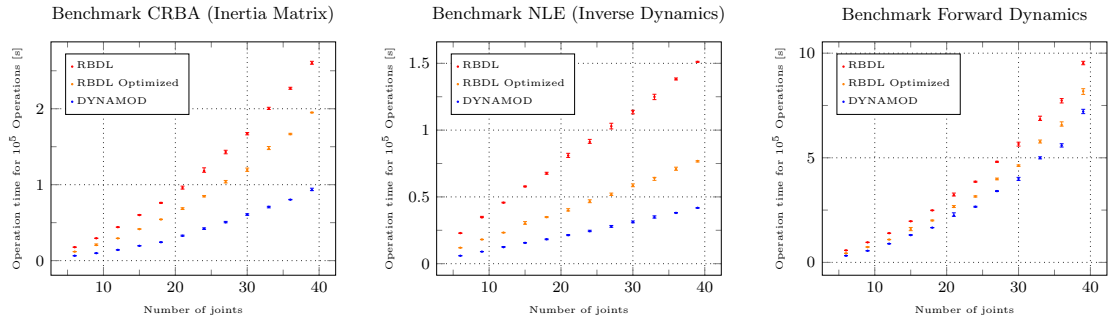
All quantities are then subject to rigorous testing against reference values of the highly mature dynamic package *RBDL* [Felis, 2014b]. All numeric tests are required to have a maximal deviation smaller than 10^{-13} to confirm its consistency.

Despite the general checks of the model based on its redundant representation, model specific verifications need to be conducted on all important parts of the model specific interface code. However, the detailed outline for each implemented model of this work is outside the scope of this paragraph.

2.3 Benchmark

Finally, it is interesting to compare the computational efficiency of the resulting symbolic representation to *State of Art* dynamic library code. In the following analysis run-time comparisons were conducted between the implementations of CRBA, RNEA and the system consisting of (2.23a) and (2.23b) generated from *RBDL* [Felis, 2014b] and the symbolic representation originating from *DYNAMOD*. The distinction between *RBDL* and *RBDL-optimized* is done to show the effect of mathematical integration of complex joint, e.g. 3D rotational joint, versus the concatenation of three single rotational joints.

The benchmarks were conducted on a Intel Core i7 930 CPU at 2.80 GHz and consisted of



(a) Benchmark of CRBA in different implementations against the generated symbolic code (b) Benchmark of RNEA in different implementations against the generated symbolic code (c) Benchmark of Forward Dynamics Lagrangian (2.23a) & (2.23b) system in different implementations compared to computations based on the symbolic code representation

Figure 3.2: Benchmark of different operations of recursive algorithms [Featherstone, 2007, Felis, 2014b] compared to the generated symbolic code from the *DYNAMOD* package. All benchmark sets consist of 10 chunks of 10^5 operations. The graphs show the mean as well as min and max values of the computation time per 10^5 operations in error bar style.

10×10^5 computations per operation of random samplings. In Figure 3.2a and 3.2b only the dynamic quantities were computed. For Figure 3.2c the complete system consisting of (2.23a) and (2.23b) is assembled and solved with a conventional QR decomposition (based on Householder transformations with additional column pivoting [Guennebaud et al., 2010]).

All graphs show small deviations around the mean value and hence, reflect sufficient quality of the measurement. The results are shown in Figure 3.2 for two different implementations of 3D rotational joints between local reference frames in *RBDL*. From a comparison of Figure 3.2a and 3.2b against Figure 3.2c it is clearly observable that an increasing part of the computational time is used to solve the complete system 7.84% and 29.42% for 6 joints towards 66.16% and 56.83% for 39 joints of *DYNAMOD* and *RBDL*, respectively. Furthermore, Figure 3.2a shows hints for a quadratic complexity, while Figure 3.2b clearly shows a linear complexity of the algorithms. In both Figures 3.2a and 3.2b *DYNAMOD* features lower computation times for the dynamic quantity then the models with different joint implementations of *RBDL*.

This comparison reveals an interesting fact of the symbolic representation of the model description. A clear gain in computation velocity is already visible between the runtime-time measurement of the *RBDL* library with the complex 3D rotational joint versus its implementation with single rotational joints. In the pure symbolic representation the formalism of joint types is completely resolved resulting in highly efficient arithmetic expressions. Furthermore, subsequent caching of arithmetic expressions reduces the number of basic arithmetic and the evaluation of trigonometric expressions. As the caching is only applied on a per code-file basis further gain in performance might be achieved with a complete resolution towards all code files.

3 Concluding Remarks

The above sections give a short outline of the initial development, the essential experiences with respect to the problem of consistent code development. Necessary verification strategies prior to a potential integration of such code in an embracing direct multiple shooting based optimal control algorithm is explained. Furthermore, the technical contributions of the implemented software modules, with respect to the dynamic package *HuMAnS* [Wieber et al., 2006] the inspiration of the adopted formalism was based on, are discussed.

The chapter concludes with a small benchmark comparison of the implementation against the highly efficient *State of Art* and mature dynamic library *RBDL* [Felis, 2014b]. From the results, a complete resolution of the local reference frame structure into symbolic expressions shows good potential to gain computational performance, even over highly optimized recursive methods.

With respect to the application in optimization the symbolic representation of the model description, yields the possibility to use symbolic or automatic differentiation [Nocedal and Wright, 2000, Walther and Griewank, 2012] to efficiently compute partial derivatives of the DAE system to replace the differentiation usually based on finite differences for higher accuracy of the gradient calculations.

On one hand the usage of the recursive dynamic library renders the model formulation setup at a certain extend independent of topology of the model that is given based on its description. On the other hand, changes of the topology are relatively unlikely to occur during the optimization process. Within this respect the full parametrization based on the easily accessible symbolic representation of the model description is an important gain in flexibility.

From a technical point of view the dependency to the commercial package Maple™ is problematic, as it is not possible to form a self-contained repository without external dependencies. At the time of writing investigations for an appropriate alternative are ongoing and potential candidates are being explored. The *python*based package *SymPy* [Joyner et al., 2012] seems to be so far an interesting and comprising solution.

4 Direct Approach for Optimal Control

All subsequent discussions of this work are based on the solution of various multi-stage OCP formulations. The standard formulation that will be adopted in all subsequent parts consists of a Bolza-Type objective that is minimized with respect to a Multi-Point Boundary Value Problem (MPBVP) of a set of ODEs in the following form,

$$\min_{\substack{x(\cdot), u(\cdot), \\ t_j, 1 \leq j \leq n_{\text{mos}}}} \int_{t_0}^{t_{n_{\text{mos}}}} L(\tau, x(\tau), u(\tau)) \, d\tau + E(t_{n_{\text{mos}}}, x(t_{n_{\text{mos}}})) \quad (4.1a)$$

$$\text{s.t.} \quad \dot{x}(t) = f^j(x(t), u(t)), \quad t \in [t_j, t_{j+1}], \quad (4.1b)$$

$$0 \leq r_{\text{mix}}^j(x(t), u(t)), \quad t \in [t_j, t_{j+1}], \quad (4.1c)$$

$$0 = r_s^j(x(t_j^+)) + r_e^j(x(t_{j+1}^-)), \quad (4.1d)$$

$$x(t_{j+1}^+) = x(t_{j+1}^-) + \Delta^j(t_{j+1}^-, x(t_{j+1}^-)). \quad (4.1e)$$

The time horizon $t \in [t_0, t_{n_{\text{mos}}}]$ is partitioned into $n_{\text{mos}} \in \mathbb{N}$ model stages,

$$[t_j, t_{j+1}], \quad 0 \leq j < n_{\text{mos}} - 1.$$

The sequence of the model stages is assumed to be fixed. The Bolza-type objective function (4.1a) is minimized on the given variable time horizon, depending on the differential state trajectories $x : [t_0, t_{n_{\text{mos}}}] \rightarrow \mathbb{R}^{n_x}$ of the system, and the control trajectories $u : [t_0, t_{n_{\text{mos}}}] \rightarrow \mathbb{R}^{n_u}$ to be determined during the optimization. The dynamics (4.1b) of the system are given by a set of ODEs with per-stage, distinct right hand sides $f^j : \mathbb{R}^{n_x} \times \mathbb{R}^{n_u} \rightarrow \mathbb{R}^{n_x}$. The model stage boundary points t_j , $1 \leq j \leq n$, are implicitly determined by the linearly coupled boundary constraints $r_s^j, r_e^j : \mathbb{R}^{n_x} \rightarrow \mathbb{R}^{n_{s,j}}$ (4.1d). Discontinuities in the state trajectory $x(\cdot)$ can occur in these boundary points as determined by transition functions $\Delta^j : [t_0, t_{n_{\text{mos}}-1}] \times \mathbb{R}^{n_x} \rightarrow \mathbb{R}^{n_x}$ (4.1e). Superscripts t_j^- and t_j^+ indicate evaluations of the system state trajectories from left and right side limits, respectively. In addition, the OCP is also constrained by mixed state-control path constraints $r_{\text{mix}}^j : \mathbb{R}^{n_x} \times \mathbb{R}^{n_u} \rightarrow \mathbb{R}^{n_b}$ (4.1c). Generally, it is assumed that all functions are at least twice continuous differentiable with respect to t , x and u .

The method that will be adopted in the following to solve this class of OCP is the direct multiple shooting approach originating from works of Bock and Plitt [Bock, 1981, Bock and Plitt, 1984]. This approach has been further developed [Leineweber et al., 2003a,b] and implemented in the software package MUSCOD-II that is document in [Leineweber, 1995, 1999]. The modeling software that has been thoroughly discussed in its theoretical foundations in the Chapters 2 and 3 and the Appendix A, B, C and G is built as a separate library and dynamically linked to the solver executable at run-time.

In Chapter 2 the set of differential equations governing the rigid multi-body system with external contacts is presented as a set of DAEs. For numerical reasons, the formulation of the boundary value problem with respect to the mechanics of the rigid multi-body system is done based on a set of ODEs equivalent to the reduced index-1 DAEs with the corresponding consistency constraints on the initial values (refer to Section 3.3 on page 30). The algebraic

variables are only computed implicitly during the integration of the equivalent set of ODEs. However, they are used for constraint evaluation inside the optimization problem. Therefore all subsequent discussions will be exclusively formulated on the OCPs with respect to an ODE boundary value problem.

In the following, a brief introduction to the transcription of the OCP into a Nonlinear Program (NLP) as well as the theoretical foundation and the structure of the employed Sequential Quadratic Programming (SQP) based solution process is given.

1 Transcription of the Continuous Problem

First the infinite dimensional problem formulation needs to be transformed into a problem with finite dimension. Although the time will be stated explicitly for each quantity, the final numerical problem formulation will undergo a substitution onto the time horizon of $[0, 1]$ and parametrize the duration of $h = t^{j+1} - t^j$ of each model stage j .

The subsequent sections closely follow the outline given in [Leineweber, 1995, 1999]. The exposition is limited to relevant aspects for this work. For a comprehensive description of the solver MUSCOD-II, including rigorous proofs of all theorems, the reader is referred to [Leineweber, 1995, 1999, Leineweber et al., 2003a,b, Nocedal and Wright, 2000].

1.1 Control Discretization

The controls of the system $u(\cdot)$ are discretized on a time grid,

$$t_j = \tau_0^j < \tau_1^j < \dots < \tau_{N^j}^j = t_{j+1}$$

by means of base functions parametrized by control parameters q . n_u is the number of actuated dofs. Available base functions are piecewise constant (4.4),

$$u(t) \Big|_{[\tau_k, \tau_{k+1}]} := q_k \in \mathbb{R}^{n_u}, \quad (4.4)$$

linear continuous,

$$u(t) \Big|_{[\tau_k, \tau_{k+1}]} := \frac{(q_{k,1} (\tau_{k+1} - t) + q_{k,2} (t - \tau_k))}{(\tau_{k+1} - \tau_k)}, \quad (4.5a)$$

$$k = 0, \dots, N^j - 1,$$

$$g_k^j (q_{k,1}^j, q_{k+1,0}^j) = q_{k,1}^j - q_{k+1,0}^j = 0, \quad 0 \leq j \leq n_{\text{mos}} - 1 \quad (4.5b)$$

cubic or cubic continuous. In the following, all subsequent problem formulations will adopt piecewise linear base functions.

1.2 State Discretization

The solution of the MPBVP (4.1b) of each model stage is performed based on multiple shooting [Betts, 2009]. In contrast to single shooting, the MPBVP per model stage,

$$\dot{x} = f^j(t, x(t), u(t)), \quad t \in [t_j, t_{j+1}], \quad (4.6a)$$

$$0 = r_s^j(x) + r_e^j(x), \quad 0 \leq j \leq n_{\text{mos}} - 1 \quad (4.6b)$$

is expressed as a series of parametrized IVPs that *shoot* on shorter time intervals,

$$t_j = \tau_0^j < \tau_1^j < \dots < \tau_{N^j}^j = t_{j+1},$$

than in the single shooting approach, for a desired solution,

$$\dot{x} = f(t, x(t), u(t)), \quad t \in [t_k^j, t_{k+1}^j], \quad (4.8a)$$

$$x(t_k^j) = s_k^j. \quad (4.8b)$$

The parametrization is effectively done with the intermediate initial values s_k^j of each model stage j and multiple-shooting interval k . The *defects* (resulting discontinuities in the system trajectories) need further consideration with suitable constraints that are imposed to the resulting NLP to form continuous system trajectories in the solution over all shooting intervals,

$$g_c^j(t_1^j, \dots, t_{N^j-1}^j, s_0^j, \dots, s_{N^j-1}^j, q_{0,0}^j, \dots, q_{N^j-1,1}^j) = \begin{bmatrix} x(t_1^j, s_0^j, q_{0,1}^j, q_{0,2}^j) - s_1^j \\ x(t_2^j, s_1^j, q_{1,1}^j, q_{1,2}^j) - s_2^j \\ \dots \\ x(t_{N^j}^j, s_{N^j-1}^j, q_{N^j-1,1}^j, q_{N^j-1,2}^j) - s_{N^j}^j \end{bmatrix} = 0. \quad (4.8c)$$

As in the shooting approach the boundary values, the MPBVP is supposed to satisfy, are added to the NLP as further constraint,

$$g_b^j(s_0^j, s_1^j, \dots, s_{N^j-1}^j) = r(s_0^j) + r_e(s_{N^j}^j) = 0. \quad (4.8d)$$

In the following it is assumed that the time grid for the control discretization and the parametrization of the MPBVP is synchronized. This assumption brings the important simplification that each initial value problem k on a given model stage j only depends on the time horizon (t_k^j, t_{k+1}^j) , its parametrized initial value s_k^j as well as the related control parameters $q_{k,1}^j$ and $q_{k,2}^j$. Consequently, the resulting NLP comes in a specific structure that will be exploited during the computation [Leineweber, 1995]. Furthermore, this enables parallel computation of states, controls and sensitivities.

1.3 Discretization of the Objective

Following the same strategy, the Lagrange-type objective function of each model stage j ,

$$\sum_{j=0}^{n_{\text{mos}}} \int_{t_j}^{t_{j+1}} L^j(\tau, x(\tau), u(\tau), p) \, d\tau, \quad (4.9a)$$

is computed with respect to each shooting interval k as a sum of objective terms,

$$\sum_{j=0}^{n_{\text{mos}}} \sum_{k=0}^{N^j-1} \int_{t_k^j}^{t_{k+1}^j} L^j(\tau, x(\tau, s_k^j, q_{k,1}^j, q_{k,2}^j), \varphi(\tau, q_{k,1}^j, q_{k,2}^j), p) \, d\tau. \quad (4.9b)$$

These terms may then be expressed by a function F ,

$$\sum_{j=0}^{n_{\text{mos}}} \sum_{k=0}^{N^j-1} F^{j,k}(s_k^j, q_{k,1}^j, q_{k,2}^j) \quad (4.9c)$$

Each term may then be expressed as an additional differential state $z(t)$ that is integrated inside the set of ODEs during the forward integration process. The final system that is considered during forward integration results in,

$$\begin{bmatrix} \dot{x}(t) \\ \dot{z}(t) \end{bmatrix} = \begin{bmatrix} f^j(x(t, s_k^j, q_{k,1}^j, q_{k,2}^j), \varphi(t, q_{k,1}^j, q_{k,2}^j), p) \\ L^j(t, x(t, s_k^j, q_{k,1}^j, q_{k,2}^j), \varphi(t, q_{k,1}^j, q_{k,2}^j), p) \end{bmatrix}, \quad 0 \leq j \leq n_{\text{mos}} - 1. \quad (4.10a)$$

The forward integration is done from the initial values,

$$\begin{bmatrix} z(t_k^j) \\ x(t_k^j) \end{bmatrix} = \begin{bmatrix} 0 \\ s_k^j \end{bmatrix}. \quad (4.10b)$$

The values of the objective function $F^{j,k}$ are then collected from the state values z at the end of each multiple-shooting interval,

$$F^{j,k}(s_k^j, q_{k,1}^j, q_{k,2}^j) = z(t_{k+1}^j), \quad 0 \leq j \leq n_{\text{mos}} - 1. \quad (4.11)$$

1.4 Discretization of Path Constraints

The continuous path constraints (4.1c) are discretized by evaluation at the shooting nodes only. With the strict local dependencies of the control discretization and state parametrization, the path constraints transform into,

$$h^j(t_1^j, \dots, t_{N^j}^j, s_0^j, \dots, s_{N^j-1}^j, q_{0,0}^j, \dots, q_{N^j-1,1}^j) = \begin{bmatrix} r_0^j(t_0^j, s_0^j, \varphi(t_0^j, q_{0,1}^j, q_{0,2}^j)) \\ r_1^j(t_1^j, s_1^j, \varphi(t_1^j, q_{1,1}^j, q_{1,2}^j)) \\ \dots \\ r_{N^j}^j(t_{N^j}^j, s_{N^j}^j, \varphi(t_{N^j}^j, q_{N^j,1}^j, q_{N^j,2}^j)) \end{bmatrix} \geq 0, \quad (4.12)$$

$$\leq j \leq n_{\text{mos}} - 1. \quad (4.13)$$

This transformation yields an relaxation of the continuous path constraint formulation. Accordingly, constraints with respect to the kinematics are formulated as consistency constraints in the set of DAEs. Refer to [Potschka et al., 2009] for a numerical formulation to enforce the path constraints in between the shooting nodes.

1.5 Discretized Problem Formulation

The discretized problem formulation is then expressed by the following form,

$$\min_{t,s,q} \sum_{j=0}^{n_{\text{mos}}} \sum_{k=0}^{N^j} F^{j,k}(s_k^j, q_{k,1}^j, q_{k,2}^j), \quad (4.14a)$$

$$\text{s.t. } g_c^j(t_1^j, t_2^j, \dots, t_{N^j}^j, s_0^j, \dots, s_{N^j-1}^j, q_{0,0}^j, \dots, q_{N^j-1,1}^j) = 0, \quad j \in [0 \dots n_{\text{mos}}], \quad (4.14b)$$

$$g_b^j(t_1^j, t_2^j, \dots, t_{N^j}^j, s_0^j, \dots, s_{N^j-1}^j, q_{0,0}^j, \dots, q_{N^j-1,1}^j) = 0, \quad j \in [0 \dots n_{\text{mos}}], \quad (4.14c)$$

$$h^j(t_1^j, t_2^j, \dots, t_{N^j}^j, s_0^j, \dots, s_{N^j-1}^j, q_{0,0}^j, \dots, q_{N^j-1,1}^j) \geq 0, \quad j \in [0 \dots n_{\text{mos}}], \quad (4.14d)$$

for the objective functions (4.14a), the continuity conditions (4.14b), the boundary value constraints and the path constraints (4.14c). The problem is now finite-dimensional and represented by the form of a NLP. The integration of the various Variational Differential Equations (VDEs) is performed with Internal Numerical Differentiation (IND) [Bock, 1981].

2 Theory of Constrained Nonlinear Optimization

Generally, nonlinear programs in constrained optimization theory are represented as,

$$\min_{\omega \in \mathbb{R}^n} F(\omega), \quad (4.15a)$$

$$\text{s.t. } g_i(\omega) = 0, \quad \forall i \in \mathcal{E}, \quad (4.15b)$$

$$h_i(\omega) \geq 0, \quad \forall i \in \mathcal{I}, \quad (4.15c)$$

featuring an objective (4.15a) as well as equality (4.15b) and inequality constraints (4.15c). Constrained nonlinear optimization problems can be solved numerically with different methods. Among them the SQP method that is employed in this thesis, will be outlined below. In the following the set of indices of the equality constraints will be denoted by \mathcal{E} and the set of all inequality constraints by \mathcal{I} . The SQP methods starts from an initial guess and adopts a local quadratic approximation to be solved in the end step. Then with a globalization strategy [Nocedal and Wright, 2000] it is decided how the local solution will be accepted for the comprehensive solution process. The iterative solution process is then repeated until a termination criterion is fulfilled. In the following, the theoretic foundations of nonlinear constrained optimization are briefly discussed, closely following [Nocedal and Wright, 2000]. The reader is referred to [Nocedal and Wright, 2000] Chapter 12 for complementary explanations and rigorous proofs of all presented theorems.

2.1 Problem Formulation

The problem formulation is shown in (4.15). Optimization is done over a vector of unknowns $\omega \in \mathbb{R}^n$ minimizing objective (4.15a) $F : \mathbb{R}^n \rightarrow \mathbb{R}$. Further, optimization is done with subject to the equality constraints (4.15b) $g : \mathbb{R}^n \rightarrow \mathbb{R}^{n_g}$ and the inequality constraints (4.15c) $h : \mathbb{R}^n \rightarrow \mathbb{R}^{n_h}$. In the following, it is assumed that F , h and g are at least twice continuously differentiable. Then $\nabla F : \mathbb{R}^n \rightarrow \mathbb{R}^n$, and $\nabla^2 F : \mathbb{R}^n \rightarrow \mathbb{R}^n \times \mathbb{R}^n$ represent the first and second derivative of the objective function with respect to the unknown ω , $\nabla h : \mathbb{R}^n \rightarrow \mathbb{R}^{n_h} \times \mathbb{R}^n$,

$$\nabla h = \left[\begin{array}{ccc} \frac{\partial}{\partial \omega} h_1 & \frac{\partial}{\partial \omega} h_2 & \cdots & \frac{\partial}{\partial \omega} h_{n_h} \end{array} \right], \quad (4.16a)$$

$$\nabla^2 h : \mathbb{R}^n \rightarrow \mathbb{R}^{n_h} \times \mathbb{R}^n \times \mathbb{R}^n \text{ and } \nabla g : \mathbb{R}^n \rightarrow \mathbb{R}^{n_g} \times \mathbb{R}^n,$$

$$\nabla g = \left[\begin{array}{ccc} \frac{\partial}{\partial \omega} g_1 & \frac{\partial}{\partial \omega} g_2 & \cdots & \frac{\partial}{\partial \omega} g_{n_g} \end{array} \right], \quad (4.16b)$$

$\nabla^2 g : \mathbb{R}^n \rightarrow \mathbb{R}^{n_g} \times \mathbb{R}^n \times \mathbb{R}^n$ are first, second derivative of the equality and inequality constraints, respectively. The Jacobians ∇g (4.16b) and ∇h (4.16a) contain the sensitivity of the equality (4.16b) and inequality (4.16a) constraints with respect to the unknown ω . Below, some common definitions are given before the optimality conditions can be discussed.

Definition 1 (Feasible Set) *The set,*

$$\Omega = \left\{ \omega \in \mathbb{R}^n \mid g(\omega) = 0, h(\omega) \geq 0 \right\}, \quad (4.17)$$

is called the feasible set that respects all equality and inequality constraints.

A point $\bar{\omega} \in \Omega$ is called a feasible point. All feasible points of the optimization problem are located in the feasible set.

Definition 2 (Local Minimum) Let $\bar{\omega}^* \in \Omega$ be a feasible point and $\mathcal{U}_e(\bar{\omega}^*)$ the environment around this point. The point $\bar{\omega}^*$ is called a local minimum, if and only if,

$$f(\bar{\omega}^*) \leq f(\omega) \quad \forall \omega \in \mathcal{U}_e(\bar{\omega}^*) \cap \Omega, \quad (4.18)$$

holds.

Definition 3 (Global Minimum) Let $\bar{\omega}^* \in \Omega$ be a feasible point. The point $\bar{\omega}^*$ is called a global minimum, if and only if,

$$f(\bar{\omega}^*) \leq f(\bar{\omega}) \quad \forall \bar{\omega} \in \Omega, \quad (4.19a)$$

holds. The minimum is called a strict global minimum if and only if,

$$f(\bar{\omega}^*) < f(\bar{\omega}) \quad \forall \bar{\omega} \in \Omega \setminus [\bar{\omega}^*], \quad (4.19b)$$

holds.

Definition 4 (Active Constraints) For a given point $\bar{\omega}^* \in \Omega$ a constraint is called active if $h(\bar{\omega}^*) = 0$ holds and in-active if $h(\bar{\omega}^*) > 0$ holds.

Definition 5 (Active Set) The active set of indices \mathcal{I}_A contains all indices of the active inequality constraints in the given point $\bar{\omega}^*$ and is a subset of all inequality constraint indices \mathcal{I} ,

$$\mathcal{I}_{A(\bar{\omega}^*)} = \{i \in \mathcal{I} \mid h_i(\bar{\omega}^*) = 0\}. \quad (4.20)$$

2.2 Optimality Conditions

In the following, *necessary* and *sufficient conditions* of optimality will be explained to outline their implications for the subsequent optimization studies conducted with the OCP-Solver MUSCOD-II [Leineweber, 1995, 1999]. The *necessary conditions* of optimality assume that ω^* is a local minimizer and deduce the necessary characteristics of f , g and h . The *sufficient conditions* of optimality express in the reverse case the characteristics of f , g and h , which will lead to $\bar{\omega}^*$ being a local minimizer. This leads to the concept of feasible sequences and limiting directions [Nocedal and Wright, 2000].

Definition 6 (Feasible Sequence) Let $\bar{\omega} \in \Omega$ be a feasible point. The sequence $\{z_k\}_{k=0}^{\infty}$ with $z_k \in \mathbb{R}^n$ is a feasible sequence when the following properties hold:

1. $z_k \neq \bar{\omega} \quad \forall k$,
2. $\lim_{k \rightarrow \infty} z_k = \bar{\omega}$,
3. $z_k \subseteq \Omega$ feasible for all k of sufficiently large values.

Based on definition 6, a local solution $\bar{\omega}^*$ is then characterized by,

$$f(\bar{\omega}^*) \leq f(z_k) \quad \forall k \text{ being sufficiently large,} \quad (4.21)$$

following [Nocedal and Wright, 2000]. From this concept one then derives the limiting directions d as follows.

Definition 7 (Limiting Direction) Let $\{\bar{z}_k\}_{k=k_{feas.}}^{\infty}$ be a subsequence of $\{z_k\}_{k=0}^{\infty}$ that is converging over feasible intermediates $\bar{z}_k \subseteq \Omega$ towards a feasible point $\bar{\omega} \in \Omega$. The limiting direction $d \in \mathbb{R}^n$ is defined as,

$$d = \lim_{k \rightarrow \infty} \frac{\bar{z}_k - \bar{\omega}}{\|\bar{z}_k - \bar{\omega}\|}. \quad (4.22)$$

Definition 8 (Tangential Cone) The limiting directions $d \in \mathbb{R}^n$ of various, different sequences $\{\bar{z}_k\}_{k=k_{feas.}}^{\infty}$ following Definition 7 are called tangential to the feasible set Ω in $\bar{\omega}$ and constitute the tangential cone denoted by $\mathcal{T}_{\Omega}(\bar{\omega})$ to the feasible point $\bar{\omega} \in \Omega$.

The tangential cone constitutes a subset of feasible search directions for a local minimizer $\bar{\omega}^*$ one may choose from. However, Definition 7 and 8 does not state a condition that may be easily verified based on the expressions of the constraint set h and g . Particularly, this is the case, when the constraint set is nonlinear. In this case, a first order approximation of the tangential cone from definition 8 in conjunction with a regularization condition is used [Nocedal and Wright, 2000].

Definition 9 (First Order Approximation of Tangent Cone) Let $\bar{\omega} \in \Omega$ be a feasible point with the active set $\mathcal{I}_{A(\bar{\omega})}$. The subset of the first order approximation of the tangent cone $\mathcal{T}_{\Omega,lin}(\bar{\omega})$ to the feasible set in $\bar{\omega}$ is expressed by,

$$\mathcal{T}_{\Omega,lin}(\bar{\omega}) = \left\{ \alpha d \mid \alpha > 0, \begin{array}{l} d^T \nabla h_i(\bar{\omega}) = 0, \quad \forall i \in \mathcal{E} \\ d^T \nabla g_i(\bar{\omega}) \geq 0, \quad \forall i \in \mathcal{I}_{A(\bar{\omega})} \end{array} \right\}. \quad (4.23)$$

If the constraint set consisting of g and h is linear, the tangent cone $\mathcal{T}_{\Omega}(\bar{\omega}^*)$ and its first order approximation $\mathcal{T}_{\Omega,lin}(\bar{\omega}^*)$ are equivalent. In any other case, one must verify that the first order approximation accurately reflects the geometric set of feasible search directions. These regularity conditions are called Constraint Qualification (CQ). They are part of the set of sufficient conditions, which means, that in case they are not satisfied, one may not be able to verify optimality conditions for a given feasible point $\bar{\omega}^*$. However, $\bar{\omega}^*$ can still represent a local minimizer [Nocedal and Wright, 2000].

Among the commonly used constraint qualifications are the Linear Independency Constraint Qualification (LICQ) and the Mangasarian Fromowitz Constraint Qualification (MFCQ) [Henrion, 1992].

Definition 10 (Linear Independence Constraint Qualification - LICQ) Let $\omega^* \in \Omega$ by a feasible point with an active constraint set $\mathcal{I}_{A(\omega^*)}$ and let the matrix $\nabla c(\omega^*)$ consist of all active constraint gradients (4.16). It is said that the LICQ holds if the matrix $\nabla c(\omega^*)$,

$$\nabla c(\omega^*) = \left[\{ \nabla g_i(\omega^*) \mid \forall i \in \mathcal{E} \}, \{ \nabla h_i(\omega^*) \mid \forall i \in \mathcal{I}_{A(\omega^*)} \} \right], \quad (4.24)$$

has full row rank. A point ω^* that satisfies the LICQ is called a regular point.

Definition 11 (Mangasarian-Fromowitz Constraint Qualification - MFCQ) Let $\bar{\omega}^* \in \Omega$ be a feasible point with the active constraint set $\mathcal{I}_{A(\bar{\omega}^*)}$. It is said that the MFCQ holds when the following conditions are satisfied:

1. There exists a vector $d \in \mathbb{R}^n$ such that,

$$\nabla g_i(\bar{\omega}^*)^T d = 0, \quad \forall i \in \mathcal{E}, \quad (4.25a)$$

$$\nabla h_i(\bar{\omega}^*)^T d > 0, \quad \forall i \in \mathcal{I}, \quad (4.25b)$$

hold.

2. The matrix $\nabla c_g(\omega^*)$,

$$\nabla c_g(\bar{\omega}^*) = \left[\{ \nabla g_i(\bar{\omega}^*) | \forall i \in \mathcal{E} \} \right], \quad (4.25c)$$

holding the gradients of the equality constraints has full column rank.

LICQ are more restrictive than MFCQ. There are situations when LICQ does not hold, but MFCQ does. In the following, discussion, it is assumed that LICQ holds.

Definition 12 (Lagrange Function) Given the NLP (4.15), the corresponding Lagrange function is,

$$\mathcal{L}(\omega, \lambda, \mu) := F(\omega) - \lambda^T g(\omega) - \mu^T h(\omega). \quad (4.26)$$

The vectors $\lambda \in \mathbb{R}^{n_h}$ and $\mu \in \mathbb{R}^{n_g}$ are called the Lagrange multiplier of the equality and inequality constraints, respectively.

Henceforth, the notation $\bar{\cdot}^*$ will be dropped in favor of \cdot^* as a local solution must always be feasible.

First Order Optimality Conditions

Based on Definition 12, 10 on the preceding page and 9 on the facing page, the optimality conditions for the NLP (4.15) are as follow:.

Theorem 1 (First-Order Necessary Conditions) Let $\bar{\omega}^*$ be a local solution of (4.15) and let LICQ hold in $\bar{\omega}^*$. Then vectors $\lambda^* \in \mathbb{R}^{n_h}$ and $\mu^* \in \mathbb{R}^{n_g}$ exist such that the conditions,

$$\nabla_{\omega} \mathcal{L}(\omega^*, \lambda^*, \mu^*) = 0, \quad (4.27a)$$

$$g_i(\omega^*) = 0, \quad \forall i \in \mathcal{E}, \quad (4.27b)$$

$$h_i(\omega^*) \geq 0, \quad \forall i \in \mathcal{I}_{A(\omega^*)}, \quad (4.27c)$$

$$\mu_i^* \geq 0, \quad \forall i \in \mathcal{I}_{A(\omega^*)}, \quad (4.27d)$$

$$\mu_i^* h_i(\omega^*) = 0, \quad \forall i \in \mathcal{I}_{A(\omega^*)}, \quad (4.27e)$$

hold for the point $(\bar{\omega}^*, \lambda^*, \mu^*)$.

Conditions (4.27) are known as the KARUSH–KUHN–TUCKER (KKT) conditions. A possible interpretation of the Lagrange multiplier λ and μ is the magnitude of sensitivity with respect to the relaxation of the given constraint set.

Definition 13 (Strict Complementarity) Let ω^* be a local solution of (4.15) and let λ^*, μ^* be the Lagrange multiplier satisfying the KKT-conditions (4.27). It is said that strict complementarity holds in ω^* if there is exactly one combination from,

$$(h_i(\omega^*), \mu_i^*) = \begin{cases} h_i(\omega^*) = 0 & \mu_i^* \geq 0 & \forall i \in \mathcal{I}_{A(\omega^*)} & \text{active set} \\ h_i(\omega^*) > 0 & \mu_i^* = 0 & \forall i \in \mathcal{I} \setminus \mathcal{I}_{A(\omega^*)} & \text{inactive set} \end{cases}, \quad (4.28)$$

that holds for $(h_i(\omega^*), \mu_i^*)$.

As it is stated in [Nocedal and Wright, 2000] for a given local solution ω^* of (4.15) there are multiple solutions λ^* and μ^* . However, if LICQ holds, the solution $(\omega^*, \lambda^*, \mu^*)$ is unique.

Although the KKT-Conditions (4.27) from (4.15) give local candidate solutions ω^* , there is no further information whether this local solution is a saddle point, a local maximizer or minimizer of (4.15a). Therefore it is crucial to additionally analyze the curvature of (4.15a) in a local solution ω^* .

Second Order Optimality Conditions

For the second-order optimality conditions, the set of possible search directions $\mathcal{T}_{\Omega, \text{lin}}(\omega^*)$ needs to be restricted to a smaller subset that maintains the configuration of the active set (Definition 5 on page 47) for all possible search directions ω .

Definition 14 (Critical Tangent Cone) Let $(\omega^*, \lambda^*, \mu^*)$ be a local solution of (4.15) satisfying the KKT conditions (4.27). Then one may define a subset $\mathcal{T}_{\Omega, \text{lin}, \text{crit}}(\omega^*, \lambda^*, \mu^*)$ from $\mathcal{T}_{\Omega, \text{lin}}(\omega^*)$, containing all directions $\omega \in \mathbb{R}^n$,

$$\omega \in \mathcal{T}_{\Omega, \text{lin}, \text{crit}}(\omega^*, \lambda^*, \mu^*) \Leftrightarrow \begin{cases} \nabla g_i(\omega^*)^T \omega = 0, & \forall i \in \mathcal{E} \\ \nabla h_i(\omega^*)^T \omega = 0, & \forall i \in \mathcal{I} \setminus \mathcal{I}_{A(\omega^*)} \quad \text{with } \mu_i^* > 0 \\ \nabla h_i(\omega^*)^T \omega \geq 0, & \forall i \in \mathcal{I}_{A(\omega^*)} \quad \text{with } \mu_i^* = 0 \end{cases} \quad (4.29)$$

In conjunction with Theorem 1 on the preceding page and Definition 12 on the previous page the subset $\mathcal{T}_{\Omega, \text{lin}, \text{crit}}(\omega^*, \lambda^*, \mu^*)$ contains all directions ω from $\mathcal{T}_{\Omega, \text{lin}}(\omega^*)$, where the first derivative of (4.15a) does neither state a clear ascent nor descent. Based on the curvature of F with respect to this subset, one may define *necessary* and *sufficient* second-order conditions [Nocedal and Wright, 2000].

Theorem 2 (Second-Order Necessary Conditions) Let $(\omega^*, \lambda^*, \mu^*)$ be a local solution of the problem (4.15), with (4.27) and (4.24) satisfied,

$$\omega^T \nabla_{\omega, \lambda, \mu}^2 \mathcal{L}(\omega^*, \lambda^*, \mu^*) \omega \geq 0, \quad \forall \omega \in \mathcal{T}_{\Omega, \text{lin}, \text{crit}}(\omega^*, \lambda^*, \mu^*), \quad (4.30)$$

holds.

Theorem 3 (Second-Order Sufficient Conditions) Let $(\omega^*, \lambda^*, \mu^*)$ satisfy conditions (4.27) and,

$$\omega^T \nabla_{\omega, \lambda, \mu}^2 \mathcal{L}(\omega^*, \lambda^*, \mu^*) \omega > 0, \quad \forall \omega \in \mathcal{T}_{\Omega, \text{lin}, \text{crit}}(\omega^*, \lambda^*, \mu^*), \quad (4.31)$$

then $(\omega^*, \lambda^*, \mu^*)$ is a local minimizer of (4.15).

3 Sequential Quadratic Programming

An efficient numerical method to solve NLPs, is the SQP method. The method starts at some initial value ω_0 and approximates the NLP in each iteration k with a Quadratic Program (QP) to be solved. QPs belong to a special class of optimization problems that will be discussed more in detail below. The method terminates with a globalization strategy and the complete algorithm runs until a defined termination criteria is satisfied.

Given the Lagrange function (4.26) of the NLP (4.15), the approximation is done using

second-order taylor expansion (4.32a),

$$M_{\mathcal{L}}(\omega_k + p_k, \lambda_k, \mu_k) \approx \mathcal{L}(\omega_k, \lambda_k, \mu_k) + \nabla_{\omega} \mathcal{L}(\omega_k, \lambda_k, \mu_k) p_k + \frac{1}{2} p_k^T \nabla_{\omega\omega} \mathcal{L}(\omega_k, \lambda_k, \mu_k) p_k, \quad (4.32a)$$

$$\nabla_{\omega} g_i(\omega_k) p_k + g_i(\omega_k) = 0, \quad \forall i \in \mathcal{E}, \quad (4.32b)$$

$$\nabla_{\omega} h_i(\omega_k) p_k + h_i(\omega_k) \geq 0, \quad \forall i \in \mathcal{I}. \quad (4.32c)$$

The equality (4.32b) and inequality (4.32c) constraint sets are relaxed to its first order approximation. Omitting the constant term $\mathcal{L}(\omega_k, \lambda_k, \mu_k)$ and using the fact from theorem 2, that the solution of the underlying NLP must minimize the Lagrange Function $\mathcal{L}(\omega_k, \lambda_k, \mu_k)$ on null-space of the active constraint set (4.32) is re-arranged to,

$$\min_{\omega_k, \lambda_k, \mu_k} \nabla_{\omega} F(\omega_k) p_k + \frac{1}{2} p_k^T \nabla_{\omega\omega} \mathcal{L}(\omega_k, \lambda_k, \mu_k) p_k, \quad (4.33a)$$

$$s.t. \quad \nabla_{\omega} g_i(\omega_k) p_k + g_i(\omega_k) = 0, \quad \forall i \in \mathcal{E}, \quad (4.33b)$$

$$\nabla_{\omega} h_i(\omega_k) p_k + h_i(\omega_k) \geq 0, \quad \forall i \in \mathcal{I}. \quad (4.33c)$$

3.1 Quadratic Programs

Besides the solution of QPs as integral part of the SQP method to efficiently solve NLPs, this class of optimization problems is, highly relevant to the subsequent discussion of the numerical computation of the model dynamics (4.1b) in Chapter 5 on page 54 and hence deserves a more detailed explanation here. The generic form of a QP is given by,

$$\min_{p \in \mathbb{R}^n} \frac{1}{2} p^T B p + b^T p, \quad (4.34a)$$

$$s.t. \quad G p + g = 0, \quad (4.34b)$$

$$H p + h \geq 0. \quad (4.34c)$$

The QP consists of a quadratic objective (4.34a) with symmetric matrix $B \in \mathbb{R}^{n \times n}$, gradient vector $b \in \mathbb{R}^n$ and linear equality and inequality constraints featuring the matrices $G \in \mathbb{R}^{n_g \times n}$ and $H \in \mathbb{R}^{n_h \times n}$ with full row rank, as well as the constraint vectors $g \in \mathbb{R}^{n_g}$ and $h \in \mathbb{R}^{n_h}$, respectively.

If the matrix B is positive definite and the QP is convex, the local minimizer is also a global one. For reasons of simplicity, the following discussion will be conducted on the problem formulation (4.34) without the inequality constraint set (4.34c), following to,

$$\underbrace{\begin{bmatrix} B & G^T \\ G & 0 \end{bmatrix}}_{\text{KKT matrix}} \begin{bmatrix} p^* \\ \lambda^* \end{bmatrix} = \begin{bmatrix} -b \\ -g \end{bmatrix}. \quad (4.35)$$

The KKT matrix as denoted in (4.35) is regular following Definition 15, rendering the solutions of (4.35) unique.

Definition 15 (Regularity of KKT Matrix) *Let the matrix $G \in \mathbb{R}^{m \times n}$ with $n \geq m$ have full row rank and let $Z \in \mathbb{R}^{n \times n-m}$ be a column-wise basis of the null-space of G and let $Z^T B Z$ be positive definite, then the KKT matrix from (4.35) is regular and the system (4.35) has a unique solution. The rank requirement to the matrix H is equivalent to the LICQ from Definition 10 on page 48.*

3.2 Methods to Solve the KKT-System

Various direct and iterative methods to solve the KKT system are given in [Benzi et al., 2005]. In the following, two direct methods, based on the Schur complement and the QR-Decomposition are outline below. These methods are important, also beyond the context of the solution of QPs as single step in the SQP method (see Chapter 5).

Range-Space Approach

Forming the Schur complement of (4.35) yields,

$$\begin{bmatrix} B & G^T \\ 0 & -HB^{-1}G^T \end{bmatrix} \begin{bmatrix} p^* \\ -\lambda^* \end{bmatrix} = \begin{bmatrix} -b \\ -g + GB^{-1}b \end{bmatrix}. \quad (4.36)$$

This upper triangular block structure can be solved by back-substitution, resulting in the expressions,

$$\lambda^* = -\left(GB^{-1}G^T\right)^{-1} \left(-g + GB^{-1}(b)\right), \quad (4.37a)$$

$$p^* = B^{-1} \left(-b + G^T \lambda^*\right). \quad (4.37b)$$

The range-space or schur complement approach can exploit given characteristics, such as symmetry or positive definiteness of the matrix B . This permits efficient and numerically stable operations involving the inverse B^{-1} and $GB^{-1}G^T$, e.g. a Cholesky decomposition is possible when B is positive definit. For general matrices B , computing the factorization forming the Schur-Complement is the computationally most demanding part of this approach. Moreover, ill-conditioning present in H is amplified when forming the Schur-Complement.

Null-Space Approach

Alternatively, under Definition 15 on the previous page it is possible to use an orthogonal (QR) decomposition to find bases Z and Y of the null-space and range-space of G ,

$$G^T = Q\tilde{R} = \begin{bmatrix} Y & Z \end{bmatrix} \begin{bmatrix} R \\ 0 \end{bmatrix}. \quad (4.38)$$

Here, Q is an orthonormal matrix and R is upper triangular. This decomposition allows to separate the solution p^* into range-space components p_z^* , not determined by the constraint set and the image-space components p_y^* tangential to the constraint set,

$$p^* = Yp_y^* + Zp_z^*. \quad (4.39)$$

Inserting this into (4.35) and pre-multiplying by Q^T yields,

$$\begin{bmatrix} Y^T B Y & Y^T B Z & R \\ Z^T B Y & Z^T B Z & 0 \\ R^T & 0 & 0 \end{bmatrix} \begin{bmatrix} p_y^* \\ p_z^* \\ -\lambda^* \end{bmatrix} = \begin{bmatrix} Y^T(-b) \\ Z^T(-b) \\ -h \end{bmatrix}. \quad (4.40)$$

For the range space solution p_y^* it is obtained,

$$p_y^* = -R^{-T}h. \quad (4.41)$$

For the null-space p_z^* it follows,

$$p_z^* = (Z^T B Z)^{-1} Z^T (-b - B Y p_y^*), \quad (4.42)$$

employing e.g. a Cholesky decomposition of the reduced matrix $Z^T B Z$. The dual variables, λ^* are computed from,

$$\lambda^* = R^{-1} Y^T (B p^* - b). \quad (4.43)$$

These results are thoroughly exploited in the subsequent discussion in Chapter 5 on the following page.

3.3 Inequality Constraints

Inequalities contained in the constraint set of a QP need some additional effort compared to the equality constraints. From [Nocedal and Wright, 2000] methods are distinguished into two different classes:

Penalty Methods The inequality constraints are introduced in the objective function with an appropriate weighting. This has the effect that the gradient of the objective function is mainly influenced by artificially created barriers in the neighborhood of the active inequality constraints.

Active Set Methods In this approach the working set $\mathcal{W}_{A(\omega^*)}$ - that contains active inequality and equality constraints - is to be estimated using appropriate algorithms. The solution is then determined, employing the same solution methods as in the purely equality constraint case.

The OCP MUSCOD-II employs the QP solver QPOPT [Gill et al., 1995] that is based on an active set method [Nocedal and Wright, 2000] to be briefly outlined in the following.

The initial working set $\mathcal{W}_k = \mathcal{E} \cap \mathcal{I}_{A(p^*)}$ for the solution p^* is to be estimated. For each local iteration the KKT system is solved with the given working set \mathcal{W}_k . Verification of the KKT conditions (4.27) either identifies the local minimizer or an invalid working set. If the working set is invalid either (4.27c) for some constraint i is not satisfied or (4.27d) is violated and hence, the working set must be updated. The algorithm then continues with the next local iteration. After identification of the local minimizer (x^*, λ^*, μ^*) the algorithm terminates. The resulting high number of iterations for large changes in the active set, is an issue that is successfully addressed for successive QP solutions by a *warmstart* (adoption of the previously employed working set) of the solver [Nocedal and Wright, 2000].

3.4 Quasi-Newton Methods

The construction of a complete QP necessitates the first-order derivative of the objective (4.15a) $\nabla_{\omega} F(\omega_k)$ and the second-order derivative of the Lagrange Function (4.26) $\nabla_{\omega\omega} \mathcal{L}(\omega_k, \lambda_k, \mu_k)$. The computation of the exact Hessian $B = \nabla_{\omega\omega} \mathcal{L}(\omega_k, \lambda_k, \mu_k)$ is computationally expensive and may result in an extensive loss of numerical accuracy, if finite difference based methods are used [Nocedal and Wright, 2000].

Another efficient alternative is to approximate the matrix B by means of low rank updates, starting from an initial guess by specific update formulas that employ the gradient information based on the secant condition [Nocedal and Wright, 2000]. These update formulas may be specifically tuned to preserve e.g. a special structure or positive definiteness [Nocedal and Wright, 2000].

5 Computation of Model Dynamics

The last component that is still necessary to complete the chain from the mechanical towards the OCP-Solver consists of appropriate algorithms to compute the right hand side (e.g. model dynamics (4.1b)) and all related information to the boundary (4.1d) and continuous path constraints (4.1c).

The domain of under-actuated whole-body motion generation is a highly active research field. Particularly, the focus goes towards motion generation under external contacts with constraint sets changing over time, yielding situations with complex partially over- as well as under-actuated (or so called: not sufficiently constrained) system configurations. Currently, employed algorithms are distinguished into two classes: FD and ID algorithms.

At one hand, the FD formulation is classically reported to be simple and straight-forward, but computationally highly involving as for each time-frame the complete model dynamics must be evaluated. At the other hand, inverse dynamics formulation is commonly perceived as complex but computationally more performant as system characteristics based on contacts may be computed purely kinematically. However, computations based on the ID formulation may suffer from numerical ill-conditioning and even infeasibility. Although, various reformulations of ID exist [Erez and Todorov, 2012, Flashner, 1986, Geoffroy et al., 2014, Hutter, 2013, Mistry et al., 2008, 2010, Righetti et al., 2011a,b], these methods do not guarantee physical correctness of their results, particularly, in limiting kinematic configurations, such as partially under-actuated/insufficiently constrained configurations.

Furthermore, application of these algorithms for derivation-based optimization methods is numerically problematic as most algorithms need additional efforts in reformulation to be continuously differentiable with respect to all input parameters.

In the subsequent work OCPs (4.1) based on FD and ID formulations are presented and an-

Table 5.1: Characteristics of the model computations based on either FD or ID

	Forward Dynamics	Inverse Dynamics
Control/System Input	Joint Torques τ	Joint Accelerations \ddot{q}
Initialization	Dynamics & Kinematics q, \dot{q}, τ	Kinematics q, \dot{q}, \ddot{q}
Operator	$FD : (q, \dot{q}, \tau) \longrightarrow (\ddot{q}, \lambda)$	$ID : (q, \dot{q}, \ddot{q}) \longrightarrow (\tau, \lambda)$

alyzed with respect to the discretization of the controls of the model, the initialization of the OCP formulation (refer to Table 5.1) and their convergence towards a local minimum, especially for a realistic highly complex Multi Body System (MBS) of the robotic platform HRP-2. For this purpose a new ID algorithm was developed, that yields physical correctness for over- and underactuated (insufficiently constrained) configurations and complies with all numerical requirements of the previously proposed multiple shooting approach (refer to Chapter 4 on page 42).

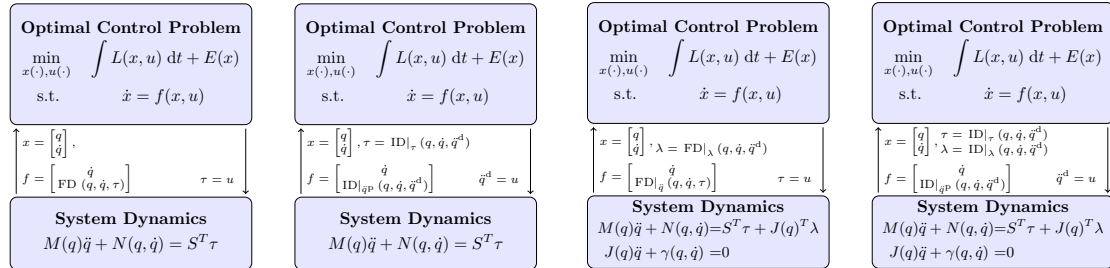
In the remainder of this chapter the FD and ID based formulation are briefly reviewed to outline the context which led to the construction of the new ID formulation. The formulation is then thoroughly verified analytically and through different OCP formulations towards its physical correctness, in comparison to the FD formulation - on an academic model (cart

pendulum) and in subsequent chapters on a realistic complex MBS of the HRP-2 robotic platform. Furthermore, a comparison of different control discretizations is presented to discuss the important aspect of how the control discretization should be selected to yield a realistic representation of the model dynamics in the OCP.

As it was observed that in the recent literature distinct terms are employed to express equivalent kinematic contact states, the remainder of this chapter will use the term *under-actuated* for systems that are *insufficiently constrained* [Del Prete, 2013], or equivalently *truly under-actuated* [Hutter, 2013] - for reasons of notational accuracy. Typical realistic under-actuated system-models are those with a floating base, e.g. legged robotics. Both model classes will be discussed more in detail in subsequent parts.

1 Expression in the Optimization Context

The classical forward and inverse dynamics case of underactuated MBS with external contacts can be formulated rigorously as constrained quadratic optimization problem with specific objectives. The final order reduced index-1 DAE system (2.23), derived from the index-3 DAE system (2.22), commonly known as descriptor-form [Brogliato et al., 2002] then follows from a simple re-arrangement including the primal and dual variables of the constrained optimization problem. With respect to the previous discussion about the solution of convex QPs in Section 3.2 on page 52 all subsequent discussions will refer to this common form of representation for notational clarity. In the following subsections the context is set with a brief introduction to the forward and inverse dynamics formulation for under-actuated MBS and its integration inside the OCP. On the top of this context the new ID formulation is then proposed in the next section.



(a) Schematic of FD OCP without external contact constraints (b) Schematic of ID OCP without external contact constraints (c) Schematic of FD OCP under external contact constraints (d) Schematic of ID OCP under external contact constraints

Figure 5.1: Scheme of FD and ID computations of the model dynamics inside the OCP formulation without (left side) and with (right-side) external contacts, respectively. This shows the different control discretizations and the form of the dynamics operator (see Table 5.1 on the preceding page)

1.1 Contact-free Forward & Inverse Dynamics Formulation

The general equation of underactuated (e.g. floating base) MBS in minimal coordinates and free space is adopted from (2.21c) in accordance to [Siciliano and Khatib, 2007]. The equation is briefly stated below for the sake of notational clarity,

$$M(q(t))\ddot{q}(t) + N(q(t), \dot{q}(t)) = S^T \tau(t). \quad (5.1)$$

It features the joint coordinates, velocities and accelerations $q, \dot{q}, \ddot{q} : \mathbb{R} \rightarrow \mathbb{R}^{n_q}$, joint torques $\tau : \mathbb{R} \rightarrow \mathbb{R}^{n_\tau}$, the symmetric positive definite joint space inertia matrix $M : \mathbb{R}^{n_q} \rightarrow \mathbb{R}^{n_q \times n_q}$, $N : \mathbb{R}^{n_q} \times \mathbb{R}^{n_q} \rightarrow \mathbb{R}^{n_q}$ the vector of nonlinear effects, e.g. Coriolis, centrifugal, and gravity terms, and a selection matrix $S \in \mathbb{R}^{n_\tau \times n_q}$ mapping the joint torques τ to the actuated dofs of the system. For brevity of exposition. Below, the dependencies on time t are omitted wherever this is obvious.

Figure 5.1a on the preceding page shows the technical integration of the contact-free forward dynamics formulation (5.1) in the OCP (4.1). Joint positions and velocities constitute the differential state vector $x := [q^T \dot{q}^T]^T$. Equation (5.1) then supplies the lower part of the right hand side f of the order-reduced differential equation (4.1b). The joint torques τ are then equivalent with the controls $u(\cdot)$ of the OCP (4.1). Integration of the accelerations \ddot{q} towards the actual joint positions q is performed in the OCP directly. The above formalism is henceforth expressed as the FdOP : $\text{FD} : \mathbb{R}^{n_q} \times \mathbb{R}^{n_q} \times \mathbb{R}^{n_\tau} \rightarrow \mathbb{R}^{n_q}$,

$$\ddot{q} = \text{FD}(q, \dot{q}, \tau) := M^{-1}(q) (S^T \tau - N(q, \dot{q})). \quad (5.2)$$

In comparison between Figure 5.1a on the previous page and 5.1b on the preceding page the distinct characteristics of Table 5.1 on page 54 with respect to the integration inside the OCP (4.1) are obvious.

In the application of the ID formulation, joint accelerations \ddot{q} are then equivalent to the controls $u(\cdot)$ of the OCP (4.1). Hence, a desirable solution would be an ID operator of the form $\tau = \text{ID}(q, \dot{q}, \ddot{q})$, that treats the accelerations as input and yields the joint torques τ as results. These torques would then enter the OCP as a state-dependent algebraic expression and the solution of the system dynamics would be trivial. In general, this is not possible and for under-actuated systems accelerations are only guaranteed to be physically correct under the premise that input accelerations are chosen carefully to be consistent to the FD on the non-actuated dofs.

As the problem of selecting physical consistent accelerations gets even harder in the contact case, the discussion is at first conducted on the contact-free case. Consequently, one may define the IdOP : $\text{ID} : \mathbb{R}^{n_q} \times \mathbb{R}^{n_q} \times \mathbb{R}^{n_q} \rightarrow \mathbb{R}^{n_\tau} \times \mathbb{R}^{n_q}$ for the contact-free setting slightly different as in,

$$\tau, \ddot{q}^{\text{phys}} = \text{ID}(q, \dot{q}, \ddot{q}^{\text{dsrd}}). \quad (5.3)$$

This operator accepts now desired accelerations \ddot{q}^{dsrd} as inputs and additionally returns physical correct accelerations \ddot{q}^{phys} . This renders again the integration of the accelerations \ddot{q}^{phys} towards the actual joint positions q possible. Despite the different implications of the controls $u(\cdot)$ both operators have same interface towards the integrator of the OCP formulation - an important feature.

In the following the previously stated **IdOp!** (**IdOp!**) will be derived by reformulating the equations of motion as QP. The equation of motion (5.1) is equivalent to the first-order necessary optimality or so called KKT conditions (4.27) of the convex quadratic minimization problem with respect to the accelerations \ddot{q} ,

$$\min_{\ddot{q}} \frac{1}{2} \ddot{q}^T M(q) \ddot{q} + (N^T(q, \dot{q}) - \tau^T S) \ddot{q}. \quad (5.4)$$

The respective Lagrange function (4.26) of (5.4) is,

$$\mathcal{L}(\ddot{q}) := \frac{1}{2} \ddot{q}^T M(q) \ddot{q} + (N^T(q, \dot{q}) - \tau^T S) \ddot{q}, \quad (5.5)$$

and its derivative with respect to \ddot{q} directly yields the contact-free equation of motion,

$$\nabla_{\ddot{q}} \mathcal{L}(\ddot{q}) = M(q)\ddot{q} + N^T(q, \dot{q}) - S^T \tau = 0. \quad (5.6)$$

This QP can be equivalently reformulated into a constrained one by dropping the actuation term $S^T \tau$ and adding an equality constraint that yields,

$$\min_{\ddot{q}} \quad \frac{1}{2} \ddot{q}^T M \ddot{q} + N^T \ddot{q}, \quad (5.7a)$$

$$\text{s.t.} \quad S \ddot{q} = S \ddot{q}^{\text{dsrd}}. \quad (5.7b)$$

The additional constraint (5.7b) ensures that the joint accelerations are equal to the desired accelerations $\ddot{q}^{\text{dsrd}} \in \mathbb{R}^{n_q}$, which are now input variables as proposed in (5.3). This leads to the following KKT system, with primal \ddot{q} and dual τ quantities, respectively. In,

$$\begin{bmatrix} M & S^T \\ S & 0 \end{bmatrix} \begin{bmatrix} \ddot{q} \\ -\tau \end{bmatrix} = \begin{bmatrix} -N \\ S \ddot{q}^{\text{dsrd}} \end{bmatrix}, \quad (5.8)$$

the first row yields again the equation of motion (5.1) and is therefore equivalent to (5.4). An orthogonal decomposition into actuated and unactuated dofs (this approach originates from [Flashner, 1986]) of the system by $\ddot{q} = S^T(S\ddot{q}) + P^T(P\ddot{q})$ and pre-multiplying $[S \ P]$, where P is the complementary selection matrix of S , i.e., $SS^T = \mathbb{I}_{n_\tau}$, $PP^T = \mathbb{I}_{n_q - n_\tau}$ and $SP^T = PS^T = 0$. System (5.8) then decomposes into,

$$\begin{bmatrix} SMS^T & SMP^T & \mathbb{I}_{n_\tau} \\ PMS^T & PMP^T & 0 \\ \mathbb{I}_{n_\tau} & 0 & 0 \end{bmatrix} \begin{bmatrix} S\ddot{q} \\ P\ddot{q} \\ -\tau \end{bmatrix} = \begin{bmatrix} -SN \\ -PN \\ S\ddot{q}^{\text{dsrd}} \end{bmatrix}. \quad (5.9)$$

The solution can then be derived consecutively by starting from the trivial last row for $S\ddot{q}$ and applying a forward substitution. This above approach is also sometimes called *hybrid dynamics* as simultaneous computation for the torques τ and physically correct accelerations \ddot{q}^{phys} are conducted (refer to [Featherstone, 2007]).

Remark 1 (Mathematical Equivalence) *One should note that contact-free and actuated dynamic systems as expressed with the intermediate of the FdOP and the IdOP inside the OCP formulation (4.1) are mathematical equivalent and yield the same results. When (4.1) is solved with direct methods the FdOP and IdOP based results, however, may differ with respect to the numerical characteristics of their respective implementation, e.g. numerical stability and discretisation errors.*

1.2 Mathematical Description of Constrained MBS in the Optimization Context

Revisiting Section 3.3 on page 32, the generation of complex motions for MBS, e.g. to generate a walking motion for a humanoid robot usually involves rigid contacts with the external environment or kinematic loops, that may change over time (compare to Section 3.3 on page 30). For notational clarity the following definitions are revisited:

- The contact functions c_i , model the distance between contact points and the environment, or, in the case of auto-collision, the MBS itself,

$$c_i(q) \geq 0 \quad \forall i \in [1, n_c] \quad \text{with} \quad c_i : \mathbb{R}^{n_q} \rightarrow \mathbb{R}. \quad (5.10)$$

- A contact becomes active when its distance function $c_i(q) = 0$ becomes zero. Hence, for a given time instant, the index set I of the active constraints is defined analogue to definition 4 on page 47 and 5 on page 47,

$$I := \{i \mid c_i(q) = 0, \forall i \in [1, n_c]\}. \quad (5.11)$$

- The size of the constraint set I is denoted by $n_I := |I|$, c_I represents the corresponding vector-valued function $(c_i)_{i \in I}$, and $J(q) := \frac{dc_I}{dq} \in \mathbb{R}^{n_I \times n_q}$ its Jacobian with respect to q .

Following Section 3 on page 26 and the comprehensive discussion in [Featherstone, 2007], there are two typical methods of introducing contacts inside the equations of motion.

In case, one is not interested in the contact reactions, a new configuration of minimal coordinates from the null-space of $J(q) := \frac{dc_I}{dq}$ is identifiable. With respect to the basis of the null-space contact constraints the equation of motion (5.1) is reprojected [Featherstone, 2007], following the approach in Section 1.2 on page 234. Although, the identification of the basis of the null-space is computationally involving, the resulting contact-free system (B.12) is of reduced size. However, it is governed by a different set of coordinates and changes in the constraint set may need further efforts to preserve differentiability over the applied coordinate transformations to keep the method applicable in the context of the OCP.

Given the case, information about the contact reactions are desired, it is sometimes advisable to maintain the original, however, redundant, non-minimal set of coordinates with respect to the set of contact constraints and solve the non-reduced constrained optimization problem directly - following Section 3.2 on page 52. This has the advantage that a set of coordinates remains valid during different contact configurations and in case desired, one may solve for the force and torque configuration in the present contacts directly.

For the remainder of this work, the decision was made for the latter (full) approach to keep a fixed set of coordinates over the complete horizon and gain full access to the contact characteristics of the system to trigger physically based contact-events in the fixed contact sequence (refer to Section 3.4 on page 53).

The equation of motion of a constrained MBS for a fixed constraint set I are then described by,

$$M(q)\ddot{q} + N(q, \dot{q}) = S^T \tau + J(q)^T \lambda \quad (5.12a)$$

$$c_I(q) = 0, \quad (5.12b)$$

for the time-frame with constant active set I (refer to (2.22)). Active contacts c_i result in an external force $\lambda_i \in \mathbb{R}$ acting on the system by means of the transposed contact Jacobian. Inactive contacts are assigned $\lambda_i = 0$ due to contact complementarity (refer to theorem 1 on page 49 as well as equation (2.22)).

Assumption 1 (Full Rank) *In the following it is assumed that the contact Jacobian $J(q)$ has full row rank, $\text{rank}(J(q)) = n_I$, for any constraint set I . This is equivalent with definition 10 on page 48.*

Remark 2 (Rank Deficiency) *Rank deficiency of the contact Jacobian indicates redundant constraints. In this case, it is always possible to replace the current constraint set by a subset that satisfies Assumption 1.*

Following Section 3.3 on page 30 index reduction transforms (5.12) into a second-order DAE of index one,

$$\begin{bmatrix} M(q) & J(q)^T \\ J(q) & 0 \end{bmatrix} \begin{bmatrix} \ddot{q} \\ -\lambda \end{bmatrix} = \begin{bmatrix} S^T \tau - N(q, \dot{q}) \\ -\gamma(q, \dot{q}) \end{bmatrix}. \quad (5.13)$$

Revisiting (5.13) equivalence of the structure and properties to the set of KKT conditions for the convex QP,

$$\min_{\ddot{q}} \frac{1}{2} \ddot{q}^T M(q) \ddot{q} + (N^T(q, \dot{q}) - S^T \tau) \ddot{q}, \quad (5.14a)$$

$$\text{s.t. } J(q) \ddot{q} = -\gamma(q, \dot{q}), \quad (5.14b)$$

for \ddot{q} is obvious. With the Lagrange multiplier λ for the equality constraint (5.14b) the Lagrange function of (5.14) follows to,

$$\begin{aligned} \mathcal{L}(\ddot{q}, \lambda) := & \frac{1}{2} \ddot{q}^T M(q) \ddot{q} + (N^T(q, \dot{q}) - S^T \tau) \ddot{q}, \\ & - \lambda^T (J(q) \ddot{q} + \gamma(q, \dot{q})) \end{aligned} \quad (5.15)$$

Following theorem 1 on page 49 a solution \ddot{q} of (5.15) satisfies the following set of conditions,

$$\nabla_{\ddot{q}} \mathcal{L}(\ddot{q}, \lambda) = M(q) \ddot{q} + N^T(q, \dot{q}) - S^T \tau - \lambda^T J(q) = 0, \quad (5.16a)$$

$$\nabla_{\lambda} \mathcal{L}(\ddot{q}, \lambda) = -J(q) \ddot{q} - \gamma(q, \dot{q}) = 0, \quad (5.16b)$$

$$\lambda^T (J(q) \ddot{q} + \gamma(q, \dot{q})) = 0. \quad (5.16c)$$

It is clearly observable that the first two equations (5.16a) and (5.16b) correspond to the rows of (5.13), while the third equation (5.16c) represents the complementarity condition (refer to theorem 1 on page 49).

1.3 Contact Handling and Forward Dynamics with Contacts

The hybrid nature of the dynamics in (4.1) arises from changes in the contact set I during the motion of the MBS. State jumps Δ_j are then caused by collisions with the external environment. Whenever a new contact event occurs, $c_i(q(t)) = 0$ for some $i \notin I$ and $t \in [t_j, t_{j+1}]$, the contact index i is added to the set I and (2.24) is solved for conservation of momentum for the new constraint set I .

As stated in Chapter 4 on page 42 the index-1 DAE formulation (5.13) will be included as ODE in the OCP (4.1) by applying the proper, previously introduced solution operators FdOP and IdOP additionally, in the presence of contacts. To this end, the operator FdOP directly arises from the outline given in the previous section. The solution of the resulting QP (5.14) then directly follows from approaches proposed in Section 3.2 on page 52.

Remark 3 For an empty contact set I , the operator FdOP reduces to the contact-free FD operator (5.2), with $\lambda = 0$.

2 Algorithms for Rank Deficient Inverse Dynamics Optimization

This section continues the previously adopted approach of the FdOP for the discussion of the IdOP, revealing the problem of the physical consistency in the case of external contacts, that is straight-forward for the FdOP. The problem is revisited from the mathematical point of view.

2.1 Rank Deficient Inverse Dynamics

Definition 16 (Full Actuation) *A constrained mechanical system is fully actuated if and only if the rank of the contact constraints Jacobian with respect to the unactuated dofs equals the number of non-actuated dofs in the system, i.e.,*

$$\text{rank}(JP^T) = n_q - n_\tau. \quad (5.17a)$$

In this definition, $P \in \mathbb{R}^{(n_q - n_\tau) \times n_q}$ is the complementary selection matrix that projects onto the non-actuated dofs, i.e., after a suitable re-ordering of entries of q , one obtains,

$$\begin{bmatrix} PP^T & 0 \\ 0 & SS^T \end{bmatrix} = \mathbb{I}_{n_q}. \quad (5.17b)$$

Definition 5.17 is equivalent to requiring that for any fully actuated MBS the non-actuated dofs are always uniquely defined by the reduced constraint equations (5.14b). The derivation of the ID solution operator for contact case again starts from (5.13) as convex optimization problem,

$$\min_{\ddot{q}} \frac{1}{2} \ddot{q}^T M \ddot{q} + N^T \ddot{q}, \quad (5.18a)$$

$$\text{s.t. } J\ddot{q} = -\gamma, \quad (5.18b)$$

$$S\ddot{q} = S\ddot{q}^{\text{dsrd}}. \quad (5.18c)$$

The KKT system then follows to,

$$\begin{bmatrix} M & J^T & S^T \\ J & 0 & 0 \\ S & 0 & 0 \end{bmatrix} \begin{bmatrix} \ddot{q} \\ -\lambda \\ -\tau \end{bmatrix} = \begin{bmatrix} -N \\ -\gamma \\ S\ddot{q}^{\text{dsrd}} \end{bmatrix}. \quad (5.19)$$

The KKT system (5.19) is only solvable, when the combined matrix $\begin{bmatrix} J & S^T \end{bmatrix}$ has full row rank. However, this does not hold when Definition 5.17 is not fulfilled. This can be clearly seen by applying the orthogonal decomposition $\ddot{q} = S^T (S\ddot{q}) + P^T (P\ddot{q})$ which transforms (5.19) into,

$$\begin{bmatrix} SMS^T & SMP^T & SJ^T & \mathbb{I} \\ PMS^T & PMP^T & PJ^T & 0 \\ JS^T & JP^T & 0 & 0 \\ \mathbb{I} & 0 & 0 & 0 \end{bmatrix} \begin{bmatrix} S\ddot{q} \\ P\ddot{q} \\ -\lambda \\ -\tau \end{bmatrix} = \begin{bmatrix} -SN \\ -PN \\ -\gamma \\ S\ddot{q}^{\text{dsrd}} \end{bmatrix}. \quad (5.20)$$

This time a solution of the KKT system by forward substitution is only possible when JP^T has full row-rank, i.e., Definition 5.17 holds. Another approach is to solve for \ddot{q} in the null-space of the kinematic constraints (5.18b) (we refer to [Benzi et al., 2005]), premultiplying by Q^T closely following (4.38) and eliminating zero terms yields,

$$\begin{bmatrix} Y^T (M\ddot{q} + N + J^T \lambda) \\ Z^T (M\ddot{q} + N) \end{bmatrix} = \begin{bmatrix} Y^T S^T \\ Z^T S^T \end{bmatrix} \tau. \quad (5.21)$$

As a consequence of Assumption 1 on page 58 and Definition 5.17 on the facing page, the matrix $Z^T S^T$ is regular and solving for the joint torques τ is immediately possible,

$$\tau = (Z^T S^T)^{-1} Z^T (M\ddot{q} + N). \quad (5.22)$$

The contact forces may then be computed in a subsequent step from (5.20). However, if a kinematic configuration is underactuated, e.g. [Mistry et al., 2008], the matrix $Z^T S^T$ will become rank deficient. Then, system (5.21) is under-constrained with respect to τ and the inverse in (5.22) does not exist. In this case, one can pre-multiply (5.22) by SZ to reflect the minimum norm solution,

$$\tau = (SZZ^T S^T)^{-1} SZZ^T (M\ddot{q} + N) \leftarrow \min_{\tilde{\tau}} \frac{1}{2} \|Z^T S \tilde{\tau} - Z^T (M\ddot{q} + N)\|_2^2. \quad (5.23)$$

According to [Hutter, 2013], the application of (5.23) as ID solution operator can cause physical inconsistency with respect to \ddot{q} . The usual solution to prevent this situations is to strictly enforce Definition 5.17 on the preceding page to hold. This is the central property of the proposed approach that must at the same time fulfill the requirements of the OCP, e.g., smoothness and continuous differentiability.

2.2 Relaxation to Overcome Rank-Deficient Inverse Dynamics

In the context of optimal control based on ID, an efficient and numerically well-defined approach to the underactuated and constrained case, i.e., systems in which Definition 5.17 on the facing page does not hold, is clearly necessary. This approach should maintain the benefits:

- Low computation times of purely kinematic projections [Righetti et al., 2011b],
- An easier, purely kinematic initialization of the problem formulation (refer to Table 5.1 on page 54).

At the same time, an effort should be made to verify that the kinematic constraints and the system dynamics are respected with satisfactory confidence on the entire motion trajectory. This issue is addressed, with the proposition of a new algorithm for the IdOP for underactuated systems. For a given set of active contacts I , the solution operator follows to,

$$(\tau, \lambda, \ddot{q}) = ID(q, \dot{q}, \ddot{q}^{\text{dsrd}}, I). \quad (5.24)$$

Reformulation of the ID problem as a convex optimization problem should additionally determine physically correct accelerations \ddot{q} such that:

- The controllable accelerations $S\ddot{q}(\cdot)$ are closest to given desired ones \ddot{q}^{dsrd} ,
- At the same time, the positional constraints and the underlying dynamics of the MBS are respected.

A common approach to overcome the problems of rank deficiency in (5.20) or (5.22) is to apply a Singular Value Decomposition (SVD) [Flashner, 1986, Nakamura, 1990, Sentis and

Khatib, 2005] to separate, actuated from unactuated dofs, as shown in,

$$Z^T (M\ddot{q} + N) = (Z^T S^T) \tau = \begin{bmatrix} U_{\parallel} & U_{\perp} \end{bmatrix} \begin{bmatrix} \Sigma & 0 \\ 0 & 0 \end{bmatrix} V^T \tau, \quad (5.25a)$$

$$U_{\perp}^T Z^T (M\ddot{q} + N) = 0, \quad (5.25b)$$

$$U_{\parallel}^T Z^T (M\ddot{q} + N) = \begin{bmatrix} \Sigma \end{bmatrix} V_{\parallel}^T \tau. \quad (5.25c)$$

Equation (5.25b) enforces the physical consistency. With a choice for the accelerations \ddot{q} that respects (5.25b), one may solve (5.25c) then, for the physically consistent joint torques τ .

Above approach is based on a SVD employing a threshold to the diagonal components of Σ to separate the distinct orthogonal subsets. Therefore, continuous differentiability of the algorithm is lost in this case. Hence, the algorithm is not suitable for a prospected integration in the OCP-formulation (4.1) and an appropriate method to overcome this problem is needed.

The rearrangement of the system will again start from the equation of motions as QP (5.18). The term \ddot{q}^{dsrd} represents the desired input accelerations to the ID operator, e.g., a control function $u(\cdot)$ within the OCP (4.1). The constraint (5.18c) then relates the accelerations \ddot{q} of the solution of the QP to the desired ones \ddot{q}^{dsrd} .

The issue here is that the joint set of constraints described by the rows of matrices $J(q)$ and S no longer needs to be regular, i.e., in general some given constraints are redundant. Depending on the right-hand side vectors γ and $S\ddot{q}^{\text{dsrd}}$, the QP may become infeasible. Therefore, various regularization strategies to address this situation are proposed and analyzed in the framework of this QP.

Relaxation of Accelerations

With the relaxation of the acceleration constraint (5.18c) one gets the optimization problem,

$$\min_{\ddot{q}, \ddot{q}^a} \frac{1}{2} \ddot{q}^T M(q) \ddot{q} + N(q, \dot{q})^T \ddot{q} + \frac{1}{2} \|S\ddot{q}^{\text{dsrd}} - S\ddot{q}^a\|_{2,K}^2, \quad (5.26a)$$

$$\text{s.t. } J(q) \ddot{q} = -\gamma(q, \dot{q}), \quad (5.26b)$$

$$S\ddot{q} = S\ddot{q}^a. \quad (5.26c)$$

An auxiliary acceleration vector $\ddot{q}^a \in \mathbb{R}^{n_q}$ is introduced that specifies the controllable part $S\ddot{q}$ of the joint torques. The connection to the desired input acceleration is made by penalizing the weighted ℓ_2 -deviation of \ddot{q}^a from the input \ddot{q}^{dsrd} in the objective (5.26a). A symmetric positive definite weight matrix $K \in \mathbb{R}^{n_q \times n_q}$ is yet to be determined. In a given ID setting, problem (5.26) is feasible for any desired input acceleration \ddot{q}^{dsrd} under Assumption 1 on page 58. The optimization problem is then transformed into the KKT system of,

$$\begin{bmatrix} M & 0 & J^T & S^T \\ 0 & S^T K S & 0 & S^T \\ \hline J & 0 & 0 & 0 \\ S & S & 0 & 0 \end{bmatrix} \begin{bmatrix} \ddot{q} \\ \ddot{q}^a \\ -\lambda \\ -\tau \end{bmatrix} = \begin{bmatrix} -N \\ S^T K S \ddot{q}^{\text{dsrd}} \\ -\gamma \\ 0 \end{bmatrix}. \quad (5.27)$$

Comparing the first rows of (5.27) and (5.13) it is obvious the the Lagrange multipliers τ are equivalent to the joint torques - compare equation (5.26c). This formulation approximates the FD case with sufficient accuracy for subsequent application in direct multiple shooting based optimization methods. However, a direct coupling between the controls of the accelerations and the physical accelerations is lost, due to the regularization. For application in optimal

control this aspect is not problematic, as the optimizer will take care of a proper choice of the input \ddot{q}^{dsrd} .

Relaxation of Forces

An alternative relaxation of the contact constraint (5.26b) and penalization of the corresponding violations in the objective, results into,

$$\min_{\ddot{q}, \lambda} \frac{1}{2} (\ddot{q}^T M(q) \ddot{q} + \lambda^T K \lambda) + \lambda^T (J \ddot{q} + \gamma) + N(q, \dot{q})^T \ddot{q}, \quad (5.28a)$$

$$\text{s.t. } S \ddot{q} = S \ddot{q}^a. \quad (5.28b)$$

The optimization problem then transforms into the full KKT system,

$$\left[\begin{array}{cc|c} M & J^T & S^T \\ J & K & 0 \\ \hline S & 0 & 0 \end{array} \right] \begin{bmatrix} \ddot{q} \\ -\lambda \\ -\tau \end{bmatrix} = \begin{bmatrix} -N \\ -\gamma \\ S \ddot{q}^{\text{dsrd}} \end{bmatrix}. \quad (5.29)$$

The weight matrix K must be chosen regular and sufficiently large to make the upper left sub-matrix positive definite. It can be seen that the contact force λ acts as a penalization weight for contact constraint violations. However, this relaxation has the effect that the kinematic contact constraints is not fulfilled with good accuracy. It is concluded that the original FD under contact constraints are not reasonably well approximated.

Relaxation of Joint Torques

The third relaxation of the joint acceleration constraint (5.26c) and penalization of the violations in the objective, leads to,

$$\min_{\ddot{q}, \tau} \frac{1}{2} (\ddot{q}^T M(q) \ddot{q} + \tau^T K \tau) + \tau^T S (\ddot{q} - \ddot{q}^{\text{dsrd}}) + N(q, \dot{q})^T \ddot{q}, \quad (5.30a)$$

$$\text{s.t. } J(q) \ddot{q} = -\gamma(q, \dot{q}). \quad (5.30b)$$

From the optimization problem (5.30) the KKT systems follows to,

$$\left[\begin{array}{cc|c} M & S^T & J^T \\ S & K & 0 \\ \hline J & 0 & 0 \end{array} \right] \begin{bmatrix} \ddot{q} \\ -\tau \\ -\lambda \end{bmatrix} = \begin{bmatrix} -N \\ S \ddot{q}^{\text{dsrd}} \\ -\gamma \end{bmatrix}. \quad (5.31)$$

Similar to the previous relaxations, the weight matrix K must be chosen regular and sufficiently large to make the upper left sub-matrix positive definite. In this relaxation the torques τ act as a penalization weight for joint acceleration constraint violations. With appropriate re-arrangements this approach is similar to the relaxation of the accelerations, but with a different expression for the weighting matrix K .

Combining All Relaxations

The weakest relaxation is given by the unconstrained convex minimization problem,

$$\min_{\ddot{q}, \tau, \lambda} \frac{1}{2} \left(\|\ddot{q}\|_{M(q)}^2 + \|\lambda\|_K^2 + \|\tau\|_K^2 \right), \quad (5.32)$$

$$- \tau^T S (\ddot{q} - \ddot{q}^{\text{dsrd}}) - \lambda^T (J \ddot{q} + \gamma) + N(q, \dot{q})^T \ddot{q}.$$

The optimization problem (5.32) then transforms into the KKT system,

$$\begin{bmatrix} M & J^T & S^T \\ J & K & 0 \\ S & 0 & \tilde{K} \end{bmatrix} \begin{bmatrix} \ddot{q} \\ -\lambda \\ -\tau \end{bmatrix} = \begin{bmatrix} -N \\ -\gamma \\ S\ddot{q}^{\text{dsrd}} \end{bmatrix}. \quad (5.33)$$

Again, the left hand side matrix must be positive definite. In contrast to the relaxations of a single quantity, e.g. acceleration, contact constraint forces or joint torques, appropriate weightings K and \tilde{K} achieve a good coupling of the final acceleration \ddot{q} with respect to the desired reference \ddot{q}^{dsrd} . However, an approximation of the FD with good accuracy can not be guaranteed any more as the kinematic contact constraints may be violated.

2.3 Solution of the KKT System

The system is then solved, based on direct methods for saddle-point systems [Benzi et al., 2005]. The algorithms should provide sufficient numerical accuracy as well as low computation times. All algorithms are subject to application in a derivative-based optimization framework for direct optimal control and thus results should be at least twice continuously differentiable with respect to all unknowns. Therefore, the use of pivoting-free approaches should be preferred over non-differentiable matrix manipulations, such as pivoting or eigenvalue computations.

At first physical accelerations \ddot{q} are decomposed orthogonally into their actuated,

$$S\ddot{q} =: v \in \mathbb{R}^{n_\tau}, \quad (5.34a)$$

and non-actuated,

$$P\ddot{q} =: w \in \mathbb{R}^{n_q - n_\tau}, \quad (5.34b)$$

parts combined to,

$$\ddot{q} = S^T v + P^T w. \quad (5.34c)$$

The selection matrices for actively controlled and passive joints are again denoted by S^T and P^T , respectively. These selection matrices satisfy the conditions,

$$SS^T = \mathbb{I}_{n_\tau}, \quad (5.34d)$$

and,

$$PP^T = \mathbb{I}_{n_q - n_\tau}, \quad (5.34e)$$

as well as the complementary condition,

$$SP^T = 0, \quad (5.34f)$$

$$PS^T = 0. \quad (5.34g)$$

For notational convenience the sub-set of desired accelerations is defined as,

$$v^{\text{dsrd}} := S\ddot{q}^{\text{dsrd}}. \quad (5.35)$$

With set of equations (5.34), (5.35) the orthogonal decomposition of the KKT system (5.27), then leads to,

$$\begin{bmatrix} SMS^T + K & SMP^T & SJ^T \\ PMS^T & PMP^T & PJ^T \\ JS^T & JP^T & 0 \end{bmatrix} \begin{bmatrix} v \\ w \\ -\lambda \end{bmatrix} = \begin{bmatrix} K v^{\text{dsrd}} - SN \\ -PN \\ \gamma \end{bmatrix}. \quad (5.36)$$

From the above discussion potential candidate choices for the weighting matrix K become obvious. The implications of these choices are discussed more in detail in the section below.

- Selection of $K = \alpha \mathbb{I} - SMS^T$ with $\alpha > 0$ renders the 1, 1-block of system (5.36) diagonal,
- Selection of $K = \alpha SMS^T$ with $\alpha > 0$ yields a 1, 1-block of the simpler structure $(1 + \alpha)SMS^T$.

Null-Space Method

A rearrangement of the reduced KKT system (5.36) results into the block system,

$$\begin{bmatrix} F & G^T \\ G & 0 \end{bmatrix} \begin{bmatrix} p \\ -\lambda \end{bmatrix} = \begin{bmatrix} -g \\ -\gamma \end{bmatrix}, \quad (5.37a)$$

$$F = \begin{bmatrix} SMS^T + K & SMP^T \\ PMS^T & PMP^T \end{bmatrix}, \quad (5.37b)$$

$$G^T = \begin{bmatrix} SJ^T \\ PJ^T \end{bmatrix}, \quad g^T = \begin{bmatrix} SN - K v^{\text{dsrd}} \\ PN \end{bmatrix}, \quad (5.37c)$$

with $p=(v,w)$ and the blocks for the Hessian-Vector (5.37b) as well as the Jacobian-matrix (5.37c). With a QR decomposition of G^T following (4.38) p is decomposed to $(u_a, w) = p = Y p_y + Z p_z$ and the system is solved using the null-space approach,

$$\begin{bmatrix} Y^T F Y & Y^T F Z & R \\ Z^T F Y & Z^T F Z & 0 \\ R^T & 0 & 0 \end{bmatrix} \begin{bmatrix} p_y \\ p_z \\ -\lambda \end{bmatrix} = \begin{bmatrix} -Y^T g \\ -Z^T g \\ -\gamma \end{bmatrix}, \quad (5.38)$$

(compare Section 3.2 on page 52). Solution of (5.38) yields the intermediate terms,

$$p_y = -R^{-T} \gamma \quad (5.39a)$$

$$p_z = (Z^T F Z)^{-1} Z^T (-F Y p_y - g) \quad (5.39b)$$

as well as the joint accelerations,

$$\ddot{q} = Y p_y + Z p_z, \quad (5.39c)$$

the joint torques,

$$\tau = K (u - S \ddot{q}), \quad (5.39d)$$

and the contact constraint forces,

$$\lambda = R^{-1} Y^T (g + F Y p_y + F Z p_z). \quad (5.39e)$$

From (5.39) it is clear that the computation of the physical accelerations \ddot{q} does not depend on the dual variables τ and λ . Thus, these values can be skipped to raise computational performance e.g. during pure forward integration. The choice $K = SMS^T$ in the final implementation is applied to ensure that F and $Z^T F Z$ are always positive definite and allow the application of a Cholesky decomposition.

Schur Complement Method

If the number of non-actuated joints $w \in \mathbb{R}^m$ and the number of contact constraints $g : \mathbb{R}^{n+m} \rightarrow \mathbb{R}^r$ is small compared to the number of the actuated joints $u \in \mathbb{R}^n$, in other words $m \ll n$ and $m \ll r$). The lower right subsystem of (5.36) then comes in a smaller dimension a fact that should be exploited. In order to do so, one may re-arrange it to block triangular form by forming the Schur-complement as in,

$$\begin{bmatrix} H & SMP^T & SJ^T \\ 0 & A & C \\ 0 & 0 & C^T A^{-1} C + B \end{bmatrix} \begin{bmatrix} v \\ w \\ -\lambda \end{bmatrix} = \begin{bmatrix} K v^{\text{dsrd}} - SN \\ a \\ C^T A^{-1} a + b \end{bmatrix}. \quad (5.40)$$

The system (5.40) contains the following matrix and vector terms,

$$H = SMS^T + K \rightarrow LL^T, \quad (5.41a)$$

$$A = \left(L^{-1} SMP^T \right)^T \underbrace{\left(SMP^T L^{-1} \right)}_{LSMP} - PMP^T \rightarrow Q_A R_A, \quad (5.41b)$$

$$C = \left(L^{-1} SMP^T \right)^T \underbrace{\left(L^{-1} SJ^T \right)}_{LSJ} + PJ^T, \quad (5.41c)$$

$$B = - \left(L^{-1} SJ^T \right)^T \left(L^{-1} SJ^T \right), \quad (5.41d)$$

$$a = - \left(L^{-1} SMP^T \right)^T \underbrace{\left(L^{-1} \left(SN - K v^{\text{dsrd}} \right) \right)}_{LSNK} + PN, \quad (5.41e)$$

$$b = - \left(L^{-1} SJ^T \right)^T \left(L^{-1} \left(SN - K v^{\text{dsrd}} \right) \right) + \gamma. \quad (5.41f)$$

With the Cholesky decompositions of H (5.41a), one may back-solve for $LSMP$, LSJ and $LSNK$ to compute the quantities A , C , B , a , and b . QR decompositions of A (5.41b) and $C^T A^{-1} C + B$ gives access to v , w and λ by three back-solves, respectively. Using these, the resulting quantities of the IdOP (5.24), being the contact constraint forces λ and related to λ , the physical acceleration \ddot{q} as well as the joint torques τ can be computed successively. The choice $K = \mathbb{I} - SMS^T$ is particularly efficient as it gives $H = H^{-1} = \mathbb{I}$.

3 Numerical Results for an Inverted Pendulum on a Cart

From the purely theoretic discussion it is difficult to entirely assess the numeric characteristics of a given algorithm, particularly in conjunction an OCP-formulation (4.1) to be solved by direct multiple shooting techniques. Therefore, the proposed algorithm is first investigated with an academic model that features the critical physical configurations of interest. Second, the algorithm is used on a more complex but realistic MBS (refer to Chapter 9 on page 124). The selected academic model is sample planar pendulum, attached on a cart, running on a rail (see Figure 5.2 on the next page). The selected set of coordinates is specifically not a minimal coordinate set to enable expression of a contact constraint set. Furthermore, the system is

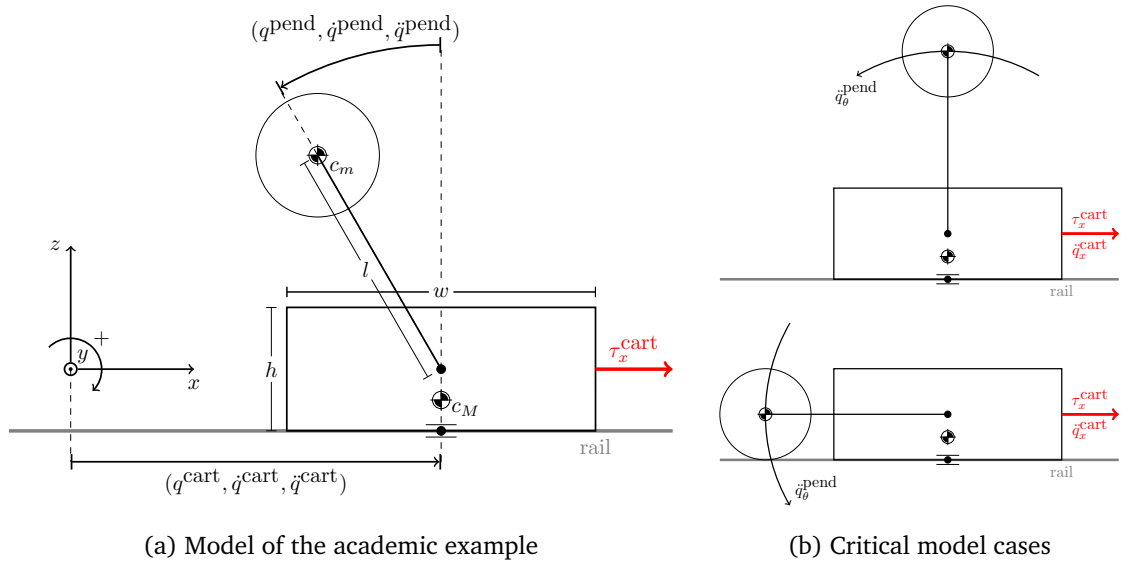


Figure 5.2: Academic example: rail pendulum

under-actuated to feature the limit configuration the previously proposed ID Op. addresses in the optimization context.

The pendulum system consists of a cart with height h , width w , depth d , mass M , and rotational moment of inertia I_{c_M} at its local center of mass c_M located underneath the geometric center of the body. The cart running on the rail, is modeled as a free-floating base in two dimensions. A non-actuated pendulum is attached to the center of the cart by a rotational joint. The pendulum has mass m and rotational inertia I_{c_m} at its local center of mass c_m located at the end of the rod with negligible mass and length l . The selected set of coordinates allows for linear motion in x - and z -directions as well as rotation around its y -axis of the cart and the pendulum attached to it. The resulting four dofs are namely the planar, free floating motion of the cart in space 2D-space and the pendulum rotation. The dof-vector is denoted as $\mathbf{q} \in \mathbb{R}^4$. The only available actuation is realized as horizontal force on the cart body and the linear actuation along the x -axis of the cart is denoted as $\tau_x^{\text{cart}} \in \mathbb{R}$. Revisiting equation (5.13) the actuation enters the model by intermediate of the selection matrix 5.42,

$$S = \begin{bmatrix} 1 & 0 & 0 & 0 \end{bmatrix}, \quad \tau = \begin{bmatrix} \tau_x^{\text{cart}} \end{bmatrix}. \quad (5.42)$$

The equations of motion in the form of (5.13) can be derived from the Lagrange formalism (2.21a). Only structural relevant parts as the joint space inertia matrix (5.43) and the contact constraint set are shown below,

$$M(\mathbf{q}) := \begin{array}{ccc} M+m & 0 & \frac{Mh}{4} \cos(q_\theta^{\text{cart}}) - lm \cos(\tilde{q}) \quad -lm \cos(\tilde{q}) \\ 0 & M+m & -\frac{Mh}{4} \sin(q_\theta^{\text{cart}}) + lm \sin(\tilde{q}) \quad lm \sin(\tilde{q}) \\ \frac{Mh}{4} \cos(q_\theta^{\text{cart}}) - lm \cos(\tilde{q}) & -\frac{Mh}{4} \sin(q_\theta^{\text{cart}}) + lm \sin(\tilde{q}) & I_{c_M,yy} + I_{c_m,yy} + \frac{Mh^2}{16} + l^2 m \quad I_{c_m,yy} + l^2 m \\ -lm \cos(\tilde{q}) & lm \sin(\tilde{q}) & I_{c_m,yy} + l^2 m \quad I_{c_m,yy} + l^2 m \end{array}, \quad (5.43)$$

$$\tilde{q} = q_\theta^{\text{cart}} + q_\theta^{\text{pend}}.$$

The vector of nonlinear effects result in a simplified form to (5.44a) with gravity terms related (featuring g) and terms depending on the Coriolis effects v_1 and v_2 , respectively. The complex blocks representing the Coriolis effects v_1 and v_2 are not relevant for the remainder of this

discussion and hence, are omitted,

$$N(q, \dot{q}) = \begin{bmatrix} v_1 \\ v_2 \\ 0 \\ 0 \end{bmatrix} + \begin{bmatrix} 0 \\ Mg + mg \\ 0 \\ -g\ell m \sin(q_\theta^{\text{pend}}) \end{bmatrix}. \quad (5.44a)$$

The cart is in frictionless contact with its rail. The rigid contact is described in accordance to (2.22) and (2.23) as bilateral holonomic constraints $c(q) = 0$ on both the z -position and rotation around the y -axis through the contact point at the bottom center of the cart. The Jacobian matrix J of the contact constraint c then follows to (5.44b).

$$J(q) = \begin{bmatrix} 0 & 1 & \frac{h}{2} \sin(q_\theta^{\text{cart}}) & 0 \\ 0 & 0 & 1 & 0 \end{bmatrix}, \quad (5.44b)$$

Remark 4 *The cart setup, especially the lowered CoM of the cart and the contact as constraint on translation and rotation, is selected for the purpose to generate a non-trivial contact force in z -direction and a torque around the y -axis of the contact point. Furthermore, this leads to a decoupling of the contact force and torque. The contact force will only depend on the dynamics of the system, while the contact torque will contain additionally effects of the cart's actuation.*

3.1 Rank Deficiency in Inverse Dynamics

The pendulum on a cart system is underactuated,

$$\text{rank}(J(q)P^T) = \text{rank} \begin{pmatrix} 1 & \frac{h}{2} \sin q_\theta^{\text{cart}} & 0 \\ 0 & 1 & 0 \end{pmatrix} \neq n_q - n_\tau, \quad (5.45)$$

according to Definition 5.17 on page 60 with contact Jacobian (5.44b) and complementary selection matrix P . Equation (5.45) shows that the motion of the unactuated pendulum is not entirely defined by the contact equation (2.23b). Additionally, in vertical positions of the pendulum $q_\theta^{\text{pend}} = \pm \frac{\pi}{2}$, the x -acceleration of the cart and the rotational acceleration of the pendulum about the y -axis are decoupled from the joint space inertia matrix. This can be seen from the zero entries in the (1, 4)- and (4, 1)-blocks of (5.43), which for $q_\theta^{\text{pend}} = \frac{\pi}{2}$ are shown in,

$$M(q) = \begin{bmatrix} M+m & 0 & \frac{Mh}{4} & 0 \\ 0 & M+m & \ell m & \ell m \\ \frac{Mh}{4} & \ell m & I_{C_{M,yy}} + I_{C_{m,yy}} + \frac{Mh^2}{16} + \ell^2 m & I_{C_{m,yy}} + \ell^2 m \\ 0 & \ell m & I_{C_{m,yy}} + \ell^2 m & I_{C_{m,yy}} + \ell^2 m \end{bmatrix}. \quad (5.46)$$

According to the discussion of the algorithms in section 2.2 on page 61, the solution of the ID problem in this singular configuration is problematic, as the dof of the pendulum rotation can not even be influenced through the horizontal cart motion over the dynamic coupling effects in the joint space inertia matrix (compare (5.43) and (5.46)). However, this problem does not occur in FD. Besides rigorous symbolic verification, numerical tests with this algorithm comparing both, the FdOP and the IdOP inside the OCP formulation (4.1) are conducted to confirm the mathematical compatibility of the IdOP with the respect to the requirements of the enveloping OCP algorithms and its accurate approximation of the FD.

3.2 OCP Formulations

For verification purposes various optimal control scenarios with a common motion sequence (up-swing) are investigated. The cart pendulum starts from a given initial solution with zero velocities, cart x - and z -position in the origin, and the pendulum pointing downwards. The different scenarios are then, as follows:

Objective: Investigation of *time optimal* and *energy optimal* motions,

Dynamics: Computations on FD and ID,

Discretization: Two different time discretizations for the control $u(\cdot)$: piecewise linear continuous (plc) and piecewise linear continuous and once integrated (plci) - equivalent to quadratic-continuous joint torques and joint accelerations for the FdOP and the IdOP, respectively.

Multiple-Shooting Grid: Various multiple-shooting interval lengths/accuracy of the discretization have been investigated.

Impacts are not considered and the cart stays in contact with its rail during the entire time horizon. In other words the set of active constraint I is constant for the whole horizon and henceforth omitted throughout this section. For time optimal control, the objective function terms follow to,

$$L(x(t), u(t), p) := 0, \quad E(x(t_{\text{fin}}), p) := t_{\text{fin}}, \quad (5.47a)$$

$$L(x(t), u(t), p) := \tau, \quad E(x(t_{\text{fin}}), p) := 0, \quad (5.47b)$$

for the minimum time and minimum actuation energy objective, respectively. Herein, τ denotes the actuation of the cart. Depending on the dynamics and discretization used in the OCP (4.1), τ may enter the right hand side as a control (FD - plc), a differential state (FD - plci), or exit the right hand side as a nonlinear algebraic expression involving the former two (ID - plc and plci).

Formulations of the Dynamic System

For a thorough discussion the OCP-formulations arising from the different scenarios are of interest. As a sufficiently detailed scheme for each operator is given in Figure 5.1 on page 55, the more interested reader is referred to the Appendix G on page 253 for a detailed description.

3.3 Results

All scenarios have been computed with using the direct multiple shooting code for optimal control MUSCOD-II [Leineweber et al., 2003a,b] and the results for the minimum time and the minimum energy objective are discussed in the subsequent paragraphs, respectively.

Time-Optimal Control

From the results of the minimum time objective (see Figure 5.3 on the next page and 5.4 on page 71) one may observe a swing-up motion of the pendulum that starts with a fore-swing runs through the singularity (gray highlighted area - singularity = dashed red line) and stops upright. As the control discretization is a piecewise linear trajectory, the actuation in Figure 5.4 on page 71 approximates a piecewise constant bang-bang solution. As no limit excess

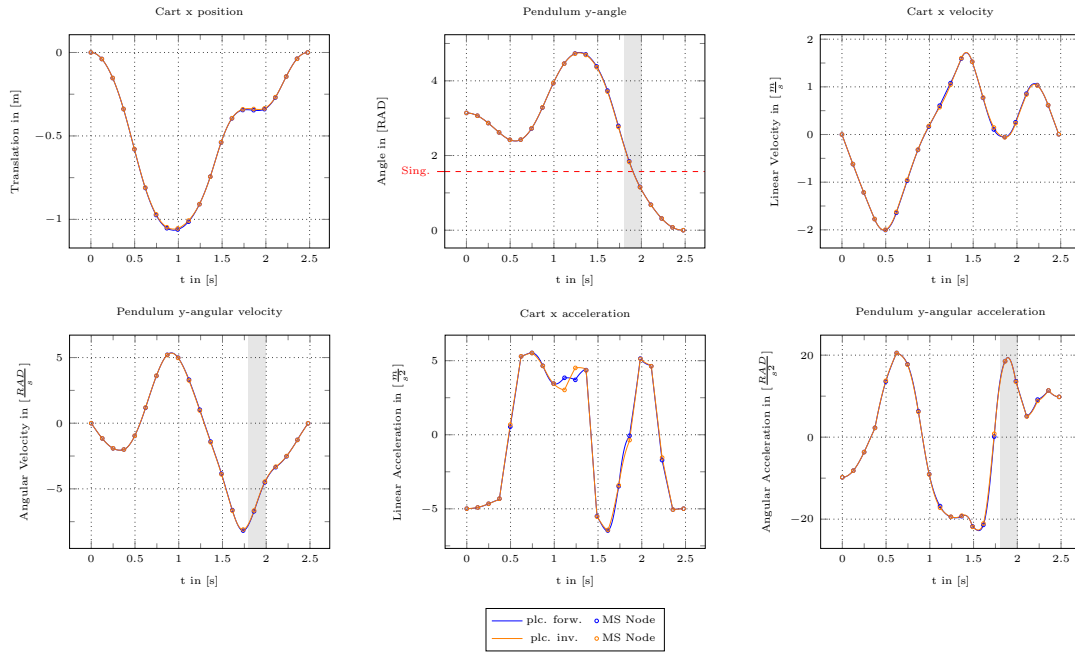


Figure 5.3: Trajectory Profile of the fastest swing-up motion of the pendulum cart within the dynamic constraints at hand. *Cart x position* represents the linear translation of the cart in x direction and *Pendulum y-angle* represents the orientation of the pendulum with respect to the cart (0 = pendulum in upright position). The Graph only show the dofs that are free to move during the simulation in position/orientation, velocity and acceleration (all other dofs are verified to stay constantly at 0 for position, velocity and acceleration). Whilst position and velocity are consistent between forward and inverse dynamics, small differences, however, remain in the acceleration profile. This difference does come from the different control discretisation between inverse and forward dynamics. The dashed red line marks the singularity where the pendulum motion is completely decoupled from the cart acceleration. The corresponding time range when the trajectory profile passes through the singularity is highlighted in gray

in the actuation is produced both solutions (forward and inverse dynamics) are feasible and show good consistency. The only differences observable are in the linear acceleration profile of the cart as well as in the actuation profile and the contact constraint reaction torque in the linear cart bearing. These differences are expected to result from the different control discretization between the forward and the IdOP. Furthermore, a decoupling of the dynamic effects influencing the contact constraint reactions is clearly observable, as discussed in Remark 4 on page 68. While the contact torque M_y shows similar perturbations between both operators, the vertical contact force F_z only depends on the pendulum motion and is nearly identical.

From the gray highlighted area, which marks the region where the pendulum passes through the singularity, it is clearly visible that there is good agreement between the resulting trajectories of the ID and the FD. Therefore, one may conclude that the IdOP correctly selects the accelerations with respect to the physical configuration.

Energy-Optimal Control

For the minimum energy objective a fixed simulation time was chosen, to further investigate the influence of different control discretizations on the FdOP and IdOP. From Figure 5.5 on page 72 and (5.6) the linear acceleration profiles are much more cracked for the plc control

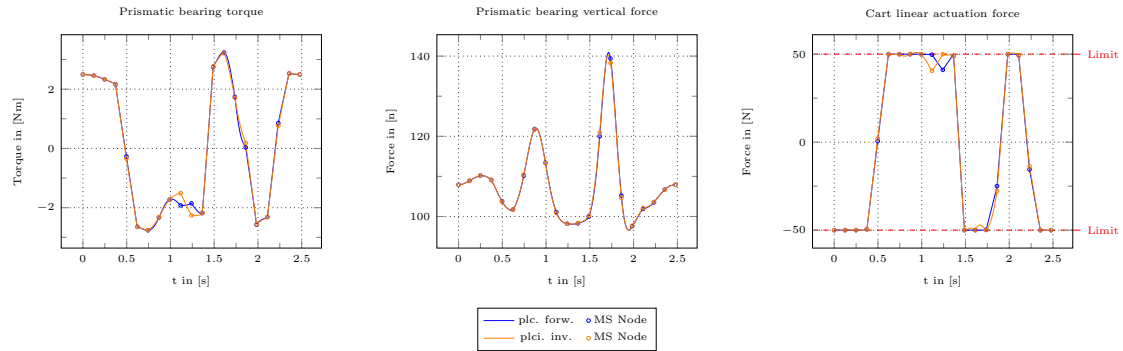


Figure 5.4: This graph shows the bearing constraint reactions as well as the actuation profile for the fastest swing-up motion within the dynamic constraints. *Prismatic bearing torque* represents the torque contact reaction and *Prismatic bearing vertical force* the vertical force on the prismatic bearing. The actuation of the cart represents a bang-bang solution. The maximum force has been limited to 50 N into both directions. The chosen actuation profile stays within the boundaries and is consequently feasible. It is clearly observable that the difference in discretisation between the FdOP and IdOP are decoupled between the vertical force and the torque in the bearing as well as the actuation force of the cart.

discretization then for plci controls. Furthermore, it is clearly visible that the linear cart trajectory in translation, velocity and acceleration differs much more between the different modes, than the trajectory in orientation, angular velocity and angular acceleration of the pendulum. Firstly, this is held to come from the different control discretization and secondly from difference between the FdOP. and the IdOP. The contact constraint reactions in Figure 5.5 on the following page show the same decoupling as for the minimum swing-up time objective. But in the actuation profile of the cart the plci control discretization features two excesses of the upper and lower limit (marked with gray dashed rectangles). This is possible as the box constraints (FdOP) as well as the decoupled interior point constraints (IdOP) used to enforce the actuation force limits are only respected on the multiple shooting nodes thus allowing for limit excess in between (refer to Section 1.4 on page 45). The large difference of the motion profiles between the plci and plci control discretization may then be explained, as the optimal control solver exploits these small infeasibilities to further reduce the objective.

The small difference between the FdOP and the IdOP with respect to orientation, angular velocity and acceleration profile (Figure 5.5 on the following page), especially in the gray highlighted time period, where the system passes through the singularity, confirm again, that the IdOP correctly selects the angular acceleration with respect to the governing physical configuration of the MBS structure and hence coincides with the FdOP. The same characteristic is observable in the profile (Figure 5.6 on page 73) of the vertical contact constraint reaction.

Discussion

From Table 5.2 on page 75 the number of iterations as well as the dimensions of the discretized problem formulations of the test cases are given. Generally the IdOP tends to produce discretized problem formulations with a higher number of constraints with respect to the OCP-formulation (4.1). The difference in the number of variables between the plc and plci control discretization is the introduction of a further system state +21 variable to handle the integration of the plc control.

The number of iterations until a stable convergence into a local optimum is reached is influenced from various aspects. For the minimum time objective the IdOP reaches faster to

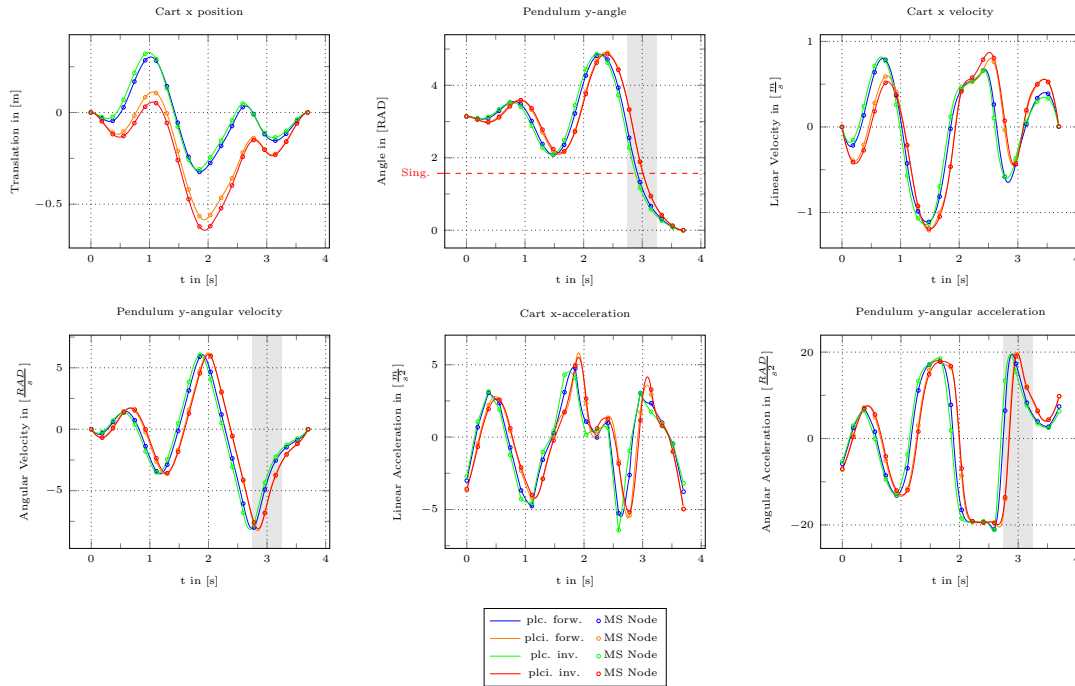


Figure 5.5: Trajectory profiles for minimum energy solution of the FD (*forw.*) and ID (*inv.*) algorithm based on two different control discretisations: plc, plci (equivalent to piecewise quadratic continuous controls). The influence of the two different discretisation schemes is clearly visible in the acceleration profiles of the different solutions - *Cart x position*. Whilst the plc profile has abrupt changes the plci is smooth. The end time of the swing-up motion is fixed. Despite the different schemes of discretisation used in the problem formulation (differences are clearly expected here) there are still small but observable differences between the solutions of the acFdOP and the IdOP with the same discretization scheme. The dashed red line marks the singularity where the pendulum motion is completely decoupled from the cart acceleration. The corresponding time range when the trajectory profile passes through the singularity is highlighted in gray

a convergence. For the minimum energy case only the plc solved based on a Quasi-Newton method shows a quicker convergence for the IdOP. In the case of an exact Newton-method the Hesse-matrix is approximated based on finite differences. This might as well explain the outliers of iterations until convergence in Table 5.2 on page 75. Here the IdOP reaches much faster a convergence for the plci case. Consequently, it is not possible to determine whether the FdOP is outperforming the IdOP or vice versa, inside the OCP formulation. Finally a big advantage of the ID is that the problem formulation may be initialized based on purely kinematic quantities (position, velocity and acceleration). Joint torques and contact constraint forces are then computed accordingly.

3.4 Node Analysis

Additionally, to each computation based on the OCP formulation (4.1), that is conducted with direct multiple-shooting techniques, an analysis of the quality of approximation of the trajectories of the dynamic model depending on the chosen discretization is highly advisable. The quality of approximation depends a various distinct aspects. Most important among these are:

- Accuracy of integration/sensitivity evaluation (refer to Section 1 on page 43)

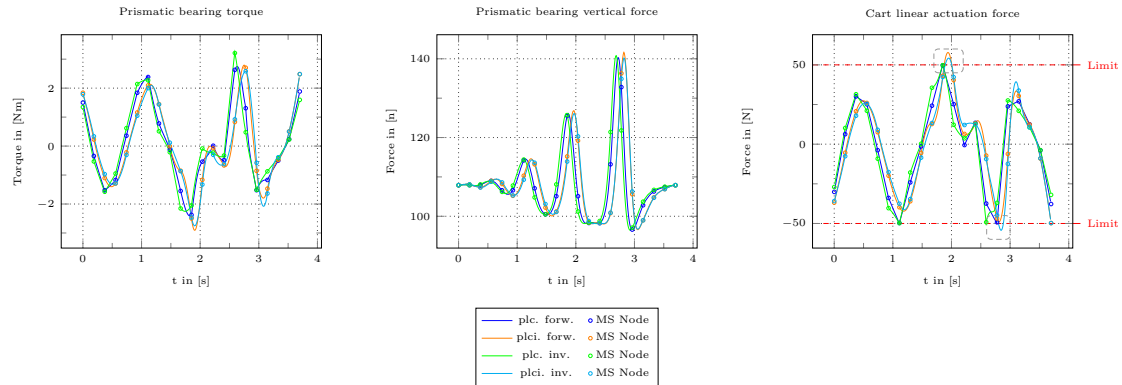


Figure 5.6: Graphs of the bearing reactions of the cart, *Prismatic bearing torque* represents the torque and *Prismatic bearing vertical force* the vertical force in the prismatic bearing of the cart. The linear propulsion is represented by *Cart linear actuation force*. The difference between the two different discretisation schemes is clearly observable as the plc actuation profile is more cracked compared to the smooth actuation profile of plci. Furthermore, small excess (marked with dashed grey rectangles) of the limits in actuation (50 [N]) are visible for the plci discretisation scheme whilst the plc keeps within the limits for FdOP and IdOP, thus the plci discretisation scheme produces slightly infeasible solutions based on the current problem formulation. With rising quality of the discretisation scheme $\text{plc} \rightarrow \text{plci}$ the difference between the forward and inverse solution becomes smaller. A decoupling between the torque in the bearing, partially related to the linear actuation, and the vertical bearing force is clearly observable.

- Number of control parameters (number of multiple-shooting nodes)
- Type of basis functions of control parametrization (plc or plci)
- Type of model - type of model input that is stimulated with the controls

Consequently, for each investigated scenario and model a specific analysis has to be conducted to cover the above mentioned aspects and to assess their individual influence on the final result after convergence. This analysis must be conducted for each combination of employed model and scenario. Depending on the model and the problem formulation the analysis can get relatively resource intensive. Thus, for the sake of brevity, only the respective analysis for the academic model, described in Section 1 on page 253, is shown as an example. For each of the subsequent optimization results such kind of analysis was conducted, its presentation however, is outside of the scope of this work.

Influence of the Discretization

From Figure 5.7 on the following page distinct features (cart position about the x -axis, pendulum orientation about the y -axis, actuation of the cart) of the converged of 16 simulations, four distinct multiple shooting configurations (21, 41, 81 and 161 nodes) for plc as well as plci control discretization for FdOP and IdOP are shown, respectively. All computation have been performed with the same termination criteria and accuracy of the integrator.

It is important to note that, despite the different scenarios, with respect to the general analysis of the IdOP in contrast to the FdOP, both operators perform with good consistency on the trajectories that purely depend on the forward dynamics (middle row of plots). Small deviations exist, however.

Generally, all 12 plots feature the same tendency, as such, all trajectories tend towards a profile with increasing number of multiple shooting nodes (top row of plots). For the dof that

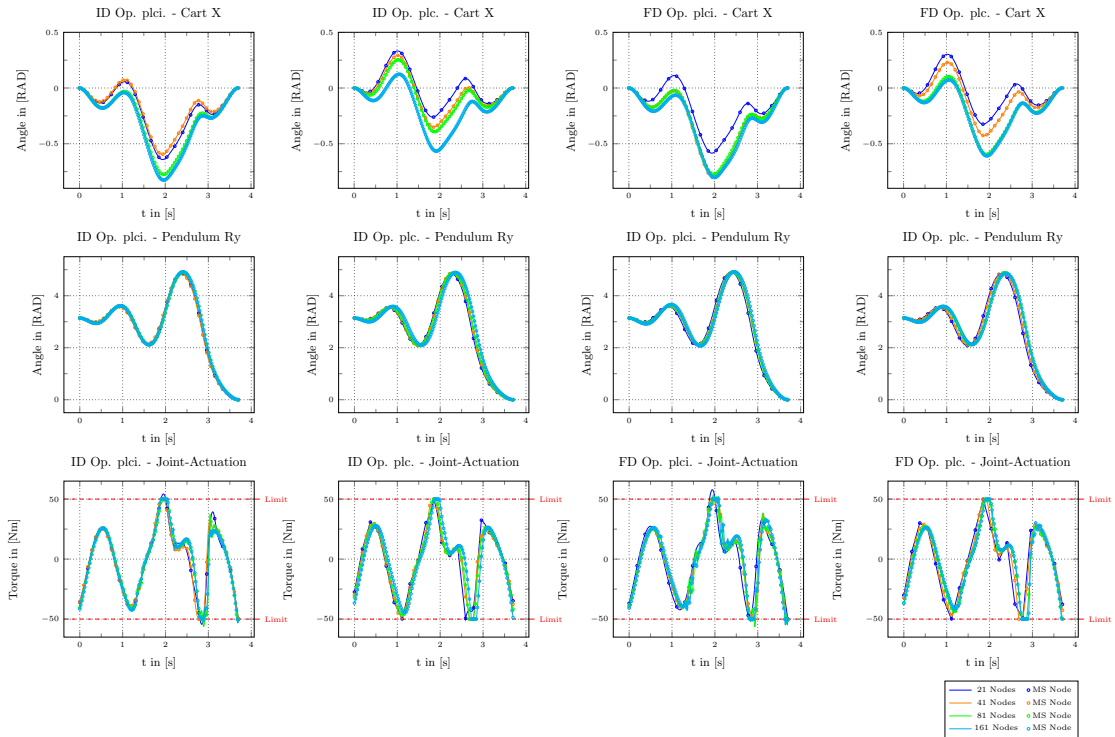


Figure 5.7: The node analysis shows how the different discretization with respect to the number of employed control parameters, the type of basis functions and the type of control parametrization influences the accuracy of the approximation of the dynamic behavior of the optimized system.

depends on the controls of the OCP-formulation (4.1) this profiles seems to be different between the different types of control discretizations (plc and plci) however, for the same control discretization FdOP and IdOP perform similar. The same relation is clear for the actuation of the system (bottom row of the plots).

It is interesting to note, that the plci control discretization seems to out-perform the plc control discretization, as despite the limit violations between the multiple shooting nodes, the plci control discretization tends faster towards the final profiles (at lower multiple-shooting node numbers) than the plc control discretization.

Finally, an obvious aspect of the higher number of multiple shooting nodes, is the reduction of limit excess of the system-actuation at higher multiple-shooting node numbers.

Discussion

The high variability of the results from the above proposed investigation underline the necessity to perform thorough analysis of each model combined with each optimization scenario to assess the quality of the finally converged optimization results. This information is crucial and should be obtained before any statement or interpretation with respect to the elaborated computations is to be made.

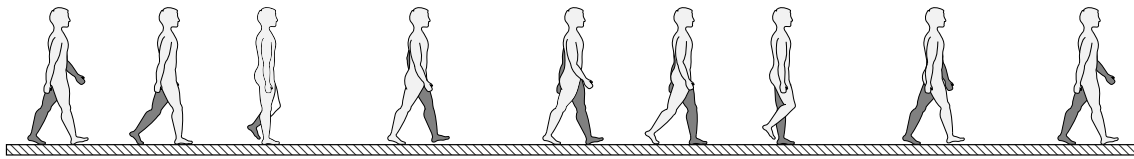
As a general experience, the plci control-discretization for both, the FdOP and the IdOP produce more smooth actuation profiles (plci versa plc) and seem to require less multiple shooting node numbers to tend towards a final trajectory profile of the dynamic system behavior.

Table 5.2: Number of NLP variables (Vars) and constraints (Cons) and number of SQP iterations (It) until a KKT tolerance less than 10^{-4} is achieved for the pendulum on a cart example. Both FD and ID are evaluated with both plc and plci control discretization, together with a BFGS approximation of the Hessian of the Lagrangian as well as with an exact Hessian.

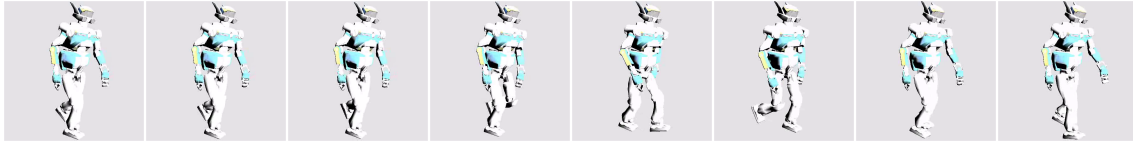
Objective	Dyn.	Disc.	Hessian	Vars.	Cons.	It.
Energy	FD	<i>plc.</i>	BFGS	209	627	142
Energy	ID	<i>plc.</i>	BFGS		652	91
Energy	FD	<i>plci.</i>	BFGS	230	672	42
Energy	ID	<i>plci.</i>	BFGS		714	70
Energy	FD	<i>plc.</i>	Exact	209	610	34
Energy	ID	<i>plc.</i>	Exact		652	35
Energy	FD	<i>plci.</i>	Exact	230	672	423
Energy	ID	<i>plci.</i>	Exact		714	21
Time	FD	<i>plc.</i>	BFGS	210	612	93
Time	ID	<i>plc.</i>	BFGS		654	44

Part

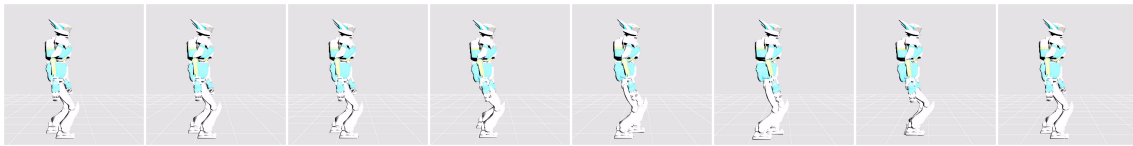
Optimal Control for HRP-2 Motions



(a) Scheme of a full stride - human walking motion



(b) Human walking motion full stride - retargeted to the kinematic structure of the robot.



(c) Full stride walking motion generated with the pattern generator from [Kajita et al., 2003a].

Figure 5.8: Different walking motions - Human motion as scheme - retarget walking motion from motion capturing on HRP-2 14 and walking motion, generated with a pattern generator

As one looks at the walking motion depicted in Figure 5.8a, the absolutely natural question comes up - why robots just can't walk around like this? - or, what would they need to actually walk more human like?

At one hand, an attempt from the human to the robot would be to simply transform the human walking motion, e.g. registered with a motion capturing system, to the robot. This process is called motion retargeting [Hecker et al., 2008], presents a relatively low complexity and is therefore in most cases real-time capable. The result is shown in Figure 5.8b. The motion has a relatively natural appearance, however, it violates several physical limits of the robots, does not respect the contact of the feet on the ground and is generally not physically consistent. At the other hand the technical attempt would be to generate a highly abstracted walking motion, based on a pattern generator (refer to Section 3.1 on page 7). The result is shown in Figure 5.8c. A direct comparison between Figure 5.8a and 5.8c as well as 5.8a and 5.8b that there is still a huge difference between both motion appearances.

Although the walking motion from Figure 5.8c respects the dynamic limits of the robot is physically feasible and performs well along with the online stabilizing control system of the robot, the gait present some odd-looking features. From Figure 5.8c one may observe a high bending of the knee throughout the complete cycle. Furthermore, the hip pitch-angle is turned slightly backward and the pelvis altitude remains perfectly constant (compare with Section 3.1 on page 7) and only little contra-lateral arm-swinging is visible.

As it was discussed in Section 1 on page 1, 2 on page 3 and 3 on page 6 the given problematic is related to multiple issues. At one hand, the kinematic structure of a given robot, in this case the robot HRP-2 N° 14 [Kaneko et al., 2004], may not fully comply with all DoG of an anthropomorphic gait and hence, the lack of one DoG may yield an exaggerated motion of a complementary DoG leading to higher energy consumption [Saunders et al., 1953]. At the other hand, as it was discussed in Section 3 on page 6, motion generation methods based on heuristics employ a highly simplified scheme and adopt various assumptions that may limit the possible subspace of potential walking motions one could choose from to walking motions with an odd looking appearance.

Therefore, not only the structure of the robot could be a limiting aspect, as well the motion generation method with its assumptions and simplifications should be investigated thoroughly. From the discussion of the hardware of HRP-2 N° 14 [Kaneko et al., 2004] in subsequent sections it is clearly observable the the robotic platform lacks a dof to perform a pelvis tilt. Therefore the robot does not fully comply with the DoG defined by [Saunders et al., 1953], hence the target of goal of designing a perfectly natural appearance of the walking gait may technically be infeasible.

The OCP based motion generation process employed in this work allows for the formulation of optimization problems to generate a whole body motion, purely based on its physical governing events and some control input, but directly respecting all kinematic and dynamic constraints. Therefore the main question would be - given the kinematic structure of the robot which aspect may change in the motion generation process, such that the motion appearance is more human like, robust and more energy-efficient?

In the following, this investigation will be performed for HRP-2 N° 14 [Kaneko et al., 2004] and it turns out (compare with the previous part) that despite the accurate dynamic model that is available, some crucial parts that are advertised in recent literature, actually need considerable efforts in modeling before any reasonably well suited motion results for that specific robot can be generated.

Related Publications: The scientific work conducted in the following chapter has been issued for publication in:

- Kai Henning Koch, Katja Mombaur, Philippe Souères. Optimization-based walking generation for humanoid robot. 10th IFAC Symposium on Robot Control (SYROCOS), 2012, Croatia
- Kai Henning Koch, Katja Mombaur, Philippe Souères. Studying the effect of different optimization criteria on humanoid walking motions. 3rd International Conference on SIMULATION MODELING AND PROGRAMMING for AUTONOMOUS ROBOTS, 2012, Japan
- Katja Mombaur, Kai Henning Koch, Martin Felis. Model-based Optimization for Robotics 日本ロボット学会, Vol 32, No.6 pp. 1-7, 2014, Japan
- Kai Henning Koch, Katja Mombaur, Olivier Stasse, Philippe Souères. Optimization based exploitation of the ankle elasticity of HRP-2 for overstepping large obstacles. IEEE-RAS International Conference on Humanoid Robots, 2014, Spain

Acknowledgment This project has been conducted in cooperation between the University of Heidelberg - IWR (Interdisciplinary Center for Scientific Computing, Heidelberg) - and the LAAS-CNRS (Toulouse) - Groupe GEPETTO. Funds from the HGS MathComp Graduate School, European Project ECHORD/GOB, the European Koroibot Project and the LAAS-CNRS for this project are gratefully acknowledged.

6 Modeling of the Humanoid Robot HRP-2

With a clear view on the scope of the modeling process and its potential application in conceptual motion generation, it will now be interesting to discuss a real world example - the humanoid robotic platform HRP-2 N° 14 (located in Toulouse). In the following, the relevant dynamic characteristics of the robot are discussed in the context of an efficient but sufficiently precise mathematical modeling. With two different modeling approaches important aspects to be carefully considered during the general modeling as transfer from the real-world into simulation are discussed. Finally it is shown how optimal control can be highly efficient in conceptual motion generation to efficiently investigate potential aspects to improve the dynamic operation of a given (robotic) platform based on its whole-body physical characteristic, breaking up with previously made assumption for simplification, that may have been helpful at one hand, but at the other hand did create limiting constraints to prevent the exploration of the full technical capacities of the (robotic) platform at hand.

1 The Humanoid Robot HRP-2 N° 14

HRP-2 N° 14 is a medium human size (1.58m) robot with 30 dofs that has been developed from a series of prototypes, namely the HRP-2L [Hirukawa et al., 2004], HRP-2LR [Kajita et al., 2004, 2005], HRP-2LT [Kajita et al., 2007a] and the HRP-2P [Hirukawa et al., 2005], during the Humanoid Robotics Project from Ministry of Economy, Trade and Industry, Japan (METI)[Hirukawa et al., 2004, Yokoi et al., 2001] Japan.

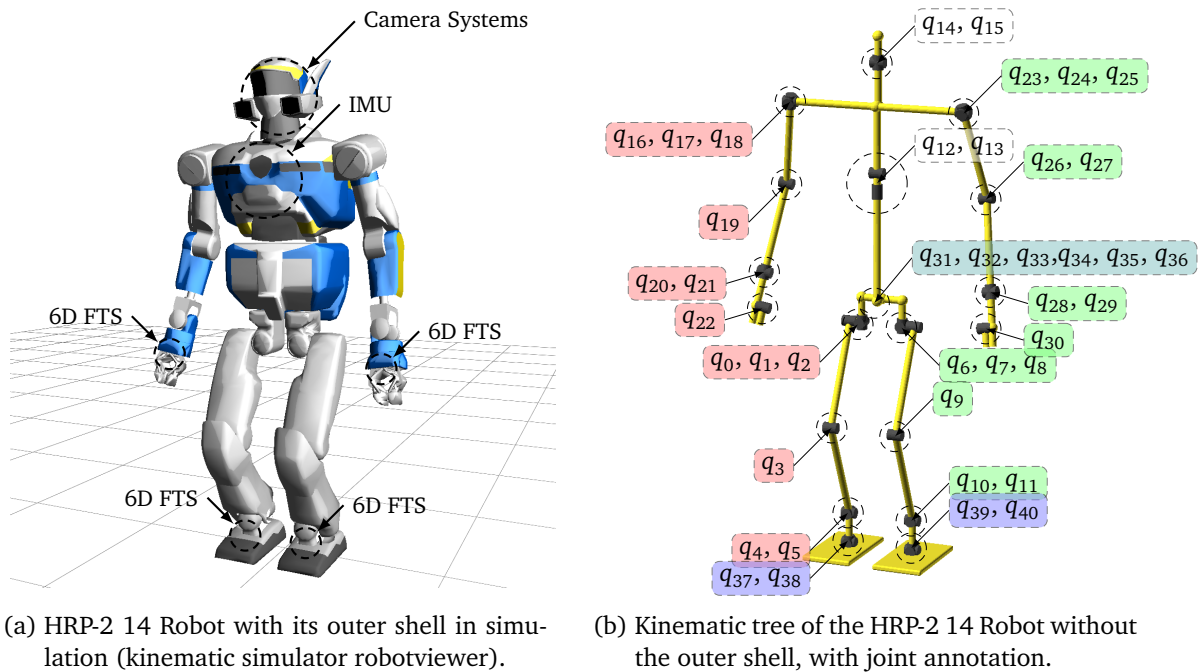
Detailed technical information can be obtained from [Kaneko et al., 2004]. From the design and experiment history of this robot series, that contains amazingly complex motion tasks as safely falling down and getting up [Hirukawa et al., 2005] as well as dynamic tasks, as hopping [Kajita et al., 2004] and running [Kajita et al., 2005, 2007b] the final platform HRP-2 N° 14 seems to be relative mature. There exists a huge number of dynamically highly challenging tasks that have been successfully implemented on this platform, such as, dynamically lifting [Arisumi et al., 2008] and carrying heavy objects [Harada et al., 2005], Walking on uneven terrain [Morisawa et al., 2012] and successfully statically and dynamically overstepping obstacles [Guan et al., 2005, Stasse et al., 2009, Verrelst et al., 2006]. Consequently the platform at hand seems to be the perfect base for practical applications of subsequent optimization studies.

1.1 Hardware

In the following all necessary characteristics of the robotic hardware will be collected and discussed to motivate the mathematical modeling of the robot for optimal control. The simulation environment used for controller design and verification of candidate motion solutions from optimal control will be addressed then in a separate chapter.

Kinematic Structure

The robot has 6 dof per leg, 2 dof in the torso element and the head as well as an additional 7 per each arm that are actuated [Kaneko et al., 2004]. Underneath the ankle-joint



(a) HRP-2 14 Robot with its outer shell in simulation (kinematic simulator robotviewer). (b) Kinematic tree of the HRP-2 14 Robot without the outer shell, with joint annotation.

Figure 6.1: Outer and schematic structure of the HRP-2 14 robot. Figure 6.1a features the location of the important sensor system of HRP-2 14 are shown. FTS represents the 6D force and torque sensors that is used in the ankle and wrist joint complexes for dynamic stabilization and interaction with the environment. Figure 6.1b shows the kinematic structure. Joints on the left and right side of the robot are emphasized green and red, respectively. The free floating base is marked with teal and the passive elastic joints are shown in blues. The force-torque sensors are installed slightly above the passive elasticity.

complex the robot has a further flexible element henceforth called the ankle elasticity [Kajita et al., 2001b, 2005, Nakaoka et al., 2007]. It is an assembly of 3 rubber bushings and serves multiple purposes (shock absorption and balance control). With respect to its importance to the secure operation of the robot this flexibility complex will be addressed in a separate section. The robot is further placed on rubber coated feet. According to [Chardonnet, 2009] this rubber coating does not substantially contribute to the elastic behavior of the complete ankle-foot complex - even though studies are ongoing how further elasticity components may be exploited [David et al., 2008]

The hip-joint of the robot is designed in a cantilever-style [Hirukawa et al., 2005, Kaneko et al., 2004]. This opens a more extended work-space to the leg, enables the robot for cross-walking and more stable operations, as the amount of candidate foot-landing positions is higher. Together with a more human-like back-pack less design and a waist joint the robot can easily stand-up from a crouched or laying configuration on the ground and use the waist joint for dynamic yaw compensation or extend the work-space of the arms. In [Kaneko et al., 2004] the authors stress as well, that large possible motion ranges of each joint for more human-like motions [Hirukawa et al., 2005, Kaneko et al., 2004]. While this is in most cases desirable one needs to be very careful not to run into self-collision issues during the motion generation process (see Figure 6.1).

In comparison with its predecessors HRP-2 N° 14 has been designed for better structural stiffness to improve the stability of the overall motion performance [Hirukawa et al., 2005, Kaneko et al., 2004]. From thorough checks of its dynamic characteristics the kinematic structure does have smaller non-symmetric portions - even though the influence was evaluated to

be relative small, this aspect may produce numerical problems during the optimization, when symmetry constraints are not appropriately formulated.

Sensor System

The HRP-2 N° 14 platform is equipped with a wide range of different sensors [Hirukawa et al., 2004, 2005, Kaneko et al., 2004] dedicated for stable motion control (joint encoder, Inertial Measurement Unit (IMU), force/torque sensors) and external environment exploration and interaction (stereo camera sets, microphone). Refer to Figure 6.1 on the previous page for the location of these sensors. In the following only the force/torque sensors and the IMU of the robot are of interest as they are part of the control algorithms for dynamic stabilization of the robot.

The IMU of HRP-2 N° 14 consists of a three axis gyroscope and accelerometer. From the raw data the global orientation of the torso link is estimated with a Kalman Filter [Sabatini, 2011] and fed into the stabilizing algorithms for posture control. The current implementation on the robot HRP-2 N° 14 does only estimate the horizontal components (roll, pitch) of the torso orientation, however different implementations for additional Yaw-Angle estimation are available but have not been employed during this work.

While 6D force/torque sensors in the wrist are mainly dedicated for environmental interaction, the same sensors in the feet are actively used to maintain the dynamic equilibrium of the robot. [Nakaoka et al., 2007] explains that the bushing assembly of the ankle elasticity complex is directly mounted underneath the force/torque sensor. Hence in the following it is assumed that the 6D stress, that is measured directly reflects the stress configuration in the ankle-elasticity complex.

Actuation System

HRP-2 N° 14 is powered with brushed DC-machines [Kaneko et al., 2004] (see 1 on page 230) based on high-gain position controllers. In comparison with its predecessors HRP-2 N° 14 has been equipped with more powerful actuators and special cooling system to enable the robot for longer continuous operation. The highly compact and low-noise design of the electrical control system is dispatched into two separated units, one for real-time (running RTLinux [Yodaiken, 2007]) and the other one for non-real-time control tasks. The motion control itself is based on multiple control cycles. The main loop is the robot controller running at 5ms [Hirukawa et al., 2003] time cycle. It consists of a stack of different algorithms for motion generation (e.g. pattern generators [Stasse et al., 2008]) and stabilization (e.g. stabilizer [Kajita et al., 2005, 2007b, 2010]) incorporating further control feedback control loops to maintain dynamic equilibrium. The motion reference is then tracked with the servo controllers featuring a position-feedback controller of the motor/encoder units in all joints, running at a smaller time-cycle [Kaneko et al., 2004]. An abstract signal scheme is shown in Figure 6.3 on page 84, please refer to [Khalil and Dombre, 2002] for a further discussion of different control schemes.

Even though simple cascaded joint controller as such shown in Figure 6.3 on page 84 are adjustable for good reduction of external perturbations, tracking quality may be reduced for reference signals with higher frequencies [Heimann et al., 2007]. Hence it is important to characterize the tracking error before any comprehensive discussion is possible. This aspect is even more important for the analysis of the dynamic equilibrium of the robot, as the stabilization and joint control are closely related.

Online Stabilization

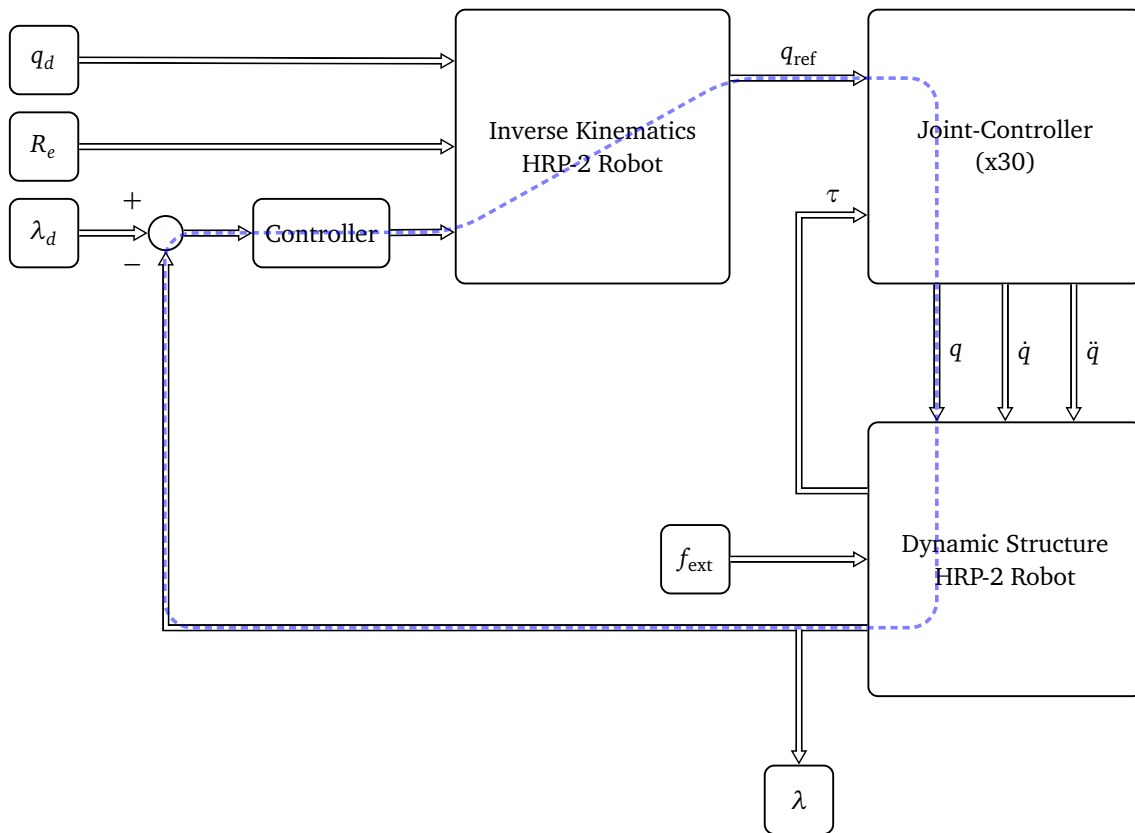


Figure 6.2: Simplified scheme of the system elements influencing the controller characteristics. The abstract block: Joint-Controller, is shown in Figure 6.3 on the following page in more detail. The stabilizing algorithms (posture control, vertical force/horizontal torque distribution) feed their reference signals to q_d , R_e and λ_d respectively. For the sake of simplicity they are not illustrated here. The control loop uses the complete lower body [Kajita et al., 2001b, 2005, 2007b, 2010] by means of an inverse kinematics to compute a manipulated joint reference trajectory q_{ref} . These reference trajectories are then tracked by each joint controller separately under external perturbations, such as external force and the nonlinear whole body dynamics. Double arrows represent vector-shaped signals. The control cycle that is concerned for the stability control is marked with the blue dashed line.

This unit in the robot-controller of the HRP-series is called stabilizer [Hirukawa et al., 2004, Kajita et al., 2005, 2007b, 2010, Yokoi et al., 2001]. While the precise structure of the heuristically combined control-loops from the current state of publications, remains a well guarded secret, the most important aspects of the utilized stabilizing control are explained in [Kajita et al., 2001b, 2005, 2007b, 2010] to be summarized below. As in the following, this will form a crucial base for the discussion of the results obtained from the optimal control work done on HRP-2 N° 14.

From [Nakamura, 1990] it is clear that position control is not suitable to follow a given force/torque reference at the end-effector. This technical issue is overcome by the introduction of a passive spring-damper system in the ankle-joint, that produces dependent on its dynamic deformation state a specific force/torque configuration [Kajita et al., 2001b] and to maintain its dynamic equilibrium despite its pure position control of the joints.

Together with the 6D force/torque sensor in the ankle joint (6D force/torque sensors are as

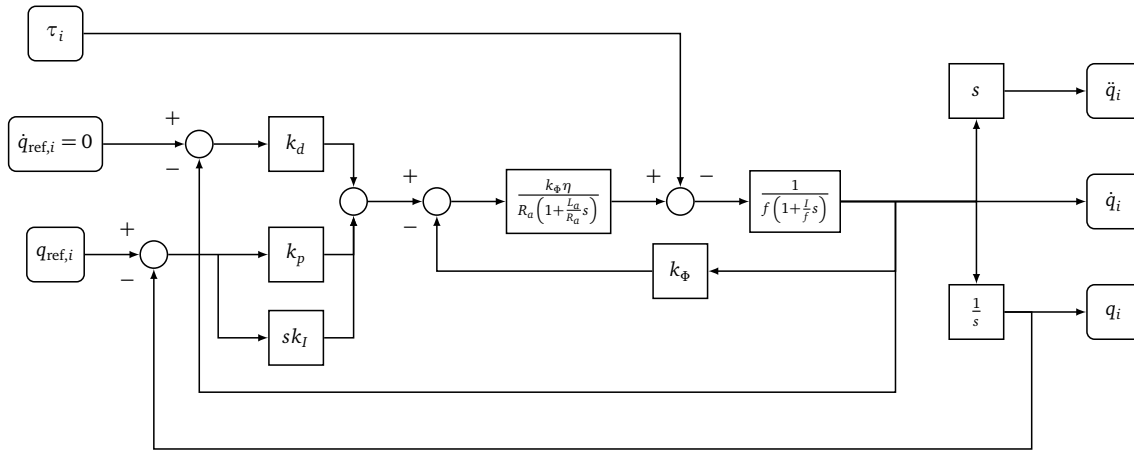


Figure 6.3: Abstract scheme of typical position based servo controller [Khalil and Dombre, 2002] including the signal blocks of a brushed DC-machine (for annotation details - refer to Section 1 on page 230). The controller tracks the motion trajectory profile of one dispatched joint given by the input reference q_{ref} . Transitions between the continuous dynamics of the DC-brushed machine and the discrete nature of the digital joint controller have been discarded for the sake of simplicity.

well mounted in the wrist joints for collaborative tasks [Mansard et al., 2009]) and the IMU in the upper torso a vertical force distribution control loop a horizontal torque distribution control loop and a posture control loop are formulated [Kajita et al., 2005, 2007b, 2010].

- The former control the vertical compression of the elasticity, tracking a heuristically determined distribution to best support the static and dynamic load of the body (reciprocal fraction of the distance ratio between ZMP and left/right foot support polygon [Kajita et al., 2010]), whilst supporting at maximum the operation of the latter loop.
- The tracking of the necessary horizontal torque profiles in the foot-ground contact serving two purposes for stabilization. Firstly the center of pressure must stay inside a feasible subspace of the contact surface to secure the foot residing firmly on the ground [Goswami, 1999] during the motion and secondly the ZMP [Vukobratović and Stepanenko, 1972] of the whole body motion in contact with the ground, must stay in a subfold of the convex polygon of support of the feet in contact to secure stable operation. The heuristics treats both horizontal torque directions separately [Kajita et al., 2007b, 2010].
 - Lateral torque direction is chosen on the same distance ratio as the vertical force distribution.
 - In the sagittal torque direction torque distribution is chosen such that it would lead to an inwards rotation of the concerned foot.
- Finally a third control loop receives the orientation estimation of the upper torso (see section 1.1 on page 82) and computes based on inverse kinematics, appropriate correction to the joint motion trajectory reference, such that the error to the desired pelvis orientation is minimized.

The inverse kinematics is referenced about the CoM [Kajita et al., 2007b, 2010] such that the manipulations tend to turn the robot around its center of gravity. Even though singularity-free inverse kinematics techniques exist [Baerlocher, 2001] the employed inverse kinematics

is prawn to situations with rather straight legs, as projection quality to some joint velocities drop considerably. This leads to abrupt, highly unstable and mostly uncontrollable motions with high velocities in the leg joints and hence should always be avoided.

From a mechanical point of view this design has two important implications about the dynamics of the robot, that should be carefully considered, as soon as it comes to the mathematical modeling. Firstly the passive spring-damper system only exerts a particular force/torque configuration upon deformation [Kajita et al., 2001b]. Thus the resulting force/torque profile mainly depends on the dynamics and the trajectories of the remaining rigid components in the structure, invoking the necessary deformation of the element. Secondly the passive spring-damper system, provides, based on its spring and damping characteristics, its own dynamics, hence substantially altering the dynamic characteristics of the MBS it is integrated in [Gross et al., 2011].

From the control point of view [Heimann et al., 2007] the necessary torque control loop featuring the controller, the high-gain servo-controllers, the highly nonlinear whole-body dynamics of the robot, including the passive dynamic elasticity and the 6D force/torque sensor, is characterized by its dynamic transfer (transfer function: reference input signal to output signal $G : \lambda_d \rightarrow \lambda$) and backdriveability (transfer function: input signal of external perturbations to output signal $G : q_d, f_{ext} \rightarrow \lambda$ - refer to Figure 6.2 on page 83) characteristics [Kajita et al., 2001b]. While the passive spring-damper system generally features a low-pass filter characteristics (see as well [Takenaka et al., 2009c]) the backdriveability¹ usually performs in a reciprocal manner. Thus, in the frequency-space, the ability to follow the desired reference and to reject external perturbations is considerably, reducing as soon as both input signals consist of higher frequencies (refer to [Kajita et al., 2001b] for results of the frequency response of transfer function and external perturbation transfer function). From 6.2 on page 83 and 6.3 on the facing page it is clear that the general form of these transfer functions is highly non-linear and complex to compute. During the design and conception of the ankle-elasticity hardware and the controller, parameter were chosen for a maximum backdriveability with the trade-off, that the high quality is only preserved in a space of very low frequencies ($\gg 10Hz$ [Kajita et al., 2001b]).

Even though it is not explicitly stated in the public available literature from the description of the stabilizing algorithms it does not seem that HRP-2 N° 14 is capable of rolling over frontal or rear rim of its feet during walking. Supported contact-states seem to be limited to either full (firm) ground contact, or non contact. This aspect has further implications on the optimal control problem formulation that will be explained in subsequent chapters.

Despite the previous discussion, it is stated in [Stasse et al., 2009] that from experience the robot with its stabilizer active dynamically behaves as such the ankle elasticity would not be present in the system. In the following chapters the relevance of this strong assumption will be discussed based on a couple of different OCP trials.

1.2 OpenHRP Motion Simulator

As accidents with the robot platform risk to quickly produce high maintenance costs, all computed motions in the following chapters have been thoroughly verified in kinematics and dynamics before they could actually be implemented very carefully on the real robotic platform. For this purpose a lightweight python based 3D kinematic viewer - Robotviewer - and a comprehensive simulation environment - OpenHRP [Hirukawa et al., 2003, 2004, Kanehiro et al., 2002, Nakaoka et al., 2007] - for controller and hardware development in simulation. OpenHRP (Open Architecture Humanoid Robotics Platform) is a collection of different mod-

¹the ability to maintain the reference output torque, despite external perturbations [Kajita et al., 2001b]

ules controlled by an Integrated Simulation Environment (ISE) based on CORBA [Vinoski, 1997]. It has been developed in parallel to the hardware series with the target to have a complete and realistic simulation of the humanoid robot hardware at hand for quick hardware development and controller design and verification. The environment basically offers the following main features: forward integration of the complete systems, including controller and actuation, computation of arbitrary contacts and collisions based upon various models for interaction with its environment and a unified controller design dispatched from the underlying hardware. Based on the CORBA implementation new modules are easily included independent of their operating system or used programming language, e.g. pattern generator for online motion generation [Kajita et al., 2003a, Stasse et al., 2008].

In the following work only a small extent of the OpenHRP environment has been used, to explore and investigate the governing constraints for a successful implementation of optimization results on the robotic platform HRP-2 N° 14. For this purpose only the pattern interpolation and the logging functionality have been adopted to initiate the robot, its controller and the stabilizer in an initial static stable posture, perform a motion computed from optimal control and drop back to a final static stable posture. The motion is encoded column-wise with the controller time-cycle of 5ms in three different files, featuring the joint position profiles, the desired global orientation profile of the pelvis and the ZMP trajectory profile with respect to the local pelvis reference frame. The logs then contain the Kalman-Filter data, the altered reference data before it is sent to the local joint controllers, and the robot data computed from the forward integration of the simulation (please refer to the appendix for the header structure of control and log files).

2 Modeling of the HRP-2 N° 14 Robot

As it is already shown in part on page 18, the mathematical modeling should always be carried out, such that the important governing physical characteristics are preserved, with a reasonable amount of computational overhead. Each decision about modeling a distinctive physical characteristic is to be considered carefully. Therefore in the following section all determining aspects during the modeling process are carefully discussed one by one.

In the following section two different modeling approaches (inelastic and elastic) are discussed in parallel.

- The inelastic model approach assumes that the robotic platform combined with the stabilizing algorithms performs dynamically, such that the elasticity in the ankle-elasticity complex would simply not exist and hence discards the ankle elasticity completely.
- The elastic model drops this assumption effectively exploiting the dynamic characteristics of the ankle-elasticity complex for motion generation. As it is shown in subsequent sections this implies further modeling steps (e.g. introduction of spring-damper systems, system identification) to adjust the model as close as possible to the real-world scenario.

As most of the decisions apply simultaneously to both approaches only the existing differences (e.g. different modelings of the spring-damper system of the ankle-elasticity complex) are discussed separately.

2.1 Modeling of the Kinematic Structure

As it is stated in Section 1.1 on page 82, the position control is tuned to accurately track a given trajectory profile and to efficiently reject any external perturbation. Besides the fact

that dry and viscous friction [Arisumi et al., 2008, Olsson et al., 1998] have a strong influence on the dynamic performance of a joint mechanism (see Section 2 on page 236 for more details), it will mostly be compensated by the position control featuring a higher joint torque magnitude (even a short overload of the machine is tolerable - see Section 1.1 on page 82) and consequently add a non-trivial offset to the optimization based joint torque reference. As the focus for this analysis is not to define the absolute min torque motion record but to moderate the motion characteristics based on abstract criteria the negligence of joint friction effects during the optimization is a reasonable choice.

In contrast to previously build platforms [Hirukawa et al., 2004] the HRP-2 N° 14 robot has been conceived for maximal rigidity of the kinematic structure [Kaneko et al., 2004] as well as a weight concentration in the pelvis (hosting the batteries), consequently the modeled MBS structure is assumed to be perfectly rigid.

Remark 5 *The global reference frame of all following optimization studies on HRP-2 N° 14 is orientated such that the X-axes point into the forward direction of the motion, the Z-axes points towards the lateral right side of the robot and Y-axes is the vertical axes. However, the re-orientation of the free-floating base adopts the Cardan convention and hence, Yaw is the rotation about the Y-axes, Pitch is the negative rotation about the Z-axes and Roll about the X-axes.*

Modeling of Gearbox

The transmission ratio in the gearboxes of the HRP-2 N° 14 are sufficiently high to respect the condition explained in Section 1.2 on page 234. Consequently, only the pure spinning velocities of the coils will be considered - coupling effects are neglected (following equation (B.12), coupling effects ${}^{L\&M}M = 0$) while discarding the inertia effects of the coils in the non-spinning axis with respect to the global motion of the local frame they are mounted on (${}^M M$ in equation (B.12)). For the sake of a lower mathematical complexity, in the following the gearbox mechanism is assumed perfectly rigid and the dynamics of the electrical part of the dc-machine are assumed to be negligible with respect to its mechanical counter part (following equation (B.5)).

Foot Ground Contact - Consistency of Mechanical Contacts

The feet are rubber coated to allow for a secure high friction ground contact. The small contribution of elasticity of the rubber coating underneath the feet will be neglected henceforth [Chardonnet, 2009]. As the problem formulation only considers feet either firmly placed on the ground, or in air, transitional stages giving evidence to highly dynamic effects (e.g. Stribeck [Olsson et al., 1998]) are not considered during the discussion below. From Section 2 on page 236 it is clear that in case of a surface contact not only the linear shear forces but as well the shear torque in the contact surface need to be evaluated to get reasonable estimation about whether the exerted stress is effectively eliminated by coulomb friction. The coulomb friction coefficient has been determined by [Chardonnet, 2009].

Physical Consistency Following the discussion from Section 3.3 on page 30 the contact modeling of the unilateral, flat surface contacts of the feet with the ground is done based on the DAE formulation with additional constraints enforcing uni-lateral contact constraint reactions, suppression of slipping (refer to Section 3.1 on page 236) and a physically consistent trajectory of the Center of Pressure (CoP) (refer to Section 3.2 on page 238).

The path constraints are formulated as constraint on the vertical contact force component,

$$f_z > 0, \quad (6.1a)$$

and as box constraint on the position of the local CoP of each foot,

$$\underline{p}_{\text{CoP},x,i} < p_{\text{CoP},x,i} < \overline{p}_{\text{CoP},x,i}, \quad : i \in \{\text{Left foot, Right foot}\}, \quad (6.1b)$$

$$\underline{p}_{\text{CoP},y,i} < p_{\text{CoP},y,i} < \overline{p}_{\text{CoP},y,i}, \quad : i \in \{\text{Left foot, Right foot}\}, \quad (6.1c)$$

during ground contact. A further criteria to ensure the dynamic feasibility of the optimized motion is the ZMP [Vukobratović and Stepanenko, 1972] constraint.

Implications to Dynamic Stability The robot HRP-2 N° 14 is modeled as a floating-base system. Therefore, it has six dofs that are not actuated. As it is shown in [Mistry et al., 2008, 2010] one can gain full access over these vacant dofs as long as the system is sufficiently constrained [Del Prete, 2013, Hutter, 2013]. Stability of a system in the sense of Lyapunov is given in [Samson et al., 1991]:

Definition 17 (Lyapunov Stability) *An equilibrium point $\tilde{x} \in \mathbb{R}^n$ of a dynamic system,*

$$\dot{x}(t) = f(t, x(t)), \quad t \geq t_0, \quad (6.2a)$$

$$x(t_0) = x_0, \quad (6.2b)$$

is considered stable in the sense of Lyapunov, if and only if it holds for every $\epsilon > 0$,

$$\|\tilde{x} - x(t)\| < \epsilon, \quad \forall t > t_0, \quad (6.2c)$$

with a real value $\delta(t_0) > 0$,

$$\|\tilde{x} - x_0\| < \delta(t_0). \quad (6.2d)$$

Technically, Definition 17 can only be achieved as long as sufficient access to all system states $x(t)$ exists. In the case of HRP-2 N° 14, a MBS with a single or multiple contacts on level-ground this relation can be formulated with the ZMP-criterion from [Vukobratović and Stepanenko, 1972]. The following definition is equivalent to the second interpretation of the ZMP in [Vukobratović and Borovac, 2004]:

Definition 18 (ZMP Criterion) *Let S_{phys} be a convex surface of a uni-lateral contact on level-ground and $p \in S_{\text{phys}}$ a point inside this convex contact surface expressed, in global reference frame I (with vertical Z -axis). The point p is on the ground,*

$$p = \begin{bmatrix} p_x & p_y & 0 \end{bmatrix}^T. \quad (6.3a)$$

In case the dynamic equilibrium of the given MBS, with N rigid bodies, can be expressed as,

$$\sum_{i=0}^N {}^{0,I}X_{O_i, B_i}^* \left(I_{O_i, B_i} a_{O_i, B_i} + v_{O_i, B_i} \times^* I_{O_i, B_i} v_{O_i, B_i} \right) = {}^{0,I}X_{p, I}^* f_{p, I}, \quad (6.3b)$$

with a single external contact reaction,

$$f_{p, I} = \begin{bmatrix} 0 & 0 & m_z & f_x & f_y & f_z \end{bmatrix}^T, \quad (6.3c)$$

that has zero horizontal torque components m_x and m_y at the point p , the dynamic equilibrium (6.3b) exists and the MBS is dynamically stable at the point p in the convex contact region S_{phys} . The point p can only exist inside S_{phys} , as for any other point $p \notin S_{phys}$ the dynamic equilibrium (6.3b) is not defined. The convex support polygon S_{phys} is spanned over all physical, uni-lateral contact points of the MBS with the level-ground plane.

Following [Goswami, 1999] this criterion, gives only a statement about stability not about the quality of stability - as soon as the point is located on the boundary ∂S_{phys} instability occurs and hence, the point never leaves the support polygon S_{phys} .

In the exceptional case of L multiple planar contact points $f_{p^i, \mathbf{I}}$, following the form of (6.3c) without slipping [Goswami, 1999], equation (6.3b) can be re-arranged to yield the point p following (6.3a),

$$p_x = \frac{\sum_i^L p_x^i (f_{p^i, \mathbf{I}})_Z}{\sum_i^L (f_{p^i, \mathbf{I}})_Z}, \quad (6.4a)$$

$$p_y = \frac{\sum_i^L p_y^i (f_{p^i, \mathbf{I}})_Z}{\sum_i^L (f_{p^i, \mathbf{I}})_Z}. \quad (6.4b)$$

Consequently, in the slip-free Single Support (SS) case the ZMP criterion [Goswami, 1999, Vukobratović and Stepanenko, 1972] is equivalent to the contact feasibility criterion defined above and in the slip-free Double Support (DS) case the ZMP is located on a line between both CoPs, of left and right foot, respectively.

The ZMP is a relative conservative criterion for dynamic stability. Alternatives are, e.g. Foot Rotation Indicator (FRI) [Goswami, 1999] or Capture Point (CP) [Pratt and Tedrake, 2006] and they have been used in recent works e.g. [Morisawa et al., 2012] for stabilization of HRP-2 N° 14. However, they have not been considered in the formulations of OCPs in this work and thus will not be described further.

Conclusion and Constraint Tuning The uni-lateral contact condition and physical consistency of each planar surface contact must be formulated as path constraint in the OCP. Furthermore, the ZMP criterion can be formulated to remain inside a defined surface ∂S_{strict} on the ground that may be much smaller than the actual physical support polygon ∂S_{phys} . For the constraint configuration in the OCP-formulation, there are two options:

1. On the one hand, maintaining the ZMP inside a strict support polygon S_{phys} , gives the OCP more freedom to move the CoP around in the local contact surface area.
2. On the other hand, if the contact feasibility is formulated sufficiently strictly the ZMP is automatically bounded inside the convex polygon of all CoPs ∂S_{CoPs} of the contact feasibility constraints and hence, might be even stricter than the original strict support polygon ∂S_{strict} for the ZMP.

As the trajectory of the CoP directly depends on the on-line stabilizing control system, the second option might be necessary, not only to control the dynamic stability of the moving robot but as well the control trajectory of the local CoP in the foot contact.

Self-Collision

Especially in position controlled robotics, usual self-collision is a critical situation [Kuffner et al., 2002], as external perturbations are rigorously rejected by the control-system resulting

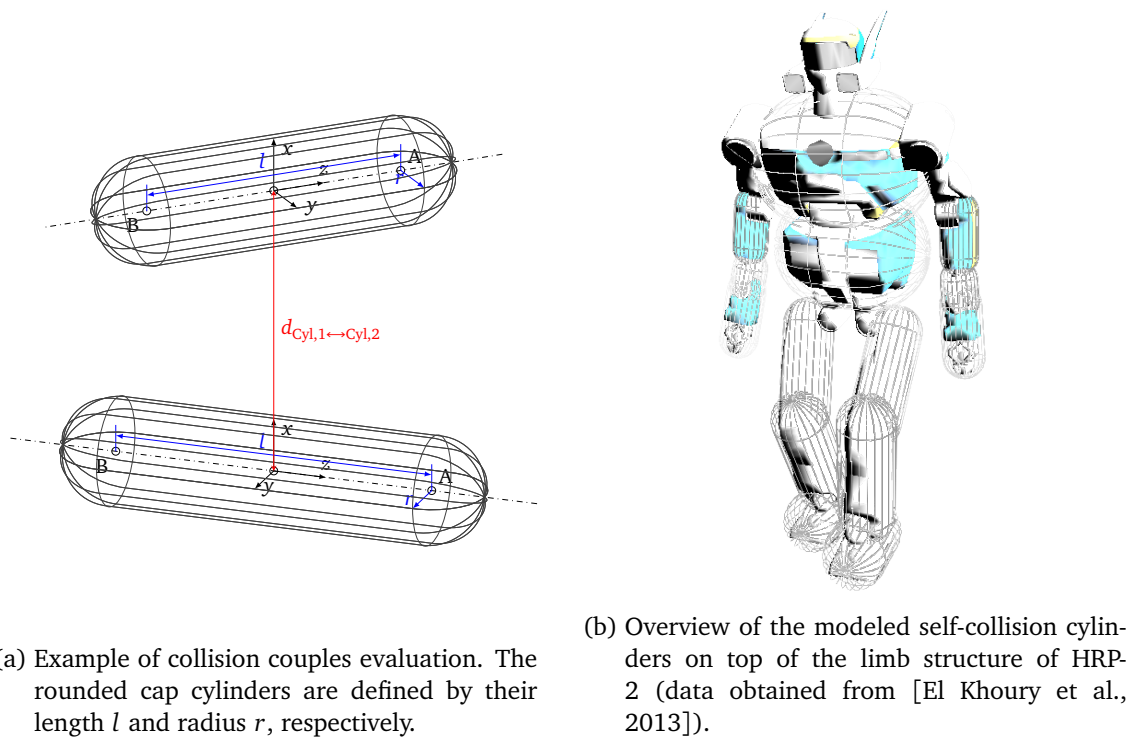


Figure 6.4: Resolution scheme of self collision modeling the broad phase has been replaced by a manual specification of the critical collision couples (Cylinder – Cylinder), figure on the right side, while the narrow phase then follows as a pure set of inequality constraints, figure on the left side.

in unexpectedly high control reactions. However, with increasing complexity of the kinematic chain, the resulting workspace is more and more complex [Brunet and Baron, 2004]. In most situations it is simply not possible to relate problematic areas in the workspace to specific limits of the motion range in the operation space of the kinematic chain. Therefore, collision checking is normally done geometrically following a broad- and a narrow phase [Mirtich, 1998]. In the broad phase the vast space of different geometrically possible collisions between different objects (see Figure 6.4b) is scanned with fast methods to obtain a reduced set of interest which is then analyzed with more sophisticated methods in the subsequent narrow phase (see Figure 6.4a).

Over the past decades a huge number of different algorithms for fast collision checking of objects with complex geometry have been proposed [Jiménez et al., 2004, Ketchel and Larochelle, 2006, 2008, Kuffner et al., 2002, Mirtich, 1998, Pan et al., 2012, Redon et al., 2002] to refer a few. Referring to the conclusions of chapter 4 integration of these methods is in most cases not possible as the continuous differentiability of these algorithms can not be confirmed with reasonable effort.

The proposed strategy in the remainder of this work is to simplify the algorithm structure. The broad phase is completely skipped and the narrow phase is performed on a fixed set of geometrical collision pairs that are further simplified to rounded cap cylinders [Ketchel and Larochelle, 2006, 2008]. Distance computation between these objects is then straight-forward and continuously differentiable [Eberly, 1999]. Thus, the problem of self-collision avoidance simplifies to a fixed set of inequality constraints, that directly integrate as path constraint-set,

$$h_{\text{collision:Cyl,1}\leftrightarrow\text{Cyl,2}}(\mathbf{q}, \mathbf{p}) = d_{\text{Cyl,1}\leftrightarrow\text{Cyl,2}}(\mathbf{q}, \mathbf{p}) - r_{\text{Cyl,1}} - r_{\text{Cyl,2}} \geq 0, \quad (6.5)$$

with the OCP-formulation (4.1). The geometric information for the distinct self-collision couples has been obtained from the solution of nonlinear optimization problems, fitting the simplified rounded cap cylinders (radius, length, global position and orientation with respect to the parent link) to the complex polygon mesh of each limb of the kinematic structure of the HRP-2 N° 14 robot [El Khoury et al., 2013]. In conclusion it should be noted that this geometric approximation is relatively coarse and might be over-restrictive in some limiting cases and hence, the selection of the individual collision pairs should be carefully processed.

Inelastic Ankle Complex

In contrast to the discussion in Section 1.1 on page 80 and 1.1 on page 125 in [Verrelst et al., 2006] states the experience that the HRP-2 N° 14 robot with the activated stabilization system dynamically behaves, such that the ankle elasticity would not be present. As the modeling is always a trade-off between computational complexity and physical representation quality of the constructed model for a maximum precision of the final results, in a first attempt the ankle-elasticity complex was discarded.

This not only saves in mathematical complexity of the model, but reduces further the computational overhead as in the elastic case highly stiff springs will alter the characteristics of the dynamics system and hence need a carefully adjusted configuration of the problem set-up (e.g. selection of integrator).

2.2 Equations of Motion

The robot is modeled in minimal coordinates (without contacts) with 30 dof for its internal branched tree structure, 4 or 6 additional dofs to account for the simple and complex elasticity model in the ankle respectively, as well as further 6 dof to model the free motion in the global reference. This coordinate configuration is preserved throughout the complete phase cycle featuring position contacts and kinematic loops. The resulting dynamic equation is then expressed as DAE system of index 3 formulated in the so-called descriptor form,

$$M(\mathbf{q}, \mathbf{p}) \ddot{\mathbf{q}} + NLE(\mathbf{q}, \dot{\mathbf{q}}, \mathbf{p}) \quad (6.6a)$$

$$+ C(\mathbf{q}, \mathbf{p}) - J(\mathbf{q}, \mathbf{p})^T \boldsymbol{\lambda} = \boldsymbol{\tau}, \quad (6.6b)$$

$$g(\mathbf{q}, \mathbf{p}) = \mathbf{0}. \quad (6.6b)$$

In this equation $M(\mathbf{q})$ represents the joint space inertia matrix which consists of the inertia matrix from the kinematic tree structure of the robot

$$M = \left(\sum_{k=0}^{n_{\text{Bodies}}} J_k^T I_k J_k \right) + M_m, \quad (6.7)$$

and an additional diagonal term M_m (6.8) containing the simplified dynamic effects of the spinning coils in the joint actuators (where I_i^m is the rotational inertia of the coil i about its spinning axis and R_i the ratio of transmission of the joint i):

$$M_{mii} = \begin{bmatrix} R_i^2 I_i^m & i \in \{\text{Actuated Joints}\} \\ 0 & i \in \{\text{Passive Joints}\} \end{bmatrix}. \quad (6.8)$$

$NLE(\mathbf{q}, \dot{\mathbf{q}})$ represents the nonlinear effects (e.g. Coriolis). Furthermore we include here the dynamic effects of the spring and damper systems,

$$NLE = \sum_{k=0}^{n_{\text{dofs}}} J_k^T (I_k \dot{J}_k \dot{\mathbf{q}} - J_k \dot{\mathbf{q}} \times^* I_k J_k \dot{\mathbf{q}}) + K_D \dot{\mathbf{q}} + K_p \mathbf{q}. \quad (6.9)$$

J_k represent the spatial Jacobian to the local reference frame of the link k respectively. I_k is the spatial inertia matrix of link k . K_D and K_p are matrices that hold spring and damping constants with respect to each of the degrees of freedom [Nakaoka et al., 2007]

Gravity effects are considered with the term $C(\mathbf{q})$. τ represents the system's actuation as torque on the joint-level (rotational). The term $g(\mathbf{q})$ expresses the scleronomous position constraints.

For higher computational efficiency, this is transformed into a DAE system of index 1:

$$\dot{\mathbf{q}} = \mathbf{v}, \quad (6.10a)$$

$$\dot{\mathbf{v}} = \mathbf{a}, \quad (6.10b)$$

$$\begin{bmatrix} M & -J^T \\ J & 0 \end{bmatrix} \begin{bmatrix} \mathbf{a} \\ \boldsymbol{\lambda} \end{bmatrix} = \begin{bmatrix} -NLE - C + \boldsymbol{\tau} \\ -\boldsymbol{\gamma} \end{bmatrix}. \quad (6.10c)$$

In forward dynamics algebraic variables $\boldsymbol{\lambda}$ (equivalent to the contact constraint forces) and acceleration $\ddot{\mathbf{q}}$ values are computed from given system's state $\mathbf{q}, \dot{\mathbf{q}}, \boldsymbol{\tau}$. Additionally, the following conditions arising from index reduction have to be respected for consistency:

$$g(\mathbf{q}(0)) = 0, \quad (6.11a)$$

$$J(\mathbf{q}(0)) \dot{\mathbf{q}}(0) = 0. \quad (6.11b)$$

The term J is represented in the classical form (6D Jacobian - refer to 3.3 on page 32). In comparison to the spatial notation, one must note that, the contact model must be computed in the classical representation (refer to equation (2.16)). The term $\boldsymbol{\gamma}$,

$$\boldsymbol{\gamma} = \left(\frac{\partial}{\partial t} \underbrace{\begin{bmatrix} j_1 & j_2 & \cdots & j_n \end{bmatrix}}_{=J} \right) \dot{\mathbf{q}} = \begin{bmatrix} \frac{\partial}{\partial \mathbf{q}} j_1 \frac{\partial}{\partial t} \mathbf{q} & \frac{\partial}{\partial \mathbf{q}} j_2 \frac{\partial}{\partial t} \mathbf{q} & \cdots & \frac{\partial}{\partial \mathbf{q}} j_n \frac{\partial}{\partial t} \mathbf{q} \end{bmatrix} \dot{\mathbf{q}}, \quad (6.12)$$

is the time derivative of J , multiplied by the velocity vector respectively that contains all active constraint directions in the contact points. When a foot enters in contact with the ground, this is modeled as an inelastic impact causing discontinuities in the joint velocities which can be computed by the following equation. $\dot{\mathbf{q}}^-$ and $\dot{\mathbf{q}}^+$ represent the velocity configuration before and after the impact respectively and $\boldsymbol{\Lambda}$ holds the complex impact impulsion:

$$\begin{bmatrix} M & -J^T \\ J & 0 \end{bmatrix} \begin{bmatrix} \dot{\mathbf{q}}^+ \\ \boldsymbol{\Lambda} \end{bmatrix} = \begin{bmatrix} M \dot{\mathbf{q}}^- \\ 0 \end{bmatrix}. \quad (6.13)$$

The dynamic equations are composed analytically, optimized and converted into C-code by means of the dynamic model builder *DYNAMOD* (refer to Chapter 3) based on 6D spatial geometry [Featherstone, 2007].

7 Inelastic Model Approach

In the following, the approach adopting the simple inelastic model will be employed to conduct two dispatched investigations. The first is a general analysis of different optimization criteria as well as governing constraints and their influence on an optimized walking gait for HRP-2 N° 14. Even though first attempts were made to push results towards a real implementation, only preliminary trials in the motion simulator OpenHRP have been conducted to appropriately prepare subsequent problem formulations.

As the primary objective of this work is to identify potential resources for further improvement of the motion capacities of the platform HRP-2 N° 14, subsequent studies build on top of the results of the first analysis but are directed towards a more limiting motion task than pure walking - overstepping of obstacles. It is shown that by breaking up common assumptions, that are governing state of art motion generation tools, it is possible to boost dynamic motion capacities to a high extent, but needs to be carefully considered as soon as one tries to bring that purely theoretic results back to a practical implementation in a real-world scenario.

Based upon the results of both studies, suggestions are made how the process of modeling should be conducted and continuously revised to assure a small gap between the characteristics of the mathematical model and its practical counter-part in a real-world scenario, whilst maintaining a minimum computational overhead.

1 A Walking Study

In the following, common parts of the problem formulation used during all optimization trials based on the inelastic modelisation approach are presented. Its influence on the resulting motion outcome and its implications to further applications of the formulations (objective and constraint) are then given in the corresponding result section. As the internal structure of the problem formulation highly depends on the motion problem at hand a specific introduction to the necessary parts is given at the beginning of each study separately.

1.1 OCP Formulation

In order to generate the results for the conceptional motion-studies, a multiple-phase optimal control problem is formulated (for details please refer to Chapter 4 on page 42) and solved subsequently. The specialized formulation (7.1a)-(7.1h) employed for the following studies is based on (4.1) and given below. It features the system states $x(t)$, the controls $u(t)$ and

system parameters p ,

$$\min_{\substack{x(\cdot), u(\cdot), p, \\ t_j, 1 \leq j \leq n_{\text{mos}}}} \sum_{i=1}^{n_{\text{mos}}} \left(\int_{\bar{t}_{i-1}}^{\bar{t}_i} \Phi_i(x(t), u(t), p) dt + \Psi_i(\bar{t}_i, x(\bar{t}_i), p) \right), \quad (7.1a)$$

$$\text{subject to } \dot{x}(t) - f_i(t, x(t), u(t), p) = 0, \quad t \in [\bar{t}_{i-1}, \bar{t}_i], \quad (7.1b)$$

$$x(\bar{t}_i^+) - h_i(x(\bar{t}_i^-)) = 0, \quad i \in \{1, 2, \dots, n_{\text{mos}} - 1\}, \quad (7.1c)$$

$$r_{eq}(x(\bar{t}_{i-1}^+), x(\bar{t}_i^-)) = 0, \quad i \in \{1, 2, \dots, n_{\text{mos}}\}, \quad (7.1d)$$

$$r_{ineq}(x(\bar{t}_{i-1}^+), x(\bar{t}_i^-)) \geq 0, \quad i \in \{1, 2, \dots, n_{\text{mos}}\}, \quad (7.1e)$$

$$g_i(x(t), u(t), p) \geq 0, \quad t \in [\bar{t}_{i-1}, \bar{t}_i], \quad (7.1f)$$

$$\underline{u} \leq u \leq \bar{u}, \quad (7.1g)$$

$$\underline{x} \leq x \leq \bar{x}. \quad (7.1h)$$

The Bolza-type objective function (7.1a) consists of a continuous Lagrange-term (Φ) and an end time related Meyer-term (Ψ) for each phase. Optimization is done with respect to the multi-point boundary value problem, consisting of the system dynamics (7.1b) as well as the equality and inequality boundary constraints (7.1d, 7.1e), and continuous path constraints (7.1f) as well as box-constraints (limits) on system states (7.1h) and controls (7.1g) for all phases.

$i \in \{1, 2, \dots, n_{\text{mos}}\}$ regroups all indices of the discrete phases, different contact states (e.g. double support, single support). \bar{t}_i^+ and \bar{t}_i^- denote the specific instant of phase transition, the former before and the latter after the phase transition. Without loss of generality it is assumed that $\bar{t}_0 = 0$. f_i is the phase dependent right hand side of a first order ODE.

Specifically in this problem formulation, the state vector of the system $x = [q, \dot{q}]^T \in \mathbb{R}^{102}$ comprises joint positions $q \in \mathbb{R}^{36}$ and velocities $\dot{q} \in \mathbb{R}^{36}$. As it was explained in Section 3.3 on page 32 the resulting DAE system of the MBS with external contacts is expressed as equivalent ODE system with consistent boundary constraints. The controls $u \in \mathbb{R}^{30}$ are injected into the system as joint torque τ (compare to equation (2.23)). Continuity of joint torque trajectories during discontinuous phase transitions needs formulation of further constraints. h_i expresses characteristics of the phase transition $(i-1) \rightarrow (i)$ (e.g. inelastic impact). $f_i, r_{eq}, r_{ineq}, g_i$ are vector functions with correspondent dimensions. This study applied the forward dynamics operator and plc control discretization (refer to Chapter 5 on page 54 for details).

1.2 Problem Structure

The modeling of a walking motion simplifies considerably, as HRP-2 N° 14 has flat feet (compare section 1 on page 80 and especially 1.1 on page 83) and seen not to be capable to roll over the front or rear rim of its foot (non existing hallux and pternion point - see section 1 on page 1) during walking. Hence the complex multi-phase walking scheme simplifies considerably to three different contact states - namely: double support (both feet in ground contact), single support left foot (left foot placed on the ground, right foot in swing phase) and single support right foot (right foot placed on the ground, left foot in swing phase). Further computational overhead is then saved by reducing the scope of the simulation to a half walking cycle only. This is possible upon formulation of an additional appropriate set of symmetry boundary constraints to the states, whilst relaxing the symmetry constraints to the controls (see Figure 6.1 on page 81) to force a symmetric motion appearance, but avoid constraint singularities that may result from a not perfectly symmetric dynamic model forced into a symmetric motion. Consequently, the problem structure consists for two phases with continues (foot lift

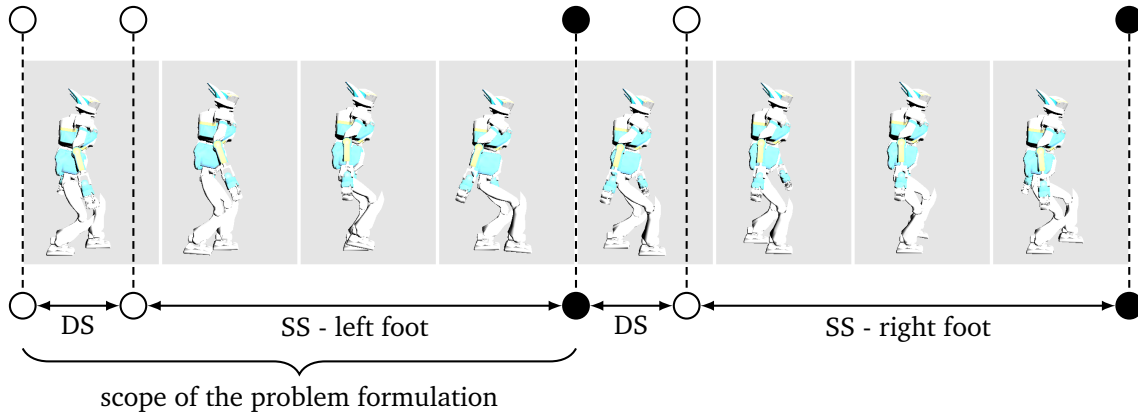


Figure 7.1: Problem structure of the walking motion study on the inelastic model. The scope of the problem formulation is reduced to a half cycle of the walking motion with additional symmetry constraints to save considerable computational overhead. Discontinues phase transitions (foot ground collision - CH) are marked with black dots while continues phase transitions (foot lift-off) are marked with white dots.

off) and discontinues (ground collision) phase transitions (the phase scheme is shown in Figure 7.1). The simulation starts with the double support phase, lifts the left foot to the right foot single support phase and ends with the ground collision. Related to the discussion in Section 3.4 on page 72, preliminary trials lead to the configuration of the initial guess for all OCP computations of this analysis, stated in Table 7.1. This configuration has been developed for good accuracy of the discretization of the state space.

Table 7.1: Model stage scheme, Multiple Shooting nodes and initial multiple shooting interval time per model stage

N	MS Nodes	Time	Contact-State	Description
SS(0)	33	0.63s	Single Support	Right foot swings
CH(1)	1	0.00s	Foot-ground Impact	Discontinues Transition
DS(2)	11	0.20s	Double Support	Load transfer - periodic coupling
Σ	45	0.83s		

1.3 Objectives

Despite the huge computational efforts generally necessary to solve problem formulations of this complexity, a determining advantage is the possibility to achieve different desired motion characteristics based on abstract high-level objectives and constraints:

- Minimum Joint Torque
- Maximum Forward Velocity
- Maximum Postural Stability
- Maximum Efficiency of Locomotion
- Minimization of Joint Velocities

In the following a first choice of different objectives drawn from literature is described to be investigated for potential further application on purpose in subsequent studies. All objectives

are summed with a global weighting α_i and in case necessary an individual one $\omega_{i,j}$. The global weighting α_i is important as soon as it comes to combination of multiple objectives. The individual weighting $\omega_{i,j}$ was seldom used but is given for the sake of completeness.

Minimum Joint Torque

This objective has been frequently applied by different authors [Bessonnet et al., 2004, Buschmann et al., 2005, Buss et al., 2003, Mombaur, 2009, Roussel et al., 1998, Schultz and Mombaur, 2010]. From the background of Section 1.1 on page 231 in Appendix B the minimization of joint torques squared, whenever they are used for a dynamic motion or a static posture, is similar to the minimization of the heat dissipation in the armature resistor of the motor coil and thus reduces the bottom-line energy consumption of the dc-machine,

$$\begin{aligned} \tau &\sim i_a (\eta k_\Phi), \\ \rightarrow \tau^2 &\sim i_a^2 (R_a) = P_{\text{loss,elec}}, \\ \rightarrow E_{\text{loss,elec}} &= \int_0^T P_{\text{loss,elec}} dt. \end{aligned} \quad (7.2)$$

This is highly interesting as it reduces the current i_a circulating in the armature and thus helps to increase the autonomous operation time of the robot on a local energy resource with fixed capacity. Further this objective should produce smooth control profiles with little oscillations. The formula is given as,

$$\min \Phi_{\text{torques}} = \alpha_{\text{torques}} \int_0^T \sum_{j=1}^N (\omega_{\text{min Torque},j} \tau_j)^2 dt. \quad (7.3)$$

As discussed in 1.1 on page 93, u_j represent the individual controls injected into the system dynamics as joint torques τ_j . α_{torques} realizes a global weighting and $\omega_{\text{torques},j}$ an individual of each joint torque separately.

Maximum Forward Velocity

As soon as we introduce objectives that minimize a part of the consumed energy from experience the resulting motion tends to become slower and thus take more time to accomplish. Besides robots that already demonstrated running [Ota, 2010, Sakagami et al., 2002] a maximization of average forward velocity during walking for most humanoid robots is highly desirable. In the case of the platform HRP-2 N° 14 it is interesting to investigate its potential limits based on optimal control. The objective is described in,

$$\max \Psi_{\text{forw Vel.}} = \alpha_{\text{forw Vel.}} \frac{l_{\text{Step}}}{T}, \quad (7.4)$$

featuring the end-time T of the simulation and the step length l_{Step} . Consequently only the average velocity will be maximized, peaks as well as strong variations are not considered.

Maximum Postural Stability

From [Goswami, 1999] it is clear that in case of a stable firm foot ground contact the CoP is equal to the ZMP [Vukobratović and Stepanenko, 1972] in case of one foot contact (one contact point) and to a weighted sum of both CoP in case of double support contact state. Logically a possible but relatively conservative measure for the postural stability of the flat

feet robot HRP-2 N° 14 is the distance of both CoP to the centroid of their ground contact surface [Buss et al., 2003], as this will automatically keep the ZMP far from the boundary of the support polygon. The objective,

$$\min \Phi_{\text{post. stab.}} = \alpha_{\text{post. stab.}} \int_0^T \sum_{e=\{Lf,Rf\}} (p_{\text{CoP}_e} - p_{\text{Centr}_e})^2 dt \quad (7.5)$$

penalizes the quadratic individual distance between the centroid position of the foot-ground contact surface p_{Centr_e} and the center of pressure p_{CoP_e} . The objective is formulated with $e = Lf$ and $e = Rf$ for single support phase on the left and right foot respectively. For the double support phase both $e = \{Lf, Rf\}$ feet are considered.

Maximum Efficiency of Locomotion

Efficiency has been defined in section 1 on page 230 for actuation systems. In the context of optimal control for walking motions, efficiency is described differently [Buss et al., 2003, Garcia et al., 1998] as the mechanical power-output of the actuation system $\dot{q}\tau$ as cost of transport over a locomotion quantity, stride/step length (in case of passive dynamic walker) [Garcia et al., 1998] or forward velocity [Buss et al., 2003] (actively controlled active walking robot). The objective,

$$\min \Phi_{\text{eff.}} = \alpha_{\text{eff.}} \int_0^T \sum_{j=1}^N \frac{\omega_{\text{eff.},j} |\dot{q}_j u_j|}{l_{\text{step}}} dt, \quad (7.6)$$

is built over both portions of energy. Those used for deceleration $\dot{q}\tau < 0$ as well as acceleration $\dot{q}\tau > 0$ re-scaled by the step length l_{step} .

Minimization of Joint Velocities

In [Morisawa et al., 2005] the authors build a pattern generator that does follow a parametric surface in contrast to a fixed hip height and show that the investigation improved the overall motion performance, and decreased the velocity peaks in the knee joints during the walking motion. Thus a minimization of joint velocities (angular rates) squared is proposed,

$$\min \Phi_{\text{joint vel.}} = \alpha_{\text{joint vel.}} \int_0^T \sum_{j=1}^N (\omega_{\text{joint vel.},j} \dot{q}_j)^2 dt, \quad (7.7)$$

to investigate the resulting for HRP-2 N° 14 while keeping the velocity profiles at low values during the walking motion.

1.4 Constraints-Set

In the following the adopted constraint set used to keep the resulting motion in a physically consistent subspace with respect to the previously described modeling decisions. The constraint-set consists of the following blocks:

Box Constraints

Box constraints are set on the system states (angular positions, velocities - see equation (7.1h)) and the controls (joint torques - see equation (7.1g)). Please refer to [Kaneko et al.,

2004] for precise limits. As it was explained in section 1.1 on page 231 the torque box constraints have been relaxed to certain extent to allow small but reasonable overload in case necessary.

Boundary Constraints

The boundary constraints regroup conditions to the phase boundary and phase transition constraints. For this study the following constraint sets have been used:

Implicit Phase Switches The implicit phase transitions are defined as: transition from double support to single support occurs when the ground contact reactions on the potential swing foot vanish - equation,

$$f_{\text{foot} \rightarrow \text{swing}} = \begin{bmatrix} 0 & 0 & 0 & 0 & 0 & 0 \end{bmatrix}^T. \quad (7.8a)$$

Transition (ground collision) from single support to double support occurs when the foot position reaches ground level with a parallel orientation to the ground plane - equations,

$$\left(X_{\text{foot}::\text{Swing}}(q) \right)_z = 0, \quad (7.8b)$$

$$\left(X_{\text{foot}::\text{Swing}}(q) \right)_{\text{roll}} = 0, \quad (7.8c)$$

$$\left(X_{\text{foot}::\text{Swing}}(q) \right)_{\text{pitch}} = 0. \quad (7.8d)$$

Symmetry & Periodicity The resulting walking half-cycle may be completed to a full cycle when the transition boundaries (initial and final phase boundary) are symmetric to each other. This symmetry can only be strictly enforced for the system states $x = \begin{bmatrix} q & \dot{q} \end{bmatrix}^T$ - equations,

$$q(0) - H_{\text{sym. sag.}}(q(T)) = 0, \quad (7.9a)$$

$$\dot{q}(0) - H_{\text{sym. sag.}}(\dot{q}(T)) = 0, \quad (7.9b)$$

but not for the joint torques (see section 1.1 on page 80). The function $H_{\text{sym. sag.}}(q)$ computes the symmetric counter part of the given configuration about the sagittal plane of the robot's kinematics structure.

Consistency Constraints From the dynamic modeling section of the robot HRP-2 N° 14 2.2 on page 91 the resulting set of index-1 DAEs (6.10) only yields the correct results when the consistency constraints,

$$X_i(q(t=0)) = 0, \quad \forall i \in \mathcal{I}_{A(q(t=0))}, \quad (7.10a)$$

$$J_i(q(t=0))\dot{q}(t=0) = 0, \quad \forall i \in \mathcal{I}_{A(q(t=0))}, \quad (7.10b)$$

are satisfied. Hence, the boundary constraint set on the initial multiple shooting node is extended by the suitable constraint sets about each active contact to enforce the kinematic consistency of the resulting solution.

Path-Constraints

The following walking analysis adopts the constraints for unilateral contacts (6.1a), the physical contact feasibility (6.1b) and (6.1c), as well as the self-collision constraint (6.5) for selected self-collision pairs between the arms, the torso, the hip as well as the legs. A potential

sliding motion of the swing foot on the ground is avoided, through a minimal ground clearance that is enforced on each corner point of the foot during the swing phase.

As the ZMP [Vukobratović and Stepanenko, 1972] constraint is considered as a rather conservative criteria for dynamic stability, this study tries to analyse potential possibilities for improvement of the motion performance, when this constraint is relaxed. Hence for all five objective functions above, the following constraint-sets have been evaluated:

- With and without ZMP constraint, restricting it to stay within a small circle below the center of the foot, during single support and in a tube with rounded caps, connecting the two foot centers, during double support.
- For the ZMP constrained case: leaving the foot placement free, or constraining the step length and step width to the values of the initial walking solution.

Overall, this results in 15 different objective function - constraint combinations.

2 Optimization Results

This study has been the first step towards the integration of the full-featured whole-body model of the HRP-2 N° 14 robot with respect to walking scenario. Although, a final implementation of the motion on the real platform was in mind, the results where not expected to directly confirm with all implied technical restrictions of the real platform. Therefore, only the walking motion, but not a complete feasible motion cycle from a static posture towards a static posture are shown here. However, it is important to form a substantial idea of the crucial aspects that one needs to be aware of, to produce realistic motion results for the given platform. Consequently, the study was designed for the following outcomes:

- As it was briefly explained in Section 3 on page 6, heuristics-based motion generation frequently makes assumptions to simplify the motion generation problem. Even though most of these assumptions are carefully chosen, it is claimed that for multi-branched kinematic chains of a similar complexity as HRP-2 N° 14, it is not possible with a reasonable effort to thoroughly assess the influences of these assumptions. Furthermore, it is not always clear how these assumptions are influencing each other. An example case which will be considered in the study below, is the adoption of the step length, which has been obtained from the pattern generator[Kajita et al., 2003a] based initial walking motion. This step length is considered as an assumption similar to the fixed pelvis height or the feet trajectories. Hence it will be interesting to observe the change in the motion when the step length is allowed to change from its initial assumption.
- An important limit for the motion generation is the ZMP-constraint - for dynamic stability. As the physical consistency does only depend on the uni-lateral (6.1a) and contact feasibility (6.1b) and (6.1c) it is interesting to relax the strict ZMP-constraint and observe the modifications in the final motion results. This is a pure hypothetical analysis, as the stabilizing algorithms will certainly not comply with this class of trajectories.
- A thorough analysis is conducted, on how the previously discussed objectives influence the generated motions resulting from the formulation (7.1) of a periodic half cycle in walking motion (see Section (1)). From these results conclusions are drawn, which objectives are to be selected and how path and boundary constraint should be reformulated for subsequent investigations of dynamic and highly limiting motions.

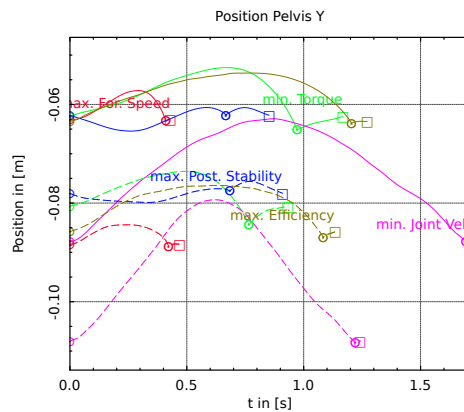


Figure 7.2: Influence of ZMP constraint on height of Pelvis (origin of Pelvis Y coordinate is reached with stretched knees) - circles display phase transitions and squares the end of the simulation - for different objectives (colored). Solid line represents results with relaxed ZMP constraint and the dashed line represents results with strict ZMP constraint

2.1 The Influence of ZMP Constraints on the Trajectory

For the control of HRP-2 N° 14 with its stabilizer turned on it is crucial to have walking trajectories that satisfy the ZMP constraints. However, this stability criteria is very strict and prevents any truly dynamic form of walking. It is often noted that many humanoid robots walk in a nearly half-sitting position, which is not quite alike humans. It can be shown that, once the ZMP constraint is ignored, the humanoid walking motions are much more upright than with the ZMP constraint. This effect occurred for all objective function studied, and the average pelvis height was increased by 2 to 4 cm (see Figure 7.2). Further investigations tried to reduce oscillations of the ZMP trajectory. It was found that among the objectives minimum torque and especially maximal postural stability produced the lowest oscillations in the ZMP trajectory particular in case of a flexible foot position.

2.2 Optimization of Different Criteria - Comparison of Free and Fixed Foot Position

Table 7.2: Step length and step width in different simulations with free foot position in comparison to the initial guess of the computations

simulation	step length	step width
initial guess	0.152m	0.144m
min. torque	0.129m	0.049m
max. forw. speed	0.171m	0.027m
min. joint speed	0.098m	0.0253m
max. postural stab.	0.158m	0.038m
max. efficiency	0.185m	0.016m

As discussed previously several heuristics based methods for walking motion generation require *a priori* fixing the position of the next foot contact on the ground and even the timing

of the step. It is claimed that making these assumption is critical. Hence an advantage of the employed optimization based approach is, that foot placement and phase times can be either fixed or left free. Fixed and free foot-placement has been adopted both. In all cases, symmetry and periodicity constraints are enforced on the solution - step timing was left free to the optimizer. The ZMP is restricted to lie within the area necessary for the stabilizer to properly track the motion on the real HRP-2 N° 14 platform.

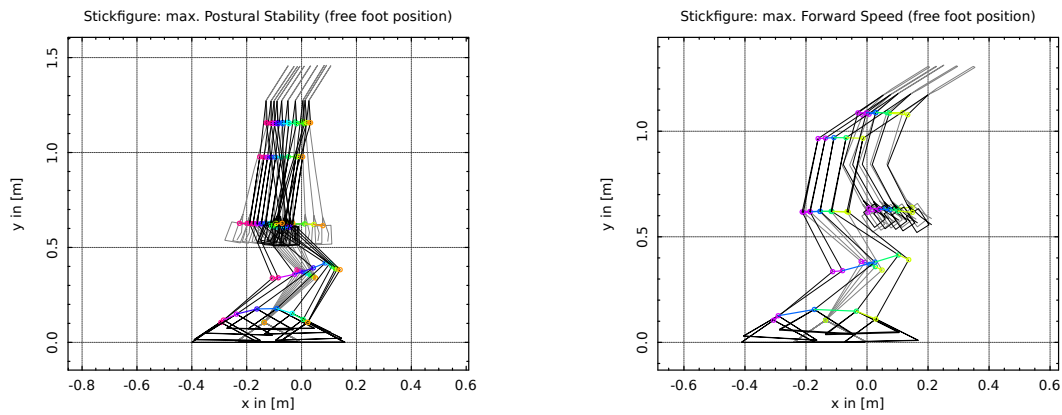
The gait characteristics with comparison to the initial guess are shown in Table 7.2 and 7.3.

Table 7.3: Mean forward velocity and duty factor of simulations with fif and frf - compared to the initial guess of the computations. The *duty factor* is defined as the fraction of time a foot is ground contact compared to the time to accomplish two steps.

simulation	mean forward speed	duty factor
initial guess	0.178 $\frac{m}{s}$	62.2%
min. torque (fif)	0.102 $\frac{m}{s}$	70.4%
min. torque (frf)	0.138 $\frac{m}{s}$	59.0%
max. forw. speed (fif)	0.228 $\frac{m}{s}$	66.1%
max. forw. speed (frf)	0.363 $\frac{m}{s}$	55.1%
min. joint speed (fif)	0.100 $\frac{m}{s}$	61.1%
min. joint speed (frf)	0.079 $\frac{m}{s}$	50.9%
max. postural stab. (fif)	0.122 $\frac{m}{s}$	65.4%
max. postural stab. (frf)	0.174 $\frac{m}{s}$	62.4%
max. Efficiency (fif)	0.090 $\frac{m}{s}$	53.0%
max. Efficiency (frf)	0.163 $\frac{m}{s}$	52.3%

Step width (Table 7.2 on the preceding page) is in all cases chosen smaller than the original $0.144m$, for the maximization of efficiency it is even reduced to $0.016m$. Step length increases in three cases and is reduced in two. Compared to the original step length of $0.152m$, the longest step length occurred for a maximization of efficiency with $0.185m$ and the shortest for the minimization of joint velocities with $0.098m$. Table 7.3 shows the average walking speed resulting from the different optimization criteria. The gait used for initialization had a walking speed of $0.178m/s$. As one could expect, the highest walking speeds result when precisely this quantity is maximized (7.4). For this objective and free foot placement but constrained ZMP, the walking speed can be increased to $0.363m/s$, i.e. $1.31km/h$ which represents an increase by a factor of 2.03, even further than for an unconstrained ZMP but a fixed foot position ($0.352m/s$). With both constraints, the same criterion only leads to $0.228m/s$. For all objective functions, except for the minimum joint velocity criterion, the relaxation of any of the constraints leads to an increased average walking speed. The contact duty fraction (measured with respect to the stride) of the feet in ground contact always increases for fixed foot placement. For the minimum torque, maximum forward velocity and postural stability criteria, values are higher than for the initial guess. However for minimum joint speed and maximum efficiency values are significantly lower.

In Figure 7.3 on the next page and Figure 7.4 on page 103, an overview is given over the whole-body appearance of the resulting motion stick figure sequences for postural stability optimization and for maximum speed optimization. In both cases with fixed and free foot positioning, it is clearly observable that the appearance changes. For forward velocity maximization the upper torso is leaned forward to make larger steps, while in the case of fixed



(a) Maximization of postural stability for free foot placement (b) Maximization of walking speed for free foot placement

Figure 7.3: Comparison of free foot placement for two criteria: maximization of postural stability (left) and maximization of walking speed (right).

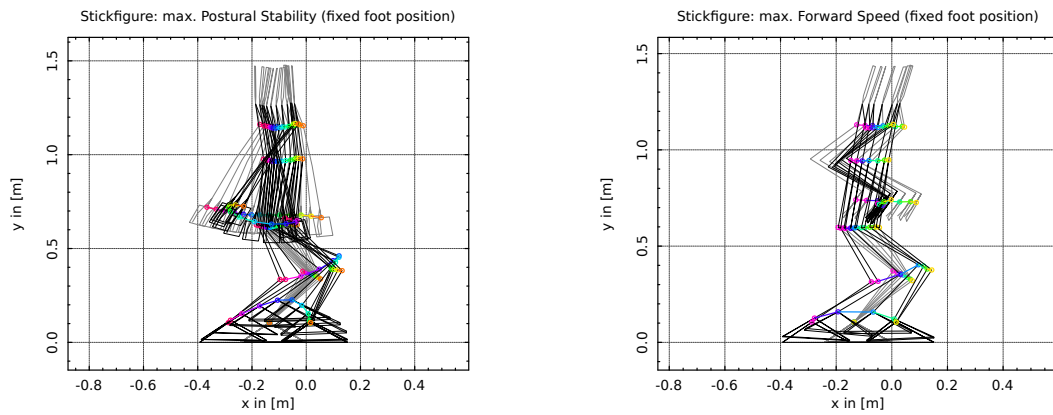
placement the upper body is kept upright to make smaller but quicker steps. The postural stability criteria does not tend towards clearly larger step lengths, however excessive arm-swinging to dynamically stabilize the whole body motion for the case of fixed foot placement is observable.

As the knee joint motion profile is a good indicator for bipedal walking characteristics, the corresponding motion trajectories deserve a closer look. For the postural stability criteria it is observable in Figure 7.5 on page 104 where the fixed foot placement (solid blue line) leads to higher value ranges for the knee joint position and velocity of left and right foot of the maximum postural stability criteria (dashed blue line). For the other criteria a similar trend is only observable for the left knee joint (support leg). An interesting fact is, that the support leg knee joint angular value range of the free foot placement case (dashed line) is significantly lower than for the fixed foot placement (solid line) case. Sole exception here is the maximum forward velocity case (see Figure 7.5 on page 104).

Furthermore, it is interesting to note that for all criteria the value range of the Z-position amplitude of the pelvis is higher for the fixed foot placement case (see Figure 7.6 on page 105). An fact that is closely related to the step width that is chosen smaller for free foot-placement to allow a more straight-forward walking motion. The same tendency is shared from the pelvis pitch motion, where much smaller amplitudes are observed for the free foot placement.

2.3 Optimization of Different Criteria - Further Criteria

Figure 7.7 on page 106 shows the linear and angular impact momentum for all 15 cases. A high impact momentum is undesirable since it results in a loss of energy and, in particular in the case of a humanoid robot, produces a high risk of destabilization and deterioration of its actuation systems. Both linear and angular impact momentum were particularly high for the maximum average velocity criterion, no matter if ZMP or foot position are constrained or relaxed. This makes the maximum velocity solution less interesting than it seemed above, and this criterion might only be useful for the real robot if additional constraints on the size of the impact are taken into account. The smallest impact momenta occur for the minimum joint velocity criterion and a relaxed ZMP, followed by the same criterion with relaxed foot position.



(a) Maximization of postural stability for fixed foot placement (b) Maximization of walking speed for fixed foot placement

Figure 7.4: Comparison of fixed foot placement for two criteria: maximization of postural stability (left) and maximization of walking speed (right).

Minimum torque, maximum efficiency and maximum postural stability result in medium size impacts. However, all impact momenta values are beyond the limit that is acceptable for an implementation on the real robotic platform.

Figure 7.8 on page 107 presents different measures for the cost of the different walking motions, namely the sum of torques squared (which corresponds to the electric power dissipation on the armature resistance of the electric motors), the cost of transport as defines above, as well as the absolute mechanical energy (Sum of all torques - by magnitude - integrated over the joint angles). Even though they have quantitatively different results, all three measures show the same tendencies: maximum velocity and maximum postural stability lead to quite costly solutions while minimum joint torques and maximization of efficiency lead to rather cheap solutions in terms of all three measures. Figures 7.9 on page 107, 7.10 on page 108, 7.11 on page 108, 7.12 on page 109 and 7.13 on page 109 show snapshot sequences of the optimal walking cycles for all five criteria. Figure 7.14 on page 109 shows the trajectories of position (top row) and orientation (bottom row) variables of the pelvis for all five objective functions (see color code explained in the first plot). In all plots the different step durations resulting from the different objectives become obvious. The top left plot describes the forward motion of the pelvis which differs significantly for the different objectives (also compare discussion about step lengths and average velocities above). The second plot in the top row shows the vertical motion of the pelvis, clearly depicting in all cases the two vertical oscillations over the two steps. The height variations of the pelvis are quite small (smaller than 1 cm) for all objective functions except for the minimum joint velocity criterion, where the variation is around 3 cm despite the small steps. This is due to the very small range of motion of the hip and the knee angles caused by this criterion which induces a high stiffness in the joints. The third plot shows the side-ward motion of the pelvis. Note that this time there is only one oscillation since the periodic cycle for orthogonal gait oscillations is two steps and not one, as for the vertical motion. The variations in side-ward directions lie between 4 cm, for the maximum speed criterion, and 10 cm, for the maximum postural stability criterion. The lower row in figure 7.14 on page 109 presents the roll, pitch and yaw angles of the pelvis. Especially noteworthy is the high amplitude of the roll angle for the minimum joint velocity criterion which again is caused by the fact that the criterion stiffens the legs. This criterion

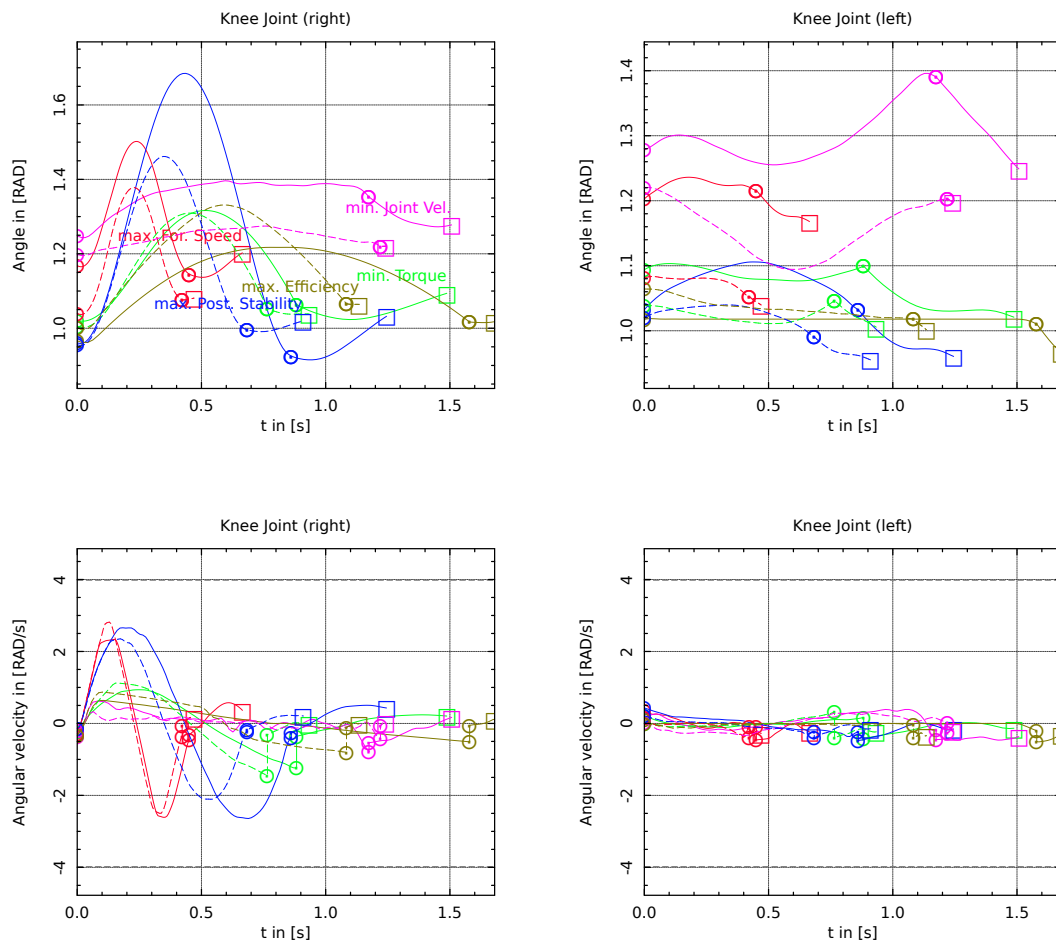


Figure 7.5: Knee joint angle and angular velocity of left (support) and right (swing) leg distinguished between strict foot position constraint (fixed - solid line) and relaxed foot position constraint (free - dashed line). Different colors indicate different objective functions as explained in the top left plot. Circles indicate model stage transitions, and squares indicate the end of the simulation (i.e. the end of the last model stage).

also leads to a significantly reduced pitch angle, i.e. the pelvis is turned backwards. In all other cases, the pelvis is bent slightly forward. For the yaw angle, in particular the maximum speed velocity stands out with much larger amplitudes than the other criteria, which is caused by the large steps performed in this mode of motion.

Figure 7.15 on page 110 shows the trajectories of the hip and knee angles in the sagittal plane for all five objective functions. The plot shows a whole walking cycle for one leg starting with the swing phase, followed by DS, then SS and again DS phase. Both angles are bent much more than in human walking motions and lead to the characteristic half-sitting position of humanoid robots. As it is shown in Section 2.1 on page 100 this behavior is clearly related to the enforcement of the ZMP constraint and a relaxation of this constraint results in a straightening of the legs and an increase of the pelvis height. As mentioned above, the oscillations linked to the minimum joint velocity criterion are very small for both knee and hip angle such that the leg is nearly straight over the full cycle. The shapes of the hip angle trajectories are very similar for the other four criteria, the only difference is the total duration of the cycle which results in more or less stretched angle trajectories. The same is true for the knee angle

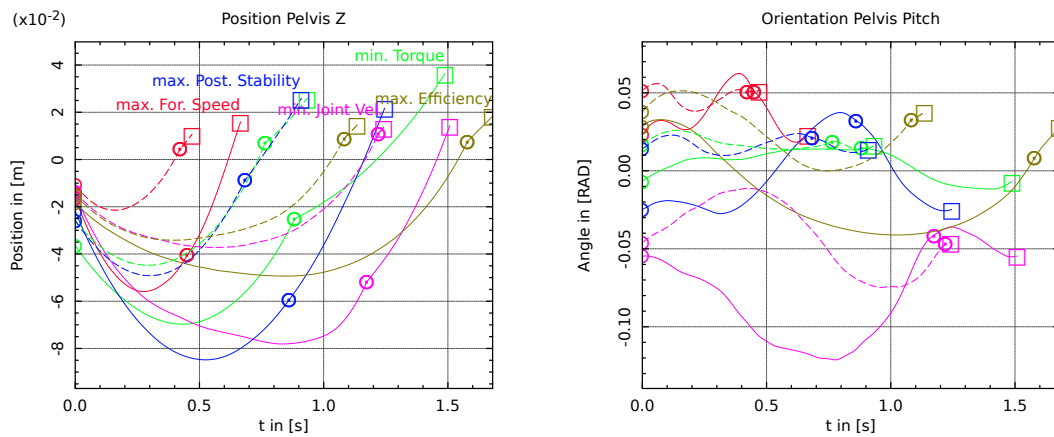


Figure 7.6: Pelvis position and orientation in Z distinguished between strict foot position constraint (fixed - solid line) and relaxed foot position constraint (free - dashed line). The axis points lateral towards the right side of the robot. Different colors indicate different objective functions as explained in the top left plot. Circles indicate model stage transitions, and squares indicate the end of the simulation(i.e. the end of the last model stage).

with slightly more pronounced differences in the amplitudes: the maximum postural stability criterion leads to the largest knee angle amplitude and the maximum efficiency criterion leads to the smallest one (but still much bigger than the minimum joint velocity knee amplitude).

In contrast to the heuristic based motion generation methods, where the foot trajectories are frequently expressed based on a parameterized trajectory, the optimization based method employed in this study freely determines the trajectory of the foot swing foot based on the whole body motion. The results are shown in Figure 7.16 on page 110. The trajectories of the sole center position as well as roll, pitch and yaw angles of the swing foot over one step are shown. Appropriate constraints (refer to Section (1.4)) in the OCP formulation avoid penetration and sliding of the swing foot on the ground. Hence, it is important to check whether the resulting motion is governed by this ground clearance constraint or whether the optimizer chooses as distinct trajectory that coincides only occasionally with the defined ground clearance barrier. The maximum postural stability criterion leads to the swing foot trajectory with the highest lift (8cm), and the minimum joint velocity with the largest side-ward variation of the foot (5cm). Changes of foot angles are generally not big over the swing phase with the highest roll and yaw angle variations again for the minimum joint velocity criterion, and the highest pitch angle variation for the maximum efficiency criterion.

Despite the fact that the ZMP constraint has a strong influence on key aspect of the motion, such as the pelvis altitude (refer to Figure 7.2 on page 100, the space that was given to the ZMP trajectory in the support polygon was still wide enough to allow for individual profiles. The results of all objectives are shown in Figure 7.17 on page 111. The foot-steps (ground-contact) are drawn including the valid polygon of support (gray tube) that was given to the optimizer to allow for a dynamically stable motion of the robot. For a clearer appearance of the motion a full stride (two steps) is drawn.

In four cases it is clearly observable that the ZMP moves to or along the boundaries of these stable areas. The constraints are quite restrictive, and the ZMP would move outside this area (gray tube) as soon as this constraint would be relaxed. However, the trajectory would still be bounded by the contact feasibility constraints of the surface contacts. The only exception represents the postural stability criterion. This criterion penalizes the individual trajectory

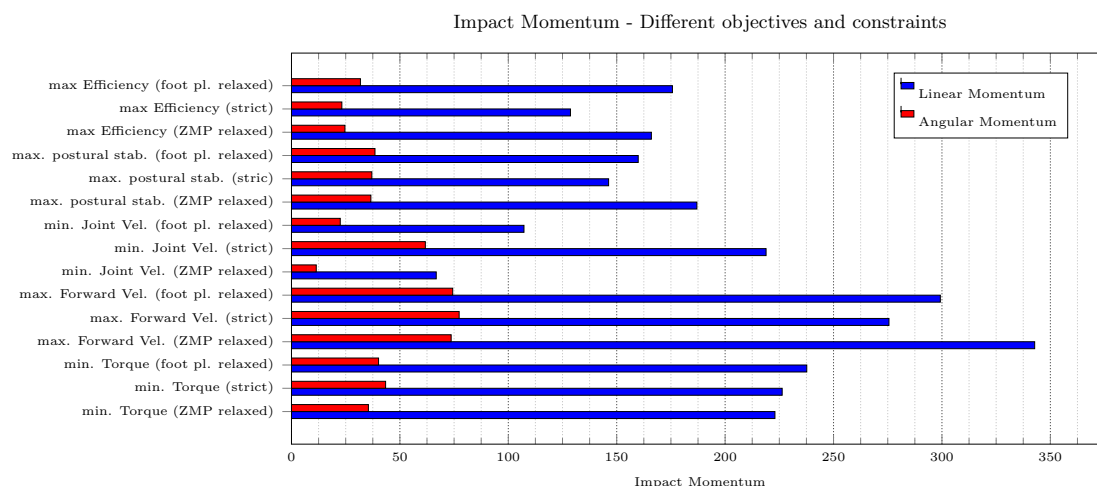


Figure 7.7: Angular and linear impact momentum from touch down during the model stage transition from SS towards DS. Even though some criteria seem to minimize the impact momentum values they are still unacceptable high for prospect motion implementation on the robot.

of each CoP underneath the sole for moving away from the center position and this yields a ZMP profile that is more shifted towards the middle line of the support polygon. In case the individual penalization is important enough the ZMP would not leave the defined retracted polygon of support even if the corresponding constraint is dropped. The minimum torque criterion and the maximum postural stability criterion produce quite smooth ZMP paths while they are more "cracked" for the other criteria.

3 Conclusion

Five different objective functions have been evaluated as well as the effect of ZMP constraint and the foot placement constraints.

A free foot placement appears to be desirable in all cases investigated. Defining the foot placement a priori in some heuristic way reduces the gait variety considerably and decreases the optimization potential. The only reason to constrain foot positioning is an environment where only limited footholds are available such as walking on step stone bridges. But on even terrain with obstacles the foot positions should be chosen freely in an optimal way according to the chosen optimization criterion. This is an important aspect that will be henceforth considered in all subsequent problem formulations.

Relaxing ZMP constraints has demonstrated some interesting perspectives - such as the possibility to walk in a more upright way than current humanoids do. For the given Robot HRP-2 N° 14, however, this option is neglected due to the restrictions of the stabilizing control system (refer to Section 1.1 on page 80). An important question for subsequent chapters to find an answer is - is the ZMP constraint correctly tuned to comply with the control system? - and are there possibilities to reformulate this constraint in a more efficient way?

The minimization of joint velocities does not appear to be a useful criterion. Even though it may intuitively seem stabilizing to avoid unnecessary joint motions, the objective leads to very stiff, non-smooth and unnatural motions with high oscillations in the pelvis height and roll angle and the foot side-wards motion as well a backward inclination of the pelvis. Consequently, further use of this criteria will be neglected.

Similarly the maximization of postural stability does not seem to be suitable either. The postu-

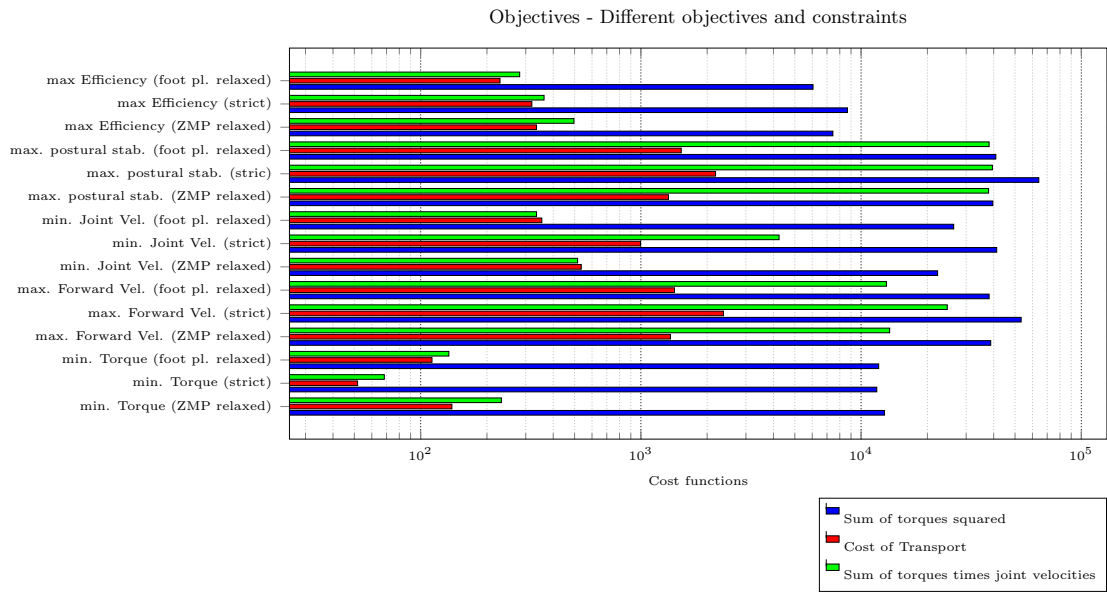


Figure 7.8: Different cost functions compared for all optimization criteria and constraint combinations: sum of torques squared, cost of transport, and absolute mechanical energy (sum of torques along angles).

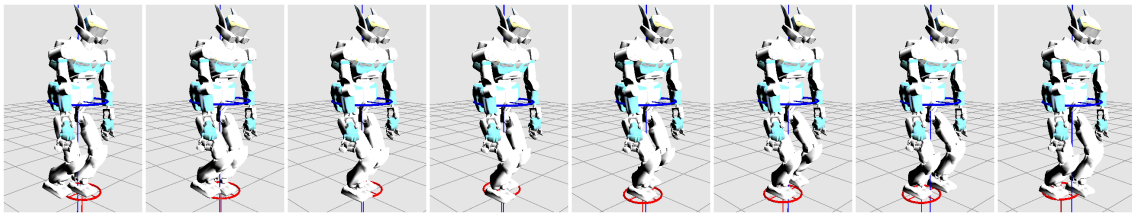


Figure 7.9: Motion sequence for minimum torque objective with free foot placement and constrained ZMP (red - ZMP position, blue - projected CoM position) for different objective functions

ral stability aspect is effectively enforced based on the ZMP constraint and further maximization of the corresponding criteria results in extremely costly solutions - in particular compared to the slow walking velocities it exhibits. The advantage of maximizing a relatively conservative stability margin does not seem to compare to the additional costs and undesirable and inefficient motion characteristics this criteria produces. However, with respect to the dynamic stability and the surface contact feasibility, one has to clearly distinguish between the local trajectory of the CoP inside the individual foot-fold and the resulting ZMP profile of the robot standing on the ground. This aspect will be discussed in the next section.

The maximization of average walking velocity is an interesting step towards investigating the dynamic limits of the given robotic platform. The computed increase of walking speed by a factor of a little more than 2 with respect to the reference solution, shows the potential that comes with whole body optimization based motion generation techniques. However, the impact magnitudes suggest that this performance will not be reachable in reality, since the associated mechanical load and potential of dynamic destabilization are assumed to exceed the capacities of the real robot.

The minimization of joint actuator torques and the maximization of walking efficiency seem to be a promising objective function, which are associated with low "energetic" costs (in all measures investigated). The minimization of torques leads to smoother motions, while the

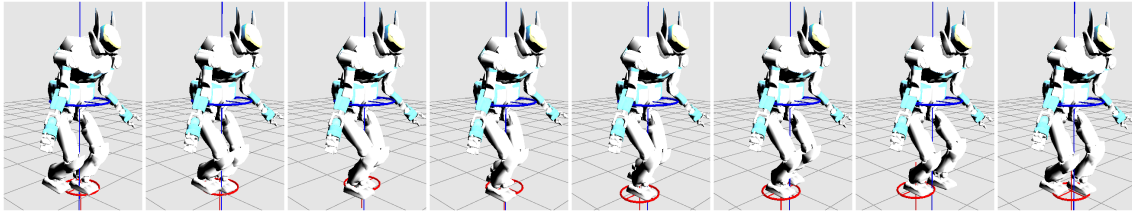


Figure 7.10: Motion sequence for maximum forward velocity objective with free foot placement and constrained ZMP (red - ZMP position, blue - projected CoM position) for different objective functions

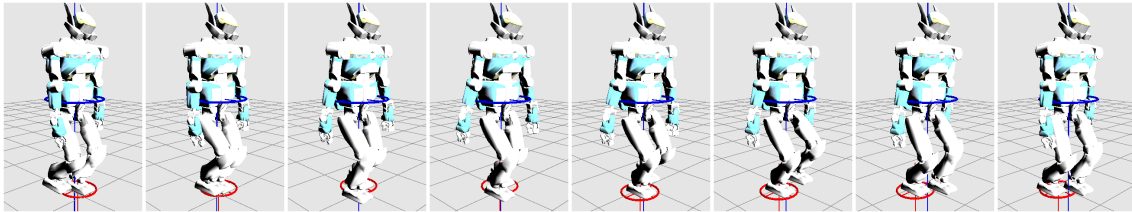


Figure 7.11: Motion sequence for maximum postural stability objective with free foot placement and constrained ZMP (red - ZMP position, blue - projected CoM position) for different objective functions

maximization of efficiency leads to faster motions with higher speeds. These motions are characterized by smaller impacts than the maximum velocity solution. However, even these reduced magnitudes are considered to reach beyond the limits the real robot may compensate during dynamic operation.

From this analysis it is concluded that:

- All subsequent formulations should leave all foot step placements as quantity to optimize along-side with the generated motion
- The magnitude of the impact-collision for all criteria most-probably exceeds the structural limit the robot is capable to compensate and hence, appropriate counter-measures must be considered in the problem formulation to reduce them to a minimum.
- Relaxation of the ZMP constraint, reveals potential for further improvement towards promising motion characteristics. This constraint should be definitely revisited and appropriate modifications of this constraint that comply with restrictions of the stabilizing control system of the real robot should be considered.
- The minimization of joint torques and maximization of the efficiency leads to low-cost and smooth motion trajectories and should definitely be considered as counter-measure to partially compensate for the relative *costly* and *non-smooth* motion profiles that are to be expected when investigations of the dynamic limits of the robot are to be performed.

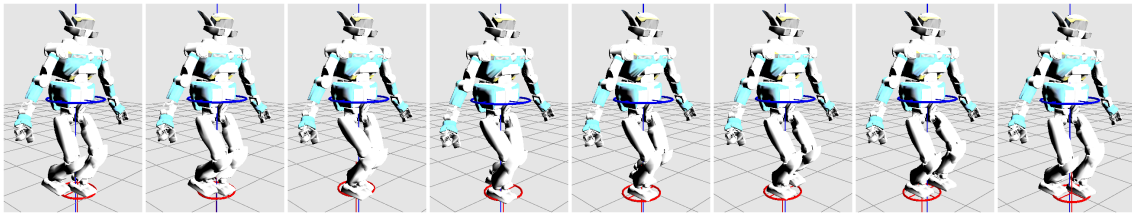


Figure 7.12: Motion sequence for maximum efficiency objective with free foot placement and constrained ZMP (red - ZMP position, blue - projected CoM position) for different objective functions

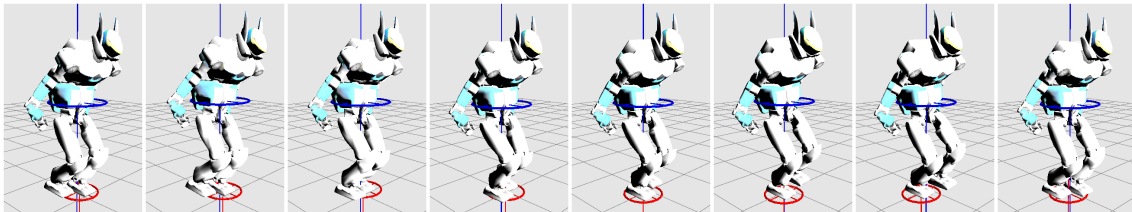


Figure 7.13: Motion sequence for minimum joint velocity objective with free foot placement and constrained ZMP (red - ZMP position, blue - projected CoM position) for different objective functions

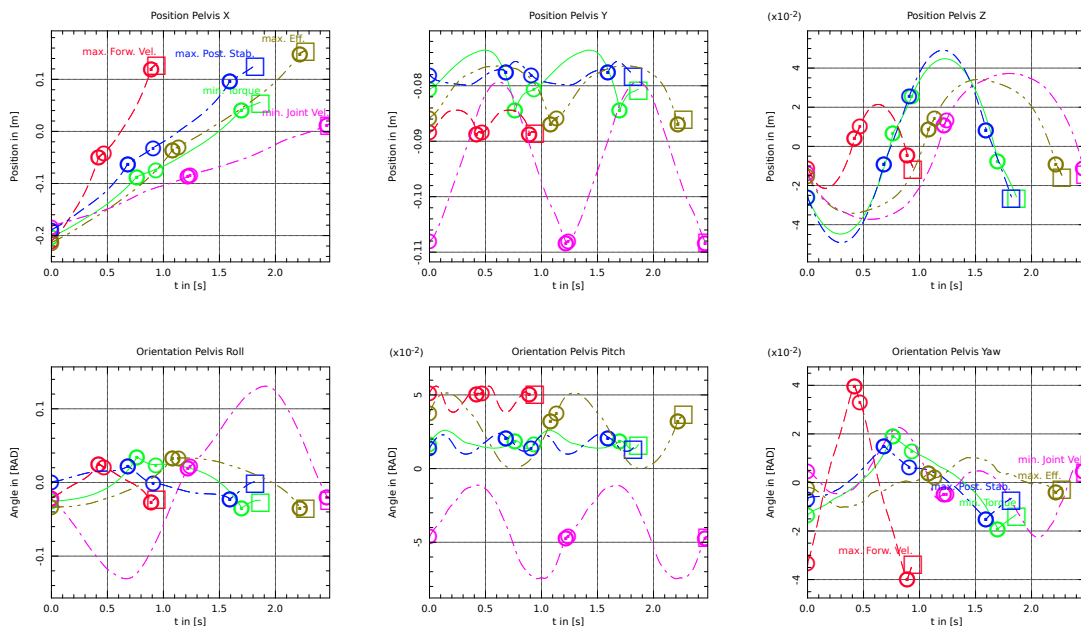


Figure 7.14: Pelvis trajectories over a full gait cycle (two steps) for the five different objective functions with constrained ZMP and free foot placement. Top: pelvis position trajectories in forward, vertical and side-ward direction. Bottom: pelvis roll, pitch and yaw angles. The gait cycle starts with the SS on the left leg, followed by DS, SS with the right leg and then DS phase (circles denote ends of phase, squares the end of the cycle).

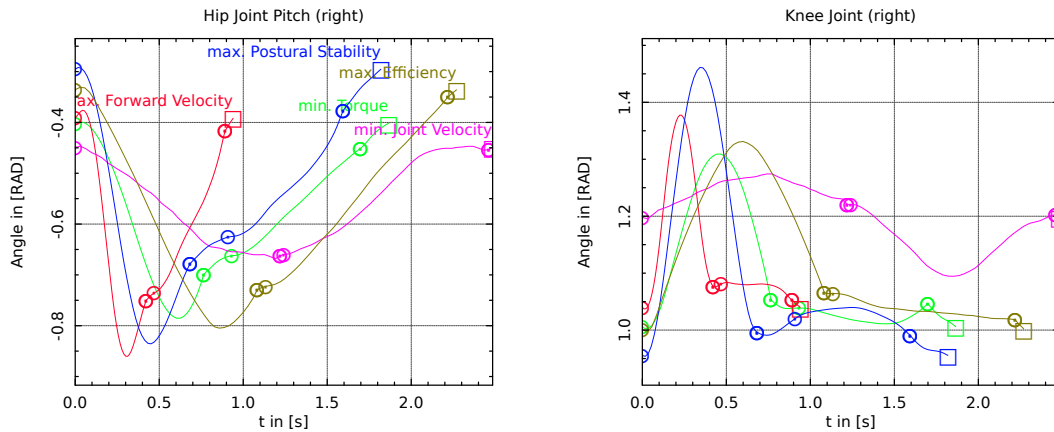


Figure 7.15: Sagittal plane hip and knee angle trajectories of one leg over a full gait cycle (two steps) for the five different objective functions with constrained ZMP and free foot placement. The gait cycle for this leg starts with the swing phase, followed by DS, SS and then DS phase (circles denote ends of phase, squares the end of the cycle).

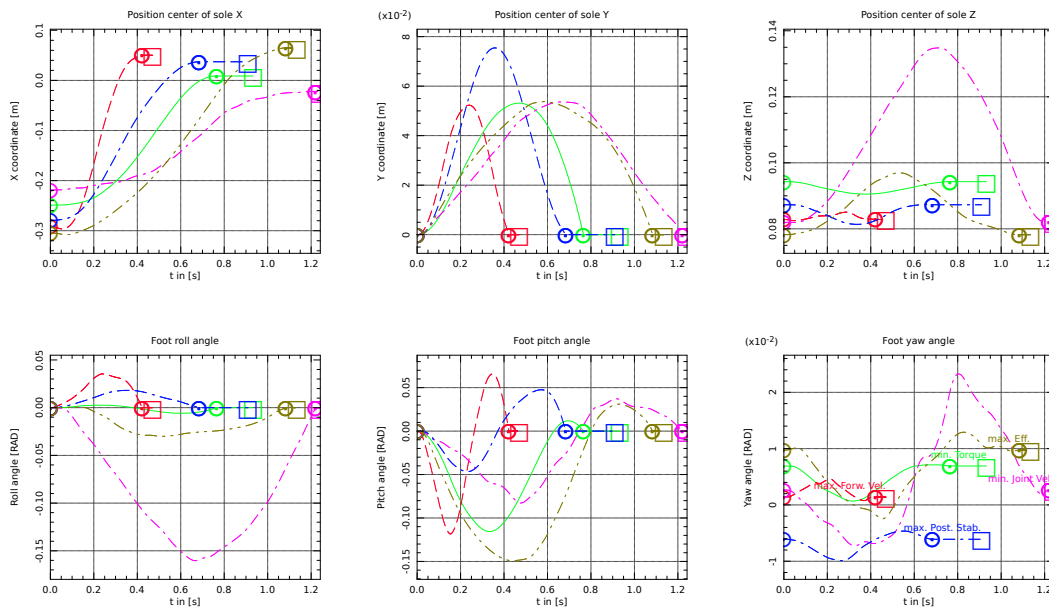


Figure 7.16: Swing foot trajectories over one step (swing phase and DS phase) for the five different objective functions with constrained ZMP and free foot placement. Top: foot sole center position trajectories in forward, vertical and side-ward direction. Bottom: foot roll, pitch and yaw angles (circles denote ends of phase, squares the end of the cycle. Same color code as in previous plots is used for the objective functions).

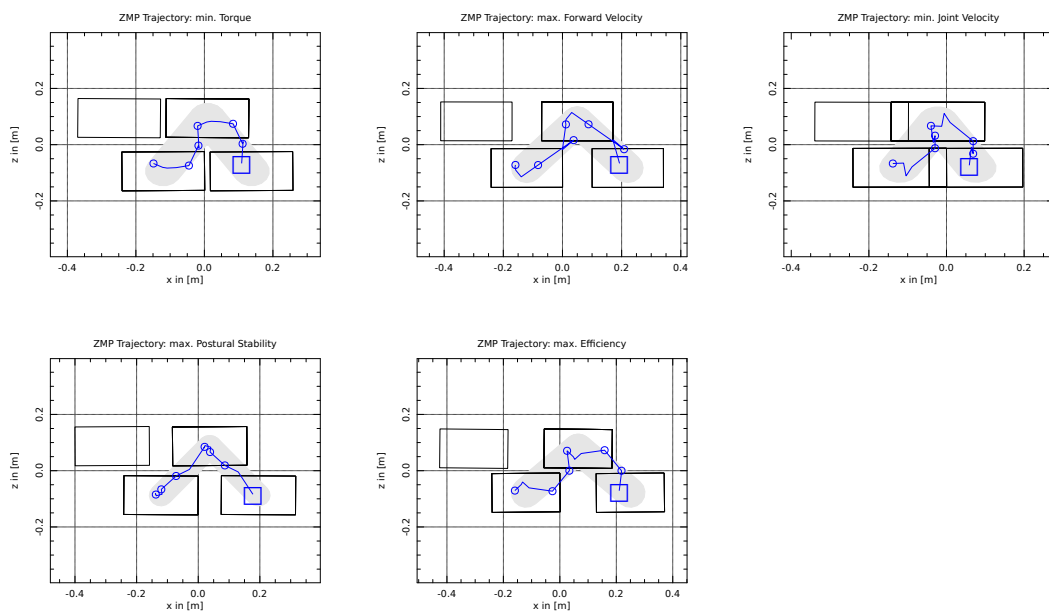
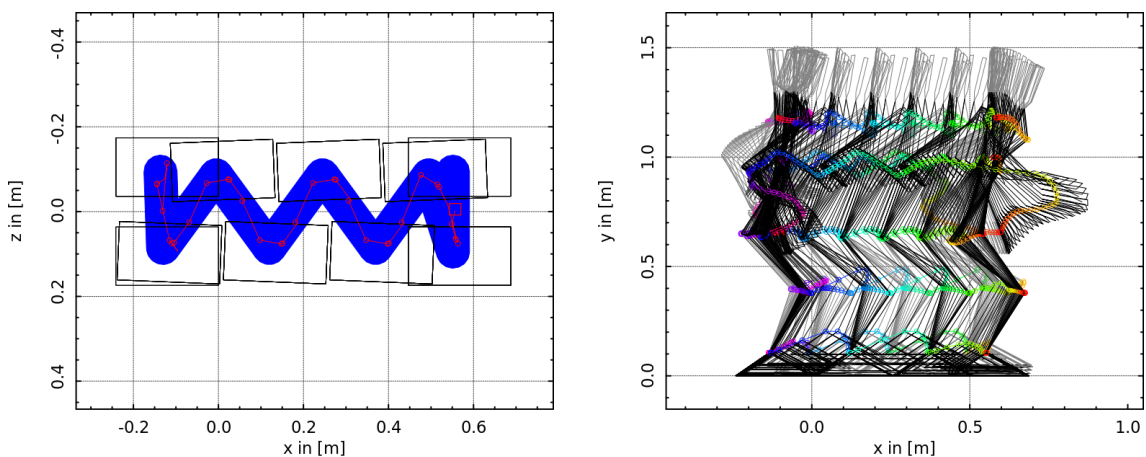
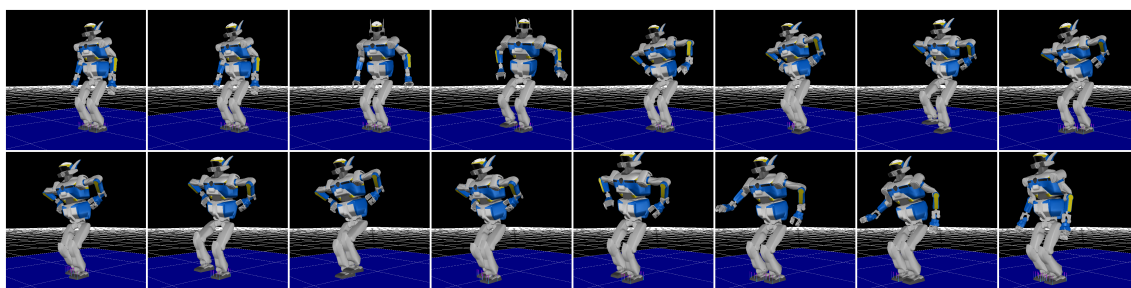


Figure 7.17: ZMP paths over a full gait cycle (two steps) for the five different objective functions with constrained ZMP and free foot placement. Grey tubes show the ZMP constraints.

8 Towards Real Motion Implementation



(a) Foot steps of a typical motion cycle with ZMP (red curve) and the feasible support polygon for the stabilizing control system (blue tube) (b) Stick-figures depicting the complete motion minimum torque motion cycle of the left graph - The color-map from: blue $t = 0$ \rightarrow $t = T_{\text{End}}$ red, shows the motion in time.



(c) Motion in the OpenHRP [Hirukawa et al., 2003] motion simulator

Figure 8.1: Realistic test motion cycle, as it has been used for first attempts to transfer experiments from the optimization tool-chain towards a real implementation on the robot.

The motion simulations from the previous chapters represent a solid preliminary investigation. However, these motions results are still far away from a potential real implementation on the robotic platform HRP-2 N° 14. A dynamic motion that should be successfully implemented on the real robot, must fulfill a couple of additional boundary constraints that have been discarded for the previous study - a static initial and final posture. A typical motion cycle that fulfills these boundary constraints is shown in Figure 8.1. On the left Figure 8.1a one can observe the free foot placement sequence that has been computed and on the right Figure 8.1b stick-figures of the compute kinematic configurations of the resulting dynamic whole-body motion. The robot starts dynamic stepping from a half-sitting posture moves forward and decelerates to finally regain its equilibrium in the static end posture. The stable motion is visible in Figure 8.1c performed in the motion simulator OpenHRP [Hirukawa et al., 2003].

From the technical point of view the motion seems to be fine as the ZMP trajectory firmly remains inside the feasible (blue) support polygon area between the foot steps (refer to Figure 8.1a on the preceding page). However, the kinematic configurations of the motion reveals features, such as a swaying upper torso motion and dynamic arm swinging. Given the kinematic constraints of the robot and the assumption that the optimization results will try to perform as much DoG as possible exaggerated motion patterns for some joints are expected. However, the influence of these motions on the dynamic stability of the robot is relatively difficult to assess, especially for a larger time horizon.

Furthermore, a walking motion alone is a motion cycle that is relatively resource intensive to compute (multiple OCP involved), but does not provide good opportunities alone to push the robot to its dynamic limits. Therefore, it was decided to suspend investigations to bring pure forward or omni-directional walking cycles to the robot in favor of a motion task that is similar to walking. This motion task should be capable to bring the robot to its limits, but perform on a smaller time horizon. This requirement is necessary to formulate and compute the motion in a monolithic OCP within reasonable computation times.

1 Motion Generation for Obstacle Overstepping

Since humanoid robots are meant to move around in unstructured environment, various approaches exist to clear obstacles with humanoid robots. Similar studies have been already conducted on the humanoid platform HRP-2 N° 14 [Guan et al., 2005, Verrelst et al., 2006]) as well as other platforms, such as: Johnnie [Seara et al., 2001], Asimo [Michel et al., 2005] and BHR-2 [Jarfi et al., 2006]. [Guan et al., 2005] conducted a kinematic feasibility analysis of obstacles to be overstepped concluding on a maximum obstacle of 24.21cm x 5cm (width x height). Dynamic overstepping was then achieved in [Verrelst et al., 2006] as part of a walking pattern, in simulation and real experiment, pushing the maximal values to 18cm x 11cm (width x height) including a safety margin of 3cm. The motion is planned for ankle and hip (including twist) trajectories from a previous geometric feasibility analysis. The whole-body motion is then generated based on the ZMP preview control pattern generator from [Kajita et al., 2003a].

Apart from the optimization based studies with a quasi-static approach [Guan et al., 2005], the investigations to dynamically overstep obstacles with HRP-2 N° 14 robot were again based on a heuristics driven motion generation method (compare Section 3 on page 6). From the conducted preliminary study, one of the concluded aspects formulated the assumption that foot placement in heuristic based motion generation methods may not be optimal and hence, it is evident to assume that in the case that these motion generation methods are employed for obstacle overstepping the result may - even though they are impressive from a technical point of view - not be optimal as well. Therefore, the remainder of this part will consider investigations to employ OCP formulations for the real HRP-2 N° 14 platform to dynamically overstep obstacles and to eventually break the stated record of: 18cm x 11cm (width x height) [Verrelst et al., 2006].

2 Problem Formulation for Obstacle Overstepping

Common parts of the problem formulation used during all optimization trials based on the inelastic modeling approach are presented, below. Its influence on the resulting motion outcome and its implications for the further discussion of the application of the employed OCP components (objective/constraint) are then given in the corresponding result section. Although most of the components of the OCP are directly exploitable for all subsequent simulations, the

structure of the OCP which incorporates these components can significantly differ between the simulations. Thus, for the sake of brevity, for each study only the new or modified components are described, while previously explained ones are referred to their respective section, where they have been introduced first.

The OCP formulation employed below is the same as in Section (1.1), with the substantial difference that in the model equation (7.1b), the forward dynamics operator was used on a plci control discretization (refer to Chapter 5 on page 54 for details).

2.1 Problem Structure of the Stepping Motion

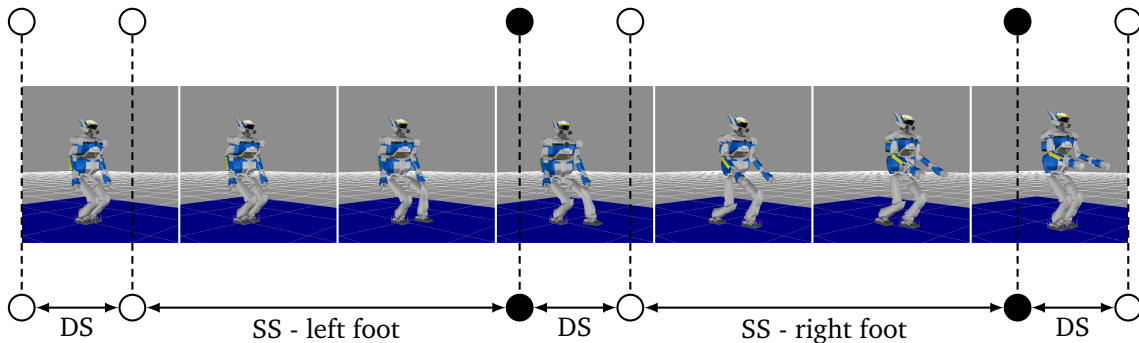


Figure 8.2: Problem structure of the stepping motion over an obstacle. The motion is simplified to 5 different contact states: double support *DS*, single support left foot *SS - left foot*, single support right foot *SS - right foot* and a final double support phase *DS*. Discontinuous phase transitions (foot ground collision - CH) are marked with black dots while continues phase transitions (foot lift-off) are marked with white dots.

The employed OCP formulation has the same structure as (7.1a)-(7.1h) in Section 1 on page 93. Hardware based simplifications of the OCP formulation directly follow from Section 1.2 on page 94 (compare section 1 on page 80 and especially 1.1 on page 83) and will not be repeated here. The motion scheme is depicted in Figure 8.2. The OCP is formulated to cover a two step walking motion from a static initial posture towards a final static posture. After a short *DS* phase, the left foot is raised and swings forward. After the ground collision (CH) and a short *DS* phase the right swing foot follows towards the final *DS* phase, to bring the robot to complete stop.

Figure 8.2 depicts the stepping scheme but not the obstacle, which is placed during the simulation at a half stride of the initial foot position.

The motion has 5 different contact states and hence features 5 distinct model stages as well as 4 model stage transitions, a OCP scope that still has a reasonable size. Related to the discussion in Section 3.4 on page 72 the OCP formulation has been adjusted to the multiple-shooting configuration and initial guess configuration stated in Table 8.1 on the next page. Compared to the values in Table 7.1 on page 95, the adopted configuration seems relatively coarse. This is related to the made trade-off between accuracy and computation time.

2.2 Objectives

Objectives are divided into:

primary (1st) Max Obstacle Height
secondary (2nd) Min End Time

tertiary (3rd) Head Stabilization and Minimum
 Variations of Square Torques

While the primary is chosen dominant together with the secondary to force a certain motion characteristic (high obstacle clearance) the tertiary objectives are carefully chosen to assure the dynamic quality (e.g. less oscillation in the controls) of the motion (refer to Section 2 on page 99).

Max Obstacle Height [1st]

The primary target of this study is to investigate the maximum expectable height of the obstacle the HRP-2 N° 14 robot platform is capable to clear within its strict realistic kinematic and dynamic limits,

$$\max \Psi_{\text{Obs. Height}} = p_{\text{Obs. Height}} \quad (8.1)$$

Min End Time [2nd]

As motion capacities of humanoid robots are still far behind those of humans, it will be, at one hand, interesting to investigate how fast the robot platform HRP-2 N° 14 is capable to clear the obstacle (in simulation of course) within its strict kinematic and dynamic limits. On the other hand, this study should clearly yield a dynamic motion to be different from the quasi static study conducted by [Guan et al., 2005],

$$\min \Psi_{\text{time}} = T_{\text{Global End-time}} \quad (8.2)$$

Head Stabilization & Min Variations of Square Torques [3rd]

In [Hicheur et al., 2005, Imai et al., 2001, Pozzo et al., 1995] it was reported that angular stabilization of the head and gaze is essential for a dynamic postural control during various manipulation and locomotion tasks. At one hand, the desired motion represents a bipedal locomotion problem and at the other hand a tedious postural balance problem. Thus it is concluded that head stabilization, towards the final target in the global reference frame, is an essential characteristic to improve postural stability. The stepping motion is directed straight

Table 8.1: Model stage scheme, Multiple Shooting nodes and initial multiple shooting interval time per model stage

N	MS-Nodes	Time	Contact-State	Description
DS(0)	4	0.50s	Double Support	From initial posture
SS(1)	12	0.99s	Single Support	Right foot swings
CH(2)	1	0.00s	Foot-ground Impact	Discontinues Transition
DS(3)	2	0.10s	Double Support	Traveling over obstacle
SS(4)	12	0.99s	Single Support	Left foot swings
CH(5)	1	0.00s	Foot-ground Impact	Discontinues Transition
DS(6)	3	0.50s	Double Support	..to final posture
Σ	35	3.08s		

forward, therefore the only exception is the pitch orientation of the head. In order to obtain a more natural motion appearance, the global orientation of the head is not constrained to remain straight forward. Instead its deviation is minimized, where $(\text{an})_{\{\text{Yaw,Pitch,Roll}\}}(x)$ is the global orientation of the head,

$$\min \Phi_{\text{Head}} = (\text{an})_{\text{Yaw}}(q)^2 + ((\text{an})_{\text{Pitch}}(q) - p_{\text{Pitch-Offset}})^2 + (\text{an})_{\text{Roll}}(q)^2. \quad (8.3)$$

As stated in [Schultz and Mombaur, 2010] it is possible to improve the motion quality further by minimizing sub-dominantly the squared variation of the torques and its first derivative respectively. This criteria was mostly integrated for technical reasons (risk of over-fitting - huge control oscillations),

$$\min \Phi_{\text{torque}} = \sum_{j=1}^{30} (\dot{\tau}_j)^2 + \sum_{j=1}^{30} (\tau_j)^2. \quad (8.4)$$

2.3 Path Constraints

The path constraints of this OCP are completely adopted from the previous walking study (refer to Section 1.4 on page 98). As it is visible from Figure 8.1 on page 112 dynamic arm-swinging and swaying motions of the upper torso occurred during successful optimization trials.

Torso Stabilization

It was found that swaying motions, even though they were dynamically compatible, give an unnatural motion appearance and could compromise the dynamic stability of the robot and should be minimized. For this study, the upper torso orientation (not the orientation of the pelvis) was fully constrained into a small motion range for its global pitch and roll,

$$\overline{(\text{an})_{\text{torso pitch}}} - (\text{an})_{\text{torso pitch}}(q) \geq 0, \quad (8.5a)$$

$$\overline{(\text{an})_{\text{torso roll}}} - (\text{an})_{\text{torso roll}}(q) \geq 0, \quad (8.5b)$$

$$(\text{an})_{\text{torso pitch}}(q) - \underline{(\text{an})_{\text{torso pitch}}} \geq 0, \quad (8.5c)$$

$$(\text{an})_{\text{torso roll}}(q) - \underline{(\text{an})_{\text{torso roll}}} \geq 0. \quad (8.5d)$$

Compared to the kinematic of the robot (see Figure 6.1 on page 81) this stabilizes the upper torso, but maintains a maximum of flexibility of the pelvis motion during the obstacle overstepping motion.

Obstacle Description

The obstacle to overcome in this study was introduced inside the OCP formulation employing the approach of the self-collision constraint (see Section 2.1 on page 89). The group of self-collision couples was simply extended in each model stage with those pairs (Robot-Limb - obstacle) to effectively prevent collision of any of the robot limbs with the obstacle. However, depending on the model stage formulation selection of the pairs must be done carefully not provoke singular configurations inside the constraint set.

2.4 Boundary Constraints

Besides the consistency constraints (7.10a) and (7.10b) that have been adopted from the previous walking study, this study regroups the following boundary constraint sets:

Implicit Phase Switches

Despite the more complex model stage scheme the implicit phase transition remain the same in the previous study (refer to Section 2.5 on page 135). Hence, for lift off, the boundary constraints (7.8a) and for the foot touch down, the boundary constraints (7.8b), (7.8c) and (7.8d) apply.

As it was found in the previous walking study (refer to Section 2 on page 99), magnitudes of the foot-ground collision were in all cases superior to the compatible limit of the real robotic platform. Therefore suitable boundary constraints had to be formulated to reduce these magnitudes to a minimum. From previous trials it was concluded that an effective reduction could only be achieved by enforcing zero 6D relative velocity of the foot contact point with respect to the ground. The resulting constraint is shown in,

$$\hat{J}_{\text{swing foot}}(q) \dot{q} = 0. \quad (8.6a)$$

Static - Initial & Final Posture

For the motion to be realizable on the real HRP-2 N° 14, it must start from a static initial posture towards a final static one, such that the stabilizing system can effectively maintain the robot its dynamic equilibrium despite external perturbation (see Section 3 on page 6). In addition, it was decided to enforce a symmetric posture of the upper and lower limbs about the sagittal layer, while the global initial and final position with respect to the obstacle was left free in the sense that the initial posture must be in front and the final posture behind the obstacle. In the constraint sets,

$$\left. \begin{array}{l} S_q \dot{q}(t=0) \\ S_q \dot{q}(t=T) \end{array} \right\} = 0, \quad (8.6b)$$

$$\left. \begin{array}{l} S_{\ddot{q}} \ddot{q}(t=0) \\ S_{\ddot{q}} \ddot{q}(t=T) \end{array} \right\} = 0, \quad (8.6c)$$

the matrix S . selects specific entries from the kinematic configuration to avoid redundancy with the consistency constraints of the set of index-1 DAEs. The symmetry of the sagittal plane and the global position in front and behind of the obstacle in constraint set

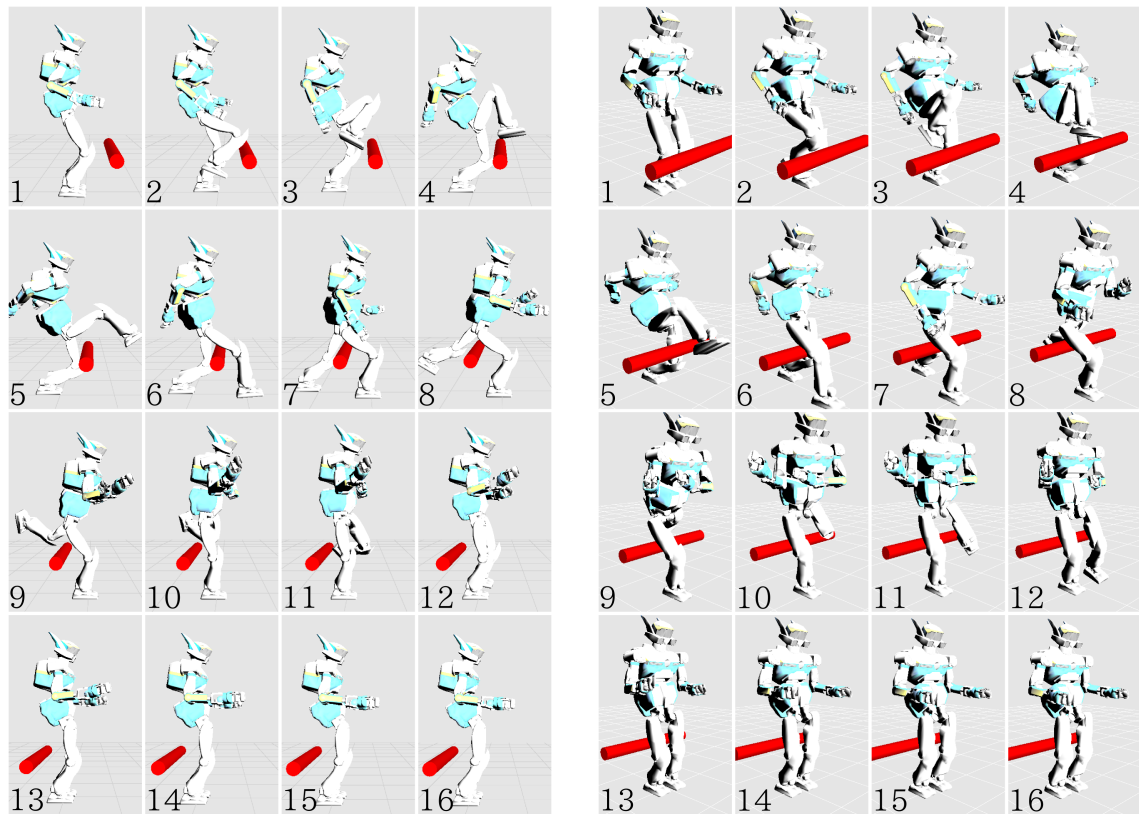
$$\left. \begin{array}{l} h_{\text{sym}}(q(t=0)) \\ h_{\text{sym}}(q(t=T)) \end{array} \right\} = 0, \quad (8.6d)$$

is enforced by the function h_{sym} .

3 Optimization Results of the Overstepping Motion

The generated motion sequence is depicted in Figure 8.3 in different view angles (refer to Table 8.1 on page 115):

From a symmetric static posture (1) one leg (in this case the right leg was chosen) is unloaded (2), lifted (3) and swinging over the obstacle (3-5) to be placed to the ground firmly behind



(a) Lateral view on the purely kinematic motion sequence of HRP-2 N° 14 overstepping the obstacle

(b) Perspective view on the purely kinematic motion sequence of HRP-2 N° 14 overstepping the obstacle

Figure 8.3: Resulting motion sequence from the preliminary study to step over a given obstacle in from different viewing angles (Sequence frames: 1-16).

(6) the obstacle. The body starts moving ahead (5), travels over the obstacle (6-9) and approaches the static end posture (10-16). The other leg (in this case the left leg) is unloaded (7), lifts (8) and swings (9-12) to reach its end posture (13) behind the obstacle. The end posture (16) is not required to be symmetric in the legs to account for additional balancing motions.

3.1 Solution Scheme of the OCP

Optimization was carried out in a two subsequent steps. First the simulation setup was employed to compute a two step walking motion from static half-sitting posture. As soon as a feasible walking trajectory was found after a few iterations, the obstacle was included in the setup to optimize for maximum obstacle height.

3.2 Results

Optimization was conducted with - 1st criterion: height of obstacle - 2nd criterion: minimum end time - 3rd criterion: head stabilization, squared sum of first derivative of joint torque (weights have been adjusted accordingly). The selected obstacle for the proposed stepping motion is a simple cylinder with a radius of 5.5 cm (painted in red in Fig 8.3 and 8.4a) fixed in horizontal orientation perpendicular to the robot's forward direction. The initial position is fixed in orientation around the vertical axis and to zero lateral shift, with symmetric posture,

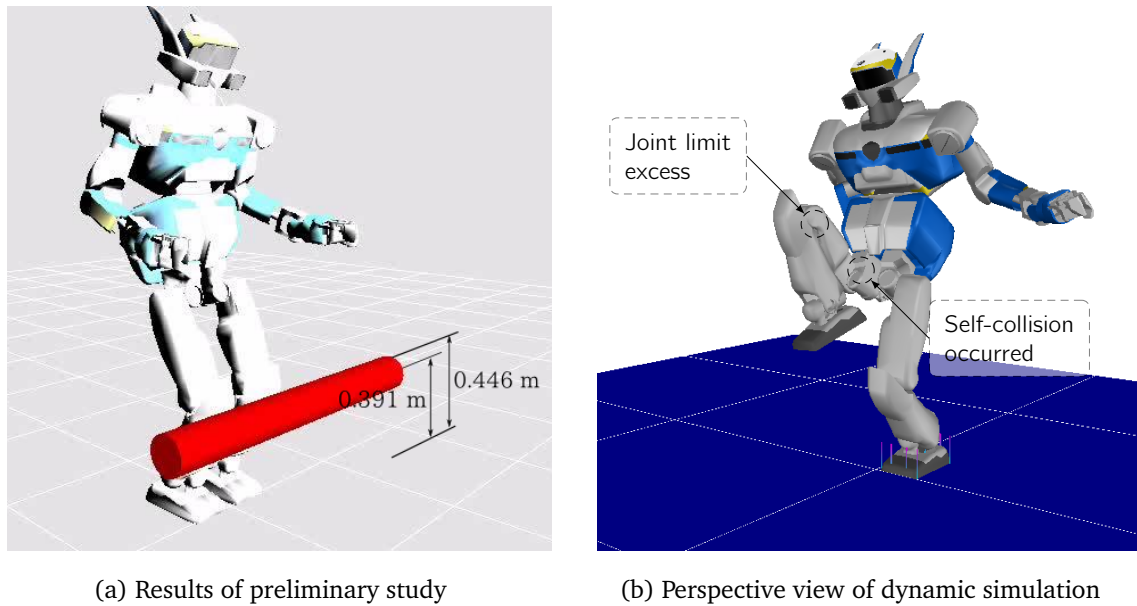


Figure 8.4: Snapshot and results from the preliminary study to dynamically overstep an obstacle. Problematic configurations are marked with dashed circles. The region the snapshot was taken from is shown in all subsequent plots with a pale blue area.

with zero joint velocities and accelerations. In the final posture the robot is forced to symmetric posture of the upper body links and the upper limb orientation with zero joint velocities and accelerations. Final foot placement was relaxed to give more flexibility to balance the final posture (refer to equation (8.6d)). The initial distance of the robot to the obstacle was chosen by optimization.

Distances between feet are measured between contact points of both feet respectively, located slightly inwards from the footfold center point, step length in forward direction, step width in orthogonal direction to the latter. From table 8.2 one may observe the phase duration chosen from the optimization. The flat time value occurred as result of the upper time limit that was accorded to the last phase in the OCP formulation (see Table 8.2).

The motion is performed in a grand total of 4.762s. The maximal recorded height

Table 8.2: Phase duration times

N	Contact-State	Duration	Description
0	DS	0.154s	From initial posture
1	SS	1.690s	Right foot swings
3	DS	0.125s	Traveling over obstacle
4	SS	1.792s	Left foot swings
6	DS	1.000s	..to final posture

successfully cleared was 0.446m and 0.391m measured from the center of the obstacle (see Figure 8.4a). The robot begins with a narrow feet arrangement of 0.157m in width and steps over the obstacle employing a step length of 0.584m to a slightly broadened step width of 0.177m (see Figure 8.5 on the next page). In the end posture the left foot is placed ahead compared to the right foot about 14.15mm. From the setup the feet are not constrained to

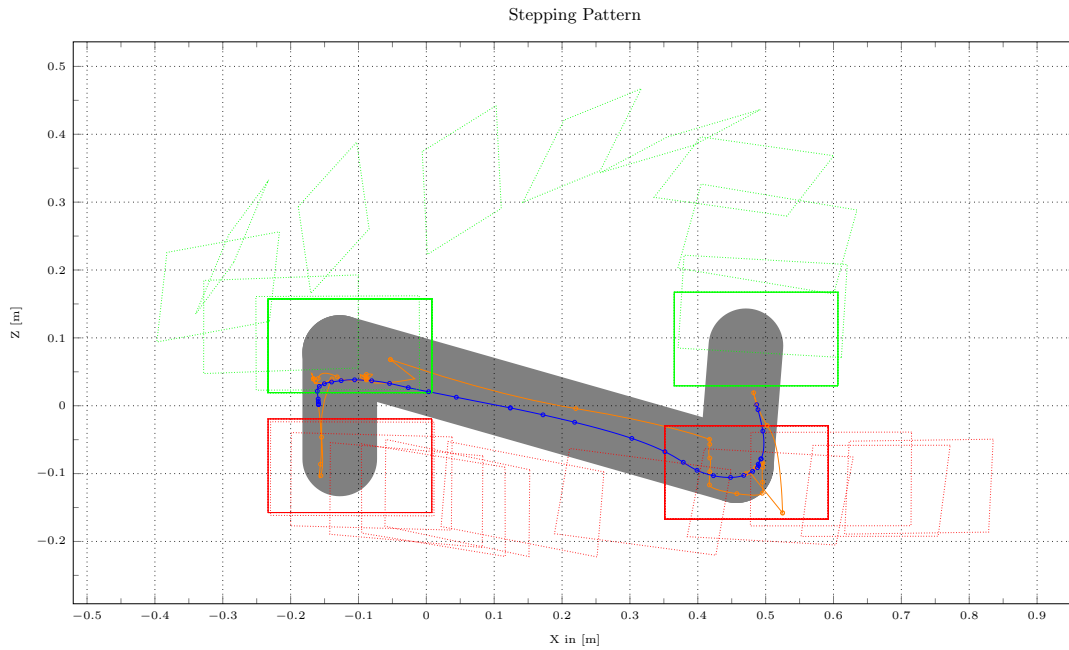


Figure 8.5: Stepping Pattern of the OCP result over the obstacle. Left and right foot are drawn in green and red, solid and dotted foot steps are drawn during ground contact and swing motion, respectively. The gray area is the accumulation of all convex support polygons of the complete motion. The CoM is drawn in blue and the ZMP in orange.

be placed in parallel. The overall motion appearance is given in Figure 8.3 on page 118 as a sequence of 16 single snapshots from different viewing angles.

From Figure 8.5 it is clearly observable that during the complex motion task the weighted CoP (blue solid line) stays with a small exception (numerical noise) at the final posture in the strict stability region (gray region) to be respected for a stable motion operation of the robot. Furthermore, this is confirmed from Figure 8.8 on page 123. During the DS(0) the weighted CoP shifts underneath the left foot it is then quickly transferred to the right foot during DS(3) before traveling back to a symmetric position during DS(6). Thus the CoM and weighted CoP trajectories are similar to those explained in [Stasse et al., 2009].

From Figure 8.3a one may observe the postural balancing strategy that was chosen during optimization. This strategy intensively employs the dynamic effects of the arm motions, swaying back and forth (Figure 8.3a on page 118 [2-8]) whilst over-stepping the obstacle and swaying to the right side and back (Figure 8.3a on page 118 [9-13]) during the left foot traveling to the final posture.

Furthermore, legs are inclined side-wards combined with a complex pelvis motion to clear the obstacle within the admissible kinematic ranges of the robot. In the leg structure most of the joints operate close to either upper or lower angular limits seldom reaching their velocity limits. Besides, the right knee joint features a critical mode of operation during SS(1). The joint trajectory reaches both upper and lower velocity and angular joint limits (observable on Figure 8.7 on page 122, 8.3a on page 118 [2-5] and in the snapshot 8.4b on the preceding page).

Despite small excess of joint limits, another issue was observed during visual verification (see Figure 8.4b on the previous page). Although joint limit excess did not occur for any joint of the right leg hip-complex, the latter features a considerable self-collision between the thigh and the cantilever-structure of the right hip structure.

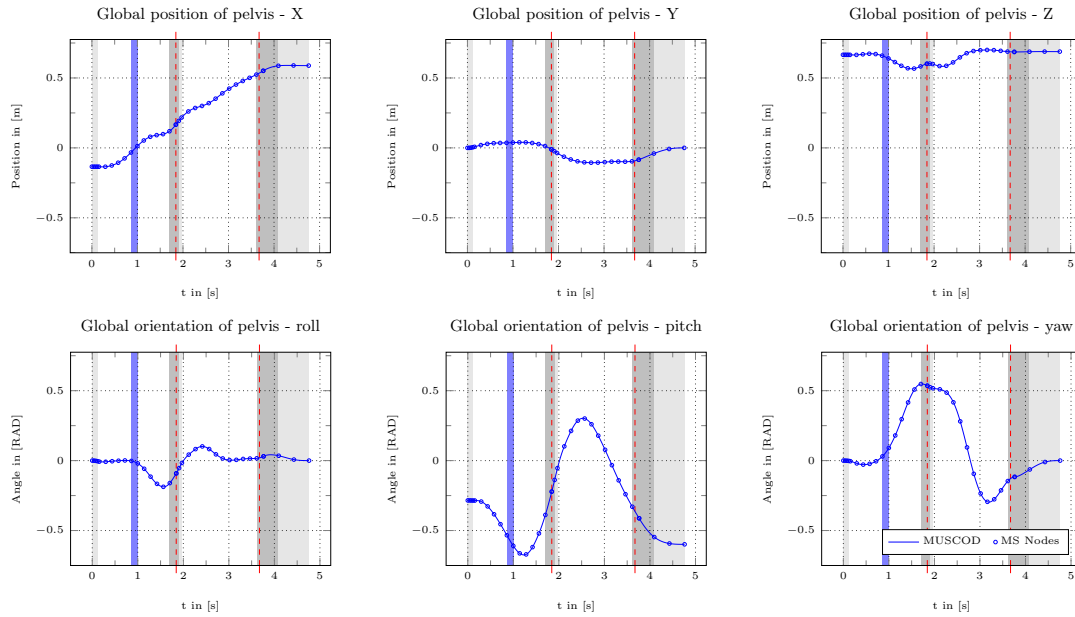


Figure 8.6: Global position and orientation of Pelvis. From this graph it is visible that the pelvis performs a complex 3D motion. Moreover, the altitude Z and all orientation angles show strong variations.

Finally, the head gaze remains stabilized globally during the whole motion (see Figure 8.3). As it is clearly observable from Figure 8.6, the pelvis features a vertical motion variation of approximately 0.14 m during the overstepping. More specifically, it drops from the initial posture to the lowest limit, regains its altitude to an intermediate peak before it reaches the final posture. Furthermore, the vertical orientation of the pelvis (see Figure 8.6) shows a variation of approximately 0.8 [RAD] while the variation of the pitch motion even reaches 1.0 [RAD]. Figure 8.3 on page 118 gives a clear look about this situation. At the beginning of the motion, the pelvis is pitched backwards to allow the right leg to travel over the obstacle. As soon as the body shifts across the obstacle, the yaw orientation of the pelvis reaches its peak to provide maximum space between the legs to avoid collision with the obstacle. As soon as the left leg is retired, the pelvis pitches forwards to allow the left leg's knee joint to raise over the obstacle. Finally, the vertical pelvis orientation reaches its inverse peak to give the left leg more space to unfold to the final posture.

3.3 Concluding Remarks

The maximum obstacle tip-height of 0.446 m (see Figure 8.4a on page 119), overstepped in 4.762 s that resulted from this preliminary study sounded interesting enough, such that a decision was made to invest further efforts into this direction. The resulting motion clearly shows the exploitation of the whole body dynamics, pelvis motion, arm swinging to maintain the dynamic balance while overstepping the obstacle. However, from the technical point of view, this result has some important problems, which will most likely prevent the implementation on the real robot:

- From Figure 8.4b on page 119, an important self-collision issue gets apparent. As stated in [Kaneko et al., 2004], the 3D cantilever type hip joint (see Figure 8.7 on the next page) shows the problematic of complex functional geometric features that may occlude the state space further beyond the specified joint limits when self-collision should not occur.

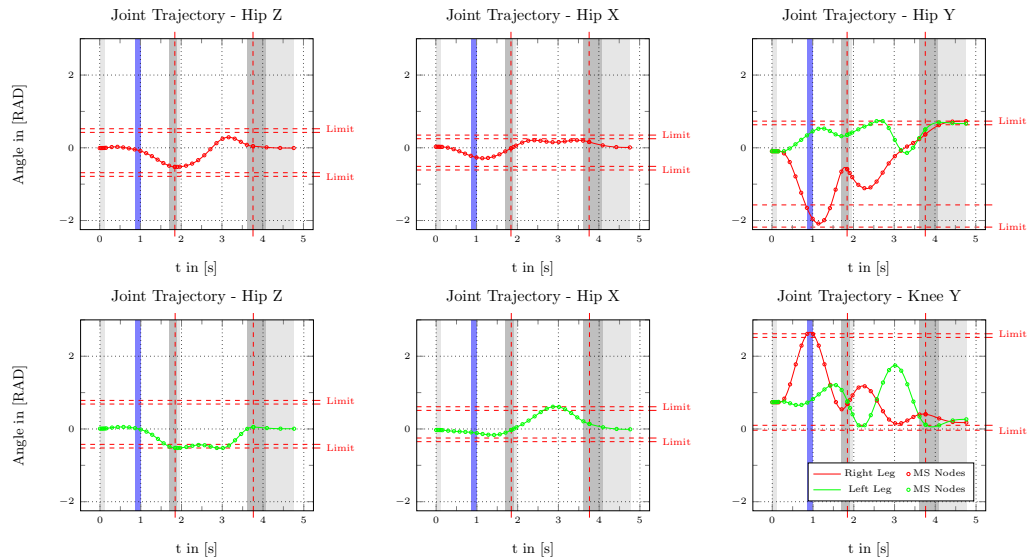


Figure 8.7: Joint trajectories of the 3D hip joint complex and the knee joint. Left and right joint trajectories have been drawn to distinct graphs in case the limits are symmetric. The rendered snapshot is shown with the pale blue mark. The outer dashed red lines represent the angular value ranges of the joints. The inner dashed lines mark a proposed security margin.

Consequently, additionally to the specified joint limits, non-linear constraints must be formulated to preserve the maximum possible flexibility of the joint complex around the occlusions that are produced by the complex functional geometry of the technical realization of the joint.

- Furthermore, Figure 8.4b on page 119 shows a control problem when it should come to a real implementation of the motion on the real robot. A well-known problem of position control (refer to Section 1 on page 230) are control deviations, especially when the control system must track a highly dynamic reference. Thus, highly dynamic motion reference trajectories that come close or exceed to the hardware angular value ranges of their respective joints, produce a considerable risk of the joint running into the hardware limits, causing considerable deterioration of the concerned actuation system, when this is not prevented with different security measures (in the case of HRP-2 N° 14). Hence, for all subsequent simulations reasonable conservative security margins on the angular value ranges must be formulated and enforced on the final solution to prevent reference trajectories coming close to the hardware limits (for a proposition see Figure 8.6 on the preceding page).
- It is observable from Figure 8.6 on the previous page performs a complex 3D motion in space. Compared the assumption of most heuristic based motion generation methods where the pelvis altitude is either fixed or follows a previously determined trajectory, the relaxation of this assumption with the given OCP formation may yield potential improvement on the final result.
- From the above motion sequence (see Figure 8.3 on page 118) the arm swinging seems to play an important role for the dynamic stabilization of the robot. In further studies this fact should be considered with great care to avoid self-collision during the final motion.

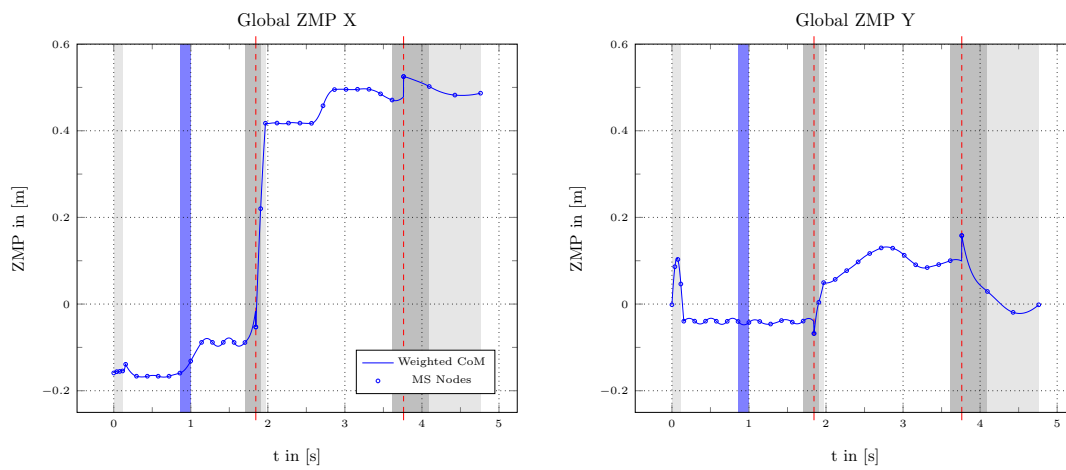


Figure 8.8: Trajectory of the weighted CoP over time. From this graph it is observable that the ZMP stays underneath the left foot until the right swing foot traveled over the obstacle, then rapidly travels to the right foot and stays there until the left foot reaches its final position.

9 A More Realistic Modeling Approach

So far - all previous studies have been conducted on the whole-body model with all related physical and dynamic constraints. The critical issues in the OCP formulation have been physical consistency and self-collision as well as excess of angular value ranges for some of the joints. However, some other crucial parts of the robotic platform, such as the control and stabilization system, external perturbations, mechanical elasticity in the kinematic structure have not been considered in a full extent. How these components will influence the final motion is indeed a tedious problem and the only possibility to actually find an answer is, to make successive tests in simulation and on the real robot - to see whether the previously made assumptions hold.

A scheme of the complete tool-chain is shown in figure 9.1. Although the tool-chain only

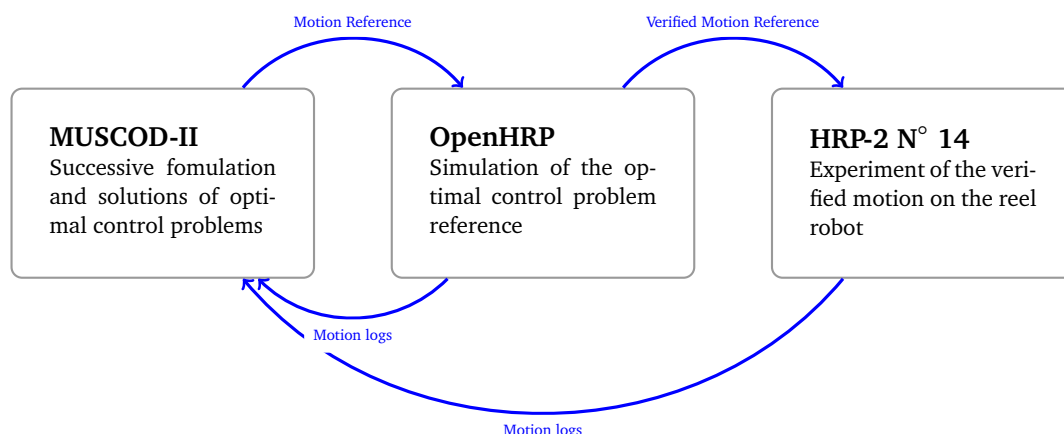


Figure 9.1: Schematics of the tool chain that has been intensively used to investigate the necessary limits and objectives that render an optimal control solution a practically feasible candidate for real motion performance. Result of an optimal control problem formulation usually undergo successive simulation trials and subsequent manipulations of the formulation until the virtual robot stably performs in simulation. This cycle is performed until all checks (e.g. joint limits, torque limits, self-collision, collision with the environment, dynamic stability etc.) are correctly verified and the motion reference is ready to be performed on the real robot. Feedback in form of the motion logs is used to appreciate potential problems in the formulation or to identify open parameters.

consist of a cascade of 3 blocks the cycle time for one iteration is considerably high which makes intensive and individual checking of essential motion features a relatively costly process. In the following the pursued strategy will be explained to minimize necessary iterations to explore the given tool-chain as quickly as possible.

1 Difference Between Reality and Modeling

Figure 9.2 on the facing page shows the dynamic simulation of the motion that has been computed during the preliminary study and confirms the assumptions from Section 3.3 that

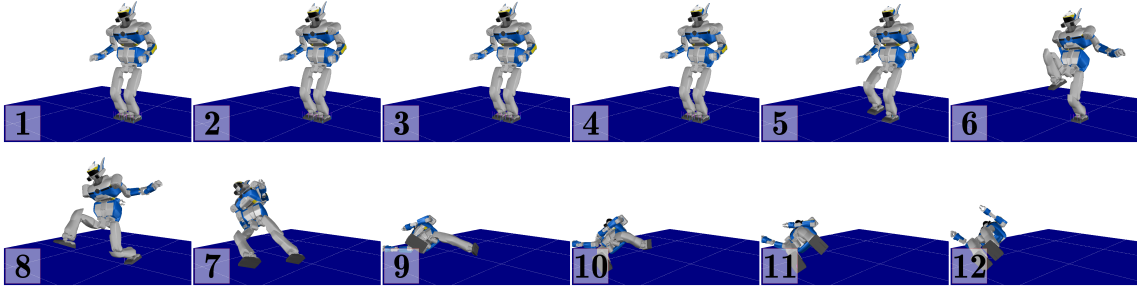


Figure 9.2: A challenging motion that is compatible with the obvious physical constraints of the robot completely fails in the OpenHRP [Nakaoka et al., 2007] motion simulator.

the motion in its present form can not be performed by the robotic platform HRP-2 N° 14. Despite the technical incompatibilities of the motion, another aspect that needs attention is the complex and heuristic control system built on top of an similarly complex kinematic structure. Thus the general problem that the robot suddenly loses balance is formed by multiple combined aspects, such as the dynamic characteristics of the passive elasticity in the ankle joint, the tracking error of the joint motion controllers and non-compatibility of the motion reference input with respect to the stabilizing algorithms.

The following chapters propose a complementary modeling discussion of the hardware elements of the robot that were not considered during the previous studies. Therefore, the next two studies will be tuned, such that the resulting motion of the OCP formulation works in concert with the hardware and control system of the real robot platform HRP-2 N° 14.

1.1 Ankle Elasticity Complex

In the following, the modeling of the robot will break with the suggestion in literature [Verrelst et al., 2006] that the robot with its stabilizing algorithms active, behaves as if the ankle elasticity would not be present (refer to Section 1.1). Based on this decision, three different variants of the modeling approach of the ankle-elasticity complex are discussed. Analysis of the third approach will not be discussed further, but is given for the sake of completeness, as future efforts are planned to expand the study at hand to the third case.

A mechanical modeling of the passive ankle elasticity of HRP-2 N° 14 is proposed in [Nakaoka et al., 2007]. They simplify the 3 point elastic joint complex into a linear elasticity system of three degrees of freedom (one linear vertical dof and two rotational horizontal dofs). The modeling is then constructed such that dynamical effects between the vertical linear component and the horizontal rotational components are decoupled. In equation,

$$\tau_{T_z} = k_{S,T_z} q_{T_z} - k_{D,T_z} \dot{q}_{T_z}, \quad (9.1a)$$

$$\begin{bmatrix} \tau_{R_x} \\ \tau_{R_y} \end{bmatrix} = -K_{S,R_x,R_y} \begin{bmatrix} q_{R_x} \\ q_{R_y} \end{bmatrix} - K_{D,R_x,R_y} \begin{bmatrix} \dot{q}_{R_x} \\ \dot{q}_{R_y} \end{bmatrix}, \quad (9.1b)$$

$\tau_{(\cdot)}$ represents the corresponding actuation of the set of minimal coordinates $q_{(\cdot)}$ (linear coordinates represent forces and rotational coordinates result in torques respectively). Spring k_{S,T_z} and damping k_{D,T_z} constants are scalars, while K_{S,R_x,R_y} and K_{D,R_x,R_y} are constant matrices. For numerical stability in simulation [Nakaoka et al., 2007] the modeling of the passive elasticity was further augmented with a small (compared to the rigid body inertia) abstract inertia term to suppress oscillation resulting from high spring constants during the forward integration process.

For optimal control computations a simplified two dof model as well as a complex but more realistic three dof modeling have been implemented. The ultimate goal was to first investigate the simplified model to gain sufficient numerical experience and then shift the analysis to the more complex model. However, the analysis of the simplified two dof elasticity model took a substantial effort, such that the more complex model was postponed beyond the scope of this work. A short explanation of its structure is given anyway for the sake of completeness.

Simple Elastic Model

From the analysis in [Kajita et al., 2001b] it is clear that for small variations on the vertical force component the center of pressure and hence the stability of the uni-lateral foot-ground contact mainly depends on the horizontal rotational contact reactions and consequently on the rotational deformation of the passive elasticity complex in the ankle. Hence, it was decided to adopt only equation (9.1b) in a slightly modified form to set up the modeling of the ankle elasticity,

$$\begin{bmatrix} \tau_{R_x} \\ \tau_{R_y} \end{bmatrix} = - \begin{bmatrix} k_{S,R_{xx}} & k_{S,R_{xy}} \\ k_{S,R_{yx}} & k_{S,R_{yy}} \end{bmatrix} \begin{bmatrix} q_{R_x} \\ q_{R_y} \end{bmatrix} - \begin{bmatrix} k_{D,R_{xx}} & k_{D,R_{xy}} \\ k_{D,R_{yx}} & k_{D,R_{yy}} \end{bmatrix} \begin{bmatrix} \dot{q}_{R_x} \\ \dot{q}_{R_y} \end{bmatrix} + \begin{bmatrix} O_{R_x} \\ O_{R_y} \end{bmatrix}. \quad (9.2)$$

In the following it is assumed that the elasticity and damping effects are linear and decoupled and that the elasticity is equal and symmetric on both ankles. The latter assumption was adopted for the sake of simplicity. Recent results about the model identification of the elasticity of HRP-2 N° 14 clarify [Mikami et al., 2014] that this assumption may turn out to be not sufficiently close to reality.

However, the two rotational axes may have correlated effects and an angular offset from zero may exist in the elasticity. The scalars $k_{S,R_{xx}}$, $k_{S,R_{xy}}$, $k_{S,R_{yx}}$ and $k_{S,R_{yy}}$ represent the linear spring constants and the scalars $k_{D,R_{xx}}$, $k_{D,R_{xy}}$, $k_{D,R_{yx}}$ and $k_{D,R_{yy}}$ the linear damping constants respectively. O_{R_x} and O_{R_y} introduce the angular offset from the neutral position into the model.

The proposed model adds 10 new parameters to the robot modeling that will need to be identified from simulation and real world experiments. As soon as sufficient knowledge about the simplified model parameters and adequate experiments of the numerical difficulties are available the ultimate goal would be to augment this simplified linear model to a more complex possibly non-linear model.

Complex Elastic Model

The following more complex modeling of the ankle elasticity is based on the assumption that the elasticity complex still follows the kinematics of the three dof structure (one vertical linear dof - two horizontal rotational dofs) but gives evidence to highly correlated possibly non-linear elasticity and damping effects. The modeling process starts directly from the three dispatched bushings - in the following called b_1 , b_2 and b_3 .

The elastic action and the corresponding damping are then retrieved from the individual bushing based on its dynamic deformation with an additional regularization. This regularization is necessary as the direction of the spring/damping action gets undefined in the neutral point and hence would create a singularity. Various different strategies are possible to prevent these singular configurations. The assumption adopted in this implementation is that the bushing is attached rigidly to the sensor mount and only exerts a vertical force on the underlying foot

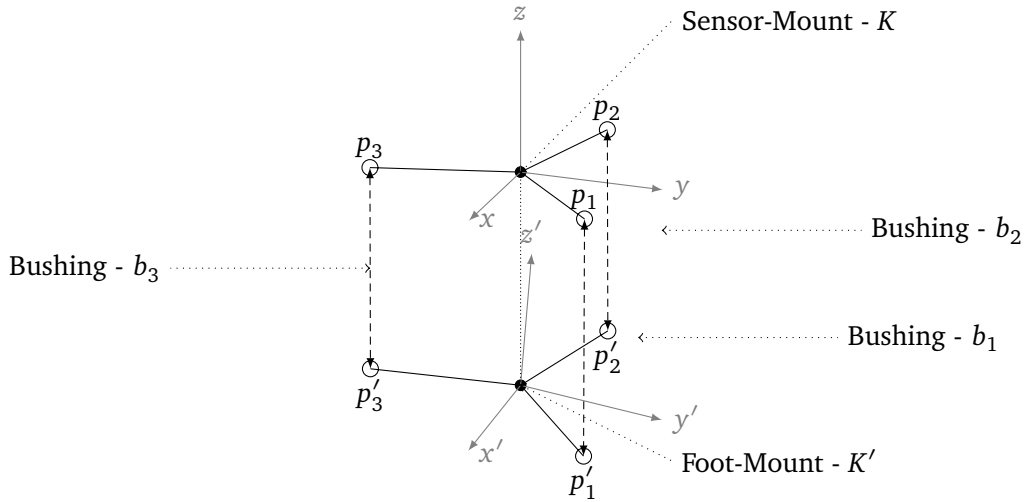


Figure 9.3: Scheme of the complex elasticity - in this scheme bushings are directly considered based on their local deformation. For better visibility the sensor mount (to the ankle joint complex) and the foot mount (to the foot plate) have been drawn pulled apart. The local coordinate system of the sensor mount is called K and that of the foot mount K' . The fixed global reference is called I .

plate. This will only be sufficiently accurate for small deformations - which should hold in most cases given the high rigidity of the rubber bushings. With this assumption this spring model may be conveniently expressed in 6D spatial algebra. In equation,

$$\begin{bmatrix} \tau_{S,T_z,i} \\ \tau_{S,R_x,i} \\ \tau_{S,R_y,i} \end{bmatrix} = \left(J_0^{K'} \right)^T K'_0 X_{K'_i}^* X_{K'_i}^{K'} X_{K'_i}^* \begin{bmatrix} 0 \\ 0 \\ 0 \\ 0 \\ 0 \\ -f_S \left({}^K H_I^I H_{K'} \mathbf{p}'_i - \mathbf{p}_i, l_{\text{off},i} \right) \end{bmatrix}, \quad (9.3a)$$

$$\begin{bmatrix} \tau_{D,T_z,i} \\ \tau_{D,R_x,i} \\ \tau_{D,R_y,i} \end{bmatrix} = \left(J_0^{K'} \right)^T K'_0 X_{K'_i}^* X_{K'_i}^{K'} X_{K'_i}^* \begin{bmatrix} 0 \\ 0 \\ 0 \\ 0 \\ 0 \\ -f_D \left({}^{K'}_{p'_i} X_{K'_i}^{K'} X_{K'_i}^{K'} J^{K'}_0 \dot{\mathbf{q}} \right) \end{bmatrix}, \quad (9.3b)$$

$$\begin{bmatrix} \tau_{T_z} \\ \tau_{R_x} \\ \tau_{R_y} \end{bmatrix} = \sum_{i=1}^3 \left(\begin{bmatrix} \tau_{S,T_z,i} \\ \tau_{S,R_x,i} \\ \tau_{S,R_y,i} \end{bmatrix} \right) + \sum_{i=1}^3 \left(\begin{bmatrix} \tau_{D,T_z,i} \\ \tau_{D,R_x,i} \\ \tau_{D,R_y,i} \end{bmatrix} \right), \quad (9.3c)$$

the elastic force depends on the vector between both connection points of the bushing (sensor mount - foot mount) and an additional length offset. The function can have non-linear elements. The purely vertical component in the system of the sensor mount K is then rotated into the system of the foot mount K' and shifted to the origin by the corresponding pluecker transformations. The 6D Jacobian then projects the 6D spatial force vector onto the generalized set of coordinates used for the modeling of the elasticity complex. Equation (9.3b) follows the same regularization strategy. Here the set of minimal coordinates of the elasticity complex is

projected into 6D spatial velocities in the origin of the foot mount transferred to the mount point of the corresponding bushing i and rotated into the system of the sensor mount. The purely vertical damping action is then computed from this vector - again the function may have as well non-linear elements. The complete elasticity action is then simply the sum of all bushings.

1.2 Control System & Stabilizing Algorithms

In Section 1.1 the high-gain position control system as well as the heuristics of the online stabilizing algorithms are thoroughly discussed. The unavoidable conclusion from this discussion is, that the weighted CoP, equivalent to the ZMP (under certain assumptions [Goswami, 1999] - compare Section 2.1 on page 87), follows from the individual CoP in each foot-ground surface contact. In that sense, controlling the CoP and *just enforcing some* physical consistent surface contacts, partially neglects the full complexity of the control problem. As suggested in Section 2.1 on page 87 for stability implications in the OCP formulation and from the explanation in [Goswami, 1999] it follows that, as soon as each individual CoP trajectory is controlled properly, the resulting ZMP will be equivalent to the weighted geometric sum of the individual CoPs and its trajectory will automatically reside in the support polygon for the robot to maintain its dynamic equilibrium. In the following it will be outlined that not the ZMP but controlling the local CoP trajectory with respect to the online control system is problematic.

Implications of the Control System

Furthermore, revisiting the cascaded control system of HRP-2 N° 14 (refer to Figure 6.3 on page 84 - the blue dashed circle marks the important control loop) control theory strongly suggests that the tuning of each individual control loop in a classic cascaded loop control system, such that, all of them work together in concert is difficult [Heimann et al., 2007]. As the parameters and the precise controller layout is not available it must be assumed that the control loops are not properly decoupled by a descending time constant and hence an aggressive tuning may lead to excessive oscillations of the output signal with respect to the input reference. It is important to note here that the input reference for the control system is the ZMP position however the ultimate output signals are the individual CoP trajectories that are equal to the input reference in single support and combine to the input signal in double support contact state. Thus, it is not always possible (double support contact state) to directly control the intermediate output signal.

Consequently, if one assumes excessive oscillations in the intermediate output signal around the reference signal, it is suggested to foresee a large security margin, such that the final output signal may oscillate but still remain inside the desired value range. Therefore all subsequent studies drop the constraint set that enforces the ZMP inside a given support polygon and reduce the contact feasibility constraint (position of the CoP with respect to the contact center point (6.1b) and (6.1c) to such a small region that a sufficiently security margin is left over for the control system to act inside the domain of physical consistency.

A final aspect should be added with respect to the internal geometric computations inside the control system. As experience suggests (refer to the discussion in Section 1.1 on page 83) the inverse kinematics implementation, which provides the relation between the foot contact points and the joint-angle based motion reference seems not to be singularity-free. Hence, as soon as the robot starts to tend towards kinematic configurations with stretched knees, oscillations around the reference trajectory and violent control actions are very likely to occur, as a situation that should be circumvented for a stable and dynamic motion operation.

Implications of the Sensory System

An integral part of the stabilizing control algorithms is the estimation of the upper torso orientation to appropriately control the pelvis orientation and the force/torque reference in the foot-ground contacts (refer to the previous section). Estimation of the orientation is done based on a classic Kalman-Filter. As it is known from [Sabatini, 2011] orientation-estimation may degrade with a dynamic motion of the body part where the IMU is located (upper torso for HRP-2 N° 14 - refer to Figure 6.1a on page 81). Consequently either the torso's or pelvis's angular motion needs to be reduced during motion performance.

A further particularity about HRP-2 N° 14 is, that the implementation of the Kalman-Filter that is in place seems to initialize inappropriately when the robot has an initial posture of the pelvis and upper torso that differ in roll and pitch orientation from the strict direction of the gravity vector. Hence, all subsequent OCP formulation will need to adopt suitable boundary constraints and path constraints, such that the Kalman-Filter implementation on the robot initializes properly and the orientation-estimation remains sufficiently accurate to support a proper operation of the the stabilizing control system.

1.3 The Correct Strategy

Unfortunately, above conclusions combined with the experiences collected during the previous studies, tend to create a high number unknown parameters in the system. Thus it is important to come in with a specific strategy to formulate the OCP that work well despite these unknown parameters and eventually provide complementary information to either construct assumptions or directly determine suitable values for these unknown system parameters. Figure 9.4 on the following page shows the strategy that was chosen and finally led to a successful and repeatable transfer of computed motions to the real robot platform.

This strategy exclusively employed a modified version of the OCP formulation from Chapter 8 and adopted the previously introduced FD and ID operator (refer to Chapter 5) to compute a high number of motion trials and test the results until a first stable motion performance was reached in the motion simulator OpenHRP. From that point on the scheme from Figure 9.4 on the next page was pursued.

The following study between FD and ID Op. was drawn from step (★) (see Figure 9.4 on the following page) and shows an intermediate solution of the stepping motion without obstacle to assess the characteristics of the local convergence of FD and ID Op. based OCP formulations for a complex systems such as the robot platform HRP-2 N° 14.

2 Comparison: FdOP & IdOP for HRP-2 N° 14

This section continues at some part the investigation about the numerical behavior of the FdOP compared to the IdOP that has been initialized in Chapter 5 and continuous a survey of the comparison on a more realistic, full-featured dynamic model of the HRP-2 N° 14 robot. Generally this analysis would be applicable to any given robot, as long as it comes along with a sufficiently accurate and well known dynamic model. As the focus of this investigation continues towards situation of potential under-actuation of an employed dynamic model with respect to its constraint configuration, a case study based on the humanoid robotic platform HRP-2 N° 14 [Kaneko et al., 2004] with a modeled passive elasticity in the ankle joint lends itself as a perfect example to achieve both. Finalization of the investigation on FdOP and IdOP based OCP formulations and further progress towards a real motion implementation on the real robot HRP-2 N° 14.

Hence, it is interesting to analyze whether the complex behavior of the model is accurately

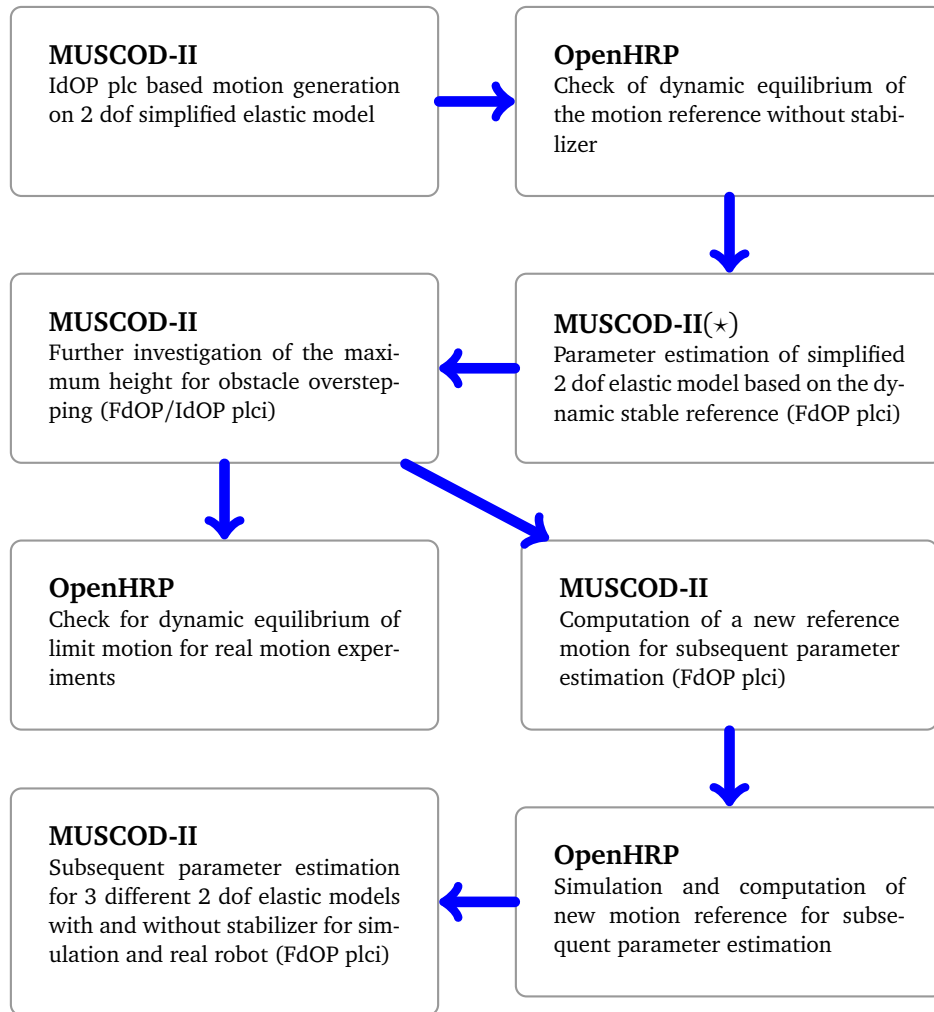


Figure 9.4: Computational scheme with lumped iterations that has been successfully used to investigate the necessary motion characteristics. The unknown system parameters have been determined to improve the OCP formulation for dynamically stable motion performance on the real robot.

reflected between both operators and agrees sufficiently well with the subsequent verification computed in the dynamic motion simulator OpenHRP.

The problem formulation recycles most of the components that have been used for the preliminary investigation to dynamically overcome obstacles (refer to Chapter 8) and improves the OCP incorporating the most recent conclusions and findings about the hardware and control system (refer to Section 1 on page 124). For the sake of completeness the problem structure follows below.

2.1 Problem Structure

The OCP formulation essentially adopts the same structure as employed in Chapter 8, (7.1a)-(7.1h) in Section 1 on page 93. However, assumptions on the hardware have been revisited, hence the dynamic model equation was altered to reflect these aspects (a brief discussion will follow below). The motion scheme is depicted in Figure 9.5. The OCP is formulated to cover a two step walking motion from a static initial posture towards a static final posture. After a

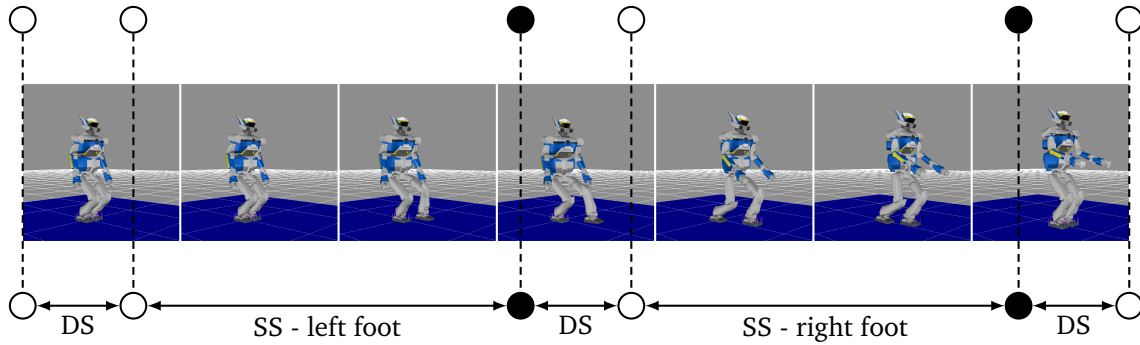


Figure 9.5: Problem structure of the stepping motion over the obstacle. The motion is simplified to 5 different contact states: double support *DS*, single support left foot *SS - left foot*, single support right foot *SS - right foot* and a final double support phase *DS*. Discontinuous phase transitions *CH* (foot ground collision) are marked with black dots while continuous phase transitions *TR* (foot lift-off) are marked with white dots.

Table 9.1: Model stage scheme, Multiple Shooting nodes and initial multiple shooting interval time per model stage

N	MS-Nodes	Time	Contact-State	Description
DS(0)	10	0.53s	Double Support	From initial posture
TR(1)	0	0.00s	Continuous Transition	Right foot lift-off
SS(2)	10	1.17s	Single Support	Right foot swings
CH(3)	1	0.00s	Foot-Ground Impact	Discontinues Transition
DS(4)	4	0.10s	Double Support	Traveling over obstacle
TR(5)	1	0.00s	Continuous Transition	Left foot lift-off
SS(6)	10	0.90s	Single Support	Left foot swings
CH(7)	1	0.00s	Foot-Ground Impact	Discontinues Transition
DS(8)	9	0.68s	Double Support	..to final posture
Σ	47	3.38s		

short DS phase, the left foot is raised and swings forward. After the ground collision and a short DS phase the right swing foot follows towards the final DS phase, to bring the robot to a complete stop. For this study, a pure stepping motion was analyzed. Based on these results and its conclusion, the obstacle will be added in the next section to confirm the efficiency of this approach.

The motion has 5 different contact states and hence features 5 distinct model stages as well as 4 model stage transitions. In contrast to the previous studies model stage durations have been adopted from previous trials and fixed to support a direct comparison between the FdOP and IdOP based results. Related to the discussion in Section 3.4 on page 72 the OCP formulation has been adjusted to the grid and initial guess configuration stated in Table 9.1. The additional TR featuring the model stage scheme have been added to comply with the requirements of the IdOP algorithms and allow for direct switch between FdOP and IdOP computations. Compared to the values in Table 8.1 on page 115, the adopted configuration was tuned for better accuracy to support the investigation. Both, FdOP and IdOP based OCP formulations have been constructed with plci control discretization.

2.2 Extension of the Dynamic Model

Following the discussion in Section 1 on page 124 the integration of the *simple elastic model* to represent the passive-dynamic elasticity of the ankle joint complex necessities a partial reconstruction of the dynamic model. The set of index-1 DAEs representing the equations of motions is stated below,

$$\dot{\mathbf{q}} = \mathbf{v}, \quad (9.4a)$$

$$\dot{\mathbf{v}} = \mathbf{a}, \quad (9.4b)$$

$$\begin{bmatrix} M & -J^T \\ J & 0 \end{bmatrix} \begin{bmatrix} \mathbf{a} \\ \boldsymbol{\lambda} \end{bmatrix} = \begin{bmatrix} -NLE - C + \boldsymbol{\tau} \\ -\gamma \end{bmatrix}. \quad (9.4c)$$

The compatibility between FdOP and IdOP is kept with a modification to the term of the nonlinear effects $NLE(q, \dot{q})$. Incorporation of the effects of passive-dynamic elasticity from (9.2) is performed as shown in,

$$NLE_{\text{elast}} = NLE_{\text{inelast}} + K_D \dot{\mathbf{q}} + K_P \mathbf{q}. \quad (9.5)$$

K_D and K_P are matrices that hold spring and damping constants for each of the degrees of freedom [Nakaoka et al., 2007].

2.3 Objectives

Following the discussion from Section 1 on page 124 the objective topology had to be rebuild, to support the reformulation of the model equations as well as the implications arising from the control system and the online stabilizing algorithms:

- | | |
|---|---|
| <ul style="list-style-type: none"> • Minimal Excitation of the Ankle Elasticity • Minimal Linear Vertical Momentum of CoM • Minimal Vertical Angular Momentum Change about CoM & Vertical Contact Shear Torque | <ul style="list-style-type: none"> • Minimal Deviation between whole-body (WB) ZMP and Table Cart (TB) ZMP • Head Stabilization • Minimum Joint Torque (τ) • Trajectory Smoothing |
|---|---|

The influence of all objectives is controlled by individual weights ω_{name} . These are adjusted such that some essential objectives are *dominant* over other objectives that appear *sub-dominant* to finally achieve the desired motion characteristics that comply at most with the requirements of the real HRP-2 N° 14 robot. From the preliminary study of Chapter 8 the objectives minimum joint torque (7.2) as well as the head stabilization (8.3) have been adopted. The newly introduced objective terms follow below:

Minimal Excitation of the Ankle Elasticity

At one hand, a distortion free signal transmission and good backdriveability of the controller is only guaranteed in a small range of low frequencies [Kajita et al., 2001b]. At the other hand, the proposed linear model of the ankle elasticity [Nakaoka et al., 2007] is only expected to give sufficiently accurate results in a small range around the neutral working point. Hence, the controller will only be able to follow smooth trajectories (low spectrum in the frequency domain) and the prediction will only be valuable at small angular ranges. This motion

characteristic is achieved with the objective formulation below,

$$\begin{aligned} \min \Phi_{\text{Elasticity}} &= \omega_{\text{Acc}} \sum_{i \in \text{Elast}} \ddot{q}_i^2 \\ &+ \omega_{\text{Vel}} \sum_{i \in \text{Elast}} \dot{q}_i^2 + \omega_{\text{Pos}} \sum_{i \in \text{Elast}} q_i^2. \end{aligned} \quad (9.6)$$

Minimal Linear Vertical Momentum of CoM

Apart from the proposed elasticity model [Nakaoka et al., 2007] where vertical linear excitations and horizontal rotational excitations are uncorrelated, it is likely that for highly dynamic motions this assumption may not be sufficiently accurate. As the vertical elasticity component has been discarded (similar to [Mikami et al., 2014]) during the modeling process, the resulting motion should contain the least possible perturbations in the vertical force component and hence a smooth vertical linear momentum trajectory with small variations should be produced,

$$\begin{aligned} \min \Phi_{\text{Linear Momentum}} &= \omega_{\text{LinMomZ}} \left(L_{\text{CoM}}^z \right)^2 \\ &+ \omega_{\partial \text{LinMomZ}} \left(\frac{\partial}{\partial t} L_{\text{CoM}}^z \right)^2. \end{aligned} \quad (9.7)$$

Minimal Vertical Angular Momentum Change about CoM & Vertical Contact Shear Torque

Dynamic linear and rotational motions of the upper body with respect to its feet are probable to result in a saturation of the transferable shear stress in the uni-lateral ground contact and most likely provoke slipping of the foot. Also, the risk of slipping, and hence an uncontrollable/undesired dynamic state of the robot, is even higher as soon as the center of pressure moves towards the boundaries of the support polygon.

$$\min \Phi_{\text{Angular Momentum}} = \omega_{\partial \text{AngMomZ}} \left(\frac{\partial}{\partial t} H_{\text{CoM}}^z \right)^2, \quad (9.8)$$

$$\min \Phi_{\text{Contact Torque}} = \omega_{\text{ContactZ}} \left(f_{\text{Contact foot}}^{mZ} \right)^2. \quad (9.9)$$

Minimal Deviation Between Whole Body ZMP and Table Cart ZMP

The difference between the whole body ZMP [Vukobratović and Stepanenko, 1972] and the 3D-LIPM [Kajita et al., 2003a, 2005], is the effect of the change of the horizontal components of the angular momentum about the CoM. This dynamic quantity may compensate for a part of the necessary horizontal contact torque upon variations of the acceleration of the CoM about the ground,

$$\min \Phi_{\text{ZMP - 3D-LIPM}} = \omega_{\text{ZMP}} \left| \text{ZMP}_{\text{whole body}}^{x,y} - \text{ZMP}_{\text{Table Cart}}^{x,y} \right|_2^2. \quad (9.10)$$

Alternatively, it is possible that the optimization tends to exploit this effect to improve the dynamics of the motion, but hence may fail to comply with potential assumptions about the heuristics inside the stabilizer [Kajita et al., 2007b]. This would risk in a highly unstable motion that should be avoided if possible.

Trajectory Smoothing Options

The problem formulation based on the FdOP gives access to the first derivative of the joint torques $\dot{\tau}$. This is exploited as stated in [Buschmann et al., 2007, Schultz and Mombaur, 2010] to further improve the motion-quality,

$$\min \Phi_{\text{diff. torque}} = \omega_{\text{torque}} \sum_{j=1}^{n_{\text{dof}}} (\dot{\tau}_j)^2. \quad (9.11)$$

This objective is similar to (8.4) from Section 2 on page 113, however, the implication with respect to the employed operator does change. Thus the criteria is formulated again for the sake of clarity. Similarly, the problem formulation based on the IdOP gives access to the abstract jerk \dot{u} (compare to Section 2 on page 59),

$$\min \Phi_{\text{jerk}} = \omega_{\text{jerk}} \sum_{j=1}^{30} (\dot{u}_j)^2. \quad (9.12)$$

2.4 Path Constraints

Despite the common constraint set that is adopted from previous studies, such as uni-lateral contact condition, foot clearance and self-collision for selected collision pairs (refer to Section 1.4 on page 98), the following additional modifications have been performed:

Restriction of the Physical Consistency

The area in which the CoP may move during the foot-ground contact state (6.1b) and (6.1c) is reduced to a small squared patch of 2cm width to support a large security margin for the control system to act during operation.

Maximum CoM Height

A further implication of the control system is (see Section 1 on page 124) that the generated motion should not feature kinematic configuration with knee joint positions close to an extended leg. At one hand these configurations are avoided with a further introduction of a box constraint on the system state trajectories for both knee joints. At the other hand this situation was easily circumvented through the introduction of a maximum height above ground constraint on the CoM of the robot. In most cases this constraint was observed to be only active during the first few iterations when a continuous stepping motion was evolving. In subsequent iterations the CoM altitude usually never reached this altitude again and thus the constraint remained inactive,

$$\overline{h_{\text{CoM}}} - h_{\text{CoM}}(q) \geq 0. \quad (9.13a)$$

Pelvis Stabilization

Following the discussion from Section 1 on page 124 that the stabilizing control system actively controls the orientation of the pelvis with respect to the estimation of the orientation of the upper torso unit, a decision was made to replace the orientation stabilization of the torso in the preliminary study from Chapter 8 with a stabilization of the pelvis about roll and pitch orientation. The valid motion range for both angles was fixed to $(-0.005, +0.005)$ [RAD].

The quantity $(an)_{(\cdot)}$ represents the orientation angle about (\cdot) .

$$\overline{(an)_{\text{pelvis pitch}}} - (an)_{\text{pelvis pitch}}(q) \geq 0 \quad (9.13b)$$

$$\overline{(an)_{\text{pelvis roll}}} - (an)_{\text{pelvis roll}}(q) \geq 0 \quad (9.13c)$$

$$(an)_{\text{pelvis pitch}}(q) - \overline{(an)_{\text{pelvis pitch}}} \geq 0 \quad (9.13d)$$

$$(an)_{\text{pelvis roll}}(q) - \overline{(an)_{\text{pelvis roll}}} \geq 0 \quad (9.13e)$$

2.5 Boundary Constraints

The consistency constraints (7.10a) and (7.10b) have been adopted from the walking study (see Section 1 on page 93). The implicit phase switching scheme with zero collision-impact (8.6a) and the boundary constraint on the initial and final static posture (8.6d), (8.6b) and (8.6c) with singularity resolution of the kinematic loop of the DS contact state have been adopted from the previous overstepping study (see Section 2 on page 113). Additionally, the following boundary constraints have been added:

Vertical Pelvis and Torso for Initial Posture

For a stable motion performance of the robot the proper initialization of the Kalman-Filter based estimation of the orientation is highly important. As suggested in Section 1 on page 124, the robot must start in the suitable configuration such that the initialization succeeds and the estimation may proceed to provide the pelvis orientation with good accuracy to the stabilizing control system,

$$(an)_{\text{pelvis pitch}}(q) = 0, \quad (9.14a)$$

$$(an)_{\text{pelvis roll}}(q) = 0, \quad (9.14b)$$

$$(an)_{\text{torso pitch}}(q) = 0, \quad (9.14c)$$

$$(an)_{\text{torso roll}}(q) = 0. \quad (9.14d)$$

Static - Initial & Final Posture of the Passive Elasticity

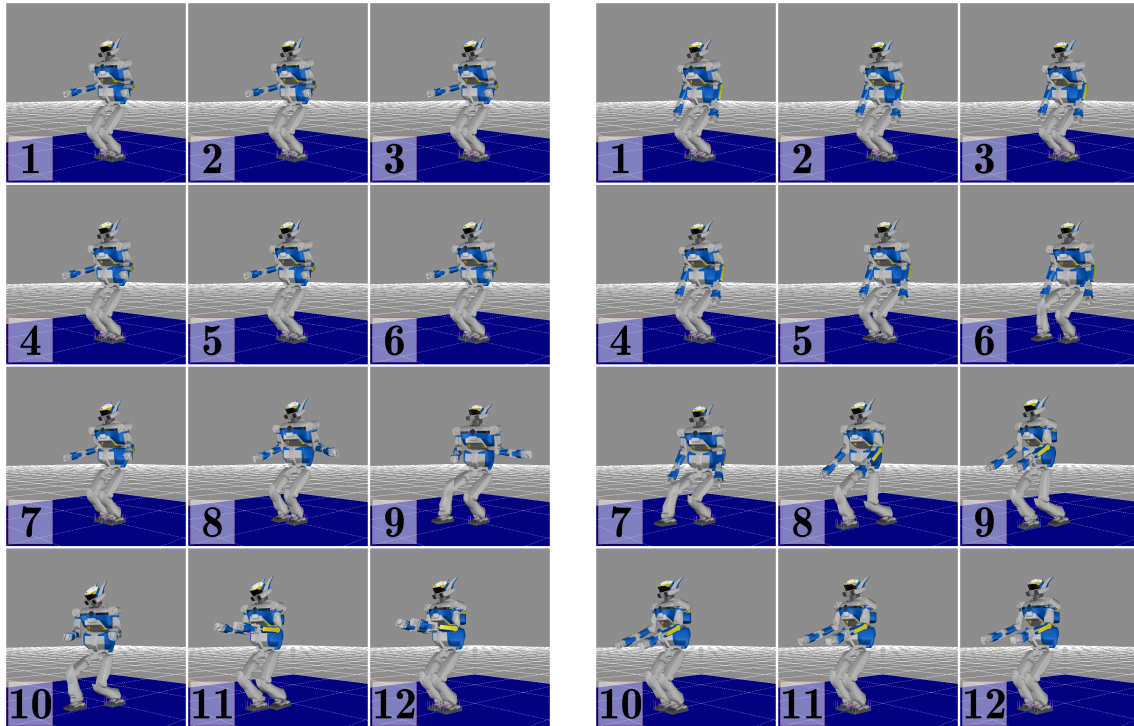
In addition to the static posture (refer to Section 2.1 on page 114) the motion is constraint to initialize with a static passive-dynamic elasticity (at best in its equilibrium position) and re-stabilize the robot towards a static posture with respect to the passive-dynamic elasticity. Again, the constraint sets (8.6b) and (8.6c) must be carefully adjusted to avoid redundancy with the consistency constraints of the set of index-1 DAEs over the kinematic loop with the ground contact of both feet,

$$\left. \begin{array}{l} S_{\text{elast},\dot{q}} \dot{\mathbf{q}}(t=0) \\ S_{\text{elast},\dot{q}} \dot{\mathbf{q}}(t=T) \end{array} \right\} = 0, \quad (9.14e)$$

$$\left. \begin{array}{l} S_{\text{elast},\ddot{q}} \ddot{\mathbf{q}}(t=0) \\ S_{\text{elast},\ddot{q}} \ddot{\mathbf{q}}(t=T) \end{array} \right\} = 0. \quad (9.14f)$$

2.6 Optimization Based on FdOP and IdOP

The characteristics of the direct multiple shooting approach (see Chapter 4 for details) are exploited in the following. The optimization is initialized without any information about the



(a) Image sequence of the dynamically stable forward dynamics based motion solution in the OpenHRP [Nakaoka et al., 2007] motion simulator.

(b) Image sequence of the dynamically stable inverse dynamics based motion solution in the OpenHRP [Nakaoka et al., 2007] motion simulator.

Figure 9.6: Comparison of the resulting motion trajectory profiles for the forward and inverse dynamics solution operator.

final motion, (fixed, common half-sitting position of HRP-2 N° 14 [Kaneko et al., 2004]) employing the fact that the initial state trajectories do not need to be continuously defined over the whole time horizon. Motion generation is then conducted employing two different optimization stages. First, the problem formulation is set up with highly relaxed path constraints to find a continuously defined stepping motion over the whole time horizon (refer to Chapter 4). Second, constraint-relaxation is reduced to force the desired motion characteristics and the setup is brought to convergence. In the following, solutions of the forward and inverse operators are presented and different aspects of problem formulations are discussed. The optimization is initialized with the fixed half-sitting posture of the robot. Motion generation is then applied in two steps: A fixed number of SQP iterations with relaxed path constraints are carried out to generate a continuous motion reference. From this motion reference, the relaxation of the path-constraints is reduced until convergence of the original OCP is observed.

3 Results

Table 9.2 on the next page shows the most significant computational characteristics of the FD and ID based problem formulation. From an identical overall problem size, in the identified local minima, the ID based problem formulation tends to use less function evaluations and integration steps than the FD based one. Given the large problem size, the homotopy to

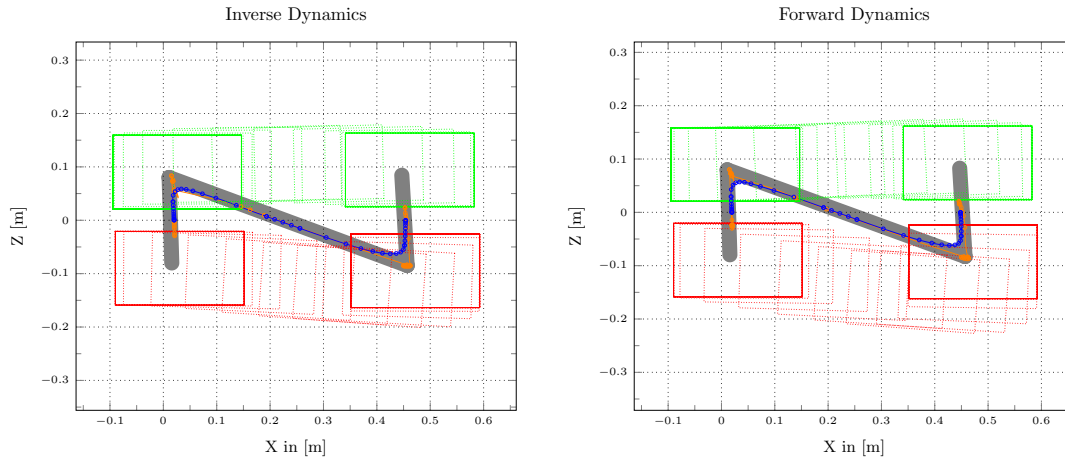


Figure 9.7: Stepping patterns of both feet for the reference solutions. The feet are represented with projection on the ground floor (green - left foot, red - right foot). The support foot patterns are drawn solid, swing foot patterns with a dotted line. The whole-body ZMP-trajectory profile is drawn in orange and the CoM trajectory profile in blue. The restricted support polygon in which the ZMP trajectory profile needs to stay at all time is drawn in gray.

Table 9.2: Problem size, number of function evaluations around the local minimum of convergence of the HRP-2 N° 14 motion generation problem formulation, for the forward and inverse dynamics operator.

	Forward Dynamics (FdOP)	Inverse Dynamics (IdOP)
Discretization	$\dot{\tau}$	\ddot{q}
Hessian-Matrix	BFGS	BFGS
Dimension	8147	8147
Constraint dimension	24419	24419
Function Evaluations	445587	471907
Int. Steps	2980	3104

identify the local minimum is relatively complex and hence does not lend itself to a direct comparison. Generally, for the ID formulation the OCP solver tends to identify the local minimum in a smaller number of SQP iterations than for the FD formulation.

Comparison of General Motion Appearance

Small differences in the appearance of the FD and ID based motion can be observed in Figure 9.6a on the facing page and 9.6b on the preceding page. The fixed time horizon for the stepping motion is 3.38s. The foot placement is observable from Figure 9.7). Both motions references perform stable (with minor manipulations of the stabilizing algorithms, compare Figure 9.11 on page 141) in the motion simulation OpenHRP and were successfully cleared for execution on the real platform.

In the motion resulting from the FdOP. one may observe clearly the whole body balancing strategy that is employed. The arms are swinging side-wards to the left to balance the robot towards the end of the single support phase of the left leg. The arms then move forward again to bring the robot to a complete stop at the end of the motion. Furthermore, a very signifi-

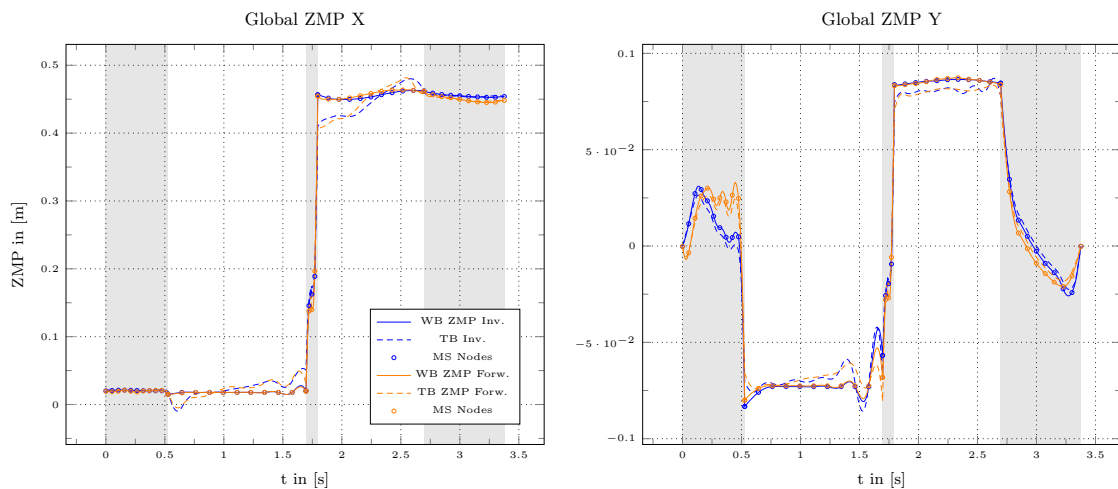


Figure 9.8: Global trajectory of the WB-ZMP (solid line) and the TB-ZMP (dashed line) of the both, the inverse and forward dynamics based motion solution on the ground floor plane (XZ). For a clearer view on the solution the multiple shooting nodes of the inverse and forward dynamics based optimization results are given.

cant head swaying is observable during the complete stepping motion (refer to Figure 9.6a on page 136).

In contrast to the FD based motion, the initial pose features only slightly bent arms in the ID case, but during the end-phase of the left foot SS, the arm perform a side-wards motion to the keep the dynamic balance of the robot. Finally, the elbow is bent to bring the robot to a complete stop in the static end posture (refer to Figure 9.6b).

Comparison of Discretization-based Characteristics

Figure 9.10 on page 140 shows the vertical component of the GCR profiles from the optimization based solution and the results from the OpenHRP simulator. In contrast to the inverse pendulum model (Section 3 on page 66), the resulting full 6D contact reactions are much more complex. Apart from minor timing issues in the phase transitions, the off-line optimal control solution and the replayed simulation of the virtual robot including its control and stabilizing algorithms in OpenHRP are in good agreement.

A closer comparison of the optimal solutions obtained using both operators (Figure 9.9 on the next page) shows better agreement during the SS phases (white background) than during the DS phases (gray background). Besides the influence of the slightly different trajectory profiles, this deviation is attributed to the kinematic loop that forces the chosen regulation strategy in the ID operator to project from the remaining free acceleration to the full set of dual variables. Here, these are the joint torques and the GCR forces. In the ID case these are more prone to noise than in the FD case. In contrast to the ID, in the FD case, the OCP has access to the full set of joint torques to be projected to the accelerations and the dual variables. Therefore, high peaks are observed in the blue curve in all graphs of Figure 9.9 on the facing page).

From Figure 9.9 on the next page it is directly observable that the deviations in the ZMP trajectory profile (refer to Figure 9.8) between forward and inverse dynamics are further support by the form of the trajectory profiles of these components. The force components on the ground (F_x & F_y) as well as the vertical torque component (M_z) show a good agreement during the SS phases. However, during the DS phases the kinematic loop in the system clearly shows a deviation between the forward and inverse dynamics based solution. These components

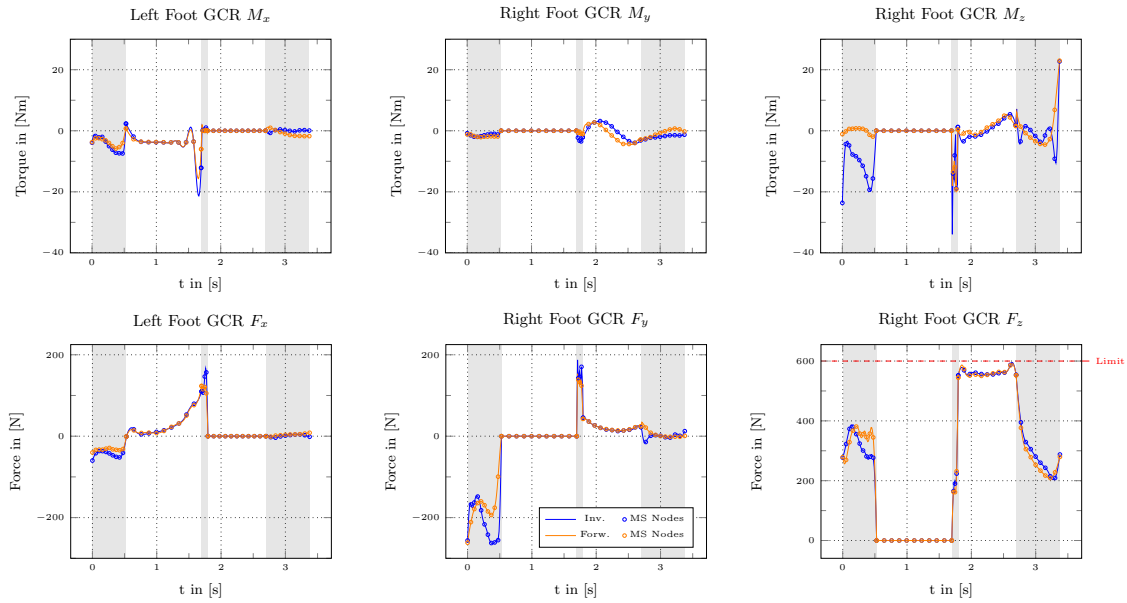


Figure 9.9: A selection of interesting GCR of left and right foot for the inverse and forward dynamics solution are shown above. The torque components in X, Y (M_x & M_y) and the vertical component (F_z) are directly related to the center of pressure and determine an equivalent form of the Zero Moment Point [Vukobratović and Stepanenko, 1972] (dynamic stability of the robot).

determine the friction stress situation in the unilateral foot-ground contact which may lead to slipping of the robot during motion when it is not carefully considered. The red dashed line represents the limit force that is permanently supported by the robots foot structure, however peak forces during ground collision may slightly exceed this limit without deteriorating the kinematic structure and sensors.

Besides smaller offsets in Figure 9.10 on the next page shows good agreement between the optimal control solution of forward and inverse dynamics and the OpenHRP Simulation. There are however small timing differences in the transition between single to DS and vice versa. From Figure 9.8 on the facing page the difference between both profiles (whole body and table cart) ZMP is small, despite the motion from the initial static posture. Near the transition point, oscillation of the table cart ZMP around the ZMP trajectory are clearly visible.

Discussion

While differences exist, both problem formulations lead to dynamically stable motion performances and agree reasonably well with trajectories computed by the OpenHRP simulator. Hence, it is concluded that both solution operators produce physically consistent motions and approximate the passive elastic characteristics of the robot’s ankle complex with satisfactory quality. However, convergence to different local minima of the optimal control problem occurred.

From the comparison of the results it can be observed that the FD and the ID operator perform with different quality with respect to resolving kinematic loops. Deviation of the trajectory profiles of both solutions in the DS case are clearly visible. From the algorithmic point of view, the results of the FD are re-identified by the ID operator with good accuracy. With respect to the ID formulation, a kinematic loop always constructs analytic dependencies between some of the acceleration controls and hence restricts the free parameter space to a smaller subspace

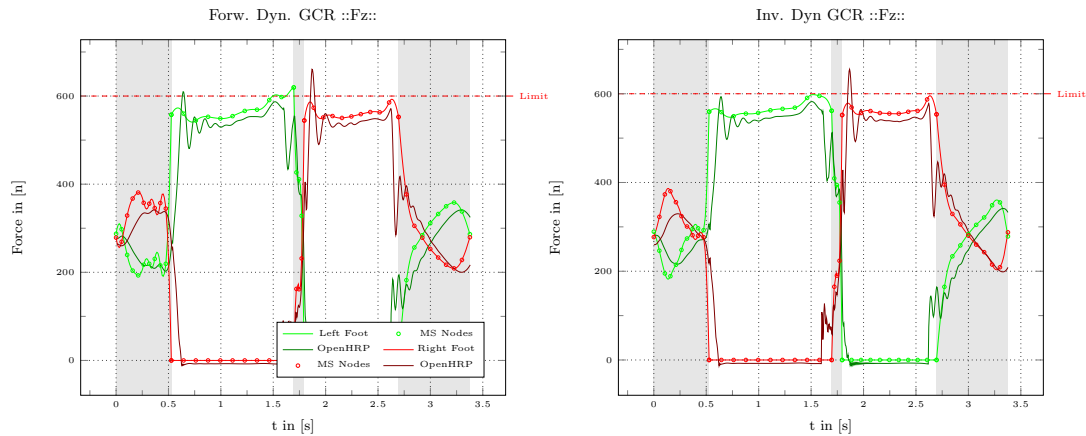


Figure 9.10: The left graph shows the vertical force component of the GCR of the forward dynamics based solution and the right graph those of the inverse dynamics based solution respectively. The left foot profile is drawn in pale green and the right foot in pale red. The forward dynamics based simulation of OpenHRP [Nakaoka et al., 2007] is drawn in the corresponding dark color.

from which the optimization algorithm can choose an optimal trajectory.

Apart from the comparison between FdOP and IdOP based solutions, Figure 9.11 reveals some important aspects. For both generated motions, the stabilized reference (dark - dashed line) and the performed motion (pale - solid line) only feature small deviations from the OCP based motion result.

3.1 Concluding Remarks

Although the operators converged towards different local minima, the above study supports the switching between both operators for rapid testing cycles of OCP based motion generation and verification inside the OpenHRP simulator. With respect to kinematic loops, the FdOP seems to give more flexibility to the Optimization-Solver to influence the final motion results inside the kinematic loop. Hence, the quick but inaccurate trial cycles at the beginning of the computation sequence in Figure 9.4 on page 130 have been conducted based on the IdOP whilst the more accurate computations (e.g. estimation of model parameters) have been based on the FdOP.

The results support as well the conclusion that the re-formulation of the OCP rendered the motion result more realistic with respect to the requirements of the hardware and the online control-system. This conclusion is further supported by the small deviations of the performed motion of the robot with the online stabilizing control system active in the OpenHRP motion-simulator. A desirable direction of investigation would be to further improve on this aspect.

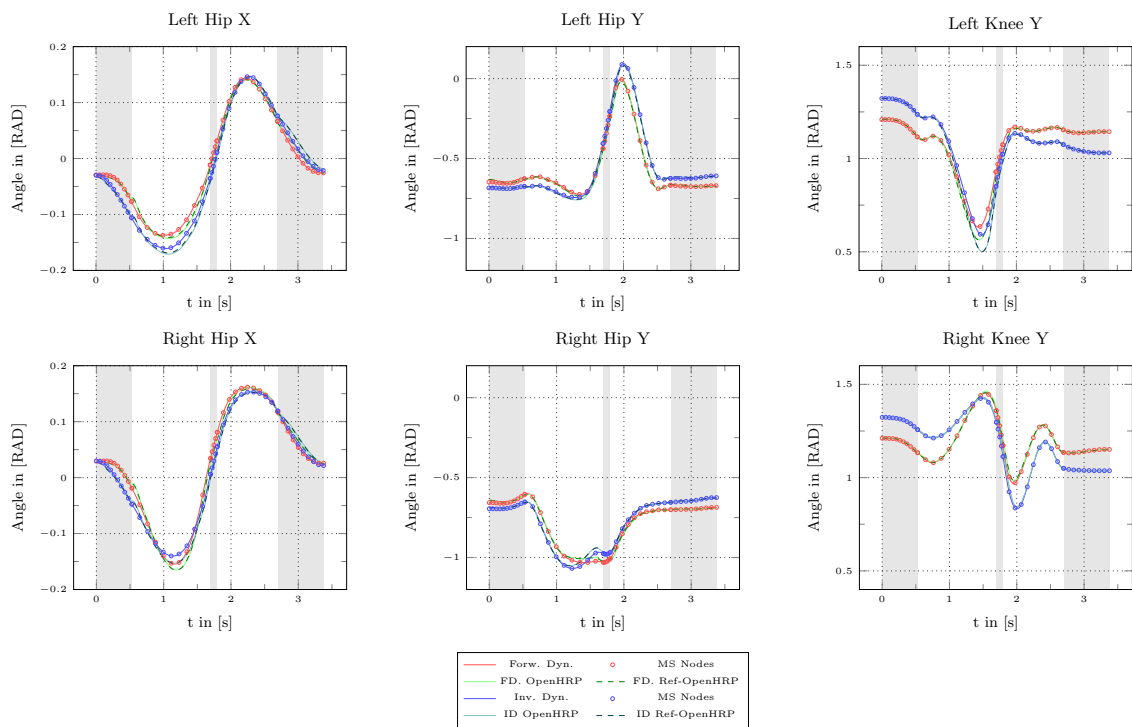


Figure 9.11: The graph on the left and right side show the horizontal rotational components of the hip joint complex and the knee joint for the forward and inverse dynamics based solution respectively. In the graph left and right joint complex are drawn in green and red colors respectively. The pale color is the optimal control motion solution including the positions of the multiple shooting nodes. The dark color shows the solution of the OpenHRP-Simulation. The dashed line represents the reference signal that is computed from the stabilizing algorithms and the solid line the output of the virtual joint encoders.

10 Implementation on the Real HRP-2 N° 14

The ultimate goal of this investigation was to determine the essential requirements upon which a robust transfer of motion results from the off-line OCP based motion generation towards the real robot is possible. Due to the fact that the dynamic limits to qualify a motion for the real robot HRP-2 N° 14 are relatively strict and the robot does not tolerate breach of its limitations, the major part of the investigations has to be conducted off-line. Additionally, the dynamic behavior of the robot in simulation inside OpenHRP and the real robot HRP-2 N° 14 substantially differs, such that is not always clear, whether a challenging motion that performs well inside OpenHRP, performs correctly on the real robot HRP-2 N° 14.

In the following, the experience from all previously conducted simulations will be combined to determine a selection of objectives to generate an OCP based dynamic challenging motion that performs reasonably well inside the motion simulator OpenHRP and on the real robot HRP-2 N° 14. Furthermore, the formulation of the OCP is based on a closer identification of the ankle elasticity model (compare Section 1.1 on page 125). However, details of this identification are outside the scope of this work. Measurements of the stable motion performance in simulation and on the real robot are analyzed to determine potential improvements to the OCP formulation this study was based on.

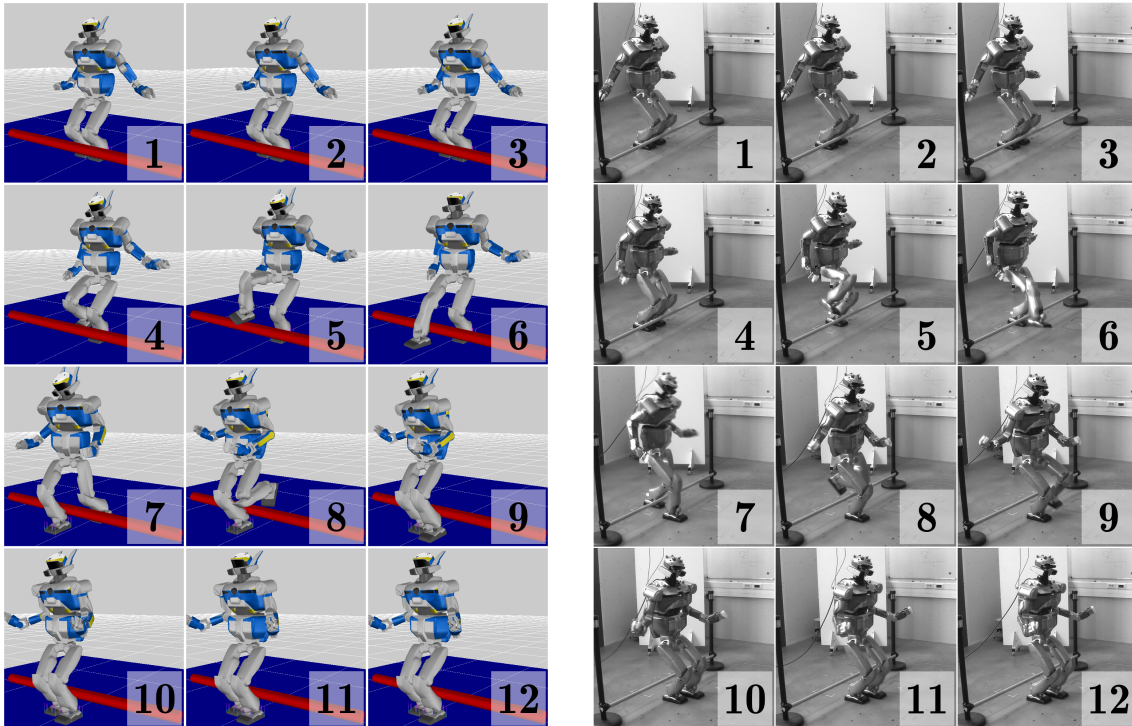
1 General Idea & Realization

The advantage of OCP based motion generation is the formulation of abstract objectives to flexibly control all characteristics of the generated motion. Given the situation that the robot must perform a motion in stable operation - which abstract motion criteria may be formulated to maintain the motion characteristics, despite investigations of its dynamic limits? - A strategy that is implemented in this section is to minimize the controller action for example: In case one would like to push the robot to its dynamic limits, the stress on the related control system should be small. In consequence a candidate solution should be computed such that particularly the control action of the stabilizer is minimal. In this respect, the control system should be able to operate safely, despite perturbations, originating from model deficiencies and the external environment.

Interestingly it turns out that this goal can be directly achieved with the previously employed set of objectives (refer to Chapter 9 on page 124). While the objectives (9.7) and (9.8) keep the motion characteristics inside the domain where the previously made model assumptions are confirmed to be valid, the objectives (9.10) and (9.6) tend to minimize the stress on the online stabilizing control system. Similar results were already observed in the previously presented study (refer to Chapter 9 on page 124). The conclusion from Section 3.1 on page 140 directly leads towards the necessary modifications of the OCP formulation.

1.1 Problem Structure

The employed problem formulation was adopted from Chapter 9 on page 124 with small modifications. The model stage scheme with the chosen multiple shooting grid is given in Table 10.1 on page 144 (the final motion sequence is depicted in Figure 10.1). The motion initiates from a static posture towards unloading the right foot (1-3, highlighted in gray). The



(a) Image sequence of the dynamically stable motion performance to clear an obstacle of 20 [cm] tip-height in the motion simulation of OpenHRP.

(b) Image sequence of the dynamically stable motion performance to clear an obstacle of 20 [cm] tip-height in real experiments.

Figure 10.1: Image sequence of the motion successfully clear an obstacle of 20 [cm] maximum height in simulation and real experiments

right foot lifts off and travels over the obstacle (4-6). Following the ground impact of the right foot, a short DS phase (highlighted in gray) is used to transfer the body support on the right leg and unload the left foot (6-7). Then the left foot lifts off and travels over the obstacle (7-9). After ground impact of the left foot, the robot enters a re-stabilization phase that ends in a static posture (10-12, highlighted in gray).

The shooting grid was found to be sufficiently accurate to support the desired investigation. The OCP was then formulated based on the **FdOp!** (**FdOp!**) with plci control discretization.

1.2 Objectives

While the set of objectives strictly remained the same with respect to the previous analysis in Chapter 9 on page 124, the weighting of the individual objectives were modified to produce a minimal control action of the stabilizing algorithms.

1.3 Constraints Sets

Similar to the objectives the constraint set was adopted with small modifications towards even stricter constraint configurations,

Table 10.1: Model stage scheme, Multiple Shooting nodes and initial multiple shooting interval time per model stage

N	MS-Nodes	Time	Contact-State	Description
DS(0)	10	0.63s	Double Support	From initial posture
TR(1)	0	0.00s	Continuous Transition	Right foot lift-off
SS(2)	10	1.38s	Single Support	Right foot swings
CH(3)	1	0.00s	Foot-ground Impact	Discontinues Transition
DS(4)	4	0.10s	Double Support	Traveling over obstacle
TR(5)	1	0.00s	Continuous Transition	Left foot lift-off
SS(6)	10	1.33s	Single Support	Left foot swings
CH(7)	1	0.00s	Foot-ground Impact	Discontinues Transition
DS(8)	9	0.94s	Double Support	..to final posture
Σ	47	4.38s		

Path Constraints

The path constraints directly employed the uni-lateral contact condition, foot clearance and self-collision for selected collision pairs, including couples between the robotic limbs and the obstacle (refer to Section 1.4 on page 98). Furthermore, the maximum CoM altitude constraint 9.13a on page 134 and the pelvis stabilization in orientation (9.13b) - (9.13e) where adopted from Chapter 9 on page 124.

The contact feasibility constraint (6.1b) and (6.1c) was further reduced to a squared patch of 1cm width.

Boundary Constraints

The adopted set consisted of the consistency constraints (7.10a) and (7.10b), the implicit phase switching scheme with zero collision-impact (8.6a), the initial torso and pelvis orientation towards the gravity vector (9.14a) - (9.14d), the boundary constraint on the initial and final static posture (8.6d), (8.6b) and (8.6c) as well as for the passive dynamic elasticity (9.14e) and (9.14f).

For the boundary constraint on the initial static posture (8.6d), the symmetry of the lower limbs was relaxed to give the OCP solver more flexibility to initiate the motion.

Box Constraints

Velocity and joint torque limits of the actuation system remained untouched. The angular value range of the joints were reduced by the security margin. In the case of the hip joint complex and the knee joint, the security margin was successively augmented during multiple iterations to avoid self-collision of the complex geometry (refer to Figure 8.4b on page 119) of the functional structure of the joint complex and unstable reactions of the control system during the motion performance.

Homotopy Towards the Final Result

For this study a different homotopy towards the final solution was selected. A dominant maximum obstacle height objective was suspended. The obstacle was introduced inside the OCP formulation and shifted to higher altitudes by each iteration, whilst closely observing the

variation of the motion characteristics combined with frequent tests in the OpenHRP motion-simulator.

Therefore, the optimization was carried out in three steps. First the simulation setup was employed to compute a two step walking motion from static half-sitting posture. As soon as a feasible walking trajectory was found after a few iterations, the obstacle was included in the setup to optimize a stepping motion over the obstacle until a certain obstacle height was reached. Finally, the motion was further optimized to reach a maximum smoothness whilst preserving desired trajectory characteristics.

2 Results

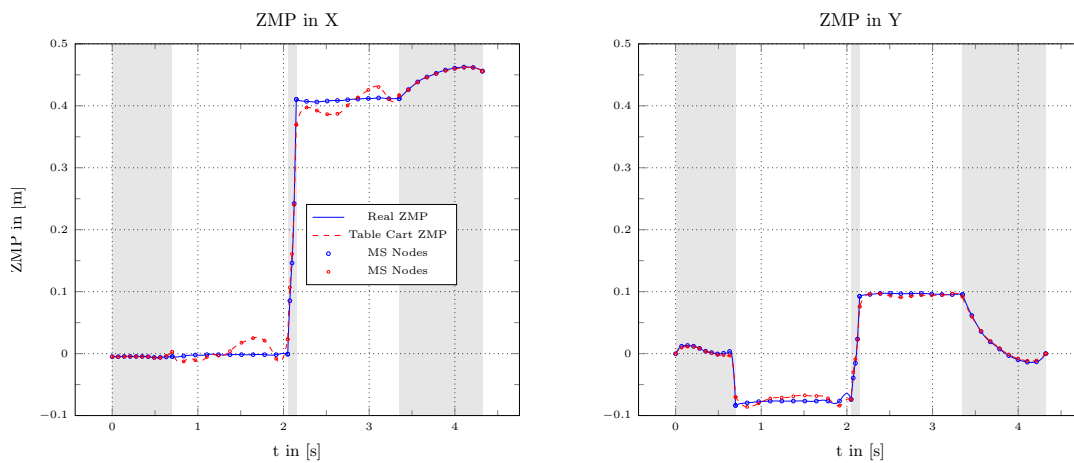


Figure 10.2: Plot of the different trajectories of the WB-ZMP and the highly simplified TB-ZMP frequently used for stable motion generation of humanoid robots.

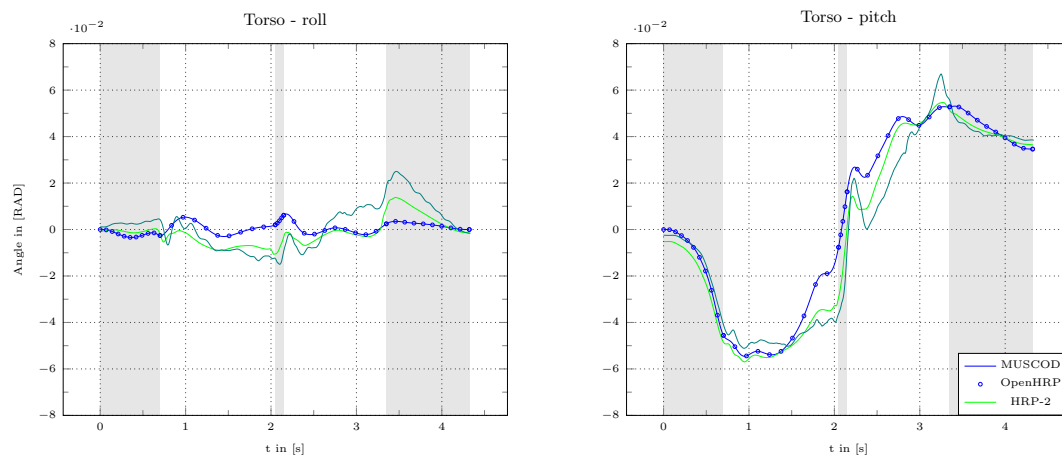


Figure 10.3: Comparison of horizontal components of the torso orientation that are computed during optimization (MUSCOD-II), and estimated in the simulation of the virtual robot (OpenHRP), as well as during the experiment on HRP-2 N° 14. Whilst the roll angle shows higher deviations the pitch orientation follows nicely the optimization results.

As the interest of this analysis is not to investigate the maximum obstacle height, but to assess the quality of this approach, optimization has not been tuned towards a maximum obstacle

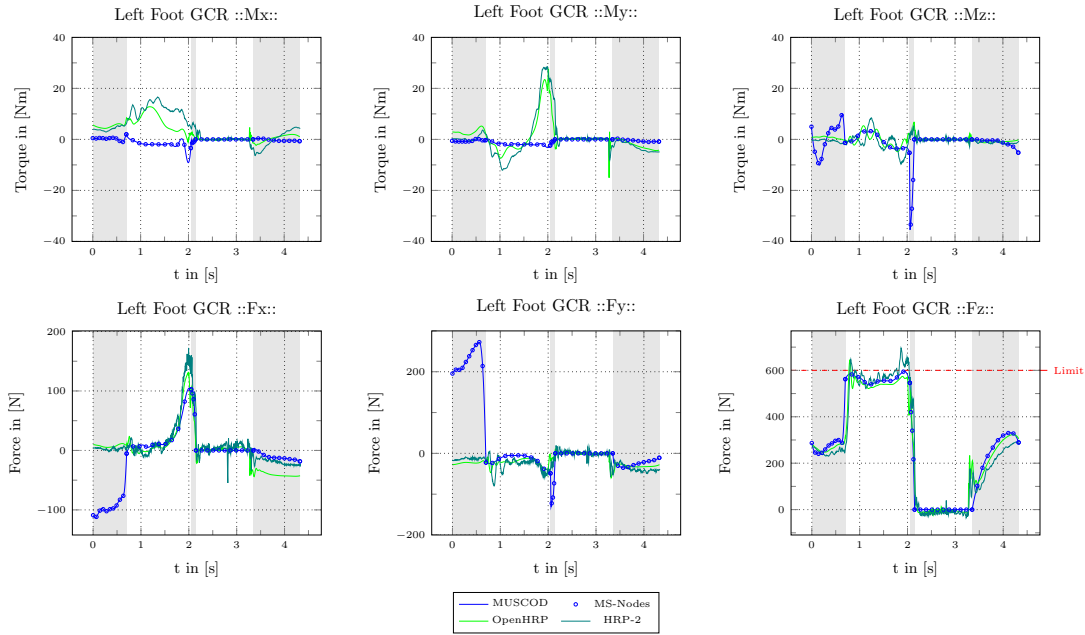


Figure 10.4: Comparison of the left foot GCR for optimization results (MUSCOD-II), the simulation of the virtual robot (OpenHRP), as well as during the experiment on HRP-2 N° 14. Close trajectories are observable for the contact forces F_x, F_y, F_z (vertical force) and the M_z (vertical torque). The stabilizing algorithms manipulate the components M_x, M_y as well as F_z . The vertical force limit should be kept firmly, however small peaks are not a problem.

height, but a suitably smooth motion combined with a reasonable obstacle height for safe investigation during real experiments. Thus, the homotopy was adjusted towards an obstacle height of 20cm (height) x 11cm (width) including safety margin. Even though it was **not** the ultimate goal the finally attained obstacle height clearly **exceeded** the current record of the HRP-2 N° 14 of 18cm in real experiments held by [Verrelst et al., 2006] by 2cm. An aspect that clearly shows the quality of the proposed method.

The obstacle was successfully cleared in 4.32 [s] (result of optimization), in 4.33 [s] and 4.34 [s] with the virtual robot in simulation and the real robot platform respectively. The optimization freely chooses a step-length of 0.415 [m] and a relatively narrow foot arrangement of 0.17 [m] between feet to clear the obstacle. The robot starts from a nearly symmetric posture and a narrow feet arrangement (0.16 [m] lateral offset, 0.005 [m] sagittal offset) into a slightly larger arrangement to re-stabilize the robot (0.19 [m] lateral offset, 0.09 [m] sagittal offset) into the final static posture (see Figure 10.1 on page 143). The simulation of the virtual robot and the real experiment showed a smooth motion without slipping, medium ground impact collisions and no destabilizing.

The analysis of the objectives revealed that the optimization converged mostly with desired motion characteristics as dominant objectives: minimum excitement of the ankle elasticity in horizontal and vertical direction, minimal difference between WB-ZMP and TB-ZMP.

From Figure 10.4 it is clearly observable that the WB model in our optimization framework, the virtual robot, as well as the real robot show similar motion characteristics. The force/torque control loop only concerns the ground contact reactions M_x, M_y and F_z . Apart from noise and different initial conditions in the optimization and the simulator OpenHRP the ground contact reactions F_x, F_y, M_z and even F_z closely follow the computed results. Thus it is concluded that perturbation from vertical excitement of the elasticity has been canceled out sufficiently. Contrary M_x and M_y show large deviation and consequently some chosen motion

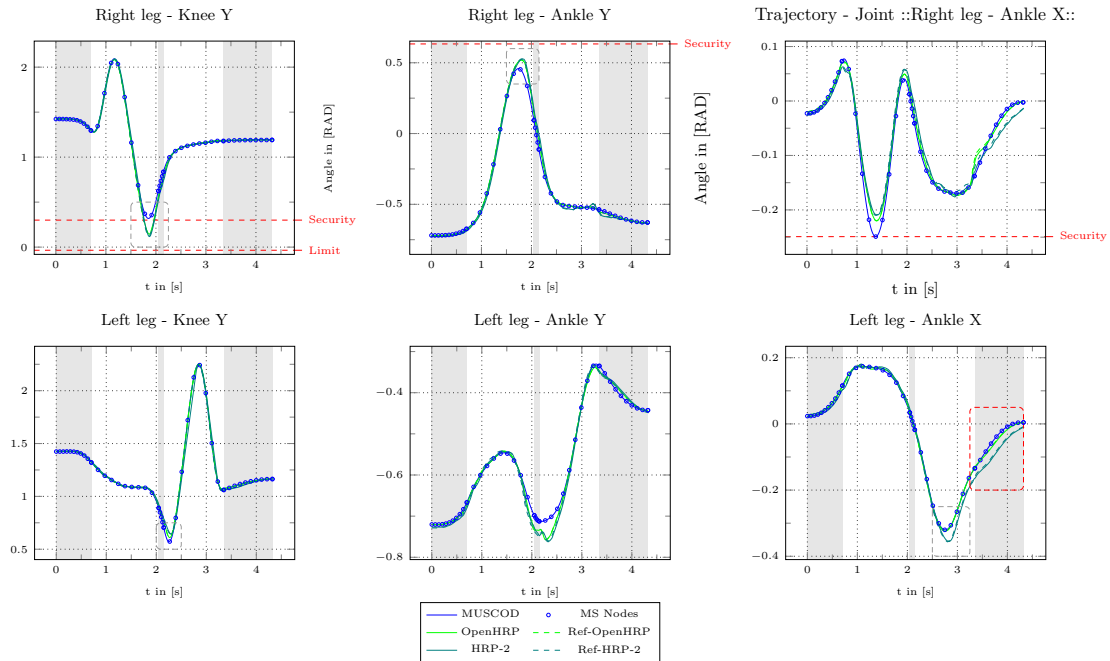


Figure 10.5: Comparison of some joint trajectories for the lower torso part, for optimization results (MUSCOD-II), the simulation of the virtual robot (OpenHRP), as well as during the experiment on HRP-2 N° 14. The control reference (scattered line) and the system’s output (solid line) are drawn separately for verification. The limit marks the absolute maximum angle range for the corresponding joint. The security limit was the actual limit chosen during the optimization to enforce safe operation. The dashed gray/red rectangle show parts of the trajectory where the stabilizer actively manipulated the motion to preserve dynamic stability. In red rectangles even the simulation and the real robot act substantially different.

characteristics of the computed reference need still improvement.

This is further confirmed from Figure 10.5. Deviation from the computed reference during the real experiment and even the simulation are clearly observable in the ankle joint as well as in the knee joint of both legs. This verifies as well the aspect that the whole lower body is used to apply the manipulation of the trajectories of the stabilizer (compare [Kajita et al., 2005, 2007b]). Besides these deviations, the overall trajectories coincide relatively well most of the time. Furthermore, the deviation of the posture control, visible in the global orientation of the torso stays small (see Figure 10.3). Thus, it is concluded, that the employed strategy was successful, despite, modeling errors (elasticity, mass distribution). However, the reference trajectory still shows small deviations from the OCP solution and therefore is still not fully compatible, hence a dynamic error between generated motion and the real robot still exists (compare Section 3 on page 6). At some point this may be as well attributed to the potential differences between the robot in simulation (OpenHRP) and real robot HRP-2 N° 14 (see Figure 10.5 red mark).

A comparison between Figure 10.2 on page 145 and 10.6 on the next page reveals an interesting fact. Figure 10.2 on page 145 shows deviations between the WB-ZMP and the TB-ZMP (as this objective was not triggered to be the first dominant one - these deviations are reasonable). Apart from the high peaks during the phase transitions (SSs \leftrightarrow DS) a high correlation between the deviations in Figure 10.2 on page 145 and 10.6 on the following page. Same tendency is visible on Figure 10.4 on the preceding page (see plot M_y !). Even though the CoP was constrained to move only in a squared area of 1 [cm] x 1 [cm] (blue line), the final result

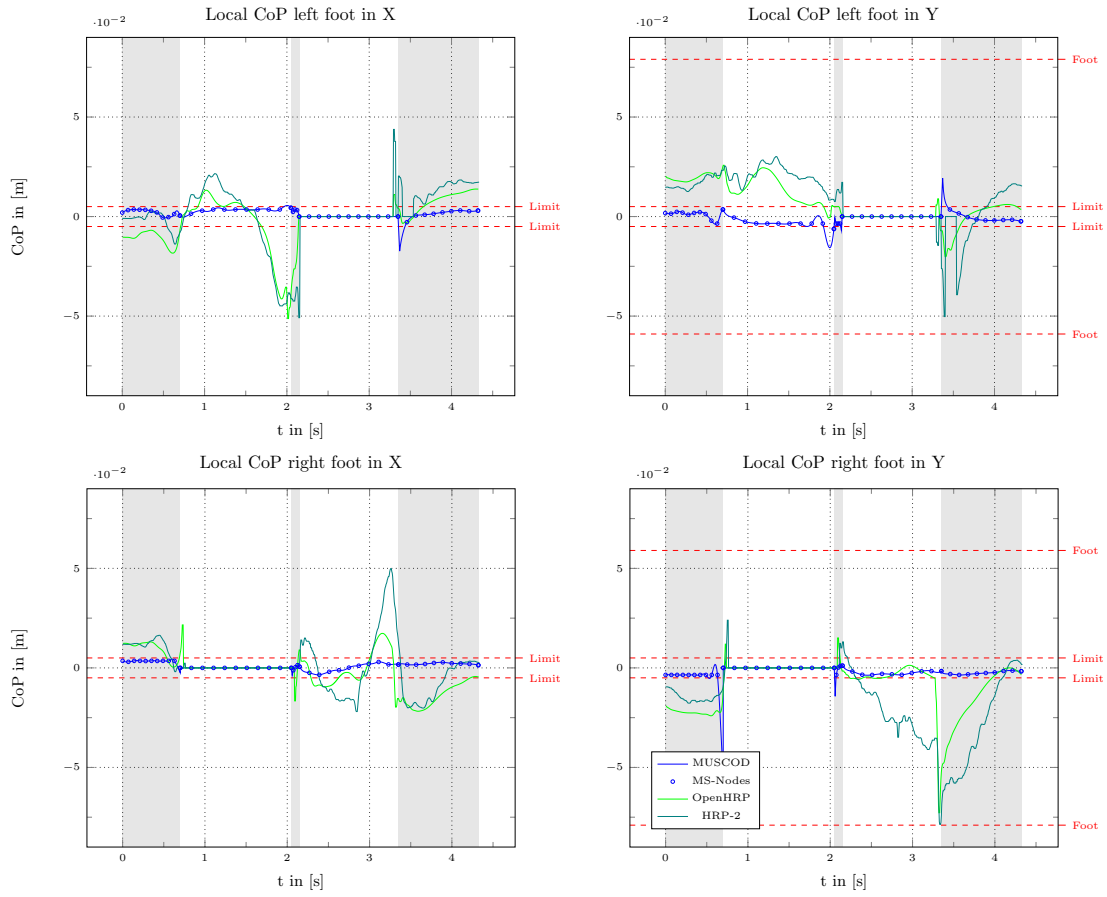


Figure 10.6: Plot of the trajectories of the local center of pressure of each foot in X and Y for optimization results (MUSCOD-II), the simulation of the virtual robot (OpenHRP), as well as during the experiment on HRP-2 N° 14. High peaks occur during the transition phase caused by the vertical contact force dropping to 0. The mark *foot* represents the physical boundary of the foot. As soon as the CoP reaches this boundary the contact stability is breached. The mark *limit* represents the constraint that was used during optimization.

of the stabilizer moves the CoM in a much larger area of approximately 10 [cm] x 10 [cm], which is however still compatible with the geometry of the foot (see Figure 10.6). Besides simplifications in the modeling of the elasticity, this might give room to further assumptions:

- As it was already assumed in Section 1 on page 124 the force/torque control loop is possible tuned to important control parameters and hence producing unstable oscillations around the given reference input signal.
- Possibly the stabilizing algorithm is internally following a reference similar to the TB-ZMP [Kajita et al., 2005]. The local CoP in the left foot - especially during SS - moves to the opposite direction of the observable deviation between the WB and the TB-ZMP. Thus, the stabilizing algorithm seems to not account for the dynamic compensation based on the angular momentum and consequently deviates from the computed reference.

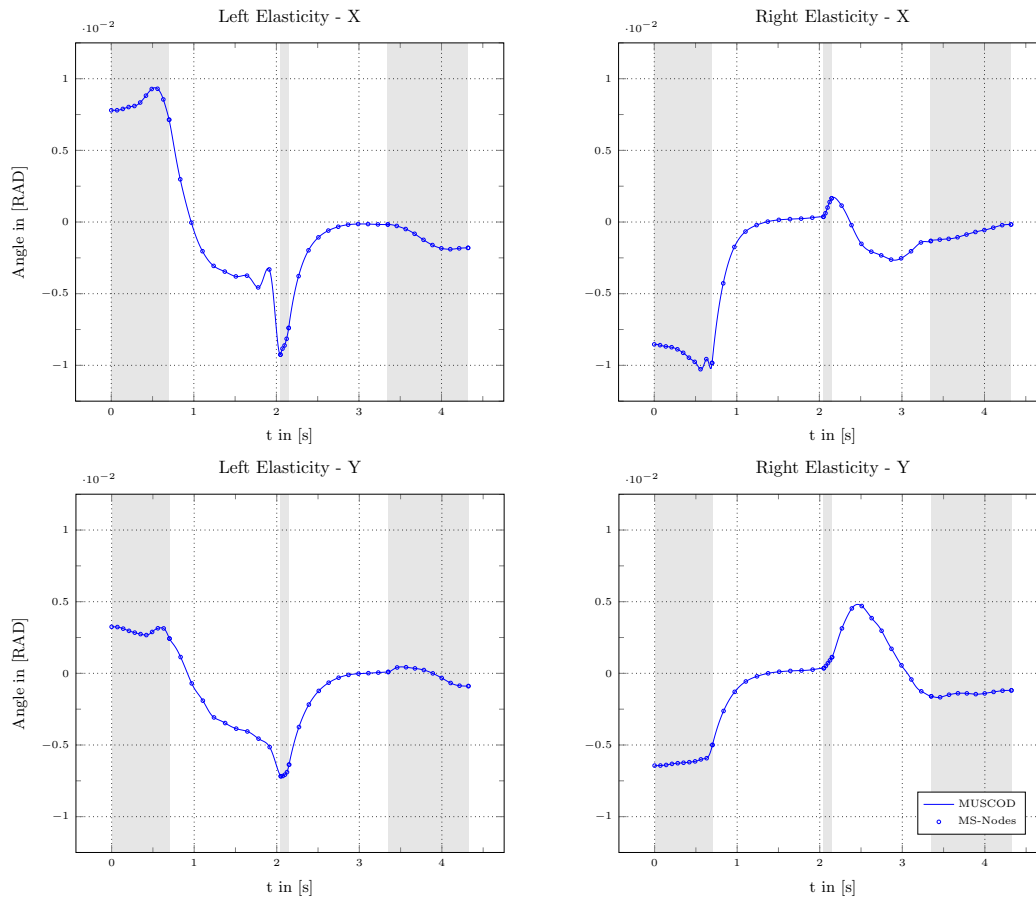


Figure 10.7: Above left and right graph show the rotary motion of the elasticity in X and below left and right graph in Y of left and right foot, respectively.

2.1 Analysis of the Motion Experiment

Based on multiple identification passes of the passive dynamic elasticity, the rotary motion of the simplified model of the ankle elasticity is estimated during the motion performance. The results for the above study is given in Figure 10.7. It is interesting to observe that the angular value range of all passive joints lie approximately inside the range $[-1.0, 1.0] \times 10^{-2}$. Therefore, the position control should reflect a resolution that has a clearly distinct lower magnitude.

This means alternatively, that the pure position control of the joints should have a sufficiently high accuracy. In the following, it is assumed for a moment that the ankle joint falls together with the passive rotational joint. The inertia of the upper body is sufficiently high for it, not to follow the movement that is exerted from the active actuated joint on the passive joint. Then, the torque that is exerted and hence, the directly related CoP trajectory depend on the tracking resolution of the position control loop of the active joint that excites the passive elasticity in the ankle. If the position control loop is not accurate enough, it may have problems to dynamically track a given CoP trajectory.

As it has been explained in Section 1 on page 80 there are three reference signals one has to be aware of when discussing about motion implementation on the real HRP-2 N° 14 robot. The first one is the motion reference itself - in the following called *MUSCOD-Ref*. In the case

of this study it results directly from computation of the OCP. This reference trajectory enters the online stabilizing control system of the robot and is altered to maintain the dynamic equilibrium of the robot - in the following called *OpenHRP-Ref*. This reference trajectory is then sent to the local joint controllers that track the motion on each joint. The measured trajectory reference that comes back from the joint encoders is then the motion profile that was actually performed - in the following called *OpenHRP*. Thus, the difference between the computed motion trajectory and the reference the stabilizer computes to maintain the dynamic equilibrium is denoted Δ_{Stab} ,

$$\Delta_{\text{Stab}} = \text{OpenHRP-Ref} - \text{MUSCOD-Ref}. \quad (10.1a)$$

The control deviation follows to Δ_{Contr} ,

$$\Delta_{\text{Contr}} = \text{OpenHRP} - \text{OpenHRP-Ref}, \quad (10.1b)$$

and the total deviation between the computed reference and the performed motion to Δ_{Total} ,

$$\Delta_{\text{Total}} = \text{OpenHRP} - \text{MUSCOD-Ref}. \quad (10.1c)$$

In the following the focus is set to the control deviation Δ_{Contr} . A first characterization of the magnitude of the control deviation based on the normal distribution is given with Table 10.2. In case we cannot reject the hypothesis that the samples of control deviation follow approximately a normal distribution, Table 10.2 would give a first idea on the tracking quality of the local joint controller.

For the virtual robot this tracking quality is around order of magnitude 10^{-3} . However, for

Table 10.2: Control-deviations in form of mean (μ) and standard deviation (σ_{n-1}) of the local joint controller of the lower limbs of virtual and the real robot

Joint	Virtual Robot (OpenHRP)		Real Robot (HRP-2 N° 14)		Description
	Mean (μ)	Std. Dev. (σ_{n-1})	Mean (μ)	Std. Dev. (σ_{n-1})	
0	2.31E-004	1.80E-003	-8.77E-004	8.55E-003	Hip Z - Right
1	-1.12E-003	1.46E-003	-8.43E-004	3.67E-003	Hip X - Right
2	3.31E-004	4.12E-003	9.71E-005	1.23E-002	Hip Y - Right
3	-2.68E-003	6.29E-003	-5.40E-003	2.49E-002	Knee Y - Right
4	-1.23E-004	4.19E-003	1.39E-004	1.25E-002	Ankle Y - Right
5	4.28E-004	2.11E-003	1.59E-003	5.30E-003	Ankle X - Right
6	-1.64E-004	1.64E-003	-9.54E-004	9.28E-003	Hip Z - Left
7	1.11E-003	1.28E-003	7.82E-004	3.34E-003	Hip X - Left
8	-3.80E-004	4.09E-003	3.95E-004	1.33E-002	Hip Y - Left
9	-2.93E-003	6.83E-003	-8.04E-004	3.30E-002	Knee Y - Left
10	4.44E-005	1.97E-003	6.77E-004	5.66E-003	Ankle Y - Left
11	-5.69E-004	2.04E-003	-5.37E-004	5.10E-003	Ankle X - Left

the real robot, the order of magnitudes 10^{-2} and 10^{-3} are clearly observable. Especially, for the joint about the Y-axis (Right: Hip, Knee and Ankle) the control deviations are particularly important. Thus, with respect to the simple reasoning above, the real robot shows deviations in the position control of the joints in a magnitude similar to the motion range estimated for the passive elasticity (see Figure 10.7 on the previous page). This could be another indicator

for the circumstance that the stabilizing control has problems to accurately track the given motion reference in form of a given force/torque reference or a CoP trajectory profile for a dynamic motion.

2.2 Concluding Remarks

The final study built on top of all the experiences from the previous studies available and successfully exploited the strength of OCP formulation to control specific motion characteristics by abstract high-level objectives. The objective that was successfully exploited tended to minimize the control effort of the online stabilizing control system. By preserving these motion characteristics the dynamic limits of the HRP-2 N° 14 robot were efficiently investigated on a challenging dynamic motion to step over an obstacle with just two steps from a static initial posture towards a static final posture. The study was confirmed with successful trials in simulation and experiments on the real robotic platform. Even though maximizing of the obstacle height was not the primary target of this study, the record of HRP-2 N° 14 dynamically stepping over an obstacle was improved from 18cm to 20cm.

Furthermore, preliminary analysis of the performed motion in simulation and on the real robot revealed a considerable control deviation of the local joint controllers. Compared to the estimation of the necessary trajectory profile of the passive dynamic elasticity in the ankle joint complex it seems that the accuracy of the local joint reference tracking might considerably compromise the ground contact reaction profile to preserve the dynamic equilibrium during motion operations.

Based on this information a possible improvement of the present investigation would be a more precise estimation of the control-deviation and to use optimization to exploit the complex and redundant lower limb structure of the robot to minimize the influence of the control deviation on the generated motion trajectory of the crucial parts of the kinematic chain - the feet or arms.

Part

Optimal Control for Exo-Skeletons

As it was outlined in the introduction 4 on page 11 exo-skeletons are combining the complex technical situation of design (compare Section 2 on page 3) and control (compare Section 3 on page 6) with a problem of close interaction between the human operator and the actual device. As the human is effectively put inside the loop, its intelligence is exploited to accomplish robust walking motions. However, an important number of potential technical safety issues, e.g. hyperstaticity [Cempini et al., 2013], joint motion ranges, compliance and robustness to human induced instabilities [Kazerooni and Snyder, 1995] remain. Thus from an engineering point of view, before one may give clearance to a prototype device for real world experiments, problems to the physical integrity of the human operator must be identified and addressed before.

If one looks at exo-skeletons from the point of view of product development [Albers et al., 2009], the complexity and the advanced level of integration of realized technical solutions [del Ama et al., 2012, Dollar and Herr, 2008, Herr, 2009, Herr and Kornbluh, 2004, Pons, 2010] clearly suggest to consider these devices as mechatronic systems [Buur and Andreasen, 1990]. A system complex with a close integration of mechanics, electronics and software. Specific guidelines for the development of these mechatronic systems as engineering product exist, e.g. the V-Model for industrial application [VDI, 2004]. An important problem that is frequently stressed in various discussions of the development of such systems (e.g. refer to [Heimann et al., 2007]) is the aspect of modeling and simulation, of the mechanics, the actuation system and the high- and low-level control system. This approach is proposed to manage the usual complexity of such devices and to properly describe the technical interdependencies between the various system components.

The trend in product development goes from the classical *over-the-wall engineering*, where system components are developed separately to form the final product, towards a comprehensive and interdisciplinary approach. Therefore, a common idea is to propose a development study that employs model-based optimal control for conceptual design. The proposed development study is different from the common approach *divide and conquer*, as the focus is shifted from a problem simplification by separation into system units towards a comprehensive system with simplified modeling of all system components. The human is in the center of this approach and the exo-skeleton is build around. The approach is iterative in the sense that each iteration substantiates further the characteristics of the given components but always preserves the complete system to resolve the complex interdependencies between the distinct system components. The optimization during each iteration is then conducted on task motions – *in this case it will be walking* – that represent the desired tasks the final system should be able to perform.

The purpose of this study is to perform the first iteration of the proposed development approach. As such, the study consists of a comprehensive investigation on how the kinematic constraints and dynamic augmentation through a virtual exoskeleton do possibly alter the mechanics of the wearing human operator. The effects of the exo-skeleton are investigated during straight line walking. Furthermore, the approximate limiting characteristics, in terms of motion and actuation trajectory profiles, of such a device performing the same motion task with a purely passive human inside are investigated. These profiles are computed from the desired task motions being fitted to the corresponding model setup. The model setup consists of a human operator wearing the exoskeleton, based on whole-body optimal control.

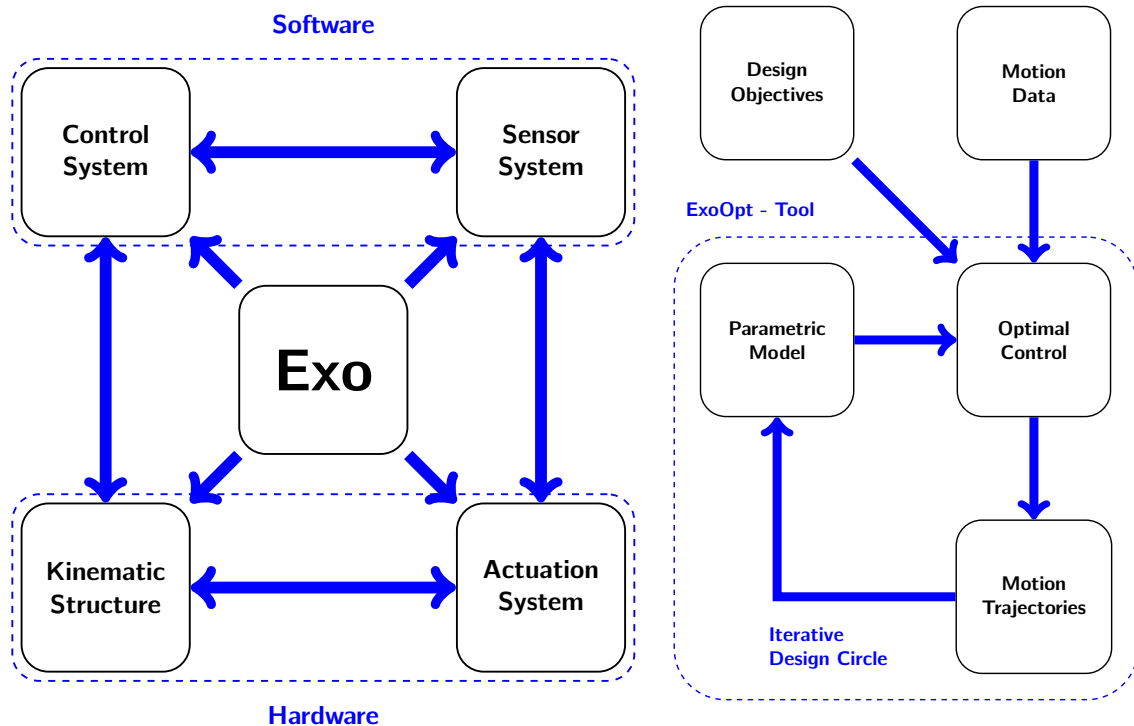
The complete tool-chain that is built to process the motion tasks, formulate the specific OCPs and visualize the results for further analysis is grouped together in a new proposed framework *ExoOpt* that will be presented and thoroughly discussed in the following chapters.

Related Publications: The work in this chapter has been issued for publication in:

- Kai Henning Koch, Katja Mombaur. ExoOpt - A tool for Evaluating Exo-Skeleton Designs using Model-Based Optimization. International Workshop on Wearable Robotics, 2014, Spain

Acknowledgement This project has been conducted in cooperation between the University of Heidelberg - IWR (Interdisciplinary Center for Scientific Computing, Heidelberg) - and the KIT (Karlsruhe Institute of Technology) - Institute of Anthropomatics - in the frame of MTH (Medical Technology for Health) of HEiKA (Heidelberg Karlsruhe Research Partnership). Funds from HEiKA for this project are gratefully acknowledged.

11 Integrated Modeling Approach for Exo-Skeletons



(a) Different components of an exo-skeleton construction and its interdependencies that need to be carefully considered during the design process. The upper level shows the software components for motion generation and interaction with the operator and the lower level the hardware components.

(b) Scope of the tool *ExoOpt* and *Iterative Design Circle* that uses the formulation of subsequent optimal control problems to substantiate the unknown parameterized characteristics of the complex Human-Exo model based on motion data and desired design objectives.

Figure 11.1: On the left side the abstract main components of an exo skeleton construction are shown. During conception these components should not be considered separately - as it is frequently done (references) but packed into a comprehensive approach. This approach then iteratively substantiates all unknown parameters based on the complete system design.

After a discussion of different target applications of exo-skeletons (see Section 4 on page 11) the following chapters will focus on the application of optimal control for preliminary conceptual studies for an exo-skeleton device targeted towards medical applications in mobility support and rehabilitation purposes. As it is discussed in [del Ama et al., 2012, Dollar and Herr, 2008, Herr, 2009] the conception of such an exo-skeleton device is generally a collection of highly complex tasks that involves a lot of technological experience, time, energy, material

and financial resources. From [Kwa et al., 2009, Raj et al., 2011, Valiente, 2005, Walsh et al., 2007] it seems that due to the high complexity in the design process of these devices it is not always clear whether the initially selected approach leads to the desired final system properties (e.g. augmented metabolism costs for passive dynamic exo-skeletons [Valiente, 2005, Walsh et al., 2007], undesired weight distribution of the device [Kwa et al., 2009]).

As discussed in the introduction, the problem is well known in conceptual product design [Heimann et al., 2007] and various attempts are made to efficiently support and improve the conceptual work of engineers [Buur and Andreasen, 1990, VDI, 2004] towards a fully functional product that fulfills all previously defined requirements. Therefore the following work attempts to efficiently exploit the capacities of optimal control to push this methodology a step further. The proposed strategy combines the iterative substantiation of functional and design aspects, but is always based on the whole system model. This integrative approach has the particular advantage that the target system is always handled in its comprehensive form, resolving the various interdependencies between the different system components. This should provide a more detailed and confident view on the final characteristics the system will probably have, as soon as the first prototype is built.

Figure 11.1a on the facing page shows the abstract main components of an exo-skeleton. The design challenge consists of combining these different components together while efficiently resolving all the interdependencies [Buur and Andreasen, 1990, Heimann et al., 2007]. The resulting conception is highly interdisciplinary as all interdependencies between the environment and sub-components need to be analyzed prior to adjusting the setup, such that they work together in an optimal manner and comply with all product requirements. Therefore, during the conception and design process there will be frequently unknown characteristics to be expressed as parameters henceforth. As the development moves towards a realistic product, these parameters will need to be substantiated. In the following, this will be accomplished based on an iteration such that the final design is substantiated step by step during iteration of the investigation process.

As it is shown for the example of a motion related task investigation in Figure 11.1b on the preceding page, optimal control can help to iteratively substantiate all unknown parameters. The advantage is that the study can always be conducted on the comprehensive system, even though, some system characteristics are initially not sufficiently determined. Additionally from the full optimization results, further conclusions are possible about the quality of the resulting characteristics with respect to the given scenario. However, as it has been explained previously (see Chapter 2 - 5) the modeling approach in OCP formulations is different from the classical simulation approach in the sense that frequent verifications of the desired characteristics in a classical simulator (e.g. OpenHRP [Hirukawa et al., 2003]) are considered necessary to keep the OCP formulation as close to the reality as possible.

1 Examples of Different Exo-Skeleton Conception Approaches

In the following, two well documented designs of exo-skeletons and their development, namely BLEEX [Chu et al., 2005, Kazerooni et al., 2005] (for military use) and MINA [Kwa et al., 2009, Raj et al., 2011] (for use in rehabilitation) will be analyzed. Based on these analysis the contribution of this work towards the complex design challenge for a lower limb exo-skeleton in medical rehabilitation and mobility will be discussed.

1.1 BLEEX

The BLEEX Berkely Lower Extremity Exoskeleton is - to the knowledge of the author - the first energetically autonomous load-carrying exo-skeleton that has been successfully tested in the laboratory as well as in outdoor environments. It is hydraulically actuated (linear pistons that act over a lever on rotational joints) and can carry a load of 34 kg with a maximal walking speed of $1.3 \frac{m}{s}$. The exo-skeleton comes with highly innovative features, such as a novel sensor-control-approach [Kazerooni et al., 2005] and a lightweight, highly portable power-unit [Raade et al., 2003]. As the design of the control system is explicitly based on the pilot's control actions to maintain stability [Kazerooni et al., 2005], the exo-skeleton requires a healthy pilot for safe operation and seeks to augment physical strength and endurance for load carrying tasks. The structural load from the payload is directed through the exo-skeleton towards the ground without affecting the pilot.

System-Overview

Table 11.1: Overview about the joint limits of BLEEX [Chu et al., 2005]

Joint	Actuation	min [DEG]	max [DEG]
Hip rotation	passive	NN	NN
Hip extension-flexion	active	10	115
Hip abduction-adduction	active	NN	NN
Knee extension-flexion	active	5	126
Ankle dorsi-plantar flexion	active	-45	45
Ankle inversion-eversion	passive	NN	NN
Ankle rotation	passive	NN	NN

The exo-skeleton has 7 dofs in each leg. 4 dofs are actively actuated, 3 dofs are passive and equipped with spring-damper systems (see Table 11.1). The kinematic structure consists of lateral outward frames for thigh and shank, a foot construction to host a part of the sensor system and a rear-brace to carry the power-unit, the control-system and the payload as a huge back-pack. The pilot is rigidly fixed to the machine by means of a fast clip mechanism on the feet and with the torso by means of a custom vest and belts. All other links, e.g. thigh and shank are highly compliant.

From a vast experience with systems with humans in the loop [Kazerooni and Guo, 1993, Kazerooni and Snyder, 1995, Kazerooni et al., 2005] the creators of BLEEX came up with an innovative approach to incorporate the human action in the loop. In contrast to [Hayashi et al., 2005, Kawamoto et al., 2003] the direct measurement of force interactions between human soft tissue and rigid engineering structure with state of the art technology for determining the users motion intention at that time was stately not possible with a sufficient repeatability and robustness for various different pilots [Kazerooni et al., 2005]. Thus the creators of BLEEX chose a novel approach without any direct measurements of the pilot-exo-skeleton interaction, to strictly focus on measurement on the exo-skeleton itself. The key aspect as that the human in the loop is considered as external perturbation and opposed to classical control-engineering [Heimann et al., 2007] the sensitivity of the control-system towards these perturbations is selectively maximized. The implemented model-based controller, computes a variable (in magnitude) feed-forward compensation [Khalil and Dombre, 2002] (compare other publications about feed-forward control with consideration of additional ex-

ternal contact forces [Mistry et al., 2010, Righetti et al., 2011b]) of the dynamic effects of the exo-skeleton with respect to its actual kinematic configuration. The controller does not generate inherently stable motions of the exo-skeleton device, but provides the pilot with a high bandwidth-sensitivity to react on his motions, such that he can stabilize both (exo-skeleton and himself) by highly dynamic motions (e.g. steps, swaying, squatting). This approach does not depend on any information about the human pilot as in [Hayashi et al., 2005, Kawamoto et al., 2003]. However, the controller is sensitive to dynamic-model deficiencies [Kazerooni et al., 2005] and actual tuning of the compensation factor.

The previously mentioned controller-approach needs, in addition to the modeling information only the kinematic configuration (joint encoders) and a feedback about the feet ground contact states (force distribution sensors at 4 points in the foot plate).

Conceptional Approach

The approach used for the conception of the complete system is explained in [Chu et al., 2005]. It is relatively straight-forward and offers a good base to explain the innovation of the described work below. The conception attempts to bring together the functional and design based aspects iteratively for a given set of application scenarios. As BLEEX is destined for bipedal transport tasks, the creators of BLEEX use different Clinical Gait Analysis (CGA) to determine the limiting kinematic and dynamic characteristics of each joint:

- The ankle joint mostly acts as a spring-damper with average mechanical power-output (positive) during the progression phase [Chu et al., 2005, Shamaei et al., 2011]. The torque profile is uni-directional during the complete stance phase, thus allowing choice of an uni-directional hydraulic actuator [Chu et al., 2005].
- The knee joint acts mainly as damper [Chu et al., 2005] with medium mechanical power-absorption (negative), in contrast to [Shamaei and Dollar, 2011] where the knee action is described as pure spring action. The torque profile features peaks into both, positive and negative direction and thus a bi-directional actuation is chosen.
- The hip joint has both mechanical power absorption during stance and output during the toe-off [Chu et al., 2005] to propel the torso forward [Dollar and Herr, 2008]. The corresponding torque profile features positive and negative peaks. Hence, a bi-directional actuator is necessary at this joint.

As the CGA-data is not directly transferable for the following conceptional analysis of the exo-skeleton it is rescaled to feature [Chu et al., 2005]:

1. 75 kg (target weight including 34kg of pay-load in a back-pack)
2. walking velocity of $1.3 \frac{m}{s}$
3. a pelvic tilt angle

However, precise information about the algorithms used to accomplish the desired non-trivial data-transformation is not stated in [Chu et al., 2005]. Based on these information peak forces of the actuation components are determined and compared to the CGA based on the non-linear kinematics to give a suitable security margin. Even though the conception of the non-linear kinematics seems to be based on the limiting motion data [Chu et al., 2005] no further information is supplied about dynamic optimality. Finally these information are combined to compute the instantaneous and average hydraulic energy consumption of the system for the dimensioning of the portable hydraulic power-unit. Different mock-ups with Fused

Decomposition Modeling (FDM) [Montero et al., 2001] were built to check for motion ranges and ergonomy.

1.2 MINA

MINA [Kwa et al., 2009] a second generation exo-skeleton built on top of experiences with the Florida Institute for Human and Machine Cognition (IHMC)-Mobility Assist Exoskeleton (MAE) [Raj et al., 2011] is targeted towards assistance in mobility for paralyzed people. The exo-skeleton is electrically actuated, torque controlled and - to the knowledge of the author - neither energetically nor operationally autonomous. Real experiments have only been reported for studies inside the laboratory. The exo-skeleton incorporates some highly innovative improvements in its Human Machine Interface (HMI) to provide the pilot with vital information about his dynamic balance state he would not be able to assess on its own. The exo-skeleton mimics as closely as possible an anthropomorphic structure and is rigidly connected to each limb (in contrast to pseudo anthropomorphic structures [Miao et al., 2013]). The exo-skeleton enforces a specific desired kinematic configuration of the lower body but does carry only its own weight. The pilots weight is supported only by its own bone structure, while standing upright.

System Overview

The following system overview compares both, the IHMC *Mobility Assist Exo-Skeleton* [Kwa et al., 2009] and the MINA exo-skeleton [Raj et al., 2011] as the documentation is mostly complementary although there are technical differences between both constructions that will be addressed below. While IHMC-MAE is equipped with 5 dofs, 3 actuated and 2 passive

Table 11.2: Overview about the joint limits of the IHMC Mobility Assist Exo-Skeleton [Kwa et al., 2009]

Joint	Actuation	min [DEG]	max [DEG]
Hip extension-flexion	active	-30	42
Hip abduction-adduction	active	-30	25
Hip rotation	passive	-10	10
Knee extension-flexion	active	-90	0
Ankle dorsi-plantar flexion	passive	-35	25

dofs (see Table 11.2 for details), MINA only has 3 dofs (ankle dorsi-plantar flexion has been replaced with a flexible foot-fold made of carbon fiber). Here only the flexion-extension dofs are actuated. Both exo-skeletons use rotatory actuation-systems equipped with a harmonic drive gearbox and an electric motor. The IHMC-MAE is additionally equipped with large elasticities between the gearbox output shaft and the kinematic structure of the exo-skeleton [Kwa et al., 2009]. With MINA the elastic deflection of the Harmonic Drives were judged to be sufficient [Raj et al., 2011] to form a Serial Elastic Actuator (SEA) [Vallery et al., 2008] with fixed stiffness. In both setups the output-torque of the exo-skeleton is measured by means of a comparison between the readings of an encoder on the motor-shaft and on the final joint-output. The actuators are capable of both - position and torque control [Kwa et al., 2009, Raj et al., 2011]. The kinematic structure is represented with nested aluminum tubes to account for precise adjustments to individual limb sizes, such that the rigid joints are best aligned with the those of the pilot [Raj et al., 2011]. The pilot himself is attached to the exo-skeleton with its torso to a curved back-plate (hosts the computing unit and the servo-modules) with straps

at shoulder and pelvis. Belts then connect thigh and foot to the remaining structure to allow the exo-skeleton to completely determine the kinematic structure of the lower limbs of the pilot.

Both exo-skeletons are capable of torque and position control [Kwa et al., 2009, Raj et al., 2011]. These control schemes are used during the able-body-user mode and the paralyzed-body-user mode. In the former mode the torque-control is used to keep a fixed specified torque on each actuated joint to allow at one hand for a natural gait and on the other minimize disalignments between the kinematic structure of the exo-skeleton and the limbs of the user. This mode is used to record different gaits from healthy subjects for later post-processing and re-play. As MINA does not have an actuated ankle joint the recorded healthy subject was asked to exaggerate ground clearance (led to similar gaits chosen for slippery ground-conditions) to assure ground clearance as well as during re-play of the same motion. In the latter mode the position control is activated and the previously recorded and processed gaits are then replayed with the paralyzed user inside the exo-skeleton. At present the MINA still needs a further pilot that controls the motion re-play process, while the paralyzed user walks forward maintaining its dynamic stability by the use of additional crutches [Raj et al., 2011]. Besides the IHMC-MAE was reported to have additional control modes. Furthermore, exo-skeleton is equipped with a *zero assistance* mode where the exo-skeleton was set to gravity compensation and a *performance enhancement* mode to assist a healthy user e.g. with load carrying tasks [Kwa et al., 2009].

The sensor system of MINA consists of rotational and linear encoders to measure motor-shaft and joint positions (estimation of output torque) as well as a F-Scan sensor array [Catalfamo et al., 2008], containing 960 dispatched pressure sensors to detect the ground contact reactions. The MINA exo-skeleton comes with a highly innovative HMI that uses the sensory substitution paradigm to render an alternative, intuitive access to vital dynamic information during operation of the system, such as, joint positions and torques, ground reaction forces as well as center of pressure [Raj et al., 2011].

Conceptional Approach

The necessary torque, velocity and trajectory profiles were determined from CGA. The creators IHMC-MAE measured the peak and Root Mean Square (RMS) power output requirements of each joint. Maximum torque output was fixed to $80 Nm$, the velocity limit to $6.8 \frac{rad}{s}$ and a corresponding low impedance SEA was developed. As it is stated [Kwa et al., 2009], bipedal locomotion requires dynamic torque profiles at a high mean level - thus the low bandwidth of the low impedance SEA at high output torques was clearly a problem. From the design scheme in [Kwa et al., 2009] it is clearly observable that the actuation system for the abduction-adduction joint has a large overhang on the rear side of the construction. The creators mention that this construction shifted the CoM back in such a manner that studies for gait rehabilitation and disability assistance were hampered. This led to a reconstruction of the device to replace the abduction-adduction as well as the rotation joint with rigid links as these were not deterministic for straight line walking performance [Kwa et al., 2009]. This design decision has been preserved during the conception of the second generation - MINA [Raj et al., 2011], while the ankle plantar-dorsi flexion joint has additionally been omitted. From tests with able bodied users in disability assistance mode it is stated that gait playback was only successful when the user intentionally interacted with the exo-skeleton [Kwa et al., 2009], e.g. unloading the future swing foot.

1.3 Concluding Remarks

Even though only a small scope of the above hand-picked examples about exo-skeleton conception have been discussed the inherent complexity of these projects is clearly observable. Due to the time and money constraints of the project the following work is based on, the author may only offer a far more restricted scope, hence a study that remains purely theoretic for the time being. However in contrast to the above examples the potential contribution of an integrative approach based on optimal control in conception should be clearly visible from various aspects.

Weight Distribution

As it is outlined in [Herr and Popovic, 2008, Kwa et al., 2009] the correct weight distribution, position of each individual as much as of the comprehensive CoM is very important, not to impede the user during dynamic operation with the exo-skeleton. As those devices generally consist of a lot of different parts with different shapes, materials densities and finally different highly complex global trajectory profiles during various dynamic motions of the user, the research of an intelligent weight distribution has a highly redundant non-unique solution space. At this point whole body control optimization can help to efficiently analyze different solutions and formulate abstract criteria to investigate an optimal weight distribution that would be optimal with respect to the desired modes of operation e.g. as well as with respect to the consumed energy or the output torque of the actuation system to improve energetic autonomy of the overall system at a very early stage of development.

Conception of Actuation Systems

From [Chu et al., 2005, Heimann et al., 2007, Kwa et al., 2009, Vallery et al., 2008] it is clearly observable that conception of an actuation system, be it linear or non-linear, determines not only the pure power output characteristics of the dispatched motor/gearbox module but as well a large part of the comprehensive system dynamics based on the interaction between the actuation system with the remaining dynamic MBS structure and between the different actuation systems that act on the former. Thus, design decisions that are taken for one actuation module virtually concern the characteristics of the whole device. At this point whole body optimal control provides an efficient method to investigate different designs of actuation systems considering its comprehensive influence based on the full system. Furthermore, interesting characteristics of the actuation systems in question are parametrized to be investigated in parallel with respect to different motion tasks and abstract optimality criteria while the optimal values for these parameters and the sensitivity of these parameters with respect to the initial setting give further information about how the given actuation system should be finally realized.

Studies of System Characteristics

The conception of the device in [Chu et al., 2005] based on CGA from different sources gives evidence to highly complex methods of rescaling (see Section 1.1 on page 158 above). As performing manipulation on data based on dynamic models in contact with its environment (in most cases during bipedal motion tasks the human or device/humanoid robot tends to have complex contact reactions with its environment) is a highly complex non-trivial task this may be at one hand a resource for errors, caused by in-appropriate assumptions and simplifications but on the other hand provide the designer with lots of potential improvements applicable on the desired system. Again, optimal control can help at this point to efficiently

investigate the essential system characteristics of a future device, based on a given task motion portfolio. Furthermore, it is possible to analyze the sensitivities of the system's characteristics with respect to small deviations of the target task motion portfolio, or to achieve a certain degree of generalization of the target motions with respect to selected system characteristics based on the formulation of abstract optimality criteria.

Ergonomics

As it is observable from literature the joints between proximal and distal limbs may have a highly complex kinematic characteristics (e.g. hip joint [Kang et al., 2002, Menschik, 1997], knee joint [Grood and Suntay, 1983, Morrison, 1970], ankle joint [Isman and Inman, 1969]). They consist of compliant tissue, such that lubrication [Menschik, 1997], load and constraint condition [Bottlang et al., 2000], as well as inter-subject variability may add even further deviations to these characteristics. As soon as these joints are technically approximated with 1-dof hinges (e.g. knee, elbow) or 3-dof ball-and-socket [Baerlocher and Boulic, 2001] (e.g. shoulder, hip, ankle), mis-alignments between the human kinematic chain and the corresponding one of the exo-skeleton are unavoidable [Pons, 2010]. This effect is called *hyperstaticity* [Cempini et al., 2013] and results in parasitic mostly uncontrollable loads on the human limb (exo-skeleton - human attachment points) and joint structure to create discomfort and even risk of injury [Cempini et al., 2013]. An attempt to quantify this amount of discomfort was given in [Esmaeili et al., 2011] based on a stochastic *one-fits-all* approach. As *in-vivo* measurements are not feasible with a reasonable amount of material and effort [Cempini et al., 2013], a proposed strategy is to add passive dofs to the robotic link structure [Jarrassé and Morel, 2012, Schiele and van der Helm, 2006] to account for this misalignment with: redundancy to allow flexible kinematic adaptability, observability of the dynamics of the comprehensive model as well as projection of the actuation torque to the desired dof without parasitic load on the human joint structure [Cempini et al., 2013]. All of these approaches will generally lead to modeling with a high number of parameters that will need to be identified during the conception phase. Whole body optimal control gives an efficient method to formulate this identification problem with respect to desired task-motions as well as abstract design criteria (e.g. separation of control-ability and adaptability [Cempini et al., 2013]) and to propose solutions based on the comprehensive dynamic model. Furthermore, most of the studies have been conducted for rehabilitation purposes of the upper limb structure [Cempini et al., 2013, Jarrassé and Morel, 2012, Schiele and van der Helm, 2006] in contrast to the lower limb structure [Cai et al., 2011]. Again optimal control would be an efficient method to compare strategies that have been previously adopted for upper limb structure to lower limb structures effectively investigating compatible kinematic, dynamic characteristics as well as load profiles of the exo-skeleton and the human pilot during operation.

2 Optimization Based - Comprehensive Approach

In [Cempini et al., 2013] the authors complain that a large number of design approaches have been driven around the robotic structure, while less attention has been given to the human. An issue that that should be clearly addressed during the following study.

From the examples above the high amount of interaction between the separate system components that need to be considered already during very early stages of the development is clearly visible. Even though optimal control, as it was used in the following thesis has as well its short-comings, to be discussed in the following modeling sections, it can provide a highly efficient method to formulate an abstract conceptual modeling problem of a system that is

mostly unknown and to iteratively substantiate a clear view over all system components. The innovative aspect is that all investigations are done on the comprehensive system model such that track of the complete system behavior is never lost. Furthermore, optimal control can be employed as well to generalize a given set of system characteristics that at some point be even contradictory, to find the best solution to fit all characteristics with a specified optimality.

2.1 Scope of this Work

In the following sections the scope of the modeling framework *ExoOpt* (see Figure 11.1b on page 156) is explained based on one iteration cycle for a preliminary parameter study of an abstract exo-skeleton device. This preliminary study tries to give an answer to the following questions:

1. What limiting characteristics of the actuation will be necessary to perform the desired task?
2. What kind of actuation systems (direct drives, SEA or Parallel Elastic Actuator (PEA) [Vallery et al., 2008]) will be best suited for this task?
3. Is it possible to perform the desired motion tasks with a reasonable amount of used energy?
4. What motion characteristics change due to the constraining kinematics, such as non-elastic foot, missing dofs in the exo-skeleton (see as well [del Ama et al., 2012, Dollar and Herr, 2008, Herr, 2009])?
5. How high will be the maximal structural load in a first estimation that needs to be supported by the exo-skeleton - hyperstaticity [Cempini et al., 2013]?

For the analysis at hand the portfolio of desired motion tasks was limited to different straight-line walking tasks (level-ground and slope walking) based upon the experiences made during this analysis, the task portfolio should be expanded towards other motions (particular motions that further push the device to its limits, such as sit-down, standing up) such that a complete set of benchmark settings is available that thoroughly determine the necessary dynamic characteristics of the future device.

The analysis for this first iteration then consists of multiple fits of a parametrized dynamic model of a human pilot wearing the exo-skeleton against the walking motion data. Based on this setup different weights of the exo-skeleton and the human pilot have been conducted, tuned for a good generalization, to explore the characteristics of the comprehensive system as well as its internal interactions.

2.2 The Tool *ExoOpt*

The tool *ExoOpt* is not a monolithic GUI-application, but a collection of thoroughly tested modules built around the OCP framework MUSCOD-II [Leineweber, 1995] to simplify the formulation of OCPs for conceptual investigation. The collection contains a parametric dynamic model builder that connects to third-party packages for convenient model-data exchange and 3D visualization of the resulting motion data. The remainder consists of modules to formulate different modeling constraints, pre-process initial conditions for the problem-formulation as well as post-process and visualize the final results.

12 Exoskeleton Modeling for Optimization

As soon as it comes to modeling, again, there is this important trade-off to make, between the complexity and quality of the model with respect of its estimation of the real-world scenario. In contrast to the case of motion generation and implementation on a real-world scenario (see chapter 6 on page 80) where a lack of crucial information almost always leads to a loss in model quality that will need to be addressed appropriately (through parameter identification). Upon an initial guess of the unknown properties the latter may be conveniently parametrized to form the characteristics of the comprehensive model while different scenarios are investigated. The huge difference is that at one hand the unknown characteristics of a real-world system are frequently abstract and neither easy parametrizable nor directly accessible (see chapter 10 on page 142). On the other hand the OCP formulation gives a unique access to the evolution of the system states and its parametrized characteristics during the complete motion simulation. This information is usually not present in real-world test scenarios e.g. during experiments with prototypes and need to be measured and estimated, evolving complex computations (e.g. Kalman-Filter based estimations [Sabatini, 2011]). This fact is highly beneficial as soon as substantiation of unknown system characteristics is to be made.

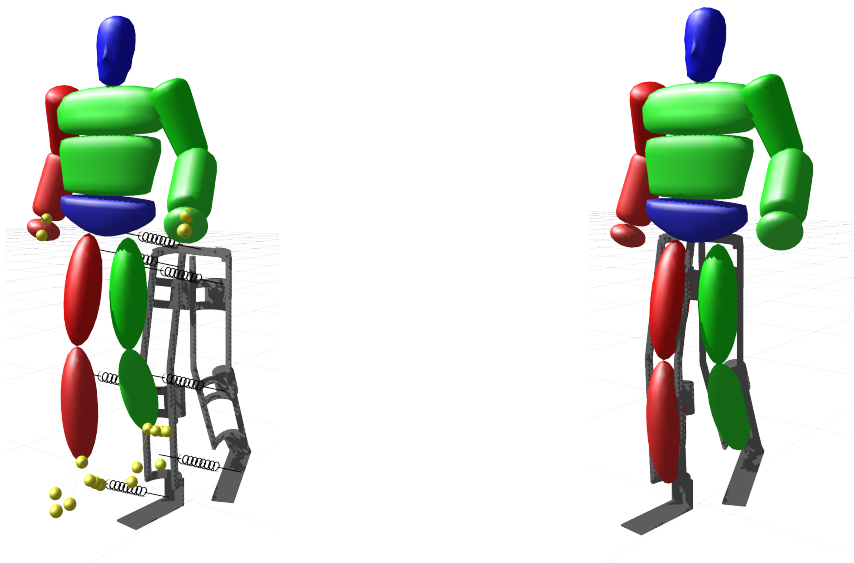
In the following different modeling approaches are discussed and the final decision for a specific one is outlined. Then the complete modeling process including all its simplifications is outlined to give a comprehensive overview about the kinematics and dynamics of the employed system for the following investigation. Furthermore, it is important to discuss the limits of this investigation. Hence, what kind of information this study may produce and how these are to be interpreted correctly.

1 Modeling of a Human Inside an Exo-Skeleton

The ultimate goal of this investigation is to assess the general performances of the comprehensive abstract system and the potential interactions between the human pilot and the exoskeleton trying to operate in concert. This conceptual study is directed towards the conception and construction of an exo-skeleton to support partially and fully lower-body paralyzed people in mobility. Therefore, interactions between the exo-skeleton and the human pilot are particularly interesting for the case where there is nearly no contribution from the human pilot during operation.

1.1 Preliminaries

An *ideal* modeling approach that would allow such kind of studies is shown in Figure 12.1a. It consists of two dispatched models, one for the exo-skeleton and one for the human that moves independently from each other in space. Both models are then joined together by means of multiple spring-damper systems and viscous-elastic contacts [Güler et al., 1998] that model the links that would attach the soft tissue of the human pilot to the real exo-skeleton prototype in a realistic scenario. In this problem-setup one could model conveniently different benchmark scenarios. For a given task-motion (e.g. walking), this setup *could* accomplish the following investigations - determining:



- (a) The final prospected modeling approach. Here a complete independent human and exo-skeleton model are combined in one simulation. The interdependencies between both models are resolved based on rheological models [Gross et al., 2011].
- (b) The currently realized modeling approach. Human and exo-skeleton are combined and simplified into one model.

Figure 12.1: Different modeling alternatives

1. the mechanical power as well as the joint trajectory and velocity profiles, for different scenarios assuming that the human pilot is only capable of supplying a fraction of the nominal torque profile for either all or a sub-selection of joints [Kwa et al., 2009, Raj et al., 2011]. This includes as well the investigation of dynamic joint characteristics [Shamaei and Dollar, 2011, Shamaei et al., 2011].
2. the closest similar motion with respect to constraints in joint trajectory, velocity or torque profile of human pilot and/or exo-skeletons or motion constraints (e.g. self-collision, obstacles) [Xiang et al., 2010].
3. a first estimation of the functional load that is transmitted over the interfaces between the links of the exo-skeleton for further mechanical design studies [Gross et al., 2004] and technical conception of the joints.
4. the coupling forces and torques between the exo-skeleton and the human pilot to maintain the ensemble in close motion configurations - state of hyperstaticity [Cempini et al., 2013]. Generally this information is critical with respect to security and user-comfort [Esmaili et al., 2011]. At one hand, the coupling reaction are directly dependent on the stiffness of the corresponding links. On the other hand, the location of the links with respect to the limbs do have an important impact on the trade-off between the stiffness of the links and the misalignment of the human pilot with respect to the exo-skeleton. Furthermore, the misalignment between the joints of the human and the exo-skeleton will produce further load cycle in the kinematic structure of both system components that will have to be analyzed as it may case damage to either the limbs [Cai et al., 2011] of the pilot or the structure of the exo-skeleton or both [Cempini

et al., 2013, Malosio et al., 2011].

5. the trajectory profile of the partial (human, exo-skeleton) and comprehensive CoM, which might give evidence how much the exo-skeleton actually hampers the human motion [Kwa et al., 2009].
6. the angular momentum trajectory profiles with respect to the corresponding CoM, provide further information on how the dynamics characteristics of the moving comprehensive system change with respect to dynamic stability and recovery [Herr and Popovic, 2008, Pratt et al., 2006, Pratt and Tedrake, 2006].
7. dynamic interdependency between the necessary exo-skeleton joint actuation, given the situation the human pilot cannot supply the full joint torque that would be necessary to perform a desired motion.

All this information is an important requirement during the conception process to achieve maximum confidence into the quality of the simulation and the results of the conducted investigation before a first already highly specialized prototype may be built. However, the following short analyzes sheds a different light on the previously proposed setup.

Let us assume that the exo-skeleton will consist of 6 dof per leg, including the free-floating motion with respect to the global reference frame results in 18 dofs. The human will be modeled with at least 3 dofs per joint. In a first approximation including the free motion with respect to the global reference the model ends up with a minimum of 51 dofs and the complete model setup will then feature at least 69 dofs. In case of the final problem formulation with order reduction and higher order input control the system will have a minimum number of 183 system states.

Eventually the number of dofs might be much larger to account for the additional anthropomorphic soft-tissue based joint-modeling [Bottlang et al., 2000, Flores, 2011, Grood and Sun-tay, 1983, Isman and Inman, 1969, Kang et al., 2002, Menschik, 1997, Morrison, 1970, Sheehan, 2010], as well as the additional passive redundancy joints for self-adaption [Cempini et al., 2013]) and 45 control inputs.

From the necessary computational resources to solve such a complex problem formulation, this should not be a real issue. Yet the experience shows that one should start first with a simpler setup that achieves similar results. Based on this setup, one should test the numerical setting in quicker iteration cycles before attempts are reasonable to further complicate things for more detailed and realistic investigations.

Hence, the following work discusses a study that was conducted on a smaller, simplified setup where the human pilot and the exo-skeleton have been reduced to a comprehensive model (see Figure 12.1b on the facing page for more details). The resulting problem formulation will then only have approximately 90 system-states and 26 control inputs, a setup with much less complexity that is better suited for these prospected preliminary investigations.

Unfortunately this approach will shadow and merge some of the above information, more particularly the aspects 3 on the preceding page, 4 on the facing page and 7. More precisely, kinematics and the dynamics of the pilot and the exo-skeleton will be merged, such that the comprehensive model will reflect the dynamics and kinematics of both, the human pilot and the exo-skeleton. The kinematics are merged to represent the human pilot effectively wearing the exo-skeleton, that is based on a first approach of simplified state-of-art technology, with more constrained kinematics (less flexible) than the human body. Both model parts give evidence to different parametrization (length, weight) to investigate its influence on the multi-body dynamics while performing the walking motion.

As simplification are mostly unavoidable to keep the complexity of the resulting mathematical

model at a reasonable level, whilst preserving the essential physical characteristics for the target analyzes, all modeling decisions will be precisely documented in the following. First both model instances will be discussed thoroughly one by one, to be joined together in the final conclusion. During this conclusion important implications for the modeling will be revisited and summarized.

1.2 Modeling of Human

In the following it is assumed without exception that the global reference, points with its X-axis always towards the direction of motion, with its Y-axis horizontally to the left-hand side and with its Z-axis upwards (vertical axis). All local reference frames in neutral configuration follow the same orientation.

Human Body

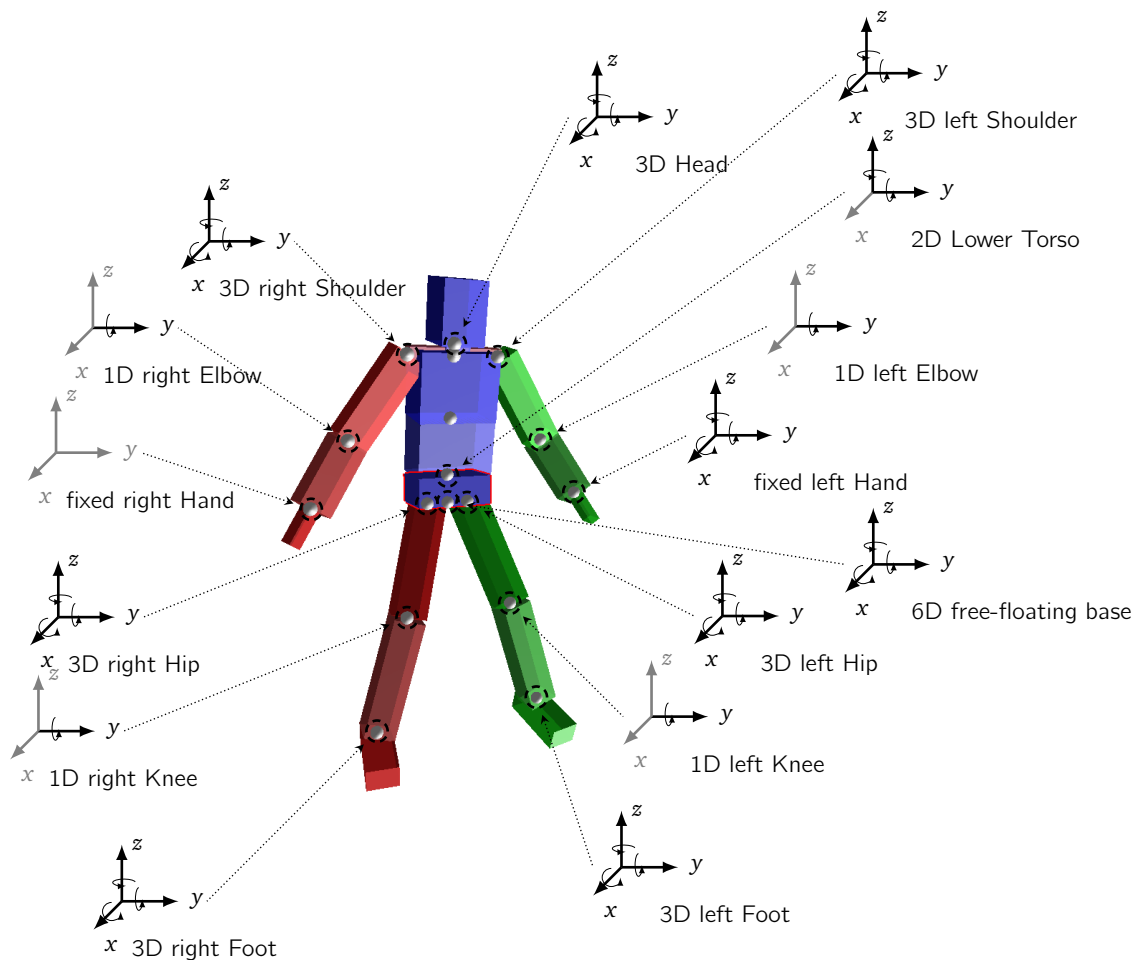


Figure 12.2: Modeling of Heiman-Model

The dynamic model of the human pilot has been built based on a standard human rigid-body dynamic model - called *Heiman* - for optimal control studies. It has been established from standard literature data [de Leva, 1996a, Dumas et al., 2007a,b, Winter, 1990] (gender and data source is chosen upon model-built) that has been compared with optimization based

walking scenario (see [Brinkmann, 2013] for details) and completed where values have been found to be non-consistent. The Heiman-Model itself consists of legs (Thigh, Shank, Foot) a pelvis element that connects to the torso (middle and upper torso) and regroups arms (upper arm, lower arm, hand) and a head segment (see Figure 12.2 on the facing page and 2 on page 241 in Appendix C for more details).

Angular Parametrization of the Joints The parametrizations of the joint angles follow the Euler-Convention Y, X', Z'' [Khalil and Dombre, 2002] of ball-and-socket joints (modeled as spherical joints [Baerlocher and Boulic, 2001]). It was judged that singularities in this joint parametrization are sufficiently far from the range of motion considered during the following investigations (compared to Appendix C). Particularly for the lower human torso, the assumption of a spherical ball-and-socket joint might be relatively accurate for the hip [Kang et al., 2002, Menschik, 1997] and for the ankle joint [Isman and Inman, 1969, Sheehan, 2010], but represents a simplified modeling for the knee-joint [Grood and Suntay, 1983, Morrison, 1970], to be approximated as single dof extension/flection joint. However with respect to the simplified problem formulation, this modeling approach is largely sufficient as joint misalignment and ergonomics are not of major interest during the following preliminary study. Despite the dof convention used for the joints of the human body, the orientation free-floating base (6D :: 3D translation, 3D rotation) is always expressed in the Cardan [Khalil and Dombre, 2002] convention (Z, Y', X'') .

Parametrization of Kinematic and Dynamic Properties For a parametric modeling (see Appendix C for a more detailed description) among the available resources in literature, there exist at least three sufficiently complete anthropomorphic data-sets [de Leva, 1996a, Dempster, 1955, Dumas et al., 2007a,b] appropriate for dynamic modeling of the human body. These data-sets are inherently different.

Based on the higher probability of a more general data set (less precision for a single specimen however) and the fact that the data-set [de Leva, 1996a] gives dynamic values for dispatched upper and middle trunk as well as a pelvis limb, the decision was made to adopt the latter data source for the following analyzes as it was not clear, whether more flexibility in the upper torso might be necessary for subsequent analyzes on different tasks motion, such as e.g. bending, sit-down, stand-up motions.

The dynamic data has been further parametrized by individual fractional rescaling $s_{m(i)}, s_{l(i)}$ on per limb basis to account for closer patient adjustments based on anthropometric measurements. The employed in 6D spatial algebra [Featherstone, 2006] then follows to mass

$$m_i = m_{\%,i} m_{\text{total}} s_{m(i)}, \quad (12.1a)$$

limb segment length,

$$l_i = l_{\%,i} l_{\text{total}} s_{l(i)}, \quad (12.1b)$$

longitudinal CoM position,

$${}^{\text{ref},i} \text{CoM}_i (l_i) = \begin{bmatrix} 0.0 & 0.0 & \text{CoM}_{z_{\%,i}} l_{\%,i} s_{l(i)} \end{bmatrix}^T, \quad (12.1c)$$

and the inertia tensor,

$${}^{\text{ref},i}I_i(l_i, m_i) = \begin{bmatrix} {}^{\text{CoM}}I_i(l_i, m_i) + m_i \text{CoM}_i(l_i) \times \text{CoM}_i(l_i) \times^T & \text{CoM}_i(l_i) \times \\ \text{CoM}_i(l_i) \times^T & I_{m_i} \end{bmatrix}. \quad (12.1d)$$

Improvement of the Human Foot Model A correct geometric foot modeling is crucial to the accuracy of the computed GCR from the model. As it was discussed in Section 3.3 on page 32 the GCR are a substantial part of the dynamic behavior of the model. Furthermore, they are directly related to the dynamic stability (compare Section 2.1 on page 87). Therefore, the geometric modeling of the foot contact will have an important influence on the final motion resulting from the optimization.

The exo-skeleton pilot does not get into contact with the ground directly. The interaction

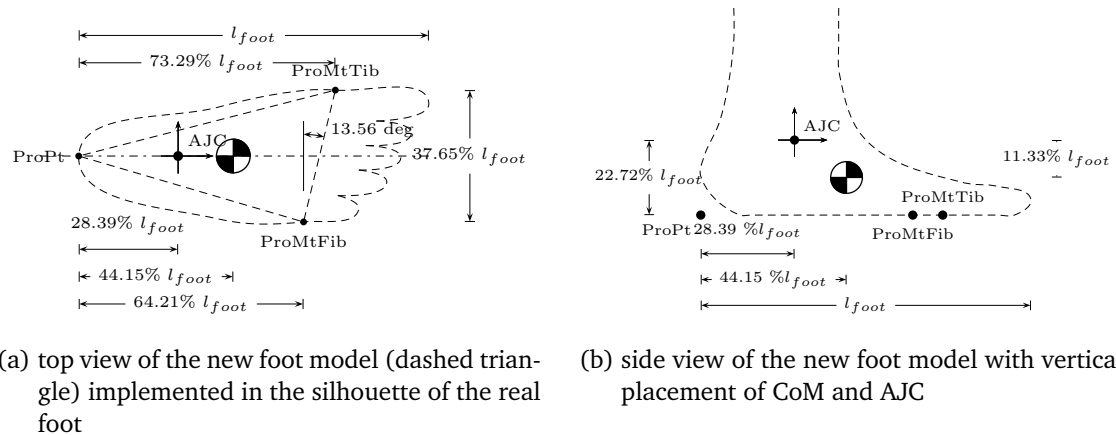
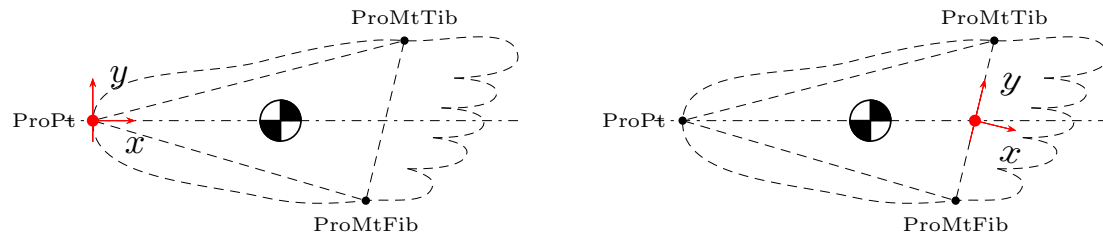


Figure 12.3: Improved contact modeling of the foot based on [de Leva, 1996a, Hawes and Sovak, 1994, Isman and Inman, 1969, Moreira et al., 2009, Onyshko and Winter, 1980, Sheehan, 2010, Winter, 1990]. The points *ProMtTib*, *ProMtFib* and *PrpPt* are the ground projections of the corresponding landmarks *Metatarsal Tibiale*, *Metatarsal Fibulare* and *Pternion* respectively. These points are then used during the mathematical contact modeling for heel-hinging (Pternion) and toe-hinging (Metatarsal-phalangeal). AJC denotes origin of the local reference frame and the ankle joint center

occurs always through the exo-skeleton's foot assembly. From the above reasoning, the definition of a suitable contact model with respect to human anatomy should however be carefully considered. At the beginning of this analyzes, a more accurate geometric sketch of the foot assembly of the exo-skeleton was not available. Thus, due to the lack of more accurate design sketches of the foot assembly, it was concluded that for the following preliminary investigation the geometry should be kept reasonably close to the functional geometry of the foot, but model the foot as a rigid body. This should produce GCR profiles between the foot assembly and the ground that are reasonably close to human walking but respect the fact that there will be a rigid plate between the foot and the ground. The purpose is to compute first for walking trajectories with a reasonable anthropomorphic contact geometry. Second, as soon as more accurate design sketches of the foot assembly are available, the contact geometry should be altered to investigate the related effects, e.g. excessive mechanical efforts or various motion appearances of the resulting walking motion.

Consequently, on the one hand, the foot-ground contact model should feature characteristics close to the natural geometry. On the other hand, the foot should mechanically behave as a rigid foot plate, without the intrinsic elasticity characteristics in the foot [Hicks, 1954]) and

rolling contact conditions [Lankarani and Nikravesh, 1990, Millard et al., 2009, Moreira et al., 2009] or viscous-elastic contact [Güler et al., 1998]. As it was already stated in [Brinkmann, 2013], neither the data-set of [Dumas et al., 2007a,b] nor the one of de Leva [de Leva, 1996a] feature the essential geometrical information about the foot such that one could build a sufficiently accurate contact model for subsequent optimization studies. For this purpose the closer



(a) Contact model that has been used for heel contact, for heel strike as well as the rolling motion. (b) Contact model that has been used for fore-foot contact, the toe rolling and the toe strike.

Figure 12.4: Different contact points that have been used to simulate the foot ground contact reactions of the human gait during the preliminary optimization study

geometry of the foot and the ankle joint were assessed from literature based on landmarks from foot classifications [Hawes and Sovak, 1994], e.g. used in shoe last fabrication [Sheng, 2010]. Furthermore, [Hawes and Sovak, 1994] featured comprehensive and generalized data-sets of foot landmark measurements from healthy, randomly drawn ethnically Caucasian people (age between 18-85 years) that compared reasonably well to alternative, but less comprehensive post-war studies in North America and Scandinavia. These data-sets were found to be compatible to the resources used in [de Leva, 1996a]. Remaining unclear geometric information were then established based on [Isman and Inman, 1969, Sheehan, 2010] for the AJC, the lateral landmark positions and vertical placement of the CoM [Onyshko and Winter, 1980, Winter, 1990]. The lateral placement of the CoM was employed from [de Leva, 1996a]. These information were then rescaled with respect to segment lengths [de Leva, 1996a] and merged with the employed data set (details about landmarks and lengths are shown in Figure 12.3 on the facing page).

As it is explained in Chapter 2 and 3 6D point-wise contact modeling is superior to 3D point contact in terms of robustness for necessary model-globalization. In Figure 12.4 the two different contact points and the orientation of each local contact reference system is shown (compare Section 3.3 on page 32), respectively. In [Bessonnet et al., 2004] it was stated that toe rolling is done in the direction of the line between the projected landmarks metatarsale tibiale and metatarsale fibulare. The orientations were chosen, such that distinct elementary rotational directions with respect to the given contact situation, e.g. heel or toe rolling, are easily controllable. However, in parallel to the theoretic argumentation that the kinematic structure of the ankle joint complex of the exo-skeleton might be severely over-constraining. Corresponding observation were made during first optimization trials to support this hypothesis. Hence, the heel and the toe rolling were defined as a pure point contact, not to block the other rotational dofs. The orientation of the local contact reference frame was preserved, however.

This particular modeling scheme however will lead to an abrupt change in the profile of the foot-ground contact reactions during the phase transition of the toe strike, as the contact model reference frame abruptly changes its location (position and orientation), which will be clearly visible in the results.

1.3 Modeling of the Exo-Skeleton

In the following, a brief description of the abstract kinematic and dynamic modeling, as well as its parametrization is given. As the real model was about to be conceived in parallel in the laboratory of the cooperation partner at KIT, the following study was based upon an abstract, but flexible approach such that the abstract model may be replaced with more accurate design blueprints as soon as they become available.

Kinematic Structure

The prospected kinematics of the exo-skeleton as it has been designed from the cooperation partner at KIT is shown as full scheme in Figure 12.5 on the next page. The exo-skeleton was conceived for this preliminary study to consist of 13 rigid segments connected with 1 dof rotational joints to comply with the current state of art technology in bearing construction and actuation-systems to keep the concept as realistic as possible. The exo-skeleton will be attached to the human pilot at the pelvic frame - the bracket, that will join both leg assemblies together.

Figure 12.11 on page 181, 12.9 on page 179 and 12.10 on page 180 show the joint configurations individually including the positive direction for motion and joint torque. The hip joint complex was conceived with rotational joints for extension/flection (Right Hip X, Left Hip X) and abduction/adduction (Right Hip Z, Left Hip Z) dofs. The internal/external rotation (Right Hip Y, Left Hip Y) is achieved with a curved linear joint that wraps around the human hip and braces extension/flection and the abduction/adduction dof (see Figure 12.11 on page 181). This configuration simplifies as well the numerical setup as, from human motion range data [Kaneko et al., 2004] it is observable that this angular parametrization keeps the mathematical singularities [Baerlocher and Boulic, 2001] outside of the feasible motion space.

The knee joint is highly simplified (compare to Section 1 on page 239 in Appendix C) as it only features a single flection/extension (Right Knee Y, Left Knee Y) dof (see Figure 12.9 on page 179). Apart from the highly complex configuration in the human ankle joint complex (see Section 1 on page 239 in Appendix C) the ankle joint is simplified to dorsi/plantar flection (Right Ankle Y, Left Ankle Y) and inversion/eversion (Right Ankle X, Left Ankle X - see Figure 12.10 on page 180).

As the soft-tissue based natural joint kinematics changes based on the inter-subject variability, external constraints or load conditions, the strategy of close approximation of the natural joint-center based on a rigid exo-skeleton design is considered problematic in literature [Cempini et al., 2013]. However technologically, this joint arrangement should create various opportunities to comprise further passive joints in later design iterations, to represent a suitable initial point for this preliminary analyzes. All local reference frames are then placed in coincidence with those of the human model to simplify the subsequent merge process.

Actuation System

Following the desired level of simplification during modeling and the actual implementation of the actuation systems different considerations, such as kinematic loops and additional dynamic characteristics, may need to be considered during the modeling (compare Section 1 on page 230 in Appendix B). A main target of this preliminary study is a first attempt to identify the potential applications for Variable Impedance Actuator (VIA) (refer to [Vanderborght et al., 2013] for a comprehensive review) or passive spring-damper systems in the actuated joints of the exo-skeleton. Therefore the modeling should be kept as abstract as possible not to bias the analyzes by any pre-major technological decisions. The prospected strategy based

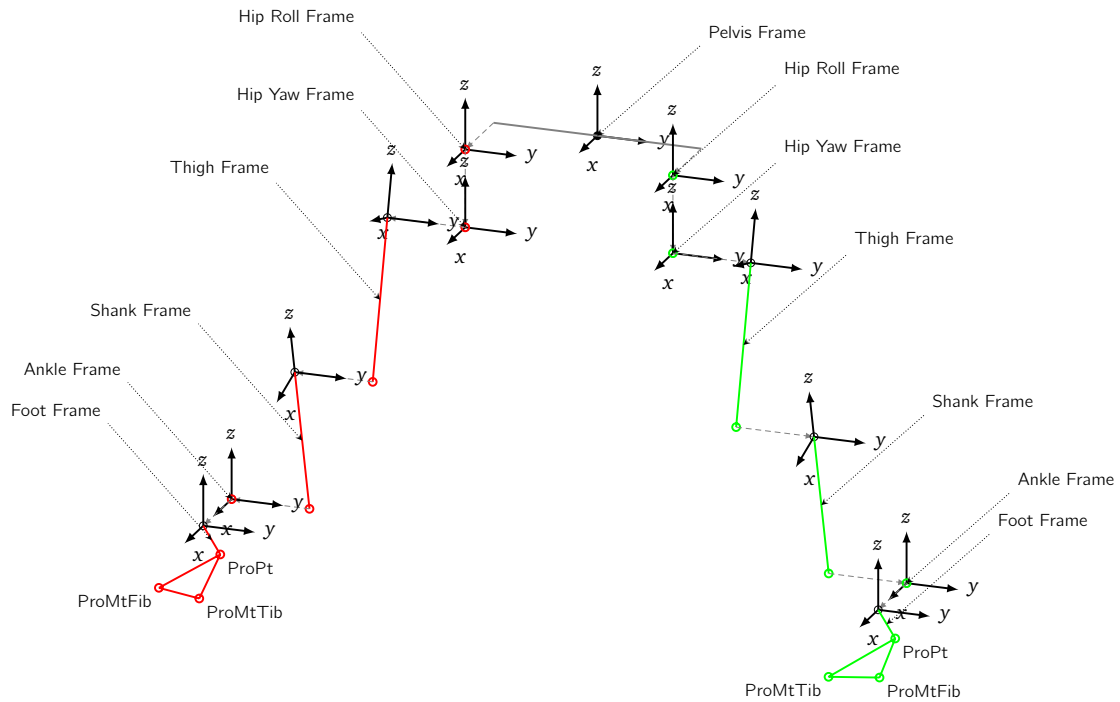


Figure 12.5: The kinematic scheme of the exo-skeleton on which all subsequent discussions will be based on. The kinematic structure of the pelvis is drawn in gray, the left and the right leg are represented by green and red colors respectively. Explosion of all frame is done following their corresponding joint axis to the parent frame. All local frame coordinate systems are drawn in black.

on the comprehensive model approach is the technological outsourcing of complex low-level dynamic characteristics from the high-level control system into a smart design of the functional structure of the device [Vanderborght et al., 2013] to simplify and homogeneously distribute technological complexity among low-level mechanics and the high-level actuation control-system.

However it is intended to use a specific SEA-actuator design in at least 2 of the actuated joints in each leg (Y-axis in the knee, Y-axis in the ankle). The actuator uses a rotational DC-machine and a rotational-to-linear transmission to drive a crank-mechanism through a die-spring. This crank-mechanism is already an integrative part of the functional structure of the exo-skeleton. This actuator design decision promises two important aspects that will impact even the abstract modeling process:

Kinematic Loop The actuator concept introduces a non-linear kinematic loop between the functional structure of the exo-skeleton and the actuator bracket between the crank-tip points (see Figure 12.6b on the next page). As it is described in Section 3.3 on page 30 (compare Section 1.2 on page 234 Appendix B), the dynamic modeling is first performed on a serial tree (all closure loops are cut open). The loop closure is then handled by formulation and solution of the corresponding DAE-System featuring the complete kinematic and constraint forces on the point of the loop closure. However the following static case analyzes based on virtual work [Gross et al., 2006], will already provide essential information for the later dynamic modeling and show interesting insights into the kinematic behavior. Hence, this will be worth a few lines of discussion.

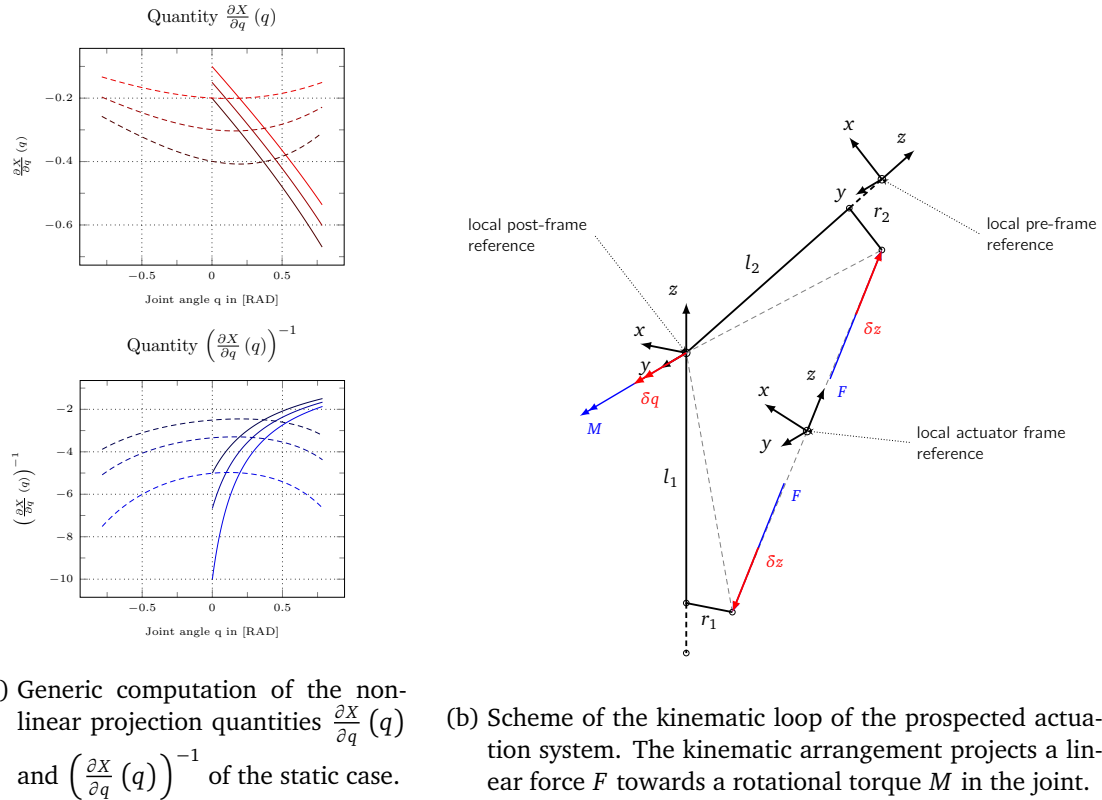


Figure 12.6: Analyses of the kinematic loop of the actuation system. Figure 12.6a shows the projection of the static load for different geometric parameters. Higher brightness levels have been chosen for smaller fractions $\frac{r_{1,2}}{l_{1,2}}$. Solid line of the knee joint, dashed line of the ankle joint. Figure 12.6b shows the geometric scheme of the kinematic loop. In case of the knee joint *pre-frame* and *post-frame* are equal to *Thigh Frame* and *Shank Frame* (solid line). In case of the ankle joint *pre-frame* and *post-frame* are equal to *Shank Frame* and *Foot Frame* respectively (see figure 12.5) (dashed line).

The kinematic-loop introduces a non-linear transfer function of the actuator position, velocity and torque towards the rotational actuated joint in the functional structure of the exoskeleton. In the following, this will be briefly analyzed on the principle of virtual work for a static setting (compare Section 3.2 on page 28). Equivalent to the dynamic case, the principle of virtual work provides a highly efficient way to express static equilibrium conditions for properly-constrained and even under-constrained mechanisms. The mathematical derivation is done by means of virtual displacements that are compatible with the kinematics configuration of the system. A relation between the motion δz of the linear part of the loop and δq of the rotational part of the loop follows to:

$$\underbrace{\frac{\partial X}{\partial t}}_{\delta z}(q) = \frac{\partial X}{\partial q}(q) \underbrace{\frac{\partial q}{\partial t}}_{\delta q}. \quad (12.2a)$$

The virtual work balance then follows to,

$$\delta W = F \delta z - M \delta q = 0, \quad \delta q \neq 0, \quad \delta z \neq 0. \quad (12.2b)$$

In the static case the virtual work in the rotational part δq of the loop must be the same as in the linear part δx of the loop for the static equilibrium to hold. Therefore, equation (12.2b) can be re-arranged to,

$$\begin{aligned} F \frac{\partial X(q)}{\partial q} \delta q - M \delta q &= 0, \\ \underbrace{\left(F \frac{\partial X(q)}{\partial q} - M \right)}_{=0} \delta q &= 0. \end{aligned} \quad (12.2c)$$

Thus, the torque in the knee or the ankle joint is related with the linear actuator force by,

$$M = F \frac{\partial X(q)}{\partial q}. \quad (12.2d)$$

The nonlinear projection (12.2d) from the torque towards the force is expressed as,

$$x(q) = \left(l_1^2 + r_1^2 + l_2^2 + r_2^2 - 2\sqrt{l_1^2 + r_1^2} \sqrt{l_2^2 + r_2^2} \cos \left(q + \arctan \left(\frac{r_1}{l_1} \right) + \arctan \left(\frac{r_2}{l_2} \right) \right) \right)^{\frac{1}{2}}, \quad (12.2e)$$

and,

$$\frac{\partial X}{\partial q}(q) = - \frac{2\sqrt{l_1^2 + r_1^2} \sqrt{l_2^2 + r_2^2} \sin \left(q + \arctan \left(\frac{r_1}{l_1} \right) + \arctan \left(\frac{r_2}{l_2} \right) \right)}{X(q)^2}, \quad (12.2f)$$

respectively. In Figure 12.6a on the preceding page this relationship is plotted for different fractions $\frac{r_{1,2}}{l_{1,2}}$. Higher brightness levels have been chosen for smaller fractions respectively. In Figure 12.6b on the facing page the sign inversion of the static projection (with respect to the chosen reference system convention) is clearly observable (12.2f). From the bottom-Figure in 12.6a on the preceding page one can clearly observe that the quality of the projection from $\dot{z} \rightarrow \dot{q}$ significantly degrades for decreasing joint angles q . Thus small changes in z will result in huge changes in q and hence a position of q controlled based on the intermediate of z might get problematic. At the same time the projection of the joint torque $F \rightarrow M$ significantly decreases (top-Figure 12.6a on the facing page). This effect is explained mechanically through the aspect that the torque lever for M decreases with smaller joint angles q and hence the structure of the kinematic loop is increasingly set under load. Finally from Figure 12.6a on the preceding page it is clearly observable that with a corresponding choice for $l_{1,2}$ and $r_{1,2}$ the setup is kept far from the singularities for the complete motion range of the joint.

Apart from this relatively simple static analyze, it is clearly observable that the impact of this nonlinear projection on the system, even during the preliminary study should be kept in mind during analyzes of the results. Of course dynamic results resolving the kinematic loop based on the whole body dynamics will yield further complex results. However, this relationship already shows, that control of position and the capacity to apply a joint torque on the rotational joint by intermediate of this prospected actuation system significantly degrades as soon as the joint angle approaches smaller values. This might quickly become a key issue to limit the systems characteristics and should be carefully considered during subsequent iterations in the conception phase.

Dynamical Coupling Based on the kinematic loop the actuator design inserts trailing masses that dynamically interact with the functional structure of the exo-skeleton, such that a sim-

plified abstract modeling of the geometry was conducted to account for its dynamic effects during this analyzes. This decision was made on the design documentation of the IHMC exo-skeleton series [Kwa et al., 2009], as actuation systems mounted on the rear of the construction were found to dynamically impede the human pilot during walking (see section 1.2 on page 160).

Concluding Remarks & Modeling Decision With a clear view on the previously investigated properties, at one hand, integration of the abstract actuation system in the model would be clearly preferable, as the impact on the comprehensive system characteristics is expected to be highly relevant. However, by the time of the conception of this preliminary analyzes, good initial values for these parameters were not available. Furthermore, a complete modeling would integrate 4 additional kinematic loops in the system model to be resolved during optimization computation and, with respect to the initially chosen parameters, already limit the characteristics of the system such that the preliminary analyzes is significantly blurred or might suffer from numerical instabilities. Hence, the full-featured actuation system will be considered in a subsequent analyzes. The following study is limited to the rotational joint level. The mass concentration of the driving unit of the actuation system will be considered in a first approximation fixed to limb-frame it is mounted to. The results will then be analyzed with respect to the previously described characteristics of the prospected actuation system design.

Parametric Modeling of the Exo-Skeleton

The modeling strategy of the mechanical properties of the exo-skeleton basically follows the same approach as the modeling of the human pilot (see Section 1.2 on page 168) with one substantial difference: the parametrization of its the mass. While the human pilot is globally characterized by total mass and total body length (m, l) the exo-skeleton is characterized based on its material density (strong assumption of homogeneous density though-out the part volume) and its total body mass (δ, l). Hence, the mass,

$$m_i = \delta_{\%,i} m_{\%,i} \left(l_{\text{total}} s_{l(i)} \right)^3 s_{m(i)}, \quad (12.3a)$$

the segment length,

$$l_i = l_{\%,i} l_{\text{total}} s_{l(i)}, \quad (12.3b)$$

the CoM,

$$\text{ref},i \text{CoM}_i(l_i) = \begin{bmatrix} 0.0 & 0.0 & \text{CoM}_{z_{\%,i}} l_{\%,i} s_{l(i)} \end{bmatrix}^T, \quad (12.3c)$$

as well as the inertia tensor,

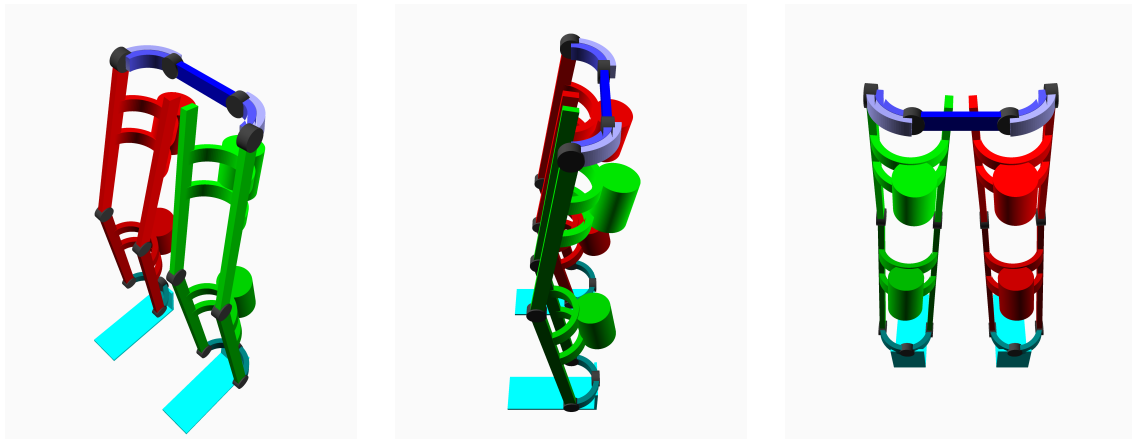
$$\text{ref},i I_i(l_i, m_i) = \begin{bmatrix} \text{CoM} I_i(l_i, m_i) + m_i \text{CoM}_i(l_i) \times \text{CoM}_i(l_i) \times^T i & \text{CoM}_i(l_i) \times \\ \text{CoM}_i(l_i) \times^T & I m_i \end{bmatrix}, \quad (12.3d)$$

are synchronized to the human model, based on the body length l_{total} , while the mass does not follow the human body but increases automatically based on the fixed density with higher body length. This modeling-decision was made to prepare for more complicated model setups, where the exo-skeleton would consist of parts that scale to adapt to the individual inter-subject variability of the patient (e.g. adaptive parts: frames, brackets, fixation mechanisms) and those that remain fixed (e.g. off-the-shelf components: mechanical transmissions. control-

components, batteries). However for the time being all parts of the exo-skeleton are assumed to scale to the geometric configuration of the human pilot.

An important aspect of this preliminary analyzes is a highly flexible and yet simple design for parametrization of the resulting geometry, for a subsequent integration into the optimization approach of the complete system (please see Section A on page 218 for a comprehensive discussion on the computation of dynamic characteristics of parametrized geometries). As for the design of this preliminary study a highly simplified geometry was used and the question about a suitable design parametrization was still an open question, decision was made to go with the approach of constructive solid geometry (see subSection 2 on page 222) but to keep the approach sufficiently flexible to exchange the underlying construction method at any-time. This would be necessary, as soon as the prospective design studies are released from the cooperation partner to be simulated and analyzed based on the same setup.

The final mechanical design of the chosen modeling approach is visualized in Figure 12.7 from different perspectives. The pelvis frame including the brackets around the hip joint are colored in different blue levels. Left and right leg are tinted in different green and red levels respectively. The foot is painted in cyan. The complete geometry has been modeled with 2 different primitives, rectangular blocks and full as well as partial cylinder splices. The computation of the resulting dynamic characteristics follows from subsection 2 on page 222. Parametrization of the geometry has been prepared but kept fixed through-out the following analyzes.



(a) Abstract schematic modeling of the dynamic structure of the exo-skeleton part of the model - perspective view

(b) Abstract schematic modeling of the dynamic structure of the exo-skeleton part of the model -front view

(c) Abstract schematic modeling of the dynamic structure of the exo-skeleton part of the model - rear view

Figure 12.7: Final model

2 Estimation of Structural Load

A critical issue in engineering products is technical failure. From a conceptional point of view the complete product safety life-cycle [Lee et al., 2012] has to be conceived carefully with respect to the targeted application, to prevent potentially hazardous incidents for any dependent third-party. This incorporates the management of the functional safety during the conception, the product development as well as the service cycle after its release towards the

proper decommission. An important aspect during the product development is the assessment of failure risk and its appropriate management by design for its software and hardware applications [Braun and Mottok, 2013, Sauer et al., 2012]. This assessments is conducted from the the early conception phase onwards and hence should be considered appropriately as well during this preliminary study. The literature of standard industrial guidelines for product development management is vast and definitely outside the scope of this work. Hence, its rigorous application is not possible in this preliminary design stage. However, the results of this study should be specifically focused towards investigations, to support at maximum future design decisions, as well about functional safety of the final exo-skeleton device and thus appropriate representation of the results data is important.

Mechanical safety of hardware is at most supported by proper decisions about design and manufacturing materials with respect of the targeted applications. Static and dynamic characteristic limits of engineering materials are very difficult to assess [Sauer et al., 2012, Shackelford, 2008], hence an accurate estimation of instantaneous and long-time load cycles during the life-span of the developed product at hand is a vital information for the choice of design and material application to prevent misconception and risk of severe mechanical failure during operation. Besides the necessary discussion of potential design concepts and proper actuation system characteristics, this preliminary study will give additional focus to estimate load information on the structural geometry of the device with respect to its articulated interfaces. This information is processed to support in parallel a proper mechanical design of the technical articulation. Thus a small discussion is given in Appendix D.

From the kinematic configuration of the exo-skeleton the most probable bearing types that

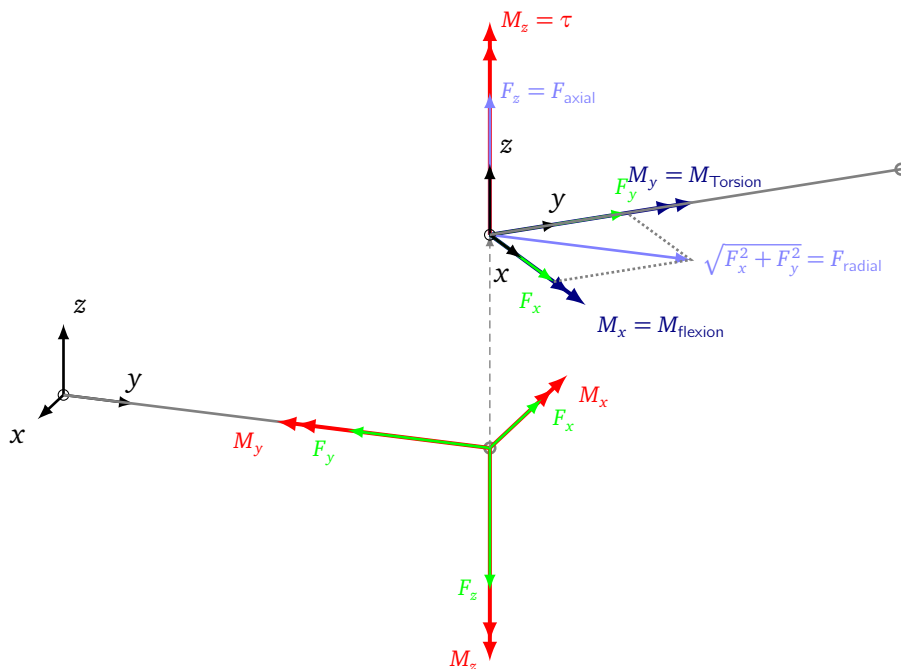


Figure 12.8: Exemplary joint scheme as it is used for the computation of the structural stress to be transmitted over the joint interface. The revolute (hinge) joint has a dof about the Z-axis - both frames are exploded correspondingly. Forces are represented in green, torques in red. The torques that are computed for the conception of the kinematic structure are highlighted with pale blue F_{axial} , F_{radial} and the corresponding torques are highlighted in dark blue $M_{flexion}$, $M_{torsion}$ respectively

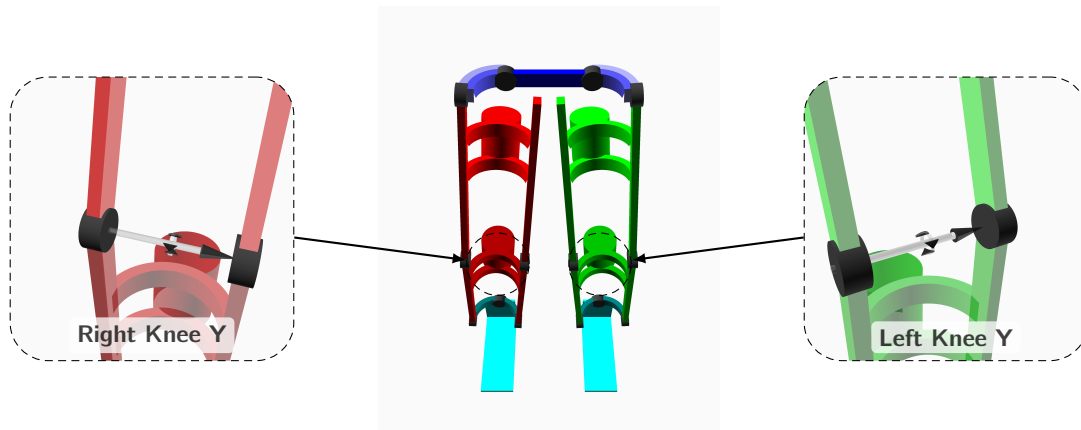


Figure 12.9: Modeling of the single joint kinematics of the Knee Joint complex. The knee joint is represented by a simple dual hinge about the Y-axis to effectively reduce flexion and torsion load in the kinematic structure. In each detailed view the joint axis with the corresponding positive rotational direction (black arrows) is shown.

will be adopted are rotational ball bearings and curved linear ball bearings. Hence it is interesting to analyze the load situation between the functional structure of the exo-skeleton, following Figure 12.8 on the preceding page. In the given example the rotational degree of freedom is realized about the Z-axis. Radial F_{radial} and axial F_{axial} load are defined around the same axis respectively. From (D.1b) and (D.1c) the maximal radial force component and its motion profile is more important than the actual dispatched magnitude with respect to the X and Y-axis. Without loss of generality the neutral position is defined when parent and child reference frames coincide with its orientation. In this configuration the torque load with respect to the transitional line between parent and child joint-center is defined as torsional load M_{Torsion} and the orthogonal component to joint-axis and the former as the flexion load M_{Flexion} . Besides the mechanical joint reactions between the components of the functional exo-structure for further investigations of the necessary geometric modeling [Gross et al., 2011, Mattheck, 2006], this data representation supports in parallel preliminary investigations about different appropriate bearing types for the prospected construction.

3 Concluding Remarks

After all governing aspects of the modeling approach have been discussed separately, one may proceed to merge both models into the simplified instance as explained in 1.1 on page 165 and continue with its exploration. The volume of the data resulting of this preliminary analyzes, should provide a first estimation of important limiting characteristics for kinematics and dynamics, critical load situations, as well as potential compatible passive/active actuator systems to best support the desired motion tasks of the prospected device. However, as stated at the beginning of Section 1.1 on page 165, various applied model simplifications introduce important limits to the applicability of the results to the real-world case, to be considered carefully. Therefore, a short discussion about kinematic and dynamic implications of the merged model in terms of the subsequent problem formulation of the optimization setup and the correct interpretation of its results will be given.

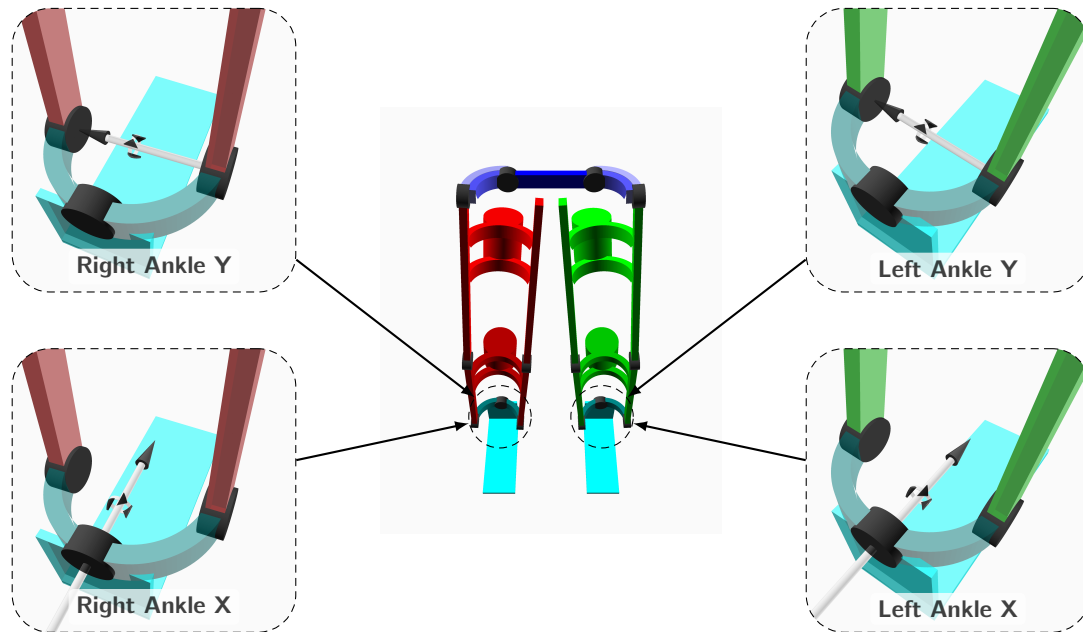


Figure 12.10: Modeling of the single joint kinematics of the Ankle Joint complex. The ankle joint is dispatched into a single hinge about the Y-axis (*left/right ankle X*) and a second hinge about the X-axis (*right/left ankle Y*). In each detailed view the joint axis with the corresponding positive rotational direction (black arrows) is shown.

3.1 Kinematic Implications

As the simplified kinematics of the exo-skeleton (see Figure 12.5 on page 173) will henceforth shadow the highly complex and variable human kinematic of the lower limbs (compare Section 1 on page 239 in Appendix C) the human pilot is forced to move in concert with the exo-skeleton. While the hip and the knee joint are at least compatible with the simplified kinematic modeling of the exo-skeleton, it is clearly not the case for the ankle joint complex (compare Section 1 on page 239 in Appendix C). This fact is problematic and raises the following two aspects to be considered during the analyzes of the results.

The prospected motion of the task to be investigated will be obtained from a healthy human specimen. Hence, it is assumed that the kinematics are most probably not fully compatible with the modeled joint complex at the ankle. Therefore, the configuration of the foot ground contact in the optimization setup might provoke slightly unnatural motion of the feet. From [Diebel, 2006] it is clear that orientations resulting from a 2 dof single rotational joint complex may not be rigorously recovered by a 2 dof joint complex with a different configuration of the joint axis compared to the former. Hence, these misalignments, which are not-visible in the following analyzes, will most probably be supported either by the human soft-tissue and bone structure or a relative motion of the foot against the exo-skeleton structure. Therefore, this issue should be ultimately investigated in subsequent iterations of this study.

3.2 Dynamic Implications

The merge process of the dynamic characteristics per segment is done based on (A.11) (see Appendix A) following the governing kinematic structure of the exo-skeleton. This implies at one hand, that the simplified dynamic tree structure of the exo-skeleton will show close

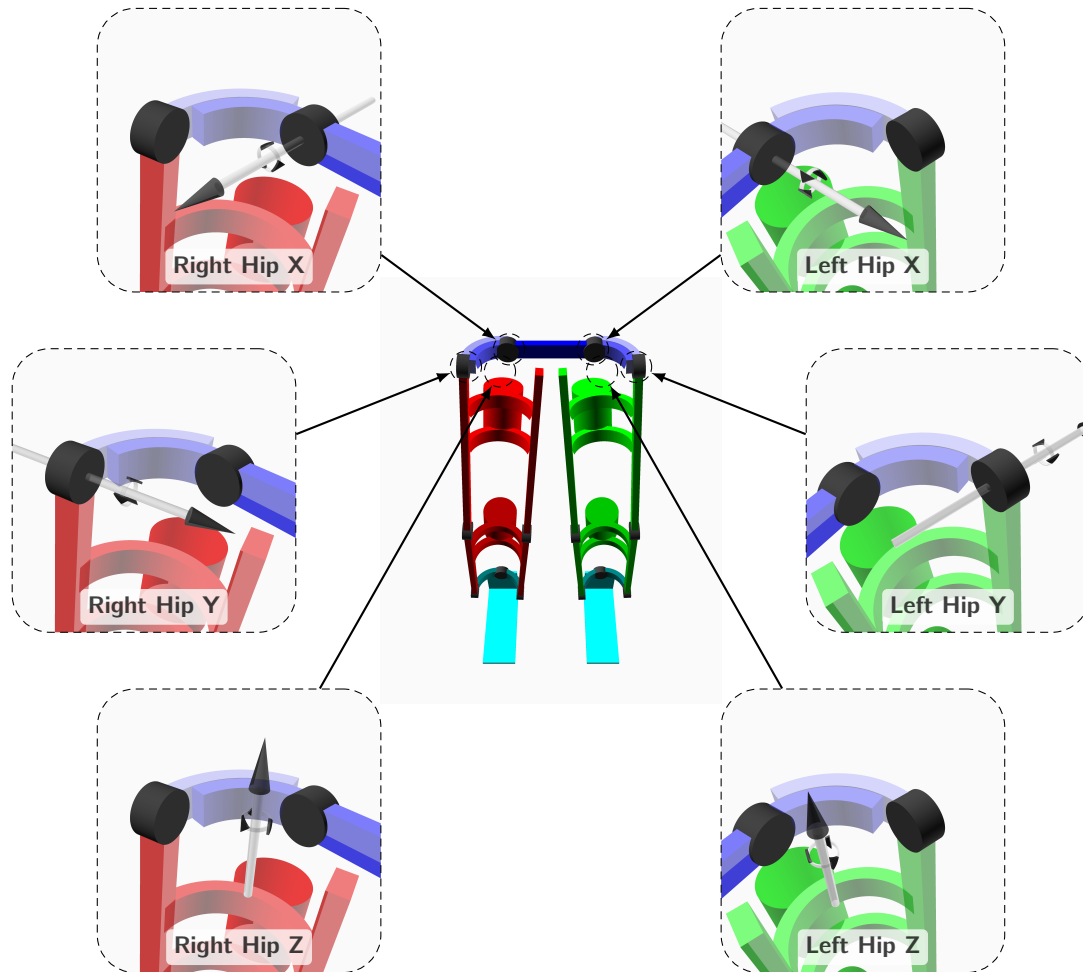
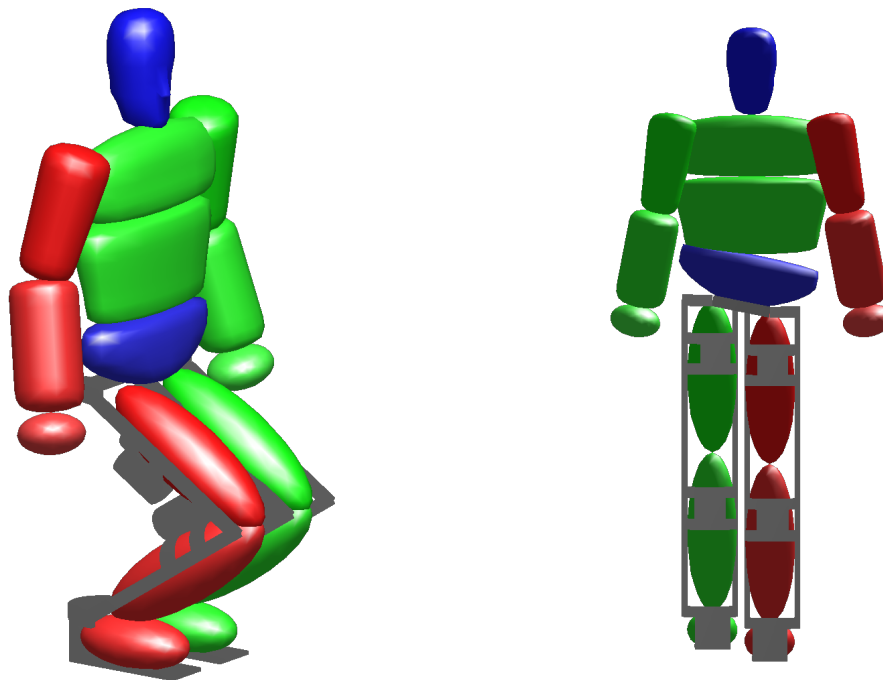


Figure 12.11: Modeling of the single joint kinematics of the Hip Joint complex. The hip joint represents a 3 dof flexibility. The technological solution of the tedious task to shift the technical joint center close to the natural one of the human operator results in a complex kinematical setting. The order is as follows: From the pelvic frame a rotation about the X-axis (*right/left Hip X*) is achieved with a hinge. The rotation about Z (*right/left Hip Z*) is done with a revolute linear joint and the rotation about the Y-axis (*right/left Hip Y*) finally build with a further hinge. In each detailed view the joint axis with the corresponding positive rotational direction (black arrows) is shown.

dynamic characteristics to the desired setup of a human pilot effectively wearing the exoskeleton, however this modeling approach has some important limits that should be briefly outlined:

As discussed above, miss-alignment of the human soft-tissue joints and the rigid exo-skeleton structure is technically suppressed. Hence it will not be possible to capture the additional mechanical load originating from the elastic linkage between the human pilot and the exoskeleton during dynamic motions.

Further the distribution of the mechanical load in the construction differs to the case of an exo-skeleton, mechanically dispatched from the human pilot, in that sense that the proposed setup should be considered as if the exo-skeleton is directly fixed to the human bones. In the case of human soft tissue load transmission will most probably be orthogonal to the contact surface [Jarrassé and Morel, 2012]. Depending on different kinematic configurations the



- (a) Crouched posture of the modeling setup. As the human pilot is mostly seated on the exo-structure the dynamic load from the torso may directly be transferred orthogonal through the contact surfaces to the exo-skeleton structure.
- (b) When standing on *one* leg only contact surfaces orthogonal to the load direction are the foot-folds. Hence, the load from the upper torso travels through all the bones towards the feet until it may enter the exo-skeleton structure.

Figure 12.12: Two different example key frame configurations that will lead to highly different load distributions as soon as the contribution of the human pilot with respect to the joint actuation diminishes. The depicted posture in Figure 12.12a results in a short and direct load transmission path. In Figure 12.12b the load needs to travel from the lifted left foot further through the complete structure before it arrives at the right foot in contact with the ground. This creates a more complex mechanical load distribution.

dynamic load of the human will then either be supported by smaller, Figure 12.12a, or larger, Figure 12.12b, load path [Albers et al., 2009] in the functional structure. The longer these load paths get, the higher its probability of accumulation, leading to complex structural stress probabilities. Assessment of the necessary actuation profile may not distinguish between the contribution of the human pilot and the exo-skeleton. The simulation computes a resulting actuation that is needed to produce the desired dynamic motion with the complete model setup.

4 Equations of Motion

After thorough discussion of the modeling strategy and all performed simplifications the model should be expressed in mathematical form to be embedded in the problem formulation presented in the next chapter. The branched tree structure finally consists of 32 dofs, 6 dofs as free motion linkage to the global reference frame, 12 dofs in the lower limb structure, 6 dofs for head to upper torso to pelvis junctions and finally 4 dofs for each arm. The hands have been modeled dynamically but the wrist was frozen, as its contribution to the overall

dynamics of the desired tasks motions was determined to be of minor importance. Although, the initial coordinate setting of the free moving model is not minimal as soon as contact with its environment with one or multiple limbs does occur, will be preserved throughout the complete simulation setting. Contacts with the environment will always be represented with single contact points and resolved in 6D, three translations and three rotations (compare Section 3.3 on page 32). Redundancy in the coordinates will then be computed by resolution of the evolving kinematic loops. The resulting dynamic equation is then expressed as DAE system of index 3 formulated in the so-called descriptor form,

$$M(q, p) \ddot{q} + NLE(q, \dot{q}, p) + C(q, p) - J(q, p)^T \lambda = \tau, \quad (12.4a)$$

$$g(q, p) = 0. \quad (12.4b)$$

In this equation $M(q)$ represents the joint space inertia matrix which consists of the merged inertia matrices for each distinct moving limb in the exo-human model,

$$M = \left(\sum_{k=0}^{N_{\text{Bodies}}} J_k^T I_k J_k \right). \quad (12.4c)$$

$NLE(q, \dot{q})$ represents the nonlinear effects (e.g. Coriolis). In order to keep the formulation compatible with forward and inverse dynamics computation, e.g. for optimization or convenient complementary initial value generation (compare Chapter 5), all additional influences that are not rigorously part of the joint actuation system, e.g. spring/damper systems, should be contained in this quantity.

$$NLE = \sum_{k=0}^{N_{\text{Bodies}}} J_k^T (I_k \dot{J}_k \dot{q} - J_k \dot{q} \times^* I_k J_k \dot{q}). \quad (12.4d)$$

J_k represent the spatial Jacobian to the local reference frame of the link k respectively. I_k is the spatial inertia matrix of link k .

Parametrized gravity effects are considered with the term $C(p, q)$. τ represents the system's actuation as torque on the joint-level (rotational). The term $g(q)$ expresses the scleronous position constraints, that will be expressed with respect to the local contact coordinate system. For higher computational efficiency, this is transformed into a DAE system of index 1,

$$\dot{q} = v, \quad (12.5a)$$

$$\dot{v} = a, \quad (12.5b)$$

$$\begin{bmatrix} M & -J^T \\ J & 0 \end{bmatrix} \begin{bmatrix} a \\ \lambda \end{bmatrix} = \begin{bmatrix} -NLE - C + \tau \\ -\gamma \end{bmatrix}. \quad (12.5c)$$

In forward dynamics, algebraic variables λ (equivalent to the contact constraint forces) and acceleration \ddot{q} values are computed from given system's state q, \dot{q}, τ . Additionally, the order reduction of the DAE requires that the consistency constraint (compare Chapter 2 on page 19) are fulfilled. The term J is the classical (not the spatial!) analytical 6D Jacobian and $\gamma = \frac{\partial}{\partial t}(J) \dot{q}$ its time derivative multiplied by the velocity vector respectively that contains all active constraint directions in the contact points.

When the projected pternion or the projected metatarsale landmarks 12.3 on page 170 enter in contact with the ground, this is modeled as an inelastic impact causing discontinuities in the joint velocities, which can be computed by the following equation. \dot{q}^- and \dot{q}^+ represent the velocity configuration before and after the impact respectively and Λ holds the complex

impact impulsion,

$$\begin{bmatrix} M & -J^T \\ J & 0 \end{bmatrix} \begin{bmatrix} \dot{q}^+ \\ \Lambda \end{bmatrix} = \begin{bmatrix} M\dot{q}^- \\ 0 \end{bmatrix}. \quad (12.6)$$

The dynamic equations are again composed analytically, optimized and converted into C-code by means of the dynamic model builder *DYNAMOD* (refer to Chapter 3).

13 Problem Formulation - Walking Studies

As the modeling and its implications for the results of the optimization study have been thoroughly discussed it is in the following embedded into the context of the optimization setup to investigate the characteristics of a specific dynamic motion task. On one hand, different motion tasks necessity different physical characteristics on the other hand the motion tasks themselves are highly dependent on the individual kinematic and dynamic properties of the human pilot. Hence, a comprehensive investigation should be based on both: a complete set of all limiting motion tasks to define a convex setting of the characteristics to allow for all considered motion tasks to be performed as well as a sufficiently feature reach assembly of individual specimens performing the tasks to assess how accurately the convex setting of the necessary characteristics of the prospected device may be defined.

Due to time constraints, this preliminary study had to be limited to a small sub-manifold of tasks, namely different straight line walking motions and the sufficiently accurate walking data of one subject (body height $1.9m$, body weight $76.0kg$) received clearance for scientific exploitation. Different specimens, at least for the dynamic data, was then achieved by rescaling the target model to different body weights such that approximately the same kinematic motion data could be used over all the investigation trials.

Consequently, results of this investigation already give interesting insights into the essential dynamic characteristics of the prospected device, however for a stochastic significant representation of a given target population and a comprehensive benchmark definition of the prospected device this investigation clearly needs to be extended to a larger set of task motions, performed by a significantly representing sub-set of human specimens.

The technique adopted for all subsequent computations is to fit the task motion of the real specimen against the dynamic model setup and to observe how controls and parameters of this setup evaluate in comparison over the different task motions and and the different human specimen performing it.

1 Scope of this Simulation

The purpose of this study is the preliminary investigation of the implications introduced by the altered kinematic constraints and the augmented dynamics of different humans walking in a straight line on level ground, effectively wearing the exo-skeleton. Furthermore, it is interesting to compare these results with the same setting walking straight line up and down a slope of varying angle of elevation. As previously discussed (see Section 1 on page 1), bipedal walking motions provide potential simplifications in the mathematical problem formulation, upon the two relative strong assumptions that: the motion is periodic over one stride and symmetric over one half-stride (step). Despite the given deviation from the symmetry the motion may contain, these assumptions are reasonable for this analyzes and hence the optimization problem will only be formulated on a half stride.

A typical result for level ground walking is shown in Figure ?? on page ??. While the trajectories of CoM and Waist in XZ-plane (Figure 13.3a on page 192) are reasonable periodic over the subsequent strides the projected one in XY-plane (Figure 13.3b on page 192) shows small deviations from a symmetric and periodic trajectory profile. The magnified scale (by 6

times) in Y for clearer visibility, however signifies that deviations are small compared to the overall trajectories and it was concluded that the other half of the stride would not present significantly different optimization results.

Hence the study was conceived on seven sets containing 15 simulations each (see Table 13.1). An additional 7 simulations were computed for verification purposes of the optimization problem formulation, as it will be discussed below.

Table 13.1: Sets of simulations that were conducted during this preliminary study. A set always consists of a distinct slope angle and all possible combinations for exo-skeleton and Human Pilot mass.

Num of Simulations	slope angle [DEG]	Human Mass [kg]	Exo Mass [kg]
x15	0.0	60.0, 70.0, 76.0, 80.0, 90.0	10.0, 20.0, 30.0
x15	+2.5	60.0, 70.0, 76.0, 80.0, 90.0	10.0, 20.0, 30.0
x15	+5.0	60.0, 70.0, 76.0, 80.0, 90.0	10.0, 20.0, 30.0
x15	+7.5	60.0, 70.0, 76.0, 80.0, 90.0	10.0, 20.0, 30.0
x15	-2.5	60.0, 70.0, 76.0, 80.0, 90.0	10.0, 20.0, 30.0
x15	-5.0	60.0, 70.0, 76.0, 80.0, 90.0	10.0, 20.0, 30.0
x15	-7.5	60.0, 70.0, 76.0, 80.0, 90.0	10.0, 20.0, 30.0

1.1 Investigation of Suitable Event Sequence

Figure 13.1 on the next page shows a typical walking sequence equivalent to [Dollar and Herr, 2008], featuring the specific motion phases with respect to the various physical contact states, e.g. swing and stance, including the partially non-continuous transitional events. As it was discussed in Chapter 4 on page 42 the implementation of the optimal control solver does not support random permutation of the phase sequence, hence for the quality of the results, it is critical that a proper *a priori* estimation of the phase sequence is made that fits perfectly to the given task motion. For phase is 1, 3 and 4, this information is well distinct from the motion capture data. However, the transitions before and after phase 2 are critical as it may not be clearly determined from the point cloud data and force plate measurement whether Sequence A, *Event: Toe off* before *Event: Toe strike*, or Sequence B, *Event: Toe strike* before *Event: Toe off*, would be most appropriate one for the given problem formulation. Within this respect, potential implications of the adopted mathematical non-elastic foot modeling based on contact points are difficult to assess and hence should be solved with respect to the comprehensive problem formulation. The adopted technique in the following is to compute sample analysis for both sequences and to compare its quality of fit to find the most appropriate one.

This method should be used with great care - compare Chapter 5 - as the optimal control solver efficiently exploits any infeasibility to maximize the specified objective (compare Section 3 on page 66). In case these infeasibilities are physically related the results risk to be highly misleading. However, in the given situation the physical correctness will not be influence, thus the method fits the purpose.

1.2 Problem Formulation

All subsequent studies are based on a particular OCP formulation that consists of a combination of a continuous Lagrange-type objective and a discrete least square term formulated on

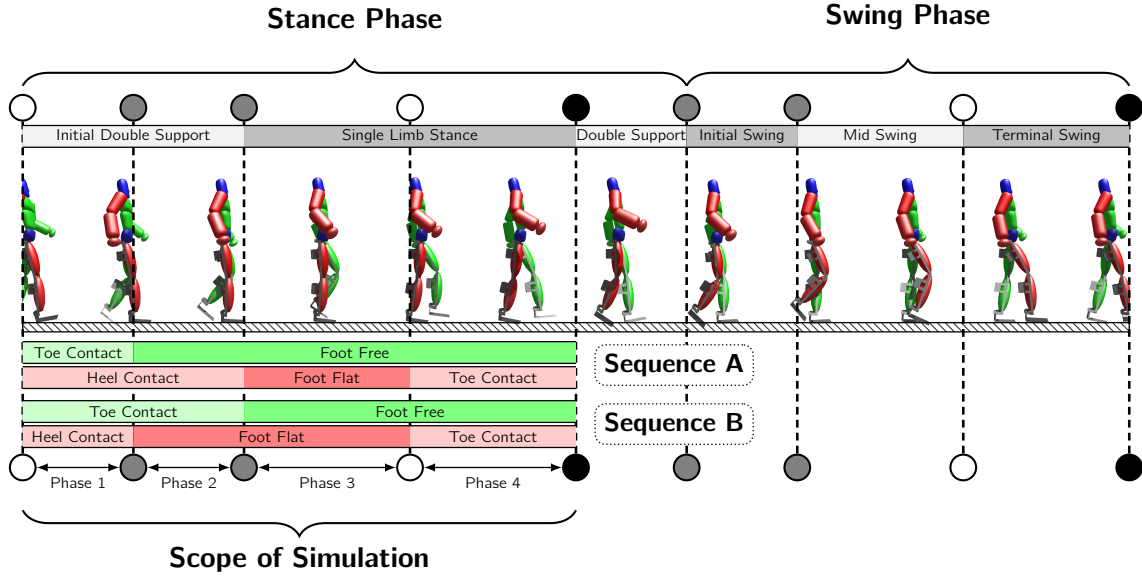


Figure 13.1: The two investigated plausible phase sequences of the walking motion. Dashed lines signify phase transitions, the type of the phase transition is noted with the upper and lower circles. White shows continues phases transitions, black show discontinues phase transitions and gray circle notify that the transition is continues or discontinues following the choice of the sequence. Contact state of the left and right foot are drawn in green and red, respectively. Contact phases are distinct with different brightness levels.

each shooting node (compare Chapter 4) over the model stage scheme given in Figure 13.1,

$$\begin{aligned} \min_{x(\cdot), u(\cdot), p} \quad & \sum_{i=1}^{n_{\text{mos}}} \int_{\bar{t}_{i-1}}^{\bar{t}_i} \Phi_i(x(t), u(t), p) dt + \frac{1}{2} \sum_{s=0}^{n_{\text{shooting}}} \sum_{l=0}^{n_{\text{dof}}} |q_l(t_s) - y_l(t_s)|_{C_{q_k^s}}^2, & (13.1a) \\ \text{subject to} \quad & \dot{x}(t) - f_i(t, x(t), u(t), p) = 0, \quad t \in [\bar{t}_{i-1}, \bar{t}_i], & (13.1b) \\ & x(\bar{t}_i^+) - h_i(x(\bar{t}_i^-)) = 0, \quad i \in \{1, 2, \dots, n_{\text{mos}} - 1\}, & (13.1c) \\ & r_{\text{eq}}(x(\bar{t}_{i-1}^+), x(\bar{t}_i^-)) = 0, \quad i \in \{1, 2, \dots, n_{\text{mos}}\}, & (13.1d) \\ & r_{\text{ineq}}(x(\bar{t}_{i-1}^+), x(\bar{t}_i^-)) \geq 0, \quad i \in \{1, 2, \dots, n_{\text{mos}}\}, & (13.1e) \\ & g_i(x(t), u(t), p) \geq 0, \quad t \in [\bar{t}_{i-1}, \bar{t}_i], & (13.1f) \\ & \underline{u} \leq u \leq \bar{u}, & (13.1g) \\ & \underline{x} \leq x \leq \bar{x}. & (13.1h) \end{aligned}$$

The discrete least square term is formulated as fit of the joint trajectory profiles towards the desired motion task (in this study – walking). The combination with the continuous Lagrange-type is specifically tuned to maintain a good quality of the fit (e.g. prevent *over-fitting*). Optimization is performed with respect to the multi-point boundary value problem consisting of the system dynamics (13.1b), equality and inequality boundary constraints (13.1d), (13.1e) for all model stages j . Furthermore, continuous path constraints (13.1f) as well as box-constraints (limits) on system states (13.1h) and controls (13.1g) are formulated.

The expression $\sum_{s=0}^{n_{\text{shooting}}} (\cdot)$ denotes a complete enumeration over all multiple shooting nodes k of all model stages i in the discrete least square term (see model stage scheme in Table 13.2). \bar{t}_i^+ and \bar{t}_i^- denote the specific instant of phase transition, the former before and the latter

after the phase transition. Without loss of generality it is assumed that $\hat{t}_s = 0$. f_i is the phase dependent right hand side of a first order ODE.

Specifically in this problem formulation the state vector of the system $x = [q \ \dot{q} \ \tau]^T \in \mathbb{R}^{102}$ comprises joint positions $q \in \mathbb{R}^{36}$, the velocities $\dot{q} \in \mathbb{R}^{36}$ (reduction to first order ODE) and the joint torques $\tau \in \mathbb{R}^{30}$. The controls $u \in \mathbb{R}^{30}$ are once integrate before they are injected into the system as joint torque τ . Therefore, the control discretization is equivalent to plci. Continuity of the first derivative of the joint torque trajectories during phase transitions needs formulation of further constraints. This was omitted in this OCP formulation. h_i expresses characteristics of the phase transition $(i - 1) \rightarrow (j)$ (e.g. inelastic impact). $f^i, r_{eq}, r_{ineq}, g^i$ are vector functions with correspondent dimension. The end time of each phase has been assumed fixed, and hence is not explicit part of the problem formulation.

The configuration of the OCP formulation of sequence A for level-ground walking consisting of multiple shooting nodes, fixed durations and contact states for each model stage is given in Table 13.2. For each slope and sequence the configuration was specifically adjusted to the initial reference from motion capturing. The different model parametrizations were then computed on the specific sequence-slope configuration. The set-up was tuned towards a trade-off between high accuracy and medium to high computational complexity.

Table 13.2: OCP formulation for sequence A – level-ground walking: Model stage scheme, Multiple Shooting nodes and initial multiple shooting interval time per model stage

N	MS Nodes	Time	Left-Foot	Right-Foot	Description
DS(0)	5	0.083s	Toe Contact	Heel Contact	Double Support
TR(1)	1	0.000s	Lift-Off	Heel Contact	Continuous Transition
SS(2)	3	0.050s	Free	Heel Contact	Single Support
CH(3)	1	0.000s	Free	Toe Strike	Discontinuous Transition
SS(4)	12	0.317s	Free	Flat Contact	Single Support
TR(5)	1	0.000s	Free	Heel Lift-Off	Continuous Transition
SS(6)	7	0.092s	Free	Toe Contact	Single Support
Σ	30	0.542s			

Integration of Ground-Slope

As it was discussed in Chapter 2, 6D contact modeling in the model processor *DYNAMOD* is independent from the external geometry, the contact is modeled with. However, in the mathematical problem formulation it is easier not to incline the ground floor layer, but to re-orient the gravity field towards the correct slope angle with respect to the ground layer. Within this respect the recorded reference of the motion task is altered to reflect the new global reference frame. All reference motions will then show the same qualitative shape as in Figure 13.3 on page 192. For a more convenient visualization the motion data is then projected back to the initial global reference.

Objectives

The objective during all subsequent studies has been weighted to a dominant discrete least-square term and a sub-dominant Lagrange-type term to contain a minimization of the joint

torques,

$$\Phi_{\min \text{ Torque}} = \omega_{\min \text{ Torque}} \sum_{s=0}^m \tau_s^2, \quad (13.2a)$$

and the first order derivation of the joint torques,

$$\Phi_{\min \partial \text{ Torque}} = \omega_{\min \partial \text{ Torque}} \sum_{s=0}^m \dot{\tau}_s^2. \quad (13.2b)$$

This should smooth the trajectory profiles of the resulting fit as it prevents the optimization from applying excessive control reactions to rigorously minimize the error between the model and the reference motion.

The motion data that is used for the discrete least-square originates from point cloud data that was measured with a motion capturing system. The motion capturing data is re-projected on the nonlinear kinematics of the model following an inverse kinematics fit method of [Sugihara, 2009]. The measurement error of the point cloud data that should usually be provided by the motion capturing system was not available by the time of this analyzes. Therefore, error propagation could not be performed and hence, $C_{q_k^*,s}$ is assumed to be the identity matrix. Consequently, the trajectory profile samples of the desired motion task in joint space have been assumed to be uncorrelated and distributed with respected to $\mathcal{N}(0, 1)$. However, a short outline to a possible first approximation of the error propagation through the inverse kinematics fit of [Sugihara, 2009] is given in E.

Constraints

The constraint set includes the consistency constraints, path constraints as well as the boundary constraints. The boundary constraints act as implicit phase switches to the simulation physical correct, although this problem formulation does not contain the time as explicit parameter to be optimized.

Path Constraints The constraint-set contains the path constraint to maintain the uni-lateral force constraint in all foot-ground contact points and a simple inequality constraint on the vertical coordinate on the external landmarks of the feet (see Section 1.2 on page 170) to prevent the swing foot from penetration of the floor. Ground friction was not modeled. In contrast to the problem formulation of HRP-2 N° 14 (compare Chapter 6) no minimum ground clearance was enforced either to embed a maximum of flexibility to the problem formulation to adopt the desired motion task.

Boundary Constraints From Figure 13.1 on page 187 the boundary constraint arrangement follows. In Sequence A the contact constraint reactions of the left foot must vanish before lift-off (Phase 1→2), as soon as the foot fold of the right foot is parallel to the ground layer the toes collide with the ground, toe strike (Phase 2→3), the projected pternion landmark was already at ground level. As soon as the component of the ground reaction contact torque parallel to the ground level and orthogonal to the line of projected metatarsale fibular and projected metatarsale tibiale landmark vanishes, the ground reaction on the projected pternion landmark is equivalently zero and the heel may lift of ground (Phase 3→4). Finally the projected pternion landmark of the left foot reaches ground level and triggers the heel strike (Phase 4→End). In contrast, sequence B the toe strike of the right foot occurs before the lift off of the left foot.

2 Tool-Chain

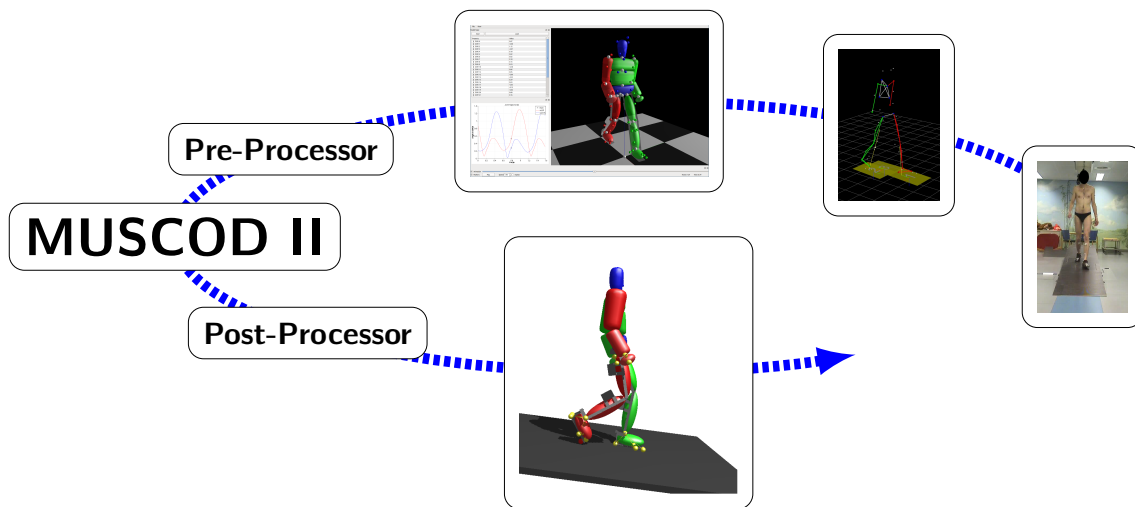


Figure 13.2: Toolchain that has been used to conduct this preliminary study. Walking motion on level ground and various slopes walking up as well as walking down has been registered with a Vicon motion capturing system under clinical conditions.

Figure 13.2 shows the complete structure of the tool-chain for the preliminary study. First the tasks motion were recorded from a healthy specimen under clinical conditions (specimen: author - 76.0 kg total body weight, 1.90 m total body length) with a Vicon motion capturing system including force plate measurements. The motion capturing data has been intensively analyzed with tools originating from the *bio-mechanics toolkit* [Barre and Armand, 2014]. However, gait event detection only partially succeeded with tools from [Ghoussayni et al., 2004], such that the subsequent model verification on each task motion sample was necessary to assess the quality of the modeling hypothesis in the problem formulation. Final decision about the proposition of gait events has been revised after rigorous visual inspection. Next the point cloud information need to be transformed into a model based representation, to be introduced into the previously explained problem formulation. Additionally during this step individual parameters, such as the particular limb lengths need to be detected and registered to the parametrized model setup such that model has maximum of kinematic and dynamic compatibility to motion task. A desirable approach would have been e.g. the automatically reconfiguring skeleton estimation method described in [Kirk et al., 2005]. The available walking motion trajectories were not sufficient to resolve all ambiguities of the complex model kinematics. Such that a highly successful approach of a different project, including the implemented software *Puppeteer*, has been adopted and embedded into the tool-chain. This method is thoroughly based on visual inspection. In a 3D model visualizer, distinct key-frames are selected and the model is manually adjusted such it fits best into the point-cloud. Finally the kinematic motion trajectory is estimated from these previously configured key-frames with an inverse kinematics based Levenberg-Marquardt method [Sugihara, 2009]. The resulting motion trajectories and its model are analyzed and pre-processed with respect to the gravity field and the global reference frame. An example of the resulting data is shown in Figure 13.3 on page 192. All walking simulations are recomputed to the level ground case with the corresponding gravity field orientation. After successful convergence of the optimal control solver the inverse process is applied for visualization and analyzes and comparison of the results. Pre- and post-processor software tools are equipped with on-line-plotting func-

tions based on the *Visualization Toolkit* and publication ready plot functionality based on \LaTeX 's powerful pgfplot package. Visualization during pre- and post-processing is done on the highly versatile tool MeshUp [Felis, 2014a].

3 Verification & Tuning of Problem Formulation

Table 13.3: Comparison of RMS-Error of the converged fit with either Phase Sequence A or B - these values have been employed as quality estimation and decision has been made to adopt either A or B for the computation of the preliminary study.

Slope angle [DEG]	\sum RMS-Error Sequence A	\sum RMS-Error Sequence B	Decision
0.0	0.288	0.434	Sequence A
+2.5	0.286	0.462	Sequence A
+5.0	0.356	0.440	Sequence A
+7.5	0.379	0.430	Sequence A
-2.5	0.300	0.345	Sequence A
-5.0	0.335	0.391	Sequence A
-7.5	0.388	0.427	Sequence A

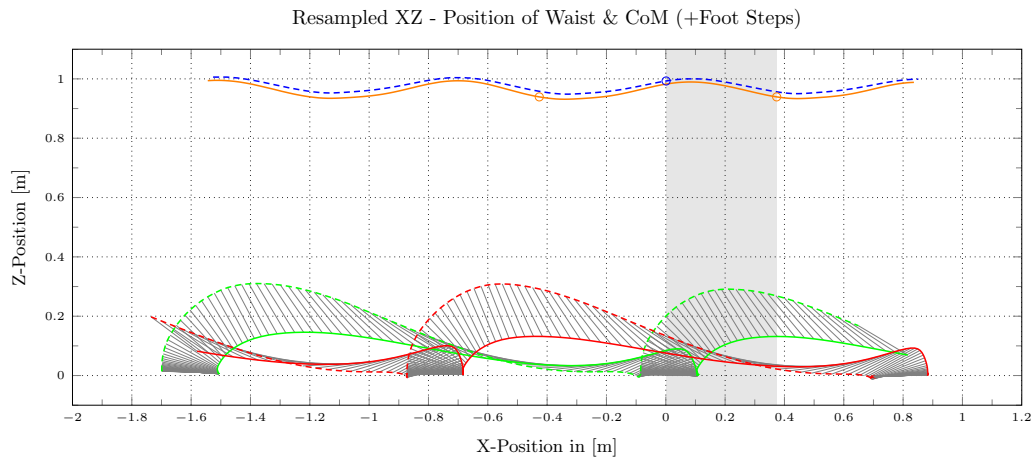
As it was previously outlined, before intensive computations are launched, one need to verify whether the chosen phase sequence in the problem formulation appropriately approximates the given task motion with respect of the kinematics, dynamics and the contact modeling, respectively. For this purpose 14 pre-trials have been conducted and its quality of fit was measured with the summed RMS between the resulting trajectory profiles of the optimization problem and the reference originating from the motion capturing experiments.

From Table 13.3 it is well observable that Sequence A produces higher fit qualities than Sequence B. Hence all subsequent 105 simulations of this preliminary study were computed based on Sequence A. However, one should note this result is highly individual, thus for another task motion even from the same human specimen this investigation has to be reconsidered to check whether the problem formulation is appropriately configured.

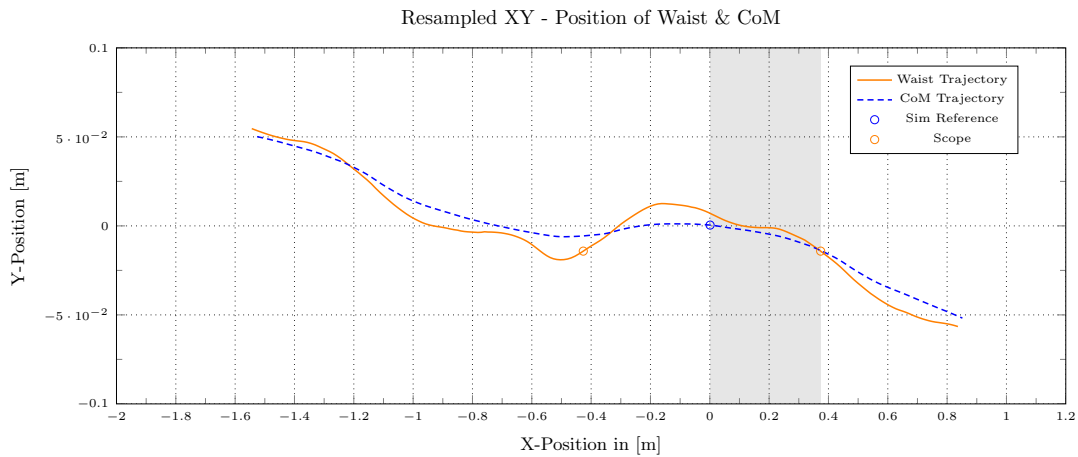
Even though the modeling of the foot contact during the 14 pre-trials has been configured as flexible as possible (compare Section 4 on page 182) per joint RMS error showed larger deviations for the joints directly related to the limbs in contact with the environment, e.g. ankle roll, ankle pitch as well as the global free-floating base (see Figure 14.2 on page 194). Consequently, it was concluded that the initial kinematic motion reference originating from [Sugihara, 2009] was not sufficiently accurate with respect to the strict mathematical contact modeling, although from visual inspection the motion looks correct (see Figure 13.3 on the following page). Thus, importance of the Lagrange-type objective with respect to the discrete least-square was increased to support at maximum the trade-off in the investigation of a motion that represents at best the given motion reference of the initial task motion, but is compatible to the kinematics of the contact constraints without the provocation of excessive control reactions.

As previously discussed in Chapter 5 the quality of the discretization greatly depends on the control type and the number of multiple shooting nodes. Based on the experience made in the previous works control type was fixed as piecewise linear and the model was conducted in forward dynamics with the controls once integrated to produce smooth trajectory profiles. The node count for all simulations of this preliminary study was fixed to 31, as that proved to be highly sufficient for comparable studies. However, as soon as selected features from the

overall study have to be investigated more precisely based on the comprehensive whole body approach these tuning parameter will have to be revisited and adjusted again.



(a) Re-sampled motion from motion capturing data in XZ plane with foot fold motion, waist and CoM trajectory of the model



(b) Re-sample motion from motion capturing data in XY plane with foot fold motion, waist and CoM trajectory of the model. The Y-scale has been magnified about 6-times for a clearer visibility on the CoM and Waist Trajectory profile.

Figure 13.3: Re-sample motion from motion capturing experiments projected into XY and XZ planes. The reference (blue circle) as well as the part subtracted as initial values for the optimization setup (gray area) have been marked separately.

14 Walking Studies

In the following selected results among all 105 converged simulations will be presented and its implication for the current state of conception as well as for subsequent more detailed studies to further substantiate the model base towards a realistic design to be built outlined. For an efficient discussion first the results of the level ground study will be discussed, further explanations are then given in case this particular result changed between the level ground and the slope walking case. Finally the slope walking case is then comprehensively compared to the level ground walking case.

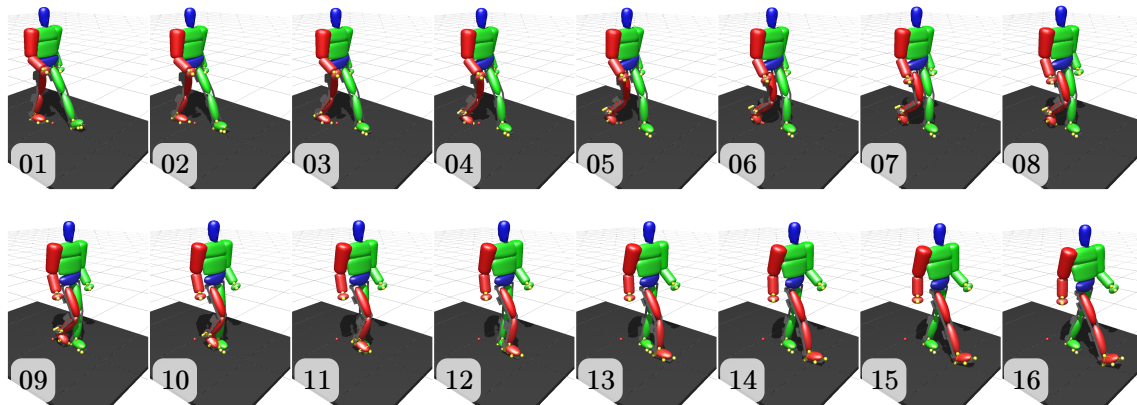


Figure 14.1: Image sequence of the post-processed optimization result, half-cycle walking motion of the exo-skeleton-Human assembly.

1 The Level-Ground Case

Figure 14.2 on the next page shows small average RMS-Errors, in the range of $[0.0, 3.3] \times 10^{-2}$ [RAD], and standard deviation, in the range of $[0.0, 3.8] \times 10^{-3}$ [RAD]. Hence deviations between the single simulations are relatively small. Furthermore, the upper torso including the arm motion is not part of any kinematic loop and thus deviation from the motion reference is the smallest. The lower body limbs, green and red highlighting, are part of the kinematic loop with respect to the foot ground contact in single support and part of multiple kinematic loops in case of double support. In addition the foot must respond to an even more constraining configuration as soon as the foot-fold is firmly placed to the ground. Thus, from the description in [Sugihara, 2009] one would expect higher deviation from the reference motion as these kinematic constraints are not considered during the transformation of the reference task motion from the initial point cloud of the motion capturing experiments. This shows the agreement of the form of the final results with the previous discussion and related decisions from Chapter 12 and 13.

In the following the comprehensive results of trajectory profiles and kinematic as well as dynamic characteristics resulting from the level ground study will be presented and thoroughly discussed with respect to the conception of the prospected device. The color convention for

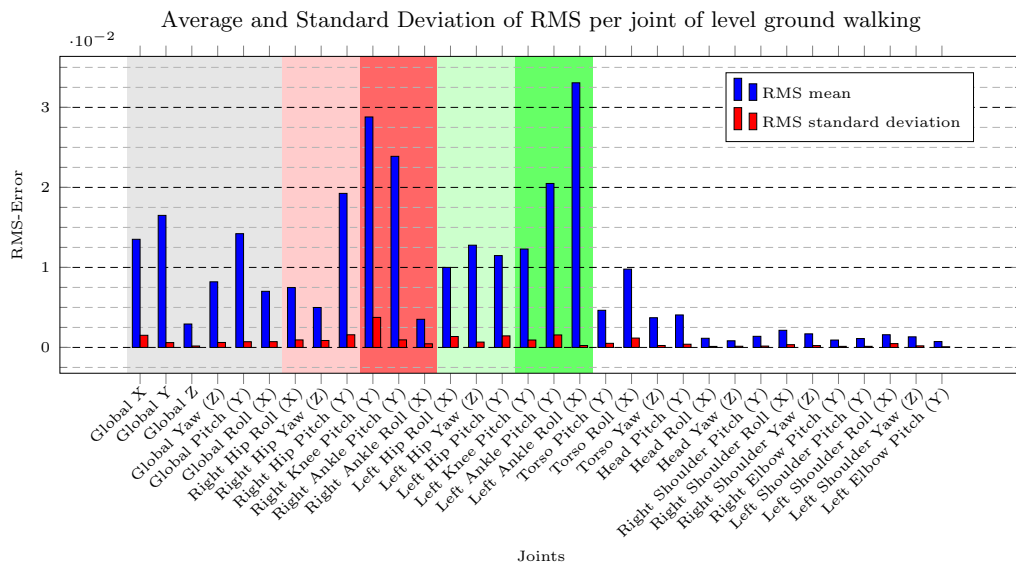


Figure 14.2: Average and Standard deviation of RMS errors per joint of the level ground case. The global free-floating joint is marked with the gray area. The left and right leg are marked with green and red area, respectively. In addition the knee as well as the ankle joint complex are marked in dark.

all plots will be defined in Hue Saturation Value (HSV) color a space. Distinct exo-skeleton masses are marked with different hue values, and human mass values with different brightness values, the higher the mass the less bright the color strip.

The representation of the results will be focused to the global questions below:

1. What are governing characteristics: min, max and variability of the joint trajectory profiles, e.g. angular value and velocity as well as the actuation torque, such that a preliminary choice of suitable actuation system performance for each joint is possible.
2. Is it possible to observe flow cycles of energy in the motion characteristic of each joint? This helps to identify energy dissipation or dynamic energy storage/release characteristics, which could lead to the integration of passive or actively controlled spring damper systems to efficiently support the active actuation system and to improve overall energy consumption and autonomy of the device.
3. How do the technical tasks of weight support, bipedal propulsion and balance control translate into the load configuration of the articulations and hence to the internal stress of the frame parts of the prospected device. Such that it will be possible to make a first preliminary choice of suitable bearing constructions and deselection of unsuitable solid body structures for the design of the functional structure of the device.
4. How do the above values change with respect to different body-masses of the human pilot and different masses of the exo-skeleton? Which aspect has a greater influence on the variability of the results? - How do the balance characteristics are altered on variation of the masses?

In the following result section, the convention for a spring damper system will be in conjunction with the definition of the actuation direction in rigid MBSs, without exception, such that a positive deviation of the spring-damper complex from the static zero-pose always provokes

a negative reaction force back towards the zero-post. Thus the resulting hysteresis curve is flipped about the vertical axis compared to most hysteresis curves found in classical textbooks for vibrational mechanics.

1.1 Joint-Complex::Hip

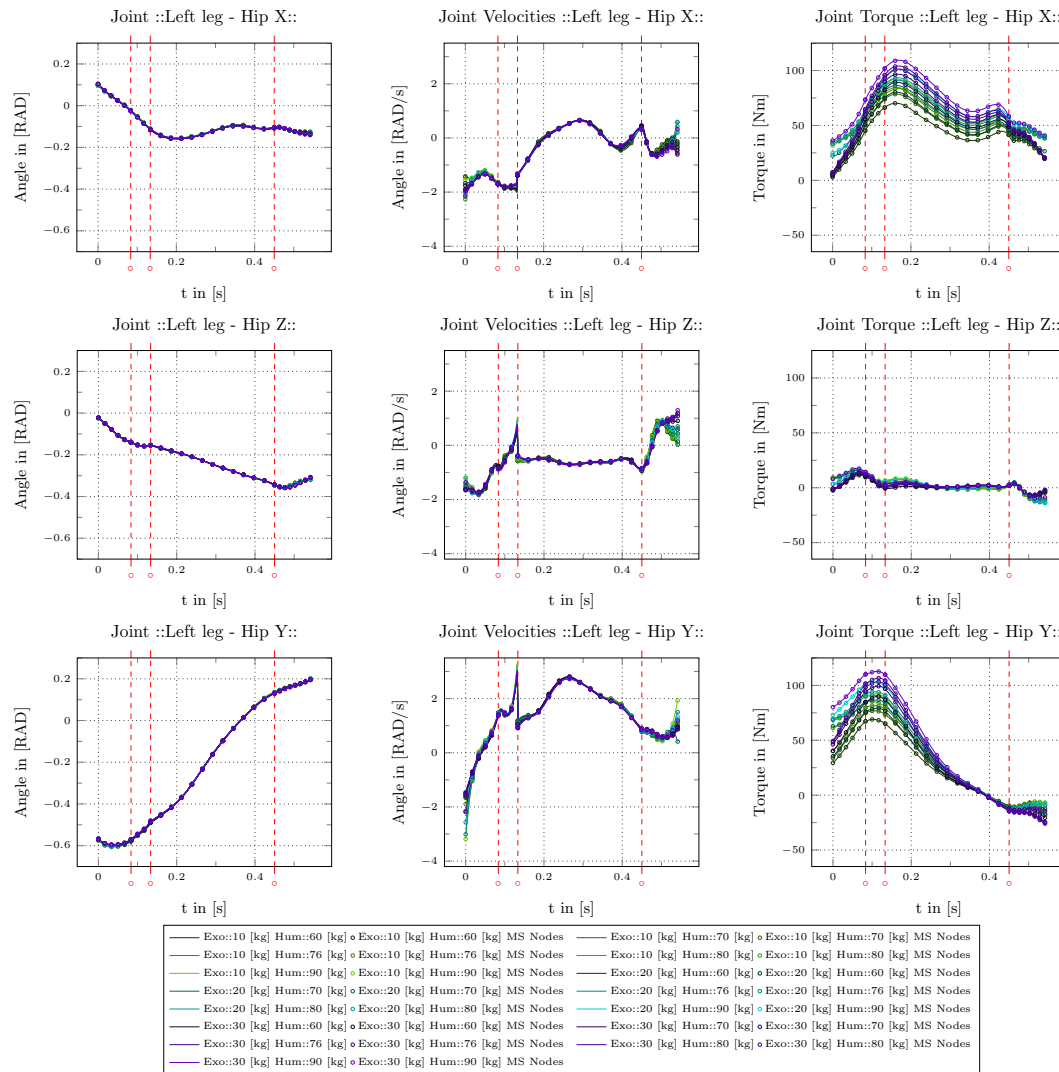


Figure 14.3: Trajectory profiles - position, velocity, torque for the Hip Joint complex X, Z, Y of the support leg

As stated in [Dollar and Herr, 2008] the human hip joint complex contributes the majority of the mechanical work. The trajectory profiles stay inside a medium angular range. Results will be presented and discussed, dispatched into support and swing leg. All numeric values of the discussion are presented in Table 14.1 on page 198.

Trajectory Profiles - Support Leg (left)

In the trajectory profiles for joint angle and velocity there are only small mutual deviations, except the boundary values of the velocity profiles. This is acceptable as the discrete least-

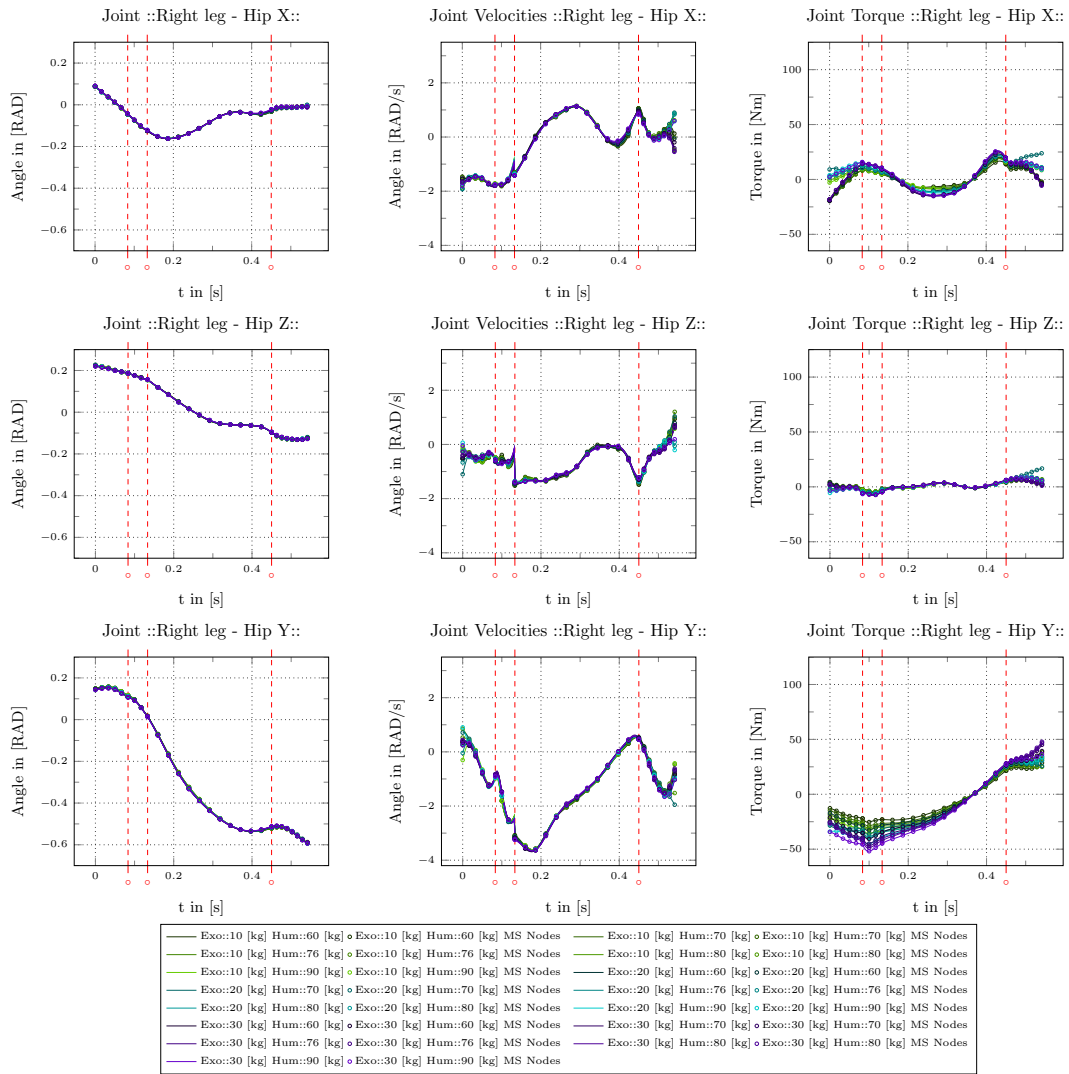


Figure 14.4: Trajectory profiles - position, velocity, torque for the Hip Joint complex X, Z, Y of the swing leg

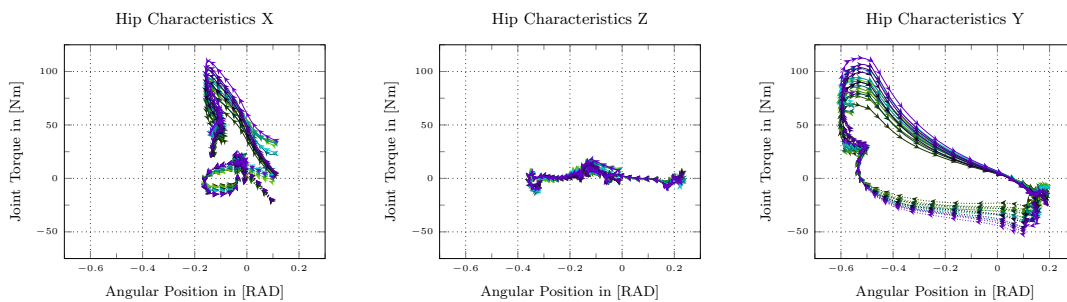


Figure 14.5: Trajectory Characteristics of Hip Joint complex. The left leg - support - leg is drawn with a solid line and the right - swing - leg is represented with a densely dotted line. As the time scale is missing in these charts the direction with raising time is represented with small arrows drawn on the curve.

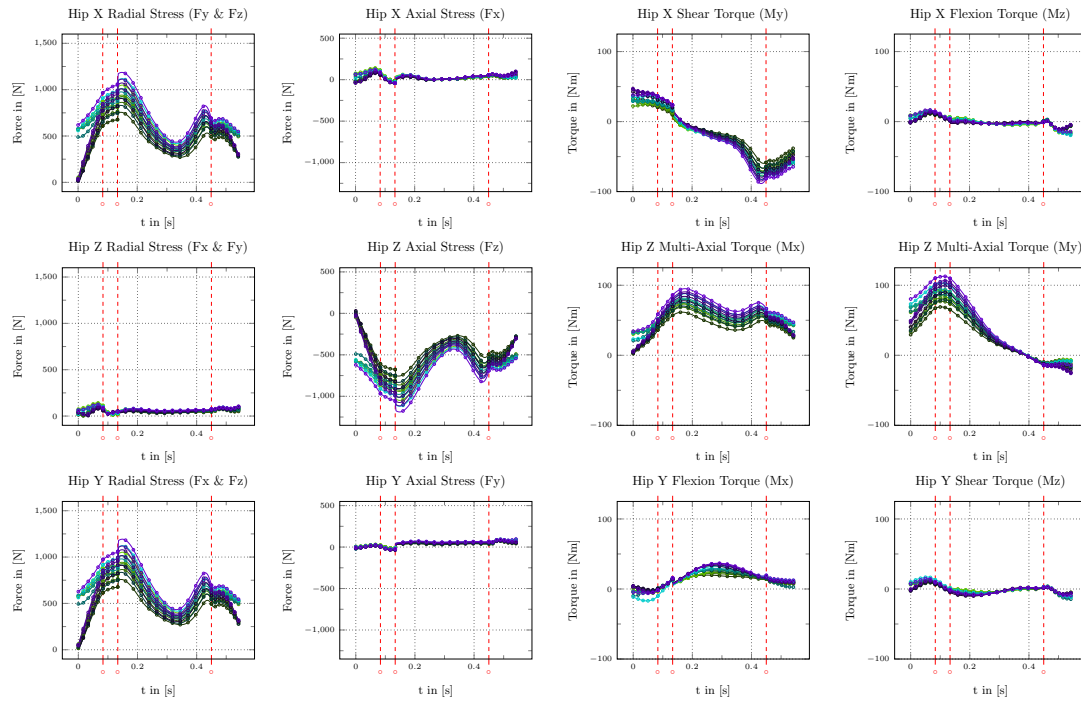


Figure 14.6: Structural load of Hip Joint complex of the support leg

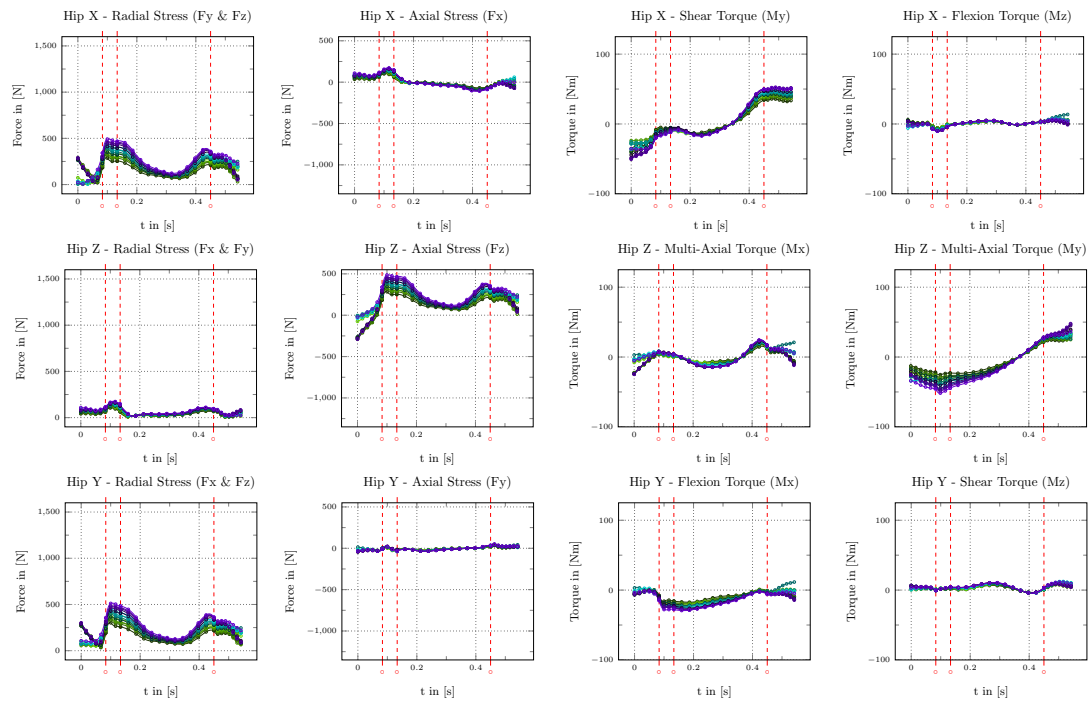


Figure 14.7: Structural load of Hip Joint complex of the swing leg

square objective is only defined with respect to the angular reference. Roll and Yaw dof are only acting in a small angular range. Their velocity ranges have medium magnitude. In contrast the pitch dof has a much larger range for angular and velocity values, respectively. While

Table 14.1: Value ranges of the various characteristics of the hip joint complex. The values marked in gray show components of a multi axial torque load on the articulation as it is not possible to distinguish this configuration towards deflectional and torsional load. Hence the torque highlighted in gray in the upper and lower row is oriented towards the X-axis and Y-axis, respectively.

Charact.	Left leg						Right leg					
	Hip X		Hip Z		Hip Y		Hip X		Hip Z		Hip Y	
	min	max	min	max	min	max	min	max	min	max	min	max
q [RAD]	-0.16	0.11	-0.36	-0.02	-0.61	0.21	-0.16	0.09	-0.13	0.23	-0.59	0.15
\dot{q} [$\frac{\text{RAD}}{\text{s}}$]	-2.28	0.59	-1.87	1.32	-3.23	3.46	-1.91	1.14	-1.55	1.23	-3.66	0.91
τ [Nm]	2.5	109.8	-14.07	17.78	-26.06	113.4	-19.13	0.23	-7.71	16.86	-52.35	48.23
\dot{q}_{step} [$\frac{\text{RAD}}{\text{s}}$]	0.69		1.57		2.44		0.54		1.45		0.91	
$F_{\text{Rad.l}}$ [N]	-100	1600.0	0.0	142.5	20.83	1201.4	0.0	491.3	5.03	177.2	28.25	514.12
$F_{\text{Ax.}}$ [N]	-48.89	142.2	-1194.	25.97	-38.89	96.83	-109.4	172.4	-293.1	490.1	-44.76	49.23
$M_{\text{Flex.}}$ [Nm]	-19.57	16.99	2.19	95.9	-14.72	17.14	-10.45	13.56	-24.93	24.12	-4.6	12.3
$M_{\text{Tors.}}$ [Nm]	-88.56	47.08	26.02	113.0	-16.74	36.95	-50.91	52.36	-51.46	47.95	-29.40	11.57

joint torque on the Yaw dof is relatively low, the roll and the pitch dof feature higher range magnitudes. The peak value of the torque profile is reached shortly after toe strike for the roll articulation and during the toe strike transition for the pitch articulation. In conjunction with the angular trajectory profiles the roll and pitch dof seem to have a major contribution in supporting the upper body, while the pitch contributes in addition to the locomotion. Besides the visible influence of human body mass the exo-skeleton mass has a distinct effect as it shifts the actuation profiles to higher torque levels. The Yaw dof seems to be decoupled from this load situation. From the actuation torque profile it seems to compensate for the vertical torque of the non symmetric ground contact reaction torque with respect to the center of gravity during bipedal locomotion. During toe strike all dofs feature high maximum discontinuities in their velocity profile.

Trajectory Profiles - Swing Leg (right)

In comparison to support leg the hip joint complex of the swing leg does show similar magnitudes of angular value ranges as well as velocity value ranges, for roll and yaw, respectively. From the second phase onwards the toes lift off and the swing motion is performed, which is clearly reflected in the angular value ranges and the velocity range of the pitch dof. In contrast to the support leg the range of the actuation profile shows a small magnitude for the roll and yaw dof, compared to the value range of the trajectory profile of the pitch dof, where the peak torque in negative direction is reached after (!) toe off event in the second motion phase (compare with Figure 13.1 on page 187). In case of the swing leg the influence of the exo-skeleton mass on the actuation profiles of roll and yaw dof is relatively small. However the pitch dof shows a distinct shift of the profiles to higher torque levels for higher exo-skeleton masses. Although the swing leg is not in contact during toe strike of the opposite leg propagation of a considerable magnitude of discontinuity in the velocity profile is clearly observable.

Trajectory Characteristics

The characteristic charts of the hip joint complex show left and right in the same plot. During the support motion the roll dof seems to act like a spring with a small damping, visible from the small hysteresis performed. In the swing motion the joint seems to act as pure damper as the hysteresis is distorted towards a circle approximately symmetric to the horizontal axis. In the case of the Yaw dof the trajectory characteristic shows a more or less free motion of the articulation, only with a small magnitude of actuation. For the pitch dof an active power output is clearly observable during both the swing and support phase. First in the swing phase the torque has a negative magnitude driving the joint angle into the negative value range. Nearby the transition into the support phase the joint torque changes the direction driving the joint trajectory back into the positive value range. As the hysteresis has been traveled in the opposite direction then it would be the case for a spring damper the system, mechanical power has been contributed here during the walking motion cycle.

Structural Load - Support Leg (left)

For the roll and pitch articulation the axial loads F_{Ax} are relatively small compared to the radial one F_{Rad} . In the yaw articulation the inverse case is observable. All load components, radial as well as axial, show highly dynamic trajectory profiles. The axial load components features positive and negative magnitudes. High magnitudes are observable for the torsional torque load M_{Flex} of the roll articulation, the multi-axial torques in M_x and M_y of the yaw articulation. While the trajectory profile of M_{Flex} of the roll articulation seems to have no dominant direction the multi-axial trajectory profiles of the Yaw articulations clearly show the positive torque direction to be dominant. The lower magnitudes in deflection load of the roll articulation M_{Rad} and both torque loads of the pitch articulation M_{Flex} and M_{Rad} , respectively, do not seem to have a dominant direction either.

The support of the body weight is clearly observable in the radial load component F_{Rad} of roll and pitch articulation and in the axial component F_{Ax} of the yaw joint. The axial load of the roll and the radial load magnitude of the yaw articulation are expected to originate from the foot pushing the body ahead during the locomotion. The radial load of the pitch articulation should show a similar profile, however it is shadowed by the much higher influence of the body mass support into this direction. As the torque magnitudes of the roll M_{Tors} , the multi-axial M_x and M_y as well as the pitch M_{Tors} , related to the support of the body weight, show already important magnitudes even though these joints are located closely to the human pilot.

Structural Load - Swing Leg (right)

Compared to the support leg one would generally expect load magnitudes here, that are much smaller. This is the case for the radial component F_{Rad} of the roll and pitch articulation, as well as the axial component F_{Ax} , respectively. Furthermore, this is true for the deflectional load M_{Flex} of the roll articulation, the multi-axial torque M_x and M_y of the yaw articulation, as well as both torque loads M_{Flex} and M_{Tors} of the pitch articulation. However, magnitude of axial component F_{Ax} of the roll articulation and radial component F_{Rad} are higher than in the case of the support leg. With respect to the variability of trajectory profile only the axial load component F_{Ax} of the yaw articulation and the torsional load component M_{Tors} of the pitch articulation seem to have a clearly dominant load direction, the former positive the latter negative. Differences in the load profiles, although much smaller than in the case of the support leg, is clearly visible. Generally the higher human and exo-skeleton mass the higher load profile magnitude get. Even though it exists a large amount of superposition of the different parameter settings, influence of the exo mass on the final load profiles seems to

be higher.

The transmission of the body mass is clearly replaced here with the dynamic interaction of the swing leg that is lifted off ground and swings ahead. The higher axial load component F_{Ax} of the roll articulation and the radial load component F_{Rad} of the yaw articulation can be explained from the fact the swing leg must accelerate to a higher forward velocity and decelerate in order to travel ahead of the human body.

1.2 Joint-Complex::Knee

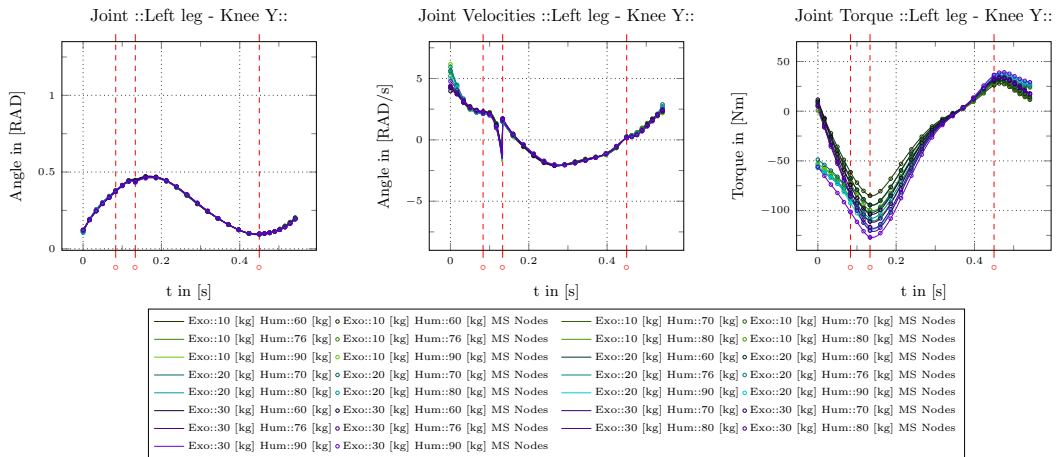


Figure 14.8: Trajectory profiles - position, velocity, torque for the Hip Knee complex Y of the support leg

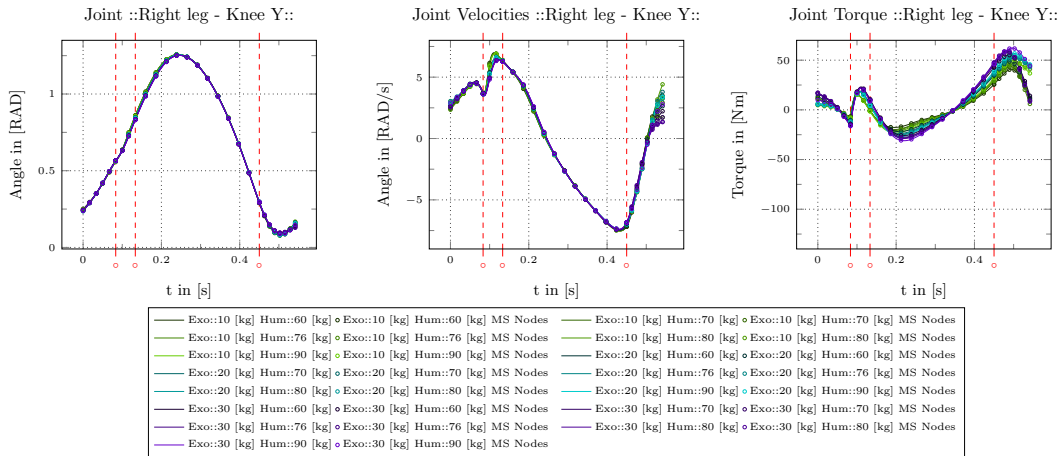


Figure 14.9: Trajectory profiles - position, velocity, torque for the Hip Knee complex Y of the swing leg

As stated in [Dollar and Herr, 2008] the knee articulation acts partially as a damper. A more precise study in [Shamaei and Dollar, 2011] identified stages, with a ballistic motion, the swing phase, and stages where the knee articulation would act equivalently to a torsional spring. Hence it is of major interest, whether this physical characteristic is preserved in the case of the human pilot effectively wearing the exo-skeleton.

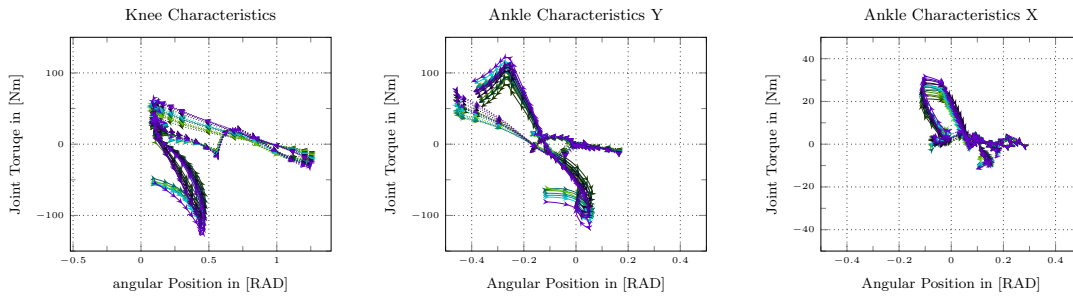


Figure 14.10: Trajectory Characteristics of Knee Joint complex. The left leg - support - leg is drawn with a solid line and the right - swing - leg is represented with a densely dotted line. As the time scale is missing in these charts the direction with raising time is represented with small arrows drawn on the curve. For visibility purposes the plot of the characteristics about the X-axis has been magnified compared to the knee and ankle characteristics about the Y-axis.

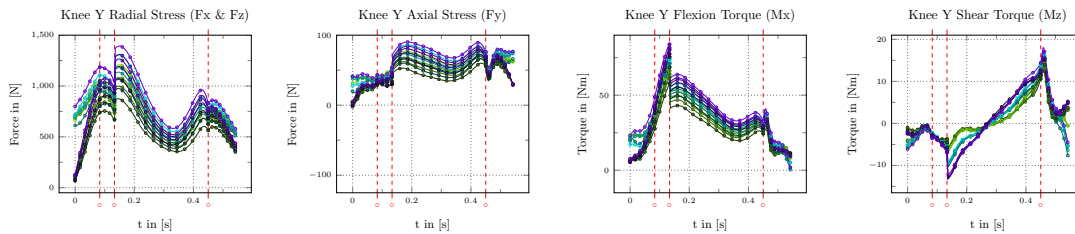


Figure 14.11: Structural load of Knee Joint complex

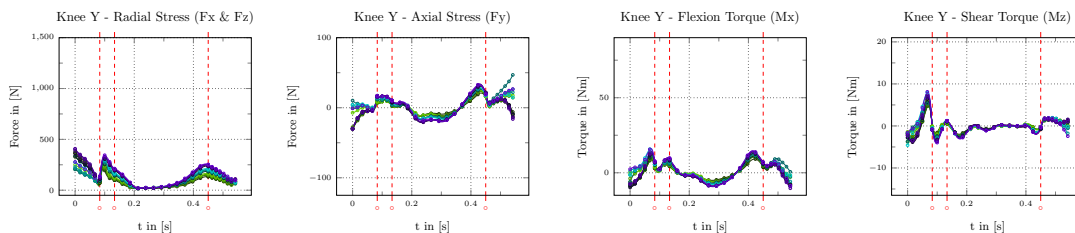


Figure 14.12: Structural load of Knee Joint complex

Trajectory Profiles

It is clearly observable that the active value range and the velocity profile of the knee articulation has much higher magnitude during the swing phase then during the support phase. While the velocity discontinuity of the toe strike was clearly visible even in the hip joint complex of the freely moving swing leg, it is not visible in the velocity profile of the knee joint of the swing leg. However the velocity profile of the support leg features a distinct discontinuity. The actuation profile features a small value range during the ballistic motion and a much higher peak magnitude during the support phase. The peak value is reached without exception during the toe strike transition. In the case of the swing leg the actuation profile shows a clear lift off phase, first peak directly after the toe lift off event, acceleration towards walking direction, second peak, and deceleration before heel strike, third positive peak. The trajectory profile confirms this observation. Influence of the human mass on the actuation profiles relatively

Table 14.2: Value ranges of the various characteristics of the knee joint complex.

Charact.	Left leg - Knee		Right leg - Knee	
	min	max	min	max
q [RAD]	0.093	0.47	0.073	1.26
\dot{q} $\left[\frac{\text{RAD}}{\text{s}}\right]$	-2.10	6.20	-7.44	6.92
τ [Nm]	-126.5	38.24	-30.60	61.75
\dot{q}_{step} $\left[\frac{\text{RAD}}{\text{s}}\right]$		3.56		0.0
$F_{\text{Rad.l}}$ [N]	62.5	1390.6	13.79	418.4
$F_{\text{Ax.}}$ [N]	-2.18	90.34	-30.45	47.27
$M_{\text{Flex.}}$ [Nm]	0.0	84.44	-10.31	16.25
$M_{\text{Tors.}}$ [Nm]	-13.25	18.04	-4.63	8.06

small but clearly visible, compared to the large influence of the exo-skeleton mass towards larger magnitudes of the actuation profiles.

Trajectory Characteristics

In left graph of Figure 14.10 on the preceding page a similar curve to that published in [Shamaei and Dollar, 2011] is clearly observable. The swing phase clearly show a ballistic motion in the knee articulation, however during the support phase the profile features a deviation from the thin spring-style hysteresis featured in [Shamaei and Dollar, 2011]. As the velocity profile during the same phase initiates with a magnitude this gives evidence to velocity damping effects present in the knee joint. Again distinct trajectory profiles are visible for different exo-skeleton masses. In contrast the human mass does not seem to have an equivalent influence.

Structural Load

In the case of the swing leg the structural load in the knee articulation is much lower than in the case of the support leg. This is explained from the fact that at one hand the swing leg does not support the body weight and at the other hand the current modeling does not consider the longer load cycle, as a large part of the body weight in the realistic case may only be support by the foot plate, effectively transmitting the complete structural load through the human pilot down to the foot complex and back though the frame structure of the exo-skeleton (compare Section 3 on page 179).

In the case of the support leg, the transmission of the body weight through the leg structure is clearly visible from the overall higher magnitude of the load profiles. Particularly, the radial load component $F_{\text{Rad.}}$ shows a high peak directly after the toe strike transition. Furthermore, the deflectional component of the torque load M_{Flex} shows a high magnitude which seems to the originate from the fact that the leg that supports the weight needs to bear as well the structural load the results from the fact that the center of gravity is not located directly over the supporting leg.

In all cases a high influence of human and exo-skeleton mass is clearly observable, as higher mass always leads to more structural load in the knee articulation. However in the torsional component of the torque load, major different between the influence of the human compared to the exo-skeleton mass is visible. While the profiles for different human masses are bundled

they are clearly distinct for different exo-skeleton masses.

1.3 Joint-Complex::Ankle

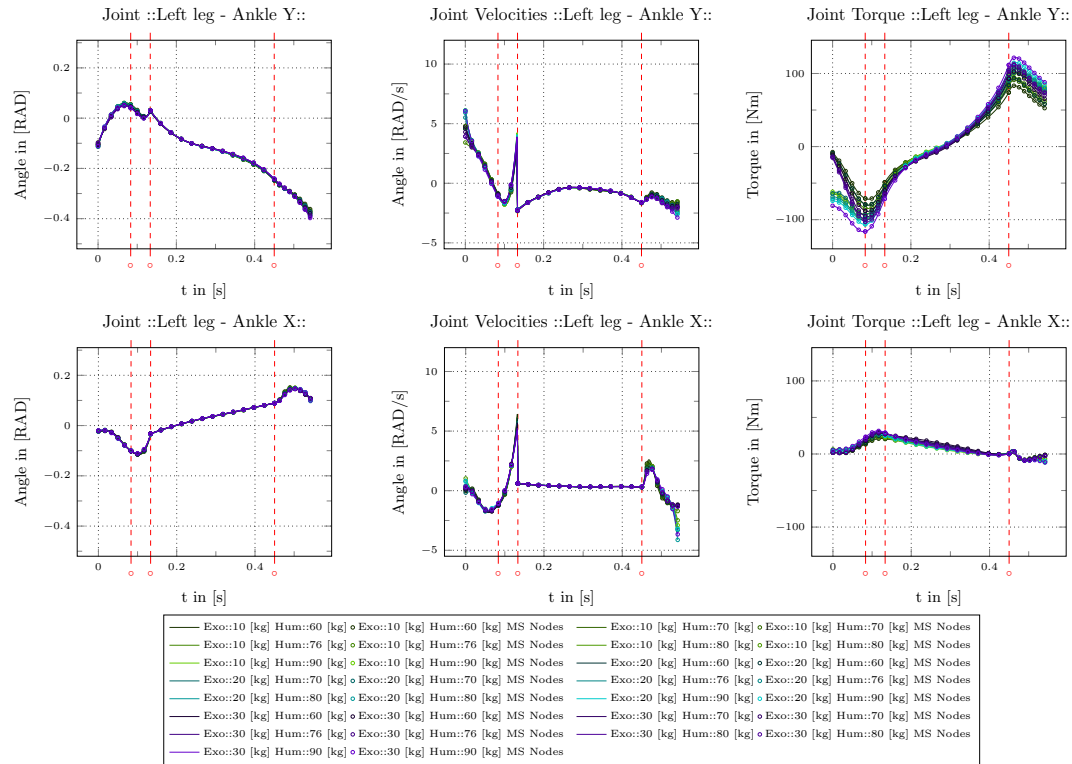


Figure 14.13: Trajectory profiles - position, velocity, torque for the Ankle Joint complex X, Y of the support leg

The ankle joint acts during walking as spring [Dollar and Herr, 2008]. More precisely [Sham-aei et al., 2011], the ankle joint in the Y-axis act as a spring during normal speed level-ground walking, but adds actively power when it comes to higher gait velocities and uphill walking, while energy is dissipated during downhill walking a slope. Furthermore, the cooperation partner mentioned the desire to replace a potentially necessary actuation system in the roll articulation by a purely passive spring-damper system. As to the knowledge of the author there is currently that discusses precisely this design step, the focus of this study for the ankle joint complex is directed towards the influence of slope walking on the overall ankle joint characteristics and more particular towards the question whether roll articulation acts approximately as a passive spring/damper system.

Trajectory Profiles

In the support phase the value range of the joint trajectory profiles are of relatively small magnitude when compared to the free-motion during the swing phase. However during toe-strike a large discontinuity in both velocity profiles is clearly observable, which does not seem to propagate into the opposite leg during its swing phase. During the support phase an actuation profile with high maximal magnitude has been observed for the pitch, while the roll joint actuation profile remains at much lower values. This high actuation profile for the pitch articulation remains until the lift off of the toes and entrance of the concerned leg into the

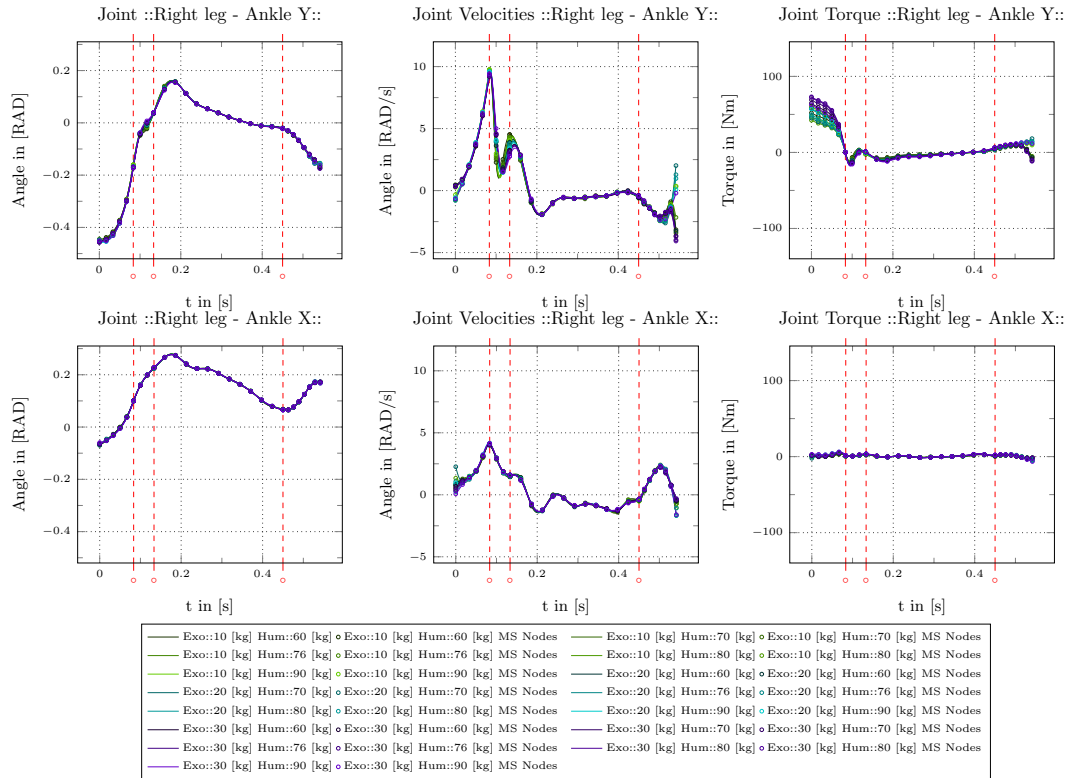


Figure 14.14: Trajectory profiles - position, velocity, torque for the Ankle Joint complex X, Y of the swing leg

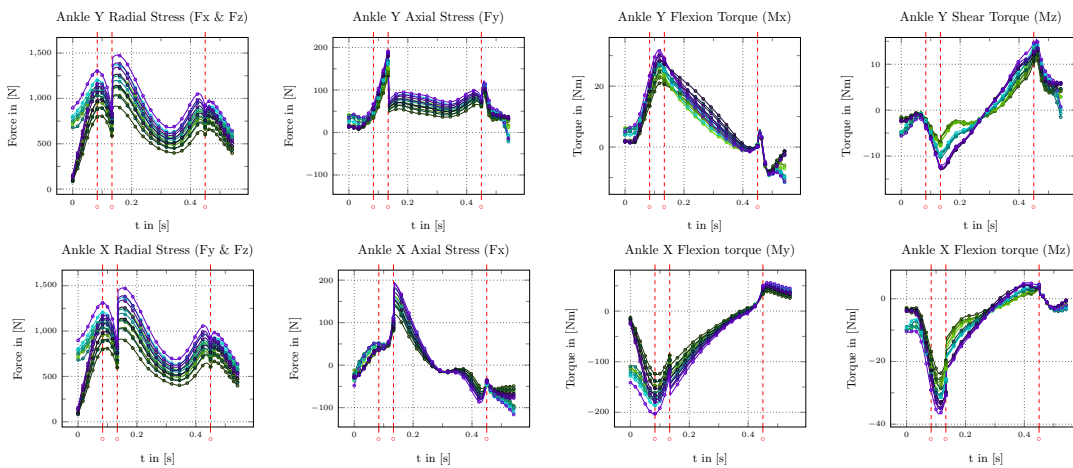


Figure 14.15: Structural load of Knee Joint complex of the support leg

swing motion, but then stays at higher values than the profile of the roll articulation. Values of the actuation profile for the roll articulation are already considerably reduced before the toes lift off. During the free motion of the swing the actuation of the roll joint remains at very small values. However the motion range and the variability of the velocity are the most important for the free motion. During the support phase an influence of the different masses is clearly visible while the impact of the exo-skeleton seems to more important towards higher

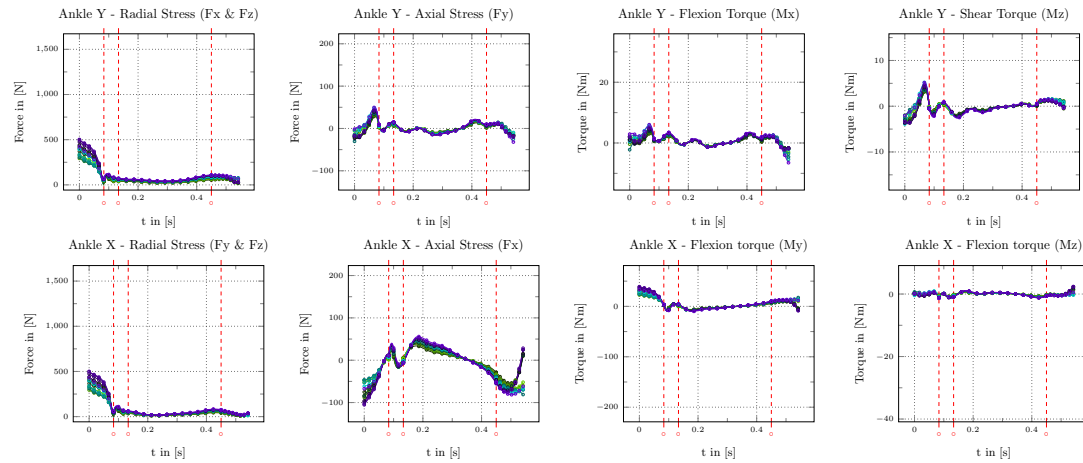


Figure 14.16: Structural load of Knee Joint complex of the swing leg

Table 14.3: Value ranges of the various characteristics of the ankle joint complex. The torque load components have been presented into dispatched lines for the sake of readability, as they are not producing a mechanically similar effect.

Charact.	Left leg				Right leg			
	Ankle Y		Ankle X		Ankle Y		Ankle X	
	min	max	min	max	min	max	min	max
q [RAD]	-0.400	0.060	-0.115	0.151	-0.458	0.156	-0.070	0.278
\dot{q} $\left[\frac{\text{RAD}}{\text{s}}\right]$	-2.86	6.15	-4.16	6.40	-4.10	9.75	-1.69	4-17
τ [Nm]	-116.1	120.3	-11.46	31.43	-17.65	73.8	-6.44	6.15
\dot{q}_{step} $\left[\frac{\text{RAD}}{\text{s}}\right]$		6.57		5.84		0.0		0.0
$F_{\text{Rad.l}}$ [N]	81.7	1479.	81.97	1475.	8.72	502.9	8.72	500.0
$F_{\text{Ax.}}$ [N]	-21.12	191.3	-116.4	194.9	-32.0	49.9	-105.4	55.06
$M_{\text{Flex. X}}$ [Nm]	-11.65	31.65			-6.52	6.00		
$M_{\text{Flex. Y}}$ [Nm]			-20.31	56.49			-10.29	39.02
$M_{\text{Tors. Z}}$ [Nm]	-13.00	15.33			-3.90	5.19		
$M_{\text{Flex. Z}}$ [Nm]			-36.12	4.93			-1.35	2.39

actuation torque profile magnitudes. During the swing phase this effect mostly vanishes.

Trajectory Characteristics

Despite a spring-like behavior at the beginning of the swing phase of the pitch articulation, the motion characteristics reflect those of a free motion after the toe off transition. From the transition of the heel-strike to the toe strike the motion characteristics transform from controlled towards a spring-like form. After the heel off transition, the joint angle trajectory keeps progressing while the torque magnitude decreases, which opens the thin hysteresis that formed previously. In case of the roll articulation, the free motion during swing is clearly visible. However after the heel- and toe strike it is clearly visible that a hysteresis towards positive actuation torque and negative joint angles is formed, which is traveled in the opposite

direction then it would be the case for a spring/damper system. Hence energy is actively added here and the joint does not act purely passive during the support phase. The influence of different human masses is hardly, while the influence of different exo-skeleton masses shows high influence in the case of the pitch articulation and relatively small impact on the roll articulation of the ankle joint complex.

Structural Load

After the toe-off transition the magnitude of the radial load component $F_{\text{Rad.}}$ of the pitch as well as the roll joint decreases to relatively small values. The magnitude of the axial load component $F_{\text{Ax.}}$ for the pitch joint shows only a peak and its maximum value shortly before the toe-off transition. The same quantity for the roll joint stays in a similar value range. The variation of these values seem to originate from the dynamics of the free moving foot assembly. The torque load components for the pitch articulations remain at relatively small exception for both joints. Only exception is the deflectional component about the Y-axis of the roll joint. Here a load concentration is clearly visible shortly before the toe-off transition that comes from the that the articulation is shifted outside of the away from the actual pivot point and hence has to bear an additional moment from linear load transmitted over the pivot point. However, one should note, as previously discussed in Section 1.2 on page 200, the chosen modeling approach does not capture the case where the human is mainly supported throughout the foot assembly and hence the low structural load result should be considered carefully, to be investigated during further studies.

During the support phase the complete body weight has to be support through the given joint structure. Radial $F_{\text{Rad.}}$ and axial $F_{\text{Ax.}}$ load component clearly reflect the transmission of the body weight. While the body seems to be well balanced over the foot smaller value range of the torque load components of the pitch joint, the torque load component about the Y-axis of the roll joint shows high peak loads based on the shift away from the pivot point. In contrast to the swing phases an influence of the different human masses in conjunction with the different exo-skeleton masses is clearly observable. The impact of the exo-skeleton mass seems to be higher than that of the human masses. Interesting examples are the torque load component about the Z-axis of both articulations. Here, adjustment of the exo-skeleton mass leads to bundled distinct curves of different human masses.

1.4 Angular Momentum

Stability control for bipedal walking devices is an important aspect in bipedal locomotion problems (refer to section [Stability]) and hence highly relevant for this preliminary study. In [Goswami and Kallem, 2004] the authors state that for determination of the stability of the orientation of the device the state of the angular momentum in conjunction with its first derivative is necessary while the latter is then used to develop appropriate strategies for re-stabilization. Thus, in Figure 14.17 on the next page the profiles of angular momentum and its first derivation of the complete model with respect to its CoM resulting from the computations for level ground walking in this preliminary study are shown.

From the previously adopted assumptions of symmetry and periodicity (refer to Section 1 on page 185), the medio-lateral component should be periodic with respect the half cycle, while vertical and anterior-posterior component should show a symmetric evolution per half-cycle and a periodic trajectory profile with respect to the full walking cycle. From the analysis in Figure 14.17 on the next page the magnitudes of the angular momentum profile about the X (anterior-posterior) and the Z (vertical) axis are relatively small compared to the profile about the Y (medio-lateral) axis. This means that the walking device performs a distinct pitch

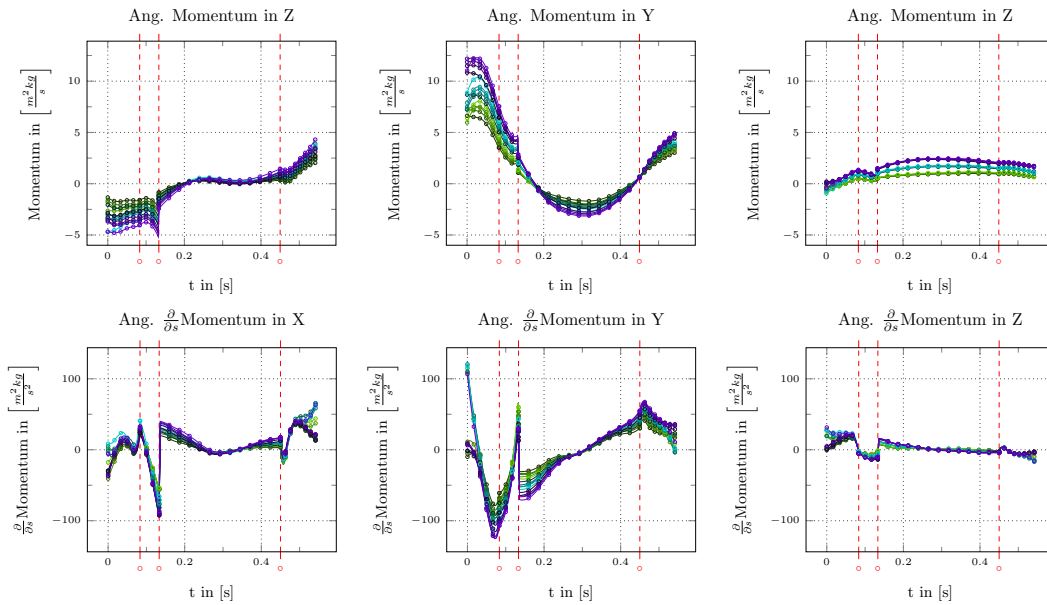


Figure 14.17: Angular momentum and first derivation of angular momentum formulated in the global reference frame with respect to the CoM, about X (anterior-posterior), Y (medio-lateral), Z (vertical) axis

oscillation when walking forward. In all directions the influence of the exo-skeleton mass is clearly more important than the one of the human mass. Particularly in the vertical component the human mass seems to have no influence at all.

The first derivative of the angular momentum shows as well the highest magnitude for the profile in the medio-lateral direction. Then it follows the magnitude of the anterior-posterior as well as the vertical direction. The medio-lateral component shows clearly a deceleration of the body's rotational movement of tipping forward. The toe-strike introduces strong discontinuity. After this discontinuity the device flips rotational motion to backwards until the heel-off transition, where it restart rotating forward again. The rotational motion about the anterior-posterior direction is periodic on the full cycle. During the left foot in support the device rotates slow to the left and flips motion direction after the discontinuity at the toe-strike transition into other direction. The vertical direction shows as well a rotational motion that flips towards the left side before the toe-off transition and is maintained despite the discontinuity at the toe-strike transition, towards the end of the half-cycle. For a comparative walking study on different slopes please refer to the annexe.

2 Concluding Remarks

After the level-ground walking case has been thoroughly discussed, the interpretation of the results with respect to subsequent modeling decisions and further prospected studies based on these results will be briefly outlined.

2.1 Implications for Actuation System

A selected actuation system for a given application, should operate inside the specified maximum ratings with maximum stability, tolerate overload situation and operate at maximum

energy efficiency. Besides the dynamics of the necessary angular trajectory as well as the velocity profiles, including discontinuities, e.g. shocks, and energy cycling characteristics give further information about potentially appropriate passive or active actuator types. The actuation system of the prospected device has to operate closely together with the human pilot inside the exo-skeleton such that a high adaptability, robust reaction to environmental perturbations and maximum safety during interaction with its environment [Vanderborght et al., 2013] are essential characteristics which generally rule out the conventional stiff high-gain position control found among industrial and humanoid [Hirukawa et al., 2004, Yokoi et al., 2001] robots.

Application of SEA

From [Vanderborght et al., 2013] VIA systems are distinguished from the physical point of view into device with active impedance by control, inherent compliance and those with inherent damping. Devices with actively controlled impedance do not contain a physical compliant element but a stiff actuator with a high bandwidth controller that actively simulates the compliance based on a feedback control loop. Although, these devices are highly flexible with respect to simulated stiffness and damping [Bischoff et al., 2010], their practical bandwidth cannot account for mechanical shocks. As these discontinuities are visible for the majority of the velocity profiles, this type of actuation system will most probably not be suitable.

The alternative, devices with a physical compliance are distinguished in fixed and variable compliance actuators. The fixed type [Kong et al., 2010, Vallery et al., 2008], also called SEA simply consists of a spring placed between the output shaft of the actuator and the motor. The variable stiffness of the actuator is resolved as a torque control problem at the output shaft, transformed to a position control-problem based on the fixed stiffness of the spring [Vanderborght et al., 2013]. On one hand these actuators have a simple mechanical structure, can store and release energy and are highly customizable, but on the other hand suffer from a low bandwidth transfer function. This is due to the physical stiffness and the adopted stable control law when the actuators is required to follow a highly dynamic reference trajectory [Vallery et al., 2008]. In contrast to the SEA the Variable Compliance Actuator (VCA) are technically more complex, however stiffness is controlled by either pre-loading nonlinear springs, changing the transmission between output-shaft and elastic element or by physically altering the elasticity characteristics of the spring. The control of variability is shifted from the control loop into a technically *smart design*. Hence, the achievable bandwidth is much higher and energy storage/release operations may consume less energy for active control than in the SEA case, at the price of at least one additional motor and further complex functional structure.

Hip Joint Complex In case of the roll and pitch dof of the hip joint (Figure 14.3 on page 195 and 14.4 on page 196), the velocity range is relatively small when compared for example to the knee pitch dof or the pitch dof of the ankle joint complex (compare Figure 14.8 on page 200, 14.9 on page 200, 14.13 on page 203 and 14.14 on page 204). However, a high stiffness would be required as the necessary maximum ratings for the joint torque are high for both joints. From the motion characteristics in Figure 14.5 on page 196 the roll joint approximately acts as a highly stiff spring. Thus, application of an SEA would be highly beneficial. In contrast, the pitch dof is mainly conceived for mechanical power output and the yaw dof is approximately performing a free motion. The application of SEAs before VCAs should be rigorously tested against motions that require higher dynamic contribution of the hip joint complex, such as push recovery or sit-down and standing-up motions to confirm suitability.

Application of Prospected Nonlinear SEA As it is observable from Figure 14.8 on page 200 and 14.9 on page 200, for the knee joint, although the trajectory profiles approach relatively small values before the toe off transition and at the heel off transition, the rotational joint requirements are small. However, from Figure 14.13 on page 203 and 14.14 on page 204 it is visible that high joint torque is not only required during small joint angle (toe off transition), but as well at higher joint angles (heel off transition). In the former configuration of the ankle joint, the nonlinear projection would be the most appropriate (compare Figure 12.5 on page 173). However, in the latter configuration, the nonlinear projection degrades in quality. Finally it should be noted that the knee as well as the ankle joint complex are confronted with high maximum ratings and dynamic velocity profiles such that the physical characteristics of the device including the nonlinear transmission originating from the kinematic loop should be further tested and adjusted to confirm its application with good accuracy and efficiency.

Passive Spring-Damper in the Ankle Joint

From Figure 14.10 on page 201 it is clearly visible that energy is actively added to the system in a certain extent. Thus, during the presently analyzed motion the joint does not act as a purely passive spring-damper system, but must be actively power to support the walking motion in its present form.

2.2 Implications for Structural Design

For this preliminary study the articulations have only been considered on an abstract level to avoid any *a priori* technological decisions. However, as stated in Section 2 on page 177 cyclic interdependencies between decision about adoption of specific design and articulation types and the kinematic as well as dynamic characteristics of the prospected device exist. Such that an investigation of a proper and technological sound selection can only be conducted iteratively. In the following, interpretation of the structural load results in a first attempt to define a potential candidate solution for the articulation system, that should then further be analyzed during subsequent studies.

For the structural load the most important information are normally originating from the support leg. However, there are situations where important information are coming as well from the swing leg.

Hip Frame & Articulation

In Figure 14.6 on page 197 and 14.7 on page 197 the load situation of the roll and pitch joint clearly qualifies these articulations as pure radial bearings, high radial and low axial load. Further, the dominant torque load on the articulation is exerted in medio-lateral direction for the roll joint and in the anterior-posterior direction for the pitch joint. As the magnitude of the dominant torque load is relatively high, especially for the roll articulation, the axial load frequently changes direction and the functional limb structure should not be strained with further structural load. In this case, a 2-point moving, fixed articulation with the pelvic bracket holding the shaft, would be a promising candidate solution.

In contrast the yaw articulation shows a small radial but an intense axial load. The multi-axial torque load with respect to the anterior-posterior as well as the medio-lateral direction shows high peak magnitudes. The abstract geometry of this articulation was suggested as curved linear bearing from our cooperation partner. With respect to the resulting load situation this technical solution is questionable as it would provoke highly non homogeneous load distribution with accumulation on the extremities of the bearing construction.

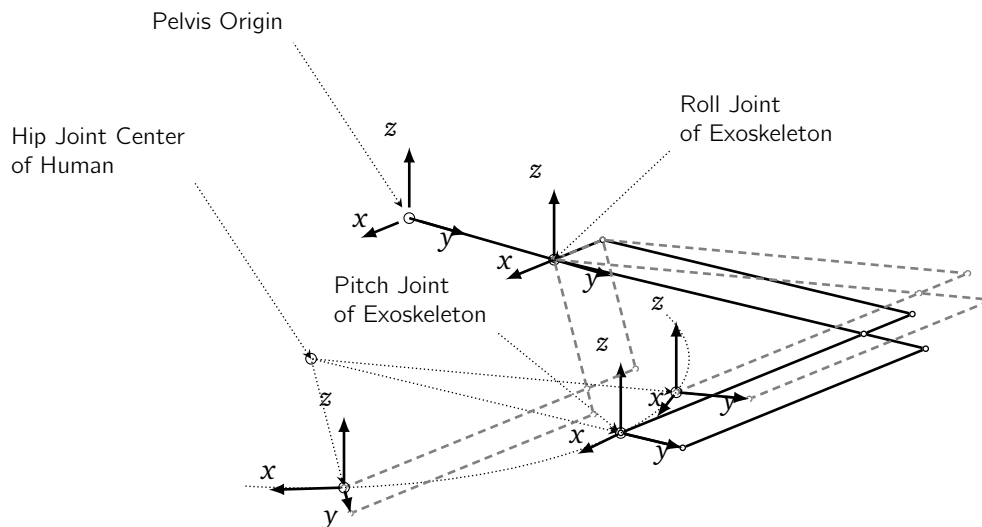


Figure 14.18: New lever scheme proposition for yaw axis hip joint complex

A technologically more simple, robust and flexible solution is shown in Figure 14.18. This lever mechanism approximates the same motion as the curved linear bearing mechanism, but is realizable with inclined 2-point or 2-point axial, radial bearing arrangements, solutions that are technically, highly mature. Furthermore, this solutions have zero floating motion into the axial direction. Therefore, this candidate solution would considerably simplify integration of an SEA actuation system [Vanderborgh et al., 2013] or further passive joints [Cempini et al., 2013] to account for hyperstaticity. Additionally, a modification of the lengths of the levers more complex motions and individual adjustments to patients are possible [Cempini et al., 2013].

The structure itself is confronted to a high amount of multi-axial deflectional and torsional torque and resulting into shear and superposed normal stress. As the horizontal load torque components are dominant a compatible lightweight frame should have a hollow rectangular structure with a higher dimension orthogonal to the horizontal directions to account for higher mechanical rigidity into that direction.

Upper Leg

The thigh frame is loaded with multi-axial deflectional torque (the torque in medio-lateral is the most dominant) and high normal stress. The shear stress, and torsional torque load are relatively small. A compatible frame structure must bear a high load at the hip pitch articulation while the load may then be distributed towards the other side of the leg frame. At this point the anterior-posterior component of the torque is dispatched into pure normal stress, while the medio-lateral component however remains. The section should be hollow to skip structure not transmitting structural load with a larger dimension into anterior-posterior than into medio-lateral.

The articulation is split in two components on each side of the leg. Accordingly all torque loads translate into additional axial and radial load components. As the elasticity of the construction probably does not support a classical distinct 2-point bearing arrangement, a small angular double-bearing O-arrangement should be a potential candidate solution for subsequent studies.

Lower Leg & Foot Assembly

The shank frame more or less follows the same load configuration than the thigh frame. However, the normal and axial load components tend to become dominant over the deflectional torque load components. Hence, the dimension of the section of the structure should be reduced to allow for less weight of the complete frame.

The articulation follows the principle as previously discussed in the knee articulation. With a dispatched complex on both sides of the leg, the torque load is completely resolved into radial and axial load components. For lightweight and low space requirements the same bearing arrangement as above should be a potential candidate solution.

For the frame segment between the ankle-pitch joint and the ankle-roll that has been suggested as passive spring-damper system from our cooperation partner it should be noted that, in case a classical articulation is to be mounted behind of the human heel, the abstract lever from the pivot towards the real implementation of the joint produces a high deflectional torque load that must dynamically be transmitted by the candidate bearing system. The frame structure itself should then be designed as lightweight and technically stiff as possible with respect to the dominant deflectional load component present. As the detailed design structure in this part of the exo-skeleton is still unclear more substantial decision are only possible after subsequent investigations.

2.3 Angular Momentum

A highly valuable contribution to the evolution of angular momentum during bipedal walking of humans was published in [Herr and Popovic, 2008]. The authors analyzed the angular momentum and the rate of angular momentum change of people walking based on motion capturing experiments with force plate measurements and a dynamic model appropriately adjusted with respect to the measured person. A principal component analysis of the data revealed that despite the small total angular moment about all three spatial axis, high angular momentum quantities of single limbs are mutually canceled between different limb groups. In the case of the anterior-posterior direction (X-axis) it was stated that momentum about arms, thigh and neck are negligible and cancellation is done between the segment groups (foot, calf, chest, head) and (pelvis, abdomen). For the medio-lateral direction (Y-axis) cancellation of the momentum is done between adjacent lower limbs. The momentum of arm, abdomen, pelvis, chest, neck and head are negligible. Finally for the vertical direction (Z-axis) the cancellation occurs between the segment groups, (legs) and (arms, pelvis, abdomen, chest, neck, head). This is as well confirmed from studies in [Collins et al., 2009]. Furthermore, the authors discuss the hypothesis that the physical phase-lock of zero-angular momentum for dynamic stability does not exist. As angular momentum, actively produced by dynamic limb movement, can be exploited to compensate dynamic effects of highly unstable kinematic configuration to maintain postural stability.

With respect to the exo-skeleton the observed strategy of mutual cancellation of the momentum between different limbs should work perfectly for the medio-lateral direction. However, for the anterior-posterior as well as vertical direction one would expect a higher impact of the exo-skeleton mass on the total angular momentum with respect to these directions as the dynamic augmentation of the exo-skeleton should disturb the characteristics of the cancellation. Interestingly from Figure 14.17 on page 207 the anterior-posterior direction shows the highest value range in magnitude and the influence of the exo-skeleton mass seems to be similar with respect to the anterior-posterior as well as the medio-lateral direction. A strong impact of the exo-skeleton mass is only visible in the case of the momentum component in the vertical direction.

15 Conclusions

1 OCP Formulations and Dynamic Modeling

In Chapter 2 - 5 and Appendix A - C the complete tool-chain of the formulation of whole-body based OCPs is discussed. Starting from the basics in rigid MBS dynamics towards the modeling of complex technical components and physical phenomena, the focus shifts to sufficiently smooth algorithms to compute the model inside OCP formulation. Final computational verification of the proposed algorithms is performed with the software package MUSCOD-II based on a direct multiple shooting approach.

From literature (see Chapter 2 - 5 and Appendix A - C) about dynamics simulation, optimization as well as control of under-actuated systems under external contacts, the forward dynamics computations, were always be stated as straight forward but numerically involving, whilst the inverse dynamics method, was perceived to be problematic in some cases, but computationally more efficient. For the integration of both methods inside the OCP formulation – for the case of the inverse dynamics of under-actuated systems under external contact constraints – a new formulation was needed.

Therefore, a new inverse dynamics algorithm has been developed to be numerically sufficiently smooth and yield physical consistent results despite problematic contact situations versus the actuation, e.g. insufficiently constrained configurations. This algorithm was implemented and thoroughly tested separately and inside different OCP formulations, for an academic model and a more realistic complex humanoid robot model. In all tests, good consistency between forward and inverse dynamics formulation was observed. While it is not possible to state that the inverse dynamics formulation outperforms the forward dynamics formulation separately and inside the OCP formulation, the inverse dynamics formulation has the clear advantage that the initial values for optimization are purely based on kinematics and hence easy to obtain.

2 Modeling and Optimal Control for HRP-2 N° 14

The Chapter 6 - 10 discuss a realistic implementation of OCP based motion generation for the humanoid robot HRP-2 N° 14 from METI, Humanoid Robotics Project (HRP) [Hirukawa et al., 2004]. From the first motivation to employ whole-body based optimal control to compute different motions, e.g. walking, with a more natural and human-like overall appearance, the humanoid robot HRP-2 N° 14 is explored, from literature (see Chapter 6 - 10) and based on various optimization trials. As large parts of the on-line stabilizing control architecture of the robot are kept confidential by the robot's manufacturer, particular approaches must be employed to treat these system components as black box and tune the OCP formulation to circumvent these unknown system parameter during the computations.

The first study that is presented shows a general investigation of how different biologically and technically inspired abstract motion objectives influence the resulting motion characteristics. It is concluded that the objectives: *minimum joint torque* and *maximum efficiency* lead to smooth and efficient energy cost motions. These are generally desirable motion criteria. The usage of maximum postural stability and minimum joint velocity is discontinued as the

resulting motion appearance is unnatural and leads to high energy costs. The maximum forward velocity plays an exceptional role as tuning a motion – e.g. walking – towards higher velocities generally yields higher energy costs but helps to push the motion performance of the robot towards its dynamic limits.

The basic idea is to employ the capacity of OCPs to formulate abstract objectives to generate a motion that at one hand yields a challenging dynamic motion and at the other hand maintains the dynamic equilibrium of the robot. The benchmark task to be employed for this study was decided to be a dynamic two-step motion over an obstacle. The first study featured an interesting **maximum obstacle tip-height** of **44.6cm** and **obstacle width** of **11cm**. These results were highly encouraging to continue research to bring this motion to the real robot HRP-2 N° 14. Furthermore, this study revealed crucial information about complex self-collision and dynamic ground contact destabilization to be avoided by appropriate modification of the OCP formulation.

Besides, various experiences from motion trials in simulation, an important decision about modeling the passive dynamic elasticity in the ankle joint complex of the robot, was made against suggestions from literature. Based on these decisions about the robot modeling, the computed motions became consistent to simulated dynamics of the robot in the OpenHRP motion simulator. Consistency was found for forward dynamics and the newly formulated inverse dynamics operator for under-actuated systems under constraints. Based on these results suitable objective functions were formulated to minimize the control effort of the black box on-line stabilizing framework, effectively preserving the dynamic equilibrium of the robot while the motion was modified towards dynamically overstepping an obstacle. The final result was then confirmed in simulation and real experiments. The robot safely overstepped an obstacle of **20cm x 11cm (height x width)**, redefining the record of 18cm x 11cm (height x width) to the present knowledge of the author previously held by [Verrelst et al., 2006].

Based on system identification of the passive dynamic ankle elasticity conducted along side the investigation of the dynamic limits of the robotic platform, an analysis of the tracking behavior of the local joint controllers revealed control-deviations similar to the necessary accuracy of the stabilizing system. On one hand, this findings may explain unexpected destabilizations of the robotic platform during a given motion. On the other hand, future studies could exploit these findings to formulate criteria to efficiently exploit the kinematically redundant lower-limb structure of the robot to effectively compensate the influence of the control deviations of the local joint-controllers with respect to the motion of the foot on the ground.

3 Conceptional Work for Exos

In the presented study, the first iteration of an integrated modeling approach has been performed. This modeling approach considered a comprehensive whole-body model with a human pilot inside a lower limb exo-skeleton. The chosen modeling effectively resolves the interdependencies between all modeled system components. Thus, the set-up lends itself for an iterative substantiation of the governing system characteristics, even though, most of these are just based on a suitable initial guess.

The design study in this work has been conducted on level-ground as well as slope (2.5 [DEG], 5.0 [DEG] and 7.5 [DEG] up and down) walking. However, preliminary analyzes showed that for the first set of modeling decisions all significant information were found in the level-ground walking case. Therefore only this set of results was discussed. At the present state of the system description the characteristics have been addressed and substantiated: Actuation-systems, Articulations and different patient characteristics.

3.1 Actuation Systems

The torque maximum ratings that have been found during this analysis are highest for the hip joint complex 109.8 [Nm] about the X-axes and 113.4 [Nm] about the Y-axes. Highest peak values of joint torque are into the positive direction. The joint velocities are highest with $3.66 \left[\frac{\text{RAD}}{\text{s}} \right]$ for the Y-axes and high peak velocities occur into both motion directions.

Highest maximum ratings for the joint torques have been detected at the knee joint with 126.6 [Nm]. The peak value of the torque is towards negative direction only. Relatively high peak values into both directions have been observed for the joint velocity with $7.44 \left[\frac{\text{RAD}}{\text{s}} \right]$.

The highest velocity peak values have been detected for the ankle joint complex. The Y-axes has maximum ratings about $9.75 \left[\frac{\text{RAD}}{\text{s}} \right]$ and $6.4 \left[\frac{\text{RAD}}{\text{s}} \right]$ about the X-axes. The peak joint torque for the Y-axes with 120.3 [Nm] is smaller as the peak value of the knee joint. Peak values for the joint torque occur into both directions. The joint for the X-axes with a peak value of 31.43 [Nm] is considerably lower than that of the Y-axes.

Discontinuities of the joint velocity profiles occur in all trajectory profiles. They are smallest for the hip joint complex $2.44 \left[\frac{\text{RAD}}{\text{s}} \right]$ and highest for the ankle joint complex $6.57 \left[\frac{\text{RAD}}{\text{s}} \right]$. Therefore, pure position control or VIA without a physical compliance is technically problematic. Thus, the prospected application of SEAs in the actuated joints is consistent with the simulation results. However, from the analyzes of the nonlinear transfer-function of the SEA towards the kinematics and kinetics at the joint-output, further iterations will be necessary to determine the best system characteristics of the actuation system (e.g. spring constant, motor ratings, ballscrew ratings) to achieve the best trade-off between energy efficiency, control effort and motion appearance of the whole-body motion of the human-exo-skeleton system.

The verification of the design suggestion of the cooperation partner to introduce a purely spring-damper system at the X-axes in the ankle joint complex. However, in the results of this study the X-axes of the ankle featured not only dissipation but as well contribution of mechanical energy into the system. Therefore, it is strongly recommended to substantiate this design decision with further simulations without actuation at the X-axes in the ankle joint complex to verify the resulting maximum ratings of all other joints and the general motion appearance.

3.2 Functional Structure

The structural load in this analysis is restricted to the force and torque components on the articulations of the MBS that have been computed based on a merged model (compare Section 2 on page 177) without explicit modeling of the kinematic loops of the actuation system. Therefore, the maximum ratings are not important as they are subject to change due to hyperstaticity and separate load cycles, as soon as the model is split into a separate human and exo-skeleton as well as modeling of the kinematic loops of the actuation is performed in the next iteration of this integrated design study. However, this information is highly valuable as a comparison between the torque and force components already gives information about appropriate articulation systems and the global design of the functional frame structure to be tested in simulation of the next iteration.

The load situation in the hip joint complex clearly suggests a 2-point moving, fixed articulation in the X-axes and Y-axes to transmit the high radial force and torsional torque load (especially for the X-axes). The curved linear bearing construction for the articulation on the Z-axes that has been proposed by our cooperation partner was observed to produce inhomogeneous load distributions and accumulations on the extremities of the bearing rail. Thus, an alternative for this technically problematic solution is proposed (see Figure 14.18 on page 210).

The exo-skeleton structure of the upper leg must transmit a high accumulation of deflection and torsional torque from the hip articulation towards the knee articulation. At the knee ar-

tication the torque load resolves mostly into a force load. Therefore, the frame structure of the upper leg should be designed as a hollow structure. As this enables transmission of high torque loads with a lightweight structure.

Similar to the upper leg structure the lower leg structure shows a higher accumulation of the torque load nearby the knee articulation that resolves towards a force load nearby the ankle joint complex. The articulation for the Y-axes at the knee and the ankle joint is split to both sides of the human leg. Thus, the technical realization could employ double bearings in O-arrangement to keep the functional structure small and robust.

From an analyzes of the dynamic influence of the exo-skeleton on the walking motion of the human only a strong influence of the mass of the exo-skeleton on the vertical angular component was observed. As this component is compensated with the upper body (e.g. motion of the arms) and the foot contact on the ground, problematic dynamic influence on the walking motion should be minimal.

In the presented thesis, OCP formulations based on whole-body dynamics have been successfully employed in two distinct engineering applications: motion generation for humanoid robots and conceptional design studies for a lower-limb exo-skeleton. From the point of engineering the formulation of OCPs and there solution for the exploration of mechatronic systems has two highly valuable aspects:

1. The desired, frequently relatively complex, system characteristics can be formulated in an abstract mathematical form.
2. Correct modeling of the full system effectively resolves the complex interdependencies between the components and gives a direct access on the system, e.g. modification of a single parameter that frequently influences the whole system – an important fact.

Especially, for the conception and application of complex mechatronic systems that are supposed to interact with its environment. The application of optimal control can help to explore and improve the characteristics of a complete system to effectively skip some premature prototyping stages. With the future increase in computational power, this could reduce development costs and improve safety during development of complex mechatronic products such as exo-skeletons and humanoid robots and their application.

Appendices

A Computation of Dynamic Characteristics

From the discussion in section 1 on page 19 the dynamic quantities mass m (A.1a), CoM r_{CoM} (A.1b) and the inertia tensor I (A.1c) have only been discussed theoretically. As soon as it comes to real computation in simulation and optimization these quantities will have to be evaluated based on the prospected geometry with a maximum of computational efficiency. Furthermore the chosen computational method should:

- allow for geometries with arbitrary shapes
- compute the dynamic quantity with a maximum of accuracy
- easily support continuously differentiable parametrization for ease of versatile and flexible modeling for geometrical shape optimization

In the following different computational methods to compute the desired mechanical quantities, from 3D geometry, based on the assumption of a homogeneous density,

$$m = \int_V \rho dV, \quad (\text{A.1a})$$

being the mass,

$$r_{\text{CM}} = \frac{1}{m} \int_V \mathbf{r} \rho dV, \quad (\text{A.1b})$$

being the CoM and,

$$I = \int_V \begin{bmatrix} r_y^2 + r_z^2 & -r_x r_y & -r_x r_z \\ -r_x r_y & r_x^2 + r_z^2 & -r_y r_z \\ -r_x r_z & -r_y r_z & r_y^2 + r_x^2 \end{bmatrix} \rho dV, \quad (\text{A.1c})$$

being the inertia tensor, are briefly reviewed and discussed. The focus lies on the question of how these methods are to be exploited efficiently during the remainder of this work.

1 Preliminaries

The computational representation of any 3D geometry of arbitrary shape as polygonal data (polyhedron in the volume-case), originating from point clouds is a relatively common and well studied problem. An early work of [Boissonnat, 1984] shows the application of surface and volume-based determination-methods of the structure from point cloud data. While the former is verified locally, essentially works in a 2D representation and therefore has lower complexity and memory requirements it is local and only performs when the discretization is sufficiently accurate. The latter uses the Delaunay triangulation [Delaunay, 1934] on the complete volume with an iterative refinement being general and more robust. Besides this representation of the data, it simultaneously offers convenient access to the dynamic quantities,

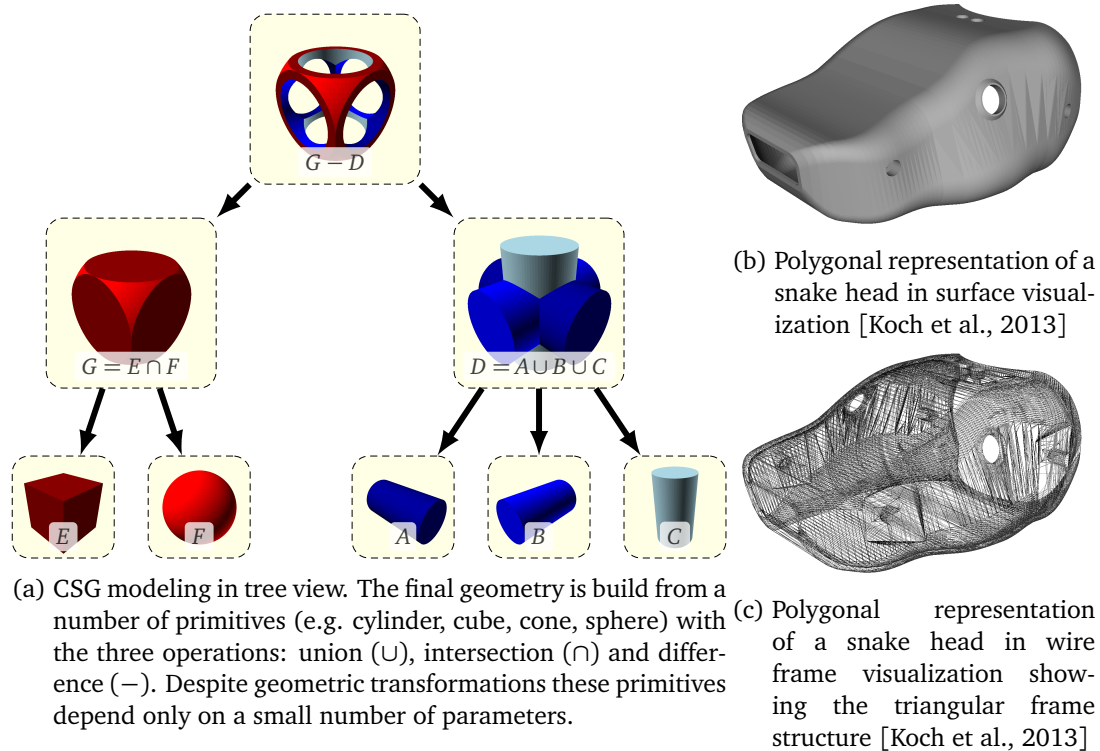


Figure A.1: Different modeling approaches to represent complex shapes in 3D geometry. Figure A.1a shows a typical construction tree of CSG modeling. Figure A.1b and A.1c show a complex geometry based on CSG and resampled to polygonate representation (Figure A.1b - as surface model & Figure A.1c - as wire frame model).

is directly exploitable for finite element applications for stress and thermal dynamic analysis (based on meshes) [Boissonnat, 1984] and may be used for re-sampling and rectification operations on the data itself [Rypl and Bittnar, 2004]. The polygonal representation is relatively flexible, is easily stored (e.g. in stereo-lithography-format STL for rapid-prototyping [Montero et al., 2001]), but is relatively in-accessible, when a geometry needs to be established and is not available as point cloud. An alternative approach would be the primitive base provided within this paper. d constructive solid geometry [Kirsch and Döllner, 2005] which is intensively based on computational geometry algorithms [Fabri et al., 1998]. Here, the modeled geometry is established based on geometric primitives that are joined based on the elementary operations: Union, Intersection and Subtraction [Kirsch and Döllner, 2005] (see figure A.4). For further potential application during optimization, these methods will be shortly discussed while focus is set on:

- a generic access to the governing characteristics to support parametrization - symbolic computations are preferable
- its continuous differentiability with respect to the parametrization (a common requirement as it will be explained below) of the results

From the mathematical point of view [Best, 1964] the computation of mechanical characteristics of a given geometry may be expressed as a simple computation of multi-order moments. The most general formula of [Best, 1964] is found simplified for the case for 3D volumes in most other publication [Dobrovolskis, 1996, Gonzalez-Ochoa et al., 1998, Ling Lien and Kajiya, 1984, Pozo et al., 2011, Ravi and Srinivasan, 1990]. A collection of important defini-

tions and theorems [Merzinger and Wirth, 2002] that will be used during the remainder of this discussion are given below. Even though most of the definitions and theorems are not limited to certain dimension, application in physics or mechanical engineering usually focus on $\dim(S) = 2$ surface and $\dim(V) = 3$ volume spaces, and hence the discussion will be conducted accordingly.

1.1 Divergence Theorem

A very important theorem not only in mathematics but as well in mechanics and physics is the *Gauss Divergence Theorem* [Merzinger and Wirth, 2002]. From the technological point of view this theorem relates to the flow characteristics in volume V of a continuously differentiable vector field \mathbf{f} to its flow $\mathbf{f}\mathbf{n}$ over the boundary S of the volume V . The physical signification of the divergence operator div is the determination of a source $\text{div}(F) > 0$ or a sink $\text{div}(F) < 0$ [Merzinger and Wirth, 2002].

Theorem 4 *Let F be a vector-field in \mathbb{R}^3 with $F : \mathbb{R}^3 \rightarrow \mathbb{R}^3$ continuously differentiable. Let the space $\mathbb{D} \subset \mathbb{R}^3$ be closed and a subset $V \subset D$ be bounded and the boundary $S \subset V$ be smooth for $x \in S$. Further let \mathbf{n} with $|\mathbf{n}| = 1$ be the outward unit normal on the boundary S . Then it holds (refer to [Merzinger and Wirth, 2002]):*

$$\int_V \text{div}(\mathbf{f}) \, dV = \iint_S \mathbf{f}\mathbf{n} \, dS. \quad (\text{A.2})$$

1.2 Surface Integral

It is a frequently employed tool in engineering to efficiently parametrize a complex surface and to apply non-trivial coordinate transformations during various operations e.g. integration [Merzinger and Wirth, 2002]. This definition is employed for example in [Dobrovolskis, 1996] to efficiently compute the dynamical characteristics of elementary tetrahedron. First the parametrization of the desired surface needs to be defined:

Definition 19 *Let $\mathbb{D} \subset \mathbb{R}^2$ be a subset that is closed and bounded and φ with $\varphi : \mathbb{R}^2 \rightarrow \mathbb{R}^3$ a continuously differentiable projection of the surface S with $S = \varphi(\mathbb{D})$, then $\varphi(u, v)$ is called a parametrization of the surface S ,*

$$\varphi(u, v) = \begin{bmatrix} \varphi_x(u, v) & \varphi_y(u, v) & \varphi_z(u, v) \end{bmatrix}^T. \quad (\text{A.3})$$

Definition 20 *Let $\varphi_u = \frac{\partial \varphi}{\partial u} \Big|_{u_r, v_r} du$ and $\varphi_v = \frac{\partial \varphi}{\partial v} \Big|_{u_r, v_r} dv$ the infinitesimal tangent vectors on the surface S at (u_r, v_r) . For a regular parametrization φ should never be parallel on all S . In case of a regular parametrization one may define the scalar,*

$$dS = \|\varphi_u \times \varphi_v\| \, dudv, \quad (\text{A.4a})$$

and the vectorial,

$$d\mathbf{s} = \frac{\varphi_u \times \varphi_v}{\|\varphi_u \times \varphi_v\|} dS = (\varphi_u \times \varphi_v) \, dudv, \quad (\text{A.4b})$$

surface element.

Based on the above definitions 19 and 20 one may then apply the coordinate transformation in the scalar and the vectorial case of the surface integral:

Definition 21 Let f with $f : \mathbb{R}^3 \mapsto \mathbb{R}$ be a scalar function on S with regular parametrization $\varphi : \mathbb{D} \mapsto \mathbb{R}^3$ with $\mathbb{D} \subset \mathbb{R}^2$ then the scalar surface integral of S is defined as:

$$\iint_S f(x, y, z) \, dS = \iint_{\mathbb{D}} f(\varphi(u, v)) \|\varphi_u \times \varphi_v\| \, dudv. \quad (\text{A.5})$$

Definition 22 Let f with $f : \mathbb{R}^3 \mapsto \mathbb{R}^3$ be a vectorial function on S with regular parametrization $\varphi : \mathbb{D} \mapsto \mathbb{R}^3$ with $\mathbb{D} \subset \mathbb{R}^2$ then the vectorial surface integral of S is defined as:

$$\iint_S f(x, y, z) \, ds = \iint_{\mathbb{D}} f(\varphi(u, v)) (\varphi_u \times \varphi_v) \, dudv. \quad (\text{A.6})$$

1.3 Volume Integral

Besides the surface integral, the volume integral is commonly used in mechanics [Gross et al., 2006, 2004, Merzinger and Wirth, 2002] with various coordinate changes to compute the dynamical characteristics of rigid bodies. This tool is intensively used for dynamical characterization of shape primitives [Gross et al., 2004] and elementary tetrahedron [ling Lien and Kajiya, 1984, Pozo et al., 2011].

Definition 23 Let φ with $\varphi : \mathbb{R}^3 \mapsto \mathbb{R}^3$ be a continuously differentiable coordinate transformation from $V_{xyz} \subset \mathbb{R}^3$ to $V_{uvw} \subset \mathbb{R}^3$,

$$\varphi(u, v, w) = \begin{bmatrix} \varphi_x(u, v, w) & \varphi_y(u, v, w) & \varphi_z(u, v, w) \end{bmatrix}^T, \quad (\text{A.7a})$$

then the infinitesimal volume element changes by the determinant of the Jacobian,

$$d(x, y, z) = \begin{vmatrix} \frac{\partial \varphi_x}{\partial u}(u, v, w) & \frac{\partial \varphi_x}{\partial v}(u, v, w) & \frac{\partial \varphi_x}{\partial w}(u, v, w) \\ \frac{\partial \varphi_y}{\partial u}(u, v, w) & \frac{\partial \varphi_y}{\partial v}(u, v, w) & \frac{\partial \varphi_y}{\partial w}(u, v, w) \\ \frac{\partial \varphi_z}{\partial u}(u, v, w) & \frac{\partial \varphi_z}{\partial v}(u, v, w) & \frac{\partial \varphi_z}{\partial w}(u, v, w) \end{vmatrix} d(u, v, w), \quad (\text{A.7b})$$

of the coordinate transformation.

The coordinate transformation inside the volume integral then follows to:

Definition 24 Let φ with $\varphi : \mathbb{R}^3 \mapsto \mathbb{R}^3$ be the previously defined coordinate transformation and f with $f : \mathbb{R}^3 \mapsto \mathbb{R}$ a scalar function, then it follows for the coordinate in the volume integral,

$$\int_{V_{xyz}} f(x, y, z) \, dV(x, y, z) = \int_{V_{uvw}} f(\varphi(u, v, w)) \left| \frac{\partial(x, y, z)}{\partial(u, v, w)} \right| \, dudvdw. \quad (\text{A.8})$$

1.4 Parallel Axis Theorem

As soon as reference point transformations for dynamic characteristics need to be performed, the expressions (A.9)¹ proves highly valuable. The parallel axis theorem (A.9) allows to apply a shift operation of the motion axis from the center of gravity towards an external point and backwards. Inertia tensors that are expressed with respect to the same coordinate systems

¹Interestingly this theorem is already in Europe known under at least 4 different names: *Parallel Axis Theorem* - England, *Satz von Steiner* - Germany, *théorème d'huygens* - France, *teorema di Huygens-Steiner* - Italy

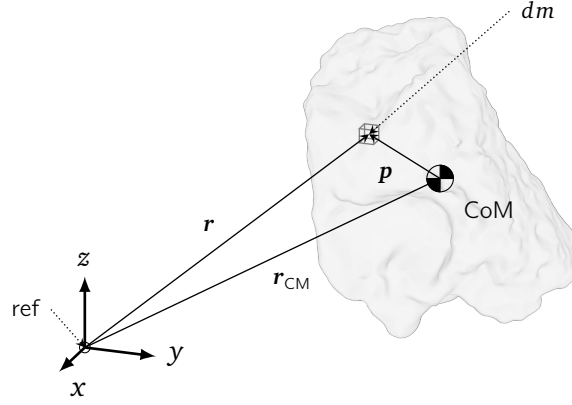


Figure A.2: Basic scheme underlying the determination of the dynamic characteristics (mass, center of gravity and inertia tensor) of a freely moving rigid body.

and reference point may be joint with simple sum and subtraction operations.

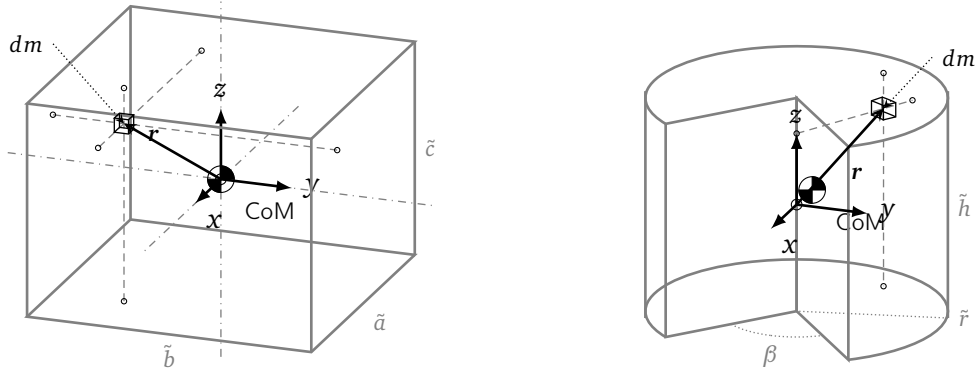
$${}^{\text{ref},o}I_{,K}^A = {}^{\text{ref},\text{CoM}}I_{,K}^A + m r_{o \rightarrow \text{CoM}} \times r_{o \rightarrow \text{CoM}} \times^T \quad (\text{A.9})$$

The parallel axis theorem is derived from figure A.2 based on a coordinate substitution assuming that the transformation is done based on the intermediate of the center of mass. For certain transformations it may happen that the inertia-tensor is shifted out of its parallel axis and loses its previous diagonal form,

$$\begin{aligned} \int_V \mathbf{r} \times \mathbf{r} \times^T dm &= \varrho \int_V \begin{bmatrix} r_y^2 + r_z^2 & -r_x r_y & -r_x r_z \\ -r_x r_y & r_x^2 + r_z^2 & -r_y r_z \\ -r_x r_z & -r_y r_z & r_x^2 + r_y^2 \end{bmatrix} dV \\ &= \varrho \int_V \begin{bmatrix} p_y^2 + p_z^2 & -p_x p_y & -p_x p_z \\ -p_x p_y & p_x^2 + p_z^2 & -p_y p_z \\ -p_x p_z & -p_y p_z & p_x^2 + p_y^2 \end{bmatrix} dV \\ &+ \varrho \int_V \begin{bmatrix} r_{\text{CM},y}^2 + r_{\text{CM},z}^2 & -r_{\text{CM},x} r_{\text{CM},y} & -r_{\text{CM},x} r_{\text{CM},z} \\ -r_{\text{CM},x} r_{\text{CM},y} & r_{\text{CM},x}^2 + r_{\text{CM},z}^2 & -r_{\text{CM},y} r_{\text{CM},z} \\ -r_{\text{CM},x} r_{\text{CM},z} & -r_{\text{CM},y} r_{\text{CM},z} & r_{\text{CM},x}^2 + r_{\text{CM},y}^2 \end{bmatrix} dV \quad . \quad (\text{A.10}) \\ &+ \underbrace{\varrho \int_V \begin{bmatrix} -2r_{\text{CM},y} r_y - 2r_{\text{CM},z} r_z & r_{\text{CM},x} r_y + r_{\text{CM},y} r_x & r_{\text{CM},x} r_z + r_{\text{CM},z} r_x \\ r_{\text{CM},y} r_x + r_{\text{CM},x} r_y & -2r_{\text{CM},x} r_x - 2r_{\text{CM},z} r_z & r_{\text{CM},y} r_z + r_{\text{CM},z} r_y \\ r_{\text{CM},z} r_x + r_{\text{CM},x} r_z & r_{\text{CM},z} r_y + r_{\text{CM},y} r_z & -2r_{\text{CM},x} r_x - 2r_{\text{CM},y} r_y \end{bmatrix} dV}_{=0} \\ &= \int_V \mathbf{p} \times \mathbf{p} \times^T dm + m r_{o \rightarrow \text{CM}} \times r_{o \rightarrow \text{CM}} \times^T \end{aligned}$$

2 Constructive Solid Geometry

From the knowledge of the author, mathematical foundations of this construction method have been first published in [Requicha and Tilove, 1978]. The constructive combination of different primitives is a relatively simple and accessible modeling strategy [Kirsch and Döllner, 2005], yet, with an increasing number of available primitives, coding efforts to support its construction raise [Lee and Requicha, 1981, Ling Lien and Kajiya, 1984]. Even though these



- (a) Computation of inertia tensor of a simple cube. The principle axis coincide in this simple case with the axis of the chosen reference frame
- (b) Integration of a splice with variable opening angle β . As soon as $\beta > 0$ the principal axis do not coincide any more with the symmetrically placed coordinate system, and hence the CoM is not found in the origin any more.

Figure A.3: Basic schemes for the computation of the dynamic characteristics of two different primitives: a cube (left) and a cylindric splice (right).

primitives normally depend from only a few parameters (e.g. cylinder, radius, length) including potential 6D transformation (3D-rotation, 3D-translation) between the merge-operations. Furthermore, the construction is done following a hierarchical tree structure [Kirsch and Döllner, 2005]. These aspects can conveniently be exploited for the computation of the mechanical characteristics. Based on the fact stated in 1.4 on page 221 that inertia tensors with respect to the same coordinate reference can be merged easily [Lee and Requicha, 1981] proposes a divide and conquer strategy that follows the tree and applies the parallel axis theorem (A.9), coordinate re-transformations, and (A.11a) - (A.11b) following the union and intersection,

$$\text{ref},o I_k^{A \cup B} = \text{ref},o I_k^A + \text{ref},o I_k^B - \text{ref},o I_k^{A \cap B}, \quad (\text{A.11a})$$

and difference,

$$\text{ref},o I_k^{A \setminus B} = \text{ref},o I_k^A - \text{ref},o I_k^{A \cap B}, \quad (\text{A.11b})$$

operations respectively.

At the top-level of the algorithm one needs to compute the dynamic characteristics of the primitives itself. For ease of parametrization forming the analytic expressions as closed form solutions is an essential requirement. In the following, an example of two different primitives (see Figure A.3), that will be intensively employed along the remainder of this work, is given and its implications are shortly discussed. For reasons of scope the discussion is limited to the most interesting aspect (inertia computation). Nevertheless, all aspects equally apply for the adjacent characteristics (CoM, mass, volume).

The computation of the inertia of the cube primitive,

$$\begin{aligned} \text{ref,CM} I_{\text{cube}} &= \int_{-\frac{c}{2}}^{\frac{c}{2}} \int_{-\frac{b}{2}}^{\frac{b}{2}} \int_{-\frac{a}{2}}^{\frac{a}{2}} \begin{bmatrix} y^2 + z^2 & -xy & -xz \\ -xy & x^2 + z^2 & -yz \\ -xz & -yz & y^2 + x^2 \end{bmatrix} \rho dx dy dz \\ &= \begin{bmatrix} m \frac{b^2+c^2}{12} & 0 & 0 \\ 0 & m \frac{a^2+c^2}{12} & 0 \\ 0 & 0 & m \frac{a^2+b^2}{12} \end{bmatrix}, \end{aligned} \quad (\text{A.12})$$

(see figure A.4b on the facing page) is relatively simple. The principal axes coincide with those of the reference frame and hence the CoM is directly located at the origin. The topology of V is a simple bounding and integration is straight-forward (A.12). Since a closed form solution exists symbolic handling of the expressions is possible.

In the case of the cylinder splice the representation of the topology V is more complicated. As soon as an opening angle $\tilde{\beta} > 0$ is allowed the primitive loses its rotational symmetric properties and the topology is even further complicated. This may be efficiently simplified with definition 24. A coordinate transformation based on (A.7a) and (A.7b),

$$\varphi(\alpha, r, h) = \begin{bmatrix} r \sin(\alpha) \\ r \cos(\alpha) \\ h \end{bmatrix}, \quad (\text{A.13a})$$

is applied towards polar-coordinates,

$$dx dy dz = \begin{vmatrix} r \cos(\alpha) & \sin(\alpha) & 0 \\ -r \sin(\alpha) & \cos(\alpha) & 0 \\ 0 & 0 & 1 \end{vmatrix} d\alpha dr dh. \quad (\text{A.13b})$$

Hence, the resulting topology reduces efficiently back to a bounding box. The inertia term then follows to,

$$\begin{aligned} \text{ref,o} I_{\text{splice}} &= \int_V \begin{bmatrix} y^2 + z^2 & -xy & -xz \\ -xy & x^2 + z^2 & -yz \\ -xz & -yz & y^2 + x^2 \end{bmatrix} \rho dx dy dz \\ &= \int_V \begin{bmatrix} r^2 \cos^2(\alpha) + h^2 & -r^2 \cos(\alpha) \sin(\alpha) & -r \sin(\alpha) \\ -r^2 \cos(\alpha) \sin(\alpha) & r^2 \sin^2(\alpha) + h^2 & -r \cos(\alpha) \\ -r \sin(\alpha) & -r \cos(\alpha) & r^2 \end{bmatrix} \rho r d\alpha dr dh. \end{aligned} \quad (\text{A.13c})$$

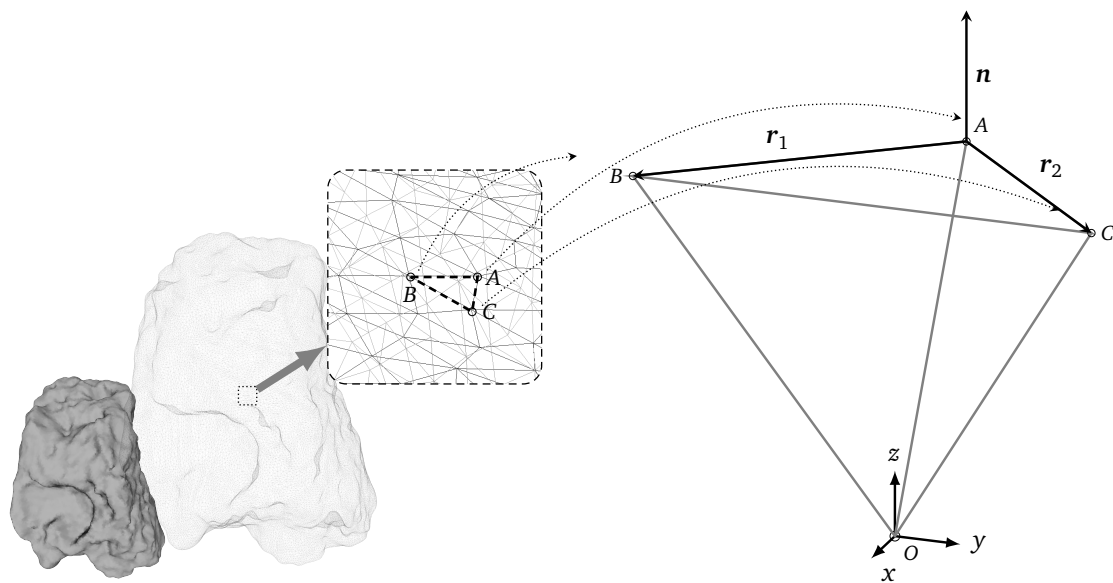
The complete resulting algebraic expressions are beyond the scope of this discussion, however a simple closed form solution exists and hence symbolic handling of the computation is possible. Hence, the examples above (see figure A.3) show that generic access to the dynamic characteristics (based on symbolic computations) is possible on the top level of the simple primitives. With a rigorous application of the divide and conquer method, (A.11a) and (A.11b) (see [Lee and Requicha, 1981, Requicha and Tilove, 1978] for details) this generic access should be preservable but is very probable to result in highly complex symbolic expressions. However, with a strict setting of the divide and conquer to process the construction of the geometry it is possible to keep the expression continuously differentiable with respect to its parametrization.

Furthermore, as it is explained in [Lien and Kajiya, 1984] the necessary algorithmic and

computational effort is considerably increasing with higher complexity of the design (see A.1b on page 219 and `vrefsuf::snakeWireFrame`), particularly when it comes to non-trivial operations like sweeping.

At a given point it might be more important to trade accuracy for efficiency and hence apply a discretization scheme to transform the highly complex primitive based representation of the design into a more generic one, volume- or surface-based. This gives further modeling opportunities, however with this discretization step, it is almost certain that continuous differentiability with respect to the parametrization is lost.

3 Polygonal Representation



(a) Polygonal representation of an arbitrary free-form (block island meteoroid [Capraro, 2014]), as surface model, as wireframe model and a detailed view on the triangulated structure.

(b) Scheme of a tetrahedra used for determination of the dynamic characteristics of the complete geometry, under the assumption of a uniformly distributed density.

Figure A.4: Almost any geometric shape be it convex or non-convex can be approximated with a collection of triangular facets classical surface shape representation [Boissonnat, 1984]. Depending on the complexity of the shape at hand the number of facets needs to be adjusted accordingly [Dobrovolskis, 1996]. Figure A.4a shows the free-form [Capraro, 2014] in surface representation, in wireframe representation and takes out an exemplairy triangular facet for further computations in Figure A.4b.

The polygonal representation of an arbitrary volumetric geometry can be tracked back relatively far [Boissonnat, 1984, Ling Lien and Kajiya, 1984, Pozo et al., 2011] and is a quite versatile method to express as well a volume just by its bounding surface when compared to other analytical approaches such as subsequent slicing [Ravi and Srinivasan, 1990]. However this technique can reach its numerical limits, when the design features highly thin structures [Boissonnat, 1984]. In [Dobrovolskis, 1996] approximate values about the quality of the approximation of volumetric geometries based on its surface discretization are given, however these apply to large bodies like asteroids. For mechanical engineering applications (see figure A.1b on page 219 and A.1c on page 219) facet numbers as high as 40.000 are reasonable. Furthermore modern CAD systems offer this kind of data format (vertices & triangu-

lated facets between those vertices) directly based on common formats such as STL (stereolithography [Rypl and Bittnar, 2004]).

A relatively recent and compact review about geometric moment computation methods for polygonal-data is given in [Pozo et al., 2011]. In this review others identify two different approaches. The track splits at the point where the volume integral has to be computed. All approaches are traced back to [Best, 1964], solving the moment over the volume of the tetrahedron. The works of [Ling Lien and Kajiya, 1984, Pozo et al., 2011] propose an efficient solution approximate and exact [Pozo et al., 2011] to solve the volume-integral directly (leading to relatively complex formulas), while approaches presented in [Dobrovolskis, 1996, Li, 1993, Liggett, 1988, Mirtich, 1996] apply theorem 4 to transform the volume integral into a surface based integral. Apart from an efficient and simple method derived directly from the previously established surface integral [Dobrovolskis, 1996], [Li, 1993, Liggett, 1988, Mirtich, 1996] further apply Greens Theorem [Merzinger and Wirth, 2002] to transform the surface integral into a line-integral before evaluation. In the following the approach from [Dobrovolskis, 1996] will be discussed shortly, as the presented formulas seem to be best suited for a symbolic application to preserve generic access.

Compared to the case of constructive solid geometry (see section 2 on page 222), computation of the dynamic characteristics is straight-forward, even without knowledge about the hierarchical construction history. According to [Pozo et al., 2011], computational complexity does only linearly scale with the number of facets $O(n)$ and with the order of the computed momentum N to $O(N^9)$ (in the case of this study it holds $N < 3$) and generally not with the complexity and feature-richness of the given design, however direct access to geometrical features is relatively difficult when compared to the constructive solid geometry approach.

From [Dobrovolskis, 1996] for the tetrahedron with one of its vertices placed on the origin (A, B, C, O) , $\mathbf{r}_1, \mathbf{r}_2$ being,

$$\mathbf{r}_{i,1} = \mathbf{b} - \mathbf{a}, \quad (\text{A.14a})$$

$$\mathbf{r}_{i,2} = \mathbf{c} - \mathbf{a}, \quad (\text{A.14b})$$

$$\mathbf{n}_i = \mathbf{r}_{i,1} \times \mathbf{r}_{i,2}, \quad (\text{A.14c})$$

the edge vectors and \mathbf{n} the facet normal, it follows directly for the facet surface,

$$S_{i,\text{Facet}} = \frac{1}{2} \|\mathbf{n}_i\|, \quad (\text{A.14d})$$

the tetrahedron volume (A.14e)

$$V_{i,\text{tetrah}} = \frac{1}{6} \mathbf{a} \cdot \mathbf{n}_i, \quad (\text{A.14e})$$

and its CoM,:

$$\mathbf{r}_{i,\text{CM}} = \frac{1}{4} (\mathbf{a} + \mathbf{b} + \mathbf{c}). \quad (\text{A.14f})$$

For the inertia tensor, however, a few more operations are necessary [Dobrovolskis, 1996]. The computation of the inertia matrix from (A.1c) can be dispatched into 6 different elementary momentum quantities $(r_x^2), (r_y^2), (r_z^2), (r_x r_y), (r_x r_z), (r_y r_z)$ to be computed separately. Thus, an integral of the form,

$$P_{i,j} = \int_V ij \rho dV \quad (i, j) = [r_x, r_y, r_z], \quad (\text{A.15})$$

needs to be solved for each quantity. As theorem 4 is to be used, [Dobrovolskis, 1996] proposes to express the general elementary momentum quantity (A.16a) and hence the volume-integral collapses to a simplified surface integral (A.16c), as it holds $\mathbf{f}_{i,j} \cdot \mathbf{n}_{S \neq \text{Facet}} = 0$. The vector \mathbf{n}_S is the normalized, outwards pointing surface vector. The final form further includes the application of the vectorial surface elements of definition 20 and a coordinate transformation (A.16b).

$$\mathbf{f}_{i,j} = \frac{1}{5} ij \begin{bmatrix} r_x \\ r_y \\ r_z \end{bmatrix}, \quad (\text{A.16a})$$

$$\varphi(u, v) = \mathbf{a} + u\mathbf{r}_1 + v\mathbf{r}_2, \quad (\text{A.16b})$$

$$\begin{aligned} P_{i,j} &= \varrho \int_V \text{div}(\mathbf{f}_{i,j}) dV = \varrho \int_{S_{\text{Facet}}} \mathbf{f}_{i,j} \mathbf{n}_S dS \\ &= \varrho \frac{1}{5} \int_S (ij) (\varphi(u, v)) \underbrace{\mathbf{r}(\varphi(u, v)) (\mathbf{r}_1 \times \mathbf{r}_2)}_{\mathbf{r}(\varphi(u, v)) \frac{(\mathbf{r}_1 \times \mathbf{r}_2)}{\|\mathbf{r}_1 \times \mathbf{r}_2\|} \|\varphi(u, v)\| = 6V_{i,\text{tetrah}}} dudv \\ &= \varrho \frac{6}{5} V_{i,\text{tetrah}} \int_0^1 \int_0^{1-v} (ij) (\varphi(u, v)) dudv \end{aligned} \quad (\text{A.16c})$$

The final integration then yields a compact form that only depends on the 3D vertex coordinates of the concerned tetrahedron. The essential dynamic characteristics are then the mass

$$m_\Sigma = \sum V_{i,\text{tetrah}} \varrho, \quad (\text{A.17a})$$

the CoM

$$\mathbf{r}_{\Sigma, \text{CM}} = \frac{\sum V_{i,\text{tetrah}} \mathbf{r}_{i, \text{CM}}}{V_{\Sigma, \text{tetrah}}}, \quad (\text{A.17b})$$

and the inertia tensor with respect to the CoM,

$${}^{\text{ref,CM}} I_\Sigma = \sum {}^{\text{ref,o}} I_i - m \mathbf{r}_{\mathbf{o} \rightarrow \text{CM}} \times \mathbf{r}_{\mathbf{o} \rightarrow \text{CM}} \times^T, \quad (\text{A.17c})$$

but aligned to its principal axis. One should note that non-convex shapes represent facets with an outwards normal that points towards the origin. As the above form (A.16c) then consistently yields a negative result the summation of all facets (A.17c) automatically respects the expressions of combination (A.11). [Dobrovolskis, 1996] shows a convenient mathematical method how to directly transform the inertia tensor into the diagonal form of its principal axis.

The complete set of dynamic characteristics does only depend on the concerned vertex coordinates and does not include any operations (such as $\|\cdot\|$ or $\sqrt{\cdot}$) that would fail the expressions from being continuously differentiable e.g. with respect to the vertex coordinates. Thus, the expressions should give a generic access for parameterization of the dynamic characteristics. From the point of view of numerical stability of the expressions, particularly the cross product term $\mathbf{r}_{i,1} \times \mathbf{r}_{i,2}$ should be verified intensively for potential numerical instabilities as highly distorted elementary tetrahedron are frequently observed [Pozo et al., 2011] in polygon surface

data originating from common component design in mechanical engineering.

4 Concluding Remarks

In the above section two exemplary candidate solutions are discussed to establish a functional, highly complex geometry and to assess its dynamic characteristics. For a potential exploitation of these characteristics for optimal control, it is important that these computations can be represented symbolically to offer a generic access for easy parametrization of geometric features.

In the case of the polygonal representation the resulting expressions scale with complexity $O(m)$ and $O(n^2)$ for the number of facets m and the order of desired momentum $n (= 2)$ [Pozo et al., 2011]. At least the expressions directly depend on the coordinates of the concerned nodes [Dobrovolskis, 1996]. In case of the constructive solid geometry, first the complexity of the resulting expressions depends on the computation for each concerned primitive and second on their non-trivial combinations. Clearly a trade-off between efforts to establish a high number of different primitives and the computations to combine these primitives geometrically is necessary [Lien and Kajiya, 1984]. However, more complex merging operations, such as sweeping, may quickly stretch efforts and implied programming efforts to their limits [Lien and Kajiya, 1984]. The number of involved primitives is generally much smaller than the number of facets used to build the same design in polygonal representation. And hence, so is the number of geometric features, one may want to control in the constructive solid geometry design. The error of the dynamic characteristics is roughly proportional to the square of the precision of the geometric approximation [Dobrovolskis, 1996].

As designs from constructive solid geometry may be directly discretized to polygonal representation, this could lead to the assumption that designs with fewer geometric features in constructive solid geometry yield less complex symbolic expressions for its dynamic characteristics and better control of its features than in the case of the same geometry in polygonal representation. This situation may change with an increasing number of geometric features in constructive solid geometry as the number of additional facets and hence the overall complexity of the computations required to accomplish the further modeled geometric features may be assumed to increase slower. Even though the direct control about geometric features (e.g. radius of a cylinder, length of a block) is lost during discretization to polygonal data, however, effective feature control is still possible e.g. by specifying a skeleton of lower degrees of freedom to reference all vertex coordinates to (a popular technique in computer animation called skinning [Kavan et al., 2010]). Within some limits this should yield again low-dimensional, symbolically parameterized and continuously differentiable expressions of the dynamic characteristics.

Another technical issue that enters the global picture is versatility and portability of the represented information. Whilst the polygonal-data is easily transportable in various containers (e.g. STL [Rypl and Bittnar, 2004]) the design information of constructive solid geometry are highly system specific and a direct exchange is not always possible, or at least requires a considerable effort in standardization. However a given design based on constructive solid geometry can always be discretized into a different format - such as STL for simpler data exchange.

However, the polygon representation still remains an approximation (precision see [Dobrovolskis, 1996, Mirtich, 1996, Pozo et al., 2011]) compared to the exact primitive-based representation, and this applies equally for any characteristic that is computed based on this specific representation. Thus, different attempts in literature are observable to improve the quality of this approximation at maximum whilst preserving its computational simplicity of the dynamic

characteristics. A highly comprising approach has been published in [Gonzalez-Ochoa et al., 1998]. The authors represent complex geometries with a few three- and four-edge patches based on surface splines [Peters, 1995]. Based on this representation the same computational approach is conducted as in [Dobrovolskis, 1996, Gonzalez-Ochoa et al., 1998]. The resulting expressions are highly optimized and suitable for quick computations even of relatively complex geometries. As proof of quality the authors present impressively quick-estimations of the dynamic characteristics of the flexibly changing complex geometries for physical simulations [Gonzalez-Ochoa et al., 1998]. However, no information about numerical stability are provided within this paper.

B Modeling of Technical Components

The robotic platform and theoretically modeled devices for subsequent optimization do consist of a large number of components (e.g. kinematic structure, bearings, contact surface, power transmissions units) that imply different physical characteristics to be modeled as precisely as necessary, such that the optimization solver can correctly exploit the physical characteristics of the complete system. In the following a brief introduction and discussion of the modeled element characteristics for the optimization studies of this work is given below.

1 Actuation Systems

Actuation systems in the abstract sense are just power converters that transform electrical into mechanical power [Heimann et al., 2007], satisfying further constraints, such as, type/magnitude of movement or force/torque by speed ratio. The system basically follows the scheme in Figure B.1a on the next page with a power intake gait (e.g. electrical power) a power output gait (e.g. electrical power) and a power loss gait (e.g. heat dissipation) over the system boundary. With the relationship between power and energy,

$$W_{t_1 \rightarrow t_2} = \int_{t_1}^{t_2} P(t), \quad (\text{B.1a})$$

and the assumption that the internal energy state $E(t)$ of the converter is stationary $\frac{\partial}{\partial t} E(t) = 0$ a pure balance of energy flows over the system boundary gaits leads to the power-balance,

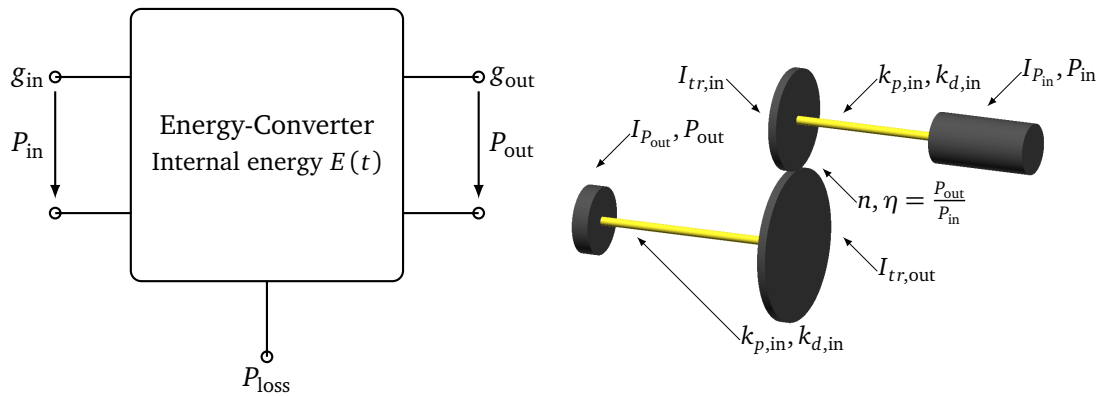
$$\frac{\partial}{\partial t} E(t) = P_{\text{in}} - P_{\text{out}} - P_{\text{loss}} = 0. \quad (\text{B.1b})$$

Based on this balance one may then define the efficiency η ,

$$\eta = \frac{P_{\text{out}}}{P_{\text{in}}}, \quad (\text{B.1c})$$

of the energy converter [Heimann et al., 2007]. The previously defined efficiency η (B.1c) is substantially different from the efficiency term that will be defined for walking motions in subsequent chapters. Therefore it is important to clearly define each term separately, as the efficiency η for power converters will be used through the complete modeling section. However, for most optimization computation η will be set to 1 in a first attempt, until better data is available (e.g. system identification).

Besides fluid-based actuators, which are, related to their power-transmission to system-weight ratio, less common in medium size robotic platforms (e.g. exception always remain [Bentivegna et al., 2007]), electrical actuation systems coming in various different forms and specifications are very frequently found [Hirukawa et al., 2004]. As the application part of this work is dedicated to the robotic platform HRP-2 14 [Kaneko et al., 2004] which is solely powered by this type of actuation system, the physical characteristics and their implications for the mathematical modeling are shortly addressed in the subsequent sections.



- (a) Abstract view of an actuation system as energy converter with power intake gait P_{in} , g_{in} , power output gait P_{out} , g_{out} and power loss gait P_{loss} , including its internal energy state $E(t)$
- (b) Simplified mechanical view of an actuation system with a power-intake P_{in} and its equivalent inertia (e.g. as electric motor) a power transmission unit with transmission ratio i , efficiency η and equivalent inertia's $I_{tr,in}$, $I_{tr,out}$ (e.g. chain-drive, timing belt, spurring gears), elastic deformation $k_{p,in}$, $k_{p,in}$ and damping $k_{d,in}$, $k_{d,out}$ as well as a power output P_{out} and its equivalent inertia I_{out} .

Figure B.1: Abstract scheme for a power converter and a direct example as abstract actuation system with electrical power intake as motor, mechanical transmission and power output

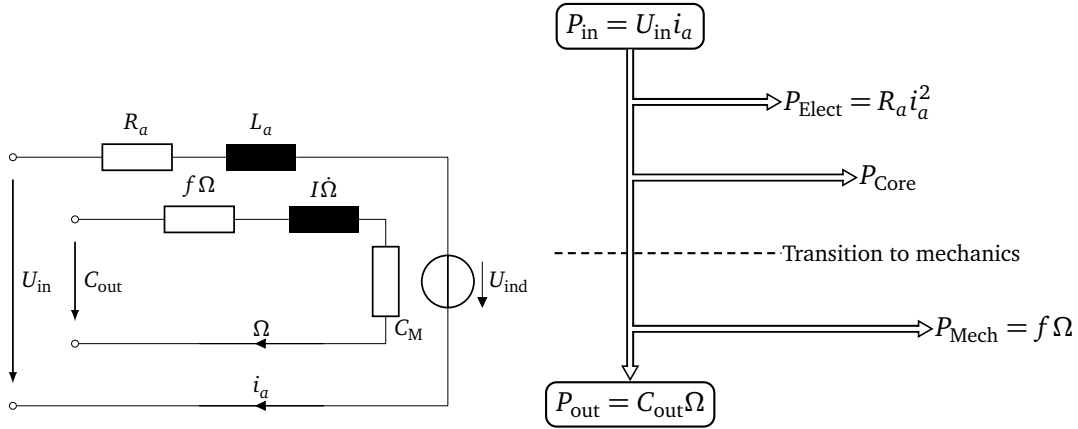
1.1 Electric Actuation Systems

A simplified sketch of an electrical motor including a transmission system is shown in Figure B.2a on the following page. They are relatively lightweight, flexible, robust, come in various forms, allow for high energy flow in forward and inverse direction and hence, are conveniently controllable. Most common principles are synchronous and asynchronous three-phase machines as well as reluctance (e.g. stepping motors) and induction based machines. An important capacity of these motors is that overload (for a short time) in the power-throughput (not the velocity-output !) is not a serious problem, if the machine is given sufficient time to dissipate the additionally produced heat to recover its operational thermal balance.

The optimization problems targeted to a practical application do, for a certain extend, exploit the dynamic characteristics of the, very commonly employed, brushed DC-machines, while others are neglected. In turn a short introduction to the governing physics and the mathematical modeling equations will be given upon which all following discussions will then be based on.

Brushed DC-machines [Heimann et al., 2007] are based on the principle of the Lorentz force (this forces transforms into a torque on the motor coil C_{Motor}) acting on an electric conductor in a magnetic field [Schulz et al., 2007]. At the same time this conductor moves in the magnetic field producing a rate of change in the magnetic flux and hence an electromagnetic force U_{ind} . The following discussion is now limited to shunt connection machines [Grote and Feldhusen, 2011, Heimann et al., 2007] as their characteristics are the most close with permanent magnet machines, which are commonly mounted as miniature motors on common medium size robotic platform (e.g. HRP-2 14, refer [Kaneko et al., 2004]).

The general scheme of the machine is shown in Figure B.2a on the next page. Kirchoff's



- (a) Electric (outer) and equivalent mechanical (inner) circuit loops of a brushed DC-machine. The outer loop is determined by the armature resistor R_a , the inductivity of the coil armature L_a and the electromagnetic force U_{ind} . The mechanical loop is determined by the transmitted torque C_{in} , viscous friction losses $f\Omega$ and the rotational inertia of the coil.
- (b) Scheme of power transfer and adjacent power losses in a brushed DC-machine from the power intake $U_{\text{in}}i_a$ to the mechanical power output $C_{\text{out}}\Omega$

Figure B.2: Schematic description of dynamic characteristics and power transmission of a brushed DC-machine

junction rule then gives the first governing differential equation,

$$U_{\text{in}} = \frac{\partial i_a}{\partial t} L_a + R_a i_a + U_{\text{ind}}, \quad (\text{B.2a})$$

of the electric circuit, featuring the electric armature resistance R_a and the armature inductivity L_a of the coil. In the input voltage of the machine is U_{in} and the current circulating in the armature is represented with i_a . The second governing differential equation,

$$C_{\text{Motor}} = \frac{\partial \Omega}{\partial t} I_m + C_{\text{out}} + f\Omega, \quad (\text{B.2b})$$

simply follows from Newton's law (torque-balance on the coil-axis of the machine), featuring the inertia of the coil I_m the viscous friction constant f the motor output torque C_{out} as well as the torque that is internally produced by the machine C_{Motor} . Both differential equations are then linked together on a simplified power transmission based on four-terminal-theory [Heimann et al., 2007] featuring in a simple manner the present core-losses (material based hysteresis losses, eddy-currents) and stray-loads. Finally by substitution of,

$$U_{\text{ind}} = \frac{\partial \Phi}{\partial t} = k_{\Phi} \Omega, \quad (\text{B.2c})$$

and,

$$\eta = \frac{P_{\text{mech}}}{P_{\text{elec}}} = \frac{C_{\text{Motor}} \Omega}{U_{\text{ind}} i_a}, \quad (\text{B.2d})$$

into (B.2a) and (B.2b) the governing set of differential equations results to the electrical part,

$$\frac{\partial i_a}{\partial t} = -\frac{R_a i_a}{L_a} - \frac{k_\Phi \Omega}{L_a} + \frac{U_{\text{in}}}{L_a}, \quad (\text{B.2e})$$

and the mechanical part (B.2f)

$$\frac{\partial \Omega}{\partial t} I_m = \eta k_\Phi i_a - C_{\text{out}} - f \Omega. \quad (\text{B.2f})$$

The following discussion is based on the static case with the following assumptions: $\frac{\partial i_a}{\partial t} = 0$ and $\frac{\partial \Omega}{\partial t} I_m = 0$. The static power intake and the mechanical power output of the machine then computes to,

$$U_{\text{in}} i_a = R_a i_a^2 + k_\Phi \Omega i_a, \quad (\text{B.3a})$$

and,

$$C_{\text{out}} \Omega = \eta k_\Phi i_a \Omega - f \Omega^2, \quad (\text{B.3b})$$

respectively. From this set of equations it follows that besides the mechanical output the term C_{out}^2 is proportional to $\sim i_a^2$ and thus a good indicator for the armature losses $R_a I_a^2$ [Buss et al., 2003], a characteristic that is intensively exploited in all subsequent optimization studies.

From a control engineering point of view it is interesting to analysis the dynamics of the brushed DC-machine to seek for possible simplifications, whilst keeping the most important physical characteristics. After a transformation into the frequency space [Heimann et al., 2007] and some re-arrangements equations for the armature current,

$$i_a(s) = \frac{U(s) - k_\Phi \Omega(s)}{R_a \left(1 + \frac{L_a}{R_a} s\right)}, \quad (\text{B.4a})$$

and the coil spinning velocity,

$$\Omega(s) = \frac{i_a(s) k_\Phi \eta - C_{\text{out}}(s)}{f \left(1 + \frac{I}{f} s\right)}, \quad (\text{B.4b})$$

are found. According to [Grote and Feldhusen, 2011, Heimann et al., 2007] it generally holds that $\frac{I}{f} \gg \frac{L_a}{R_a}$. In a first approximation the dynamics of the electric loop are negligible effectively eliminating the armature current from the set of equations - resulting in the simplified dynamic equation,

$$\frac{\partial \Omega}{\partial t} I = \frac{\eta k_\Phi}{R_a} (U_{\text{in}} - \Omega k_\Phi) - C_{\text{out}} - f \Omega, \quad (\text{B.5})$$

featuring the inertial effects of the spinning coil an input torque component (proportional to the input voltage U_{ind}) and a dissipation term (proportional to the spinning angular velocity of the coil). This simplified equation will be used for the modeling of the determining characteristics of all brushed DC-machine driven actuation in subsequent discussions.

1.2 Abstract Dynamic Modeling of Transmission Units

From a technical point of view a gearbox [Grote and Feldhusen, 2011] (e.g. spurring gears, belt drives, coils) is just an assembly of multiple moving parts that are either rigidly or compliantly connected. From the modeling perspective these bodies give usually an addition to the normal kinematic tree with further degrees of freedom to express their functional motion on top of external motion of the device they are rigidly mounted to [Featherstone, 2007]. Depending on the assumption concerning the design of the robot and its modeling, the mathematical expression can be simplified to a certain extend and conveniently used in forward and inverse dynamics [Siciliano and Khatib, 2007].

The general equation of motion without contacts is,

$$M(q)\ddot{q} + NLE(q, \dot{q}) = \tau. \quad (\text{B.6})$$

The state of the fully actuated system is with q , \dot{q} and \ddot{q} under the external actuation τ . The discussion of the underacted part is analogous but involves more complicated formulas and thus will not be shown here. With the additional rigid bodys of the complete structure, the state vector of the system may be dispatched into $q = [x \ y]^T$ featuring the states x of the system and the additional degrees of freedom y to express their functional motions (e.g. spin motion of the motor coil). The inertia matrix of the complete system is then expressed as in,

$$M = \sum_i \left({}^L J_i^T(q) {}^L I_i {}^L J_i(q) \right) + \sum_j \left({}^M J_j^T(q) {}^M I_j {}^M J_j(q) \right), \quad (\text{B.7a})$$

and the nonlinear effects in,

$$\begin{aligned} NLE = & \sum_j \left({}^L J_i^T {}^L I_i {}^L J_i \dot{q} - {}^L J_i^T {}^L J_i \dot{q} \times {}^L I_i {}^L J_i \dot{q} \right) \\ & + \sum_j \left({}^M J_j^T {}^M I_j {}^M J_j \dot{q} - {}^M J_j^T {}^M J_j \dot{q} \times {}^M I_j {}^M J_j \dot{q} \right), \end{aligned} \quad (\text{B.7b})$$

as part of the pure dynamics of the kinematic structure and a coupling between the dynamics of both, the kinematic structure and the moving parts of the actuation system. ${}^L J_i$ and ${}^M J_j$ in equation (B.7a) and (B.7b) represent the 6D spatial Jacobi-Matrix with respect to the origin of structure frame i or the local actuation system component j respectively and expressed in the local reference of the frame. ${}^L I_i$ and ${}^M I_j$ are the 6D spatial inertia matrices of the frame i and the actuation system component j respectively with respect to the local origin expressed in the local reference frame. In most cases the determining dynamical parts of an actuation system do have rotational-symmetric shape about their functional motion axis and homogeneous density while the motion is a pure rotation. Further more the degrees of freedom of the components of the actuation system linked with a constant transmission ratio. In turn, the 6D inertia tensor of the actuation components simplifies to a diagonal matrix. With the further assumption that deformations stay in purely elastic domain, the dynamic equation of the system drops in the form of,

$$\begin{aligned} & \begin{bmatrix} {}^L M + {}^M M + {}^{L\&M} M (B^{-1}) {}^{L\&M} M^T & {}^{L\&M} M \\ {}^{L\&M} M^T & B \end{bmatrix} \begin{bmatrix} \ddot{x} \\ \ddot{y} \end{bmatrix} + \begin{bmatrix} {}^L C + {}^{L\&M} C \\ {}^M C \end{bmatrix} \\ & = \begin{bmatrix} k_d (N^{-1} \dot{y} - \dot{x}) + k_p (N^{-1} y - x) \\ k_d N^{-1} (N \dot{x} - \dot{y}) + k_p N^{-1} (N x - y) + \tau \end{bmatrix}, \end{aligned} \quad (\text{B.8})$$

following [Siciliano and Khatib, 2007] which lends itself easily for further discussions. The matrices ${}^L M$ and ${}^M M$ contain the pure inertia effects of the kinematic structure and the actuation system (other diagonal inertia terms that are with respect to the acceleration of the kinematic structure. B contains the inertia terms of all components of the actuation system with respect to the functional acceleration (e.g. spinning acceleration of the motor coil) and ${}^{L\&M} M$ regroups all dynamic couplings between the actuation system and the kinematic structure. The matrix N is diagonal and regroups all transmission ratios n_j between the specific coupled degrees of freedom $x \rightarrow y$. Depending on the design of the robotic system, the matrix S is highly structured (upper triangular when all actuation systems are mounted to there parent link of the joint they are driving) and the inertia matrix may only depend on the system states x [Siciliano and Khatib, 2007], aspects that can be exploited for an efficient resolution of the system.

As the degrees of freedom of the actuation components y do usually have much higher turning rates $n_j \gg 1$ and the influence of the term ${}^{L\&M} M$ raises with $\sim n_j$ compared to the influence of B with $\sim n_j^2$, for sufficiently high transmission ratios ≤ 100 the dynamic coupling between the components of the actuation system and the kinematic structure are sufficiently small to be negligible [Siciliano and Khatib, 2007] and the upper and the lower part of the dynamic equation gets decoupled.

For the assumption that the actuation system is perfectly rigid the following assumptions holds,

$$\begin{aligned} k_p &\rightarrow \infty, \\ N^{-1}y, N^{-1}\dot{y} &\rightarrow x, \dot{x}. \end{aligned} \tag{B.9}$$

It is then possible to express the motor states based on the system states $q(x)$, in the case of the discussed system $q(x) = \begin{bmatrix} x & Nx \end{bmatrix}^t$. As stated in [Featherstone, 2007] the dynamic equation may be reduced by substitution with the Jacobian-Matrix $G(x)$ and Hessian-Vector $\dot{G}(x, \dot{x})$ of the coordinate transformation of $q(x)$. Further pre-multiplying with the Jacobian-Matrix $G(x)$. The projected dynamic equation results to,

$$G^T M (G\ddot{x} + \dot{G}) + G^T N L E = G^T \tau. \tag{B.10}$$

For the simple case above (B.8) G and \dot{G} yield the form of,

$$G(x) = \begin{bmatrix} 1 & 0 & 0 \\ 0 & \ddots & 0 \\ 0 & 0 & 1 \\ n_1 & 0 & 0 \\ 0 & \ddots & 0 \\ 0 & 0 & n_{..} \end{bmatrix} = \begin{bmatrix} I \\ N \end{bmatrix}, \tag{B.11a}$$

and,

$$\dot{G}(x, \dot{x}) = 0, \tag{B.11b}$$

with the transformation ratios n_i . The dynamic equation then transforms into,

$$\left({}^L M + {}^M M + {}^{L\&M} M (B^{-1}) {}^{L\&M} M^T + {}^{L\&M} M N + N^T {}^{L\&M} M^T + N^T B N \right) \ddot{x}, \tag{B.12a}$$

$$+ \left({}^L C + {}^{L\&M} C + N^T {}^M C \right) = \tau. \tag{B.12b}$$

This dynamic equation expresses the full dynamics of the multi-body system including the coupling effects with the components of the actuation system - under the assumption of perfectly rigid links (see [Featherstone, 2007, Siciliano and Khatib, 2007]).

2 Modeling Friction

As it is stated in various sources, e.g. [Arisumi et al., 2008, Townsend and Salisbury, 1987], friction has an important physical influence that should be considered during the modeling of technical components, like joints, gearboxes as well as contact between rigid bodies. An introduction to static and dynamic friction models, as well as explanations about friction compensation for motion control based on those models is given in [Olsson et al., 1998]. They conclude that dynamic friction models generally perform over static models, while being almost as simple as the former when it comes to integration into a given control law (refer to [Bliman and M.Sorine, 1995]).

In the optimization studies, dry and viscous friction being modeled, either as static or dynamic quantity, would have an influence on the final motion result. However, the focus of interest during these studies was the investigation of the dynamics of a comprehensive model. As parameters for static friction modeling are given in literature, for technical joints [Albers et al., 2005, Sauer et al., 2012], the robot HRP-2 14 [Arisumi et al., 2008, Chardonnet, 2009] and for human joints [Morrison, 1970], the static case has been prepared by appropriate model parametrizations, but not used for optimization of the present results.

3 Modeling of Surface Contacts

As it was outlined in Section 3.3 on page 30 the modeling strategy for the optimization problem formulation is different to the purely dynamic simulation in the sense that, for the physical consistency of the model, the final resulting trajectory is either circumventing a given phenomena or influenced from it. In the former case the phenomena is not modeled and appropriate measures, e.g. constraints, are taken to maintain consistency of the optimization problem formulation. In the latter case the phenomena is modeled and thus part of the optimization problem.

As it was previously explained in Section 3.3 on page 30 uni-lateral constraints are modeled as bilateral contacts with additional consistency constraints. In case this 6D bilateral point contact represents a surface contact, despite the force component normal to the surface, the contact surface pair may as well transmit tangential force and torque components as well as vertical torque components. Consequently, these constraints must be formulated inside the constraint to enforce physical consistency.

3.1 Friction in Unilateral Contacts

Based on [Albers et al., 2005, Olsson et al., 1998, Sauer et al., 2012] it is assumed that force-components orthogonal to the surface normal can only be transmitted when a sufficiently high normal force component is present. In engineering mechanics the static relation these force components is expressed through Coulomb friction,

$$F_t = F_n \mu, \tag{B.13}$$

[Olsson et al., 1998] relating the normal force component F_n and the tangential force component F_t of the friction coefficient μ . Determination of this coefficient is highly problematic

as it depends various aspects, such as microscopic characteristics of the contact surfaces, lubrication.

Although this is only a coarse approximation, it is a simple and thus valuable indicator for the physical consistency of the contact state. In the case of the surface contact, however, there is a problem. Despite the tangential force component, the transmitted vertical torque component, with respect to the surface normal, is not taken into account. Hence, a second indicator to be based on (B.13) is necessary to enforce the physical consistency. The following approach explicitly avoids hyperstaticity to keep the computations tractable for the given optimization problem.

The pair of contacts transmits a stress field $\boldsymbol{\sigma} \in \mathbb{R}^3$, distributed among their common surface S_C with the boundary ∂S_C . The spatial contact force reaction $\hat{\mathbf{f}}$ referenced to the position of the contact point is the resultant of this stress field from,

$$\mathbf{f} = \int_{S_C} \boldsymbol{\sigma} dS, \quad (\text{B.14a})$$

$$\mathbf{m}^{\text{Contact}} = \int_{S_C} \mathbf{r} \times \boldsymbol{\sigma} dS, \quad (\text{B.14b})$$

under the assumption that the vertical of the force field is a linear plane,

$$\boldsymbol{\sigma} \mathbf{n}_\perp = ar_{\parallel,1} + br_{\parallel,2} + c. \quad (\text{B.14c})$$

For the orthogonal component $\boldsymbol{\sigma} \mathbf{n}_\perp$ of the stress field, based on (B.14a) and (B.14b) one may observe that this component only depends on the tangent torque components $m_{\parallel,1}^{\text{Contact}}$ and $m_{\parallel,2}^{\text{Contact}}$ as well as the orthogonal force component f_\perp . From this relation the orthogonal stress field components are determined by reverse identification from the 6D contact reactions,

$$\begin{bmatrix} \int_{S_C} r_{\parallel,1} dS & \int_{S_C} r_{\parallel,2} dS & \int_{S_C} dS \\ \int_{S_C} r_{\parallel,1} r_{\parallel,2} dS & \int_{S_C} r_{\parallel,2}^2 dS & \int_{S_C} r_{\parallel,2} dS \\ -\int_{S_C} r_{\parallel,1}^2 dS & -\int_{S_C} r_{\parallel,2} r_{\parallel,1} dS & -\int_{S_C} r_{\parallel,1} dS \end{bmatrix} \begin{bmatrix} a \\ b \\ c \end{bmatrix} = \begin{bmatrix} f_\perp \\ m_{\parallel,1}^{\text{Contact}} \\ m_{\parallel,2}^{\text{Contact}} \end{bmatrix}. \quad (\text{B.15a})$$

Based on the estimated orthogonal stress field component $\boldsymbol{\sigma} \in \mathbb{R}^3$ a comparative value $m_{t,\max}$,

$$m_{t,\max} = \int_{S_C} \mu \mathbf{n}_\perp \boldsymbol{\sigma} \sqrt{r_{\parallel,1}^2 + r_{\parallel,2}^2} dS, \quad (\text{B.15b})$$

is computed. For the maximal admissible orthogonal torque component this is then computed on the assumption of Coulomb friction (B.13).

For more complex contact surface boundaries above equations lend them selves perfectly for simplifications based on the curl-theorem [Merzinger and Wirth, 2002] to reduce the surface integral to a line integral on ∂S_C . For the implementation (B.15b) is transformed to polar coordinate base. As conclusion, consistency with respect to friction, e.g. no slip, of the unilateral contact is assumed upon respect of the two constraints,

$$\sqrt{f_{\parallel,1}^2 + f_{\parallel,2}^2} < f_\perp \mu, \quad (\text{B.16a})$$

and,

$$m_{\perp}^{\text{Contact}} < m_{t,\text{max}}. \quad (\text{B.16b})$$

3.2 CoP Position

From (B.14b) another important information can be obtained. If one discards the component $m_{\perp}^{\text{Contact}}$ orthogonal to the contact surface there exists a reference point of the integral where the remaining torque $m_{\parallel,1}^{\text{Contact}}$ and $m_{\parallel,2}^{\text{Contact}}$ components disappear. In the domain of robotics this point is called center of pressure (in the following CoP) [Goswami, 1999, Vukobratović and Stepanenko, 1972] and is adopted to rate the stability of unilateral ground contacts. It happens to coincide [Goswami, 1999] with the ZMP [Vukobratović and Stepanenko, 1972], when it is not located on the boundary ∂S_C of the contact surface and for perfectly inelastic surfaces that do not slip against each other. As the CoP,

$$\text{CoP}_{\parallel,1} = -\frac{m_{\parallel,2}^{\text{Contact}}}{f_{\perp}}, \quad (\text{B.17a})$$

$$\text{CoP}_{\parallel,2} = \frac{m_{\parallel,1}^{\text{Contact}}}{f_{\perp}}, \quad (\text{B.17b})$$

can physically never leave the contact surface it is not possible to measure a rate of instability with this formalism, but only a margin of stability as a generalized distance to the boundary ∂S_C of the contact surface. Within this respect, literature suggests different methods, such as FRI [Popovic et al., 2005] to measure the stability for example in foot-ground contact states. However, based on its appealing simplicity, this formalism has been adopted similarly to [Ramos et al., 2011, Saab et al., 2011]. The contact is declared feasible when the CoP remains inside a more restricted sub-manifold of the contact surface. This proved to be a sufficiently conservative assumption, as well with respect to real experiments on HRP-2 14 discussed in subsequent chapters.

C Human Body Data

As soon as a comprehensive study of the dynamic whole body motion is to be conducted, partial or full modeling of the human body is an essential requirement. In case the human body is assumed to consist of perfectly rigid bodies – a strong assumption with respect to the soft tissues a human body – the minimal necessary data-set consists of kinematic chain data of the dispatched body-limbs as well as the inertia tensor, the mass and the placement of the local CoM for each limb segment. These values need to be measured from real bodies.

1 Kinematic Data

A difficult process in modeling of biological structures for subsequent simulation and optimization studies is the assessment of the kinematic characteristics of the soft-tissue based joints [Bottlang et al., 2000, Flores, 2011, Grood and Suntay, 1983, Isman and Inman, 1969, Kang et al., 2002, Menschik, 1997, Morrison, 1970]. These characteristics not only depend on the individual variety present in nature but as well from the instantaneous kinematic constraint and load configuration, such that, a rigorous projection to prismatic and rotational joints must be carefully considered to achieve a desired modeling accuracy. In the following, the necessary accuracy to support the subsequent studies and discussions is estimated to be more important for the lower than for the upper part. Consequently, this discussion will be limited to the lower limb kinematics.

1.1 Hip Joint

Mechanically the human hip joint articulation is located between the hip and the femur and consists of a conchoid rotational femoral head moving in a acetabulum of same shape but slightly larger dimension [Menschik, 1997]. The authors in [Menschik, 1997] measured the geometry of joints from cadavers with a highly precise CNC-Measurement machine to support the above hypothesis which effectively changes the previously purely sliding motion into a combination of rolling and sliding. However most studies determine the hip joint center employing various invasive or non-invasive methods [Kirkwood et al., 1999] and assume the hip joint center as a spherical joint (see Figure C.1 on the following page). This proved to be sufficiently accurate for most motion studies. However, the above aspect should be kept in mind when it comes to kinematic constraints and particular load situations.

1.2 Knee Joint

The knee joints, femur and tibia bone consist of a larger medial and smaller lateral condyles with variable curvature, sliding in its geometrical counterparts of the tibia bone. Lateral motion is mostly prevented by the intercondyloid eminence. [Morrison, 1970] gives a review about the knee mechanics. The authors measured muscle forces compared with force plate data and whole body kinematics to estimate ligament force and the vertical and medio lateral load transmitted through the knee joint. [Grood and Suntay, 1983] analyzed the knee from a geometrical point of view. Besides the main dof in the media-lateral direction, they identify a

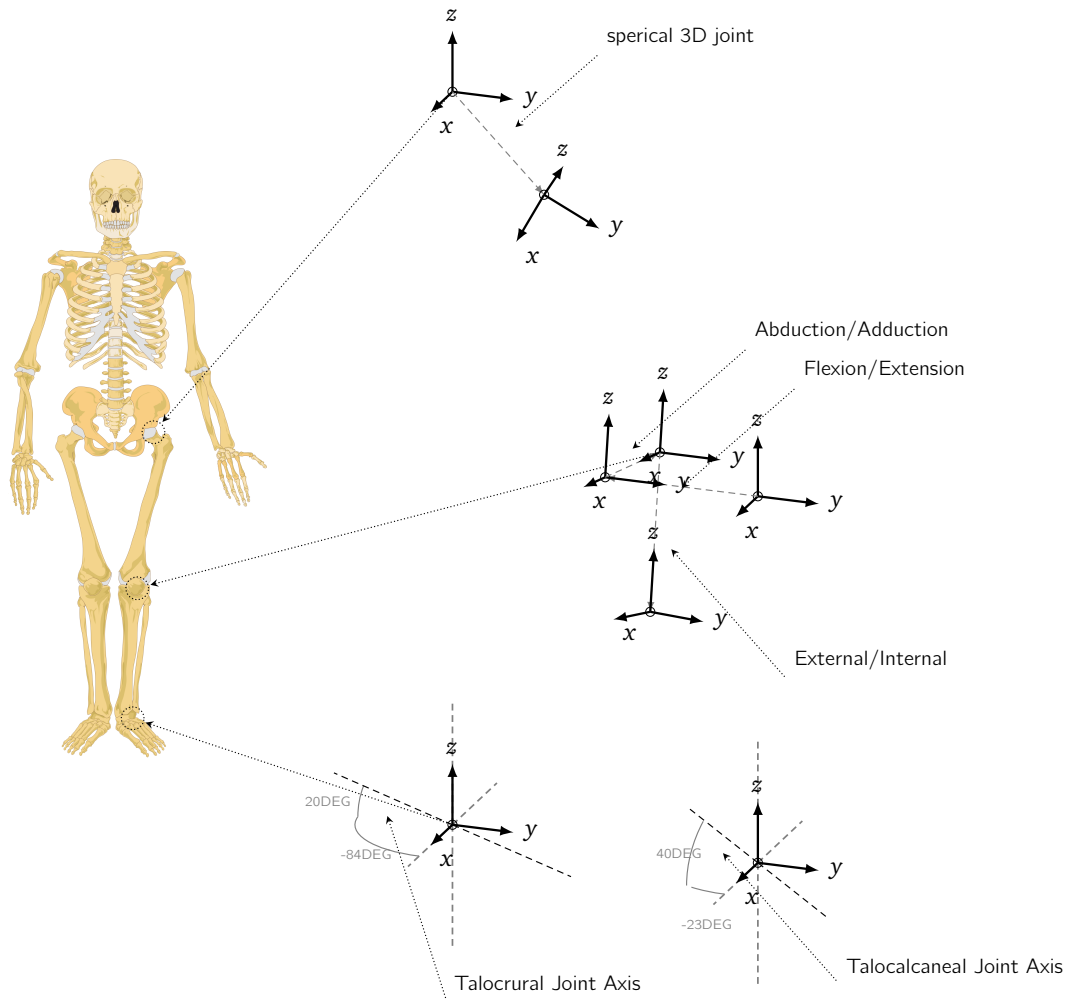


Figure C.1: The kinematic scheme of a human body with joint axis configurations from literature [Hägström, 2008]. The choice of the coordinate systems closely follows the convention frequently observed in clinical articles, with the Z-axis pointing upright, the Y-axis pointing into the lateral direction and the X-axis orthogonal to the latter and the former axis.

configuration (see Figure C.1) of three rotational and three prismatic dofs to describe the full kinematic configuration space following sequence dependent and independent conventions. The results are expressed based on the Denavit-Hartenberg Convention convention [Heimann et al., 2007]. The proposed sequence starts with flexion/extension and a prismatic joint around the Y-axis, continues with abduction/adduction and a prismatic joint around the X-axis and ends with external/internal rotation and the corresponding prismatic joint around the Z-axis.

1.3 Ankle Joint

The kinematic configuration of the ankle joint complex at the end of the tibia and fibula bones was analyzed by [Isman and Inman, 1969] carrying out large scale measurements on cadaver specimens. They identified the orientation and location of the talocrural and the talocalcaneal joints dispatched in space to be represented as single dof joints. Both axes show a complex configuration in space (see Figure C.1). The authors state as well that the measurements

contained a large variety between the specimens, such that an efficient exploitation of the geometric data for manufacturing of braces would highly depend on separate adjustments of the geometry on a per specimen bases. In Figure C.1 on the preceding page the Z-axis coincides with the long axis of the tibia and the X-axis with the middle line of the foot. The talocrural joint axis is inclined about -84DEG around the Z-axis and -20DEG around the Y-axis. The talocalcaneal joint axis is oriented about -23DEG around the Z-axis and about -40DEG around the Y-axis. For better visibility joint axis have been shown dispatched. Furthermore, the talocalcaneal joint axis is located about 5mm orthogonal below the talocrural joint axis [Isman and Inman, 1969].

2 Dynamic Data

Different measurement methods have been documented in literature from measurements, on disassembled cadavers [Clauser et al., 1969, Dempster, 1955] or *in vivo* tests using either gamma-ray scanning technics [Zatsiorsky et al., 1990] or stereo-photogrammetric techniques [McConville et al., 1980, Young et al., 1983]. The *in vivo* measurement use photographic techniques to estimate the 3D shape or analyze the tissue properties underneath the skin and to compute the inertia properties from assumption e.g. upon density (homogeneous in case of [McConville et al., 1980, Young et al., 1983]). The dynamics properties have then been established separately for male and female gender, based on linear regression upon a large number of sample measurements with respect to scaling parameters (length and mass). As it is outlined in [de Leva, 1996a, Dumas et al., 2007a,b] the data sets are only consistent for similar age, corporal constitution, gender and ethnic origin. As soon as measurement-samples outside of the population are considered non-linear regression methods are possible as long as anthropometric measurements are supplied with the raw data-sets [Dumas et al., 2007a].

The problem for the modeling case is that most of the data-sets are not given with respect to the joint centers between the limbs of the human body, but with respect to a setting of bone-based landmarks. This is a general problem as the computed segment lengths are generally neither consistent with the kinematic chain nor support arbitrary movements of the segments without rescaling [de Leva, 1996a]. During the past few decades efforts have been conducted to adjust those data sets for kinematic modeling. While the gait analysis community mainly works with data-sets from [Dempster, 1955] in the modeling community complete data-sets from [de Leva, 1996a, Dumas et al., 2007a,b] have been commonly established. In the following, a short introduction to both data-sets will be given to motivate a later decision for one of them. All data sets are given as fraction values with respect to a characteristic length l (complete body length) and the total body mass m .

3 Data-Set from McConville et. al. and Young et. al.

This complete data-set [Dumas et al., 2007a,b] for dynamic modeling has been adjusted from measurements sets in [McConville et al., 1980] (31 adult male - mean age 27.5 years, mean weight 80.5 kg, mean statue 1.77 m) and [Young et al., 1983] (46 adult female - mean age 31.2 years, mean weight 63.9 kg, mean statue 1.61 m). It comprises a full set of 15 segments with upper and middle torso merged together. Dynamic data has been computed from 3D surface points and an assumption of constant density $1 \frac{g}{cm^3}$ per slice. The adjustment of the segment coordinate systems to the joint centers has been consistently done based on anthropometric measurements from the same raw data-sets [McConville et al., 1980, Young et al., 1983]. However the authors suggest that *in vivo* measurements of the joint centers

should be preferred over the provided data for motion analysis tasks [Dumas et al., 2007a]. The data-set consists of a tabular arrangement of the segment masses,

$$m_i = m_{\%,i} m_{\text{total}}, \quad (\text{C.1a})$$

the lengths,

$$l_i = l_{\%,i} l_{\text{total}}, \quad (\text{C.1b})$$

measured from proximal to distal joint centers, the CoM positions,

$${}^{\text{ref},i}\text{CoM}_i(l_i) = \left[\text{CoM}_{x\%,i} l_i \quad \text{CoM}_{y\%,i} l_i \quad \text{CoM}_{z\%,i} l_i \right]^T, \quad (\text{C.1c})$$

in the local reference frames and the inertia tensor,

$${}^{\text{ref},i}I_i^{\text{CoM}}(l_i, m_i) = \begin{bmatrix} \left(r_{xx\%,i} l_i \right)^2 m_i & \left(r_{xy\%,i} l_i \right)^2 m_i & \left(r_{xz\%,i} l_i \right)^2 m_i \\ \left(r_{yx\%,i} l_i \right)^2 m_i & \left(r_{yy\%,i} l_i \right)^2 m_i & \left(r_{yz\%,i} l_i \right)^2 m_i \\ \left(r_{zx\%,i} l_i \right)^2 m_i & \left(r_{zy\%,i} l_i \right)^2 m_i & \left(r_{zz\%,i} l_i \right)^2 m_i \end{bmatrix}, \quad (\text{C.1d})$$

of each segment. The principal axis of the inertia tensor do generally not coincide with the axis of the local reference frames. The inertia tensor is given with respect to the CoM.

4 Data-Set from Zatsiorsky et. al.

Earlier in [de Leva, 1996a] Paolo de Leva published a data-set that was based on measurements from caucasian male and female college-aged persons [Zatsiorsky and Seluyanov, 1983, Zatsiorsky et al., 1990]. The problem was that Zatsiorsky et. al. did not report the anthropometric measurements that should go along with the previously published data-sets. Hence the adjustments was based on the original data sets [Zatsiorsky and Seluyanov, 1983, Zatsiorsky et al., 1990] (ethnic resource Russians) but merged at least 5 carefully chosen different data resources [Chandler et al., 1975, Clauser et al., 1969, Gordon et al., 1988, Hinrichs, 1990, Staff, 1978] (contain *in vivo* as well as measurements on cadaver) to complement all missing anthropometric measurements by means of various adjustments and re-scaling. The dynamic data-set comprises 16 segments featuring a torso in three segments (upper, middle trunk and pelvis). Furthermore [de Leva, 1996a] shows a comparison between the bony landmarks based and the data-set that was adjusted to the joint center points. The final data-set then consists of tabular data, featuring the segment lengths,

$$l_i = l_{\%,i} l_{\text{total}}, \quad (\text{C.2a})$$

the segment masses,

$$m_i = m_{\%,i} m_{\text{total}}, \quad (\text{C.2b})$$

the CoM placement which is assumed to lay on the line between proximal and distal joint centers,

$${}^{\text{ref},i}\text{CoM}_i(l_i) = \left[0.0 \quad 0.0 \quad \text{CoM}_{z\%,i} l_i \right]^T, \quad (\text{C.2c})$$

and the inertia tensor,

$${}^{\text{ref},i}I_i(l_i, m_i) = \begin{bmatrix} (r_{xx\%,i} l_i)^2 m_i & 0.0 & 0.0 \\ 0.0 & (r_{yy\%,i} l_i)^2 m_i & 0.0 \\ 0.0 & 0.0 & (r_{zz\%,i} l_i)^2 m_i \end{bmatrix}, \quad (\text{C.2d})$$

for each link, respectively. Generally it is assumed that the principle axis of the inertia tensor of each element coincide with axis of the local segment's reference frame. The inertia tensor is given with respect to the CoM.

5 Concluding Remarks

While the data-set from [Dumas et al., 2007a,b] was based and adjusted from dynamic data and its corresponding anthropometric measurements [McConville et al., 1980, Young et al., 1983] (alternative resources have only been used for data verification purposes), its counterpart [de Leva, 1996a] was based on body data from ethnic Russians [Zatsiorsky and Seluyanov, 1983, Zatsiorsky et al., 1990] but used various alternative, *in vivo* [Chandler et al., 1975, Gordon et al., 1988, Hinrichs, 1990, Staff, 1978] as well as data measurements from cadavers [Clauser et al., 1969] to compute all necessary anthropometric values that were not documented with the initial data resource. Assuming that the choice among the alternative data resources has been carefully decided and verified, one may conclude that the latter presents a better generalization among ethnic origin and body statue, than the former which has been established on data from a well defined population of samples.

At one hand the data-set from [McConville et al., 1980, Young et al., 1983] was computed based on the assumption of a constant density overall 2D-slices to build the 3D segment representation, while the established values clearly show in case of the inertia tensor, principal axis that do not coincide with the local reference frames of the limb segments and CoM positions that feature deviations from the line between proximal and distal joint centers. At the other hand [Zatsiorsky and Seluyanov, 1983, Zatsiorsky et al., 1990] used gamma-ray scanning techniques to analyze the characteristics of the soft tissue underneath the skin, however the data-set is governed by the strong assumption that all CoM are placed on the line in between the proximal and the distal joint centers and the principal axis of the inertia tensor coincide with the axis of the local reference frame of each limb segment.

D Conception of Bearings

The purpose of this technical component is the creation of prismatic or rotational relative motion between two different rigid bodies with least effort as well as robust (high stiffness, good damping characteristics) load transmission into any orthogonal direction. Thus, either contact surfaces should translate with least counter-effort against motion direction or the relative motion should be translated into a rolling motion between the contact surfaces. A comprehensive introduction to bearings as technical realization of articulation-complexes is given in [Albers et al., 2005, Grote and Feldhusen, 2011] and most of the descriptions featuring below are borrowed from these sources.

From the previous experience of joint motion trajectory profiles of bipedal locomotion, the joints will be most probably confronted with highly varying joint velocities, medium load impacts and frequent permutations of the spinning direction. Furthermore, prototyping applications are bound to highly flexible and generalized manufacturing processes [Sauer et al., 2012], thus, functional tolerance of lower geometric accuracy and deviations from defined functional surface qualities is clearly necessary to efficiently support the prototyping process.

1 Bearing Classes

Bearings are classified from its functional structure in floating bearings and rolling bearings. In the case of floating bearings a shaft with a defined external structure is floating inside a lubricated bushing. Depending on the lubrication principle these bearings are distinguished in dynamic and static types. Both types are robust to high continues and impact loads. While the dynamic type is technically very simple but unsuited for low speeds and frequent stop-and-go operations, the static-type bearing has much lower friction force, but is technically much more complex [Grote and Feldhusen, 2011]. These bearings generally have good damping characteristics and low space requirements [Albers et al., 2005].

The rolling bearings change the relative translation between both contact surfaces by means of an intermediate functional structure into a rolling motion. Depending on the external load characteristics and necessary tolerance of the bearing complex to external angular and translational deviations, this intermediate structure has spherical, straight, conic or convex cylindrical forms, rolling in-between both relatively translating contact surfaces, which normally are equipped with a groove for additional guidance. The rolling components are in most cases further surrounded by a casing that prevents direct mutual contact of its contact surfaces moving into opposite directions. Based on the elasticity of the functional structure, the point (spherical) or line contact (cylindrical) transforms into a small ellipsoid or rectangular surface transmitting high pressure [Hertz, 1882, Sauer et al., 2012]. Its location inside the groove depends on the external load and kinematic conditions. A given load is frequently inhomogeneously distributed between multiple rolling components [Albers et al., 2005]. At one hand, the concentration of the contact load in a small surface limits the maximum (low cycle), continues (e.g. creeping) and impact pressure (high cycle) before the structure suffers from permanent material failure. On the other hand however, in conjunction with the rolling kinematics the lubrication separates the rolling contact surface at much lower velocity [Albers et al., 2005], resulting in low static friction forces and reduced wear of the contact surfaces.

Furthermore, this type of bearing complex is highly standardized as boxed technical component, suitable for life-time lubrication and may tolerate much higher angular displacements between both contact surfaces than roller bearings. Even though ball bearings have lower damping capabilities and higher space requirements, they are most probably suited to highly flexible applications during prototyping over the previously described floating type bearings.

2 Conception of Ball Bearings

From the preferred load direction ball bearings are geometrically conceived as either radial, axial or as angular contact bearings, being a combination of both [Grote and Feldhusen, 2011]. Besides pure radial or axial bearings that may only support load orthogonal to their preferred direction, when a sufficiently high load into preferred direction is present, angular contact bearings always produce e.g. an axial load dependent on the radial load magnitude, that needs to be supported by the shaft, the support structure as well as adjacent bearings and thus should be considered during conception [Albers et al., 2005]. A full introduction in bearing conception is clearly outside the scope of this discussion (see [Albers et al., 2005, Grote and Feldhusen, 2011] for a comprehensive introduction and discussion). In the following the basic principles are described to motivate the adopted form of data presentation and its discussion in the subsequent result Section.

Load situations of roller bearings are divided into static, e.g. high peak loads during slow motion or complete stop, and dynamic configurations, e.g. fixed or moving load during higher motion velocities. The largest admissible static and dynamic load of bearings are dependent on the highly inhomogeneous internal load distribution, based on the load direction, geometry of the functional contact surface, the number of rolling components and its elastic deformation [Hertz, 1882, Sauer et al., 2012], in comparison with the materials characteristics. As previously discussed, the precision of materials mechanical characteristics are, however, varying and thus renders generally secure statements of maximum supported load conditions relatively difficult. A common definition that has been adopted in the conception of ball bearings are the static C_0 and dynamic C load rating. In static conception, applied loads should not supersede a permanent materials deformation of 0.01% of the spherical rolling components. A decision about whether a given bearing is eligible to hold the given load, is then determined from a comparison,

$$S_0 = \frac{C_0}{P_0}, \quad (\text{D.1a})$$

of the static load rating C_0 with the equivalent static bearing load P_0 from equation (D.1b). With a static safety factor of $S_0 > 1$ the bearing should hold, however, further requirements to precision and more demanding load situations may raise need for even higher safety factors. It is important to note that in equations,

$$P_0 = \max(X_0 F_r + Y_0 F_a, F_r), \quad (\text{D.1b})$$

$$P = X F_r + Y F_a, \quad (\text{D.1c})$$

both P and P_0 are the equivalent load quantities highly specific to the given bearing type. They are computed from the axial F_a and radial load component F_r as well as their corresponding radial X_0, X and axial Y_0, Y load static and dynamic load factors, which are dependent on the load situation and bearing topology. For the dynamic case, the high variety of the material characteristics with respect to the highly dynamic internal load conditions of the bearing renders concepts, equivalent to the static method, impractical. A more efficient approach is to

empirically measure a statistically appropriate number of bearings and determine the dynamic load C for which about 90% of the samples survive 10^6 rounds (e.g. for rotatory bearings). From,

$$L_{10} = \left(\frac{C}{P}\right)^p \quad [10^6 \text{ rounds}] \quad p = \begin{cases} 3 & : \text{ ball bearings} \\ \frac{10}{3} & : \text{ roller bearings} \\ \dots & : \text{ load dependent} \end{cases}, \quad (\text{D.1d})$$

and with the equivalent dynamic load P a conceptional life-cycle limit in 10^6 rounds may then be computed from the motion profile of the prospected life-cycle, for a selected bearing type.

E Meta Motion Capture Data

The data originating from the motion capturing system is provided as moving point cloud. The measured point trajectories $\hat{p} \in \mathbb{R}^3$,

$$\hat{p}(t) = \begin{bmatrix} p_x(t) \\ p_y(t) \\ p_z(t) \end{bmatrix} + u(t), \quad (\text{E.1a})$$

with respect to time t consist of the true trajectories $p \in \mathbb{R}^3$ and the measurement error $u \in \mathbb{R}^3$, that is henceforth assumed to follow a multivariate normal distribution with offset μ and Covariance Matrix C ,

$$\hat{u} \sim \mathcal{N}(\mu, C). \quad (\text{E.1b})$$

The transition from the point-cloud data to the actual kinematics of the model that will be used during this study is complex as it depends at one hand on the individual kinematics of the measured individual, the actual marker placement during the preparation phase as well as dislocation of markers due to the elasticity of the human soft-tissue.

When it is assumed for a moment that these previously mentioned information, e.g. model kinematics and local marker placement, are available, one could solve for the model kinematics based on a nonlinear optimization problem. In [Sugihara, 2009] the author discusses the application of a Gauss-Newton method with Levenberg-Marquardt regularization. The essence is the choice of the regularization factor that is bound again to the weighted residual, which leads to a numerical robust problem formulation to converge comparably quickly to a reasonable solution despite redundancy and singularities in the nonlinear model kinematics. In addition the authors compares his method against other approaches from literature showing the robustness and efficiency. When this method is used, it is a crucial aspect that information of the measurement error of the initial point cloud data is propagated through this nonlinear transformation to assess the quality of the resulting meta capture data for the subsequent study. The robust inverse kinematic fit in [Sugihara, 2009] minimizes the criteria,

$$\min_{q_k} \frac{1}{2} r_k^T W_e r_k + \frac{1}{2} \Delta q_k^T W_n \Delta q_k, \quad (\text{E.2a})$$

with iterate Δq_k ,

$$\Delta q_k = q_{k+1} - q_k, \quad (\text{E.2b})$$

and the side-term r_k ,

$$r_k = e(q_k, p_s) - \frac{\partial}{\partial q} e(q_k, p_s) \Delta q_k. \quad (\text{E.2c})$$

Computations are based on the residuum of the global marker positions of the whole body kinematics for each tag $X(q)$ and the point-cloud data p at the frame s ,

$$e(q, p) = \begin{bmatrix} p_{x,1} - X_{x,1}(q) \\ p_{y,1} - X_{y,1}(q) \\ p_{z,1} - X_{z,1}(q) \\ p_{x,2} - X_{x,2}(q) \\ \vdots \\ p_{z,n} - X_{z,n}(q) \end{bmatrix}^T. \quad (\text{E.2d})$$

The iteration number is represented with k . Upon convergence the kinematics for the frame s is described by,

$$q_k^* = q_{k-1} + H_{k-1}^{-1} g_{k-1} \quad (\text{E.2e})$$

$$H_{k-1} = \left(\left(\frac{\partial}{\partial q} e(q_{k-1}, p_s) \right)^T W_e \frac{\partial}{\partial q} e(q_{k-1}, p_s) + W_n \right), \quad (\text{E.2f})$$

$$g_{k-1} = \left(\left(\frac{\partial}{\partial q} e(q_{k-1}, p_s) \right)^T + e_{k-1} \right), \quad (\text{E.2g})$$

$$W_n = \left((e(q_{k-1}, p_s))^t W_e e(q_{k-1}, p_s) + \omega \right) I. \quad (\text{E.2h})$$

From variational calculus in error analyzes, probabilistic effect of a linear transformation f ,

$$f : X \in \mathbb{R}^n \rightarrow Y \in \mathbb{R}^m, \quad Y = f(X) = AX, \quad (\text{E.3a})$$

it follows, if X follows a multi-dimensional normal distribution, so does Y with,

$$X \sim N(\mu_X, C_X), \quad Y \sim N(\mu_Y, C_Y). \quad (\text{E.3b})$$

The covariance matrices C_X are related C_Y with expression,

$$C_Y = AC_X A^T, \quad (\text{E.3c})$$

and the mean values μ_x and μ_y base on the expression, respectively,

$$\mu_Y = A\mu_X. \quad (\text{E.3d})$$

The error propagation for nonlinear transformations is highly complex. Analytical investigation is only possible in some exceptional cases. However, it is possible for a first approximation to linearize the expressions on a desired working point x_0 based on a Taylor expansion and to apply the error calculus on this linearized expression,

$$q_k(p_k) = q_k^* + \begin{bmatrix} \frac{\partial}{\partial p_1} q_k^* & \dots & \frac{\partial}{\partial p_n} q_k^* \end{bmatrix} \begin{bmatrix} \Delta p_1 \\ \Delta p_1 \\ \vdots \\ \Delta p_n \end{bmatrix} = q_k^* + B\Delta p. \quad (\text{E.4a})$$

from the iterate (E.2e) at the convergence point it follows for the first derivative B with respect to the point cloud p_i ,

$$\frac{\partial}{\partial p_i} q_k^* = \frac{\partial}{\partial p_i} H_k^{-1} g_k + H_k^{-1} \frac{\partial}{\partial p_i} g_k. \quad (\text{E.4b})$$

Elements $\frac{\partial}{\partial p_i} H_k^{-1}$ and $\frac{\partial}{\partial p_i} g_k$ of expression (E.4b) follow from matrix calculus to,

$$\frac{\partial}{\partial p_i} H_k^{-1} = H_k^{-1} \frac{\partial}{\partial p_i} H_k H_k^{-1} = H_k^{-1} (2W_e e(q_k, p_s))_i I H_k^{-1}, \quad (\text{E.4c})$$

$$\frac{\partial}{\partial p_i} g_k = \left(\frac{\partial}{\partial q} e(q_k, p_s) \right)^T W_e \begin{bmatrix} 0 \\ 1_{\rightarrow i} \\ 0 \\ \vdots \end{bmatrix}, \quad (\text{E.4d})$$

respectively. The propagation of the covariance matrix of the point cloud data p_i towards the kinematic of the model then follows to,

$$C_{q_k^*, s} = B C_{p_1, p_2, \dots, s} B^T. \quad (\text{E.4e})$$

These computations are then conducted for each kinematic configuration at the frame s . The covariance matrix $C_{p_1, p_2, \dots, s}$ of the complete point-cloud setting at frame s contains the variance C_{p_i} of each point as block diagonal or further non-diagonal elements in case the measurements are not uncorrelated. The expression $(\dots)_i$ selects the i -th component of the vector. Due to the fact that $C_{p_1, p_2, \dots, s}$ or related information originating from the used Vicon system were not available at the time of this study, error propagation towards the application of the least-square was not applied.

F Model Description of DYNAMOD

1 Kinematics

File F.1 KinematicData.maple

```
1
2 # frame number
3 NSOL := 3:
4
5 # Degree of freedom number
6 GNDDL := 6:
7 PNDDL := 12:
8 NDDL := PNDDL+GNDDL:
9
10 # Definitions of coordinates and generalized speeds
11 q := vector(NDDL):
12 qdot := vector(NDDL):
13
14 actuation_joint_mask:= [seq(1,n=1..PNDDL), seq(0,n=PNDDL+1..PNDDL+GNDDL)]:
15
16 #Cardan rotation: we begin with rotation around x, and after around y and
17 #finally around z.
18
19 ## define parameter arrays – this will be used to define the corresponding
20 ## structure to hold the parameters in the C-Code
21 ## NOTE do not use XX_x (x = 1..) because they are reserved for parametric
22 ## inertia testing and Im because it is used by maple itself !!
23
24 m:= vector(3);
25 lx:= vector(3);
26 ly:= vector(3);
27 lz:= vector(3);
28 tx:= vector(3);
29 ty:= vector(3);
30 tz:= vector(3);
31 Rx:= vector(3);
32 Ry:= vector(3);
33 Rz:= vector(3);
34
35 CoMx:= vector(3);
36 CoMy:= vector(3);
37 CoMz:= vector(3);
38
39 Ixx:= vector(3);
40 Iyy:= vector(3);
41 Izz:= vector(3);
42 Ixy:= vector(3);
43 Ixz:= vector(3);
44 Iyz:= vector(3);
45
46 Ri:= vector(18);
47 IR:= vector(18);
```

```

48 Grav:= vector(3);
49
50 ## to declare a parameter array it has to feature in the list of
51 ## parameter in DOUBLE SINGLE QUOTA !!!
52 parameter:= [ 'Grav', 'lx', 'ly', 'lz', 'tx', 'ty', 'tz', 'm', '
    CoMx', 'CoMy', 'CoMz', 'Ixx', 'Iyy', 'Izz', 'Ixy', 'Ixz', '
    Iyz', 'Ri', 'IR' ];
53
54
55 # Frame 1 : rotation absolute frame (x direction to front of robot,
56 # y vertically upwards, z to the right of robot) to frame defined by
57 # (x direction to front of robot, y to the left of robot, z vertically
58 # upwards)
59 ref_1      := 0:
60 Rx_1      := q[6]:
61 Ry_1      := q[5]:
62 Rz_1      := q[4]:
63 Tx_1      := q[1]+lx[1]:
64 Ty_1      := q[2]+ly[1]:
65 Tz_1      := q[3]+lz[1]:
66 Label_1   := "GLOBAL":
67
68 # Frame 2 :
69 ref_2      := 1:
70 Rx_2      := q[12]:
71 Ry_2      := q[11]:
72 Rz_2      := q[10]:
73 Tx_2      := q[7]+lx[2]:
74 Ty_2      := q[8]+ly[2]:
75 Tz_2      := q[9]+lz[2]:
76 Label_2   := "LEAF_A":
77
78 # Frame 3 :
79 ref_3      := 1:
80 Rx_3      := q[18]:
81 Ry_3      := q[17]:
82 Rz_3      := q[16]:
83 Tx_3      := q[13]+lx[3]:
84 Ty_3      := q[14]+ly[3]:
85 Tz_3      := q[15]+lz[3]:
86 Label_3   := "LEAF_B":

```

2 Dynamics

File F.2 DynamicData.maple

```

1 # Gear ratio of transmissions
2 TransmGearR := vector([ Ri[1], Ri[2], Ri[3], Ri[4], Ri[5], Ri[6], Ri[7], Ri[8],
    Ri[9], Ri[10], Ri[11], Ri[12], Ri[13], Ri[14], Ri[15], Ri[16], Ri[17],
    Ri[18]]):
3
4 # Rotor Inertia
5 RotorInertia := vector([IR[1], IR[2], IR[3], IR[4], IR[5], IR[6], IR[7], IR
    [8], IR[9], IR[10], IR[11], IR[12], IR[13], IR[14], IR[15], IR[16], IR[17],
    IR[18]]):
6
7 # gravity vector

```

```

8 Gravity := vector([Grav[1], Grav[2], Grav[3]]):
9
10 # Rigid Body 1 :
11 m_1 := m[1]:
12 G_1 := vector([ CoMx[1], CoMy[1], CoMz[1]]):
13 IG_1 := matrix([[Ixx[1], Ixy[1], Ixz[1]], [Ixy[1], Iyy[1], Iyz[1]], [Ixz[1], Iyz
      [1], Izz[1]]]):
14
15 # Rigid Body 3 :
16 m_2 := m[2]:
17 G_2 := vector([CoMx[2], CoMy[2], CoMz[2]]):
18 IG_2 := matrix([[Ixx[2], Ixy[2], Ixz[2]], [Ixy[2], Iyy[2], Iyz[2]], [Ixz[2], Iyz
      [2], Izz[2]]]):
19
20 # Rigid Body 4 :
21 m_3 := m[3]:
22 G_3 := vector([CoMx[3], CoMy[3], CoMz [3]]):
23 IG_3 := matrix([[Ixx[3], Ixy[3], Ixz[3]], [Ixy[3], Iyy[3], Iyz[3]], [Ixz[3], Iyz
      [3], Izz[3]]]):

```

3 Tags & Contacts

File F.3 AdditionalData.maple

```

1 # Definition of important tags
2
3 # Number of link contacts – 6D HuMAnS
4 NLNCONT:= 3:
5
6 # reference frames for link contacts – 6D HuMAnS
7 lncontact:= [1,2,3]:
8
9
10 # Number of tags
11 NTAG := 3:
12
13 # Tag 1 :
14 reftag_1 := 1:
15 tag_1 := vector([tx[1], ty[1], tz[1]]*1e-3):
16 tagLabel_1 := "tagA":
17
18 # Tag 2 :
19 reftag_2 := 2:
20 tag_2 := vector([tx[2], ty[2], tz[2]]*1e-3):
21 tagLabel_2 := "tagB":
22
23 # Tag 3 :
24 reftag_3 := 3:
25 tag_3 := vector([tx[3], ty[3], tz[3]]*1e-3):
26 tagLabel_3 := "tagC":

```

G FdOP and IdOP based OCP-Formulations

1 Formulations of the Dynamic System

For a thorough discussion this section briefly explains each OCP-formulation scenario in detail. Following Figure 5.1 on page 55 it is important to note the configuration of the states vector and the type of controls controls as well as resulting form of the ODE right hand side functions.

1.1 Forward Dynamics FD; Piecewise Linear Continuous Controls plc

For this discretization of the controls $u(\cdot)$, the FD of the model are given by,

$$x := \begin{bmatrix} x_1 \\ x_2 \end{bmatrix} = \begin{bmatrix} q \\ \dot{q} \end{bmatrix}, \quad u := [\tau], \quad f(x, u) := \begin{bmatrix} x_2 \\ \text{FD}|_{\dot{q}}(x_1, x_2, u) \end{bmatrix}, \quad (\text{G.1})$$

where $\text{FD}|_{\dot{q}}(x_1, x_2, u)$ denotes results of the FdOP. Controls of the OCP (4.1) and the joint-actuation τ (5.13) are equivalent (refer to Figure 5.1c on page 55).

1.2 Forward Dynamics FD; Piecewise Linear Continuous and once Integrated Controls plci

This discretization is equivalent to piecewise quadratic continuous joint-actuation τ , based on the same controls $u(\cdot)$ as in the previous scenario, additionally integrated once. The resulting model configuration is given in,

$$x := \begin{bmatrix} x_1 \\ x_2 \\ x_3 \end{bmatrix} = \begin{bmatrix} q \\ \dot{q} \\ \tau \end{bmatrix}, \quad u := [\dot{\tau}], \quad f(x, u) := \begin{bmatrix} x_2 \\ \text{FD}|_{\dot{q}}(x_1, x_2, x_3) \\ u \end{bmatrix}. \quad (\text{G.2})$$

It is important to note that OCP-controls and joint-actuation τ are not equivalent in this scenario (refer to Figure 5.1c on page 55).

1.3 Inverse Dynamics ID; Piecewise Linear Continuous Controls plc

In contrast to the FdOP-based scenarios the discretization of the controls $u(\cdot)$ for the IdOP is now related to the desired accelerations \ddot{q}^{dsrd} . The model configuration is shown in,

$$x := \begin{bmatrix} x_1 \\ x_2 \end{bmatrix} = \begin{bmatrix} q \\ \dot{q} \end{bmatrix}, \quad u := [\ddot{q}], \quad f(x, u) := \begin{bmatrix} x_2 \\ \text{ID}|_{\dot{q}}(x_1, x_2, u) \end{bmatrix}, \quad (\text{G.3})$$

where the definition of the IdOP (5.24) is embedded in the term $\text{ID}|_{\dot{q}}(x_1, x_2, u)$, which also returns physical correct accelerations \ddot{q} of the system (refer to Figure 5.1d on page 55). The actuation-torque τ of the system is an algebraic expression of states and controls given back

Table G.1: Box constraints on joints, velocities and torques of the cart pendulum used in the OCP.

dof or actuation	lower limit	upper limit	unit
q_x^{cart}	-100	100	[m]
q_z^{cart}	-100	100	[m]
q_θ^{cart}	-100	100	[rad]
q_θ^{pend}	-100	100	[rad]
\dot{q}_x^{cart}	-100	100	[m/s]
\dot{q}_z^{cart}	-100	100	[m/s]
$\dot{q}_\theta^{\text{cart}}$	-100	100	[rad/s]
$\dot{q}_\theta^{\text{pend}}$	-100	100	[rad/s]
τ_x^{cart}	-50	50	[N]
t_{fin} (select constant for min. Energy)	> 0	3.7	[t]

as result from the IdOP,

$$\tau := \text{ID}|_\tau(x_1, x_2, u). \quad (\text{G.4})$$

The actuation-torque is then used in the energy minimal objective (5.47b) or in the minimal time case in the torque constraints.

1.4 Inverse Dynamics ID; Piecewise Linear Continuous Controls and once Integrated Controls plci

For a piecewise linear continuous discretization of the controls $u(\cdot)$, which are additionally integrated once, it is again important to note that the controls are not equivalent to the desired joint accelerations. This configuration is equivalent to piecewise quadratic continuous desired joint accelerations \ddot{q}^{dsrd} with respect to the previous scenario. The model configuration is given in,

$$x := \begin{bmatrix} x_1 \\ x_2 \\ x_3 \end{bmatrix} = \begin{bmatrix} q \\ \dot{q} \\ \ddot{q} \end{bmatrix}, \quad u := [\ddot{q}], \quad f(x, u) := \begin{bmatrix} x_2 \\ \text{ID}|_{\ddot{q}}(x_1, x_2, x_3) \\ u \end{bmatrix}, \quad (\text{G.5})$$

(refer to Figure 5.1d on page 55). The actuation-torque τ of the system is an algebraic expression of system-states given back as result from the IdOP,

$$\tau := \text{ID}|_\tau(x_1, x_2, x_3). \quad (\text{G.6})$$

The cart and pendulum dynamics are subject to constraints that enforce joint limits, actuation limits, influencing the desired up-swing motion of the pendulum. These limits are expressed as box constraints,

$$q_{\text{lo}} \leq q \leq q_{\text{up}}, \quad \dot{q}_{\text{lo}} \leq \dot{q} \leq \dot{q}_{\text{up}}, \quad \tau_{\text{lo}} \leq \tau \leq \tau_{\text{up}}. \quad (\text{G.7a})$$

State constraints are chosen to be sufficiently high for these quantities to be considered unbounded in the OCP context (refer to Table G.1). The remaining bounds on the joint torques τ are given in Table G.1. Finally the up-swing motion is modulated with the boundary con-

straints,

$$r^{s,\text{eq}} = \begin{bmatrix} q - \bar{q} \\ \dot{q} \\ \ddot{q} \end{bmatrix} = 0, \quad \bar{q} := \begin{bmatrix} 0 \\ 0 \\ 0 \\ -\pi \end{bmatrix}, \quad r^{e,\text{eq}} = \begin{bmatrix} q \\ \dot{q} \\ \ddot{q} \end{bmatrix} = 0, \quad (\text{G.7b})$$

for joint positions, velocities, and accelerations. For the minimal energy scenario, the free end-time was fixed to $t_{\text{fin}} = 3.7$ [s] (refer to Table G.1 on the preceding page) for uniqueness of the solution.

Bibliography

- M. Ackermann and A. J. van den Bogert. Optimality principles for model-based prediction of human gait. *Journal of Biomechanics*, 43(6):1055–1060, 2010. ISSN 0021-9290. doi: <http://dx.doi.org/10.1016/j.jbiomech.2009.12.012>. URL <http://www.sciencedirect.com/science/article/pii/S0021929009007210>.
- A. Albers, L. Deters, J. Feldhusen, E. Leidich, H. Linke, G. Poll, B. Sauer, and J. Wallaschek. *Konstruktionselemente des Maschinenbaus 2 : Grundlagen von Maschinenelementen für Antriebsaufgaben*. Springer-Lehrbuch. Springer Verlag, 2005.
- A. Albers, M. Braun, P. Clarkson, H. Enkler, and D. Wynn. Contact and channel modelling to support the early design of technical systems. In *International Conference on Engineering Design*, volume 5: Design Methods and Tools, Part 1, pages 5–61. Design Society, August 2009. URL <http://publications.eng.cam.ac.uk/435864/>.
- H. Arisumi, S. Miossec, J.-R. Chardonnet, and K. Yokoi. Dynamic lifting by whole body motion of humanoid robots. In *IEEE/RSJ International Conference on Intelligent Robots and Systems (IROS)*, pages 668–675, Sept 2008. doi: 10.1109/IROS.2008.4651195.
- U. Ascher, H. Chin, L. Petzold, and S. Reich. Stabilization of constrained mechanical systems with DAEs and invariant manifolds. *J. Mech. Struct. Machines*, 23:135–157, 1994. doi: 10.1.1.26.1624. URL <http://citeseerx.ist.psu.edu/viewdoc/download?doi=10.1.1.26.1624&rep=rep1&type=pdf>.
- P. Baerlocher. *Inverse kinematics techniques of the interactive posture control of articulated figures*. PhD thesis, Lausanne, EPFL, Lausanne, 2001. URL <http://opac.inria.fr/record=b1072118>. Th. doct. : Informatique.
- P. Baerlocher and R. Boulic. Parametrization and range of motion of the ball-and-socket joint. In N. Magnenat-Thalmann and D. Thalmann, editors, *Deformable Avatars*, volume 68 of *IFIP — The International Federation for Information Processing*, pages 180–190. Springer US, 2001. ISBN 978-1-4757-4930-4. doi: 10.1007/978-0-306-47002-8_16. URL http://dx.doi.org/10.1007/978-0-306-47002-8_16.
- A. Barre and S. Armand. Biomechanical ToolKit: Open-source framework to visualize and process biomechanical data. *Computer Methods and Programs in Biomedicine*, 114(1):80 – 87, 2014. ISSN 0169-2607. doi: <http://dx.doi.org/10.1016/j.cmpb.2014.01.012>. URL <http://www.sciencedirect.com/science/article/pii/S0169260714000248>.
- R. Beckett and K. Chang. An evaluation of the kinematics of gait by minimum energy. *Journal of Biomechanics*, 1(2):147 – 159, 1968. ISSN 0021-9290. doi: [http://dx.doi.org/10.1016/0021-9290\(68\)90017-1](http://dx.doi.org/10.1016/0021-9290(68)90017-1). URL <http://www.sciencedirect.com/science/article/pii/0021929068900171>.
- D. Bentivegna, C. Atkeson, and J.-Y. Kim. Compliant control of a hydraulic humanoid joint. In *IEEE/RAS International Conference on Humanoid Robots*, pages 483–489, Nov 2007. doi: 10.1109/ICHR.2007.4813914.
- M. Benzi, G. H. Golub, and J. Liesen. Numerical solution of saddle point problems. *Acta Numerica*, 14:1–137, 5 2005. ISSN 1474-0508. doi: 10.1017/S0962492904000212. URL http://journals.cambridge.org/article_S0962492904000212.
- G. Bessonnet, P. Sardain, and S. Chessé. Optimal motion synthesis – dynamic modeling and numerical solving aspects. *Multibody System Dynamics*, 8(3):257–278, 2002. ISSN 1384-5640. doi: 10.1023/A:1020928112173. URL <http://dx.doi.org/10.1023/A%3A1020928112173>.
- G. Bessonnet, S. Chessé, and P. Sardain. Optimal gait synthesis of a seven-link planar biped. *The International Journal of Robotics Research*, 23(10-11):1059–1073, 2004. doi: 10.1177/0278364904047393. URL <http://ijr.sagepub.com/content/23/10-11/1059.abstract>.
- G. C. Best. Helpful formulas for integrating polynomials in three dimensions. *Mathematics of Computation*, 18(86):310–312, 1964. ISSN 00255718. URL <http://www.jstor.org/stable/2003308>.
- J. T. Betts. *Practical Methods for Optimal Control and Estimation Using Nonlinear Programming*. Cambridge University Press, New York, NY, USA, 2nd edition, 2009. ISBN 0898716888, 9780898716887.
- R. Bischoff, J. Kurth, G. Schreiber, R. Koeppel, A. Albu-Schaeffer, A. Beyer, O. Eiberger, S. Haddadin, A. Stemmer, G. Grunwald, and G. Hirzinger. The KUKA-DLR lightweight robot arm - a new reference platform for robotics research and manufacturing. In *Robotics (ISR), 2010 41st International Symposium on and 2010 6th German Conference on Robotics (ROBOTIK)*, pages 1–8, June 2010.
- P.-A. Bliman and M. Sorine. Easy-to-use realistic dry friction models for automatic control. In A. Isidori, S. Bittanti, E. Mosca, A. De Luca, M. D. Di Benedetto, and G. Oriolo, editors, *European Control Conference*, volume 2, pages 3788–3794, September 1995. URL <https://books.google.de/books?id=t-Mii70R05IC>.
- H. Bock. Numerical treatment of inverse problems in chemical reaction kinetics. In K. H. Ebert,

BIBLIOGRAPHY

- P. Deuffhard, and W. Jäger, editors, *Modelling of Chemical Reaction Systems*, volume 18 of *Springer Series in Chemical Physics*, chapter 9, pages 102–125. Springer Berlin Heidelberg, 1981. ISBN 978-3-642-68222-3. doi: 10.1007/978-3-642-68220-9_8. URL http://dx.doi.org/10.1007/978-3-642-68220-9_8.
- H. Bock and K. Plitt. A multiple shooting algorithm for direct solution of optimal control problems. In A. MacFarlane and H. Rauch, editors, *IFAC World Congress*, volume 9, pages 242–247. International Federation of Automatic Control, July 1984.
- J.-D. Boissonnat. Geometric structures for three-dimensional shape representation. *ACM Trans. Graph.*, 3(4):266–286, October 1984. ISSN 0730-0301. doi: 10.1145/357346.357349. URL <http://doi.acm.org/10.1145/357346.357349>.
- M. Bottlang, S. M. Madey, C. M. Steyers, J. L. Marsh, and T. D. Brown. Assessment of elbow joint kinematics in passive motion by electromagnetic motion tracking. *Journal of Orthopedics Research*, 18(2):195–202, Mar 2000.
- J. Braun and J. Mottok. Fail-safe and fail-operational systems safeguarded with coded processing. In *EUROCON, 2013 IEEE*, pages 1878–1885, July 2013. doi: 10.1109/EUROCON.2013.6625234.
- M. Brinkmann. Vergleich von Regressionsgleichungen zur bestimmung von anthropometrischen Daten in der Gangdynamik. Technical report, Interdisciplinary Center of Scientific Computing, University of Heidelberg, 2013. URL <http://mo.uni-hd.de/bachelorarbeit/bachelorarbeit-brinkmann.pdf>.
- B. Brogliato, A. A. t. Dam, L. Paoli, F. Genot, and M. Abadie. Numerical simulation of finite dimensional multibody nonsmooth mechanical systems. *ASME Applied Mechanics Reviews*, 55(2):107–150, 2002. doi: 10.1115/1.1454112. URL <http://dx.doi.org/10.1115/1.1454112>.
- S. Brunet and L. Baron. Workspace computation of parallel manipulators using 2k-trees with collision detection. In T. Huang, editor, *World Congress in Mechanism and Machine Science*. International Federation for the Promotion of Mechanism and Machine Science (IFToMM), 2004.
- J. Buchli, M. Kalakrishnan, M. Mistry, P. Pastor, and S. Schaal. Compliant quadruped locomotion over rough terrain. In *IEEE/RSJ International Conference on Intelligent Robots and Systems (IROS)*, pages 814–820, Oct 2009. doi: 10.1109/IROS.2009.5354681.
- T. Buschmann, S. Lohmeier, H. Ulbrich, and F. Pfeiffer. Optimization based gait pattern generation for a biped robot. In *IEEE/RAS International Conference on Humanoid Robots*, pages 98–103, Dec 2005. doi: 10.1109/ICHR.2005.1573552.
- T. Buschmann, S. Lohmeier, M. Bachmayer, H. Ulbrich, and F. Pfeiffer. A collocation method for real-time walking pattern generation. In *IEEE/RAS International Conference on Humanoid Robots*, pages 1–6, Nov 2007. doi: 10.1109/ICHR.2007.4813841.
- T. Buschmann, S. Lohmeier, and H. Ulbrich. Humanoid robot lola: Design and walking control. *Journal of Physiology-Paris*, 103(3–5):141 – 148, 2009. ISSN 0928-4257. doi: <http://dx.doi.org/10.1016/j.jphysparis.2009.07.008>. URL <http://www.sciencedirect.com/science/article/pii/S0928425709000400>. Neurorobotics.
- M. Buss, M. Hardt, J. Kiener, M. Sobotka, M. Stelzer, O. von Stryk, and D. Wollherr. Towards an autonomous, humanoid, and dynamically walking robot: Modeling, optimal trajectory planning, hardware architecture, and experiments. In *IEEE/RAS International Conference on Humanoid Robots*, pages 2491–2496, 2003.
- J. Buur and M. Andreasen. *A theoretical approach to mechatronics design*. PhD thesis, Department of Management Engineering, 1990. URL http://orbit.dtu.dk/services/downloadRegister/96900446/Buur_PhD_Mechatronics_Design.pdf.
- V. A. D. Cai, P. Bidaud, V. Hayward, F. Gosselin, and E. Desailly. Self-adjusting, isostatic exoskeleton for the human knee joint. In *Annual International Conference of the IEEE Engineering in Medicine and Biology Society, EMBC*, pages 612–618, Aug 2011. doi: 10.1109/IEMBS.2011.6090136.
- K. Capraro. Block island - mars exploration rover oppertunity, 2014. URL <http://nasa3d.arc.nasa.gov/detail/block-island>.
- P. Catalfamo, D. Moser, S. Ghossayni, and D. Ewins. Detection of gait events using an f-scan in-shoe pressure measurement system. *Gait & Posture*, 28(3):420 – 426, 2008. ISSN 0966-6362. doi: <http://dx.doi.org/10.1016/j.gaitpost.2008.01.019>. URL <http://www.sciencedirect.com/science/article/pii/S096663620800043X>.
- M. Cempini, S. De Rossi, T. Lenzi, N. Vitiello, and M. Carrozza. Self-alignment mechanisms for assistive wearable robots: A kinetostatic compatibility method. *IEEE Transaction on Robotics*, 29(1):236–250, Feb 2013. ISSN 1552-3098. doi: 10.1109/TRO.2012.2226381.
- R. Chandler, C. Clauser, J. McConville, H. Reynolds, and J. Young. Investigation of inertial properties of the human body (AMRL TR 74-137). Technical Report NTIS No, AD-A016 485, Wright-Patterson Air Force Base, OH, 1975.
- P. H. Channon, S. H. Hopkins, and D. T. Pham. Derivation of optimal walking motions for a bipedal walking robot. *Robotica*, 10:165–172, 3 1992. ISSN 1469-8668. doi: 10.1017/S026357470000758X. URL http://journals.cambridge.org/article_S026357470000758X.
- B. Char, K. Geddes, W. Gentleman, and G. Gonnat. The design of maple: A compact, portable, and powerful computer algebra system. In J. van Hulzen, editor, *Computer Algebra*, volume 162 of *Lecture Notes in Computer Science*, pages 101–115. Springer Berlin Heidelberg, 1983. ISBN 978-3-540-

- 12868-7. doi: 10.1007/3-540-12868-9_95. URL http://dx.doi.org/10.1007/3-540-12868-9_95.
- J.-R. Chardonnet. *Real-Time Dynamic Model for Animation of Poly-Articulated Objects in Constrained Environments with Contact with Friction and Local Deformations: Application to Humanoids and Virtual Avatars*. Theses, Université Montpellier II - Sciences et Techniques du Languedoc, June 2009. URL <https://tel.archives-ouvertes.fr/tel-00406932>.
- C.-M. Chew, E. Choong, A.-N. Poo, and G.-S. Hong. From science fiction to reality - humanoid robots. In *Humanoid, Nanotechnology, Information Technology, Communication and Control Environment and Management*, 2003. URL <http://guppy.mpe.nus.edu.sg/~mpeccm/papers/hnicem1.pdf>.
- L. Chou, S. Song, and L. Draganich. Predicting the kinematics and kinetics of gait based on the optimum trajectory of the swing limb. *Journal of Biomechanics*, 28(4):377 – 385, 1995. ISSN 0021-9290. doi: [http://dx.doi.org/10.1016/0021-9290\(94\)00083-G](http://dx.doi.org/10.1016/0021-9290(94)00083-G). URL <http://www.sciencedirect.com/science/article/pii/002192909400083G>.
- C. Chow and D. Jacobson. Studies of human locomotion via optimal programming. *Mathematical Biosciences*, 10(3–4):239 – 306, 1971. ISSN 0025-5564. doi: [http://dx.doi.org/10.1016/0025-5564\(71\)90062-9](http://dx.doi.org/10.1016/0025-5564(71)90062-9). URL <http://www.sciencedirect.com/science/article/pii/0025556471900629>.
- A. Chu, H. Kazerooni, and A. Zoss. On the biomimetic design of the Berkeley Lower Extremity Exoskeleton (BLEEX). In *IEEE/RAS International Conference on Robotics and Automation (ICRA)*, pages 4345–4352, April 2005. doi: 10.1109/ROBOT.2005.1570789.
- C. Clauser, J. McConville, and J. Young. *Weight, volume, and center of mass of segments of the human body*, volume 32 of *AMRL-TR*. Aerospace Medical Research Laboratory, Aerospace Medical Division, Air Force Systems Command, 1969. URL <http://books.google.de/books?id=7bk8AAAAIAAJ>.
- S. Collins and A. Ruina. A bipedal walking robot with efficient and human-like gait. In *IEEE/RAS International Conference on Robotics and Automation (ICRA)*, pages 1983–1988, April 2005. doi: 10.1109/ROBOT.2005.1570404.
- S. H. Collins, M. Wisse, and A. Ruina. A three-dimensional passive-dynamic walking robot with two legs and knees. *International Journal of Robotics Research*, 20(7):607–615, 2001. doi: 10.1177/02783640122067561. URL <http://ijr.sagepub.com/content/20/7/607.abstract>.
- S. H. Collins, P. G. Adamczyk, and A. D. Kuo. Dynamic arm swinging in human walking. *Proceedings of the Royal Society of London B: Biological Sciences*, 2009. ISSN 0962-8452. doi: 10.1098/rspb.2009.0664.
- C. Dang. Silhouette humain asexue, February 2013. URL http://commons.wikimedia.org/w/index.php?title=File:Silhouette_humain_asexue_anterieur_posterieur.svg&redirect=no.
- A. David, J.-R. Chardonnet, A. Kheddar, K. Kaneko, and K. Yokoi. Study of an external passive shock-absorbing mechanism for walking robots. In *IEEE/RAS International Conference on Humanoid Robots*, pages 435–440, Dec 2008. doi: 10.1109/ICHR.2008.4755991.
- P. de Leva. Adjustments to Zatsiorsky-Seluyanov's segment inertia parameters. *Journal of Biomechanics*, 29(9):1223 – 1230, 1996a. ISSN 0021-9290. doi: [http://dx.doi.org/10.1016/0021-9290\(95\)00178-6](http://dx.doi.org/10.1016/0021-9290(95)00178-6). URL <http://www.sciencedirect.com/science/article/pii/0021929095001786>.
- P. de Leva. Joint center longitudinal positions computed from a selected subset of chandler's data. *Journal of Biomechanics*, 29(9):1231 – 1233, 1996b. ISSN 0021-9290. doi: [http://dx.doi.org/10.1016/0021-9290\(96\)00021-8](http://dx.doi.org/10.1016/0021-9290(96)00021-8). URL <http://www.sciencedirect.com/science/article/pii/0021929096000218>.
- L. De Michieli, F. Nori, A. Pini Prato, and G. Sandini. Study on humanoid robot systems: An energy approach. In *IEEE/RAS International Conference on Humanoid Robots*, pages 219–226, Dec 2008. doi: 10.1109/ICHR.2008.4755948.
- X. Décoret. The XdkWrl library, 2003. URL <http://maverick.inria.fr/~Xavier.Decoret/resources/xdkwrl/html/index.html>.
- A. J. del Ama, A. D. Koutsou, J. C. Moreno, A. de-los Reyes, A. Gil-Agudo, and J. L. Pons. Review of hybrid exoskeletons to restore gait following spinal cord injury. *Journal of Rehabilitation Research & Development*, 49(4):497–514, 2012. [PubMed:22773254].
- A. Del Prete. *Control of Contact Forces using Whole-Body Force and Tactile Sensors: Theory and Implementation on the iCub Humanoid Robot*. PhD thesis, Instituto Italiano di Tecnologia, 2013. URL <http://www.iit.it/images/images/icub-facility/docs/theses/delprete.pdf>.
- B. Delaunay. Sur la sphère vide. A la mémoire de georges voronoï. *Bulletin de l'Académie des Sciences de l'URSS. Classe des sciences mathématiques et na*, 6:793–800, 1934. doi: 0010.41101|60.0946.06. URL <http://mi.mathnet.ru/izv4937>.
- W. Dempster. *Space Requirements of the Seated Operator: Geometrical, Kinematic, and Mechanical Aspects of the Body with Special Reference to the Limbs* /Wilfred Taylor Dempster. Number v. 1 in Technical report. Wright Air Development Center, Air Research and Development Command, U.S. Air Force, 1955. URL <http://deepblue.lib.umich.edu/bitstream/handle/2027.42/4540/bab9715.0001.001.txt?sequence=4&isAllowed=y>.
- J. Diebel. Representing attitude: Euler angles, unit quaternions, and rotation vectors, 2006. URL <http://ai.stanford.edu/~diebel/attitude/attitude.pdf>.
- A. R. Dobrovolskis. Inertia of any polyhedron. *Icarus*, 124(2):698–704, 1996. ISSN 0019-1035.

BIBLIOGRAPHY

- doi: <http://dx.doi.org/10.1006/icar.1996.0243>. URL <http://www.sciencedirect.com/science/article/pii/S0019103596902432>.
- A. Dollar and H. Herr. Lower extremity exoskeletons and active orthoses: Challenges and state-of-the-art. *IEEE Transaction on Robotics*, 24(1):144–158, Feb 2008. ISSN 1552-3098. doi: 10.1109/TRO.2008.915453.
- R. Dumas, L. Chèze, and J.-P. Verriest. Adjustments to McConville et al. and Young et al. body segment inertial parameters. *Journal of Biomechanics*, 40(3):543 – 553, 2007a. ISSN 0021-9290. doi: <http://dx.doi.org/10.1016/j.jbiomech.2006.02.013>. URL <http://www.sciencedirect.com/science/article/pii/S0021929006000728>.
- R. Dumas, L. Chèze, and J.-P. Verriest. Corrigendum to “Adjustments to McConville et al. and Young et al. body segment inertial parameters” [J. Biomech. 40 (2007) 543–553]. *Journal of Biomechanics*, 40(7):1651 – 1652, 2007b. ISSN 0021-9290. doi: <http://dx.doi.org/10.1016/j.jbiomech.2006.07.016>. URL <http://www.sciencedirect.com/science/article/pii/S0021929006000728>.
- D. Eberly. Distance between two line segments in 3D. Technical report, Geometric Tools, LCC, 1999.
- A. El Khoury, F. Lamiroux, and M. Taix. Optimal motion planning for humanoid robots. In *IEEE/RAS International Conference on Robotics and Automation (ICRA)*, pages 3136–3141, May 2013. doi: 10.1109/ICRA.2013.6631013.
- J. Engelsberger, A. Werner, C. Ott, B. Henze, M. Roa, G. Garofalo, R. Burger, A. Beyer, O. Eiberger, K. Schmid, and A. Albu-Schäffer. Overview of the torque-controlled humanoid robot toro. In *IEEE/RAS International Conference on Humanoid Robots*, November 2014.
- J. Engelsberger, C. Ott, and A. Albu-Schäffer. Three-dimensional bipedal walking control using divergent component of motion. In *IEEE/RSJ International Conference on Intelligent Robots and Systems (IROS)*, pages 2600–2607, Nov 2013. doi: 10.1109/IROS.2013.6696723.
- T. Erez and E. Todorov. Trajectory optimization for domains with contacts using inverse dynamics. In *IEEE/RSJ International Conference on Intelligent Robots and Systems (IROS)*, pages 4914–4919, Oct 2012. doi: 10.1109/IROS.2012.6386181.
- T. Erez, K. Lowrey, Y. Tassa, V. Kumar, S. Koley, and E. Todorov. An integrated system for real-time model predictive control of humanoid robots. In *IEEE/RAS International Conference on Humanoid Robots*, 2013.
- M. Esmaeili, K. Gamage, E. Tan, and D. Campolo. Ergonomic considerations for anthropomorphic wrist exoskeletons: A simulation study on the effects of joint misalignment. In *IEEE/RSJ International Conference on Intelligent Robots and Systems (IROS)*, pages 4905–4910, Sept 2011. doi: 10.1109/IROS.2011.6095136.
- A. Fabri, G.-J. Giezeman, L. Kettner, S. Schirra, and S. Schönherr. On the design of cgal, the computational geometry algorithms library. Research Report MPI-I-98-1-007, Max-Planck-Institut für Informatik, Im Stadtwald, D-66123 Saarbrücken, Germany, February 1998. URL <http://domino.mpi-inf.mpg.de/internet/reports.nsf/c125634c000710d1c12560400031a48c/f8e489e085e8c160412565a900544313/\protect\T1\textdollarFILE/MPI-I-98-1-007.ps>.
- R. Featherstone. Plucker basis vectors. In *IEEE/RAS International Conference on Robotics and Automation (ICRA)*, pages 1892–1897, May 2006. doi: 10.1109/ROBOT.2006.1641982.
- R. Featherstone. A beginner’s guide to 6-D vectors (part 1). *IEEE Robotics & Automation Magazine*, 17(3):83–94, Sept 2010a. ISSN 1070-9932. doi: 10.1109/MRA.2010.937853.
- R. Featherstone. A beginner’s guide to 6-D vectors (part 2) [tutorial]. *IEEE Robotics & Automation Magazine*, 17(4):88–99, Dec 2010b. ISSN 1070-9932. doi: 10.1109/MRA.2010.939560.
- R. Featherstone and D. Orin. Robot dynamics: equations and algorithms. In *IEEE/RAS International Conference on Robotics and Automation (ICRA)*, volume 1, pages 826–834, 2000. doi: 10.1109/ROBOT.2000.844153.
- R. Featherstone. *Rigid Body Dynamics Algorithms*. Springer-Verlag New York, Inc., Secaucus, NJ, USA, 2007. ISBN 0387743146.
- M. Felis. MeshUp - A visualization tool for multi-body systems based on skeletal animation and magic. online repository, 2014a. URL <https://bitbucket.org/MartinFelis/meshup>.
- M. Felis. RBDL - Rigid Body Dynamics Library. Online repository, 2014b. URL <https://bitbucket.org/rbdl/rbdl/>.
- B. Fick. Hardiman I Arm Test - Hardiman I Prototype Project. Technical Report NR 196-049, Specialty Materials Handling Products Operation General Electric Company, Specialty Materials Handlings Products Operation - General Electric Company - Schenectady, New York, 12345, 1969. URL <http://www.dtic.mil/get-tr-doc/pdf?AD=AD0701359>.
- B. Fick and J. Makinson. Final report on hardiman I prototype for machine augmentation of human strength and endurance. Technical Report NR 196-049, Specialty Materials Handling Products Operation General Electric Company, Specialty Materials Handlings Products Operation - General Electric Company - Schenectady, New York, 12345, 1971. URL <http://www.dtic.mil/dtic/tr/fulltext/u2/739735.pdf>. Summary of Programm progress though 31 August 1971.
- H. Flashner. An orthogonal decomposition approach to modal synthesis. *International Journal for Numerical Methods in Engineering*, 23(3):471–493, 1986. ISSN 1097-0207. doi: 10.1002/nme.1620230311. URL <http://dx.doi.org/10.1002/nme.1620230311>.
- P. Flores. Compliant contact force approach for forward dynamic modeling and analysis of biomechan-

- ical systems. *Procedia {IUTAM}*, 2(0):58 – 67, 2011. ISSN 2210-9838. doi: <http://dx.doi.org/10.1016/j.piutam.2011.04.006>. URL <http://www.sciencedirect.com/science/article/pii/S2210983811000071>. {IUTAM} Symposium on Human Body Dynamics.
- M. Garcia, A. Chatterjee, and A. Ruina. Efficiency, speed, and scaling of 2D passive dynamic walking. *Dynamics and Stability of Systems*, 1998.
- P. Geoffroy, N. Mansard, M. Raison, S. Achiche, and E. Todorov. From inverse kinematics to optimal control. In *Advances in Robot Kinematics*, pages 409–418. Springer, 2014. URL http://link.springer.com/chapter/10.1007/978-3-319-06698-1_42.
- S. Ghousayni, C. Stevens, S. Durham, and D. Ewins. Assessment and validation of a simple automated method for the detection of gait events and intervals. *Gait & Posture*, 20(3):266 – 272, 2004. ISSN 0966-6362. doi: <http://dx.doi.org/10.1016/j.gaitpost.2003.10.001>. URL <http://www.sciencedirect.com/science/article/pii/S0966636203001711>.
- P. Gill, W. Murray, and M. Saunders. *User's Guide For QPOPT 1.0: A Fortran Package For Quadratic Programming*, 1995. URL <http://www.cam.ucsd.edu/~peg/papers/qpopt.pdf>.
- C. Gonzalez-Ochoa, S. McCammon, and J. Peters. Computing moments of objects enclosed by piecewise polynomial surfaces. *ASM Transaction on Graphics*, 17(3):143–157, July 1998. ISSN 0730-0301. doi: 10.1145/285857.285858. URL <http://doi.acm.org/10.1145/285857.285858>.
- C. Gordon, T. Churchill, C. Clauser, B. Bradtmiller, J. McConville, I. Tebbetts, and R. Walker. 1988 anthropometric survey of U.S. Army personnel: summary statistics interim report. Technical Report NATICK/TR-89/027, U.S. Army Natick RD & E Center, Massachusetts, 1988.
- A. Goswami and V. Kallem. Rate of change of angular momentum and balance maintenance of biped robots. In *IEEE/RAS International Conference on Robotics and Automation (ICRA)*, volume 4, pages 3785–3790, April 2004. doi: 10.1109/ROBOT.2004.1308858.
- A. Goswami. Postural stability of biped robots and the foot-rotation indicator (FRI) point. *The International Journal of Robotics Research*, 18(6):523–533, 1999. doi: 10.1177/02783649922066376. URL <http://ijr.sagepub.com/content/18/6/523.abstract>.
- D. Gouaillier, V. Hugel, P. Blazevic, C. Kilner, J. Monceaux, P. Lafourcade, B. Marnier, J. Serre, and B. Maisonnier. Mechatronic design of NAO humanoid. In *Robotics and Automation, 2009. ICRA '09. IEEE International Conference on*, pages 769–774, May 2009. doi: 10.1109/ROBOT.2009.5152516.
- J. Gray. The mechanism of locomotion in snakes. *Journal of Experimental Biology*, 23(2):101–120, 1946. URL <http://jeb.biologists.org/content/23/2/101.abstract>.
- E. S. Grood and W. J. Suntay. A joint coordinate system for the clinical description of three-dimensional motions: application to the knee. *ASME Journal of Biomechanical Engineering*, 105(2):136–144, May 1983. [PubMed:6865355].
- D. Gross, W. Hauger, J. Schröder, and W. Wall. *Technische Mechanik: Statik*. Springer-Lehrbuch. Springer London, Limited, 2006. ISBN 9783540340928. URL http://books.google.de/books?id=b_gdBAAQBAJ.
- D. Gross, W. Hauger, and P. Wriggers. *Technische Mechnik 4: Hydromechanik, Elemente der Höheren Mechanik, Numerische Methoden*. Springer-Lehrbuch. Springer Verlag, 2011. ISBN 978-3-642-16827-7. doi: 10.1007/978-3-642-16828-4.
- D. Gross, W. Hauger, W. Schnell, and J. Schrader. *Technische Mechanik 3: Kinetik*. Springer-Lehrbuch. Springer, 2004. ISBN 978-3-540-22167-8. doi: 10.1007/3-540-34995-2. URL <http://books.google.de/books?id=NaN9En9K9B0C>.
- K. Grote and J. Feldhusen. *Dubbel: Taschenbuch für den Maschinenbau*. Springer Berlin Heidelberg, 2011. ISBN 9783642173066. URL <http://books.google.de/books?id=o41HW8AvXVgC>.
- Y. Guan, K. Yokoi, and K. Tanie. Feasibility: Can humanoid robots overcome given obstacles? In *IEEE/RAS International Conference on Robotics and Automation (ICRA)*, pages 1054–1059, April 2005. doi: 10.1109/ROBOT.2005.1570255.
- G. Guennebaud, B. Jacob, et al. Eigen v3. <http://eigen.tuxfamily.org>, 2010.
- H. C. Güler, N. Berme, and S. R. Simon. A viscoelastic sphere model for the representation of plantar soft tissue during simulations. *Journal of Biomechanics*, 31(9):847 – 853, 1998. ISSN 0021-9290. doi: [http://dx.doi.org/10.1016/S0021-9290\(98\)00085-2](http://dx.doi.org/10.1016/S0021-9290(98)00085-2). URL <http://www.sciencedirect.com/science/article/pii/S0021929098000852>.
- M. Häggström. Skeleton scheme of human, November 2008. URL http://upload.wikimedia.org/wikipedia/commons/c/c2/Human_skeleton_front.svg_-_no_labels.svg.
- K. Harada, S. Kajita, H. Saito, M. Morisawa, F. Kanehiro, K. Fujiwara, K. Kaneko, and H. Hirukawa. A humanoid robot carrying a heavy object. In *IEEE/RAS International Conference on Robotics and Automation (ICRA)*, pages 1712–1717, April 2005. doi: 10.1109/ROBOT.2005.1570360.
- M. Hardt, K. Kreutz-Delgado, and J. Helton. Optimal biped walking with a complete dynamical model. In *IEEE International Conference on Decision & Control*, volume 3, pages 2999–3004, 1999. doi: 10.1109/CDC.1999.831393.
- Y. Hardy, K. S. Tan, and W.-H. Steeb. *Computer Algebra With Symbolic C++*. World Scientific Publishing Co., Inc., River Edge, NJ, USA, 2008. ISBN 9789812833617, 9812833617.
- C. R. Hargraves and S. W. Paris. Direct trajectory optimization using nonlinear programming and collocation. In *(Astrodynamics Conference, Williamsburg, VA, Aug. 18-20, 1986, Technical Papers, p. 3-12) Journal of Guidance, Control, and Dynamics (ISSN 0731-5090)*, vol. 10, July-Aug. 1987, p.

BIBLIOGRAPHY

- 338-342. Previously cited in issue 23, p. 3418, Accession no. A86-47902., volume 10 of AAS/AIAA *Astrodynamics Conference*, pages 3–12, August 1987. URL http://adsabs.harvard.edu/cgi-bin/nph-bib_query?bibcode=1987asdy...10...3H.
- M. R. Hawes and D. Sovak. Quantitative morphology of the human foot in a north american population. *Ergonomics*, 37(7):1213–1226, 1994. doi: 10.1080/00140139408964899. URL <http://dx.doi.org/10.1080/00140139408964899>. PMID: 8050406.
- T. Hayashi, H. Kawamoto, and Y. Sankai. Control method of robot suit HAL working as operator's muscle using biological and dynamical information. In *IEEE/RSJ International Conference on Intelligent Robots and Systems (IROS)*, pages 3063–3068, Aug 2005. doi: 10.1109/IROS.2005.1545505.
- C. Hecker, B. Raabe, R. W. Enslow, J. DeWeese, J. Maynard, and K. van Prooijen. Real-time motion retargeting to highly varied user-created morphologies. *ACM Trans. Graph.*, 27(3):27:1–27:11, August 2008. ISSN 0730-0301. doi: 10.1145/1360612.1360626. URL <http://doi.acm.org/10.1145/1360612.1360626>.
- B. Heimann, W. Gerth, and K. Popp. *Mechatronik, Komponenten - Methoden - Beispiele*. Hanser Fachbuchverlag, Leipzig, 3 edition, 2007. URL <http://www.hanser.de/buch.asp?isbn=978-3-446-40599-8&area=Technik>. ISBN-10: 3-446-40599-2.
- R. Henrion. TECHNICAL NOTE, on constraint qualifications. *Journal of Optimization and Applications*, 72:187–196, 1992. doi: 10.1007/s10957-004-1861-9. URL link.springer.com/content/pdf/10.1007/s10957-004-1861-9.pdf.
- H. Herr. Exoskeletons and orthoses: classification, design challenges and future directions. *Journal of Neuro Engineering and Rehabilitation*, 6(1):21, 2009. ISSN 1743-0003. doi: 10.1186/1743-0003-6-21. URL <http://www.jneuroengrehab.com/content/6/1/21>.
- H. Herr and M. Popovic. Angular momentum in human walking. *Journal of Experimental Biology*, 211(4):467–481, 2008. doi: 10.1242/jeb.008573. URL <http://jeb.biologists.org/content/211/4/467.abstract>.
- H. M. Herr and R. D. Kornbluh. New horizons for orthotic and prosthetic technology: artificial muscle for ambulation. *Proc. SPIE*, 5385:1–9, 2004. doi: 10.1117/12.544510. URL <http://dx.doi.org/10.1117/12.544510>.
- H. Hertz. Ueber die berührung fester elastischer körper. *Journal für die reine und angewandte Mathematik (Crelle's Journal)*, 1882(92):Weissauer, Rainer, 1882. ISSN 1435-5345. doi: 10.1515/crll.1882.92.156. URL www.degruyter.com/view/j/crll.1882.issue-92/crll.1882.92.156/crll.1882.92.156.xml.
- H. Hicheur, S. Vieilledent, and A. Berthoz. Head motion in humans alternating between straight and curved walking path: Combination of stabilizing and anticipatory orienting mechanisms. *Neuroscience Letters*, 383(1–2):87–92, 2005. ISSN 0304-3940. doi: <http://dx.doi.org/10.1016/j.neulet.2005.03.046>. URL <http://www.sciencedirect.com/science/article/pii/S0304394005003526>.
- J. H. Hicks. The mechanics of the foot. II. The plantar aponeurosis and the arch. *Journal of Anatomy*, 88(1):25–30, Jan 1954. [PubMed Central:PMC1244640] [PubMed:13129168].
- R. N. Hinrichs. Adjustments to the segment center of mass proportions of Clauser et al. (1969). *Journal of Biomechanics*, 23(9):949 – 951, 1990. ISSN 0021-9290. doi: [http://dx.doi.org/10.1016/0021-9290\(90\)90361-6](http://dx.doi.org/10.1016/0021-9290(90)90361-6). URL <http://www.sciencedirect.com/science/article/pii/0021929090903616>.
- K. Hirai. Current and future perspective of Honda humanoid robot. In Y. Shirai and S. Hirose, editors, *Robotics Research*, pages 446–450. Springer London, 1998. ISBN 978-1-4471-1582-3. doi: 10.1007/978-1-4471-1580-9_44. URL http://dx.doi.org/10.1007/978-1-4471-1580-9_44.
- K. Hirai, M. Hirose, Y. Haikawa, and T. Takenaka. The development of Honda humanoid robot. In *IEEE/RAS International Conference on Robotics and Automation (ICRA)*, volume 2, pages 1321–1326, 1998. doi: 10.1109/ROBOT.1998.677288. URL <http://dx.doi.org/10.1109/ROBOT.1998.677288>.
- H. Hirukawa, F. Kanehiro, and S. Kajita. OpenHRP: open architecture humanoid robotics platform. In R. Jarvis and A. Zelinsky, editors, *Robotics Research*, volume 6 of *Springer Tracts in Advanced Robotics*, pages 99–112. Springer Berlin Heidelberg, 2003. ISBN 978-3-540-00550-6. doi: 10.1007/3-540-36460-9_7. URL http://dx.doi.org/10.1007/3-540-36460-9_7.
- H. Hirukawa, F. Kanehiro, K. Kaneko, S. Kajita, K. Fujiwara, Y. Kawai, F. Tomita, S. Hirai, K. Tanie, T. Isozumi, K. Akachi, T. Kawasaki, S. Ota, K. Yokoyama, H. Handa, Y. Fukase, J. ichiro Maeda, Y. Nakamura, S. Tachi, and H. Inoue. Humanoid robotics platforms developed in {HRP}. *Robotics and Autonomous Systems*, 48(4):165 – 175, 2004. ISSN 0921-8890. doi: <http://dx.doi.org/10.1016/j.robot.2004.07.007>. URL <http://www.sciencedirect.com/science/article/pii/S0921889004000946>. Humanoids 2003.
- H. Hirukawa, S. Kajita, F. Kanehiro, K. Kaneko, and T. Isozumi. The human-size humanoid robot that can walk, lie down and get up. *The International Journal of Robotics Research*, 24(9):755–769, 2005. doi: 10.1177/0278364905057217. URL <http://ijr.sagepub.com/content/24/9/755.abstract>.
- G. Hu, C. Ong, and C. Teo. Direct collocation and nonlinear programming for optimal control problem using an enhanced transcribing scheme. In *IEEE International Symposium on Computer Aided Control*

- System Design*, pages 369–374, 1999. doi: 10.1109/CACSD.1999.808676.
- M. Hutter. *StarLETH & Co. - Design and Control of Legged Robots with Compliant Actuation*. PhD thesis, ETH Zurich, 2013. URL <http://e-collection.library.ethz.ch/eserv/eth:7183/eth-7183-02.pdf>.
- R. Ierusalimsky, L. Figueiredo, and W. Celes. *Lua 5.1 Reference Manual*. Lua.Org, 2006. ISBN 8590379833. URL <http://www.lua.org/manual/5.1/manual.html>.
- T. Imai, S. T. Moore, T. Raphan, and B. Cohen. Interaction of the body, head, and eyes during walking and turning. *Experimental Brain Research*, 136(1):1–18, 2001. ISSN 0014-4819. doi: 10.1007/s002210000533. URL <http://dx.doi.org/10.1007/s002210000533>.
- T. Ishida, Y. Kuroki, and J. Yamaguchi. Mechanical system of a small biped entertainment robot. In *IEEE/RSJ International Conference on Intelligent Robots and Systems (IROS)*, volume 2, pages 1129–1134, Oct 2003. doi: 10.1109/IROS.2003.1248796.
- R. Isman and V. Inman. Anthropomorphic studies of the human foot and ankle. Technical report, Biomechanics Laboratory, University of California, 1969. URL <http://www.rehab.research.va.gov/jour/69/6/1/97.pdf>.
- A. Jarfi, Q. Huang, L. Zhang, J. Yang, Z. Wang, and S. IV. Realization and trajectory planning for obstacle stepping over by humanoid robot BHR-2. In *IEEE International Conference on Robotics and Biomimetics*, pages 1384–1389, Dec 2006. doi: 10.1109/ROBIO.2006.340131.
- N. Jarrassé and G. Morel. Connecting a human limb to an exoskeleton. *IEEE Transaction on Robotics*, 28(3):697–709, June 2012. ISSN 1552-3098. doi: 10.1109/TRO.2011.2178151.
- J. Jiménez, R. Segura, and F. Feito. Efficient collision detection between 2D polygons. In *International Conferences in Central Europe on Computer Graphics, Visualization and Computer Vision*, volume 12, pages 191–198. UNION Agency - Science Press, 2004. doi: <http://hdl.handle.net/11025/1748>. URL http://wscg.zcu.cz/wscg2004/Papers_2004_Full/B83.pdf.
- D. Joyner, O. Čertík, A. Meurer, and B. E. Granger. Open source computer algebra systems: SymPy. *ACM Communications in Computer Algebra*, 45(3/4):225–234, January 2012. ISSN 1932-2240. doi: 10.1145/2110170.2110185. URL <http://doi.acm.org/10.1145/2110170.2110185>.
- S. Kagami, K. Nishiwaki, J. Kuffner, S. Thompson, J. Chestnutt, M. Stilman, and P. Michel. Humanoid HRP2-DHRC for autonomous and interactive behavior. In S. Thrun, R. Brooks, and H. Durrant-Whyte, editors, *Robotics Research*, volume 28 of *Springer Tracts in Advanced Robotics*, pages 103–117. Springer Berlin Heidelberg, 2007. ISBN 978-3-540-48110-2. doi: 10.1007/978-3-540-48113-3_10. URL http://dx.doi.org/10.1007/978-3-540-48113-3_10.
- T. Kagawa and Y. Uno. Gait pattern generation for a power-assist device of paraplegic gait. In *IEEE International Symposium on Robot and Human Interactive Communication (ROMAN)*, pages 633–638, Sept 2009. doi: 10.1109/ROMAN.2009.5326348.
- S. Kajita and K. Tani. Study of dynamic biped locomotion on rugged terrain-theory and basic experiment. In *International Conference on Advanced Robotics ICAR, 'Robots in Unstructured Environments'*, volume 1, pages 741–746, June 1991. doi: 10.1109/ICAR.1991.240688.
- S. Kajita, F. Kanehiro, K. Kaneko, K. Yokoi, and H. Hirukawa. The 3D linear inverted pendulum mode: a simple modeling for a biped walking pattern generation. In *IEEE/RSJ International Conference on Intelligent Robots and Systems (IROS)*, volume 1, pages 239–246, 2001a. doi: 10.1109/IROS.2001.973365.
- S. Kajita, K. Yokoi, M. Saigo, and K. Tanie. Balancing a humanoid robot using backdrive concerned torque control and direct angular momentum feedback. In *IEEE/RAS International Conference on Robotics and Automation (ICRA)*, volume 4, pages 3376–3382 vol.4, 2001b. doi: 10.1109/ROBOT.2001.933139.
- S. Kajita, F. Kanehiro, K. Kaneko, K. Fujiwara, K. Yokoi, and H. Hirukawa. A realtime pattern generator for biped walking. In *IEEE/RAS International Conference on Robotics and Automation (ICRA)*, volume 1, pages 31–37 vol.1, 2002. doi: 10.1109/ROBOT.2002.1013335.
- S. Kajita, F. Kanehiro, K. Kaneko, K. Fujiwara, K. Harada, K. Yokoi, and H. Hirukawa. Biped walking pattern generation by using preview control of zero-moment point. In *IEEE/RAS International Conference on Robotics and Automation (ICRA)*, volume 2, pages 1620–1626, Sept 2003a. doi: 10.1109/ROBOT.2003.1241826.
- S. Kajita, F. Kanehiro, K. Kaneko, K. Fujiwara, K. Harada, K. Yokoi, and H. Hirukawa. Resolved momentum control: humanoid motion planning based on the linear and angular momentum. In *IEEE/RSJ International Conference on Intelligent Robots and Systems (IROS)*, volume 2, pages 1644–1650, Oct 2003b. doi: 10.1109/IROS.2003.1248880.
- S. Kajita, T. Nagasaki, K. Kaneko, K. Yokoi, and K. Tanie. A hop towards running humanoid biped. In *IEEE/RAS International Conference on Robotics and Automation (ICRA)*, volume 1, pages 629–635, April 2004. doi: 10.1109/ROBOT.2004.1307219.
- S. Kajita, T. Nagasaki, K. Kaneko, K. Yokoi, and K. Tanie. A running controller of humanoid biped HRP-2LR. In *IEEE/RAS International Conference on Robotics and Automation (ICRA)*, pages 616–622, April 2005. doi: 10.1109/ROBOT.2005.1570186.
- S. Kajita, M. Morisawa, K. Harada, K. Kaneko, F. Kanehiro, K. Fujiwara, and H. Hirukawa. Biped walking pattern generator allowing auxiliary ZMP control. In *IEEE/RSJ International Conference on Intelligent Robots and Systems (IROS)*, pages 2993–2999, Oct 2006. doi: 10.1109/IROS.2006.

- 282233.
- S. Kajita, K. Kaneko, M. Morisawa, S. Nakaoka, and H. Hirukawa. Zmp-based biped running enhanced by toe springs. In *IEEE/RAS International Conference on Robotics and Automation (ICRA)*, pages 3963–3969, April 2007a. doi: 10.1109/ROBOT.2007.364087.
- S. Kajita, T. Nagasaki, K. Kaneko, and H. Hirukawa. Zmp-based biped running control. *IEEE Robotics & Automation Magazine*, 14(2):63–72, June 2007b. ISSN 1070-9932. doi: 10.1109/MRA.2007.380655.
- S. Kajita, M. Morisawa, K. Miura, S. Nakaoka, K. Harada, K. Kaneko, F. Kanehiro, and K. Yokoi. Biped walking stabilization based on linear inverted pendulum tracking. In *IEEE/RSJ International Conference on Intelligent Robots and Systems (IROS)*, pages 4489–4496, Oct 2010. doi: 10.1109/IROS.2010.5651082.
- F. Kanehiro, K. Fujiwara, S. Kajita, K. Yokoi, K. Kaneko, H. Hirukawa, Y. Nakamura, and K. Yamane. Open architecture humanoid robotics platform. In *IEEE/RAS International Conference on Robotics and Automation (ICRA)*, volume 1, pages 24–30, 2002. doi: 10.1109/ROBOT.2002.1013334.
- F. Kanehiro, M. Morisawa, W. Suleiman, K. Kaneko, and E. Yoshida. Integrating geometric constraints into reactive leg motion generation. In *IEEE/RSJ International Conference on Intelligent Robots and Systems (IROS)*, pages 4069–4076, Oct 2010. doi: 10.1109/IROS.2010.5651634.
- K. Kaneko, F. Kanehiro, S. Kajita, K. Yokoyama, K. Akachi, T. Kawasaki, S. Ota, and T. Isozumi. Design of prototype humanoid robotics platform for HRP. In *IEEE/RSJ International Conference on Intelligent Robots and Systems (IROS)*, volume 3, pages 2431–2436, 2002. doi: 10.1109/IRDS.2002.1041632.
- K. Kaneko, F. Kanehiro, S. Kajita, H. Hirukawa, T. Kawasaki, M. Hirata, K. Akachi, and T. Isozumi. Humanoid robot HRP-2. In *IEEE/RAS International Conference on Robotics and Automation (ICRA)*, volume 2, pages 1083–1090, April 2004. doi: 10.1109/ROBOT.2004.1307969.
- K. Kaneko, K. Harada, F. Kanehiro, G. Miyamori, and K. Akachi. Humanoid robot HRP-3. In *IEEE/RSJ International Conference on Intelligent Robots and Systems (IROS)*, pages 2471–2478, Sept 2008. doi: 10.1109/IROS.2008.4650604.
- K. Kaneko, F. Kanehiro, M. Morisawa, K. Miura, S. Nakaoka, and S. Kajita. Cybernetic human HRP-4C. In *IEEE/RAS International Conference on Humanoid Robots*, pages 7–14, Dec 2009. doi: 10.1109/ICHR.2009.5379537.
- K. Kaneko, F. Kanehiro, M. Morisawa, K. Akachi, G. Miyamori, A. Hayashi, and N. Kanehira. Humanoid robot HRP-4 - humanoid robotics platform with lightweight and slim body. In *IEEE/RSJ International Conference on Intelligent Robots and Systems (IROS)*, pages 4400–4407, Sept 2011. doi: 10.1109/IROS.2011.6094465.
- M. Kang, H. Sadri, L. Moccozet, N. Magnenat-Thalmann, and P. Hoffmeyer. Accurate simulation of hip joint range of motion. In *Computer Animation*, pages 215–219, 2002. doi: 10.1109/CA.2002.1017539.
- K. Kasaoka and Y. Sankai. Predictive control estimating operator’s intention for stepping-up motion by exo-skeleton type power assist system hal. In *IEEE/RSJ International Conference on Intelligent Robots and Systems (IROS)*, volume 3, pages 1578–1583, 2001. doi: 10.1109/IROS.2001.977204.
- T. Kato, A. Takanishi, H. Jishikawa, and K. I. The realisation of the quasi-dynamic walking by the biped walking machine. In A. Morecki, G. Bianchi, and K. Kędzior, editors, *Proceedings of the Fourth Symposium on Theory and Practice of Robots and Manipulators*, page 341 – 351, 1983.
- L. Kavan, P-P Sloan, and C. O’Sullivan. Fast and efficient skinning of animated meshes. *Computer Graphics Forum*, 29(2):327–336, 2010. ISSN 1467-8659. doi: 10.1111/j.1467-8659.2009.01602.x. URL <http://dx.doi.org/10.1111/j.1467-8659.2009.01602.x>.
- H. Kawamoto, S. Kanbe, and Y. Sankai. Power assist method for HAL-3 estimating operator’s intention based on motion information. In *IEEE International Workshop on Robot and Human Interactive Communication (ROMAN)*, pages 67–72, Oct 2003. doi: 10.1109/ROMAN.2003.1251800.
- H. Kawamoto and Y. Sankai. Power assist system HAL-3 for gait disorder person. In K. Miesenberger, J. Klaus, and W. Zagler, editors, *Computers Helping People with Special Needs*, volume 2398 of *Lecture Notes in Computer Science*, pages 196–203. Springer Berlin Heidelberg, 2002. ISBN 978-3-540-43904-2. doi: 10.1007/3-540-45491-8_43. URL http://dx.doi.org/10.1007/3-540-45491-8_43.
- H. Kazerooni and J. Guo. Dynamics and control of human-robot interaction. In *American control conference*, pages 2398–2403, June 1993.
- H. Kazerooni and T. Snyder. Case study on haptic devices: Human-induced instability in power hand controllers. *Journal of Guidance, Control and Dynamics*, 18(1):108–113, 1995. doi: 10.2514/3.56664. URL <http://bleex.me.berkeley.edu/wp-content/uploads/hel-media/Publication/AIAA.GCD.V18N1.Instability%20Hand%20Controller.1995.pdf>.
- H. Kazerooni, J.-L. Racine, L. Huang, and R. Steger. On the control of the Berkeley Lower Extremity Exoskeleton (BLEEX). In *IEEE/RAS International Conference on Robotics and Automation (ICRA)*, pages 4353–4360, April 2005. doi: 10.1109/ROBOT.2005.1570790.
- J. Ketchel and P. Larochelle. Collision detection of cylindrical rigid bodies for motion planning. In *IEEE/RAS International Conference on Robotics and Automation (ICRA)*, pages 1530–1535, May 2006. doi: 10.1109/ROBOT.2006.1641925.
- J. Ketchel and P. Larochelle. Self-collision detection in spatial closed chains. *Journal of Mechanical*

- Design*, 130(9):1–9, 2008. ISSN 1050-0472. doi: 10.1115/1.2965363. URL <http://dx.doi.org/10.1115/1.2965363>.
- W. Khalil and E. Dombre. *Modeling, Identification and Control of Robots*. Taylor & Francis, Inc., Bristol, PA, USA, 3rd edition, 2002. ISBN 1560329831.
- A. Kirk, J. O'Brien, and D. Forsyth. Skeletal parameter estimation from optical motion capture data. In *IEEE Computer Society Conference on Computer Vision and Pattern Recognition, CVPR*, volume 2, page 1185, June 2005. doi: 10.1109/CVPR.2005.327.
- R. N. Kirkwood, E. G. Culham, and P. Costigan. Radiographic and non-invasive determination of the hip joint center location: effect on hip joint moments. *Clinical Biomechanics*, 14(4):227 – 235, 1999. ISSN 0268-0033. doi: [http://dx.doi.org/10.1016/S0268-0033\(98\)00073-4](http://dx.doi.org/10.1016/S0268-0033(98)00073-4). URL <http://www.sciencedirect.com/science/article/pii/S0268003398000734>.
- F. Kirsch and J. Döllner. OpenCSG: A library for image-based CSG rendering. In *Proceedings of the Annual Conference on USENIX Annual Technical Conference, ATEC '05*, pages 49–49, Berkeley, CA, USA, 2005. USENIX Association. URL <http://dl.acm.org/citation.cfm?id=1247360.1247409>.
- K. Koch, M. Nöltner, G. Plettenberg, M. Rössler, and K. Mombaur. Moving ahead in unstructured terrain - A versatile, low-cost and light-weight snake robot prototype for motion optimization. In *DGR-Days - German robotics society*, 2013. URL https://www1.iwr.uni-heidelberg.de/fileadmin/groups/orb/HenningKoch/ORBsnake/DGR2013_abstractSnake.pdf.
- K. Kong, J. Bae, and M. Tomizuka. A compact rotary series elastic actuator for knee joint assistive system. In *IEEE/RAS International Conference on Robotics and Automation (ICRA)*, pages 2940–2945, May 2010. doi: 10.1109/ROBOT.2010.5509227.
- J. Kuffner, K. Nishiwaki, S. Kagami, Y. Kuniyoshi, M. Inaba, and H. Inoue. Self-collision detection and prevention for humanoid robots. In *IEEE/RAS International Conference on Robotics and Automation (ICRA)*, volume 3, pages 2265–2270, 2002. doi: 10.1109/ROBOT.2002.1013569.
- H. K. Kwa, J. Noorden, M. Missel, T. Craig, J. Pratt, and P. Neuhaus. Development of the IHMC mobility assist exoskeleton. In *IEEE/RAS International Conference on Robotics and Automation (ICRA)*, pages 2556–2562, May 2009. doi: 10.1109/ROBOT.2009.5152394.
- H. M. Lankarani and P. E. Nikravesh. A contact force model with hysteresis damping for impact analysis of multibody systems. *Journal of Mechanical Design*, 112(3):369–376, 1990. doi: 10.1115/1.2912617. URL <http://dx.doi.org/10.1115/1.2912617>.
- M. Lee, S.-H. Hong, D.-C. Kim, and H. Kwon. Incorporating ISO 26262 development process in DFSS. In *Asia Industrial Engineering & Management Systems Conference*, 2012. URL <http://apiems.net/conf2012/T2B2.pdf>.
- Y. Lee and A. Requicha. Algorithms for computing the volume and other integral properties of solid objects. Technical Report Technical Memorandum / 35a, College of Engineering & Applied Science - The University of Rochester, University of Rochester. Production Automation Project – Rochester, N.Y., March 1981. URL <http://hdl.handle.net/1802/1182>.
- D. B. Leineweber. The theory of MUSCOD in a nutshell. Master's thesis, Interdisciplinary Center of Scientific Computing, University of Heidelberg, 1995. URL http://www.iwr.uni-heidelberg.de/groups/agbock/USER_PAGES/LEINWEBER_DANIEL/WWW/musnut.pdf.
- D. B. Leineweber. Efficient reduced SQP methods for the optimization of chemical processes described by large sparse DAE models. Reihe 3 613, VDI-Verlag GmbH, Düsseldorf, 1999. URL http://www.iwr.uni-heidelberg.de/groups/agbock/USER_PAGES/LEINWEBER_DANIEL/WWW/phddiss.pdf.
- D. B. Leineweber, I. Bauer, H. G. Bock, and J. P. Schlöder. An efficient multiple shooting based reduced {SQP} strategy for large-scale dynamic process optimization. Part I: theoretical aspects. *Computers & Chemical Engineering*, 27(2):157 – 166, 2003a. ISSN 0098-1354. doi: [http://dx.doi.org/10.1016/S0098-1354\(02\)00158-8](http://dx.doi.org/10.1016/S0098-1354(02)00158-8). URL <http://www.sciencedirect.com/science/article/pii/S0098135402001588>.
- D. B. Leineweber, A. Schäfer, H. G. Bock, and J. P. Schlöder. An efficient multiple shooting based reduced {SQP} strategy for large-scale dynamic process optimization: Part II: Software aspects and applications. *Computers & Chemical Engineering*, 27(2):167 – 174, 2003b. ISSN 0098-1354. doi: [http://dx.doi.org/10.1016/S0098-1354\(02\)00195-3](http://dx.doi.org/10.1016/S0098-1354(02)00195-3). URL <http://www.sciencedirect.com/science/article/pii/S0098135402001953>.
- B. Li. The moment calculation of polyhedra. *Pattern Recognition*, 26(8):1229 – 1233, 1993. ISSN 0031-3203. doi: [http://dx.doi.org/10.1016/0031-3203\(93\)90207-D](http://dx.doi.org/10.1016/0031-3203(93)90207-D). URL <http://www.sciencedirect.com/science/article/pii/003132039390207D>.
- J. A. Liggett. Exact formulae for areas, volumes and moments of polygons and polyhedra. *Communications in Applied Numerical Methods*, 4(6):815–820, 1988. ISSN 1555-2047. doi: 10.1002/cnm.1630040616. URL <http://dx.doi.org/10.1002/cnm.1630040616>.
- S. Ling Lien and J. Kajiyama. A symbolic method for calculating the integral properties of arbitrary nonconvex polyhedra. *Computer Graphics and Applications, IEEE*, 4(10):35–42, Oct 1984. ISSN 0272-1716. doi: 10.1109/MCG.1984.6429334.
- K. Löffler, M. Gienger, and F. Pfeiffer. Sensors and control concept of walking “Johnnie”. *The International Journal of Robotics Research*, 22(3-4):229–239, 2003. doi: 10.1177/0278364903022003007. URL <http://ijr.sagepub.com/content/22/3-4/229.abstract>.
- J. A. T. Machado and M. F. Silva. An overview of legged robots. In *MME 2006-International Symposium*

- on *Mathematical Methods in Engineering*, 2006.
- M. Malosio, N. Pedrocchi, F. Vicentini, and L. Tosatti. Analysis of elbow-joints misalignment in upper-limb exoskeleton. In *IEEE International Conference on Rehabilitation Robotics (ICORR)*, pages 1–6, June 2011. doi: 10.1109/ICORR.2011.5975393.
- N. Mansard. A dedicated solver for fast operational-space inverse dynamics. In *IEEE/RAS International Conference on Robotics and Automation (ICRA)*, pages 4943–4949, May 2012. doi: 10.1109/ICRA.2012.6224851.
- N. Mansard, O. Stasse, P. Evrard, and A. Kheddar. A versatile generalized inverted kinematics implementation for collaborative working humanoid robots: The stack of tasks. In *International Conference on Advanced Robotics ICAR*, pages 1–6, June 2009. ISBN 978-1-4244-4855-5.
- B. Martin and J. Bobrow. Minimum effort motions for open chain manipulators with task-dependent end-effector constraints. In *IEEE/RAS International Conference on Robotics and Automation (ICRA)*, volume 3, pages 2044–2049, Apr 1997. doi: 10.1109/ROBOT.1997.619174.
- K. Martin and B. Hoffman. An open source approach to developing software in a small organization. *IEEE Software*, 24(1):46–53, Jan 2007. ISSN 0740-7459. doi: 10.1109/MS.2007.5.
- C. Mattheck. *Verborgene Gestaltgesetze der Natur: Optimalformen ohne Computer*. Karlsruhe Institut of Technology (KIT), 2006. ISBN 9783923704538. URL <http://books.google.de/books?id=beIkMwAACAAJ>.
- J. McConville, T. Churchill, I. Kaleps, C. Clauser, and J. Cuzzi. Anthropometric relation of body and body segment moments of inertia. Technical Report AFAMRL-TR-80-119, Aerospace Medical Research Laboratory, Wright-Patterson Air Force Base, OH, 1980.
- T. McMahon. Mechanics of locomotion. *The International Journal of Robotics Research*, 3(2):4–28, 1984. doi: 10.1177/027836498400300202. URL <http://ijr.sagepub.com/content/3/2/4.abstract>.
- F. Menschik. The hip joint as a conchoid shape. *Journal of Biomechanics*, 30(9):971 – 973, 1997. ISSN 0021-9290. doi: [http://dx.doi.org/10.1016/S0021-9290\(97\)00051-1](http://dx.doi.org/10.1016/S0021-9290(97)00051-1). URL <http://www.sciencedirect.com/science/article/pii/S0021929097000511>.
- G. Merzinger and T. Wirth. *Repetitorium der Höheren Mathematik*. BINOMI Verlag, 2002. ISBN 978-3923923335.
- Y. Miao, F. Gao, and D. Pan. Mechanical design of a hybrid leg exoskeleton to augment load-carrying for walking. *International Journal of Advanced Robotic Systems*, 10:395:1–11, 2013. doi: 10.5772/57238.
- P. Michel, J. Chestnutt, J. Kuffner, and T. Kanade. Vision-guided humanoid footstep planning for dynamic environments. In *IEEE/RAS International Conference on Humanoid Robots*, pages 13 – 18, December 2005. URL http://www.ri.cmu.edu/pub_files/pub4/michel_philipp_2005_1/michel_philipp_2005_1.pdf.
- Y. Mikami, T. Moulard, E. Yoshida, and G. Venture. Identification of HRP-2 foot’s dynamics. In *IEEE/RSJ International Conference on Intelligent Robots and Systems (IROS)*, pages 927–932, Sept 2014. doi: 10.1109/IROS.2014.6942670.
- M. Millard, J. McPhee, and E. Kubica. Multi-step forward dynamic gait simulation. In C. Bottasso, editor, *Multibody Dynamics*, volume 12 of *Computational Methods in Applied Sciences*, pages 25–43. Springer Netherlands, 2009. ISBN 978-1-4020-8828-5. doi: 10.1007/978-1-4020-8829-2_2. URL http://dx.doi.org/10.1007/978-1-4020-8829-2_2.
- B. Mirtich. *Practical Motion Planning in Robotics: Current Approaches and Future Directions*, chapter Efficient Algorithms for Two-Phase Collision Detection, pages 203–223, (see also Technical Report TR-97-23, MERL – A MITSUBISHI ELECTRIC RESEARCH LABORATORY). Number TR-97-23. John Wiley & Sons, Ltd, 1998. ISBN 047198163X. URL <http://www.merl.com/papers/docs/tr97-23.pdf>.
- B. Mirtich. Fast and accurate computation of polyhedral mass properties. *Journal of Graphics Tools*, 1(2):31–50, February 1996. ISSN 1086-7651. doi: 10.1080/10867651.1996.10487458. URL <http://dx.doi.org/10.1080/10867651.1996.10487458>.
- M. Mistry, J. Nakanishi, G. Cheng, and S. Schaal. Inverse kinematics with floating base and constraints for full body humanoid robot control. In *IEEE/RAS International Conference on Humanoid Robots*, pages 22–27, Dec 2008. doi: 10.1109/ICHR.2008.4755926.
- M. Mistry, J. Buchli, and S. Schaal. Inverse dynamics control of floating base systems using orthogonal decomposition. In *IEEE/RAS International Conference on Robotics and Automation (ICRA)*, pages 3406–3412, May 2010. doi: 10.1109/ROBOT.2010.5509646.
- N. J. Mizen. Powered exoskeletal apparatus for amplifying human strength in response to normal body movements, June 1969. URL <http://www.freepatentsonline.com/3449769.html>.
- K. Mombaur. Using optimization to create self-stable human-like running. *Robotica*, 27:321–330, 5 2009. ISSN 1469-8668. doi: 10.1017/S0263574708004724. URL http://journals.cambridge.org/article_S0263574708004724.
- K. Mombaur. *Stability Optimization of Open-loop Controlled Walking Robots*. PhD thesis, Interdisciplinary Center of Scientific Computing, University of Heidelberg, 2001. URL <http://archiv.ub.uni-heidelberg.de/volltextserver/1796/1/archiv.gz>.
- K. Mombaur, H. Bock, J. Schloder, and R. Longman. Human-like actuated walking that is asymptotically stable without feedback. In *IEEE/RAS International Conference on Robotics and Automation (ICRA)*,

- volume 4, pages 4128–4133 vol.4, 2001. doi: 10.1109/ROBOT.2001.933263.
- M. Montero, S. Roundy, D. Odell, S.-H. Ahn, and P. Wright. Material characterization of fused deposition modeling (FDM) ABS by designed experiments. Technical report, University of California, Berkeley, 2001. URL http://groups.csail.mit.edu/drl/wiki/images/e/e7/Montero_Roundy_Odell_Ahn_Wright_2001_Material_Characterization_of_Fused_Deposition_Modeling_FDM_ABS_by_Designed_Experiments.pdf.
- I. Mordatch, J. M. Wang, E. Todorov, and V. Koltun. Animating human lower limbs using contact-invariant optimization. *ACM Transactions on Graphics*, 32(6):203:1–203:8, November 2013. ISSN 0730-0301. doi: 10.1145/2508363.2508365. URL <http://doi.acm.org/10.1145/2508363.2508365>.
- P. Moreira, M. Silva, and P. Flores. Ground foot interaction in human gait: Modeling and simulation. In J. Ambrósio, editor, *EUROMECH Solid Mechanics Conference*, pages 1–13, 2009.
- M. Morisawa, S. Kajita, K. Kaneko, K. Harada, F. Kanehiro, K. Fujiwara, and H. Hirukawa. Pattern generation of biped walking constrained on parametric surface. In *IEEE/RAS International Conference on Robotics and Automation (ICRA)*, pages 2405–2410, April 2005. doi: 10.1109/ROBOT.2005.1570473.
- M. Morisawa, S. Kajita, F. Kanehiro, K. Kaneko, K. Miura, and K. Yokoi. Balance control based on capture point error compensation for biped walking on uneven terrain. In *IEEE/RAS International Conference on Humanoid Robots*, pages 734–740, Nov 2012. doi: 10.1109/HUMANOIDS.2012.6651601.
- J. Morrison. The mechanics of the knee joint in relation to normal walking. *Journal of Biomechanics*, 3(1):51–61, 1970. ISSN 0021-9290. doi: [http://dx.doi.org/10.1016/0021-9290\(70\)90050-3](http://dx.doi.org/10.1016/0021-9290(70)90050-3). URL <http://www.sciencedirect.com/science/article/pii/0021929070900503>.
- W. Nachtigall. *Bionik: Grundlagen und Beispiele für Ingenieure und Naturwissenschaftler*. Springer Berlin Heidelberg, 2002. ISBN 9783540436607. URL <http://books.google.de/books?id=u90In822VuwC>.
- K. Nagasaka, H. Inoue, and M. Inaba. Dynamic walking pattern generation for a humanoid robot based on optimal gradient method. In *IEEE International Conference on Systems, Man, and Cybernetics*, volume 6, pages 908–913, 1999. doi: 10.1109/ICSMC.1999.816673.
- Y. Nakamura. *Advanced Robotics: Redundancy and Optimization*. Addison-Wesley Longman Publishing Co., Inc., Boston, MA, USA, 1990.
- S. Nakaoka, S. Hattori, F. Kanehiro, S. Kajita, and H. Hirukawa. Constraint-based dynamics simulator for humanoid robots with shock absorbing mechanisms. In *IEEE/RSJ International Conference on Intelligent Robots and Systems (IROS)*, pages 3641–3647, Oct 2007. doi: 10.1109/IROS.2007.4399415.
- M. Naveau, J. Carpentier, S. Barthelemy, O. Stasse, and P. Souères. METAPOD - template META-Programming applied to Dynamics: CoP-CoM trajectories filtering. In *IEEE/RAS International Conference on Humanoid Robots*, 2014.
- K. Nishiwaki, T. Sugihara, S. Kagami, F. Kanehiro, M. Inaba, and H. Inoue. Design and development of research platform for perception-action integration in humanoid robot: H6. In *IEEE/RSJ International Conference on Intelligent Robots and Systems (IROS)*, volume 3, pages 1559–1564, 2000. doi: 10.1109/IROS.2000.895195.
- K. Nishiwaki, J. Kuffner, S. Kagami, M. Inaba, and H. Inoue. The experimental humanoid robot H7: a research platform for autonomous behaviour. *Philos Trans A Math Phys Eng Sci*, 365(1850):79–107, Jan 2007. doi: 10.1098/rsta.2006.1921.
- J. Nocedal and S. J. Wright. *Numerical Optimisation*. Springer, 2000.
- Y. Ogura, H. Aikawa, K. Shimomura, A. Morishima, H. ok Lim, and A. Takanishi. Development of a new humanoid robot wabian-2. In *IEEE/RAS International Conference on Robotics and Automation (ICRA)*, pages 76–81, May 2006. doi: 10.1109/ROBOT.2006.1641164.
- H. Olsson, K. Åström, C. C. de Wit, M. Gäfvert, and P. Lischinsky. Friction models and friction compensation. *European Journal of Control*, 4(3):176–195, 1998. ISSN 0947-3580. doi: [http://dx.doi.org/10.1016/S0947-3580\(98\)70113-X](http://dx.doi.org/10.1016/S0947-3580(98)70113-X). URL <http://www.sciencedirect.com/science/article/pii/S094735809870113X>.
- S. Onyshko and D. A. Winter. A mathematical model for the dynamics of human locomotion. *Journal of Biomechanics*, 13(4):361–368, 1980. URL <http://www.me.berkeley.edu/ME239/resources/papers/1980%20-%20A%20mathematical%20model%20for%20the%20dynamics%20of%20human%20locomotion.pdf>. [PubMed:7400165].
- Y. Ota. Partner robots – from development to implementation. In *Conference on Human System Interactions*, pages 14–16, May 2010. doi: 10.1109/HSI.2010.5514594.
- C. Ott, C. Baumgartner, J. Mayr, M. Fuchs, R. Burger, D. Lee, O. Eiberger, A. Albu-Schäffer, M. Grebenstein, and G. Hirzinger. Development of a biped robot with torque controlled joints. In *IEEE/RAS International Conference on Humanoid Robots*, pages 167–173, Dec 2010. doi: 10.1109/ICHR.2010.5686340.
- J. Pan, S. Chitta, and D. Manocha. FCL: A general purpose library for collision and proximity queries. In *IEEE/RAS International Conference on Robotics and Automation (ICRA)*, 2012.
- M. G. Pandy and N. Berme. Quantitative assessment of gait determinants during single stance

- via a three-dimensional model—part 1. normal gait. *Journal of Biomechanics*, 22(6–7):717 – 724, 1989a. ISSN 0021-9290. doi: [http://dx.doi.org/10.1016/0021-9290\(89\)90022-5](http://dx.doi.org/10.1016/0021-9290(89)90022-5). URL <http://www.sciencedirect.com/science/article/pii/0021929089900225>.
- M. G. Pandy and N. Berme. Quantitative assessment of gait determinants during single stance via a three-dimensional model—part 2. pathological gait. *Journal of Biomechanics*, 22(6–7):725 – 733, 1989b. ISSN 0021-9290. doi: [http://dx.doi.org/10.1016/0021-9290\(89\)90023-7](http://dx.doi.org/10.1016/0021-9290(89)90023-7). URL <http://www.sciencedirect.com/science/article/pii/0021929089900237>.
- I.-W. Park, J.-Y. Kim, J. Lee, and J.-H. Oh. Mechanical design of humanoid robot platform KHR-3 (KAIST Humanoid Robot 3: HUBO). In *IEEE/RAS International Conference on Humanoid Robots*, pages 321–326, Dec 2005. doi: 10.1109/ICHR.2005.1573587.
- J. Perry and J. Burnfield. *Gait Analysis: Normal and Pathological Function*. SLACK, 2010. ISBN 9781556427664. URL <http://books.google.de/books?id=DICTQAAACAAJ>.
- J. Peters. C1-surface splines. *SIAM Journal on Numerical Analysis*, 32(2):645–666, 1995. ISSN 00361429. doi: 10.2307/2158416. URL <http://www.jstor.org/stable/2158416>.
- J. Plücker. Fundamental views regarding mechanics. *Philosophical Transactions Royal Society London*, 156:361–380, 1866. doi: 10.1098/rstl.1866.0016.
- J. Pons. Rehabilitation exoskeletal robotics. *IEEE Engineering in Medicine and Biology Magazine*, 29(3): 57–63, May 2010. ISSN 0739-5175. doi: 10.1109/MEMB.2010.936548.
- M. Popovic, A. Goswami, and H. Herr. Ground reference points in legged locomotion: Definitions, biological trajectories and control implications. *The International Journal of Robotics Research*, 24 (12):1013–1032, 2005. doi: 10.1177/0278364905058363.
- A. Potschka, H. Bock, and J. Schlöder. A minima tracking variant of semi-finite programming for the treatment of path constraints within direct solution of optimal control problems. *Optimization Methods and Software*, 24(2):237–252, 2009.
- J. Pozo, M.-C. Villa-Uriol, and A. Frangi. Efficient 3D geometric and zernike moments computation from unstructured surface meshes. *IEEE Transactions on Pattern Analysis and Machine Intelligence*, 33(3):471–484, March 2011. ISSN 0162-8828. doi: 10.1109/TPAMI.2010.139.
- T. Pozzo, Y. Levik, and A. Berthoz. Head and trunk movements in the frontal plane during complex dynamic equilibrium tasks in humans. *Experimental Brain Research*, 106(2):327–338, 1995. [PubMed:8566197].
- J. Pratt, J. Carff, S. Drakunov, and A. Goswami. Capture point: A step toward humanoid push recovery. In *IEEE/RAS International Conference on Humanoid Robots*, pages 200–207, Dec 2006. doi: 10.1109/ICHR.2006.321385.
- J. Pratt and S. Drakunov. Derivation and application of a conserved orbital energy for the inverted pendulum bipedal walking model. In *IEEE/RAS International Conference on Robotics and Automation (ICRA)*, pages 4653–4660, April 2007. doi: 10.1109/ROBOT.2007.364196.
- J. Pratt and R. Tedrake. Velocity-based stability margins for fast bipedal walking. In M. Diehl and K. Mombaur, editors, *Fast Motions in Biomechanics and Robotics*, volume 340 of *Lecture Notes in Control and Information Sciences*, pages 299–324. Springer Berlin Heidelberg, 2006. ISBN 978-3-540-36118-3. doi: 10.1007/978-3-540-36119-0_14. URL http://dx.doi.org/10.1007/978-3-540-36119-0_14.
- H. A. Quintero, R. J. Farris, C. Hartigan, I. Clesson, and M. Goldfarb. A powered lower limb orthosis for providing legged mobility in paraplegic individuals. *Topics in Spinal Cord Injury Rehabilitation*, 17 (1):25–33, 2011. doi: 10.1310/sci1701-25. URL <http://www.ncbi.nlm.nih.gov/pmc/articles/PMC3375739/pdf/nihms379572.pdf>.
- O. Ramos, L. Saab, S. Hak, and N. Mansard. Dynamic motion capture and edition using a stack of tasks. In *IEEE/RAS International Conference on Humanoid Robots*, pages 224–230, Oct 2011. doi: 10.1109/Humanoids.2011.6100829.
- J. Raade, T. McGee, and H. Kazerooni. Design, construction, and experimental evaluation of a monopropellant powered free piston hydraulic pump. In *ASME International Mechanical Engineering Congress*, IMECE2003-42606, pages 651–658. The American Society of Mechanical Engineers, 2003. doi: 10.1115/IMECE2003-42606. URL <http://bleex.me.berkeley.edu/wp-content/uploads/hel-media/Publication/McGee.Raade.IMECE.Monoprop%20Hydraulic%20Pump%20Design.2003.pdf>.
- A. K. Raj, P. D. Neuhaus, A. M. Moucheboeuf, J. H. Noorden, and D. V. Lecoutre. Mina: A sensorimotor robotic orthosis for mobility assistance. *Journal of Robotics*, 2011:1–8, 2011. doi: 10.1155/2011/284352. URL <http://downloads.hindawi.com/journals/jr/2011/284352.pdf>.
- B. Ravi and M. Srinivasan. Geometric property computation for boundary represented solids. In *ISME Conference on Mechanical Engineering*, 1990. URL http://www.me.iitb.ac.in/~bravi/lab/paper/1990ISME_GeomPropertyComputation.pdf.
- S. Redon, A. Kheddar, and S. Coquillart. Fast Continuous Collision Detection between Rigid Bodies. *Computer Graphics Forum*, 2002. URL <https://hal.inria.fr/inria-00390356>. The definitive version is available at www.blackwell-synergy.com.
- A. Requicha and R. Tilove. Mathematical foundations of constructive solid geometry: general topology of closed regular sets. Technical Report Technical Memorandum / 27, College of Engineering & Applied Science - The University of Rochester, University of Rochester. Production Automation Project

- Rochester, N.Y., 1978. URL <http://hdl.handle.net/1802/1209>.
- B. Rich. Clarence leonard (kelly) johnson 1910 - 1990: A biographical memoir. *National Academies Press*, page 13, 1995. URL http://www.nap.edu/openbook.php?record_id=4894&page=221.
- L. Righetti, J. Buchli, M. Mistry, and S. Schaal. Control of legged robots with optimal distribution of contact forces. In *IEEE/RAS International Conference on Humanoid Robots*, pages 318–324, Oct 2011a. doi: 10.1109/Humanoids.2011.6100832.
- L. Righetti, J. Buchli, M. Mistry, and S. Schaal. Inverse dynamics control of floating-base robots with external constraints: A unified view. In *IEEE/RAS International Conference on Robotics and Automation (ICRA)*, pages 1085–1090, May 2011b. doi: 10.1109/ICRA.2011.5980156.
- L. Roussel, C. Canudas-de Wit, and A. Goswami. Comparative study of methods for energy-optimal gait generation for biped robots. In *International Conference on Informatics and Control*, volume 3, pages 1213–1223. DTIC Document, 1997. URL <http://www.ambarish.com/paper/STPETER.ps.pdf>.
- L. Roussel, C. Canudas-de Wit, and A. Goswami. Generation of energy optimal complete gait cycles for biped robots. In *IEEE/RAS International Conference on Robotics and Automation (ICRA)*, volume 3, pages 2036–2041, May 1998. doi: 10.1109/ROBOT.1998.680615.
- D. Rypl and Z. Bittnar. Triangulation of 3d surface recovered from STL grids. *Acta Polytechnica*, 44(5): 61–67, 2004. ISSN 1210-2709. URL <https://ojs.cvut.cz/ojs/index.php/ap/article/view/620/452>.
- L. Saab, O. Ramos, N. Mansard, P. Soueres, and J.-Y. Fourquet. Generic dynamic motion generation with multiple unilateral constraints. In *IEEE/RSJ International Conference on Intelligent Robots and Systems (IROS)*, pages 4127–4133, Sept 2011. doi: 10.1109/IROS.2011.6094795.
- A. M. Sabatini. Kalman-filter-based orientation determination using inertial/magnetic sensors: Observability analysis and performance evaluation. *Sensors*, 11(10):9182–9206, 2011. ISSN 1424-8220. doi: 10.3390/s111009182. URL <http://www.mdpi.com/1424-8220/11/10/9182>.
- T. Saidouni and G. Bessonnet. Generating globally optimised sagittal gait cycles of a biped robot. *Robotica*, 21:199–210, 3 2003. ISSN 1469-8668. doi: 10.1017/S0263574702004691. URL http://journals.cambridge.org/article_S0263574702004691.
- Y. Sakagami, R. Watanabe, C. Aoyama, S. Matsunaga, N. Higaki, and K. Fujimura. The intelligent asimo: system overview and integration. In *IEEE/RSJ International Conference on Intelligent Robots and Systems (IROS)*, volume 3, pages 2478–2483, 2002. doi: 10.1109/IRDS.2002.1041641.
- C. Samson, B. Espiau, and M. L. Borgne. *Robot Control: The Task Function Approach*. Oxford University Press, 1991. ISBN 0198538057.
- B. Sauer, A. Albers, L. Deters, J. Feldhusen, E. Leidich, and H. Linke. *Konstruktionslemente des Maschinenbaus 1 Grundlagen der Berechnung and Gestaltung von Maschinenelementen*. Springer Verlag, 2012. ISBN 978-3642243004.
- J. B. d. M. Saunders, V. T. Inman, and H. D. Eberhart. THE MAJOR DETERMINANTS IN NORMAL AND PATHOLOGICAL GAIT. *The Journal of Bone & Joint Surgery*, 35(3):543–558, 1953. ISSN 0021-9355.
- A. Schiele and F. van der Helm. Kinematic design to improve ergonomics in human machine interaction. *IEEE Transactions on neural systems and rehabilitation engineering*, 14(4):456–469, Dec 2006. ISSN 1534-4320. doi: 10.1109/TNSRE.2006.881565.
- G. Schultz and K. Mombaur. Modeling and optimal control of human-like running. *IEEE/ASME Transactions on Mechatronics*, 15(5):783–792, Oct 2010. ISSN 1083-4435. doi: 10.1109/TMECH.2009.2035112.
- W. Schulz, E. Hering, G. Kurz, R. Martin, and M. Stohrer. *Physik für Ingenieure*. Engineering Online library. Springer, 2007. ISBN 9783540351481. URL <http://www.springer.com/materials/mechanics/book/978-3-642-22568-0>.
- J. F. Seara, O. Lorch, and G. Schmidt. Gaze Control for Goal-Oriented Humanoid Walking. In *IEEE/RAS International Conference on Humanoid Robots*, pages 187–195, Tokio, Japan, November 2001. URL http://www.robotic.dlr.de/fileadmin/robotic/stroblk/publications/seara_2001human.pdf.
- L. Sentis and O. Khatib. Control of free-floating humanoid robots through task prioritization. In *IEEE/RAS International Conference on Robotics and Automation (ICRA)*, pages 1718–1723, April 2005. doi: 10.1109/ROBOT.2005.1570361.
- L. Sentis, J. Park, and O. Khatib. Compliant control of multicontact and center-of-mass behaviors in humanoid robots. *IEEE Transaction on Robotics*, 26(3):483–501, June 2010. ISSN 1552-3098. doi: 10.1109/TRO.2010.2043757.
- K. Shamaei and A. Dollar. On the mechanics of the knee during the stance phase of the gait. In *IEEE International Conference on Rehabilitation Robotics (ICORR)*, pages 1–7, June 2011. doi: 10.1109/ICORR.2011.5975478.
- K. Shamaei, M. Cenciarini, and A. Dollar. On the mechanics of the ankle in the stance phase of the gait. In *Annual International Conference of the IEEE Engineering in Medicine and Biology Society, EMBC*, pages 8135–8140, Aug 2011. doi: 10.1109/IEMBS.2011.6092007.
- J. Shackelford. *Introduction to Materials Science for Engineers*. Pearson, 2008. ISBN 978-0136012603.
- F. Sheehan. The instantaneous helical axis of the subtalar and talocrural joints: a non-invasive in vivo dynamic study. *Journal of Foot and Ankle Research*, 3(1):13, 2010. ISSN 1757-1146. doi: 10.1186/1757-1146-3-13. URL <http://www.jfootankleres.com/content/3/1/13>.

BIBLIOGRAPHY

- L. Sheng. Landmark design in 3D PDM for PCA of shoe last. In *International Conference on Advanced Computer Theory and Engineering*, volume 1, pages V1–517–V1–521, Aug 2010. doi: 10.1109/ICACTE.2010.5578964.
- B. Siciliano and O. Khatib. *Springer Handbook of Robotics*. Springer-Verlag New York, Inc., Secaucus, NJ, USA, 2007. ISBN 354023957X.
- W. A. Staff. Anthropometric source book, Vol II. a handbook of anthropometric data (NASA RP-1024). Technical Report NTIS No. N79-13711, National Aeronautics and Space Administration, Texas, 1978.
- O. Stasse, B. Verrelst, B. Vanderborght, and K. Yokoi. Strategies for humanoid robots to dynamically walk over large obstacles. *IEEE Transaction on Robotics*, 25(4):960–967, Aug 2009. ISSN 1552-3098. doi: 10.1109/TRO.2009.2020354.
- O. Stasse, B. Verrelst, P.-B. Wieber, B. Vanderborght, P. Evrard, A. Kheddar, and K. Yokoi. Modular architecture for humanoid walking pattern prototyping and experiments. *Advanced Robotics*, 22(6-7):589–611, 2008. doi: 10.1163/156855308X305236. URL <http://dx.doi.org/10.1163/156855308X305236>.
- T. Sugihara. Solvability-unconcerned inverse kinematics based on Levenberg-Marquardt method with robust damping. In *IEEE/RAS International Conference on Humanoid Robots*, pages 555–560, Dec 2009. doi: 10.1109/ICHR.2009.5379515.
- Z. Sun and N. Roos. An energy efficient dynamic gait for a NAO robot. In *IEEE International Conference on Autonomous Robot Systems and Competitions (ICARSC)*, pages 267–272, May 2014. doi: 10.1109/ICARSC.2014.6849797.
- A. Takanishi, M. Ishida, Y. Yamazaki, and I. Kato. The realization of dynamic walking by the biped walking robot WL-10 RD. *Journal of the Robotics Society of Japan*, 3(4):325–336, 1985. doi: 10.7210/jrsj.3.325.
- T. Takenaka, T. Matsumoto, and T. Yoshiike. Real time motion generation and control for biped robot -1st report: Walking gait pattern generation-. In *IEEE/RSJ International Conference on Intelligent Robots and Systems (IROS)*, pages 1084–1091, Oct 2009a. doi: 10.1109/IROS.2009.5354662.
- T. Takenaka, T. Matsumoto, and T. Yoshiike. Real time motion generation and control for biped robot -3rd report: Dynamics error compensation-. In *IEEE/RSJ International Conference on Intelligent Robots and Systems (IROS)*, pages 1594–1600, Oct 2009b. doi: 10.1109/IROS.2009.5354542.
- T. Takenaka, T. Matsumoto, T. Yoshiike, T. Hasegawa, S. Shirokura, H. Kaneko, and A. Orita. Real time motion generation and control for biped robot -4th report: Integrated balance control-. In *IEEE/RSJ International Conference on Intelligent Robots and Systems (IROS)*, pages 1601–1608, Oct 2009c. doi: 10.1109/IROS.2009.5354522.
- T. Takenaka, T. Matsumoto, T. Yoshiike, and S. Shirokura. Real time motion generation and control for biped robot -2nd report: Running gait pattern generation-. In *IEEE/RSJ International Conference on Intelligent Robots and Systems (IROS)*, pages 1092–1099, Oct 2009d. doi: 10.1109/IROS.2009.5354654.
- Y. Tassa, N. Mansard, and E. Todorov. Control-limited differential dynamic programming. In *IEEE/RAS International Conference on Robotics and Automation (ICRA)*, pages 1168–1175, May 2014. doi: 10.1109/ICRA.2014.6907001.
- R. Tellez, F. Ferro, S. Garcia, E. Gomez, E. Jorge, D. Mora, D. Pinyol, J. Oliver, O. Torres, J. Velazquez, and D. Faconti. Reem-B: an autonomous lightweight human-size humanoid robot. In *IEEE/RAS International Conference on Humanoid Robots*, pages 462–468, Dec 2008. doi: 10.1109/ICHR.2008.4755995.
- E. Todorov. Implicit nonlinear complementarity: A new approach to contact dynamics. In *IEEE/RAS International Conference on Robotics and Automation (ICRA)*, pages 2322–2329, May 2010. doi: 10.1109/ROBOT.2010.5509739.
- E. Todorov, T. Erez, and Y. Tassa. MuJoCo: A physics engine for model-based control. In *IEEE/RSJ International Conference on Intelligent Robots and Systems (IROS)*, pages 5026–5033, Oct 2012. doi: 10.1109/IROS.2012.6386109.
- W. Townsend and J. Salisbury. The effect of coulomb friction and stiction on force control. In *IEEE/RAS International Conference on Robotics and Automation (ICRA)*, pages 883–889. IEEE, 1987. doi: 10.1109/ROBOT.1987.1087936.
- A. A. Transeth, K. Y. Pettersen, and P. Liljebäck. A survey on snake robot modeling and locomotion. *Robotica*, 27:999–1015, 12 2009. ISSN 1469-8668. doi: 10.1017/S0263574709005414. URL <http://journals.cambridge.org/article.S0263574709005414>.
- H. Vallery, J. Veneman, E. van Asseldonk, R. Ekkelenkamp, M. Buss, and H. van der Kooij. Compliant actuation of rehabilitation robots. *IEEE Robotics & Automation Magazine*, 10:60–69, 2008.
- A. Valiente. Design of a quasi-passive parallel leg exoskeleton to augment load carrying for walking. Master's thesis, Massachusetts Institute of Technology. Dept. of Mechanical Engineering., 2005. URL <http://hdl.handle.net/1721.1/34412>.
- B. Vanderborght, A. Albu-Schäffer, A. Bicchi, E. Burdet, D. Caldwell, R. Carloni, M. Catalano, O. Eiberger, W. Friedl, G. Ganesh, M. Garabini, M. Grebenstein, G. Grioli, S. Haddadin, H. Hoppner, A. Jafari, M. Laffranchi, D. Lefeber, F. Petit, S. Stramigioli, N. Tsagarakis, M. V. Damme, R. V. Ham, L. Visser, and S. Wolf. Variable impedance actuators: A review. *Robotics and Autonomous Systems*,

- 61(12):1601 – 1614, 2013. ISSN 0921-8890. doi: <http://dx.doi.org/10.1016/j.robot.2013.06.009>. URL <http://www.sciencedirect.com/science/article/pii/S0921889013001188>.
- VDI. Design methodology for mechatronic systems (VDI 2206). Technical report, VDI, 2004.
- B. Verrelst, K. Yokoi, O. Stasse, H. Arisumi, and B. Vanderborght. Mobility of humanoid robots: Stepping over large obstacles dynamically. In *IEEE International Conference on Mechatronics and Automation (ICMA)*, pages 1072–1079, June 2006. doi: 10.1109/ICMA.2006.257774.
- S. Vinoski. CORBA: Integrating diverse applications within distributed heterogeneous environments. *Communications Magazine, IEEE*, 35(2):46–55, Feb 1997. ISSN 0163-6804. doi: 10.1109/35.565655.
- O. von Stryk and R. Bulirsch. Direct and indirect methods for trajectory optimization. *Annals of Operations Research*, 37(1):357–373, 1992. ISSN 0254-5330. doi: 10.1007/BF02071065. URL <http://dx.doi.org/10.1007/BF02071065>.
- M. Vukobratović and J. Stepanenko. On the stability of anthropomorphic systems. *Mathematical Biosciences*, 15(1–2):1 – 37, 1972. ISSN 0025-5564. doi: [http://dx.doi.org/10.1016/0025-5564\(72\)90061-2](http://dx.doi.org/10.1016/0025-5564(72)90061-2). URL <http://www.sciencedirect.com/science/article/pii/0025556472900612>.
- M. Vukobratovic, D. Hristic, and Z. Stojiljkovic. Development of active anthropomorphic exoskeletons. *Medical and Biological Engineering*, 12(1):66–80, 1974. ISSN 0025-696X. doi: 10.1007/BF02629836. URL <http://dx.doi.org/10.1007/BF02629836>.
- M. Vukobratović and B. Borovac. ZERO-MOMENT POINT — THIRTY FIVE YEARS OF ITS LIFE. *International Journal of Humanoid Robotics*, 01(01):157–173, 2004. doi: 10.1142/S0219843604000083. URL <http://www.worldscientific.com/doi/abs/10.1142/S0219843604000083>.
- C.-J. Walsh, K. Endo, and H. Herr. A quasi-passive leg exoskeleton for load-carrying augmentation. *Journal of Humanoid Robotics*, 4:487–506, 2007.
- A. Walther and A. Griewank. Getting started with ADOL-C. In U. Naumann and O. Schenk, editors, *Combinatorial Scientific Computing*, chapter 7, pages 181–202. Chapman-Hall CRC Computational Science, 2012.
- S. Wang, W. van Dijk, and H. van der Kooij. Spring uses in exoskeleton actuation design. In *IEEE International Conference on Rehabilitation Robotics (ICORR)*, pages 1–6, June 2011. doi: 10.1109/ICORR.2011.5975471.
- P.-B. Wieber. *Modélisation et Commande d'un Robot Marcheur Anthropomorphe*. PhD thesis, INRIA Rhône-Alpes, 2000.
- P.-B. Wieber, F. Billet, L. Boissieux, and R. Pissard-Gibollet. The HuMANs toolbox, a homogenous framework for motion capture, analysis and simulation. In *International Symposium on the 3D Analysis of Human Movement*, Valenciennes, France, 2006. URL <https://hal.inria.fr/inria-00390447>.
- D. A. Winter. *Biomechanics and motor control of human movement*. A Wiley-Interscience publication. J. Wiley and sons, New York, 1990. ISBN 0-471-50908-6.
- Y. Xiang, J. Arora, and K. Abdel-Malek. Physics-based modeling and simulation of human walking: a review of optimization-based and other approaches. *Structural and Multidisciplinary Optimization*, 42(1):1–23, 2010. ISSN 1615-147X. doi: 10.1007/s00158-010-0496-8. URL <http://dx.doi.org/10.1007/s00158-010-0496-8>.
- J. Yamaguchi, E. Soga, S. Inoue, and A. Takanishi. Development of a bipedal humanoid robot-control method of whole body cooperative dynamic biped walking. In *IEEE/RAS International Conference on Robotics and Automation (ICRA)*, volume 1, pages 368–374, 1999. doi: 10.1109/ROBOT.1999.770006.
- V. Yodaiken. The RTLinux manifesto. Technical report, Department of Computer Science - New Mexico Institute of Technology, 2007. URL <http://www.yodaiken.com/papers/rtlinuxmanifesto.pdf>.
- K. Yokoi, F. Kanehiro, K. Kaneko, K. Fujiwara, S. Kajita, and H. Hirukawa. A honda humanoid robot controlled by aist software. In *IEEE/RAS International Conference on Humanoid Robots*, pages 259–264, 2001. URL https://staff.aist.go.jp/k.kaneko/publications/2001_publications/12.pdf.
- E. Yoshida, C. Esteves, I. Belousov, J.-P. Laumond, T. Sakaguchi, and K. Yokoi. Planning 3-D collision-free dynamic robotic motion through iterative reshaping. *IEEE Transaction on Robotics*, 24(5):1186–1198, Oct 2008. ISSN 1552-3098. doi: 10.1109/TRO.2008.2002312.
- J. W. Young, U. States., and C. A. Institute. *Anthropometric and mass distribution characteristics of the adult female [microform]*. Federal Aviation Administration, Office of Aviation Medicine - Washington, D.C, rev. ed. edition, 1983. URL <http://nla.gov.au/nla.cat-vn3872654>.
- V. Zatsiorsky and V. Seluyanov. The mass and inertia characteristics of the main segments of the human body. volume V, pages 1152–1159, 1983.
- V. M. Zatsiorsky, V. Seluyanov, and L. Chugunova. In vivo body segment inertial parameters determination using a gamma-scanner method. In *Biomechanics of Human Movement: Application in Rehabilitation, Sport and Ergonomics*, pages 186–202, 1990.
- G. Zeilig, H. Weingarden, M. Zwecker, I. Dudkiewicz, A. Bloch, and A. Esquenazi. Safety and tolerance of the rewalk™ exoskeleton suit for ambulation by people with complete spinal cord injury: A pilot study. *The Journal of Spinal Cord Medicine*, 35(2):96–101, 2012. doi: 10.1179/2045772312Y.0000000003. URL <http://www.ncbi.nlm.nih.gov/pmc/articles/PMC3304563/pdf/scm-35-96.pdf>.

List of Acronyms

DoG	Determinante of Gait	VDE	Variational Differential Equation
CoM	Center of Mass/Gravity	NLP	Nonlinear Program
CoP	Center of Pressure	QP	Quadratic Program
dof	Degree of Freedom	SQP	Sequential Quadratic Programming
OCP	Optimal Control Problem	KKT	KARUSH–KUHN–TUCKER
HRP	Humanoid Robotics Project	IND	Internal Numerical Differentiation
ZMP	Zero Moment Point	MBS	Multi Body System
ID	Inverse Dynamics	IMU	Inertial Measurement Unit
FD	Forward Dynamics	ISE	Integrated Simulation Environment
IdOP	Inverse Dynamics Operator	fif	Fixed Foot Position
FdOP	Forward Dynamics Operator	frf	Free Foot Position
LCP	Linear Complementary Problem	DS	Double Support
NCP	Nonlinear Complementary Problem	SS	Single Support
RNEA	Recursive Newton Euler Algorithm	CH	Impact Model-Phase Transition (discontinuous)
CRBA	Composite Rigid Body Algorithm	TR	Continuous Model-Phase Transition
VRML	Virtual Reality Modeling Language	1st	primary
URDF	Unified Robotic Description	2nd	secondary
XML	Extensible Markup Language	3rd	tertiary
SVD	Singular Value Decomposition	3D-LIPM	3D Linear Inverted Pendulum Mode
plc	piecewise linear continuous	GCR	Ground Contact Reaction
plci	piecewise linear continuous and once integrated	TB	Table Cart
FRI	Foot Rotation Indicator	WB	whole-body
CP	Capture Point	CGA	Clinical Gait Analysis
BFGS	BROYDEN–FLETCHER–GOLDFARB– SHANNO	FDM	Fused Decomposition Modeling
BVP	Boundary Value Problem	HMI	Human Machine Interface
MPBVP	Multi-Point Boundary Value Problem	IHMC	Florida Institute for Human and Machine Cognition
IVP	Initial Value Problem	VIA	Variable Impedance Actuator
METI	Ministry of Economy, Trade and Industry, Japan	SEA	Serial Elastic Actuator
CQ	Constraint Qualification	PEA	Parallel Elastic Actuator
LICQ	Linear Independency Constraint Qualification	RMS	Root Mean Square
MFCQ	Mangasarian Fromowitz Constraint Qualification	MAE	Mobility Assist Exoskeleton
DAE	Differential Algebraic Equation	AJC	Ankle Joint Center
ODE	Ordinary Differential Equation	HSV	Hue Saturation Value
		VCA	Variable Compliance Actuator
		PoR	Parameter of Restitution